Version 1.2 (2023)

Coastal Dynamics

Judith Bosboom and Marcel J.F. Stive

TU Delft open

Coastal Dynamics

Judith Bosboom and Marcel J.F. Stive

This textbook on Coastal Dynamics focuses on the interrelation between physical wave, flow and sediment transport phenomena and the resulting morphodynamics of a wide variety of coastal systems. The textbook is unique in that it explicitly connects the dynamics of open coasts and tidal basins; not only is the interaction between open coasts and tidal basins of basic importance for the evolution of most coastal systems, but describing the similarities between their physical processes is highly instructive as well. This textbook emphasizes these similarities to the benefit of understanding shared processes such as nonlinearities in flow and sediment transport. Some prior knowledge with respect to the dynamics of flow, waves and sediment transport is recommended.

Judith Bosboom
TU Delft | Faculty of Civil Engineering and Geosciences

Dr. Judith Bosboom is a senior lecturer Coastal Engineering. She developed innovative teaching methods for the topic of Coastal Dynamics. Judith has been elected best lecturer for the MSc Hydraulic Engineering multiple times. In 2016, she received both the best lecturer award for the Faculty of Civil Engineering and Geosciences and the best lecturer award for Delft University of Technology. She has successfully taught Nanjing University graduates (China) for several years.

Marcel J.F. Stive
TU Delft | Faculty of Civil Engineering and Geosciences

Prof. Marcel Stive is an emeritus professor Coastal Engineering. He assisted Judith in developing and teaching the Coastal Dynamics lectures based on his earlier involvements in lecturing and teaching. He has successfully taught Indian, Chinese, Vietnamese, Brazilian and Iranian graduates and/or professionals for several years.

TU Delft

2023 TU Delft Open
ISBN 978-94-6366-370-0
DOI 10.5074/T.2021.001
Version 1.2

textbooks.open.tudelft.nl

Cover image:
Atlantic coast, Angola
(Courtesy Stefanie Ross)

ISBN 978-94-6366-370-0
9 789463 663700

Coastal Dynamics

Delft University of Technology

Coastal Dynamics

Judith Bosboom & Marcel J.F. Stive

[This pdf document of version 1.2 provides a record of the most important changes made to versions 1.0 and 1.1. Search for §1.1 and §1.2, respectively, to find these edits and the corresponding pagenumbers. Less crucial changes are not tracked.]

Bosboom, J. and Stive, M. J. F. (2023). Coastal Dynamics. *Delft University of Technology, Delft, The Netherlands.*

Publisher	TU Delft Open
Date	11th January 2023
Cover image	Atlantic coast, Angola (courtesy Stefanie Ross)
ISBN (softback/paperback)	978-94-6366-370-0
ISBN (e-book)	978-94-6366-371-7
DOI	10.5074/T.2021.001
Version	1.2 (see 'Errata and improvements' on page 583)
Subversion (SVN) revision	1489 logged at 2023-01-11 14:53
Corresponding author	j.bosboom@tudelft.nl

The latest version of this book is available for online use and free download from the TU Delft Open Textbook repository at textbooks.open.tudelft.nl. Here, a form is also available to subscribe to update notifications and provide feedback.

The softback is printed by Holland Ridderkerk (HollandRidderkerk.nl) on behalf of the Faculty of Civil Engineering and Geosciences, Department of Hydraulic Engineering, Section of Coastal Engineering. It can be ordered at textbooks.open.tudelft.nl.
Graphics produced with [MATLAB, Inkscape, Adobe Illustrator, Adobe Photoshop] ©
Typesetting with LaTeX

Last change date: 2023-01-11

Contents

Preface

This Open Textbook is the Open Access version of lecture notes that have been developed to support and supplement the Delft University of Technology (TU Delft) first-year Master of Science (MSc) course on Coastal Dynamics. Since its introduction in the academic year 2009-2010, this first-year MSc course has been taught to MSc graduate students following the two-year Hydraulic Engineering MSc curriculum of the Faculty of Civil Engineering and Geosciences. It focuses on the interrelation between physical wave, flow and sediment transport phenomena and the resulting morphodynamics of a wide variety of coastal systems. The objective is to provide hydraulic and coastal engineering MSc students with insights into the phenomenological and theoretical, as well as applied aspects of these phenomena. The course builds upon Bachelor (BSc) and MSc courses treating the dynamics of flow, waves and sediment transport, and may serve as a basis for a course focusing on coastal modelling, as in the TU Delft curriculum. Although several valuable course monographs and books exist on the topic of coastal dynamics and coastal engineering (see Sect. 1.7), we felt that no standard teaching books existed for the purposes that we had in mind. It has been our explicit intention to connect coastal and estuarine dynamics. Not only is the interaction of coasts and estuaries of basic importance for the evolution of many coastal systems, but describing the similarities between their physical processes is highly instructive as well.

This textbook emphasizes these similarities for the benefit of understanding shared processes such as nonlinearities in flow and sediment transport. Furthermore, our textbook differs from other coastal textbooks in that we connect engineering scales with larger Holocene scales, emphasizing among other aspects the impact of leading and trailing edge coasts on coastal evolution. While primarily developed for the purpose of teaching, we hope that these notes are also useful as a reference book for MSc and PhD students.

The present form and format of this book has been developed to follow the Open Access rules and is subject to change, both in language and contents. We feel that this is a matter of evolution, strongly steered by our continuous learning through and our experience with both teaching and examination. In the years to come we will provide regular updates of this Open Textbook, also in response to comments we expect to receive from our readers.

Our list of acknowledgements is long, but our view is that the art of teaching is to accumulate and digest the efforts of many of our colleagues nationally and globally.

Last change date: 2023-01-11

First, we wish to acknowledge the efforts of all our colleagues in the Netherlands who developed earlier lecture notes that we used as inspiration for these notes: Professor Eco Bijker and Associate Professors Walt Massie and Jan van de Graaff, Professor Kees d'Angremond and MSc Liesbeth van der Velden, Professors Huib de Vriend and Zheng Bing Wang and PhDs Anneke Hibma and Edwin Elias, and Professor Job Dronkers (see 'Credits' on page 579).

Second, we wish to acknowledge some key international references that we used while developing new material that we found missing. Chapter 2, especially Sect. 2.3, is heavily inspired by Davis Jr. (1994), whose well-illustrated textbook offers a good insight into larger-scale coastal behaviour and classification. The energetics approach for cross-shore sediment transport in Sect. 6.1 and Ch. 7 is largely based on Bowen (1980), whose elegant work we still find very instructive. In a more general sense we have been inspired by a number of books we reference in Sect. 1.7, notably the books by Fredsøe and Deigaard (1992), Kamphuis (2000) and Masselink and Hughes (2003).

Further, we need to acknowledge many Delft colleagues who have contributed to our knowledge by their work and comments and/or provided us with course and lecture materials. Regarding knowledge contributions, we mention Jurjen Battjes, Leo Holthuijsen, Jacobus van de Kreeke and Han Winterwerp. Stefan Aarninkhof, Jan van Overeem, Roshanka Ranasinghe and Zheng Bing Wang gave valuable contributions to the content of our lectures. Revisions of sections of early versions of our notes by Ad Reniers, Dano Roelvink, Ad van der Spek and Zheng Bing Wang are highly appreciated. Special thanks go to Howard Southgate, who has read through our complete lecture notes in detail making relevant comments and suggestions. PhDs Stuart Pearson, Yorick Broekema and Alejandra Gijón Mancheño greatly improved the connection between the notes and the lecturing of the course. We thank our former Delft Hydraulics colleague Hans de Vroeg for providing cross-shore distributions of wave heights, longshore currents and sediment transports calculated with Unibest-CL+. Finally, we are grateful for the many suggestions we received from our students over the years.

We have invested heavily in making the illustrations and graphs "our own". For this we were assisted by many of our talented students Liang Li, Dáire Stive, Marcio Boechat Albernaz, Janbert Aarnink, Ascha Simons, Viktorija Usevičiūtė and Tim van Dam, whose creative contributions we gladly acknowledge. We thank Marcel Mol for the subject index.

TU Delft library convinced, stimulated and sponsored us to publish these notes Open Access. Their specialists Michiel de Jong, Jacqueline Michielen-van den Riet and Monique de Bont guided us to understand and comply with copyright licenses. Besides their creative qualities, Ascha Simons and Tim van Dam used their ample technical competences to successfully finish this ambitious project. The management qualities

of Carolina Piccoli to streamline this process are highly appreciated. The broad support by Stefan Aarninkhof in this venture has been essential. We thank Saskia Roselaar for proofreading the book.

As our knowledge and experience is continuously developing, lecture notes are always work-in-progress. We would be very grateful for feedback from our readers on contents and didactics. Also, we would appreciate to be informed of any copyright infringements in the textbook. We will gladly adjust and/or correct.

Judith Bosboom and Marcel J.F. Stive

Delft, The Netherlands
January 2023

Note to our readers: We would like to track the reach and use of this Open Textbook. Therefore, we would be very pleased if you could provide information on your intended use of this book using the form on the TU Delft Open Textbook repository. The form also provides options to subscribe to update notifications and give feedback.

Note to our students: No one reads a textbook more thoroughly than a student studying the material for a course. Therefore, if you find any smaller or larger mistakes in this book – from typographical errors and incorrect cross-references to unclarities and inconsistencies – we would greatly appreciate to be informed of these. In order to suggest a correction or improvement, please fill out the form accessible via the TU Delft Open Textbook repository.

1 Overview

1.1. Introduction

Throughout history, humans have extensively used the coastal zone for many purposes, such as fishing, tourism, transport of goods, water treatment and housing. Agriculture has benefited from the very fertile grounds created by marine and riverine deposits. Approximately three billion people – half the world's population – live and work within a few hundred kilometres of a coastline, notwithstanding the vulnerability of coastal areas to flooding. Due to the high population densities and extensive infrastructure and property development in coastal areas, disasters will have major consequences. Coastal engineers play an important role in both developing the coastal zone and protecting the coast and the hinterland.

In Sect. 1.2, the course contents and the position in the curriculum are explained. Sect. 1.3 lists the study goals. Section 1.4 gives some examples of the problems coastal engineers may be faced with. In doing so coastal engineers need a thorough knowledge of the natural dynamics of the coastal system. An introduction on that topic is given in Sect. 1.5. Important players in the (Dutch) coastal engineering sector are summarised in Sect. 1.6. The chapter concludes with a list of handbooks, journals, conference proceedings and internet sources for further reading (Sect. 1.7).

1.2. Coastal dynamics for coastal engineers

1.2.1. What is coastal engineering?

Coastal Engineering is the branch of civil engineering concerned with the planning, design, construction and maintenance of works in the coastal zone. Coastal engineering usually involves either 1) the transport and stabilisation of sand and other coastal sediments or 2) the construction of structures.

Measures in the first category are called *'soft' measures* since they make use of natural (soft) coastal material. Examples are beach nourishments, maintenance dredging and land reclamation.

The second category of *structures* or *'hard' measures* can be divided into various functional groups:

- Seawalls and revetments are built parallel or nearly parallel to the shoreline at the land-sea interface with the objective of preventing further shoreline recession. Seawalls are usually massive and rigid, while a revetment is an armouring of the beachface with rock armour or artificial units. Although often used, the efficacy of seawalls and revetments is debatable, as we will discuss later on (Sect. 10.6);
- Groynes are built perpendicular to the shore and usually extend out through the surf zone under normal wave and water level conditions (the surf zone or breaker zone is the zone close to the shore where waves are breaking). They help widen and protect a beach by trapping sand from the alongshore transport system (see Ch. 8) or by retaining artificially placed sand;
- Jetties are structures built at the entrance to a river or tidal basin to stabilise the entrance as well as to protect vessels navigating the entrance channel;
- Breakwaters primarily protect a shoreline or harbour anchorage area from wave attack. Breakwaters may be located completely offshore and oriented parallel to the shore (detached breakwaters), or they may be oblique and connected to the shore. Traditionally, detached breakwaters have been designed as emerged structures, but submerged breakwaters have now also become a popular option. The latter are not easily noticeable because of their low crests;
- Other structures such as submerged pipelines.

The purposes of these 'soft' and 'hard' works are diverse:

- Control of shoreline erosion;
- Defence against flooding caused by storms and/or tides;
- Development of coastal functions, for instance coastal recreation;
- Development of navigation channels and harbours.

Coastal engineering works are carried out in a highly dynamic and energetic environment. The various sources of coastal energy are:

- Marine forces (waves, tides, currents and other oceanographic phenomena);
- Terrestrial forces (river outflow);
- Atmospheric forces (coastal winds and climate).

These forces not only directly impact the planned 'soft' or 'hard' measures, but also permanently change the physical shape and structure of a coastal system. This shape of the coast is called *morphology*. Coastal morphology for a sandy stretch of coast thus is the topography of the sandy dunes and beach and the underwater topography

of the seabed. When changes occur in the external forcing, the coastal morphology will change accordingly. Changes in the forcing can have a natural cause or can be human-induced. Examples of changes in the forcing conditions are:

- High waves and piling up of water against the coast (surge) due to the occurrence of a storm;
- Long-term sea level rise;
- Changes in the wave impact on the adjacent coast due to the construction of a harbour;
- The deprivation of a coastal system of sediment supply due to the construction of a dam in a river.

Although coastal changes take place on a variety of timescales, coastal engineers and managers are mostly interested in timescales ranging from 1 year to (a few) hundred years and in large-impact events like storms causing dune erosion and flooding.

1.2.2. Position of Coastal Dynamics in the TU Delft curriculum

Coastal engineering is a very broad profession. As an illustration, the program of the two-yearly International Conference on Coastal Engineering (ICCE) includes disciplines such as hydrodynamics, coastal morphology, coastal protection, structures and ports and waterways. At TU Delft these disciplines are covered in a number of courses within the specialisations Coastal Engineering, Rivers, Ports and Waterways, Environmental Fluid Mechanics and Hydraulic Structures and Flood Risk[1].

Coastal Dynamics I and II

For an appropriate choice and design of measures, the dynamics of the forcing and response of the coastal system should be taken into account. For that reason the courses Coastal Dynamics I and II focus on the dynamics of the coastal system (waves, currents, sediment transport and morphology). Coastal Dynamics I (CIE4305), which is served by this textbook, treats the most important coastal and estuarine phenomena. Furthermore, attention is paid to functional design and impacts of engineering works. Coastal Dynamics II (CIE4309) goes into more detail regarding coastal processes and pays special attention to coastal modelling. Coastal Dynamics I is compulsory for Coastal Dynamics II.

In both Coastal Dynamics I and II the focus is on the dynamics of coastal systems built up by loose and relatively fine material (we consider mainly sand and to a lesser extent mud). This material has been delivered to the coast in recent geological history, mostly through Holocene marine and fluvial sediment supply (see Ch. 2).

[1]The Faculty of Civil Engineering is implementing a new MSc curriculum. During the transition period, we will continue to refer to the old course names and codes and update these in the near future.

Relevant prior knowledge

Fluid mechanics and wave theories are indispensable topics in coastal dynamics. Coastal Dynamics I builds upon the Bachelor courses treating flow, wave and transport dynamics. Of the MSc courses, preferably Ocean Waves (CIE4325) should be followed prior to Coastal Dynamics I. A summary of the (offshore) aspects of wind waves and tides that are relevant to Coastal Dynamics I are given in Ch. 3 and will be built on in subsequent chapters.

Related topics

The technical design of structures is not treated in Coastal Dynamics I and II. Other courses like Bed, Bank and Shoreline Protection (CIE4310) deal with this.

1.3. Study goals

At TU Delft, this textbook accompanies the course Coastal Dynamics I, which will be renamed Coastal Systems in the new curriculum. On completion of either course, the student will be able to:

1. Discuss the nature and complexity of typical coastal engineering problems (Chs. 1 and 10, but also Chs. 7 to 9);
2. Explain the imprint on present-day coastal systems – considering uninterrupted coastlines as well as tidal inlets and basins – of a) geological processes, sea level, and climate (Ch. 2); and b) fluvial, wave and tidal processes and their relative influence (Ch. 2);
3. Understand the global variation of a) coastal systems (Chs. 2 and 4); and b) wave and tidal climate (Ch. 2);
4. Analyse the hydrodynamics of waves and tides in a) the oceans (Ch. 3); b) open coasts (Ch. 5); and c) tidal basins (Ch. 5);
5. Evaluate sediment transport processes under waves, tides, and currents (Ch. 6), distinguishing between: a) cross-shore transport (Ch. 7); b) longshore transport (Ch. 8); and c) transport in tidal inlets and basins (Ch. 9);
6. Apply system knowledge to determine the morphological response to environmental conditions as well as interventions (groynes, breakwaters, nourishments, land reclamations, sand mining) of a) open coasts (Chs. 7 and 8); and b) tidal inlets and basins (Ch. 9);
7. Assess the merits and disadvantages of various coastal interventions for protection against flooding and erosion (Ch. 10).

1.4. Examples of engineering applications

1.4.1. Overview of coastal area and problems

Figure 1.1 shows a schematic plan view of a coastal area with most of the natural forcing conditions, natural features and some examples of man-made interventions in a natural coastal system. Most of the items are dealt with in these lecture notes.

The coastline in Fig. 1.1 receives sediment from rivers and is interrupted by openings called tidal or coastal inlets (see Intermezzo 9.2 for the terminology). The name *tidal* inlet refers to the fact that the tide is important in maintaining the inlet, viz. keeping the inlet from closing naturally. Tidal inlets are either found along barrier island coasts or along coasts interrupted by estuaries or lagoons. Tidal inlets and their associated basins are common features of lowland coasts all around the world.

Seen from the sea side, an estuary is an arm of the ocean that is thrust into the mouth and lower course of a river as far as the tide reaches. Estuaries receive fresh water from rivers, and salt water from the sea. Lagoons do not have a major point source of fresh water input, such as a river. These tidal systems play a crucial role in the sediment budget of the coastal zone and thus influence the long-term coastal evolution.

At the uninterrupted stretches of coast, waves are the dominant forcing agent. Wind waves and tides are treated in detail in Chs. 3 and 5 for oceanic and coastal waters respectively. The global variation in wave and tidal climate is discussed in Ch. 4.

Some examples of practical cases are given in this section by briefly discussing the following items from Fig. 1.1:

- Cross-shore profile (section A–A in Fig. 1.1);
- Morphological development in vicinity of a port;
- Delta near a river mouth;
- Tidal inlet;
- Dune erosion during a severe storm surge;
- Large artificial island in open sea.

1.4.2. Cross-shore profile

The upper panel of Fig. 1.2 shows the shape of a cross-section (called cross-shore profile) as measured perpendicular to a sandy coast at two moments in time. The lower panel shows the variation in time around an average profile. Please note that the vertical and horizontal scales of the plot are quite different. Dunes, beach and a part of the so-called shoreface can be discerned. The actual slope of the dune face is 1:3 to 1:4. The slope of the beach is decreasing from the upper part of the beach near the foot of the dunes (1:20) towards the sea; near the waterline the slope is approximately 1:50. At the shoreface some (breaker) bars are present. The average bottom slope becomes

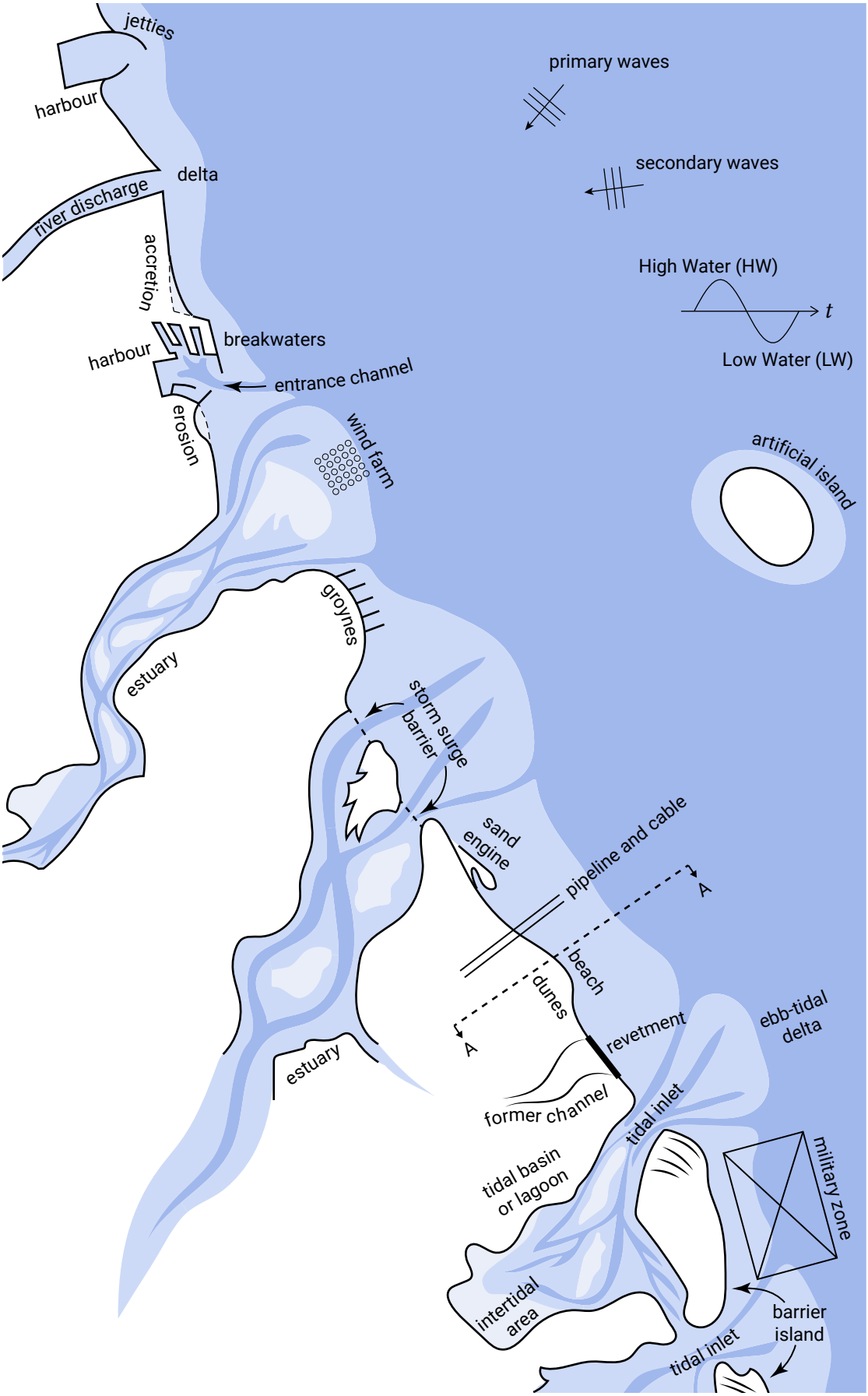

Figure 1.1: Plan view of a coastal area.

flatter with longer distance from the waterline. At the seaward end of the plot (water depth: MSL −10 m) the slope is approximately 1:125.

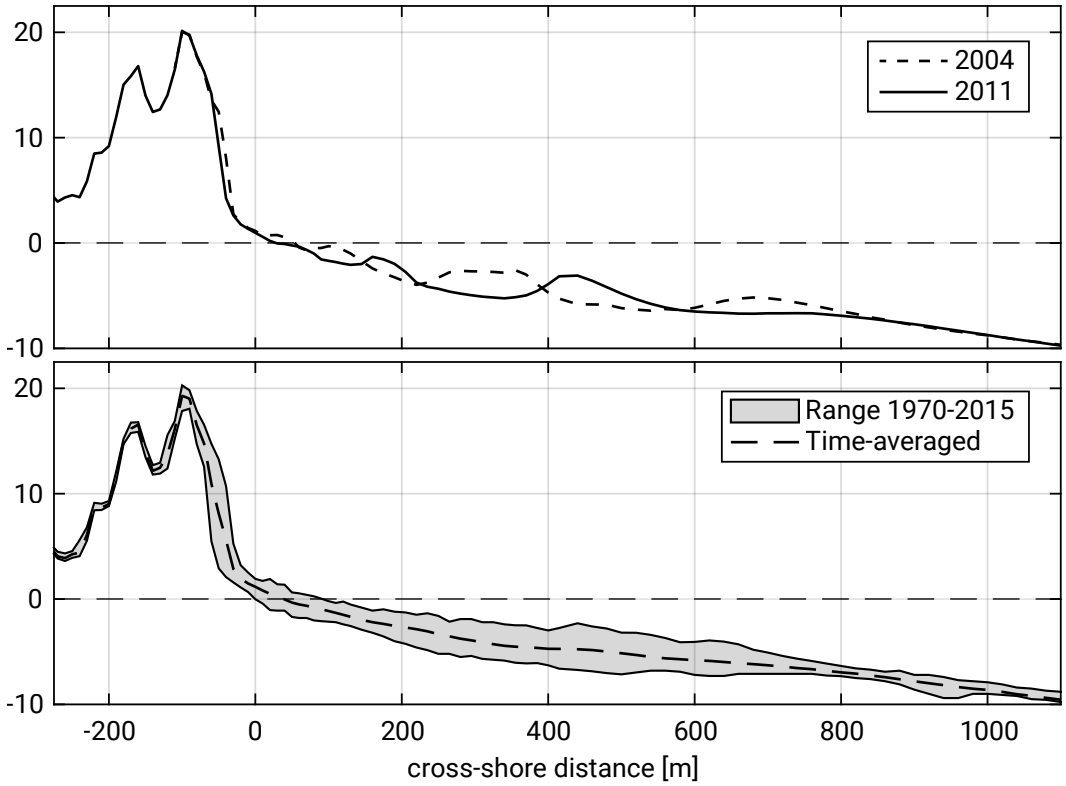

Figure 1.2: Cross-shore profiles at Egmond aan Zee (RSP 7004125) from the long-running Jarkus dataset (JARKUS, n.d.), which contains profiles of the entire Dutch coast measured in subsequent summers. The upper panel shows two instantaneous profiles, whereas the lower panel displays the temporal variation from 1970 to 2015. The cross-shore coordinate is relative to a local beach pole or *Rijksstrandpaal* (RSP) in Dutch. The elevation is relative to the Dutch reference level NAP.

The water level as indicated in Fig. 1.2 reflects the Mean Sea Level (MSL). This is the sea level averaged over a period of time such as a month or a year, such that periodic sea level changes e.g. due to waves and tides are averaged out. In the Netherlands, MSL is approximately equal to the Dutch reference level called NAP (*Normaal Amsterdams Peil*, in Dutch)[2]. The seabed consists of sandy material that generally fines when going further offshore. A typical grain size for a sandy coast is $D_{50} = 200\,\mu m$; 150 million of these particles fit into a volume of 1 litre!

Under the influence of waves, the position of the coastline (represented by the intersection of MSL and the profile) will continuously change. Variations will take place on the timescale of storms and seasons. During storms, high and long waves cause erosion of the beach. This sediment is deposited in the surf zone (the zone where the waves are breaking). A typical storm profile therefore has a narrow beach and a relatively

[2]Recently, MSL has been around NAP + 0.06 m in the Netherlands.

flat slope. Seasonality is especially evident in the Northern Hemisphere which experiences a large number of storms in winter (see Sect. 4.3.1). Hence, a storm profile is also often called a winter profile. During storms high water levels can also cause dune erosion and flooding (see Sect. 1.4.6). In summer the sand is moved back towards the beach and dunes by lower and shorter waves. This cross-shore transport of sediment causes oscillations of the coastline (Fig. 1.3), but in principle the mean position of the coastline does not change. The mean position of the coastline will only change in the case of a structural loss or gain of sediment; structural erosion may occur when sand disappears in offshore canyons or in the alongshore direction (Sect. 1.4.3). Seasonal variations are relevant to tourism (beach width) and the safety of property close to the brink (highest point) of the dune.

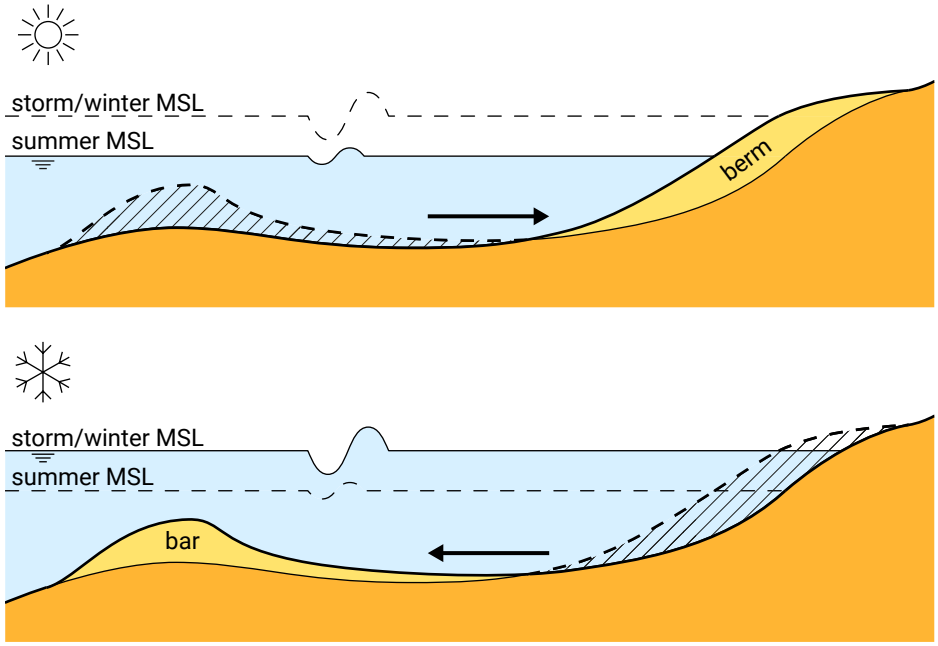

Figure 1.3: Summer and winter profiles showing the annual changes in beach profile. §1.1 In summer the beach is rich in sediment (see the berm in the upper panel). In winter the beach is lower and sediment is found further offshore (see the bar in the lower panel). [p8]

Suppose that irregular waves (also called random waves) approach the coast perpendicularly with a significant deep-water wave height of $H_{s,0} = 2\,\text{m}$ and a peak period of $T_p = 10\,\text{s}$ (for the definitions see Sects. 3.4.2 and 3.4.3). The wave height distribution along the profile (Fig. 1.4a) can be calculated with numerical models based on a spectral energy or action balance (Sects. 3.5.3 and 5.2.1). Note that the wave height in Fig. 1.4a reduces gradually when the waves approach the waterline. This is due to energy dissipation due to (partial) wave-breaking and bottom friction.

In Fig. 1.4b the maximum horizontal components of the orbital velocities near the bed are plotted as a function of the position in the cross-shore profile. Note the rather large magnitudes (§1.2 ~~≥1.0 m/s~~ §1.2 >0.6 m/s to 0.8 m/s [p8] at many positions). Realizing that the critical velocity to initiate motion in uniform flow for particles with $D_{50} = 200\,\mu\text{m}$ is approximately 0.2 m/s (see Sect. 6.3), one may understand that the waves of Fig. 1.4a

are able to stir up many particles in the cross-shore profile. The turbulence generated by breaking waves is very effective in keeping those particles away from the bed. The particles can subsequently be transported by for instance wave-generated and tidal currents (see Ch. 5). Asymmetric waves can also give a net sediment transport. Chapter 6 discusses sediment transport in general, whereas Ch. 7 focuses on cross-shore transport. Both the magnitude and direction (onshore-offshore) of the cross-shore transport may change depending on the local hydrodynamic conditions.

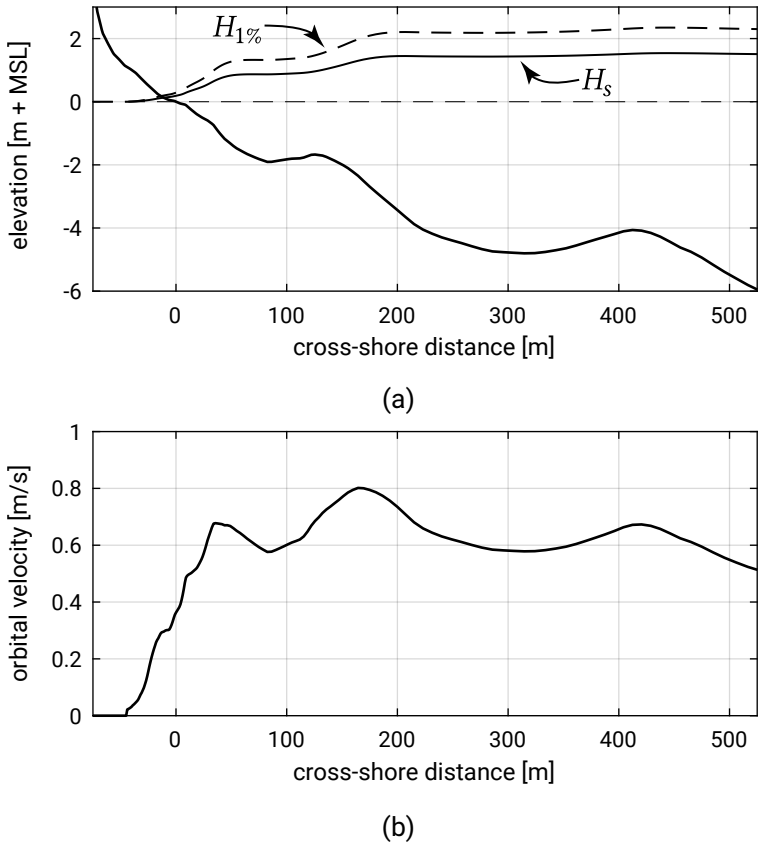

Figure 1.4: Wave height and orbital velocity along a cross-shore profile computed with XBeach (Roelvink et al., 2009) based on a JONSWAP spectrum (Sect. 3.5) with peak period $T_p = 7\,\mathrm{sec}$ and significant wave height $H_s = 1.9\,\mathrm{m}$. (a) H_s (solid line) and 1% exceedance wave height $H_{1\%}$ (dashed line) calculated from a Rayleigh distribution (Sects. 3.4.2 and 3.4.4); (b) Horizontal orbital velocity near the bed (root-mean-square velocity u_{rms}).

Often the effect of cross-shore oscillations is assumed to average out in the longer term. In those cases structural trends in coastline position are due to sediment transport *along* the coast (or more correctly due to gradients in longshore transport, as we will see in Sect. 1.4.3). Nevertheless, some important practical problems are related to changes in the shape of the profile with time (e.g. dune erosion and the behaviour of beach and shoreface nourishments).

1.4.3. Morphological development in vicinity of a port

Figure 1.5 shows in plan view a part of a uniform sandy coast. Uniform means that the depth contours are assumed to be straight and parallel. Waves obliquely approach the coast, viz. there is a non-zero angle φ between the wave crests and the depth contours (or equivalently between a wave ray and the shore normal). As the waves approach the shore, the angle becomes smaller due to refraction (Sect. 5.2.3).

Inside (and a little bit outside) the surf zone, sediment is transported along the coast, the so-called longshore transport (Ch. 8). Waves continuously stir up material from the bed. This sediment is then transported by the longshore current. This current is generated by the breaking of obliquely incident waves in the surf zone, see Sect. 5.5.5. Due to the wave action in stirring up the material, a longshore current of 1 m/s is much more effective in transporting sand than a river flow with the same magnitude.

If the coast is uniform, the sediment transport S is constant along the coast and the coast remains stable. The coastal section under consideration will only change when the amount of sediment transported into the section is different than the sediment leaving the section; or in other words: when there is a *gradient* in longshore transport rates. Erosion will occur in case of a positive gradient in the transport direction (the sediment transport is increasing along the shore, and hence more sediment is leaving than entering the section). Accretion occurs in case of a negative gradient in the drift direction. A uniform sediment transport along the coast (no gradient) does not change the coast. This leads to one of the most important notions of these lecture notes:

> Coastal changes occur in case of transport gradients. A positive gradient (an increase in sediment transport in the transport direction) leads to erosion. A negative gradient (a decrease in sediment transport in the transport direction) creates accretion. If the gradient is zero, there are no changes in morphology.

If along the uniform sandy coast a port is built with the help of two rather long breakwaters, much longer than the width of the surf zone (see Fig. 1.6), the longshore sediment transport will be interrupted. Seaward of the breakwaters no sediment transport

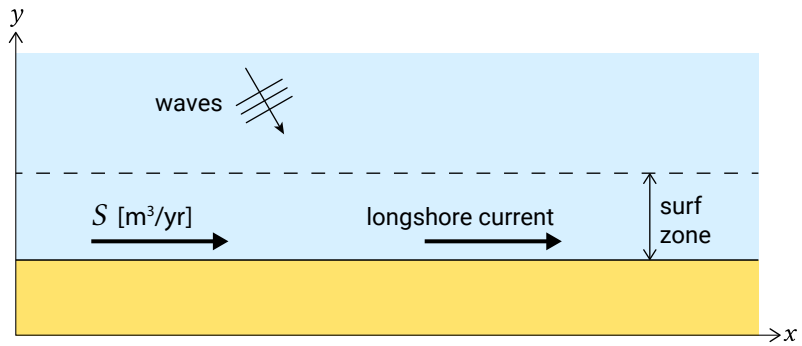

Figure 1.5: Plan view of a uniform sandy coast. In the zone where waves are breaking (called *breaker or surf zone*), a wave-driven sediment transport takes place along the coast.

is assumed to occur. On the updrift side of the port, accumulation of sand will occur (negative transport gradient); at the downdrift side (lee side) erosion will take place (due to a positive transport gradient). In Fig. 1.6 some coastline positions have been sketched as a function of time.

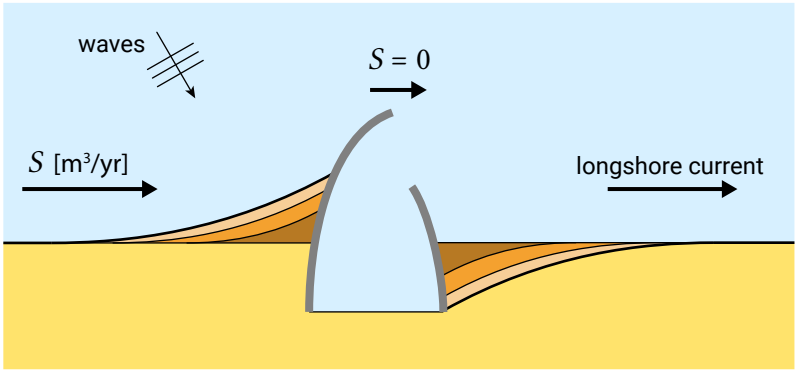

Figure 1.6: Plan view of a uniform sandy coast with port breakwaters. Note the updrift accretion and lee-side erosion. The latter is an oversimplified sketch of the real shape of lee-side erosion, see Ch. 8.

After having studied these lecture notes, you should be able to understand and describe the shapes of the coastline at updrift and downdrift sides as a function of time. It is to be expected that sooner or later the accreting coastline on the updrift side reaches the end of the updrift breakwater; you should be able to say at what time after the construction of the port this will happen. For the time being it will be clear that as long as no sediment will pass the breakwaters ($S = 0\,\mathrm{m}^3/\mathrm{yr}$ seaward of the breakwaters) the total accumulation of sand in t years after completion of the port on the updrift side will be $t \times S\ \mathrm{m}^3$ (with S the undisturbed transport rate). That is, when we assume that S in m^3/yr is expressed including pores between the grains, so that the volumes represent *deposited volumes*. (In Sect. 6.4 other units of sediment transport are discussed.) The total erosion on the lee side will be $t \times S\ \mathrm{m}^3$ as well.

In most cases accumulation will not be considered problematic by the coastal zone manager involved; valuable new land has been gained (unless sediment is deposited in navigation channels). However, the erosion on the lee side of the port will sooner or later cause serious problems. How to resolve such types of erosion problems will be discussed in Ch. 10. An obvious solution will be to artificially transfer volumes of sand from the one side of the port to the other ($S\ \mathrm{m}^3/\mathrm{yr}$ on average; a so-called sand bypass system). Summarizing:

> Engineering problems are often related to longshore transport gradients. Structural coastal problems arise when the longshore transport is changing alongshore, for instance when the longshore current is interrupted by harbour breakwaters.

In the example of Fig. 1.6, the longshore sediment transport was due to obliquely approaching waves only. If tidal currents also occur along the coast, the morphological

behaviour becomes more complicated. The combination of a wave-induced and tidal longshore current is discussed in Sect. 5.7.2.

1.4.4. Delta near a river mouth

Figure 1.7 shows in plan view a part of a sandy coast with a river outfall. Waves are assumed to approach perpendicular to the (initial straight) coastline. The river discharges a volume of water Q_r m^3/s to the sea; at the same time sediment is transported by the river; say S_r m^3/yr. S_r is expressed in m^3/yr since we are looking at large morphological timescales.

Like many rivers all over the world, the river of Fig. 1.7 acts as source of sediments for the coastal system. It is interesting to understand the interaction processes between river and sea and to be able to predict the morphological changes with time, as shown in Fig. 1.7. Such a clear delta coastline develops when the supply of riverine sediments to the coast is faster than they can be dispersed along the coast by tidal and wave-generated currents. (See Chs. 2 and 8 for a more detailed discussion of deltaic coastlines.) The stability of a deltaic coastline is very dependent on the river sediment supply. If the sediment supply is cut off or reduced by, for instance, the construction of dams, sand mining or irrigation schemes, the system is deprived of its regular supply of sediments. This leads to erosion of the coastline on either side of the river mouth and is quite common in present-day deltaic coastlines.

1.4.5. Tidal inlets and basins

Tidal inlets are openings in the shoreline, for example between two barrier islands that connect bays or lagoons to the open ocean. They are maintained (viz. kept from closing naturally) by tidal currents. Figure 1.8 shows various tidal inlets in the Wadden Sea, the Netherlands. Essential for a tidal inlet is the tidal variation in the open sea; the tide is the engine that determines most of the features of the inlet and the basin it connects to.

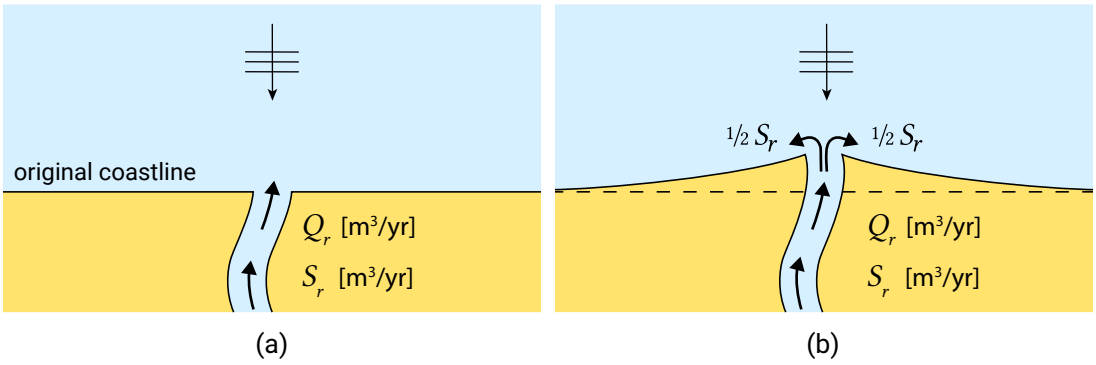

Figure 1.7: Plan view of a sandy coast with a river outfall in initial situation (a) and with a developing delta (b).

The tidal range – the difference between High Water Level (HWL) and Low Water Level (LWL) – and the surface area of the tidal basin together determine, in principle, the volumes of water that have to flow in and out through the inlet during a tide. This tidal prism is in some cases in the order of magnitude of one billion (1×10^9) m^3. For instance, during one tidal cycle about 10^9 m^3 of water enters the Texel Inlet or Marsdiep (between Texel and Den Helder, see Fig. 1.8) and leaves the Texel Inlet again.

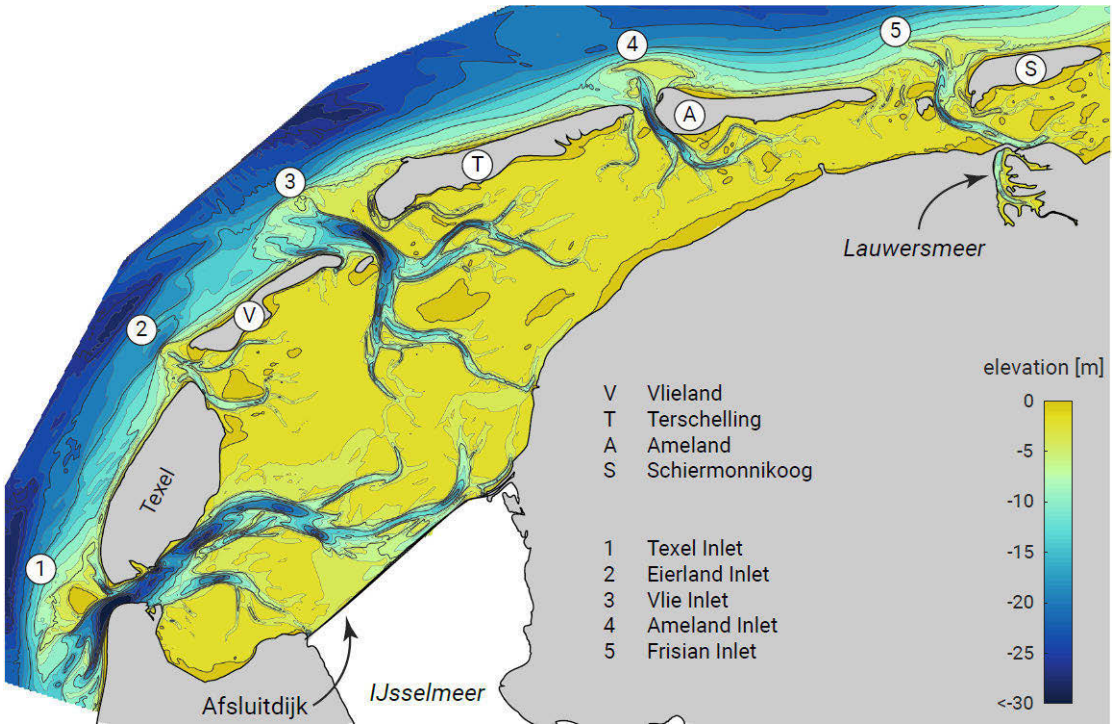

Figure 1.8: Tidal inlets in the Wadden Sea (the Netherlands). The elevations are taken from the Vaklodingen dataset (https://publicwiki.deltares.nl/display/OET/Dataset+documentation+Vaklodingen) and are w.r.t. to NAP.

A typical tidal inlet system consists of several morphological units (see Ch. 9 for more details):

- The actual entrance or tidal inlet, often dominated by a main channel;
- A shallow ebb-tidal delta seaward of the inlet that often folds around a deep channel.
- The flood basin, with possibly a distinct flood-tidal delta just landward of the inlet and an inner tidal basin consisting of the channels that are followed by the tidal currents and of the lower and higher tidal flats that alternately inundated and exposed by the tides and possibly covered by salt marshes or mangroves.

The position of the different elements of the tidal inlet system (e.g. ebb-tidal delta, flood-tidal delta, flood channels, ebb channels, shoals, tidal flats and gorge) changes over time. Figure 1.9 shows a schematic plan view of a tidal inlet with some typical notions.

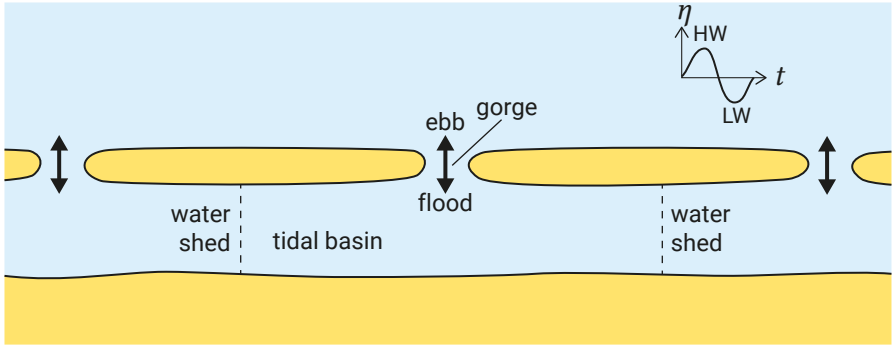

Figure 1.9: Schematic plan view of a tidal inlet system with the tidal water level variation, outflowing ebb and inflowing flood currents and watersheds. At watersheds, tidal flow through different inlets meets and tidal currents are zero.

From a morphological point of view, tidal inlets form highly dynamical systems, which are interlinked with the adjacent coast and the tidal basin or backbarrier area to which they give access. Often, unnatural constraints (e.g. coastal defence works) and the effects of human utilisation (e.g. sand mining) interfere with the natural morphodynamic behaviour. Sometimes measures are taken to restrict the dynamic behaviour of the morphological system, for instance when it complicates navigation.

1.4.6. Dune erosion and flooding during a severe storm surge

Figure 1.10 shows an instantaneous cross-shore profile (cf. Fig. 1.2). Under normal conditions the water level changes due to vertical tidal variations. On top of that, shorter variations due to waves are present. Due to changing water levels and changing wave characteristics (wave height, wave period and wave direction), cross-shore sediment transport rates (and cross-shore transport gradients) continuously change in magnitude and direction. This normal variation was already discussed in Sect. 1.4.2.

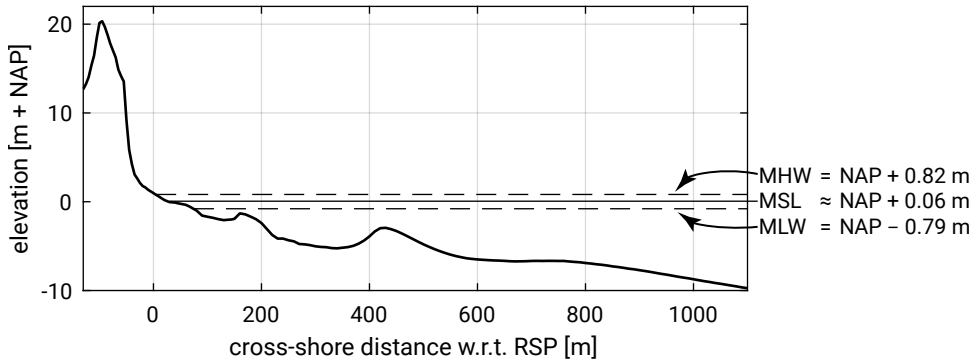

Figure 1.10: Instantaneous (summer 2011) cross-shore profile at Egmond aan Zee (RSP 7004125). Tidal elevations §1.1(see App. C) [p14] are calculated for 2018 and assumed static for the entire JARKUS period of 1965-present (JARKUS, n.d.).

During a severe storm the waves generated in the open sea will be much higher than normal. Depending on the direction and strength of the wind during the storm and

on the shape of the sea bordering the coast under consideration, water can pile up at the coastline, raising the Still Water Level (SWL) (without the effect of waves). This piling up of water is called surge.

During the severe storm surge of January 31st and February 1st 1953 in the Netherlands, the water level along the Dutch coast was about 2.5 to 3.0 m higher than normal. The wind associated with this storm came from north-westerly direction, blew over the funnel-shaped North Sea and forced the water to pile up against the coasts of the southern part of the North Sea (see Fig. 1.11). The rather small gap between United Kingdom and France (The Channel) prevented the raised water from escaping the North Sea basin. During the 1953 storm surge, many dikes in the southwestern part of the Netherlands broke. Nearly 1850 lives were lost and there were large economical consequences as well. This disaster triggered the execution of the so-called Delta plan in the Netherlands.

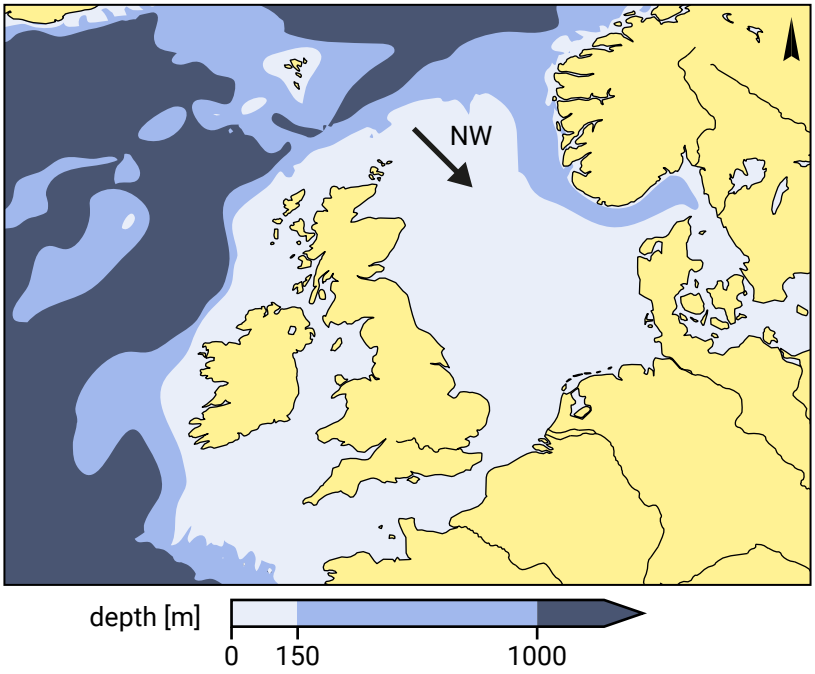

Figure 1.11: Funnel-shaped North Sea with the wind blowing from the northwest (NW). The darker the shade the deeper the water. Note the distinction between the shallower shelf region and the deeper oceanic waters. Bathymetric data from GEBCO (https://www.gebco.net/data_and_products/gridded_bathymetry_data/).

Figure 1.12 shows some characteristics of the measured and predicted water levels in Flushing (Vlissingen in Dutch). Note that the storm effect (the surge) is the difference between the actual measured and the predicted astronomical (tidal) water level variation. Note also that the surge lasted in fact a rather small period of time; within two days the storm effect rose from zero to approximately 2.8 m and fell down to zero again.

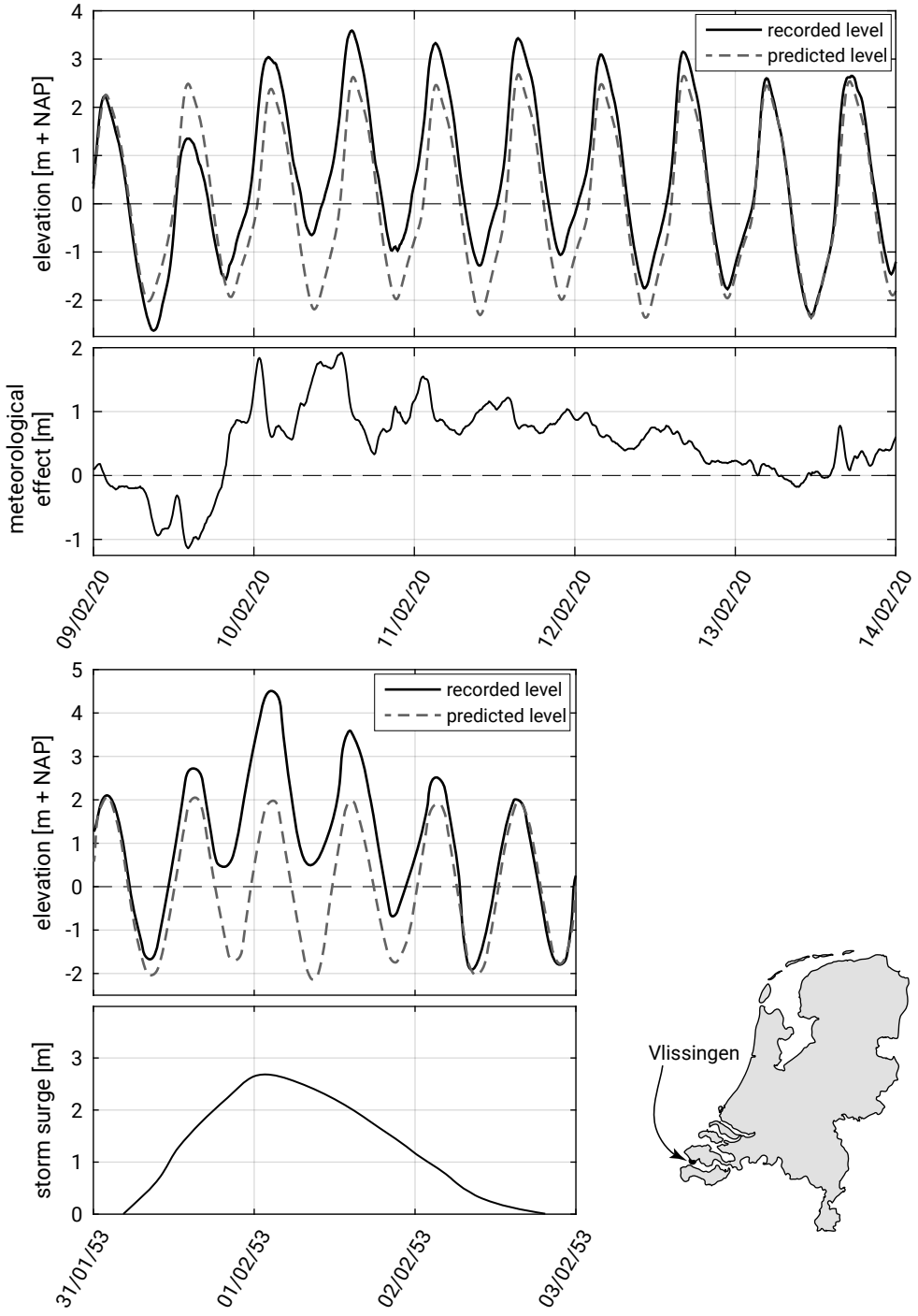

Figure 1.12: Measured and predicted water levels at Vlissingen (the Netherlands). The upper panel displays the predicted astronomical tide (grey line) and the actual measured water levels (black line) during a storm in March 2020 (https://waterinfo.rws.nl/). The difference between these two is the meteorological effect (second panel) and consists of both the storm surge and the interaction between the tide and the storm surge (see (Bijlsma et al., 1989)). The third panel shows the astronomical tide and recorded water levels during the disastrous storm of 1953. The fourth panel shows the corresponding storm surge only, which is not exactly equal to the difference between predicted and measured water levels, because of the effect of interaction between the tide and the storm surge.

In Fig. 1.13 the same cross-section as in Fig. 1.10 has been sketched, but now under maximum storm surge conditions. Not only is the SWL much higher than in Fig. 1.10, but also much higher waves are present. The SWL even exceeds the level of the dune foot; all the beaches have disappeared under water and the waves hit the dunes. It can be argued that the shape of the cross-shore profile does not correspond to the storm surge conditions (the profile shape is far out of equilibrium for these conditions). Large offshore-directed sediment transports ensure that the profile shape is transformed towards the equilibrium shape associated with the storm conditions. The dunes erode and the eroded dune material settles in deeper water, where the cross-shore profile gradually flattens (see Fig. 1.13; cf. the winter profile of Fig. 1.3).

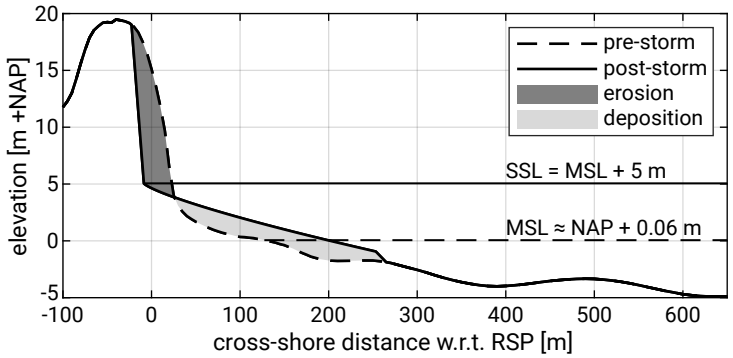

Figure 1.13: Illustration of a storm impact on the cross-shore profile. The pre-storm profile (dashed line) is a typical summer profile (summer 2015) for the Dutch coast, averaged over a 3 km long stretch near Zandvoort (data from JARKUS, n.d.). The post-storm profile (solid black line) as a consequence of a storm surge with Storm Surge Level (SSL) and storm wave conditions is estimated after (Vellinga, 1986), see Fig. 7.18 for details.

In Ch. 7 a more detailed description is given of the associated processes. For the time being it is sufficient to understand that a coastal zone manager likes to know what the loss of dune area will be under a given set of storm surge conditions, e.g. to assess the safety of properties built close to the brink of the dunes. In the Netherlands, furthermore, the safety of a large part of the population, living well below MSL behind the dunes, is at stake if a break-through of the dunes occurs.

1.4.7. Large artificial island in open sea

In densely populated areas (e.g. Japan, Taiwan or the Netherlands) it is becoming increasingly complicated to find large open areas on the mainland to start new developments (e.g. for a new airport, hosting new industries or even housing the growing population).

The open sea in front of the existing coast may be used to build an artificial island. In the Netherlands, for instance, there has been ongoing discussion whether it is useful to build an artificial island off the coast near IJmuiden for hosting an extension of Schiphol Airport. A specific airport-island requires rather large dimensions (amongst

others due to the length of runways). A typical size for such an island is 5 km. With respect to the distance of an island from the existing coast, an optimum has to be found taking into account transportation requirements, noise limitations and morphological implications.

An artificial island in open sea has large morphological implications for the existing coasts and affects the stability of coasts in a wide area. In the shadow area behind the island, the wave characteristics will fundamentally change. Another aspect of an airport-island is that the (tidal) current patterns will be affected in the vicinity of the island. The adaptation time of the existing coastal area is generally relatively long. The water depth off the coast of IJmuiden, where such an island would probably be built, is approximately 15 m. Because of this depth, the required dimensions of an island and the required level above MSL (approximately 5 m) huge volumes of sand are required to construct such an island (order of magnitude 600 million m^3 of sand.) These volumes are easily available from the bed material of the North Sea, but call for large borrow pits which also impact the morphology.

During dredging operations fine-grained silt (see Sect. 2.6.2) will also be mobilised, since within the sand deposits at the seabed often small volumes of silt occur (say 2 %). With a required volume of 600 million m^3, with 2 % silt, this results in 12 million m^3 of silt that is mobilised in the North Sea environment. The associated turbidity can have large ecological effects.

It is clear that in the final decision whether to build an artificial island or not, coastal morphology topics have to play a role.

1.4.8. Other examples

A few examples relevant to coastal engineering practice have been discussed in this section. Other examples are:

- Siltation of (dredged) navigation channels;
- Erosion near the toe of breakwaters, seawalls or offshore structures;
- Structural or gradual erosion of coasts;
- Impact of coastal protection tools, like groynes, offshore breakwaters and seawalls and revetments;
- Behaviour of artificial beach and shoreface nourishments;
- Blockage of sediment supply by a river.

In all cases sediment transports due to waves and currents are important. Compared to sediment transports due to currents alone (like in rivers), the waves enhance the sediment transport and make the calculation of the transport rates more complicated. In Ch. 6, sediment transport due to waves and currents is discussed in detail.

1.5. Coastal (morpho)dynamics

1.5.1. Definition of the coast

So far we have assumed that it was clear what we meant by 'coast'. The definition of coast however depends on the objective and the timescale under consideration. Coasts are the transition zones between oceans and continents. The coastal zone is made up of:

- the part of the land that is affected by being near to the ocean (coastlands); and
- the part of the oceans that is affected by being near to the land (coastal waters).

The coastlands encompass all terrain features that are influenced by coastal processes, like dunes, cliffs and low-lying areas (coastal plains). In a practical situation, the inland extent depends on the timescale under consideration. A coastal engineer, who is mostly concerned about timescales of years, would say that the coast extends inland as far as the influence of the tides and storm waves reaches. Although for a large estuary the limit of inland tidal propagation can be hundreds of kilometres, this definition of the landward extent is relatively narrow in the eyes of a geologist. A geologist would be aware of the fact that in former times the sea has reached higher levels than the present levels and might find evidence of that in the form of coastal deposits far from the present influence of the sea. Therefore, a geologist would include all these areas in a definition of the coast. Half of the Netherlands consisting of polders below sea level would then belong to the coast.

Similarly, the seaward limit of the coast is dependent on the timescale under consideration. Engineers have introduced the so-called depth of closure §1.2or closure depth [p19] as the most seaward point of interest. The depth of the beach profile closure is the depth beyond which repeated field observations over a certain period of time show no significant changes in bed height. It can be empirically determined by examining a series of profile measurements over a period of months to years so that both calm periods and storm conditions are included (Fig. 1.14).

The beach profile envelope in Fig. 1.14 includes typical accretional profiles built up during months of moderate wave conditions and typical erosional profiles under the influence of large storm waves. It shows that the profile is divided into an inactive offshore and a more active nearshore zone called *shoreface*. The shoreface is the part of the sandy profile affected by wave action and typically extends to water depths of 10 m to 20 m. The shoreface can further be separated into the §1.2~~shoal zone (or shoaling zone or lower shoreface)~~§1.2lower shoreface (or shoal zone) where waves gain amplitude up to the point of breaking, and the most active zone where waves are breaking and the majority of the changes takes place (§1.2~~breaker or surf zone, littoral zone or upper shoreface~~§1.2upper shoreface or littoral zone) [p19].

When considering larger timescales, we have to take into account that coastal processes have reached up to the continental shelf (Fig. 1.15) when sea levels were lower

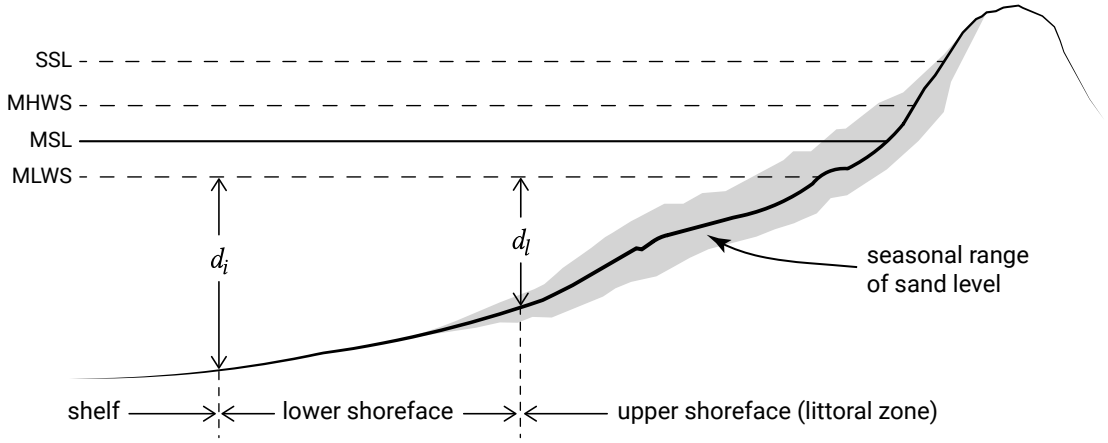

Figure 1.14: Envelope of beach profiles measured at different times, over a period of for instance a year. The two depth limits d_i and d_l correspond to the closure depth definition of Hallermeier (1978, 1981), see also Sect. 7.2.3. The profile is dynamic landward of the outer depth limit d_i. The majority of the bed dynamics takes place at depths smaller than the inner depth limit or annual closure depth d_l, where d_l is the maximum water depth for nearshore erosion by extreme conditions exceeded for twelve hours per year. The tidal levels Mean High Water Spring (MHWS) and Mean Low Water Spring (MLWS) are explained in App. C. [Figure updated] [p19]

than present. The continental shelf is the edge of a continent and is covered with relatively shallow seas up to 100 m to 200 m water depth (up to the shelf break).

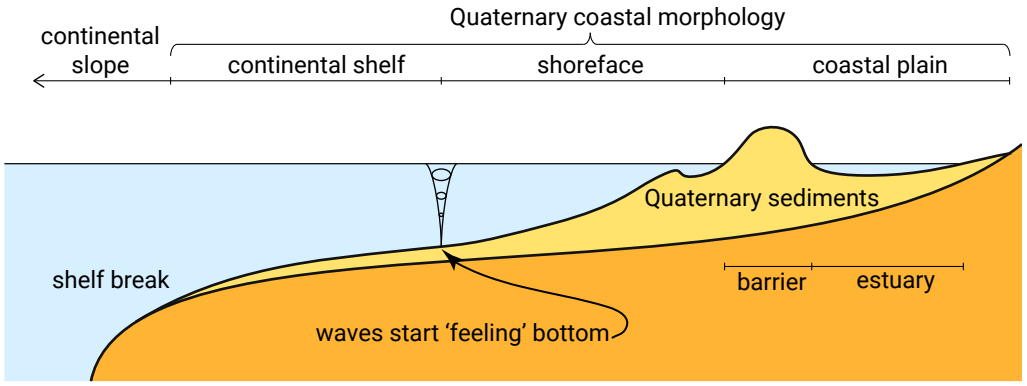

Figure 1.15: Spatial boundaries of the coastal zone. The Quaternary coastal morphology reaches up to the shelf break. The transition between the shelf and the shoreface is located where waves propagating towards the shore start feeling the bottom.

In the broadest sense of the word, we can now characterise coastal systems as relative shallow areas (i.e. depths less than order 100 m) bordered by or partly enclosed by land that are influenced by the sea and connected to the oceans, and in which ocean disturbances propagate. Due to the intensive interaction between land and water at the interfaces of the two, a large variety of coastal ocean systems has developed. The landward side includes the partially enclosed basins (such as the estuaries of Fig. 1.16b).

1.5.2. Coastal morphodynamics

In Sect. 1.4.3 we already concluded from continuity considerations that coastal changes occur in the case of gradients in sediment transport rates. This of course not only holds for the coastal stretch considered there, but for coastal systems in general. Consider for instance the sediment budgets along the estuarine and deltaic coasts of Fig. 1.16. Changes in the morphology of these systems depend on the spatial and temporal fluctuations in the sediment transport rates. In terms of a continuity equation or mass balance:

$$\frac{\partial z_b}{\partial t} + \frac{\partial S_x}{\partial x} + \frac{\partial S_y}{\partial y} = V \tag{1.1}$$

where:

$z_b(x,y,t)$	bed level above a certain horizontal datum	m
$S_x(x,y,t), S_y(x,y,t)$	sediment transport rates per m width of flow in the horizontal x- and y- direction, including the effect of porosity	$m^3/m/s$
$V(x,y,t)$	sink or source term per unit area representing local sediment gains and losses, often taken as zero	$m^3/m^2/s$

If the net sediment flux into a certain area is negative, meaning that the outgoing sediment flux is larger than the incoming one, the bottom will supply the sediment deficit (we assume that the bottom is erodible). In that case a lowering of the bottom occurs (erosion). However, while the morphology changes, the waves and tides – being dependent on the water depth – respond to the adjusted bed level. As a result the sediment transport rates change and this again affects the development of the morphology. Apparently, a feedback (named morphodynamics) exists between hydrodynamic processes and morphology. The coupling between the two is provided by sediment transport:

> Coastal morphodynamics is the mutual adjustment of morphology and hydrodynamic processes involving sediment transport.

The morphodynamic feedback can be positive or negative. In the case of negative feedback the adjustment process continues until a new situation is reached where no changes occur. An example is the response of a straight coast with normally incident waves to a beach nourishment (see also Example 8.4). Waves will disperse the sediment until eventually the coastline orientation is such that the transport gradients are zero again (hence, the end result is a straight coast again). Negative feedback thus is a stabilizing process that makes sure that after a disturbance a new equilibrium develops.

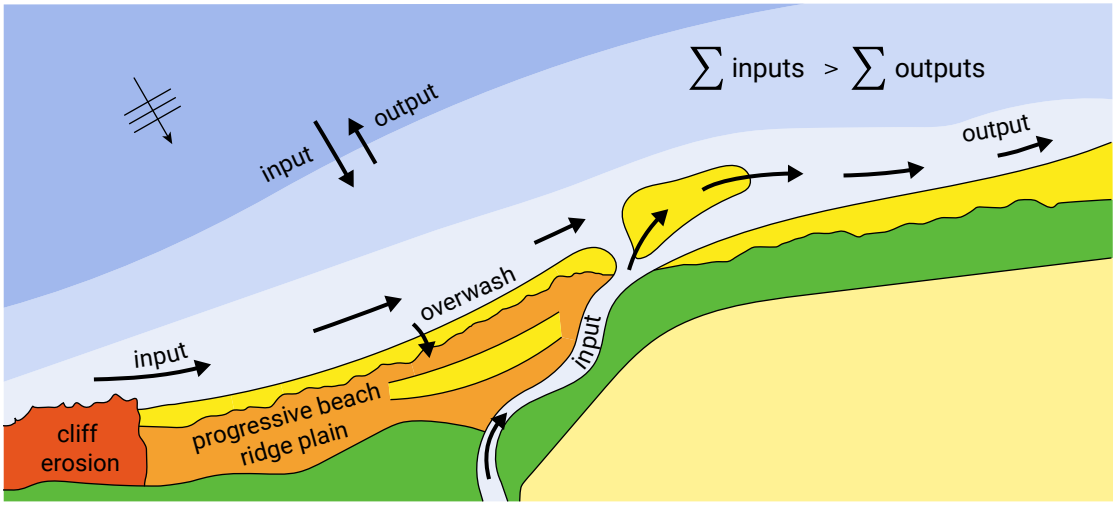

(a)

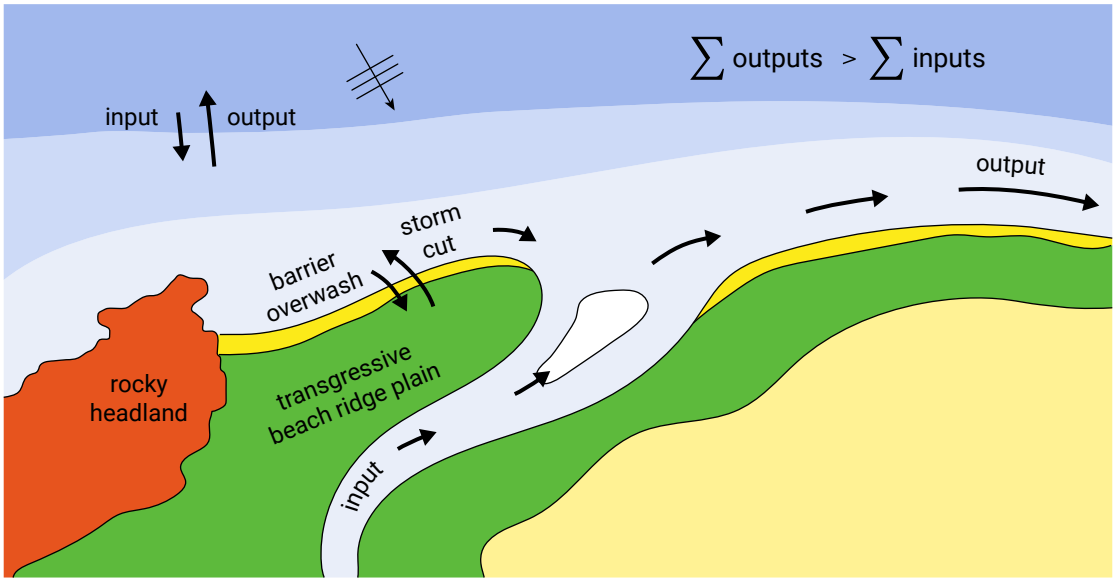

(b)

Figure 1.16: Sediment budgets along (a) deltaic and (b) estuarine coasts. In the example, the deltaic coast gains sediment; the sum of the inputs is larger than the sum of the outputs. This is reversed for the estuarine coast that loses sediment.

Note that in practice, an equilibrium is never static, since the external conditions are also changing during the adaptation process.

Positive feedback is exactly the opposite from negative feedback in that the system is pushed away from equilibrium. An example is a small disturbance of the bed, which itself generates the sediment transport convergence that makes sure that the disturbance grows larger and larger, forming a larger-scale feature, such as a shoal.

1.5.3. Time- and spatial scales

As we have seen in the previous two sections, the behaviour of a natural coastal system is dynamic on a variety of time- and spatial scales. The spatial scale is generally determined by the dimensions (in m) of a particular morphological element; it indicates the extent of the element. Examples of spatial scales (see also Fig. 1.17) are:

- A whole tidal inlet system, comprising a flood basin, an inlet gorge and an ebb or outer delta. Dimensions vary between 50 to 700 km^2. Morphological changes on such a large spatial scale generally take decades to centuries (e.g. the gradual migration of the entire inlet system);
- Large tidal channels and sand banks. Typical surface dimensions are 5 to 20 km^2, while significant changes generally take place within years to decades (such as the landing of the sand bank 'De Onrust' on the south coast of Texel around 1910);
- Smaller tidal channels and bars, with typical surface dimensions of no more than a few km^2. Significant morphological changes occur within years (such as the development and landing of the 'Bornrif' sand bar on the west coast of Ameland in the nineties of the last century);
- Accretion and erosion patterns at both sides of a port entrance, built with the help of long breakwaters. The spatial scale is several kilometres;
- Smaller bed forms like ripples and (bottom) dunes. The related spatial scales are a few metres or less.

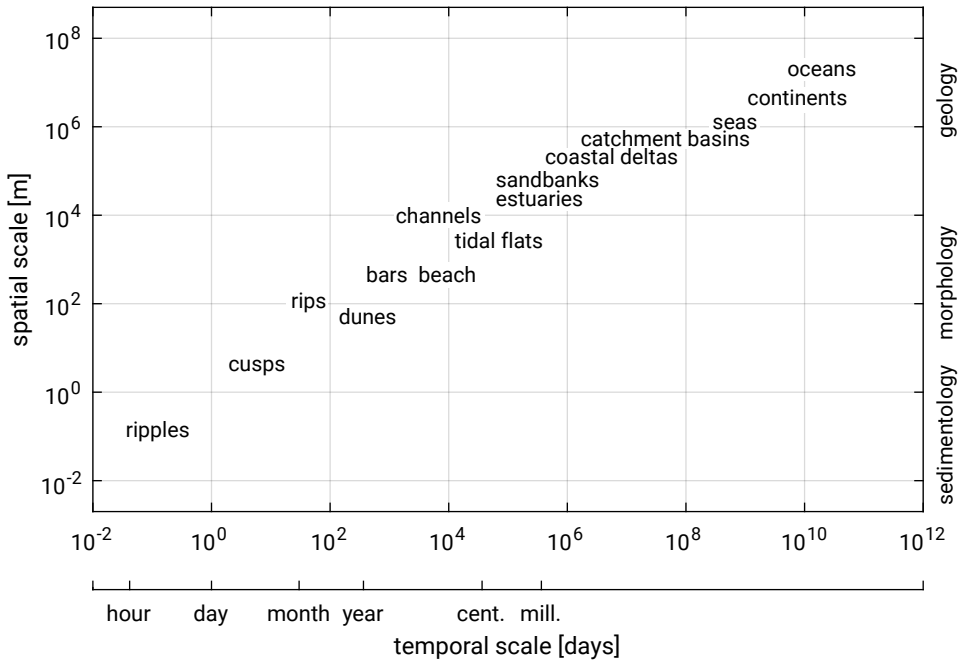

Figure 1.17: Coastal phenomena span a large range of time- and spatial scales, with time- and spatial scales being closely related. For this figure, we followed the categorisation of coastal phenomena by Dronkers (2005).

Figure 1.17 suggests that spatial and timescales are closely coupled; the larger the spatial scale of a certain feature, the larger the timescale. As an example, smaller bed forms (as mentioned in the last bullet above) not only have small spatial scales but also small timescales; the time period in which significant changes occur is a few days or less.

Examples of morphological timescales are given in Table 1.1. These examples are related to the observed morphological changes of the outer deltas of several Dutch tidal inlet systems after abrupt changes in their flood basins. The figures support the general idea that morphological timescales are directly coupled to the spatial scales of the morphological units.

Table 1.1: Examples of morphological timescales.

Morphological unit	Basin that is abruptly closed	Surface area of flood basin after closure [km^2]	Observed morphological timescale [year]
Outer delta Haringvliet	Haringvliet (1970)	120	11
Zoutkamperlaag	Lauwerszee (1969)	200	17
Outer delta Texel Inlet	Zuiderzee (1932)	680	32

A timescale is generally interpreted as the period of time (e.g. in years) required for typical morphological developments. Some researchers relate the timescale to the total duration that a morphological system needs to reach a new equilibrium situation once it has been disturbed by nature or by man (see Sect. 1.5.4). Equilibrium in this sense means that the overall sediment balance of the morphological unit is maintained (no erosion and no accretion).

A coastal engineer would generally not be interested in dynamics on very small scales like the evolution of wave ripples on the seabed or even breaker bars in the surf zone (see Sect. 1.4.2). The dynamics on these scales are generally oscillatory, which means that they have no net effect on engineering timescales. By contrast, the natural behaviour on larger (human/engineering) scales generally shows a net trend. Examples are depth reduction of an estuary due to infilling by sediments, the erosion or accretion of a delta, and the migration of a tidal inlet. Human interventions have timescales of years to decades and spatial scales of 1 km to 100 km. The coastal behaviour due to human interventions (harbours, coastal defence works, land reclamation) interferes with the natural behaviour of the coastal system on these time- and spatial scales.

Long-term sea level change acts on timescales larger than engineering scales (order of ten thousand years). This long-term tendency needs to be taken into account in the analysis on the engineering scale of the system; it provides boundary conditions for

processes and system evolution on the engineering scale. Coastal evolution on geological timescales (such as plate tectonics) is responsible for the large-scale geographical variation of coastal systems that we find around the globe nowadays. These large-scale characteristics can be considered a given for any analysis on engineering timescales. In Ch. 2 we discuss this distribution of coastal environments and – briefly – its origin.

1.5.4. Equilibrium concept

If a morphological system is not in equilibrium with the forcing (waves, tides, currents), morphological adjustments start to take place immediately; the morphological system reacts to disturbances. The rate of morphological adjustment has been observed to depend on the magnitude of the still-existing disruption (the difference between the actual situation and the equilibrium situation).

Sometimes, morphological changes are induced very abruptly, such as the closure of parts of a tidal basin. Other changes take place more slowly, such as the response of the shape of a cross-shore profile to sea level rise. Usually, the morphological response to (sudden) changes shows a certain variation with time. The process of morphological response will be fast at first and decelerates when the new equilibrium situation is approached. Often such a morphological adjustment process can be approximated with an exponential function. In terms of for instance sediment volume content of a certain morphological unit we would then have:

$$V(t) = V_{\text{old}} + \left(V_{\text{new}} - V_{\text{old}}\right)\left(1 - e^{-t/\tau}\right) \tag{1.2}$$

where:

$V(t)$	characteristic volume in morphological unit at time t	m^3
t	time after the distortion	yr
V_{old}	the (equilibrium) volume before distortion	m^3
V_{new}	the new equilibrium volume	m^3
τ	morphological timescale	yr

E.g. Stive and De Vriend (1995) and Eysink (1991) use this type of approximation to describe adaptation processes of units with large scales. Within a time t equal to the morphological timescale τ a good 63 % (namely: $1 - 1/e$) of the changes required to reach new equilibrium (namely: $V_{\text{new}} - V_{\text{old}}$) have taken place. The morphological timescale τ is the time that would be required to reach equilibrium, if the rate of morphological adjustment dV/dt would remain equal to the rate at $t = 0$:

$$\tau = \frac{\left(V_{\text{new}} - V_{\text{old}}\right)}{(dV/dt)_{t=0}} \tag{1.3}$$

Equation 1.3 can be found by differentiation of Eq. 1.2 and evaluating the resulting equation at $t = 0$. Sediment transports are supposed to drive the morphological unit

to its new equilibrium and are therefore implicitly known. Such an implicit approach to determine sediment transport rates based on the deviation from a predefined equilibrium is very different from a more process-based approach to describe sediment transport. The latter approach will be taken in Ch. 6.

1.5.5. Classification of coastal systems

Due to the intensive interaction between land and water, a large variety of coastal ocean systems has developed. Many classifications of coastal systems have been proposed that try to order the huge variety into classes with similar characteristics. In fact, so many classifications have been proposed that it seems hard to make sense of the large assortment of classifications. We will therefore not attempt to give an overview of all classification schemes, but focus instead on the points of similarity between various classifications.

In order to characterise a given coast we need to describe a minimum of four terms:

1. Geological factors:
   Any coast is the result of slow geological processes (like mountain formation) that require millions of years and result in a certain initial state of the solid boundaries (considered as given by a coastal engineer);
2. Nature and abundance of coastal 'material':
   Is the material hard (rocks, coral) and/or soft? Soft material (mud, sand, gravel, cobbles and carbonate sands) is present in depositional coastal features like deltas, beaches and mud flats. They can host vegetation such as mangroves, salt marshes, and dune vegetation;
3. Transgression or regression:
   The gradual relative sea level changes (rise or fall) that have timescales of thousands of years determine – in combination with the amount of sediment supply to the coast – whether a coast during a certain period of time has advanced (for instance a delta that has built out) or retreated (a drowned river valley). In this terminology, transgression and regression are used to describe a horizontal shift of the waterline. Hence, regression (of the sea) is equivalent to advance of the coast. Similarly, transgression (of the sea) implies retreat of the coast. Besides global effects there are regional and local effects (for instance bottom subsidence);
4. Processes that construct and erode the coast:
   Processes affecting sandy and rocky coasts are for instance wind and hydraulic forcing by waves and tides; for coral coasts and in mangrove environments or salt marshes chemical and biological processes are important. Waves and tides give rise to significantly different shapes of depositional features consisting of sand, mud and gravel. On a global scale these processes are affected by latitude and climate, whereas on a local scale they are dependent on local bathymetry.

Coastal classifications are typically based on one or more of the above four identifiers and are dependent on the scale: are we considering an entire continent or a small section of a coastline? Are we looking at developments over thousands of years or at smaller timescales? On regional (tens to hundreds of kilometres) and local scales (only a few kilometres) coastal features are dependent on the forcing by processes such as waves, tides and wind. The present book takes a mainly process-based approach and hence focuses – from Ch. 3 onwards – on regional- and local-scale features. Underlying these smaller-scale features are broader (or first-order) coastal features. The latter cover large geographical distances (thousands of kilometres) and are linked to the long-term geological process of plate tectonics and influenced by climate. On long timescales and associated spatial scales, coastal development is also connected with the expansion and retraction of ice-sheets and associated sea level changes.[3] History's legacy to coasts is described in Ch. 2.

1.6. Important parties in the Netherlands

All over the world, many governmental and non-governmental organisations, institutes, universities, consultants and contractors are active in the field of coastal dynamics. Countries in the world in which coastal engineering and coastal morphology receive significant attention are amongst others:

- Australia;
- Belgium;
- Brazil;
- China;
- Denmark;
- France;
- Germany;
- Italy;
- Japan;
- Singapore;
- South Africa;
- Spain;
- The Netherlands;
- UK;
- USA.

In the Netherlands coastal engineering has always been a very important topic for the simple reason that the ground level of large parts of the Netherlands is below MSL; see Fig. 1.18. Without dikes and dunes, people would not be able to live in these parts of the country. The Dutch governmental organisations, consultants, contractors,

[3] During the Quaternary (from 1.8 million years ago till present) the sea level fluctuated over more than 100 m vertically.

research institutes and universities that are active in the field of coastal engineering and management are described below.

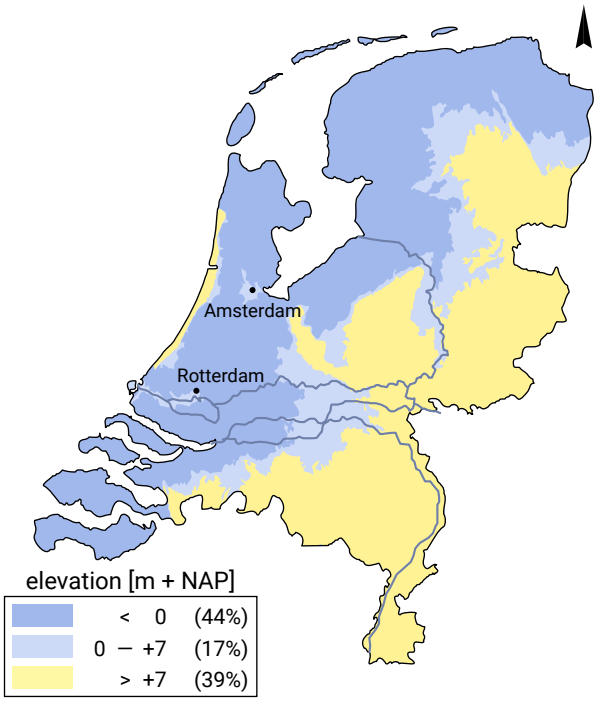

Figure 1.18: Elevation map of the Netherlands, illustrating the areas at risk of flooding. The figure is generated using the SRTM30 dataset, which is comprised of a Shuttle Radar Topography Mission (SRTM) flown in February 2000 (Farr & Kobrick, 2000) and the U.S. Geological Survey's GTOPO30 dataset. Data available on https://www.diva-gis.org/datadown.

Government

Various parts of the Directorate-General of Rijkswaterstaat (RWS) and the Directorate-General Water, which are parts of the Ministry of Transport, Public Works and Water Management, are active in the field of coastal engineering and management.

- Waterdienst Lelystad;
- Directorate North Sea;
- Regional Directorates of RWS.

The various Provinces bordering the North Sea, are – mainly at coordination level – also involved in coastal zone management. Also, the regional Water Boards play an important role in coastal zone management in the Netherlands.

Consulting companies/contractors

Many Dutch consulting companies and contractors are active in the field of coastal engineering and management, either in the design phase or in the execution of specific works. A non-exhaustive list of companies is (in alphabetical order):

- Arcadis;

- BAM;
- Boskalis;
- CDR International;
- Lievense | WSP;
- Royal HaskoningDHV;
- Svašek Hydraulics;
- Van Oord;
- Witteveen and Bos.

Research institutes

Dutch research institutes are positioned in between consulting activities and academic, more fundamental research. Institutes active in the field of coastal engineering and coastal (eco-)morphology are:

- NIOZ – The Netherlands Institute for Sea Research (Nederlands Instituut voor Onderzoek der Zee);
- Deltares – an independent institute for Delta Technology (formed in 2008 out of a merger between Delft Hydraulics, GeoDelft, parts of TNO and parts of Rijkswaterstaat).

Universities

The four Dutch universities strongly involved in education and research related to coastal engineering and coastal morphology are:

1. TU Delft – Delft University of Technology;
2. UU – Utrecht University;
3. UT – Twente University;
4. WUR – Wageningen University.

In addition, the IHE Institute for Water Education offers hydraulic engineering education to practising professionals from developing countries.

Research and management cooperation in the Netherlands

- NCK – Netherlands Centre for Coastal Research, a cooperation between TU Delft, UU, UT, RWS-Water, TNO-NiTG, Deltares, NIOZ and the Netherlands Oceanographic Institute;
- ENW – Expertise Network Water Defences (Expertise Netwerk Waterkeringen).

1.7. References

1.7.1. Lecture notes

These lecture notes are primarily developed as a student handbook and secondarily as a reference book for getting acquainted with the field of coastal dynamics and coastal engineering. More in-depth knowledge can be found in the overwhelming amount of coastal engineering literature. At several places in the lecture notes reference is made to selected literature. This is done by giving the author(s) and year of publication in the main text, whereas the full reference is given in the bibliography at the end of this book. It is of course recommended to consult other literature also. Below an overview is given of relevant text books, journals and conference proceedings.

1.7.2. Textbooks

Background information on coastal engineering and coastal morphology is provided in a number of handbooks that each have their own focus and approach. Several are mentioned here, in alphabetical order:

- Dean, R. G. (2002). *Beach Nourishment: Theory and Practice.* (Vol. 18: Advanced Series on Ocean Engineering). World Scientific Publishing
- Dean, R. G. & Dalrymple, R. A. (2004). *Coastal processes with engineering applications.* Cambridge University Press
- Dronkers, J. (2005). *Dynamics of Coastal Systems* (Vol. 25). World Scientific
- Fredsøe, J. & Deigaard, R. (1992). *Mechanics of Coastal Sediment Transport.* (Vol. 3). World Scientific, Singapore
- Kamphuis, J. W. (2000). *Introduction to Coastal Engineering and Management* (P. L.-F. Liu, Ed.; Vol. 16). World Scientific
- Komar, P. D. (1998). *Beach Processes and Sedimentation* (Second). Prentice-Hall, Upper Saddle River, New Jersey
- Masselink, G. & Hughes, M. G. (2003). *Introduction to Coastal Processes and Geomorphology.* Hodder Arnold, London
- Nielsen, P. (1992). *Coastal Bottom Boundary Layers and Sediment Transport.* World Scientific. https://doi.org/10.1142/1269
- Nielsen, P. (2009). *Coastal and Estuarine Processes.* World Scientific. https://doi.org/10.1142/7114
- Soulsby, R. L. (1997). *Dynamics of marine sands: a manual for practical applications.* Thomas Telford, London
- Van Rijn, L. C. (1999). *Principles of coastal morphology.* Aqua Publications, Amsterdam, the Netherlands.
- Whitehouse, R. J. S. (1998). *Scour at marine structures: a manual for practical applications.* Thomas Telford, London

1.7.3. Internet sources

- For translation of terminology in six languages consult waterdictionary.info;
- The *Coastal Wiki* (coastalwiki.org) is a fast-expanding source of information regarding coastal morphology, coastal engineering and coastal zone management;
- The Coastal and Hydraulics laboratory of the US Army Corps of Engineers (USACE) gives on-line access to the Coastal Engineering Manual (CEM) – type 'Coastal Engineering Manual' in a search engine like Google:

> "Coastal Engineering Manual (CEM)[4] provides a single, comprehensive technical document that incorporates tools and procedures to plan, design, construct, and maintain coastal projects. This engineering manual will include the basic principles of coastal processes, methods for computing coastal planning and design parameters, and guidance on how to formulate and conduct studies in support of coastal flooding, shore protection, and navigation projects. New sections are being added on navigation and harbour design, dredging and disposal, structure repair and rehabilitation, wetland and low-energy shore protection, risk analysis, field instrumentation, numerical simulation, the engineering process, and other topics."

1.7.4. Interesting journals

Many coastal engineering topics are discussed in scientific journals. Examples of such (mostly peer-reviewed) international journals are:

- Coastal Engineering. An international journal for coastal, harbour and offshore engineers, Elsevier Science;
- Journal of Waterway, Port, Coastal and Ocean Engineering. American Society of Civil Engineers (ASCE) Publications;
- Coastal Engineering Journal. World Scientific Publishing;
- Journal of Geophysical Research – Oceans. American Geophysical Union (AGU) Publications;
- Ocean & Coastal Management. Elsevier Science.
- Journal of Coastal Research. Coastal Education and Research Foundation;
- Shore & Beach. American Shore and Beach Preservation Association (ASBPA);
- The Open Access Journal Water. Multidisciplinary Digital Publishing Institute (MDPI).

[4] The CEM used to be called Shore Protection Manual (*Shore Protection Manual.* 1984).

1.7.5. Conference proceedings

In the field of coastal engineering many conferences are organised where recent work is first presented and subsequently collected in conference Proceedings. Four major conferences are discussed below.

International Conference on Coastal Engineering

The International Conference on Coastal Engineering (ICCE) is the world's premier forum on coastal engineering and related sciences. The Institution of Civil Engineers and the Coastal Engineering Research Council (CERC) of the American Society of Civil Engineers (ASCE) organise this bi-annual conference on theory, measurement, analysis, modelling and practice. As an illustration, the invitation brochure of ICCE 2004 mentions the following topics:

- Coastal Processes and Climate Change. Oceanography, meteorology, morphodynamics and sediment processes, macro- and micro-tidal regimes, extreme events, coastal waves, effects on coastal management;
- Flood & Coastal Defence Engineering and Management. Beach management and nourishment, coastal and beach control structures, construction techniques and performance;
- Flood Risk Management. Strategic planning, flood warning, forecasting and coastal change monitoring, data management and exchange, risk and uncertainty, decision making;
- Coastal Environment. Recreation, industrial activity, water quality, wetlands and estuaries, sustainability, environmental economics;
- Ports and Harbours. Siltation, dredging and dredged material re-use, navigation channels, optimisation, wave-structure interactions, breakwater monitoring, coastal interactions;
- Coastal Legislation, Planning and Cooperation. Government policy, funding, collaborative projects, integrated coastal zone management, international cooperation and conventions, law enforcement, effects of coastal hazards on land use planning.

Coastal Sediments

Coastal Sediments is a multi-disciplinary international conference convened for researchers and practitioners to discuss science and engineering issues of coastal sediment processes. The conference is organised every fourth year by the Committee on Coastal Engineering of the Waterway, Port, Coastal and Ocean Division of the American Society of Civil Engineers. The conference provides a high-level technical forum for the exchange of information on coastal engineering, geology, oceanography, meteorology, physical oceanography, and biology.

Coastal Dynamics

The Coastal Dynamics conferences are held under the auspices of the ASCE every four years and are technical speciality conferences bringing together field and laboratory experimentalists, theoreticians and modellers conducting research on coastal hydrodynamics and sediment transport. The proceedings of the multi-disciplinary conference are of interest to coastal engineers, coastal geologists, oceanographers, and related sciences.

Conference on Coastal and Port Engineering in Developing Countries

The mission of the Conference on Coastal and Port Engineering in Developing Countries (COPEDEC) conferences was originally to provide an international forum where coastal and port engineers from developing countries can exchange know-how and experience amongst themselves and with their colleagues from industrialised countries. In 1999, this was expanded to the following mission: To enable developing countries to have a sustainable human resources pool of highly skilled coastal and port development professionals. At the conference, which is held every four years, papers are presented on many subjects with special reference to needs in developing countries; viz.:

- Port and Harbour Infrastructure Engineering in Developing Countries. Port infrastructure design: choice of structures, design methods and techniques. Port construction: choice of materials, dredging and construction techniques. Port renovation: renovation and demolition techniques;
- Port Infrastructure Planning and Management in Developing Countries. Port planning: economic forecasts, site selection, layout and nautical aspects. Economic aspects: BOT, PPP, privatisation, containerisation. Operations and maintenance: performance, safety, management;
- Coastal Sediments and Hydrodynamics. Coastal stability, beach erosion, control and nourishment. Sedimentation, maintenance dredging of harbour basins and approach channels. Waves, currents and tides: field survey and measuring techniques;
- Coastal Zone Management in Developing Countries. Integrated coastal planning: development, implementation, evaluation. Impacts of coastal use: fisheries, infrastructure, tourism, recreation. Policy, regulations and guidelines for coastal zone management;
- Coastal and Port Environmental Aspects. Environmental Impact Assessment: pollution control and treatment. Sediment and dredging materials: isation, treatment, disposal. Waste management: reception facilities, prevention, treatment.

2

Large-scale geographical variation of coasts

2.1. Introduction

Present-day coasts show the imprint of both present-day and past processes. Coastal morphology is thus partly inherited from the past. Section 2.2 introduces the long timescales of geological processes and sea level changes and the concept of inheritance.

In Ch. 1 it was mentioned that the characterisation of a coastal system is dependent on the scale that we consider. The broadest (or first-order) features of the coast cover large geographical distances (thousands of kilometres) and are linked to the long-term geological process of plate tectonics. Plate tectonic theory and the consequences for coastal systems are discussed in Sect. 2.3.

Many of the geomorphologic features shaped or deposited during the Quaternary – consisting of the Pleistocene and Holocene – are still clearly recognisable at present. These coastal features are superimposed on the pre-existing geology that is controlled by plate tectonics. The Pleistocene legacy of rocky coasts is briefly treated in Sect. 2.4, whereas Sect. 2.5 discusses the effect of Holocene sea level changes in combination with availability (supply or loss) of sediment.

Section 2.6 deals with large-scale variations in nature and abundance of coastal material. This will be shown to be coupled to geological controls as tectonic plate setting and glacial action, and to climate. The relevant climatic effects, such as global wave height distribution and discharge of the world's largest rivers are therefore also briefly treated in Sect. 2.6. More specific information on global variation of wind, wave and tidal characteristics and their effects on coastal developments are treated in Ch. 4.

On regional (tens to hundreds of kilometres) and local scales (only a few kilometres) second- and third-order features become noticeable. In order to describe these regional

and local features, a process-based approach will be introduced in Sect. 2.7, which will be followed in the remainder of these lecture notes.

2.2. Cumulative evolution of coastal systems

2.2.1. Geological timescale

When we describe the physical history of the earth, we enter the realm of geology. Geology has produced a timescale that covers the roughly 4 to 5 billion years since the formation of planet earth. The geological timescale is divided in some main periods (geological eras) and subdivided in a much larger number of sub-periods (called periods and epochs). Since the more recent history is known in far greater detail than the initial stages of development, the sub-periods that can be distinguished become progressively shorter. Table 2.1 shows the more recent eras and periods.

The Quaternary is the present geological period and consists of the Pleistocene and the Holocene. The old names for the Pleistocene and Holocene are Diluvium and Alluvium respectively. These are the epochs of most concern to coastal engineers, extending back a total of 1.8 million years before present.

Within the period encompassed by geological history, two aspects deserve special attention in this coastal engineering textbook. First, the slow process of continental separation that started 200 million years ago has greatly impacted the formation of coastlines (Sect. 2.2.2). Second, the expansion and retraction of ice sheets and associated sea level changes[1] has strongly determined coastal development during the Quaternary (Sect. 2.3.2). Note that the modern continents essentially reached their present positions during the Quaternary, having moved no more than 100 km relative to each other since the beginning of the Quaternary.

2.2.2. Continental 'drift'

Around 200 million years ago the world's continents formed a primordial super-continent, called Pangaea (Greek for 'all earth'). The continuity of geologic features across the now widely separated continents supports this idea. The continental land masses that formed Pangaea gradually drifted from their original positions (see Fig. 2.1). They reached intermediate locations 135 million years ago, between the Jurassic and Cretaceous Periods. After almost 200 million years, the continents reached their present positions, though we can observe that they are still drifting. Nowadays, it is known that even before the formation of Pangaea, the continents were already drifting; there have been a number of cycles of continental break-up, drift, and collision, each lasting a few hundred million years.

[1] During the Quaternary the sea level fluctuated over more than 100 m vertically.

Table 2.1: Geological timescale with focus on the last 250 million years.

Era	Period		Epoch	Time before present
Cenozoic	Quaternary		**Holocene**	11,700 years
			Pleistocene (Ice age)	1.8 million years
	Tertiary	Neogene	**Pliocene**	5.3 million years
			Miocene	23.8 million years
		Paleogene	**Oligocene**	33.7 million years
			Eocene	54.8 million years
			Paleocene	65 million years
Mesozoic	Cretaceous			144 million years
	Jurassic			206 million years
	Triassic			±200 million years
				248 million years
				...
				4.75 billion years

Africa, America separated

extinction of dinosaurs

start of continent separation

formation of planet

The hypothesis that continents 'drift' was fully developed by Wegener in the beginning of the 20th century (Wegener, 1912, 1929). However, it was not until the development of the theory of plate tectonics in the 1960s that a sufficient geological explanation for that movement was found (see Sect. 2.3.1). This process of plate tectonics has had an enormous impact on the formation of coastlines and determines the broadest features of the coast. Important inherited aspects are the continental shelf configuration (mainly width and slope of the shelf) and the lithology (see Sects. 2.3.2 and 2.3.3).

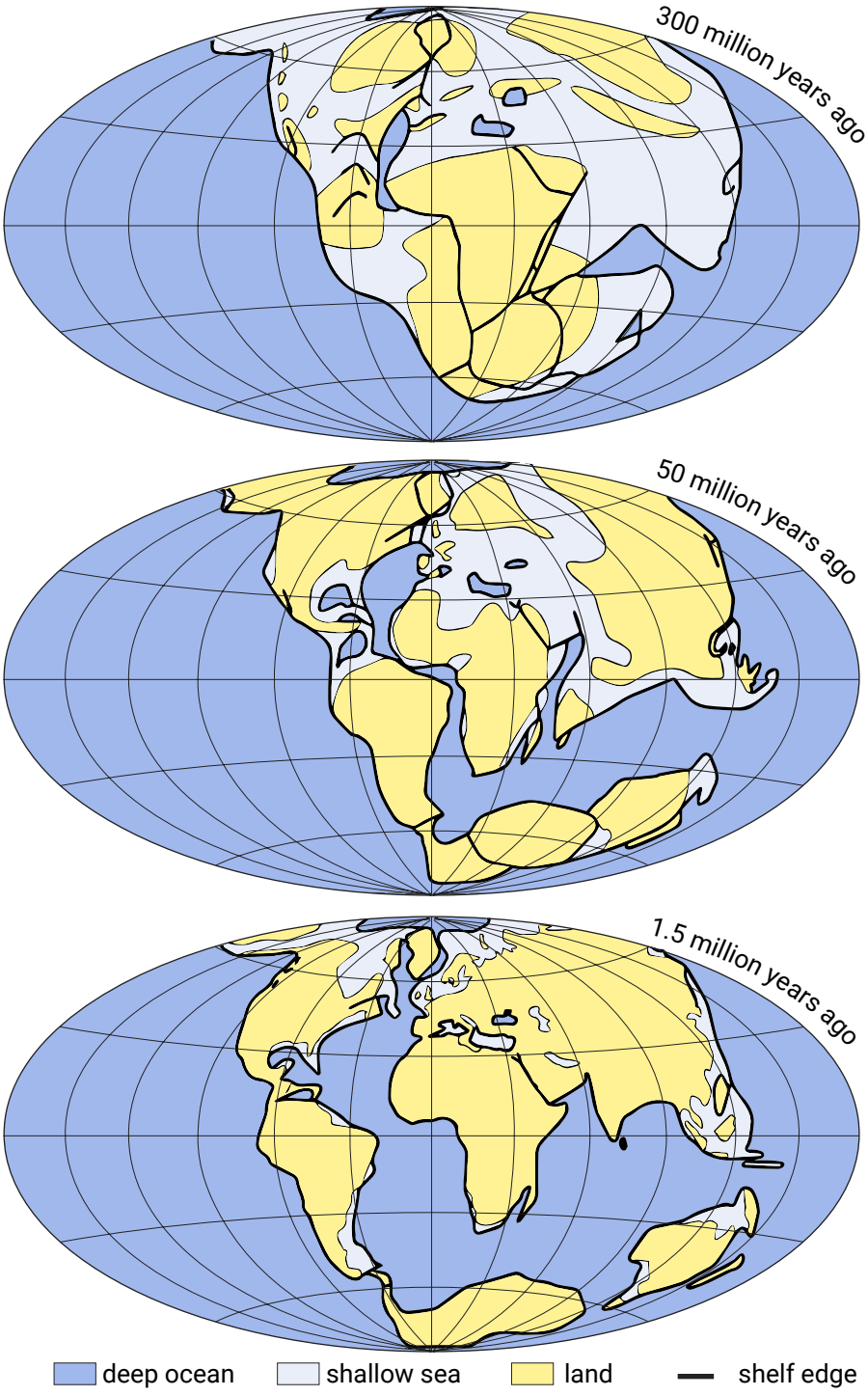

Figure 2.1: Continental drift is the movement of the earth's continents relative to each other. After Wegener (1929).

2.2.3. Pleistocene inheritance

During the Pleistocene epoch (the most recent ice age), pronounced climatic fluctuations occurred that resulted in at least eight cycles of glacials and interglacials. In glacial periods the earth experienced severe cooling and the advance of glaciers over land up to the 40th parallel in some places. Hence, glaciers periodically covered vast areas of the continents and at maximum glacial extent roughly 30 % of the earth's surface was covered by ice sheets 1500 m to 3000 m thick. Since large volumes of water were tied up in these continental ice sheets, global sea levels could temporarily drop 100 m or more. During subsequent interglacial periods, the global sea level again rose due to ice retreat and melting. The Holocene , the current geological epoch, is also an interglacial.

Pleistocene inheritance is found in coastal systems in the form of rocks formed by glaciers (Sect. 2.4) and by sediments deposited in the Pleistocene. During interglacial times in the Pleistocene drowned coastlines were common; the sea level rise allowed temporary marine incursions and hence sediment deposits into areas that are now far from the sea. In the next glacial period, these sediments were compacted by the ice cover. Buildings in the Netherlands are often built on piles touching the hard Pleistocene substrate. Many present-day morphological features date to the Holocene. They are shaped by erosion and deposition on the one hand and sea level changes on the other hand (Sect. 2.5). The sediments are either loose alluvial sediments supplied by rivers during the Holocene (from around 12 000 years ago) or older (Pleistocene). Marine processes may rework these older deposits and feed the coastal system again from the sea. §1.1This is called marine feeding [p39].

2.3. Tectonic control of coasts

2.3.1. Plate tectonic theory

Our continents are part of the lithosphere, which is the uppermost layer of the earth (containing the crust). By the 1960s, the scientific consensus was that the lithosphere is divided into 12 large, tightly fitting plates and several small ones (see Fig. 2.2).

Since these so-called tectonic or crustal plates are riding on a semi-molten underlying material (asthenosphere), the plates are in permanent motion, moving 1 cm to 10 cm per year depending on the location. Six of the large plates bear the continents; the other six are oceanic. Note that plate boundaries and continents do not exactly coincide.

Where tectonic plates diverge (mainly mid-ocean) the semi-molten asthenosphere material can be driven to the earth surface. As a result new (oceanic) earth crust is formed, resulting in the so-called oceanic ridges (Fig. 2.3). At other places, instead of divergence there is convergence. If an oceanic and continental plate meet, the denser oceanic plate dives under the continental plate (Fig. 2.3). This process of convergence

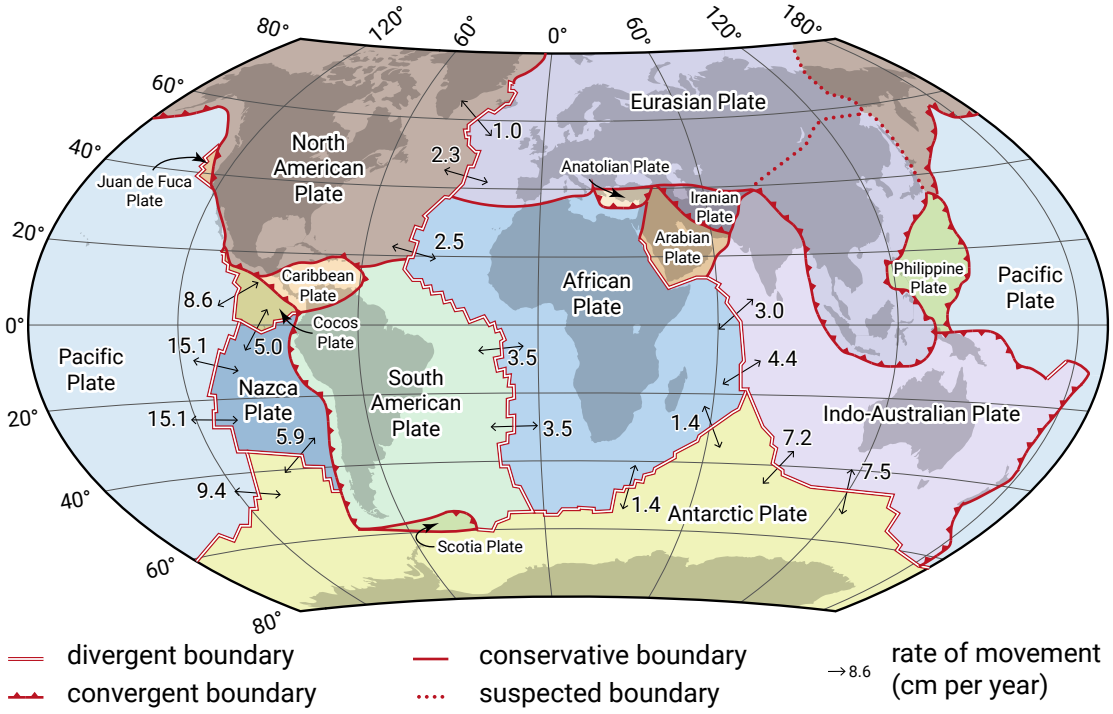

Figure 2.2: Movements of the tectonic plates: colliding or converging plates, diverging plates and plates grinding past each other (§1.1conservative or transform boundaries [p40]).

creates mountains and oceanic trenches and is often accompanied by seismic and volcanic activity (see Fig. 2.4).

The oceanic ridge system consists of the Mid-Indian Ridge, Mid-Atlantic Ridge and East Pacific Rise (see Fig. 2.4). The age of the crust on both sides of the mid-ocean ridges increases with distance from the ridge. The rates of plate divergence range

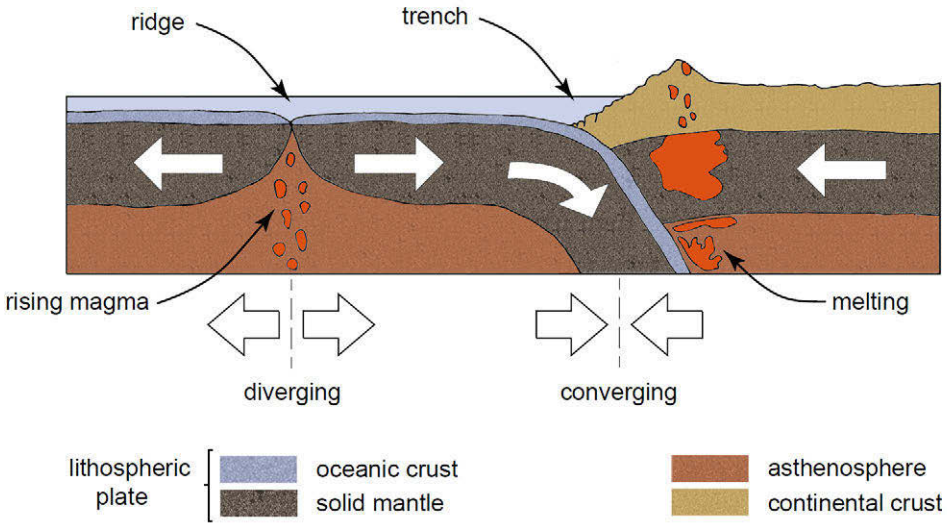

Figure 2.3: Movement in the earth's crust at convergent boundaries (subduction zones where an oceanic plate dives under a continental plate) and divergent boundaries.

from 1 to 3.5 cm/yr at the Mid-Atlantic ridge to 9 to 15 cm/yr at the East Pacific Rise in the southeastern Pacific. Nowadays, the movements are measured with the aid of satellites using very accurate geodetic positioning systems (such as Differential Global Positioning System (DGPS)).

Figure 2.5 shows the deep rift valley that runs along the axis of the Mid-Atlantic Ridge and becomes visible at the surface on Iceland in a very spectacular way.

§1.1 Figures 2.2 and 2.4 not only show convergent and divergent plate boundaries, but also conservative or transform boundaries, where plates grind past each other. There are no volcanoes at a conservative plate boundary, but earthquakes can be very destructive. An example is the San Andreas Fault in California where the Pacific and the North American plates are sliding past each other, in the same direction but at different speeds. [p41]

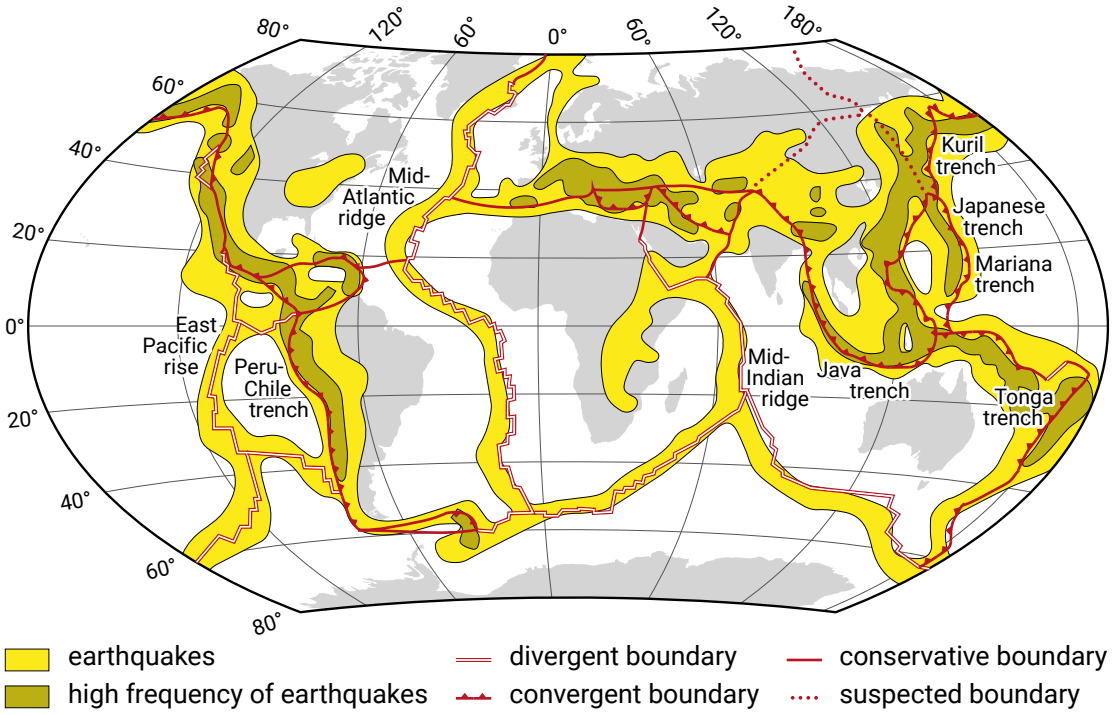

Figure 2.4: Global distribution of earthquake occurrence is associated with plate boundaries: earthquakes are found near the oceanic ridge system at diverging boundaries and near the trenches closer to continental edges at converging boundaries.

2.3.2. Tectonic plate setting of coasts

Inman and Nordstrom (1971) recognised that broad coastal characteristics such as shelf width and coastal topography are related to the position on the moving tectonic plates. Not only the proximity of a coast to a plate boundary, but also whether this boundary is converging or diverging has a huge influence on the character of that coast. Inman

Figure 2.5: Mid-Atlantic Rift passing across Thingvellir National Park, Iceland. The North American Plate is shown to the left and the Eurasian plate to the right. Photo by Matthijs Buijs ('Credits' on page 579).

and Nordstrom (1971) classified coasts into three categories according to their tectonic plate setting:

- Leading-edge or collision coasts: associated with the leading-edge of a crustal plate viz. with converging plates. They are characterised by rugged, cliffed coastlines, tectonic activity and a narrow continental shelf;
- Trailing-edge coasts or passive margins: coasts that are located away from plate boundaries and are generally tectonically stable because the continent and adjoining ocean floor are part of the same plate. They have wide continental shelves;
- Marginal sea coasts: tectonically stable coasts protected from the open ocean by island arcs at converging plate boundaries.

Figure 2.6 shows the worldwide distribution of coastal types as classified by Inman. Compare this figure with the tectonic plate setting of Fig. 2.2.

Figure 2.7 illustrates the formation of leading-edge coasts and trailing-edge coasts. It can be thought of as a cross-section of North or South America. Along the west coasts of the American continent, denser oceanic plates descend beneath the continental edge of the North and South American plates (see the plate boundaries in for instance Fig. 2.6). This collision has resulted in narrow shelves, earthquakes, coastal uplift, and the formation of mountains immediately inland from the coast: the Andes Mountains and the North American western mountain ranges. This is illustrated by Fig. 2.8, the Big Sur coast in California, USA. The rising magma may also create volcanic activity.

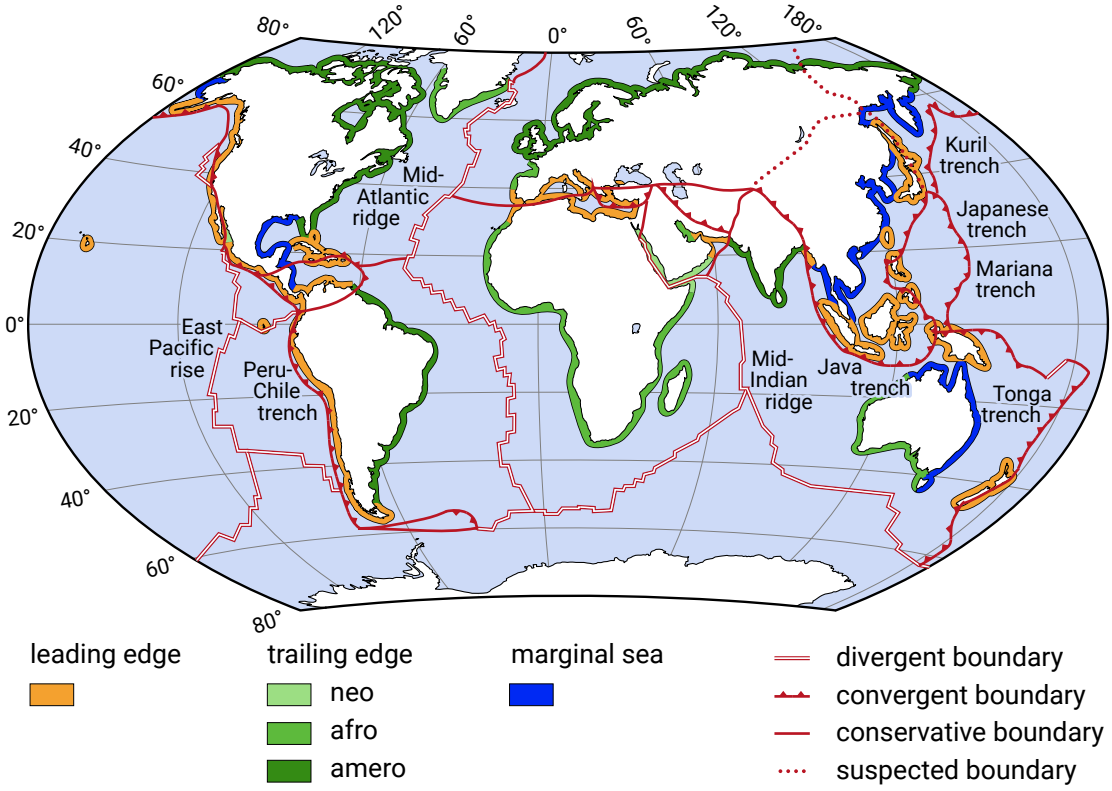

Figure 2.6: A tectonic-based classification of coasts. After Inman and Nordstrom (1971). The three classes of trailing-edge coasts are discussed below.

In contrast, the east coasts of the American continent lie within the interior of tectonic plates, and therefore experience little tectonic activity and are either stable or subside rather than being uplifted.

Trailing-edge coasts are the result of plate divergence and are facing a spreading centre. In plate tectonics, the formation of an ocean is a spreading process between two newly formed plates. At first this process results in a rift valley (the African Rift Valley being a recent example). In the next stage, the valley opens up until seawater enters; a present day example is the Red Sea. The spreading process continues, the ocean becomes wider and forms a mature ocean like the Atlantic. The mature trailing-edge coasts bordering that ocean are far away from the mid-plate spreading centre. This means that all coasts on both sides of the Atlantic Ocean in Europe, Africa, North and South America are trailing-edge coasts (e.g. the Dutch coast, see Fig. 10.9). Other examples of trailing-edge coasts are the west Australian coasts. Inman and Nordstrom have categorised the new trailing-edge coasts formed near young spreading centres as *neo-trailing-edge coasts*. Regarding the more mature trailing-edge coasts further from plate boundaries, they discern *Afro-trailing-edge coasts* and *Amero-trailing-edge coasts* based on differences in sediment supplies (see Sect. 2.3.3).

The leading-edge coasts as illustrated in Fig. 2.7 develop along the border of a land mass where the oceanic edge of one plate converges with the continental edge of another plate. They are called *continental collision coasts*. Other examples are found along the

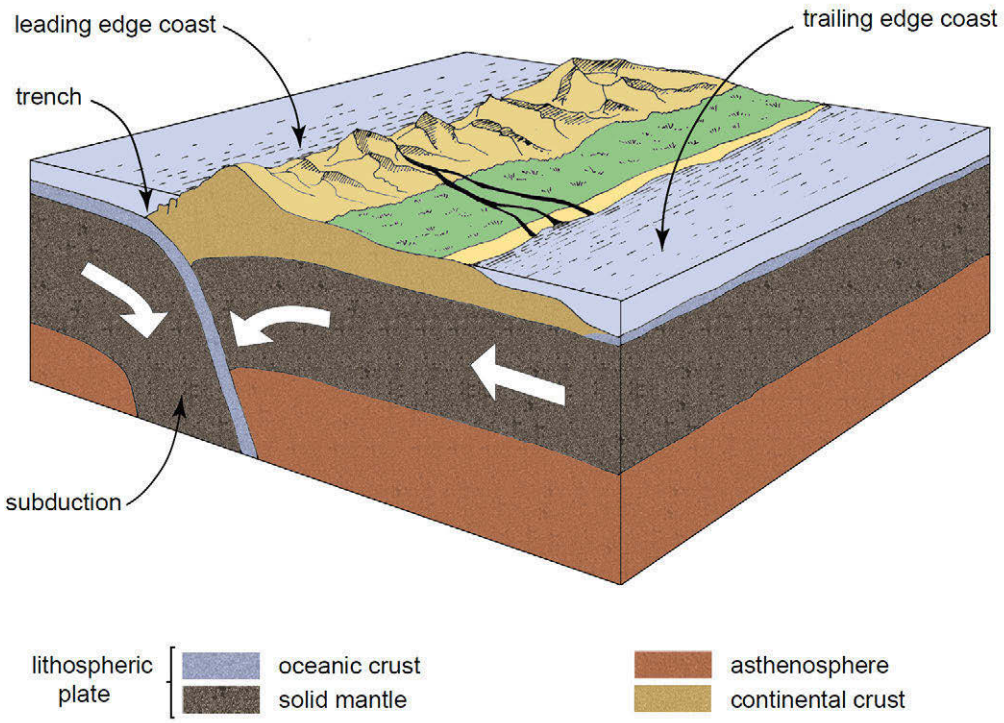

Figure 2.7: Formation of leading-edge and trailing-edge coasts. This figure can be seen as a cross-section of the American continent with the west coasts dominated by rocky coasts and a narrow and steep continental shelf and the east coasts dominated by extensive sediment deposits on a wide and flat continental shelf.

Figure 2.8: Leading-edge coast in the Big Sur region of California, USA. Photo by Marcel J.F. Stive ('Credits' on page 579).

coast of Turkey and Greece. Besides these continental collision coasts, also *island arc collision coasts* can be discerned. The latter form where two oceanic plates collide, see Fig. 2.9.

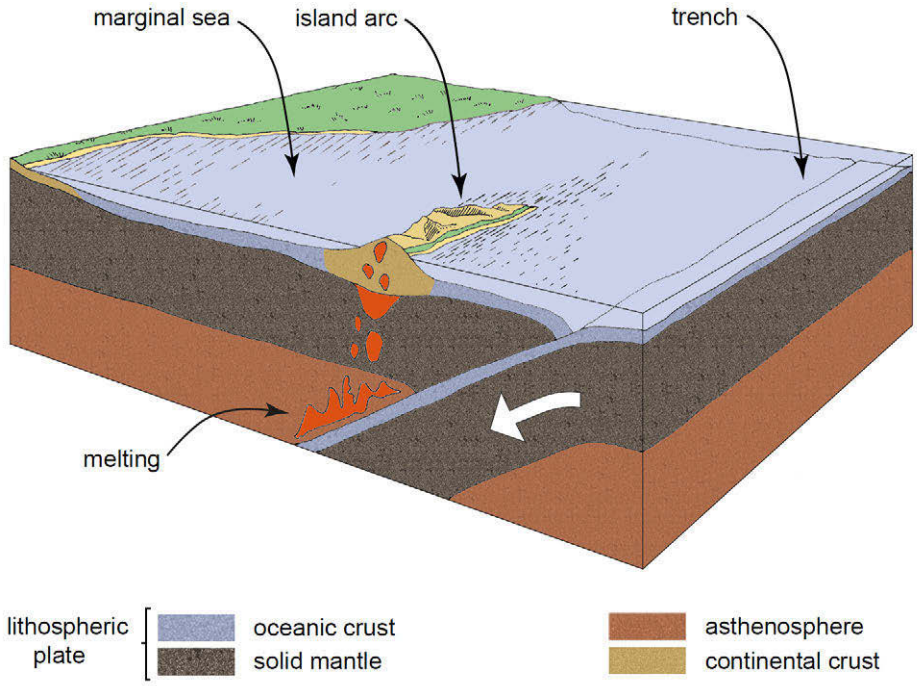

Figure 2.9: Convergence of two oceanic plates and the associated volcanic activity leads to the formation of island arc coasts.

The island arc is formed from volcanoes which erupt through the overriding plate as the descending plate melts below it. Japan, the Philippines, the Caribbean island arc and the Aleutian island arc in Alaska are examples of collision coasts located along the margin of an island arc. Other examples of island arc coasts collision coasts are found along the coasts of Borneo, Sumatra and New Guinea.

Marginal sea coasts occur in semi-protected environments including eastern Australia, the Gulf of Mexico and eastern Asian shorelines. The left part of Fig. 2.9 shows a marginal, inland sea enclosed between a land mass and a volcanic island arc at the converging plate boundary. The marginal sea coast fronting the inland sea is therefore protected from the open ocean by the volcanic island arcs (e.g. Korea) where a plate collision is occurring. Although fairly close to the convergence zone, the marginal sea coast is far enough away to be unaffected by convergence tectonics – it behaves like a trailing-edge coast.

2.3.3. First-order coastal sedimentary features

Of the aforementioned tectonically-driven coastal characteristics, shelf width is the major factor controlling coastal sedimentary features. Furthermore, differences in sediment supply are of importance. Both aspects are discussed in this section.

Continental shelf width

The world distribution of continental shelf width is given in Fig. 2.10. As can be seen from Figs. 2.6 and 2.10, there is a direct correlation between the tectonic plate setting and the continental shelf width. For instance, some of the narrowest shelves are found off the tectonically active west coasts of North and South America. Broad shelves on the other hand are common to trailing margins. Since the shelf break (see Fig. 1.15) is located at relatively constant water depths of 100 m to 200 m, narrow shelves imply steep slopes, whereas wide shelves have low gradients.

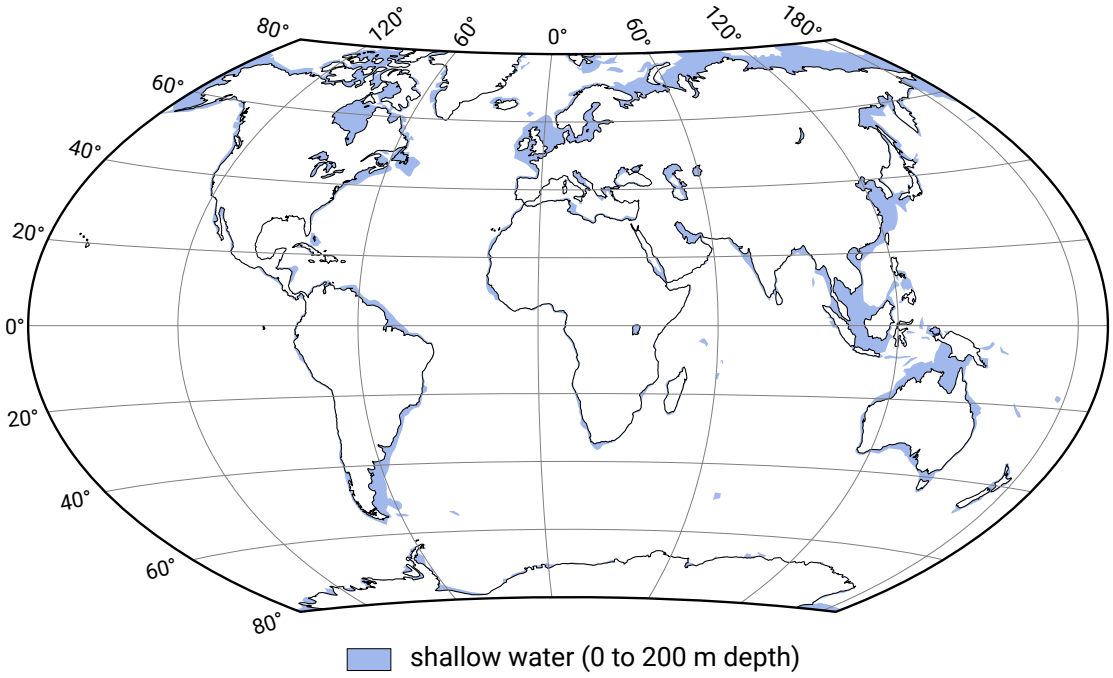

Figure 2.10: Approximate world distribution of continental shelf width indicated by near-coast regions up to 200 m water depth.

Because of their larger horizontal extent, wide and flat shelves facilitate the development of extensive sedimentary features as opposed to narrow and steep shelves. Also due to the smaller slope, the former permit more rapid coastal progradation. For this reason, large deltas and barrier islands systems have the potential to develop on coasts with wide shelves (as long as sufficient sediment is supplied). Hence, leading-edge coasts and trailing-edge coasts are dominated, respectively, by erosional features like sea cliffs, rocky headlands, etc., and depositional features like barrier islands.

The shelf width also has an effect on the hydrodynamic conditions, for instance storm surge is augmented by shelf width. Storm surge is the piling up of water against the coast due to a combination of onshore winds and low atmospheric pressure, see Ch. 5. Narrow shelves do not have enough horizontal extent for water to pile up and have lower potential surge elevations (see Fig. 5.50 and Eq. 5.90). Wind-wave heights are higher at narrow shelves since the waves are permitted to keep their height; there is no shallow sea bottom to interfere with and hence dampen the wave motion. Wider

shelves on the other hand have more frictional dampening of storm waves and thus lower wave energy. Tidal amplitudes on the contrary are generally higher at wider shelves, at least for semi-diurnal tides in non-polar areas. In those situations resonance is approached, which amplifies the tidal amplitudes at the coast (see Sect. 3.8).

As pointed out above, large mid-ocean waves lose energy as they progress across the gently sloping inner continental shelf of a trailing-edge coast. They consequently do not inhibit deposition of sediment along the coast. As long as enough sediment is supplied to the coastal system, the combination of reduced wave energy and the facilitation of sediment accumulation ensures the development of large sedimentary features on the wide and flat trailing-edge continental margins. An example are the extensive mangrove swamps and tidal flats, which cover the low-relief Amero-trailing edge coast near the mouth of the Amazon River in Brazil.

Similarly, marginal sea coasts have the potential to develop large sedimentary features due to their wide continental shelves and low wave energy (see Fig. 2.11). They are low wave energy coasts due to 1) the gentle slope and shallow waters of the continental shelves in these areas; 2) the attenuation of wave energy due to the sheltering by nearby or surrounding land masses or island arcs or ice; and 3) the restricted size of the marginal seas and hence limited fetch, restricting the size of waves that develop locally. The coastal plains of marginal sea coasts vary in width and may be bordered by hills and low mountains (e.g. Vietnam).

Figure 2.11: Marginal sea coast at Jiangsu, China. Photo by Marcel J.F. Stive ('Credits' on page 579).

In contrast, sediment delivered to leading-edge coasts is soon dispersed by the usually large waves coming from the deep ocean. Moreover, because of the narrow continental shelf, submarine canyon heads lie close to the shore. As a result, most of the sediment deposited along the coast moves offshore through canyons and thus into deeper water

beyond the shelf. Hence, the coastal zone of leading-edge coasts has relatively little sediment even if large amounts of sediments are transported to the coast by rivers.

Sediment availability

Trailing-edge coasts have typically been tectonically stable for many millions of years. All these years, erosion processes have taken place and converted hills and cliffs into coastal and submarine plains. Along these coasts, one can therefore find large deposits of sediment. They are shaped and reshaped by currents, wind and waves into barrier islands, deltas and other sedimentary shapes. For instance, the São Francisco Delta in Brazil and the Senegal Delta in Africa have developed on trailing-edge coasts.

There are differences between the trailing-edge coasts of the African continent and the east and Gulf coasts of the American continent, mainly as a result of differences in sediment supply. The American trailing-edge coasts receive large quantities of sediments, since many of the rivers originate in mountainous regions and have very large drainage basins. The latter is the result of the overall asymmetry of North America, with the largest mountains and divides located closer to the west coast. The African continent on the other hand occupies a position in the middle of a crustal plate. Due to the absence of plate collisions, it lacks significant mountains. Therefore and because of climatic conditions, accordingly smaller quantities of sediment are delivered to the coastal zone. The typical coastal features of the African continent have led to the name *Afro-trailing edge coast* for a trailing-edge coast for which the coast on the opposite side of the continent is also trailing. Although Afro-trailing edge coasts have pronounced continental shelves and coastal plains, these features are usually smaller than found at more mature coasts, and sedimentary features such as large deltas are rare.

Amero-trailing edge coasts are represented by the east coasts of North and South America and are geologically the most mature coastal areas. Amero-trailing edge coasts have a collision coast on the opposite side of the continent. In combination with the moderate climate, this has led to the development of numerous large, meandering river systems that for more than 150 million years have been carrying sediment across a gentle incline, developing broad, low-relief coastal plains and subaqueous features.

Some of the largest deltas in the world have been formed on marginal sea coasts by the great rivers of southeastern Asia and the Gulf region of the USA. Both areas have a mild climate and abundant rainfall. Hence, the combination of relatively low-energy coastal conditions and sizeable sediment loads leads to the formation of large deltas and other coastal sedimentary deposits such as tidal flats, marshes, beaches and dunes. Examples are the Mississippi River Delta in the Gulf of Mexico and the huge deltas of the Pearl, Yangtze and Yellow Rivers that empty into the South China Sea.

The steep mountain slopes of leading-edge coasts hold rapidly flowing streams and small rivers that quickly erode their beds. Because the watershed is at a high elevation near the coast, the rivers are short, steep, and straight. They may transport large

quantities of sediments directly to the coastal areas, giving no opportunity for sediments to become entrapped in a meander, on a natural levee, or on a flood plain. The rivers deposit their sediment loads into coastal bays or directly onto open beaches. The coastal deposits are relatively coarse, since the material has to be transported over just a short distance (see Sect. 2.6). However, even though mountain streams deposit large amounts of sediment on the coast, they do not produce deltas (Davis Jr., 1994). In fact, none of the world's 25 largest deltas are found on leading-edge coasts. As pointed out above, this is because this tectonic setting with narrow and steep continental shelves does not have a shallow, nearshore area on which the sediment can accumulate. Instead, sediment will be lost to deeper areas beyond the shelf break through offshore canyons. Furthermore, the dispersion of sediment by the usually large waves prevents the development of extensive sedimentary features such as deltas.

Some trailing-edge coasts look like leading-edge coasts. This holds for instance for the high-relief coast with coarse gravel beaches on the Sea of Cortez (or Gulf of California), Mexico. This coast is a *neo-trailing edge coast*. Being only a few million years old, it represents the first stage of coastal development and resembles a leading-edge coast.

2.3.4. Summary of tectonic classification

As noted by Inman and Nordstrom (1971), the tectonic setting of a coast controls the physical nature of the coast, at least at first order (that is to say, to a first approximation). The *leading-edge* or *collision coasts* are all relatively straight and mountainous and generally characterised by sea cliffs, raised terraces, and narrow continental shelves.

The *trailing-edge types of coasts* are more variable. The *Amero* and *Afro* types have low-lying depositional coastal forms such as barrier islands and the widest continental shelves. The *neo-trailing edge* coasts are typically steep with beaches backed by sea cliffs, so in many respects these neo-trailing edge coasts are similar to leading-edge coasts. The *marginal sea coasts* have the greatest diversity of form. The land may be low-lying or hilly, and the form of the coast can be dominated by local processes such as the formation of river deltas.

2.4. Pleistocene inheritance of cliffed coasts

The larger part (about 75 %) of the world's continental and island margins is lined with cliffs, consisting of rocks or cohesive clays. As we have seen in Sect. 2.3.2, cliffed coasts are commonly tectonically active convergent coasts, which produce a rocky, high-relief border. Because they are formed on continental plate margins, under which an oceanic plate is descending, virtually no continental shelf is present. The western edges of North and South America are good examples of this type of coast, as discussed above.

There are also cliffed coasts of which the origin is unrelated to plate tectonics. In these cases the adjacent continental shelf is wide, with a gentle slope. First, Pleistocene glaciers have had a hand in producing cliffed coasts. The moving ice masses gouged out steep valleys, which were subsequently drowned as the sea level rose during an interglacial period. Examples of these so-called fjords are found along the coasts of Alaska, Scandinavia and Scotland. Although their profiles are similar, some fjords are rocky and others are not. In Fig. 2.12, the rocky coast along a Norwegian fjord is shown. It was carved by a glacier.

Figure 2.12: Geirangerfjord in Norway. Photo by Marcel J.F. Stive ('Credits' on page 579).

Still other cliffed coasts are formed of glacial till, sediment deposited by glaciers beneath and at the margins of the ice. The till is over 100 m thick in some places and includes nearly any type of material, from stiff clays to sand, gravel and boulders. Some of it is well-layered and some is massive, with essentially no internal coherence. The accumulations known as end moraines tend to be linear and thick. When these end moraines meet the sea, the waves sculpt steep bluffs. Coasts formed by glacial till are also found in Scotland, Denmark and the United Kingdom.

Another variety of rocky and commonly cliffed coast is associated with areas where the continental shelf and adjacent coast are dominated by carbonate sediments as a result of skeletal shell and coral debris. In the Pleistocene, onshore winds blew the carbonate sediment landward, where it accumulated in wide beaches and dunes. In a process called lithification, the calcium carbonate grains were welded together by a cement that is created as ocean spray or percolating ground water reacts with the calcium carbonate. The evaporation of regularly wetted surfaces in arid climates enhances the lithification of the sediments. The rapid cementation converts the dunes to a rock called eolianite. The coast of North Africa is well known for its cemented sand, which

hampers dredging operations because in surveys it appears to be sand, whereas it is quite hard in reality. Similarly, on the beach we find the so-called beach rock, which can be a nuisance for dredging operations.

An example of yet another type of cliffed coasts are the Cliffs of Moher (Fig. 2.13), made up of layer upon layer of sand, silt and mud, compacted into solid rock. These sediments were carried into an ancient sea by large rivers.

Figure 2.13: Cliffs of Moher, Ireland, showing horizontal layers of rock. Photo by Alejandra Gijón Mancheño ('Credits' on page 579).

Erosion rates of cliffed coasts strongly depend on lithological factors. Typical erosion rates for rock are 10^{-1} m/yr to 1 m/yr for chalk, 10^{-3} m/yr to 10^{-2} m/yr for limestone and 10^{-3} m/yr for granite. Along rocky coasts, nearshore wave energy is often high because the size of the waves is related to the nearshore bathymetry (see Sect. 2.3.3) and to refraction patterns. The wave energy is focused on the headlands (see Fig. 5.6) and dispersed in the bays, so the headlands erode as the intervening bays fill up. Wave erosion of an indented coastline produces a straightened, cliff-bound coast, as shown in Fig. 2.14. Wave-cut platforms and isolated stacks and arches may remain offshore (see Figs. 2.15 and 2.16).

Our focus is on sandy (and to a lesser extent muddy) coastal systems and, therefore, the processes of cliff and rock erosion are not considered any further in the remainder of this book.

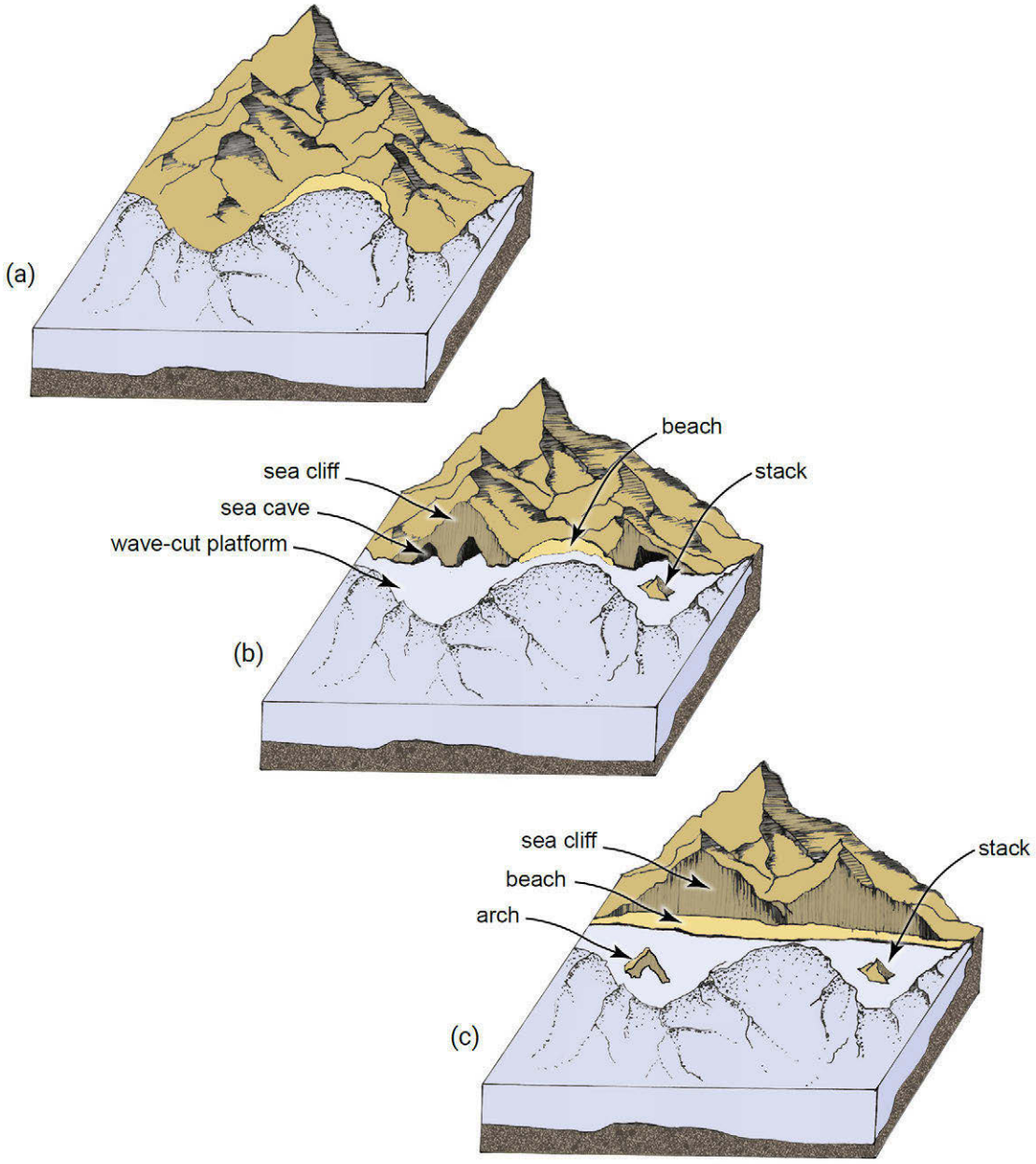

Figure 2.14: Wave-erosion effects. Along rocky coasts with headlands (a), the headlands erode due to wave focusing (b), leaving behind isolated stacks and arches (c). After De Blij and Muller (1993).

2.5. (Holocene) transgression versus regression

2.5.1. Geological sea level changes

Local mean sea level is defined as the height of the sea with respect to a land benchmark, with fluctuations caused by waves and tides smoothed out. Locally perceived changes in mean sea level (also called *relative* sea level changes) can be the result of

Figure 2.15: Cliffs with stack and arc at Falaise d'Etretat, France. Photo by Blenda Gomes Rocha ('Credits' on page 579).

Figure 2.16: Cliffs with stacks at the coast of Peniche, Portugal. Photo by Ascha Simons ('Credits' on page 579).

either vertical movements of the land or an absolute (relative to the earth-centre) movement of the sea level (Fig. 2.17). Absolute sea level changes are called eustatic changes and can be of the same order of magnitude as the vertical land movements.

Eustatic sea level changes are commonly defined as absolute vertical movements of the mean sea level, represented by the oceanic geoid[2]. §1.1This oceanic geoid is the shape that the ocean surface would take under the influence of the gravity of the earth, if

[2]The geoid is a surface of equal gravitational attraction and is§1.1, within the ocean areas, [p52] roughly equal to the mean sea level surface (if dynamic effects are ignored).

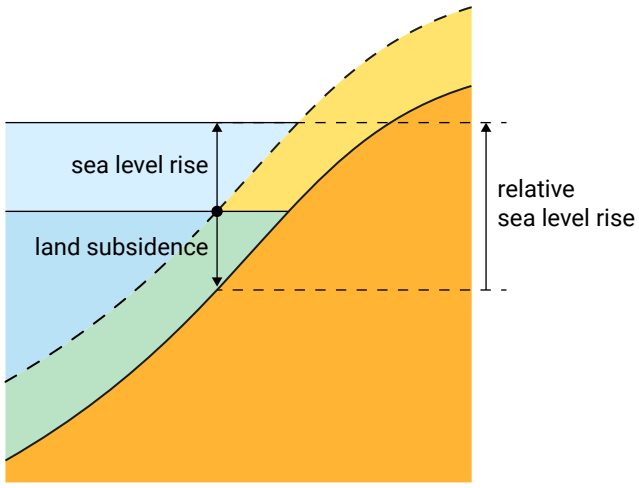

Figure 2.17: Relative sea level rise is the combined effect of absolute sea level rise and land subsidence or uplifting. It therefore is the locally perceived sea level change.

other influences such as winds and tides were absent. Therefore, it corresponds to the mean sea surface at rest. Eustatic changes are caused by: [p52]

- Changes in the volume of the ocean water through:
  - Changes in the amount of water as a result of glaciations and deglaciations i.e. the advance and retreat of ice sheets and glaciers (*glacio-eustasy*);
  - Changes in expansion of water (so-called *steric changes* due to temperature or salinity changes);
- Changes in the volume of the ocean basins due to the very slow process of tectonic plate divergence (*tectono-eustasy*), marine sedimentation or hydro-isostasy (see below);
- Changes in the distribution of water due to changes in the earth's gravitational field and hence in the shape of the oceanic geoid (*geoidal eustasy*).

Of the listed causes, the most important cause of long-term variations in eustatic sea level is changes in the amount of ocean water due to glaciations and deglaciations. Such changes have taken place often during earth's history under the influence of global temperature change, and still occur. In the Quaternary, interglacial and glacial climates alternated at the higher latitudes of the Northern Hemisphere. During the cold periods the development of enormous ice sheets and glaciers resulted in a significant lowering of the ocean level (more than 100 m) and large parts of the continental shelf became dry land or coastal swamp. The melting down of the ice sheets during the warmer periods resulted in the restoration of the ocean level.

The last listed cause should also be explained. Eustatic changes have long been believed to be worldwide and simultaneous. For that reason eustatic sea level rise was also called global sea level rise. It was only discovered in the early 1970s that the oceanic geoid is not uniform and constant. It has relief and is constantly deforming under the influence of gravitational and rotational changes as a result of, amongst

other reasons, the formation and melting of ice sheets. The changing shape of the geoid influences the worldwide distribution of water and therefore eustatic sea levels. This explains why eustatic sea level changes during the last 6000 years, as reported by several authors before this effect was taken into account, were rather divergent. §1.2The role of the formation and melting of ice sheets can be explained as follows. Large ice masses exert a gravitiational force on the ocean that results in a gradual tilt of the sea surface toward the ice sheets. If the ice melts, the gravitational attraction and hence the sea surface slope reduces. This yields a larger than average absolute sea level rise far away from the ice sheets and a smaller than average absolute sea level rise or even a sea level fall closer to the ice sheets. [p55]

Eustatic sea level changes result in deformations of the earth's crust, which is known as isostatic deformation (uplift or subsidence). The isostatic uplift or subsidence of the earth's surface can take two forms:

Glacio-isostasy is the loading and unloading by ice. It is related to the fact that the weight of the ice sheet depresses the underlying land. When the ice melts away, the land areas previously covered by ice (above about 40°N) slowly rise. Adjacent areas that were never covered with ice tend to sink. This is known as isostatic rebound and subsidence.

Hydro-isostasy is the loading and unloading by ocean water. It refers to the fact that water from melted land ice creates an additional load on the ocean floor. To attain isostatic equilibrium, the ocean floor is slowly depressed in response to sea level changes. Simultaneously, the continents are flexed upward at their margins. This 'continental levering' may be restored when the water is tied up again in continental ice sheets.

Isostatic subsidence and rebound of the lithosphere not only impact relative sea levels, but also absolute sea levels via changes in the volume of the ocean basins.

As a result of both geoidal eustasy and isostasy, the world-wide distribution of sea level change is spatially non-uniform. Clark et al. (1978) were amongst the first to model the spatially non-uniform deformation of the geoid and the earth's surface in the last 6000 years as a result of viscoelastic isostatic responses to water and ice loads. They distinguished various geographic regions based on differences in Relative Sea Level (RSL) curves in response to the retreat of Northern Hemisphere ice sheets.

Figure 2.18 shows the results of more recent model predictions of the present-day rate of worldwide sea level change in response to early Holocene deglaciation (Mitrovica & Milne, 2002). The sea level change as predicted by Mitrovica and Milne (2002) is due to isostatic adjustments to changes in ice and ocean loading (including interactions with the earth's gravitational field), assuming that Holocene deglaciation was complete 5000 years ago. Hence, the patterns reflect ongoing sea level adjustments during a time in which no meltwater is being added into the oceans. The saturated red zones

are previously glaciated areas that experience ongoing rebound due to glacial unloading and thus RSL fall. §1.2Near these areas, the reduced gravitational attraction associated with the ice mass and thus ocean unloading of the solid surface also play a role. [p55] The saturated blue zones experience RSL rise due to isostatic subsidence§1.2; the seafloor in these zones was previously levered up in response to the nearby depression of the earth's surface by mostly ice. After the decay of the ice sheets, the previously up-levered areas tend toward their pre-ice age state, resulting in sea level rise. Note also the sea level fall in equatorial basins.§1.2 This is due to the redistribution of water to fill the subsiding blue zones. Continental levering is evident in the thin bands of offshore sea level rise and onshore sea level fall along coastlines in the far field from the late Pleistocene ice sheets; due to the additional water load on oceanic regions only, the continents are flexed upward at their margins and downward offshore. The above also implies that sea level curves will differ between oceanic islands and continental margins.

The processes underlying the spatially non-uniform sea level change are further illustrated in Fig. 2.19 (see also Tamisiea et al., 2003). §1.2This figure shows both isostatic and eustatic changes. [p57] The right-hand panel clearly shows that there may be a sea level fall in the vicinity of a melted (or melting) ice sheet or glacier (cf. the saturated red areas in Fig. 2.18). This spatial non-uniformity has implications also for future sea level change in response to projected climatic change. If for instance the Greenland ice sheet were to melt significantly in the next centuries, the sea level change around the Netherlands for instance could just as well be zero.

In addition to eustatic and isostatic effects, there are other factors that locally and regionally influence relative sea level changes, for instance:

- Regional subsidence can occur due to compaction of sediments and withdrawal of subsurface fluids such as groundwater, oil, and natural gas;
- Tectonic activity can cause upward or downward movements of the shore. Areas with significant tectonic movements are for instance the earthquake zones in the western and southwestern Pacific and in the Mediterranean. In these areas shorelines can be uplifted, submerged or tilted by these (sudden) earth movements. In addition, most deltas are situated in slowly subsiding sedimentary basins (tectonic subsidence between 2 and 10 cm per century).

All factors contributing to locally perceived, relative sea level changes are summarised in Fig. 2.20.

Summarizing, curves of relative sea level rise versus time can show large local and regional variations. This is especially true during the second half of the Holocene, the last ca. 6000 years, when the land icecaps had already mostly vanished.

In Fig. 2.21 indications of Holocene sea level changes are given for a number of relatively stable areas, i.e. without major subsidence or uplift (although in the Netherlands the bottom is slowly subsiding).

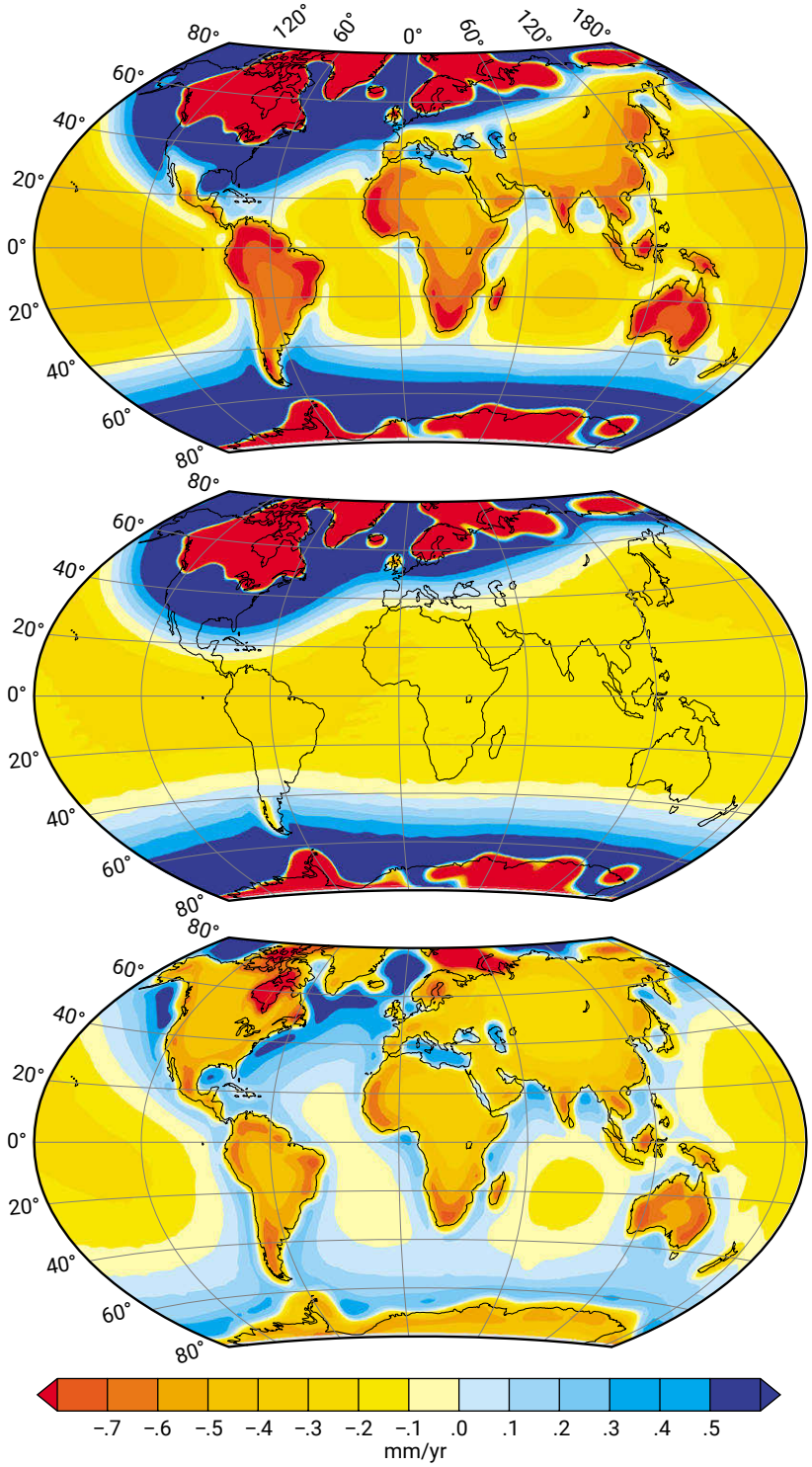

Figure 2.18: Numerical prediction of the present-day rate of change of global sea level due to isostatic adjustments (top) and the contributions to this change from ice loading (centre) and ocean loading (bottom). After Mitrovica and Milne (2002).[§1.2] [Figure corrected; missing colour patches added] [p56]

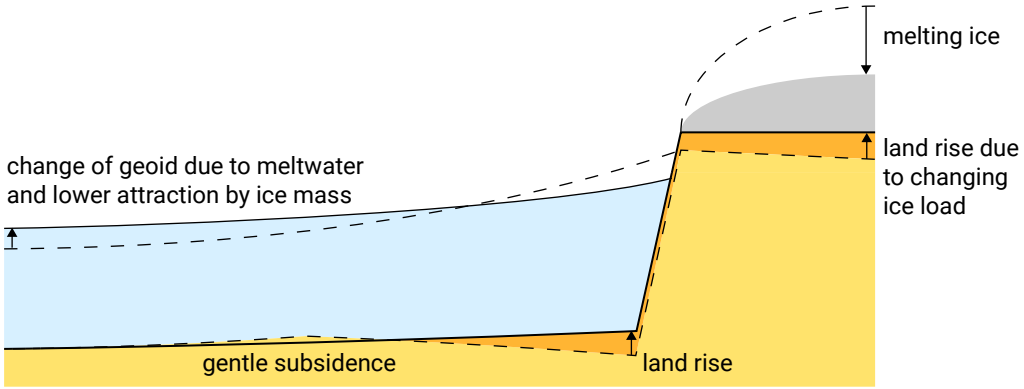

Figure 2.19: Spatially non-uniform sea level response. Dashed lines: the presence of a large ice mass leads to raised water levels in the vicinity of the ice mass (as a result of gravitational attraction) and a lowered solid surface. Solid lines: Melting of the ice sheet causes a fall of the sea surface in a large area centred on the region of mass loss. The solid surface responds to the changes in ice loading and ocean loading.[§1.2] [Figure updated] [p57]

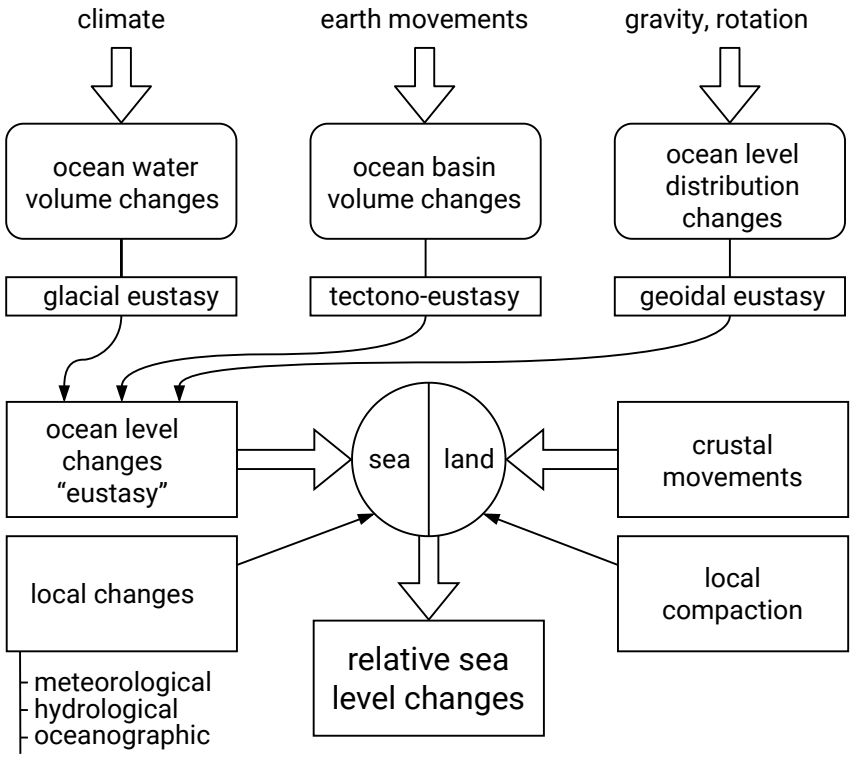

Figure 2.20: Relative mean sea level changes are the result of the three different types of eustasy, vertical crustal movements due to tectonic activity and isostasy, and local compaction.

During the 20th century, the average rate of global sea level rise was about 1.5 mm/yr to 2.0 mm/yr. Satellite measurements taken over the first decade of the 21st century indicated that the rate of sea level rise had gone up to 3.1 mm/yr. Apparently, the present-day rates of increase are in the order of magnitude of millimetres per year which is significantly larger than the recorded rates over the past few thousands of years (see Fig. 2.21). These accelerated rates of sea level rise have been interpreted as

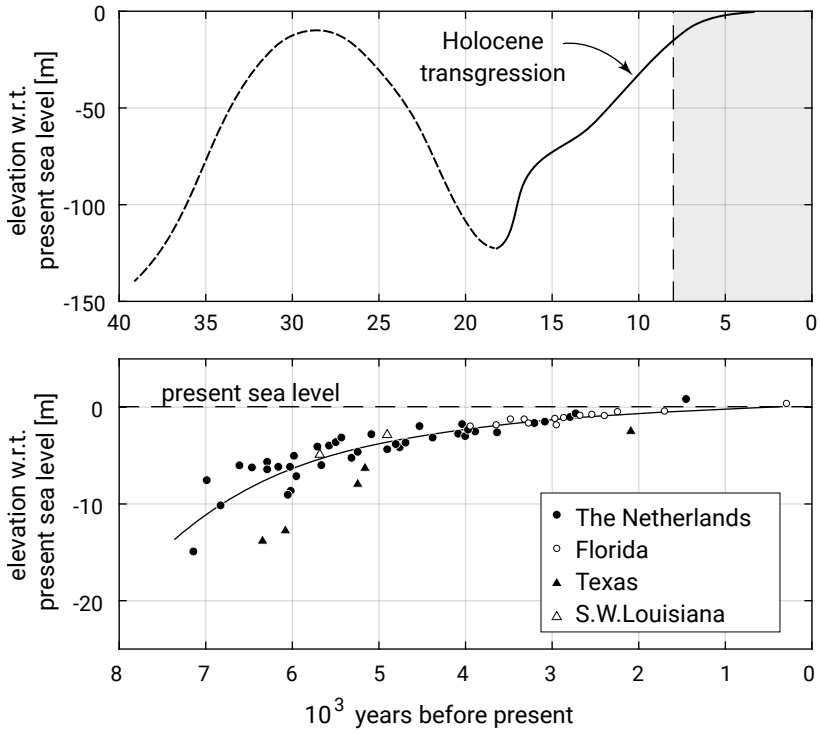

Figure 2.21: Indication of sea level changes in stable areas (no local subsidence or uplift).

evidence that atmospheric warming, since the industrial revolution, has led to thermal expansion of the oceans, melting of mountain glaciers and icecaps (Gornitz & Lebedeff, 1987) and loss of ice from the Greenland and West Antarctic ice sheets.

2.5.2. Role of sea level rise in Holocene coastal evolution

Sea level changes can affect the coastal zone very strongly. The effect of sea level rise can be understood from the well-known concept of Bruun (1954, 1962), which is briefly explained here and treated in more detail in Ch. 7. The Bruun rule assumes that the shoreface has a profile that is in equilibrium with the hydrodynamic forcing. Hence, it states that the shore profile is vertically invariant in space and time relative to mean sea level. Consequently, a sea level rise results in a water depth that is too large to be in equilibrium with the forcing. In other words: extra space has become available for sediment accumulation, the so-called *accommodation space*. In the absence of sediment sources or sinks, equilibrium is again achieved by a landward and upward shift of the profile: the shoreline retreats and a new equilibrium profile forms at the new shoreline position by moving sediments to deeper water (Fig. 2.22).

The world's coasts can be divided into two classes: *transgressive* coastal environments and *regressive* coastal environments. As the shoreline moves seaward or landward in response to sea level changes, it either exposes or inundates coastal areas and, in so doing, causes the character of the coast to change. Additionally, the position of the shoreline influences coastal processes that shape coastal environments. Inundation is

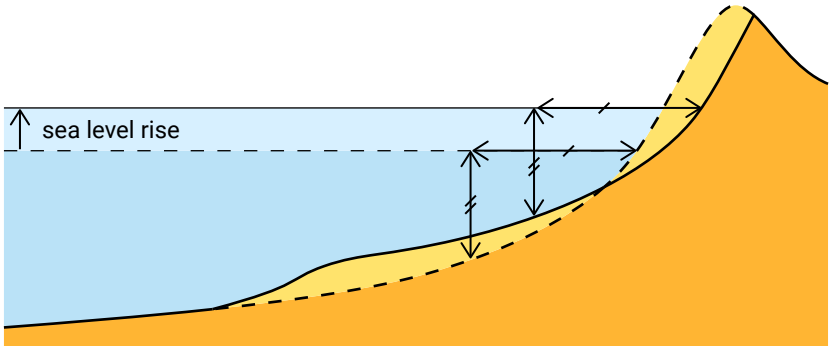

Figure 2.22: Bruun effect: the profile shape remains the same (the length of the vertical and horizontal lines respectively is constant), but the profile moves up and landward as a result of sea level rise. The volume of sediment eroded from the upper profile is equal to the deposited volume in deeper water.

also called *transgression* (§1.1 ~~or simply~~ advance§1.1 of the sea), whereas drying of the land is referred to as *regression* (§1.1 ~~or simply~~ retreat§1.1 of the sea [p59]). Transgressive coastal environments are characterised by lagoons and estuaries. We have seen before that estuaries are semi-enclosed coastal water bodies, which are on one side connected to the sea and on the other side have one or more rivers or streams flowing into it. Rias and fjords are estuaries formed through flooding of low-lying areas; rias are drowned river valleys (for instance Sydney harbour) and fjords are drowned valleys carved out by land ice (see Fig. 2.12). In regressive coastal environments the shoreline moves seaward and estuaries and lagoons that are present get filled in or abandoned.

The global distribution of transgressive and regressive systems is mainly determined by the (late) Holocene relative sea level changes. Sea level changes are relative movements and thus vary from place to place as can be seen from for instance Fig. 2.18. Transgressive coastal environments are well developed in areas that have experienced isostatic subsidence, viz. the middle and south of North America, the middle and south of Europe and the Mediterranean region. In these regions relative sea level has risen at an average rate of 1 mm/yr over the last 7000 years. On the contrary, regressive coastal systems can be found (although not exclusively) in the regions that were located far from glaciers during the last ice age. This includes most of Asia, Oceania, the middle and south of Africa, and South America. In the beginning of the Holocene these areas experienced a relative sea level rise, but this had changed to relative sea level fall later in the Holocene, resulting in a relative sea level fall in the order of a few metres over the last 7000 years. Lagoons and estuaries that have formed in the beginning of the Holocene were filled or abandoned later, so that now evidence of regression is found along those coasts.

Although the global distribution of transgressive and regressive coastal systems is mainly controlled by sea level rise, the amount of sediment supply is very important as well in controlling transgression versus regression. Clearly, sediment supply may counteract the effect of shoreline retreat. For instance, if the rate of sediment supply

keeps up with the rate of sea level rise, the accommodation space created by the sea level rise is filled by incoming sediments and the profile moves upward only; the position of the shoreline remains unchanged. Sediment can be supplied to the coast by for instance rivers and erosion from coastal cliffs or headlands. Through alongshore and cross-shore processes, waves and tides will rework the sediment supplied to the coast, resulting at a certain location in either erosion or deposition of recycled (mainly riverine) sediment. At a very high level of aggregation these sources and losses can be summarised to be represented by the term 'sediment availability'.

Figure 2.23 qualitatively summarises the effects of both relative sea level change and sediment availability on the displacement of the coastline. This type of diagram is called Curray's diagram after Curray (1964).

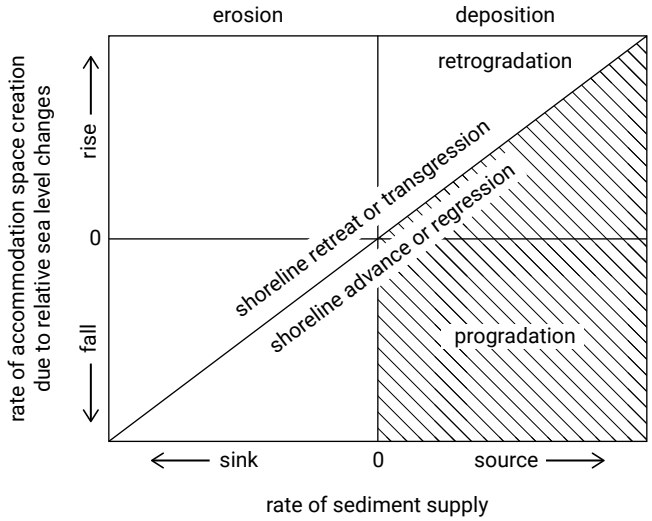

Figure 2.23: Factors controlling shoreline migration after Curray (1964). The effect of relative sea level rise is to create more space to accommodate sediments. If the rate of sediment supply equals the rate of space creation (the diagonal line), the shoreline remains stationary. If the rate of sediment supply is larger than the rate of accommodation space creation (the region below the diagonal), the shoreline advances; if it is smaller the shoreline retreats (the region above the diagonal). The dashed lines indicate progradation or building out of the coast (Intermezzo 2.1).

Curray's diagram shows that in the absence of a net sediment source or sink, regression occurs in the case of a falling sea level – called emergence in that case – and transgression occurs in the case of a rising sea level or submergence. With a net source of sediment, the transition between regression and transgression shifts towards low levels of rising relative sea level, and alternatively, with a net sink of sediment, towards low levels of falling relative sea level. In other words, in areas with erosion the shoreline generally moves landward, inundating the coast (transgression), unless the relative sea level fall is so large that the shoreline migrates seaward. Sediment supply (deposition) results in regressive shorelines moving seaward, except when the regression is counteracted by a large relative sea level rise. This building out of the coast is also called *progradation*. The various names that are used to describe the coastal response are summarized in Intermezzo 2.1.

The main conclusion from Curray's diagram is:

> Whether a shoreline migrates seaward or landward is determined by the combination of relative sea level changes and amount of sediment supply or loss. Seaward-migrating coasts are also referred to as regressive coastlines; landward-migrating coastlines are termed transgressive coastlines.

Intermezzo 2.1 Classification on the basis of sea level change

On the basis of coastal response to substantial sea level changes, various classifications have been proposed in literature. They are invariably based on the balance between sea level change and sediment supply. Some terminology used to describe the coastal response is given here (Fig. 2.24):

Regression	seaward shift of the shoreline → former sea bottom exposed
Transgression	landward shift of shoreline → inundation
Progradation	sediment is deposited such that shoreline moves seaward
Retrogradation	sediment is deposited but shoreline moves landward
Emergence	land emerges out of the water due to relative sea level fall (e.g. due to tectonic uplift: Chile)
Submergence	inland regions are flooded due to relative sea level rise

The classification of Valentin (1952) is a clear example. He simply divides the world's coasts into coasts that have advanced (due to emergence and/or deposition) and coasts that have retreated (due to submergence and/or erosion). The various definitions are also indicated in Curray's diagram.

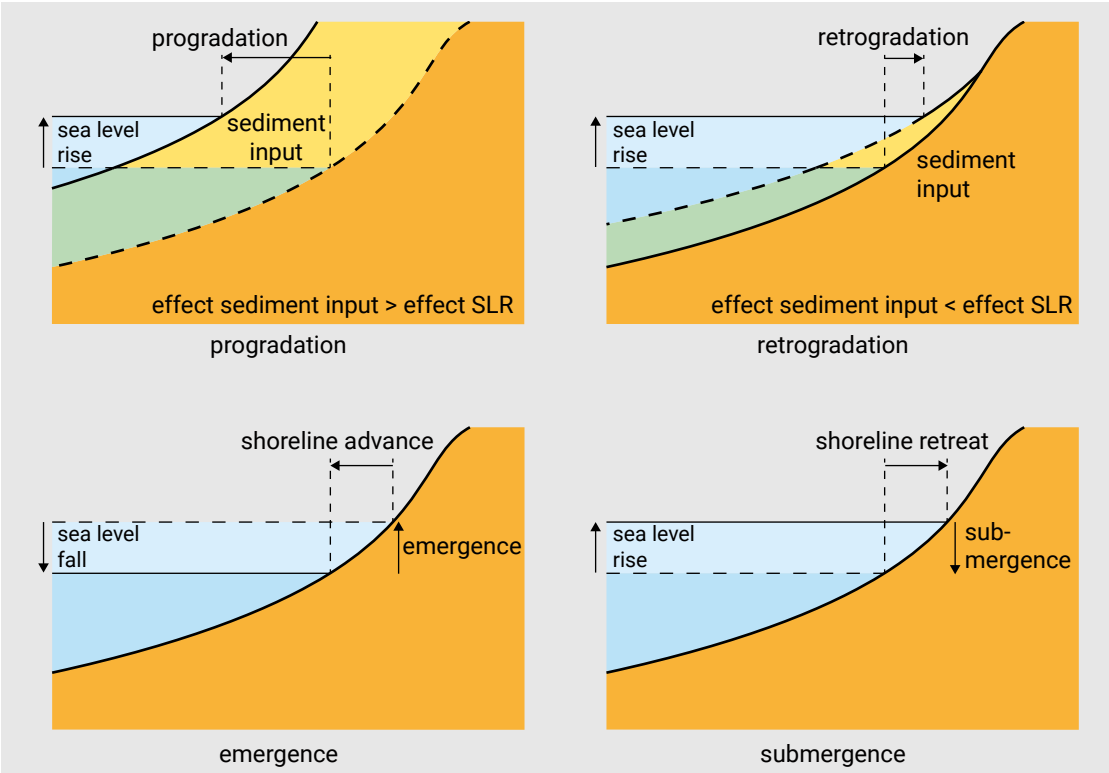

Figure 2.24: Classifications on the basis of sea level change and sediment supply. In the case of sea level rise, the occurrence of progradation or retrogradation depends on the amount of sediment input or loss. Note that the shoreline response in the sketches for emergence and submergence does not take the Bruun effect into account (see Fig. 2.22).

If the amount of erosion due to sea level rise is small compared to sediment deposition, the shoreline may migrate seaward even under conditions of relative sea level rise. The Mississippi delta (see also Intermezzo 2.2) and the central Dutch coast are good examples of regressive systems that have developed despite their location in regions with Holocene relative sea level rise. In regressive coastal environments typically deltas and extensive strand plains (sandy beach and shoreface systems) and chenier plains (muddy tidal flats) are found.

It is important to note that the characteristics of a coast show imprints of different episodes in the history of its development. Australia for instance has a large number of estuaries and lagoons, although the relative sea level fell during the late Holocene. This is related to the dry climate and therefore very low sediment supply. The estuaries that have formed during the rising of sea levels during the early Holocene can still be found at present, since not enough sediments were supplied to fill them in during the late-Holocene sea level fall. Therefore the present-day coastline still shows the signs of early Holocene transgression and does not bear the typical characteristics of regression. Classification apparently implies an integration of the developments over a certain time period. At different moments in time a certain coast might occupy a

different position in the quadrant of Fig. 2.23. The classification class is therefore dependent on the integration period. An example of a situation where progradation and transgression have alternated over the geological history is the central Dutch coast.

Intermezzo 2.2 Geological delta formation

Most of the present active deltas are geologically very young features; some are only a few hundred years old. Because a delta develops at the coast, its existence is, in part, controlled by the sea level. It therefore was and still is vulnerable to sea level rise, too. During periods of extensive glaciation, sea levels were much lower and rivers traversed the present continental shelves, dumping their sediment loads at or near the outer shelf edges. This suspended sediment cascaded down the continental slopes in turbulent, high-density flows called turbidity currents. New deltas did not form during this period, and deltas that had previously existed near the positions of present-day coasts were abandoned and entrenched by rivers as they flowed across the continental shelves. Melting glaciers brought a rapid rise of sea level, and river mouths retreated so rapidly that deltas could not develop. Finally, about 7000 years ago, the Holocene sea level rise slowed, and in some parts of the world it stabilised at approximately its present position. Where conditions were appropriate, deltas began to develop as large quantities of river sediment accumulated.

Not all present-day deltas are only a maximum of a few thousand years old. Many of them have formed on ancestral deltas built up during previous interglacial periods. A few, such as the Mississippi and Niger Deltas, are underlain by ancestral deltas that formed tens of millions of years ago. The upper regions of these mature deltas are also ancient, but their active delta lobes are only between 3000 and 6000 years old. The lower Mississippi Delta includes 16 detectable lobes. A new lobe forms whenever the location of the river mouth changes. The channels of abandoned lobes fill up with sediment, contributed both by the river, by the waves and by the tides of the coast. The present delta lobe of the Mississippi dates back only 600 years; its most active portion has developed since New Orleans was founded in 1717.

2.5.3. More recent coastal development

A worldwide inventory by Bird (1985) indicates that approximately 70 % of the world's sandy coastlines have shown retreat over a period of decades; less than 10 % have shown net progradation, while the remaining 20 % to 25 % have remained approximately stable. Recently, an analysis of satellite-derived shoreline data for 1984–2016 showed that 24 % of the world's sandy beaches–sandy beaches making up 31 % of the world's ice-free shorelines–are eroding at rates exceeding §1.1 ~~0.5~~ [p63] 0.5 m/yr, while 28 % are accreting and 48 % are stable (Luijendijk et al., 2018).

While shoreline retreat on a geological timescale is undoubtedly connected with eustatic sea level rise, it is more or less generally assumed that even the relatively small sea level changes of the last century are driving this worldwide tendency of shore retreat (cf. Vellinga & Leatherman, 1989).

The rate of sea level rise is likely to increase during the 21st century, although considerable controversy exists about the likely size of the increase. The latest[3] International Panel on Climate Change (IPCC) projections indicate a sea level rise range from §1.1 ~~0.26 m to 0.82 m for the period 2081-2100 relative to 1986-2005 (IPCC, 2014)~~ §1.1 0.28 m to 1.02 m by 2100 relative to the 1995-2014 average (IPCC, 2021) [p64]. Any future rise in the mean sea level will result in the retreat of unprotected coastlines. Low-lying countries without resources for extensive coastal defence are the most vulnerable to this danger. Figure 2.25 shows Bangladesh, which lies in the Ganges-Brahmaputra Delta on the Bay of Bengal. About 25 000 km^2 (18 % of the total land area) will be inundated with a sea level rise of 1 m. A sea level rise of 0.5 m by the year 2100, which is within the IPCC estimated range of 'global' sea level rise, would inundate more than 10 000 km^2.

It must be borne in mind though that there generally exists a complicated interaction of agents affecting shore retreat (as illustrated in Fig. 2.26). For instance, both the sea level rise relative to the land and its effects are rather site-specific. Besides the eustatic sea level rise, local contributions can for instance be due to glacial rebound, subsidence, compaction, and changes in ocean circulation. Additional (and often dominating) causes of erosion can be due to alongshore or cross-shore losses, which in their turn can be due to a variety of causes such as the physical geometry (e.g. headlands, submarine canyons), hydraulic boundary conditions (e.g. related to waves, tides, wind) or human interference (e.g. harbours, erosion-mitigating structures). As seen in Ch. 1, human interference at the land side can also influence the sediment budgets of the coastal zone, for instance by the construction of dams, as has been done in many rivers, especially in Asia.

2.6. Nature and abundance of coastal material

2.6.1. Sources of sediments deposits

This book focuses on depositional coastal environments. By that we mean coastal environments consisting of soft or loose material (mainly sand or mud) that has been deposited there at some point in the past. At present these materials might be subject to either erosion or accretion due to the impact of waves and tides. The loose material is present in the form of shorefaces, beaches and accompanying dunes and barriers. Besides by dunes, beaches can also be backed by rocky material. The loose material

[3] §1.1 ~~5th assessment report, 2014~~ §1.1 The Working Group I contribution to the 6th Assessment Report, 2021; the 5th Assessment Report was finalized in 2014 (IPCC, 2014). [p64]

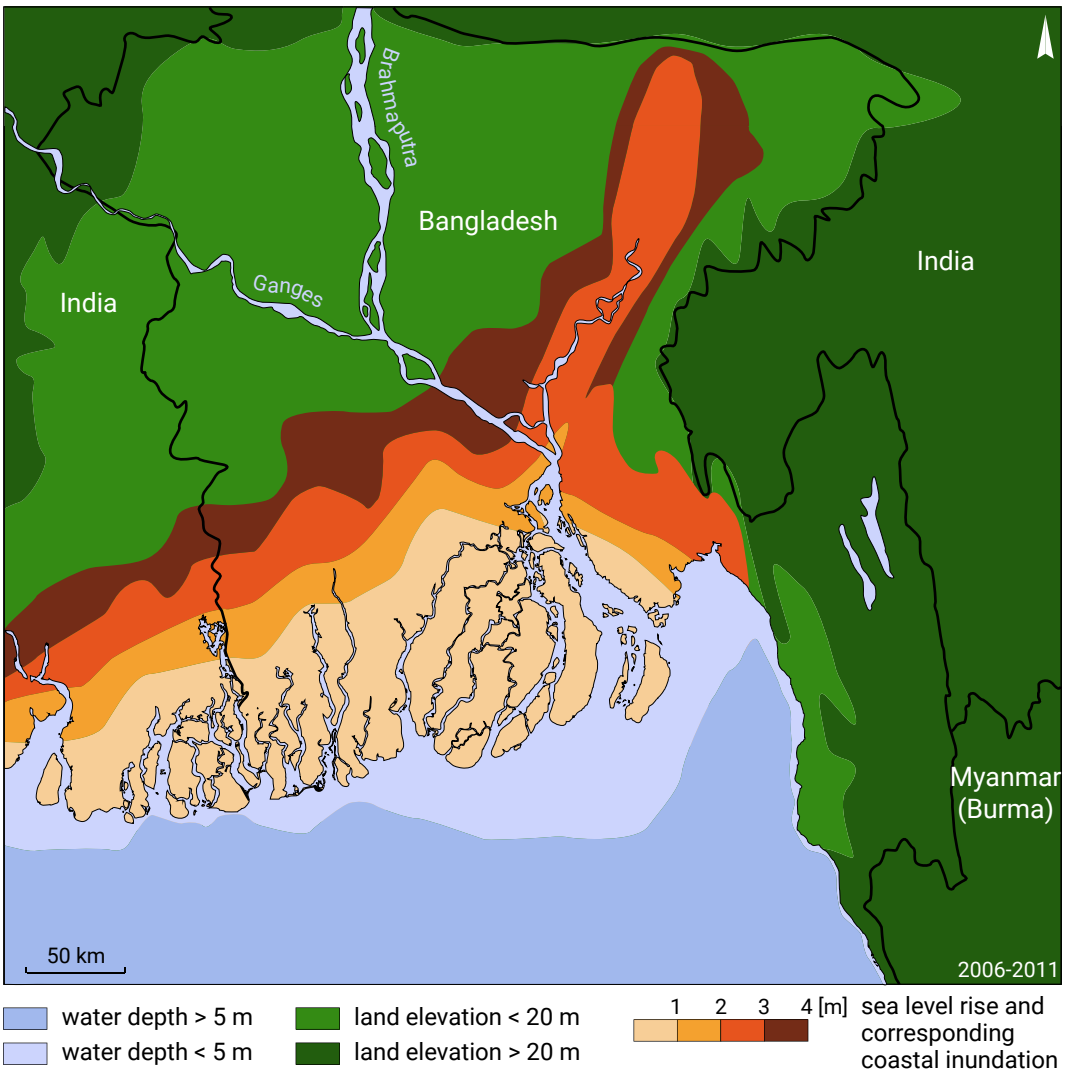

Figure 2.25: The low-lying delta of the Ganges-Brahmaputra. The map shows the extent of the projected flooding that is likely to occur for a sea level rise from 1 m up to 4 m as estimated from elevation contours.

that we find on coasts can have various origins. We distinguish continental sediments and carbonate sediments:

Continental sediments are the major type of sand of the coastal area and are formed from weathered continental rock, usually granite. They are composed of silicate minerals, with quartz and feldspar being the most abundant. Quartz is very resistant, feldspar easily weathers into fines. Granite and basalt are also the source of heavy minerals (with a density larger than quartz). Streaks and patches of dark-coloured grains – rich in heavy minerals – can be found on some beaches. The majority of continental sediments found in coastal deposits is not from current rivers, but consists of older Holocene sediments or Pleistocene sediments reworked during the Holocene by marine processes.

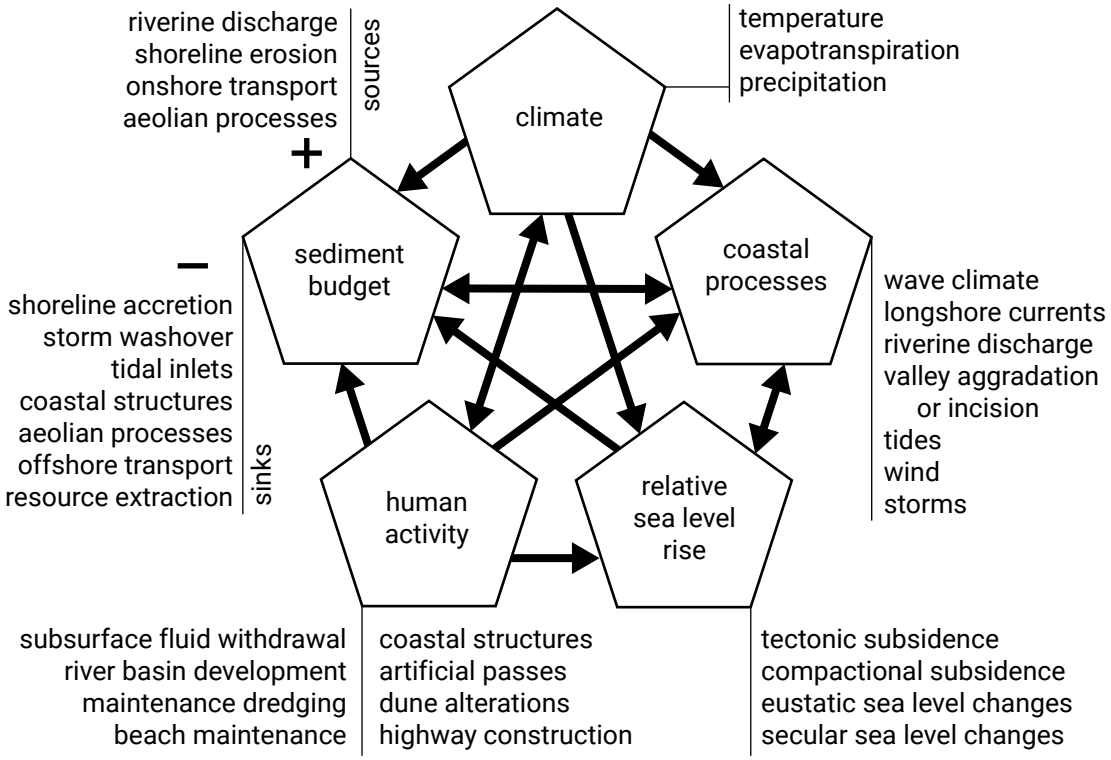

Figure 2.26: Interaction of agents affecting shore retreat and erosion according to Morton (1977).

Carbonate sediments are formed from calcium carbonate. Most of these grains are fragments of shells or remains of marine life. Marine carbonates are the second major source of sands on the coast.

2.6.2. Sediment sizes

Not only the source but also the size of sediments varies. The size of sediments found in a coastal system can range from large boulders with diameters exceeding 25 cm to very fine material like clay. The size of the sediment grains can be used to classify the sediment. An example of this classification is the Wentworth classification, often used by geologists (see Table 2.2).

According to this classification, sand is defined as grains with a size between 63 µm (lower limit very fine sand) and 2 mm (upper limit very coarse sand). Sand-sized material consists mostly of quartz or carbonate and is the most abundant coastal material. Sand is a non-cohesive material; the individual near-spherical grains do not stick together and are very resilient. Material with a grain size smaller than 63 µm can be defined as either clay or silt. While silts tend to have larger particle sizes than clays, silts and clays are mineralogically and chemically quite distinct, see Intermezzo 2.3.

Often both silt and clay particles are found together. A fluid-sediment mixture of (salt) water, silt, clay and organic materials is named *mud*. Also, some very fine sand may be present in mud.

Based on the size of the beach material, the world's beaches can be classified as muddy coasts, sandy coasts or gravel/shingle coasts. The main focus of this book is on sandy coasts, although the finer sediments of muddy coasts are also considered.

Table 2.2: Unified Soils and Wentworth classifications of sediments on the basis of size. ASTM mesh refers to the ASTM standard for sieve aperture sizes and D_n is the nominal diameter. For definition of the ϕ scale, see Sect. 6.2.2.

Unified Soils Classification	ASTM mesh	D_n [mm]	ϕ value	Wentworth Classification
cobble		256.0	−8	boulder
		76.0	−6.25	cobble
coarse gravel		64.0	−6	
		19.0	−4.25	pebble
fine gravel	4	4.76	−2.25	
coarse sand	5	4.0	−2.0	gravel
	10	2.0	−1.0	very coarse sand
	18	1.0	0.0	coarse sand
medium sand	25	0.5	1.0	
	40	0.42	1.25	medium sand
	60	0.25	2.0	fine sand
fine sand	120	0.125	3.0	
	200	0.074	3.75	very fine sand
silt	230	0.063	4.0	silt
		0.0039	8.0	clay
clay		0.0024	12.0	colloid

Intermezzo 2.3 Properties of silt and clay

Silts are soils with fine, nearly spherical grains that do not include clay minerals. Mineralogically, silt is composed of quartz and feldspar. Clay on the other hand mainly consists of clay minerals that originate from the weathering of feldspar. Chemically, clay minerals are layered metal silicates: thin plate-shaped particles held together by electrostatic forces (Figs. 2.27 and 2.28). Hence, clays have strong cohesive properties.

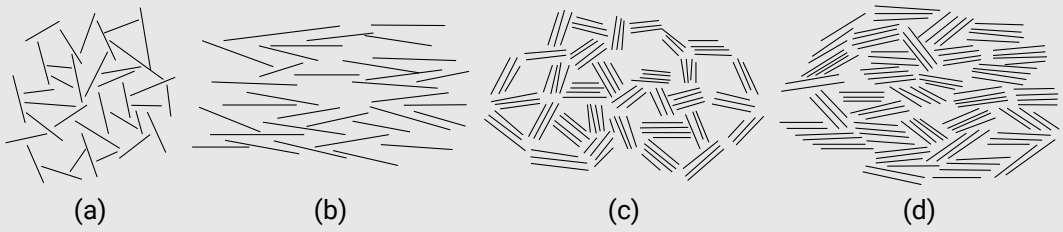

Figure 2.27: Elementary particle arrangements of clay with (a) interaction between individual particles in a 'card-house' structure (flocculation); (b) dispersed individual particles; (c) and (d) examples of group interaction showing also plate to plate contact.

Figure 2.28: 3D impression of a group of clay particles.

When the distance between particles is small enough, they can become stuck in a 'card-house' structure. This process, called flocculation, is enhanced by ionic constituents present in saline environments and the presence of organic material.

2.6.3. Geographical variation

The material present on beaches and shorefaces shows a latitudinal zonality. Figure 2.29 shows the relative frequency of inner continental shelf sediment type (up to about 60 m water depth). It was first published by Hayes (1967) who described the following correlations between coastal climatic zones and sediment types:

- Mud is most abundant off areas with high temperatures and high rainfall (humid tropics);
- Sand is abundant everywhere and increases to a maximum in the subtropics and lower mid-latitudes (between 20° to 40°). These are the intermediate zones of moderate temperatures and rainfall. Sand includes both quartz and carbonate sands;
- Gravel is most common off areas of low temperature (subpolar and polar);
- Coral is most common in areas with high (water) temperatures;
- Rock is generally more abundant in cold areas but its distribution is also strongly controlled by plate tectonic setting (see Sect. 2.3.2);
- Shell distribution shows no strong latitudinal dependency.

These patterns are strongly controlled by climatic factors influencing the availability of the material to the coast and the coastal processes.

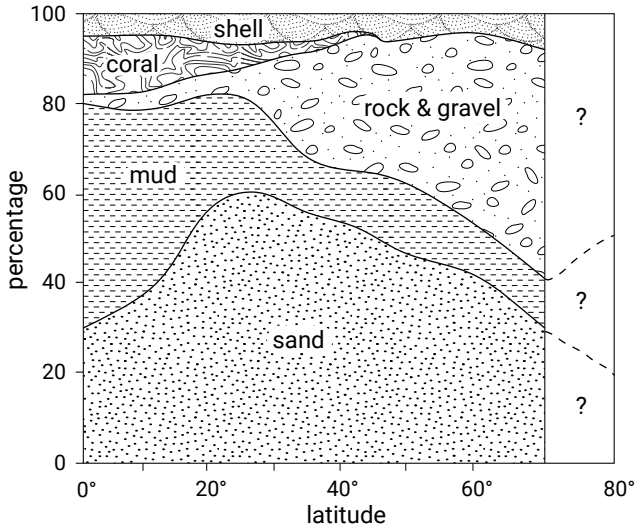

Figure 2.29: Relative frequency of inner continental shelf (up to about 60 m depth) sediment types by latitude according to Hayes (1967).

Availability of the material to the coast

The availability of the material to the coast is determined by:

1. Topographic relief and global precipitation pattern, and hence the presence or absence of large rivers, determine the availability of sediments to the coastal system (see Sect. 2.3.3). Figure 2.30 shows the global distribution of mechanical erosion and the solid discharge of the world's major rivers. This indicates that the supply of sandy sediments to the coast is largest between 40°N and 40°S. Figure 2.31 illustrates the influence of topographic relief and catchment size on the beach material;
2. The type of weathering (mechanical or chemical) determines whether a coast receives mainly sand or mud. Mud is produced through chemical weathering which is enhanced for high temperatures in the source area and for high rainfall. Hence chemical weathering is enhanced in the tropics. The ratio of mud to sand supply to the coast increases as chemical weathering increases. If chemical weathering is intense, the majority of the sediment reaching the coast is mud;
3. Pleistocene glaciation (see Sect. 2.4) has produced rocks and gravel, which are thus restricted to subpolar and polar zones. Gravel is generally too coarse to be transported to the coast by rivers (except on leading-edge coasts);
4. High water temperatures in the tropics are responsible for the growth of organisms responsible for the formation of coral and carbonate sands (see Intermezzo 2.4). Figure 2.33 shows the global distribution of coral reefs and carbonate sands. There is a latitudinal and longitudinal variation; at low latitudes and in the west of the oceans the temperature is more favourable (higher) than in the east. This is caused by the tropical trade winds blowing towards the west (see Ch. 4). By contrast, most of the sands outside the tropics, e.g. in European waters, consist of quartz minerals.

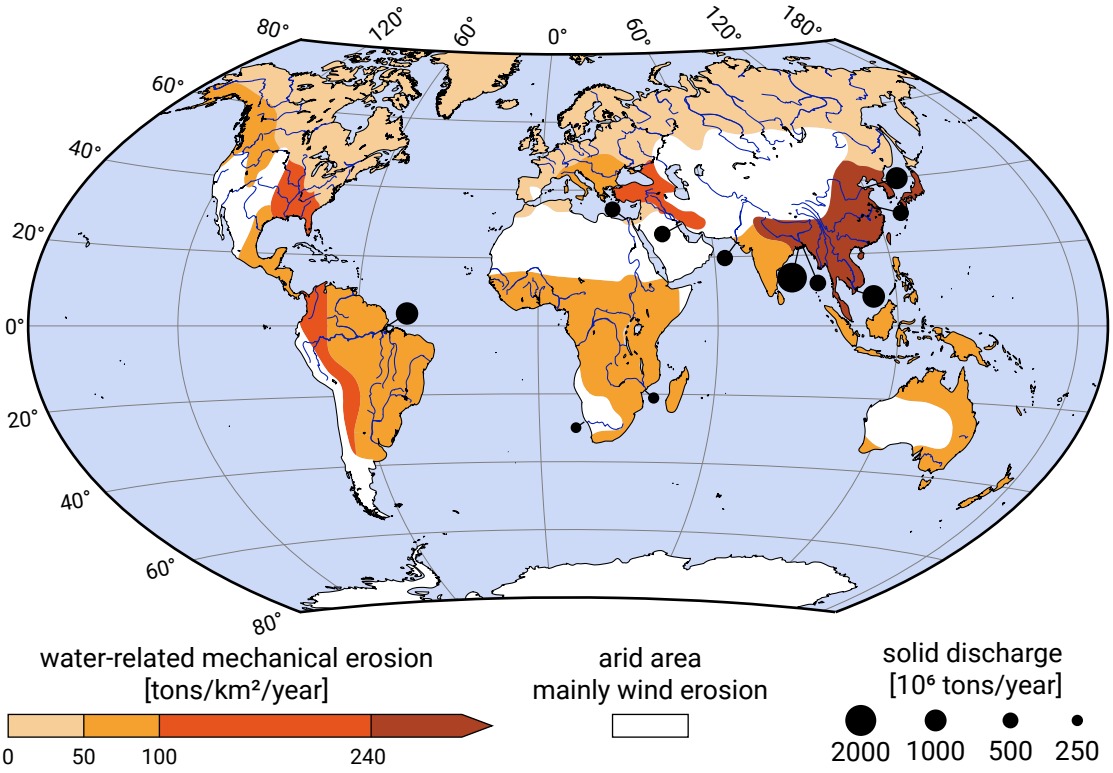

Figure 2.30: Global distribution of mechanical erosion.

Figure 2.31: Spiaggia del Cannello, a 350 m long beach on the southernmost part of the island Elba, Italy. It consists of white and black pebbles that get smaller nearer the water line. The coarse beach material is supplied by short and steep rivers. Photo by Erik Mosselman (‘Credits’ on page 579).

Intermezzo 2.4 Coral reefs

The term coral reef refers to rigid subaqueous limestone formations consisting of calcium carbonates. The limestone formations are accumulations of the cases that polyps build around themselves (using calcium from the water) and that remain

after the polyps have died. The case of one dead polyp forms the foundation of the case of a next polyp. The coral reef ecosystem is based on a closed energy cycle. Warm water and the penetration of sunlight are essential to the development of coral reefs. The Indo-Pacific region has the most extensive coral structures. In the Atlantic region the corals are most often attached to other structures and therefore are said not to be true coral reefs. Coral reefs are, like tropical rain forests, among the most complex communities on the earth, and rock-producing reef communities are among the most ancient life forms found in the fossil record. Because of their complexity, the dynamics of coral reefs are not yet well understood.

Coral reefs are important for tourism, fisheries and shoreline protection. Many low-income communities depend on reefs to protect their property against flooding by high tides and wind set-up. Unfortunately, during the last centuries coral reefs have been adversely affected by humans. Some of the most widespread impacts are water pollution from various human activities, deforestation (and thus soil erosion leading to increased turbidity), dredge and fill operations, overharvesting of fish and shellfish, and the harvesting of some corals for souvenirs. All forms of stress on the coral retard its growth. Destruction has long-lasting effects, since natural recovery would take thousands of years. Implantation experiments have not been successful.

Where reefs border the coast they are termed fringing reefs; where they lie offshore, enclosing a lagoon, they are known as barrier reefs; and where they encircle a lagoon, they are called atolls (Fig. 2.32). Barrier reefs and atolls form under the influence of relative sea level rise, the reefs growing vertically upward with the rising water level. Atolls form from fringing reefs surrounding an island. If the land sinks or the sea rises, the polyps build upwards and seawards in a ring around the island. When the island is completely submerged, a lagoon is formed with a ring of atolls around it.

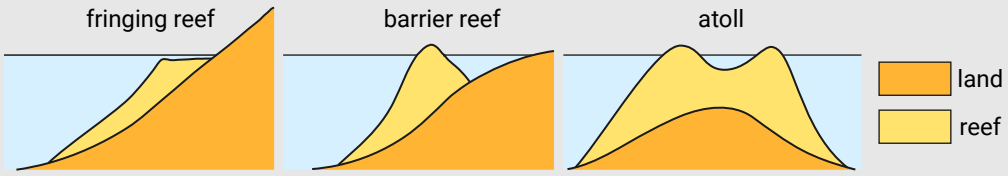

Figure 2.32: Reef types.

Atolls are primarily found in isolated groups in the western Pacific Ocean and the Indian Ocean (Maldives). Small low islands composed of carbonate sands may form on these reefs. These islands are quite vulnerable to inundation, and to tropical storms. Reef islands are naturally dynamic; carbonate sediment production, erosion, deposition and cementation can occur concurrently.

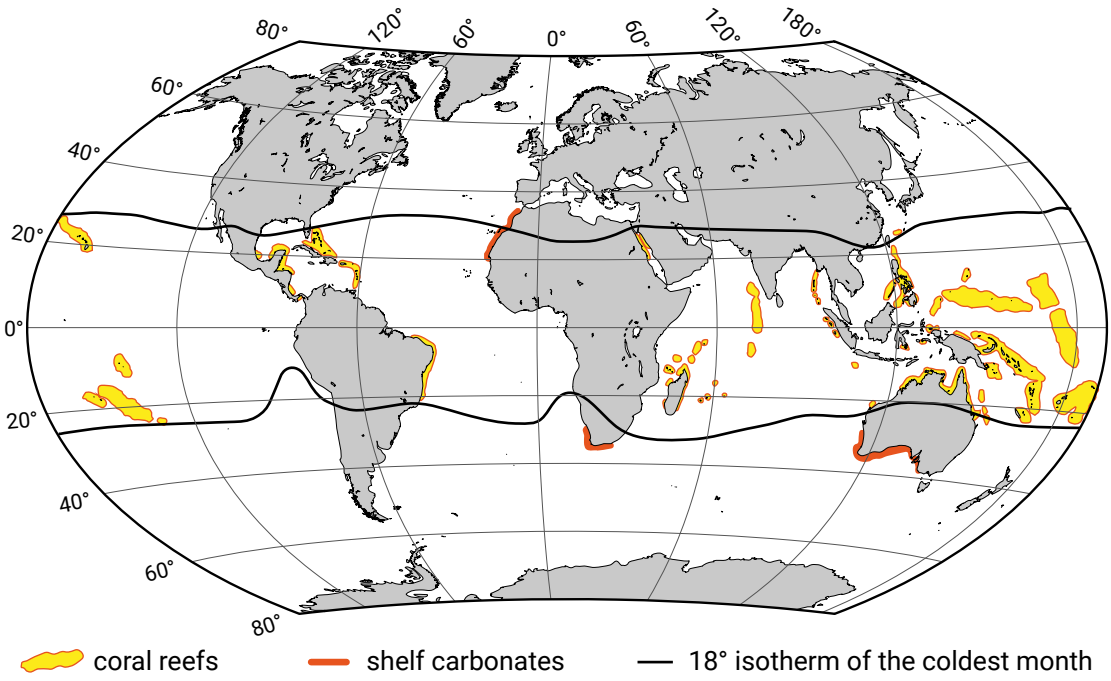

Figure 2.33: Extensive coral reefs and known areas of major supply of shelf carbonate sands to the coast are found at lower latitudes. Coasts at these latitudes are named low-latitude coasts. The occurrence of coral reefs is to a large extent governed by temperature as indicated by the 18 °C isotherm (of air) of the coldest month.

Coastal processes

Besides availability of the material, coastal processes also play an important role in determining the type of material found at a certain location:

- Erosion of rock into gravel by coastal processes;
- The winnowing out of muddy material by wave and tidal processes. In energetic wave environments, fine muddy sediment cannot settle. Sand on the other hand is deposited on the coasts in wave-agitated energetic conditions. This means that even though fines dominate many of the world's river sediment discharges, they will only deposit in low-energy conditions, such as in estuaries and far offshore. On a global scale, the moderate wave climate in the tropics and subtropics (see Ch. 4) enhances tropical mud deposition at low-latitude coasts;
- In the case of large concentrations of silt and clay particles, the concentration of the particles is large enough that enhanced deposition through flocculation can take place.

2.6.4. Muddy coasts

Muddy coasts can be found at all latitudes and on all continents, but are mostly found in tropical areas, particularly in Asia, where they settle in quiet areas and near river mouths. An example of a muddy coast is the Guyana coast in South America. This

1600 km long coast of Guyana, Surinam, French Guyana, and parts of Brazil and Venezuela consists mainly of mud transported to the coast by the Orinoco and Amazon Rivers. Along large parts of the coast, mangroves are found (see Sect. 2.6.6). Other examples of mud coasts can be found near the mouths of the Mississippi River (USA) and the Yellow River (China). Mud also plays an important role in parts of the coastal system of the Netherlands. The low-lying parts of the Netherlands are mainly formed by sediments carried by the rivers Rhine, Meuse and Scheldt. Especially the estuarine area in the southwest (Zeeland) and the Wadden Sea are influenced by mud (see Fig. 2.34). Besides, there is a large supply from the southern North Sea and the Channel.

Figure 2.34: Satellite image of the Wadden Sea from the Sentinel-2 mission of April 5, 2020. Sentinel satellite data are retrieved from satellietdataportaal.nl (https://www.spaceoffice.nl/nl/satellietdataportaal/). See also https://sentinel.esa.int/web/sentinel/missions/sentinel-2 for more information about the Sentinel-2 mission.

2.6.5. Sandy coasts

Short (2005) lists the most extensive sand coasts on each continent:

North America the southeast and Gulf coasts, both low-gradient passive-margin coasts supplied by numerous rivers including the Mississippi, with the sand reworked onshore by a high-energy wave environment. However, coastal dunes are poorly developed. Furthermore, parts of the west coast exposed to high shelf sediment supply and winds to build dunes.

South America massive long-term sand supply to the entire east coast, leading to essentially a sand barrier/dune coast from the Amazon south to Argentina. Long beach-barrier-dune systems exist for much of the coast.

Africa beach, barrier and dune systems ring most of the continent, with sand supplies by local rivers, including the Nile, Niger, and Orange, and on the most exposed coasts there is shelf supply of quartz, and in the south also of carbonate sands.

Eurasia sand dominates most of the exposed western (Europe-Mediterranean), southern (India), and eastern shores (Southeast Asia-China), with some substantial river systems and deltas and extensive sand barriers in South India and Sri Lanka.

Australia 50 % of passive-margin coast consists of sand deposits, with low-energy beaches in the north and high-energy beaches and dune systems across the south. Supply comes from rivers and shelf in the north, from shelf quartz in the southeast and from carbonate in the south and west.

2.6.6. Vegetation

Mangroves and salt marshes

On the fringes of estuaries and other basins – in the intertidal areas between high and low water level – salt-resistant vegetation can establish a foothold. The vegetation requires not only calm conditions but also a silty substratum to germinate. The silty character keeps the soil moist, also during low tidal levels. The calm conditions and the silty soil are closely related, since only in such conditions the finer particles can settle. When conditions remain favourable, the number of species increases and the plant cover gets denser. The type of vegetation depends strongly on climatic conditions. While salt marshes are mostly found in moderate climate zones (hence on mid-latitude coasts, e.g. along the southern North Sea), mangroves favour tropical and subtropical climates (see Fig. 2.35).

A salt marsh may be a few metres wide or it may occupy the entire estuary except for the tidal channels. In Fig. 2.36, a cross-section of a salt marsh is drawn. This figure shows the different zones within the marshland, that can be distinguished by the different species that are present. The upper limits of the salt marsh coincide with the landward or upper limit of the spring high tide, the highest level of regular inundation and sediment supply.

Individual marsh flats can develop into extremely valuable nature resorts. Apart from many specific vegetation species, animals use them for breeding, feeding and during seasonal migrations. Beautiful examples of such marshes in the Netherlands are the Wadden Sea and the tidal flats of Eastern and Western Scheldt (see Fig. 2.37).

For hundreds of years, the Dutch, Germans, and Danes have been converting marshes to farmland by draining them through a system of dams, dikes, and canals. This process has now been stopped, mainly because the ecological value of the tidal wetlands has been recognised and the Wadden Sea has been declared a nature reserve.

The marsh environment is quite similar to that of river and delta floodplains with channels, meandering or not, cutting through the marshy plain. This system delivers

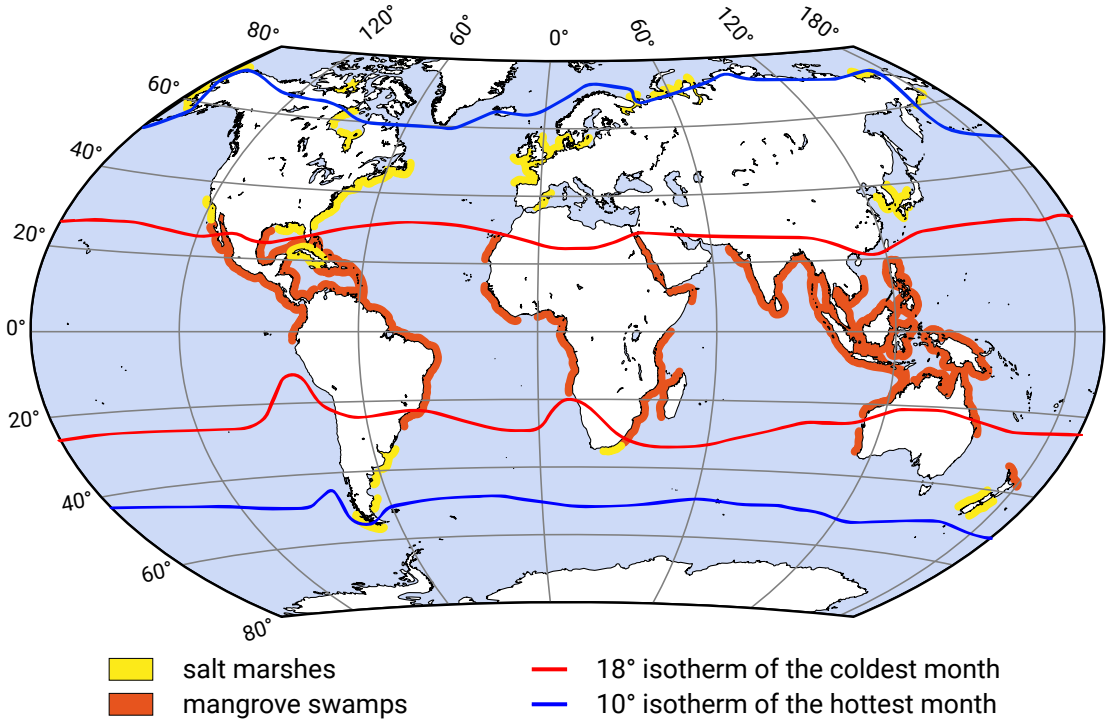

Figure 2.35: Global distribution of salt marshes and mangrove swamps. Mangroves are mostly found at low-latitude coasts and salt marshes at mid-latitude coasts. The climate zones are indicated by the isotherms of (air) temperature of the hottest and coldest months.

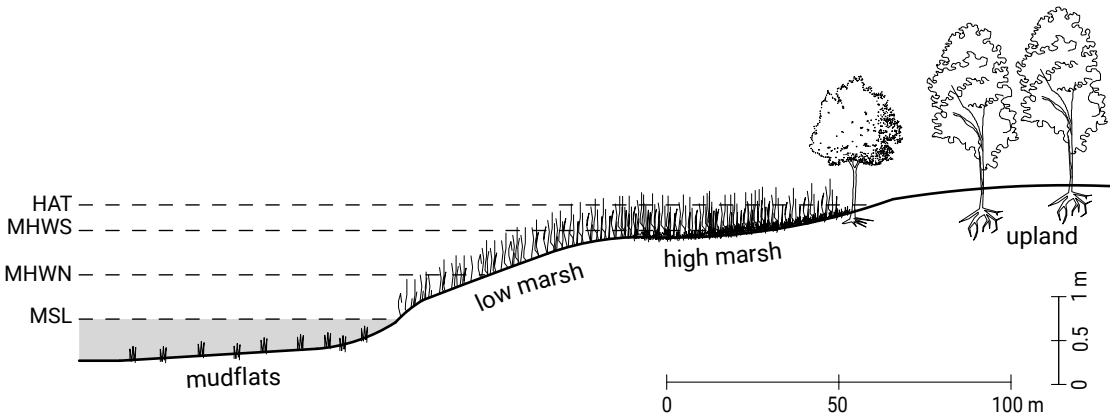

Figure 2.36: Typical cross-section of a salt marsh. The tidal levels are explained in App. C.

sediment to the marsh in two ways: by regular but slow flooding of the marsh by turbid water carried by sluggish currents that permit settling; and by storm tides that push large amounts of sediment-laden water onto the marsh and deposit considerable sediment in a short time. By reducing current velocities near the bottom, sedimentation is enhanced by the vegetation. In addition to their positive role in catching sediment to the substrate, marsh grasses are very important sediment stabilisers. They prevent or inhibit currents and waves from removing sediment from the vegetated substrate, partly by their root system (strengthening the soil), partly by reducing current velocities. An extensive marsh is a sign of a natural estuary that has largely filled with

Figure 2.37: Lower salt marsh at Western Scheldt. Photo by Marcel J.F. Stive (‘Credits’ on page 579).

sediment. Cord grass is a type of vegetation often introduced artificially to enhance siltation and formation of new farmland.

Although a paradigm for marsh development has been given here, the present global situation is one of eroding marshes due to sea level rise.

Mangroves are woody trees of various taxonomic groups (Fig. 2.38). Thick tangles of shrub and tree roots, commonly called swamps but properly known as mangles, form an almost impenetrable wall at about water level (Fig. 2.39). Most trees grow from 2 m to about 8 m high, although some are much higher, depending on the species and the environmental conditions – rare stands may be twice that height. The root systems of mangroves are not only dense, but also diverse in appearance and function. In places like tropical Australia or India, there are more than 20 species of mangroves.

Like salt marshes, mangroves accumulate and stabilise sediment and protect the coastline from erosion. They provide a resilient coastal defence against storms and hurricanes as long as the conditions are not too rough. Furthermore, mangroves play an essential role as the incubator of the coastal ecosystem. The thickets of mangrove roots at the water line provide a sheltered habitat for a special community of organisms that are adapted to an environment intermediate between land and water. Barnacles and oysters encrust the roots and branches. Fish, snails, and snakes all find protection, nesting sites, and food among the roots.

Because the mangrove swamps are rich in expensive seafood like shrimp, the shores are often turned into artificial fish and shrimp farms. Destruction of mangrove forests and their replacement by shrimp farms is a major factor responsible for the increase

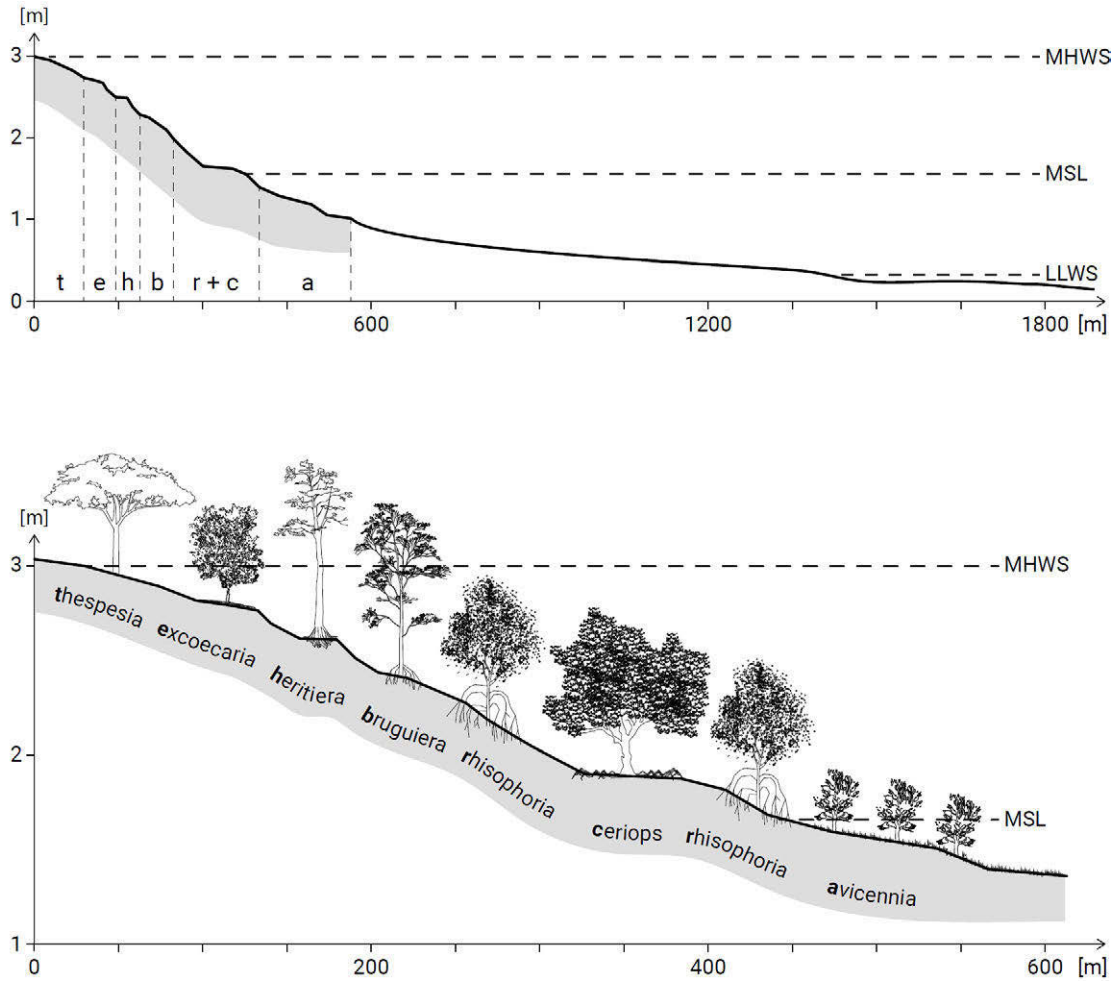

Figure 2.38: Typical cross-section of a mangrove swamp with different species present at different elevations. The tidal levels are explained in App. C.

in the severity of flooding in many coastal areas, especially in India and Indonesia. Water pollution and cutting of trees for firewood also hampers the continued growth of mangrove forest. This means that mangrove vegetation is disappearing rapidly. Once the forest has disappeared, it becomes clear how effective the forest was in preventing erosion of the generally silty coastline. Reforestation is extremely difficult since the young trees are quite vulnerable.

Dune vegetation

The beach above the high water line is another place where non-marine plant life can survive (see e.g. Fig. 2.40). On the dry beach conditions are still quite harsh: the sand has very little capacity to hold moisture, so that plants growing here must be drought-resistant. When the first vegetation develops on the dry beach, it forms a nucleus for the formation of dunes. The first vegetation provides some shelter against the wind, which enables sand to accumulate and its roots stabilise the sand. In this way, the first plants create small, slightly elevated undulations in the flat beach. These higher places provide storage areas for fresh water, creating more favourable conditions for species

Figure 2.39: Mangroves in the Mekong delta, Vietnam. Photo by Marcel J.F. Stive ('Credits' on page 579).

such as the well-known Marram (or *Helm* in Dutch). Marram has a more extensive root system and forms a dense cover with its stems and leaves. In this way, small dunes are formed, and the higher the dunes, the better the conditions for a wider variety of vegetation. In the dunes, freshwater is caught and this drains slowly to the lower parts of the slopes where species requiring more water can establish themselves. Note that part of the Dutch drinking water originates from dune water.

The vegetation cover of the dunes prevents the 'wandering' of dunes by aeolian (wind-blown) transport, which is very important since dunes form an important part of the sea defence, not only in the Netherlands, but also in other parts of the world. In the Netherlands Marram is used extensively to provide artificial protection to young dunes and to prevent wind erosion. The species are site-specific, in the sense that the composition of the soil and the climate play an important role in what species are able to survive. This means that the use of vegetation to stabilise sandy shores must always be based on observations of locally available and successful species.

2.7. Process-based classification

2.7.1. Dominance of fluvial, wave or tidal processes

Sections 2.3 and 2.5 described the classification of coastal systems on the basis of plate tectonic setting and substantial sea level changes respectively. Superimposed on these large-scale characteristics are regional- and local-scale variations in coastal landforms. One way to distinguish between features at these scales is to look at the hydraulic

Figure 2.40: Primary vegetation development at the Sand Engine (in Dutch: De Zandmotor), The Netherlands. Photo by Marcel J.F. Stive ('Credits' on page 579).

boundary forcing to the coastal system; the dominance of fluvial, wave or tidal processes can be seen to influence the shape of coastal features.

A process-based classification on the basis of the relative importance of fluvial sediment supply and wave and tidal action is relevant to trailing-edge coasts (such as the USA East Coast) and to the typical Dutch situation (being an example of a marginal sea system; other ones being the Gulf of Mexico and the Chinese coast).

Such a process-based classification of coastal systems implies that we can distinguish between various typical coastal morphologies on the basis of two criteria:

1. How important has fluvial sediment input been for shaping the coastal system?
2. Are sediment deposits being reworked by waves or tides (wave dominance or tide dominance)?

Based on the answers to those questions, the following systems can be discerned (with the numbers in the list referring to the numbers in Fig. 2.41 and the respective sketches in Fig. 2.42):

1. Wave-dominated uninterrupted coastline (or pocket beaches) with tidal influence at the lower shoreface only
2. Wave-dominated deltaic (i.e. built out by fluvial sediment supply) coastline
3. Deltaic coastline with no significant wave or tidal influence
4. Tide-dominated deltaic coastline
5. Estuary with fluvial deposits shaped by tide
6. Estuary (tide-dominated)

7. Tidal inlet system dominated by tide with combined wave and tidal influence at the inlet
8. Wave-dominated barrier system

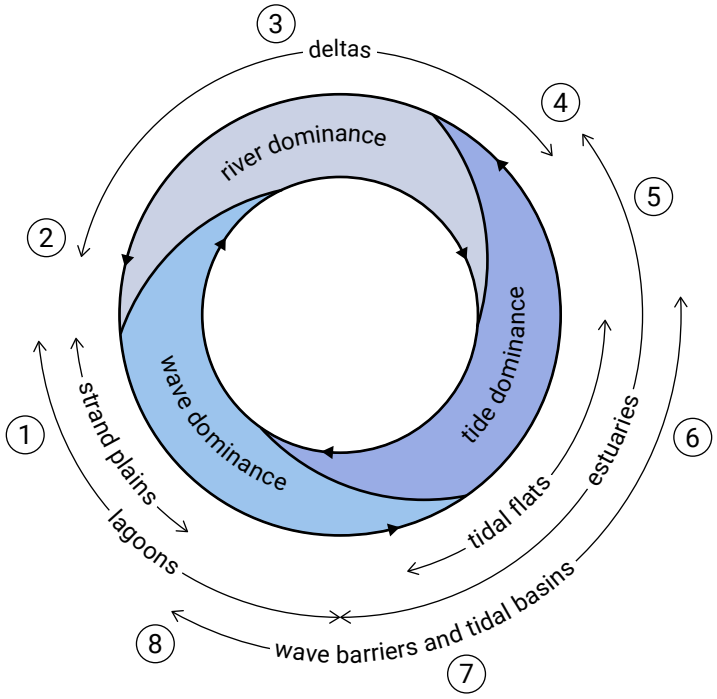

Figure 2.41: The relative influence of fluvial, wave and tidal processes influences the shape of coastal features. The numbers in the figure correspond to the typical morphologies of Fig. 2.42.

2.7.2. Ternary diagrams for progradation and transgression

Boyd et al. (1992) used the classification in prograding and transgressive coasts as a starting point and added the effect of domination by waves or tides. In prograding situations, the landside is on the winning hand, either because of a falling sea level relative to the land, or because of an excessive sediment supply. Transgression takes place either because of a rise in sea level, or because of insufficient sediment supply. Note again that the change in sea level is relative; subsidence of the land with a constant sea level has the same effect. Since Boyd et al. (1992) only §1.2 ~~take~~ §1.2 took [p80] depositional environments into account, the distinction between prograding and transgressive coasts boils down to the distinction between shoreline advance and shoreline retreat (see Fig. 2.23).

In the progressive case, deposition of river sediment leads to delta formation. When wave power and tidal power are low, the sediment of the river will build up long narrow banks on both sides of its course. Due to the gradient of the river flow, water levels at a fixed point along the river will gradually rise, since the distance of this point from the actual river mouth is increasing. At a certain moment, most likely when river discharge is high, the river starts overflowing the bank and it will erode a new, shorter channel towards the sea. The same process is continuously repeated, which leads to

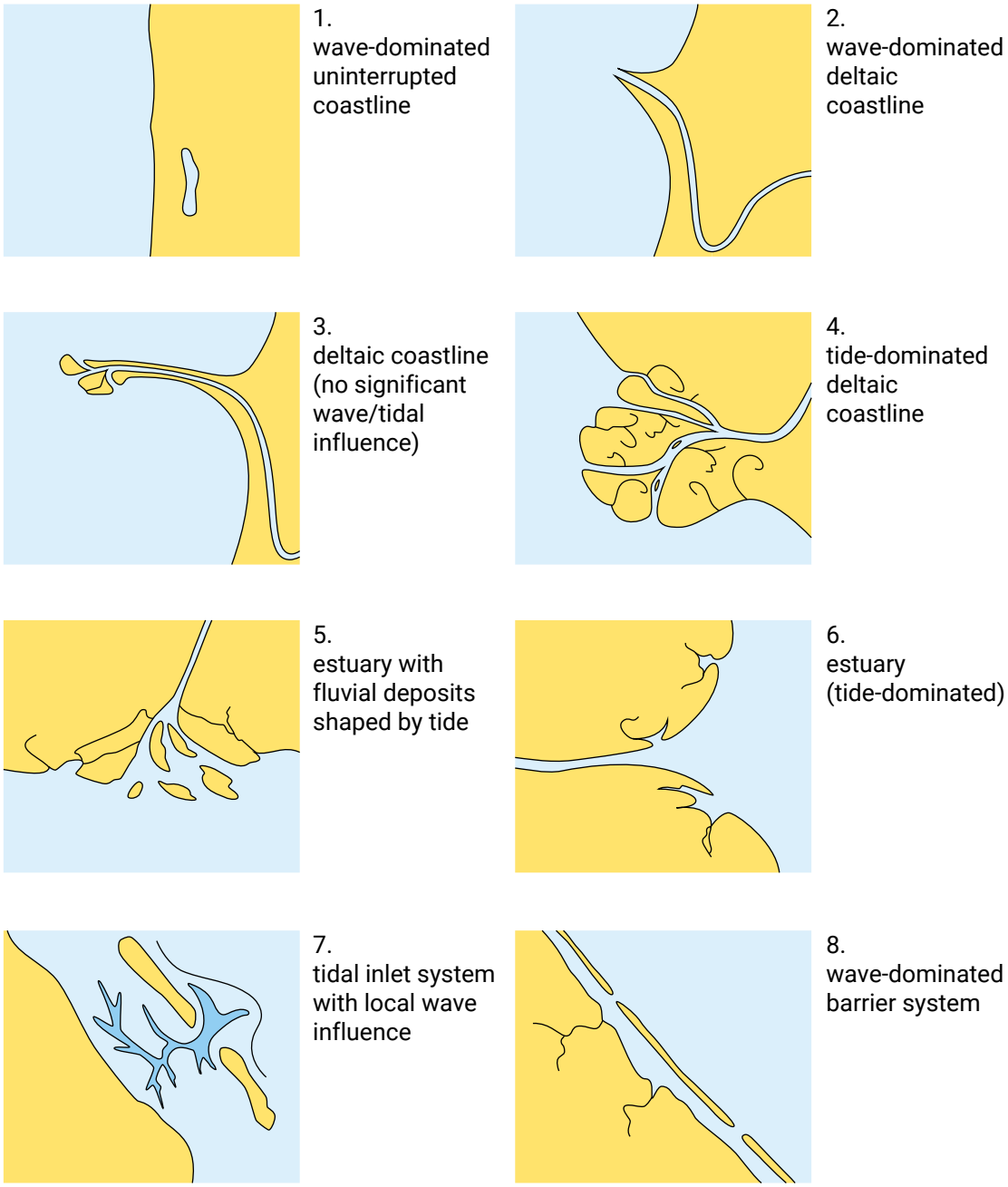

Figure 2.42: Examples of different coastal systems; the figure shows typical coastal morphologies developing in response to the relative influence of fluvial sediment supply, tide action and wave action.

an ‘elongate’ or ‘bird-foot’ delta (see also Sect. 2.7.3). Strong waves with longshore currents tend to stretch the delta coast parallel to the general orientation of the shoreline, while strong tidal action usually creates patterns perpendicular to the shoreline. Outside the influence of the river, a strand plain develops when wave action is dominant and tidal flats develop when tidal action is the strongest.

In the transgressive case, an estuary is the equivalent of a delta in the prograding case, but now, the sediment supply is not enough to keep pace with the relative sea level

rise. The sediment is no longer merely fluvial, but also has a marine source, since the flood tide or waves bring in sediment from the sea. A lagoon has a marine sediment source only, as no river is flowing into it.

Based on the various processes, Fig. 2.43 gives a classification for prograding and transgressive coasts. Figure 2.43a represents prograding situations, whereas Fig. 2.43b represents the transgressive case. Either ternary diagram presents the fluvial power on a vertical axis from the top corner (100 %) to the bottom (0 %). The coastal powers are represented on axes running from the lower two corners (100 %) to the middles of the opposite corners (0 %); the left corner indicates 100 % wave power and the right corner 100 % tidal power. The top of the triangle represents deltas; the bottom strand plains and tidal flats; estuaries are situated in between. A distinction can be made between wave- and tide-dominated estuaries. This will be further elaborated on in Ch. 9. In the ternary diagram, lagoons form the end member of the estuary spectrum.

The two diagrams together give an idea of the evolution of coastal systems over time, relative to the change in sea level and sediment supply. For instance, with a rising sea level, deltas change into estuaries (transgression). Strand plains and tidal flats vanish and become shelf when the sea level rises.

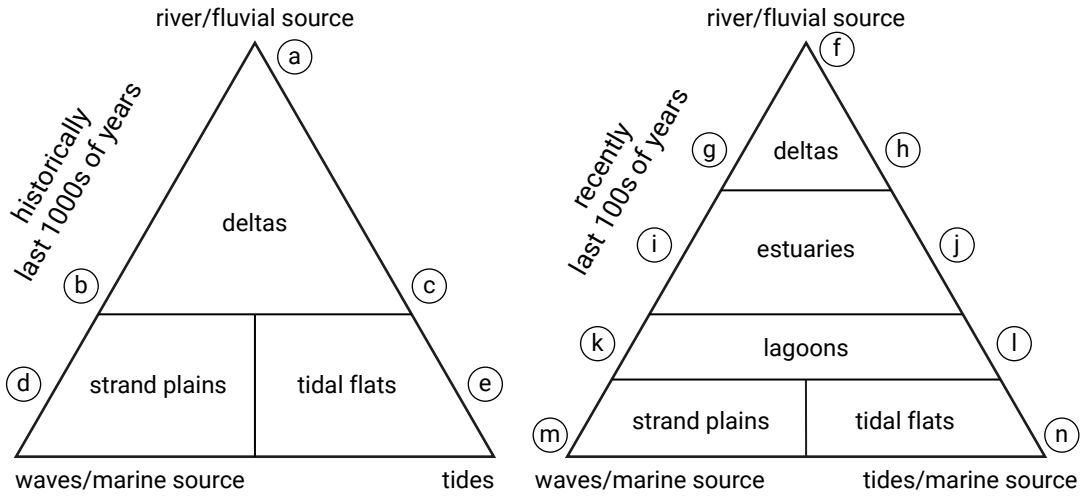

(a) high sediment supply, low rate of sea level rise, coastal progradation

(b) no or reduced sediment supply, high rate of sea level rise, marine transgression

Figure 2.43: Ternary coastal form classification diagrams for transgressive and prograding coasts (reinterpreted from Boyd et al., 1992; Dalrymple et al., 1992). The letters correspond to real-life examples listed in Table 2.3.

It is interesting to note that the triangles in Fig. 2.43 depicting deltas have been separately described by Galloway. Section 2.7.3 describes in detail how the various delta shapes are influenced by the dominance of fluvial, wave or tidal processes.

2.7.3. Classification of deltas

The formation of a delta depends on the interaction between the river flow and sediment supply on the one hand and the distribution of the river sediment by waves and tidal currents on the other hand. William Galloway recognised the relative influence of these three major factors affecting delta development (river, waves and tide) on the morphological structure. He proposed the triangular classification diagram of Fig. 2.44, in which river-dominated, tide-dominated and wave-dominated deltas are distinguished.

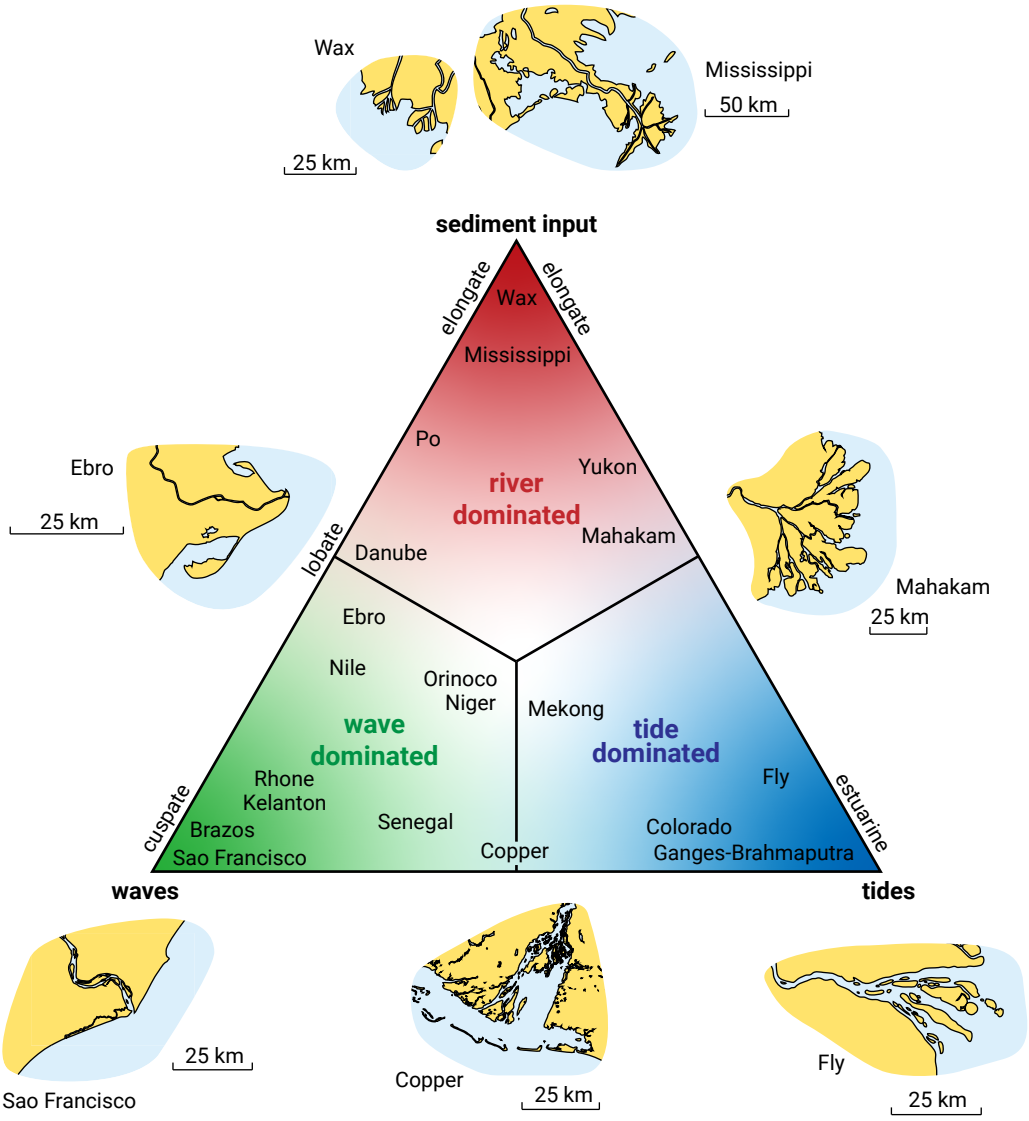

Figure 2.44: William Galloway's triangular delta classification diagram. The colors represent the relative influence of waves (green), tides (blue) and fluvial sediment input (red). After Galloway (1975).

As the water flows from the river mouth, its velocity decreases and it loses its capacity to carry sediment. Consequently, sediments accumulate in the river mouth area. As the velocity of the outflowing river water decreases, the coarse material settles

first, followed by the finer sediments. At the seaward edge of the delta front, the suspended sediment in the river water finally settles in deeper coastal water. This mud accumulation is generally very thick and extends across part of the continental shelf. The amount and configuration of sand accumulating in the delta-front depends on the relative roles of the interacting river, wave, and tidal currents.

A common type of sand accumulation is a sandbar that forms just seaward of the channel mouth and typically causes the channel to bifurcate. Another is the formation of banks along the sides of the channel. As the river deposits sand in the mouth, a situation can be reached in which the water level is affected by the sand deposits. The river can then overflow its banks and then divide into *distributary* channels. Each distributary channel then continues to transfer massive amounts of fine-grained sediment to the coastal area. When this new-born delta is situated in an environment with little tide and wave action, it is categorised as being *river-dominated*. It can grow out into a bird-foot type of delta. Examples are shown in Figs. 2.45 and 2.46 (Danube Delta and Mississippi River, respectively).

Tide-dominated deltas develop where a large difference between the high and low tides leads to strong tidal currents. On these coasts, the wave height is moderate to low, and wave-induced currents along the coast are weak. These deltas resemble estuaries because of their embayed setting of salt marshes, swamps, and tidal flats. An example of such a tide-dominated delta is the delta of the river Fly on the south coast of Papua New Guinea (Fig. 2.47).

If the wave climate is more severe, the bars at the river mouth are affected by the waves. As a result of the wave action, sand is repositioned by alongshore and cross-shore effects. Depending on the wave direction, this can lead to a delta that is symmetrical (in the case of waves perpendicular to the coast) or asymmetrical (in the case of obliquely incident waves) in shape.

Wave-dominated deltas typically have a rather smooth shoreline with well-developed beaches and dunes. The delta plain tends to have few distributaries; some deltas of this type have only a single channel. A wave-dominated delta is generally smaller than other types, because the distributing power of the waves striking the delta front is stronger than the carrying power of the river. When the wave climate is strong enough to carry all the river sediment away, the delta will shrink and eventually disappear. Two different shapes characterise these deltas. The general shape is symmetrically cuspate. One of the best examples is the delta of the São Francisco in Brazil (Fig. 2.48).

The other shape is characterised by a strong longshore current. A sand spit (an elongated and narrow accumulation of sediment that is attached to land at one end, see Ch. 8) develops and protects the extensive wetlands that cover the delta plain. An example of this is the Ebro delta (Fig. 2.49).

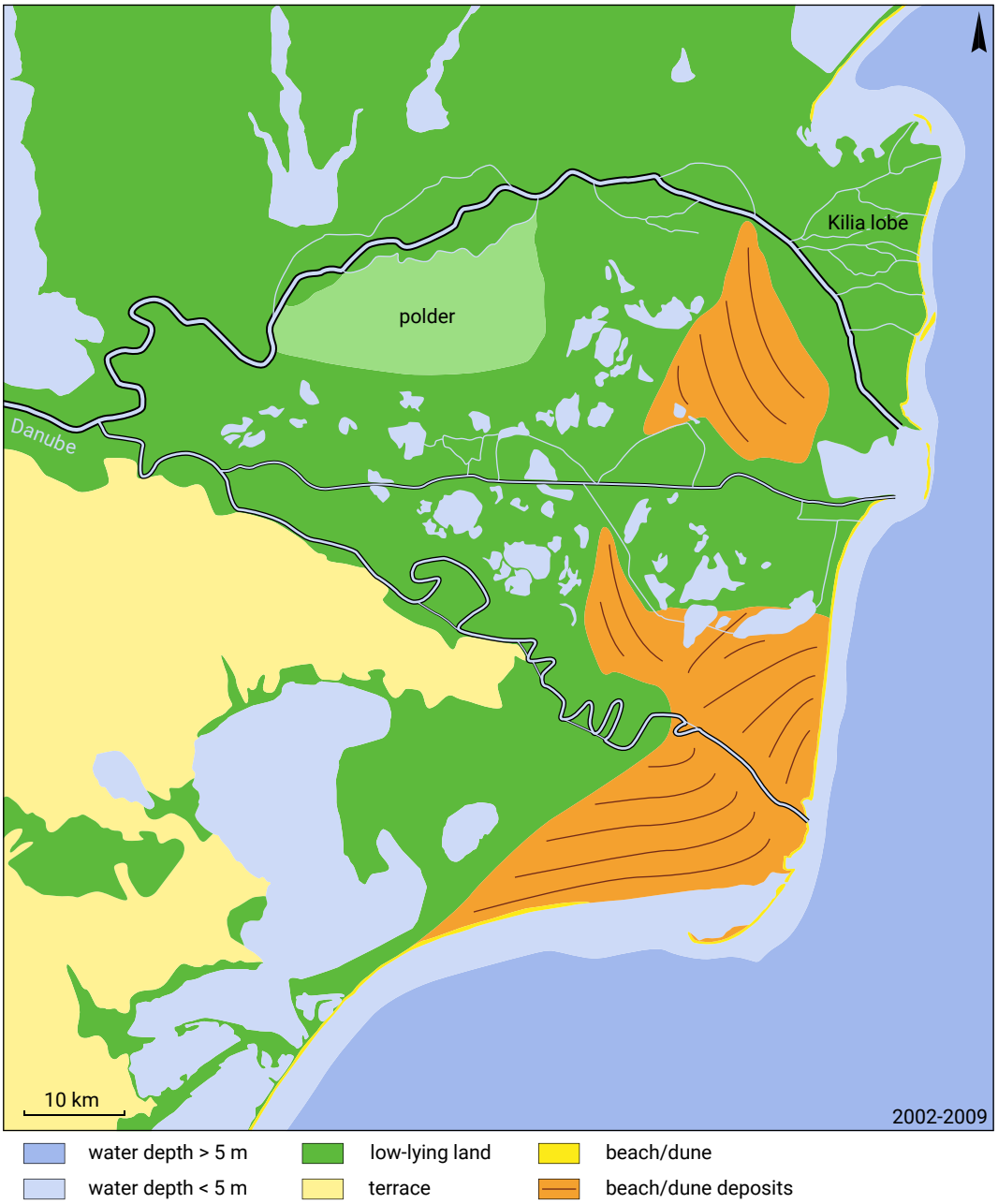

Figure 2.45: Historically, the Danube delta has developed as a river-dominated delta, as can still be recognised from the bird-foot shape of the northern Kilia Lobe. The southern part of the present-day delta shows evidence of wave dominance.

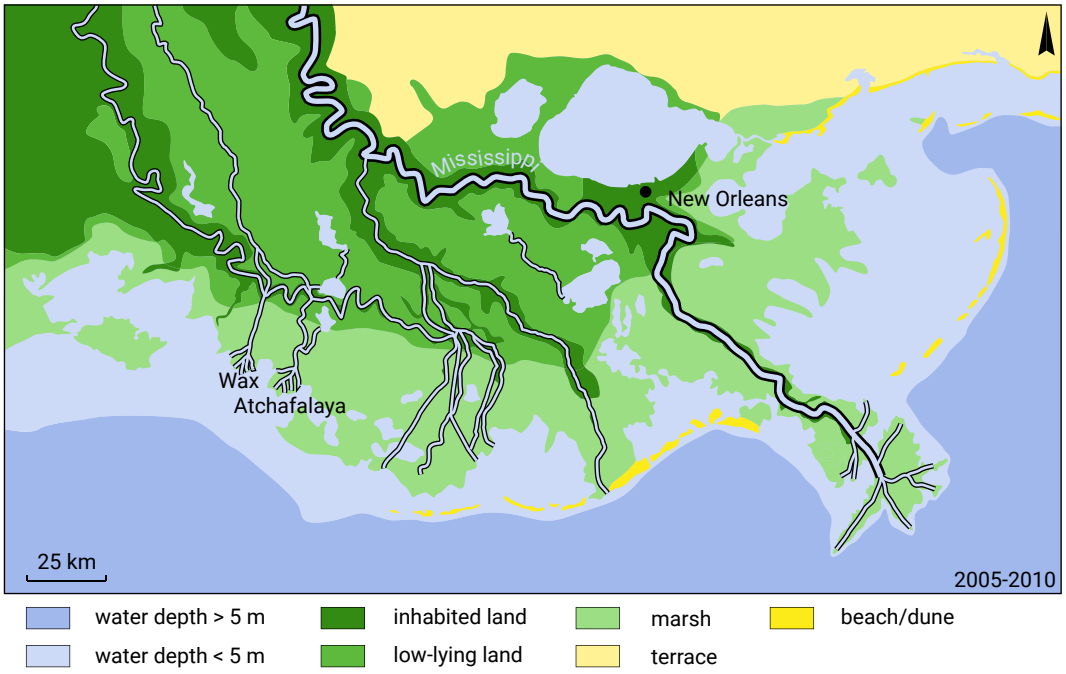

Figure 2.46: Mississippi delta system.The main branch (to the right) has developed as a bird foot delta. Its present course, however, is strongly constrained by the man-made levee system. The smaller Wax and Atchafalaya deltas (to the left) are clearer present-day examples of a bird-foot delta.

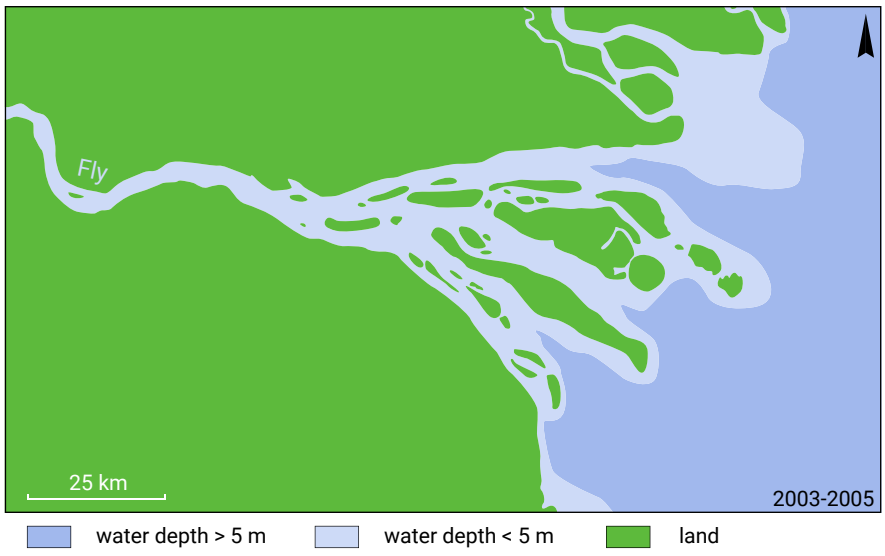

Figure 2.47: Delta of the river Fly, Papua New Guinea.

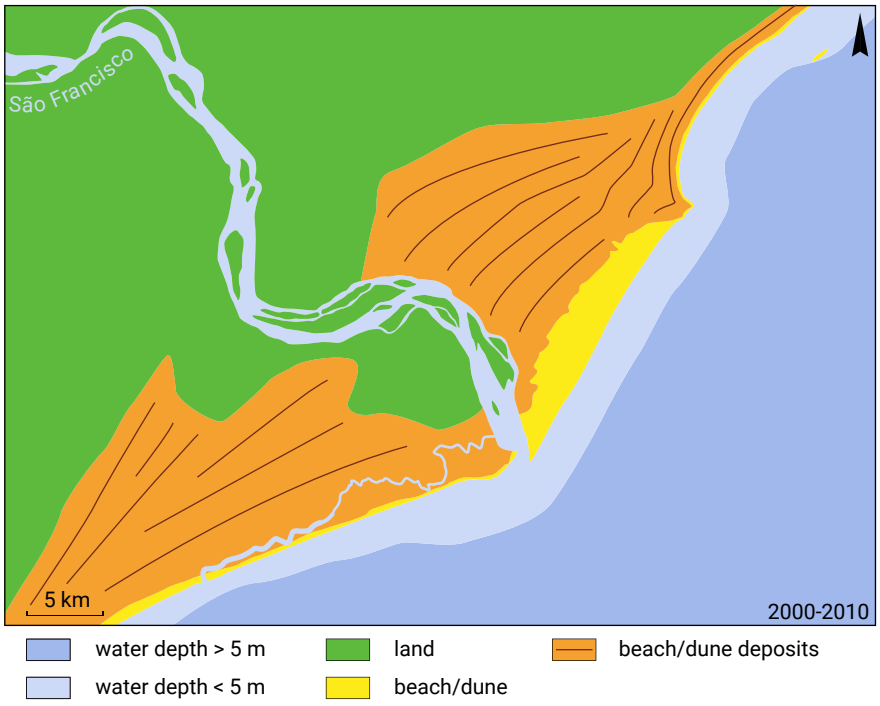

Figure 2.48: São Francisco Delta, Brazil.

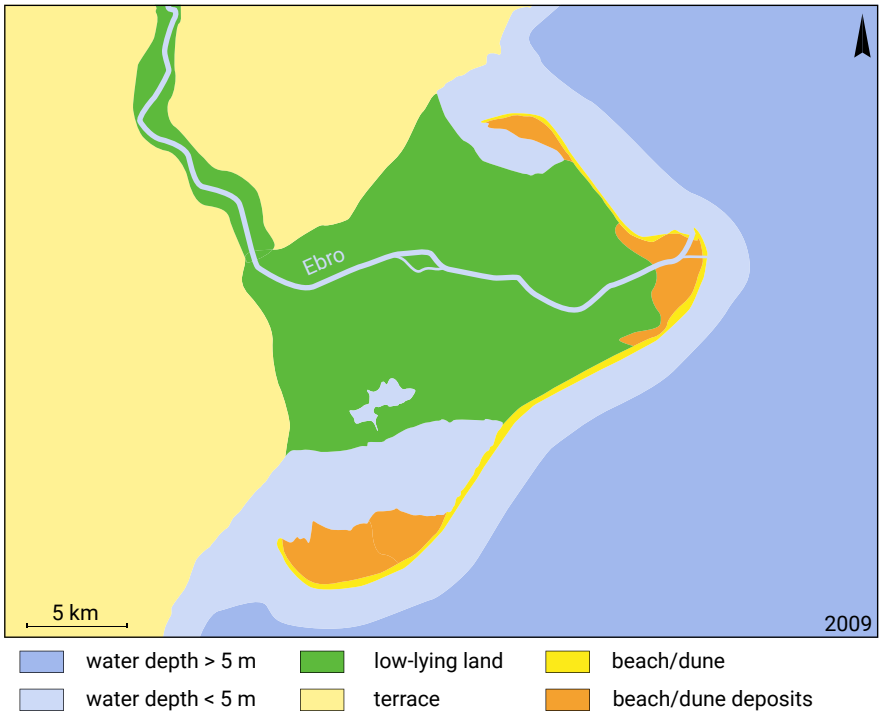

Figure 2.49: Ebro delta, Spain, with a sand spit at the southern end.

2.7.4. Overview and examples of coastal forms

Table 2.3 not only gives an overview of the variety of coastal forms but also presents real-life examples. The table distinguishes between 1) primary coastal forms (deltas, estuaries, plains and flats, and barrier and lagoon coasts); 2) secondary coastal forms based on the influence of wave action and tidal action and 3) sediment-rich and sediment-poor systems. For each resulting class, an example is given and linked to the ternary diagrams of Fig. 2.43. The latter includes the triangular classification diagram of Fig. 2.44. The typical morphologies listed in Sect. 2.7.1 can also be positioned in the ternary diagrams of Fig. 2.43.

2.8. Summary of coastal classification

Classification can be used as a means to inventory the large variety of coastal systems. It may be based on:

- Material – hard/soft, origin, size;
- Tectonic controls – e.g. Inman and Nordstrom (1971);
- Sea level criterion – e.g. Valentin (1952);
- Dominant processes.

The diversity in coastal systems is the result of the simultaneous occurrence of all coastal system determining factors in a nearly infinite number of combinations. That is why there exists no truly unique classification system of coastal ocean systems and why one encounters a large variety of classification systems in literature. Classification is scale-dependent; the tectonic classification for instance describes only the broadest features of a coast. Also in process-based classifications, the levels of aggregation can vary.

The process-based classification on the basis of the *relative* importance of fluvial sediment supply and wave and tidal action comes closest to the approach in this book, that discusses the characteristics of coastal systems based on the (hydrodynamic) boundary forcing to the coastal system and resulting sediment transport processes.

Table 2.3: Classification of coastal forms with real-life examples. The examples are indicated by letters that correspond to the letters in Fig. 2.43.

Primary coastal form	Secondary coastal form	Sediment rich	Sediment poor
Deltas	River-dominated deltas	Yellow river, China **(a)** Mississippi, USA (until ca. 1975) **(a)** Wax Lake, USA **(a)**	Mississippi, USA (ca. 1975–present) **(f)**
	Wave-dominated deltas	Sao-Francisco, Brazil **(b)**	Ebro, Spain **(g)** Senegal delta, Senegal **(g)**
	Tide-dominated deltas	Ganges (Megna estuary), Bangladesh **(c)**	Amazon, Brazil **(h)**
Estuaries	Tide-dominated estuaries	Yangtze, China (*poor in river sediment, tidal supply*) **(j)**	Pearl (Zhujiang River estuary), China **(j)** Severn estuary **(j)**
	Tide-dominated estuaries with wave-dominated ebb-delta	Columbia River estuary (*poor in river sediment, wave supply*) **(i)**	Mekong estuaries and coast, Vietnam **(i)**
Plains and flats	Strand plains (beach ridges)	Western tips of Wadden Islands, The Netherlands **(d)** Dune du Pilat, France **(d)**	Eastern tips of Wadden Islands, The Netherlands **(m)**
	Tidal plains	Jiangsu coast (radial ridges in southern part), China **(e)**	Jiangsu coast (northern part), China **(n)**
Barrier & lagoon coasts	Spatially varying dominance by waves & tide	Wadden Sea, Netherlands/Germany (between **k** and **l**)	Redfish Pass, USA (between **k** and **l**)
	Wave-dominated open and seasonally closed lagoons	Albufeira lagoon, Portugal (*wave supply*) **(k)**	Willapa Bay, USA **(k)**
	Tidal bays	Baie de St. Michel, France **(l)**	Hangzhou Bay, China **(l)**

3

Ocean waves

3.1. Introduction

This chapter deals with ocean waves. By ocean waves we mean all oscillations of the water surface generated in the ocean (see Sect. 3.2). The most important in shaping the coastal zone are the short waves generated by wind and the longer tidal motion generated by the attractive forces of the sun and the moon on the water masses of the earth. In Sect. 3.3 we look at how waves can be measured. Statistical and spectral representations of wind waves are treated in Sect. 3.4. Both wind wave generation and the propagation away from the area of wave generation are treated in Sect. 3.5. We see how ocean waves become longer and smaller when propagating away further from their source due to the phenomenon of wave frequency dispersion and due to frequency-dependent dissipation. Long term statistics are briefly discussed in Sect. 3.6. The generation of the tide is explained and the origin of the different harmonic constituents is treated in Sect. 3.7. We look into the propagation of the tide in the world's oceans and in doing so discuss propagation velocity, Coriolis forces and amphidromic systems (Sect. 3.8). Tidal analysis and prediction are the topics of Sect. 3.9.

After having taken the TU Delft courses Ocean Waves (CIE4325), Hydraulic Engineering (CTB2410, in Dutch) and Open Channel Flow (CTB3350/CIE3310-09) the larger part of this chapter on Ocean Waves should be familiar to you. This particularly holds for the Sects. 3.2 to 3.6 on wind or short waves. You will find that Sects. 3.7 to 3.9 treat the tidal generation and propagation more extensively than CTB2410 does. In CTB3350/CIE3310-09 you will have encountered some aspects of tidal propagation as well. For those without any prior knowledge of wind waves or tides in oceanic waters, this chapter deals with the main aspects that are required in order to successfully follow Coastal Dynamics I (CIE4305).

3.2. Oscillations of the ocean water surface

We can broadly define ocean waves as all sea surface variations on the timescale of seconds to months as generated in the oceans. MSL is the sea level when these fluctuations are averaged out. This definition of ocean waves includes wind waves, tides and tsunamis. Wind and atmospheric pressure changes can also cause water level variations.

The simplest way of representing a wave is by a sine or cosine function: a regular variation of the water surface at a certain location. We will see later that such a sine wave is a solution to the linearised equations describing the water motion. In such a representation the temporal variation at one location is shown in the right-hand side of Fig. 3.1.

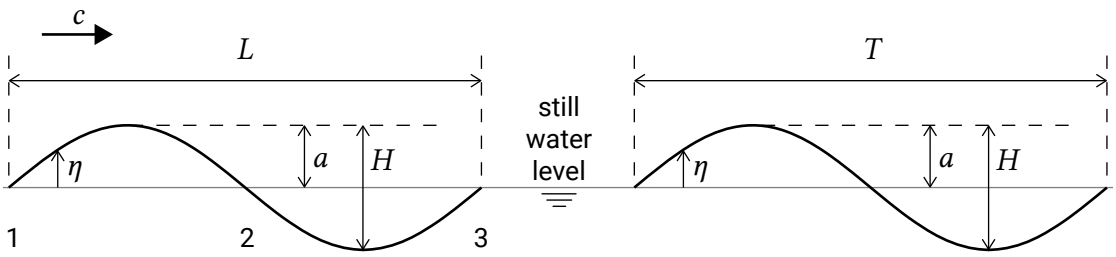

Figure 3.1: Simple representation of a wave. Left: the spatial variation is measured along the direction of wave propagation at a single moment in time. Right: the temporal variation in water level η is measured over a certain time period at a single location (at location 2 and directly following the recording of the spatial variation). A similar signal measured simultaneously at location 1 (or 3) will have opposite sign.

The wave height H is the vertical distance between the crest and the trough of the wave and equals twice the amplitude a for a sinusoidal variation. The wave period T is the time the wave needs to pass the location, the inverse of which is the frequency f, the number of waves passing a fixed location per unit time. When travelling in the ocean at a certain moment in time, the wave can be seen as a similar sinusoidal variation of the water surface, see the left-hand side of Fig. 3.1. The figure shows the wavelength L of the surface elevation deformation measured along the direction of wave propagation x. The wavelength is the length a wave will travel in the wave period T. The ratio between wave height and wavelength is called the wave steepness H/L. The surface elevation η can be described by:

$$\eta = a\sin(\omega t - kx) = a\sin S(x,t) \tag{3.1}$$

where ω is the angular frequency and k is the wavenumber according to:

$$k = \frac{2\pi}{L}; \qquad \omega = 2\pi f = \frac{2\pi}{T} \tag{3.2}$$

§1.1 The units of ω and k are rad/s and rad/m, respectively. They may also be written as 1/s and 1/m, respectively, since the radian is dimensionless, just like the degree. [p192]

The deformations propagate with the wave speed c:

$$c = \frac{L}{T} = \frac{\omega}{k} \tag{3.3}$$

In the linear (first-order) approximation, wave propagation is merely a matter of movement of the wave form, not of mass. The water particles describe orbital or oscillatory motions at particle speed and remain at the same position on average. In Sect. 5.5.1 we will see that at second order there exists a non-zero net mass flux that becomes more important for larger wave amplitudes.

There are various ways to discern between the different types of ocean waves, viz. by:

- the disturbing force, i.e. their mechanism of generation;
- the restoring force, i.e. the mechanism that dampens the wave motion;
- the length of the wave (represented by the wavelength, wave period or frequency).

These different classifications are shown in Fig. 3.2 which shows the different ocean waves as a function of their wave period. In this book we will discuss the waves that are most important for our coastal system: wind waves (normal wind waves and longer storm waves), tides, tsunamis and storm surges. The energy level as indicated in Fig. 3.2 is a qualitative reflection of the amount of energy contained in these waves and their relative frequency of occurrence. Storm surges and tsunamis contain a lot of energy but are not as frequent as ordinary wind waves. Therefore the energy contained in the wind wave range is higher.

Wind waves

Wind-generated gravity waves have periods ranging from ¼ s to 30 s. They are called gravity waves because gravity is the restoring force that dampens the wind wave motion by returning the particles to their average position in the water column. Local wind fields generate relatively short (order 10 s, larger for larger storms) random and irregular oscillations of the water surface that we call 'sea'. These wind-generated oscillations can travel large distances away from their area of generation. They will then transform into longer, faster, lower and more regular 'swell' due to a process called frequency dispersion and frequency dependent damping (see Sect. 3.5.2). Capillary waves (< ¼ s) can be seen as small ripples on the water surface, but they will die out very fast after the wind stops blowing. Their restoring force is surface tension. Infra-gravity waves are longer gravity waves with periods up to 5 minutes. Although deep-water infra-gravity waves do exist, infra-gravity waves are mainly a shallow-water phenomenon. In shallow water (groups of) wind waves can generate

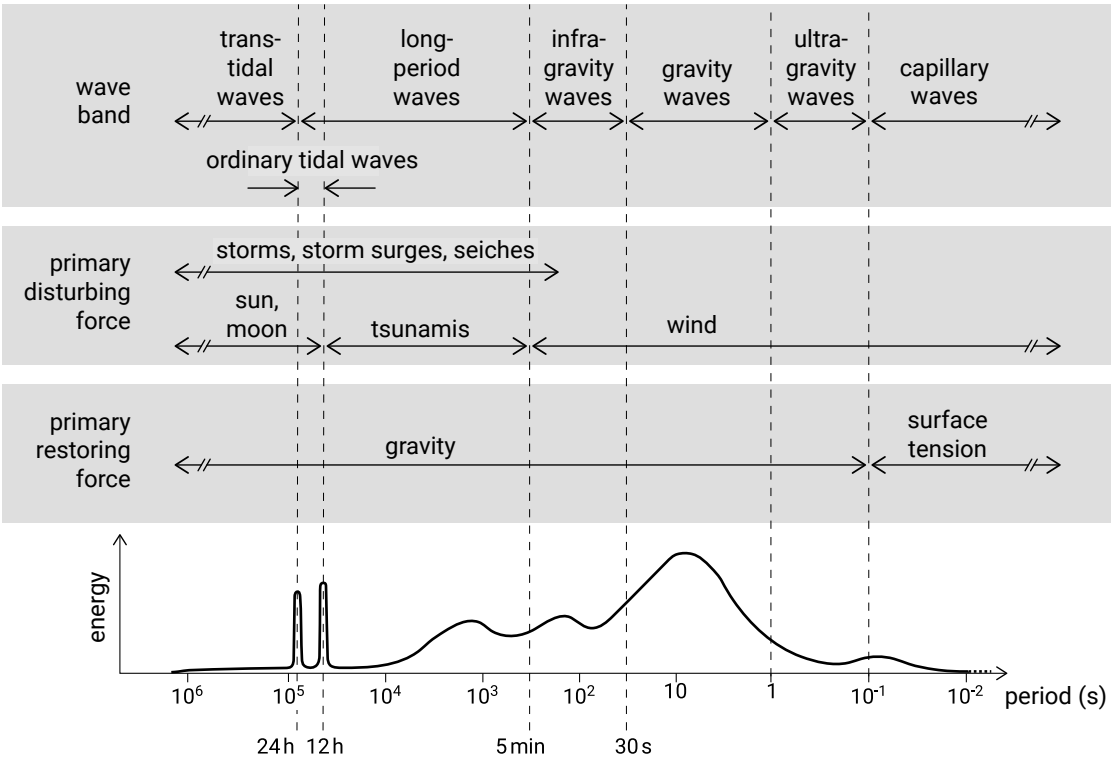

Figure 3.2: Sketch of the relative amounts of energy as a function of wave period in ocean waves. The top section gives the classification based on wavelength, the section below the classification based on the wave-generating force, and the bottom section the classification based on the restoring force. After Munk (1950) and Kinsman (1965).

longer (30 s to 5 min) waves like surf beat, which has a period of a few minutes (corresponding to the length of a wave group). This will be treated in Ch. 5. Note that the ratio of water depth to wavelength h/L or alternatively kh determines whether we are dealing with deep water (or short waves) and shallow water (or long waves).

Wind-generated gravity waves (sea and swell together) are the major supplier of energy to the coastal system. In this chapter therefore due attention is given to the generation and description of wind waves and their propagation in oceanic waters. The transformation they undergo when entering more shallow coastal waters will be treated in Ch. 5.

Tides

The tide is generated by the mutual gravitational attraction of the earth and the moon and of the earth and the sun. The frequencies of the tide are governed by the well-known movements of the earth, the moon and the sun and are mainly diurnal and semi-diurnal (see the two spikes of ordinary tidal waves in Fig. 3.2) and not continuous, in contrast to wind waves. The restoring force for long waves like tides is gravity, although the waves are influenced by Coriolis (see Intermezzo 3.1). The tide also attributes to shaping our coastal systems. Due to the once- or twice-daily rise and fall of the water level, the part of a coastal profile that is affected by waves changes during the

tidal cycle; at high tide the waves will attack more shoreward portions of the profile than at low tide. In tidal basins intertidal areas between high and low water level act as storage areas for the water brought in by the tide. The emptying and filling of the basin can give rise to large tidal currents in the inlets and keep the inlets open. Large tidal currents can also occur on open coasts around structures where convergence of the tidal current can be expected. The generation and propagation of the tide in oceanic waters will be treated in this Sects. 3.7 and 3.8. In Ch. 5 the specific processes in the coastal zone will be treated.

Intermezzo 3.1 Coriolis acceleration

Since we are interested in water motion relative to the earth, our (numerical) models are mostly formulated in a frame of reference fixed to the earth's surface. Generally, in such a reference frame, the z-axis is normal to the earth surface and outward-directed: the x-axis points east and the y-axis points north (see Fig. 3.3). Because the earth rotates around its own axis (see Sect. 3.7.2), the chosen frame of reference also rotates (i.e. accelerates towards the centre of rotation).

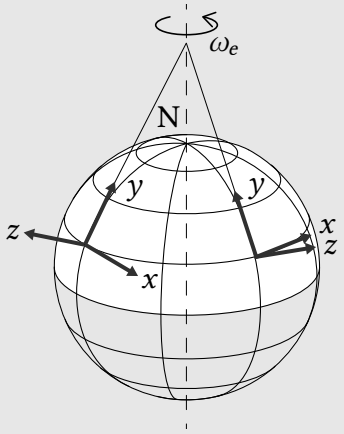

Figure 3.3: As a result of the earth's rotation any x, y, z-reference frame that is fixed to the earth's surface also rotates.[§1.1] [Latitude of right reference frame corrected] [p95]

Newton's equations of motion are valid in an inertial frame of reference: a reference frame that does not accelerate, e.g. a frame fixed to the distant stars. In order to make Newton's equations of motion valid in our rotating, non-inertial frame of reference, we need to introduce 'fictitious' centrifugal[a] and Coriolis forces. These forces are called 'pseudo-' or 'fictitious' forces since they do not arise from any physical interaction but from the choice of a non-inertial reference frame.

The Coriolis force is named after Gustave-Gaspard Coriolis who first described it in the first half of the 19$^{\text{th}}$ century. As will be explained below, this force acts on every moving particle in the rotating reference frame, at right angles to the direction of motion, to the right in the Northern Hemisphere (NH) and to the left in the Southern Hemisphere (SH). Hence, the Coriolis effect causes air and water

currents in the Northern Hemisphere to deflect to the right, and in the Southern Hemisphere to the left.

In the Northern Hemisphere the rotation of the reference frame implies an anti-clockwise rotation of the x, y-plane, the horizontal plane tangent to the earth's surface (see Fig. 3.4). When observing motion in a horizontal plane that is turning anti-clockwise, a particle travelling in a straight line (as seen from the stars) appears to be turning clockwise. To describe this deflection to the right, a Coriolis force acting to the right must be introduced in Newton's equations of motion.

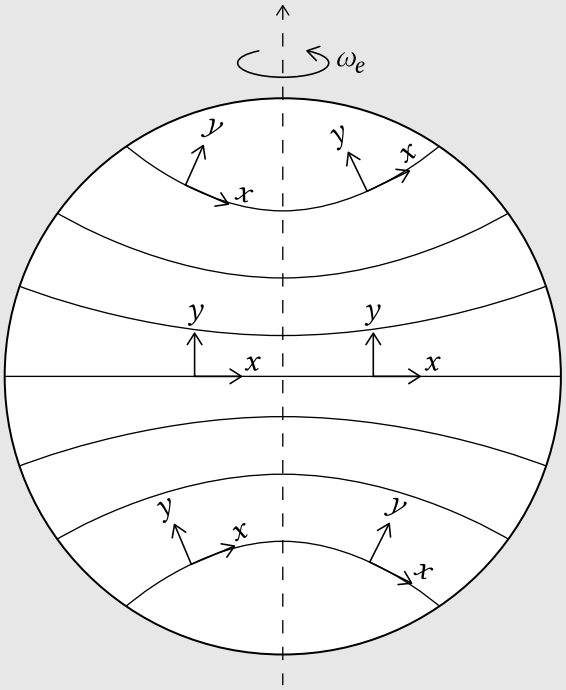

Figure 3.4: Gnomonic map projection of latitudinal lines. In such a projection great circles (the shortest distance between two locations on a spherical object) are displayed as straight lines and directions are preserved. The x, y-plane turns anti-clockwise in the NH and clockwise in the SH.

[a] The 'fictitious' centrifugal force (directed away from the axis of rotation) does not seem to be invoked by any true force, since for an observer in the rotating reference frame the centripetal acceleration of the earth (towards the rotation axis) is hidden.

In the Southern Hemisphere the x, y-plane has rotated clockwise after some time, such that the Coriolis force acts to the left (or anti-clockwise). At the equator the Coriolis force is zero[b]. This is because at the equator the earth's surface lies in a plane parallel to the earth's axis of rotation. Hence, the earth's rotation vector ω_e (see Fig. 3.4) has no component perpendicular to the earth surface and the angular velocity of the horizontal plane (the rate at which the x, y axes change direction) is zero. Going from the equator to the poles, the rotation vector is less and less parallel to the earth's surface until at the poles it is entirely perpendicular to the

earth's surface. Hence, the horizontal (i.e. parallel to the earth surface) Coriolis forces are zero at the equator and largest at the poles.

At a latitude φ, the earth-normal component of the rotation vector is $\omega_e \sin\varphi$. It represents the angular velocity of the horizontal plane (the rate at which the x, y-coordinate axes change direction). The Coriolis force is proportional to 1) the angular velocity of the horizontal plane $^{\S 1.1}\omega_e \sin\varphi$ [p97]; and to 2) the velocity of the moving particle or object in the rotating reference frame. It can be shown that the Coriolis acceleration (or Coriolis force per unit mass) to the right of the velocity V reads:

$$a_c = fV = 2\omega_e \sin\varphi V \tag{3.4}$$

where:

a_c	Coriolis acceleration	m/s^2
f	Coriolis parameter	1/s
ω_e	angular velocity of the earth	rad/s
V	current velocity	m/s
φ	latitude (positive in NH and negative in SH)	°

The earth's angular velocity $\omega_e = 72.9 \times 10^{-6}$ rad/s is based on sidereal day, i.e. the time needed by the earth to complete a rotation around its axis, 23 hours and 56 minutes. With the latitude and hence the Coriolis parameter positive in the Northern Hemisphere and negative in the Southern Hemisphere, the direction of the acceleration is to starboard in the Northern Hemisphere and to port in the Southern Hemisphere. Its magnitude is largest at the poles where $|\sin\varphi| = 1$ and zero at the equator where $\sin\varphi = 0$. At mid-latitudes (say $\varphi \approx^{\S 1.1} \pm 45°$) we have $f \approx^{\S 1.1} \pm 10^{-4}\,s^{-1}$ [p97]. However, in practice, in numerical models covering not too large areas, the parameter f can be assumed to be a constant.

Whether the Coriolis deflection is significant relative to inertia can be determined by the Rossby number, which is given by:

$$R = \frac{V}{|f|L} \tag{3.5}$$

with L is the length scale of the motion. The Rossby number can be seen as the ratio between the inertial forces and Coriolis forces, see also Sect. 3.8.3. For Rossby numbers of order 1 and smaller, Coriolis deflection is important, which is for instance the case for large-scale motions such as tides. To describe tidal motion, the

Coriolis acceleration must be introduced in Newton's equations of motion. How this is done is discussed in Sect. 3.8.3.

[b] Or more precisely: the horizontal components of the Coriolis force (in the x, y-plane) are zero. Coriolis force acts in a direction perpendicular to the rotation axis of the earth, which is normal to the earth's surface at the equator.

Tsunamis

Also indicated in Fig. 3.2, tsunamis are a specific type of wave not caused by wind but by large, impulsive displacement of the sea level. The disturbance of the water surface is usually triggered by underwater earthquakes or underwater volcanic eruptions. The surface disturbance travels away from its origin in a pattern comparable with the patterns generated by the landing of a pebble in a pond. In deep water, tsunamis are not visible because they are small in height and very long in wavelength (periods ranging from 5 min to 60 min). They may grow to devastating proportions at the coast where the water is shallow. This effect of tsunamis will be discussed in Ch. 5, whereas the propagation of tsunamis through the oceans is treated in Sect. 3.5.2. Approximately every 15 years a destructive, ocean-wide tsunami occurs.

Tsunami warning systems are in place, which recognise either seismic activity that can potentially lead to a tsunami or unusual water level variations.

Storm surges

Storm surges are elevations of the water surface with time- and spatial scales equal to those of the large storm fields that generate them. They are generated by the low atmospheric pressure and high wind speeds in a storm field. The wavelength and period are generally slightly shorter than those of tides. Storm surges can cause severe flooding because the water will pile up against the coast when they approach the coast (see Ch. 5). Examples are the flooding of New Orleans due to the storm surge associated with hurricane Katrina in 2005, the regular cyclone-induced floodings of Bangladesh and the 1953 storm surge in the Netherlands (see Sect. 1.4.6).

3.3. Measuring ocean surface elevations

Measurements of waves can be done in various ways, either at the location of the waves itself (in situ) using for instance wave buoys or poles present in the water or from some distance with remote sensing techniques like radar. The accuracy of most of the instruments is ± 10 % or better. The easiest way to measure the vertical elevation is by visual observation of individual waves from ships, a technique that has been applied for a long time.

The in-situ measurements are often aimed at obtaining the vertical elevation of the sea surface at one location, either in deep water (buoys or poles) or in the surf zone. Arrays of bottom-mounted pressure gauges can be placed just offshore of the surf zone to determine the offshore wave heights and directions which act as boundary conditions for the coastal system. Placed in deep water, it is suited to measure long wave fluctuations like tides and tsunamis (the shorter fluctuations will not reach the bottom, see Sect. 5.4).

Coastal tide gauges measure tide and mean sea level changes relative to points on land rather than to an absolute reference. These coastal tide gauges are often based on floats operating in a stilling well or on electrical measurements of water heights in a pipe. In order to arrive at absolute mean sea level changes, the local vertical land motion has to be measured and corrected for[1], see also Sect. 2.5.1. Differences in estimates for historic mean sea level changes mainly result from the uncertainties related to the local vertical motions. Therefore, although data is available for over 1750 stations worldwide and sometimes going back as far as 1700 (for Amsterdam), there are a lot of different interpretations of absolute mean sea level changes.

Nowadays the vertical movement of the land can be quite accurately recorded using satellite data, Global Positioning System (GPS) receivers and altimeters based on absolute gravity measurements.

The wave information from buoys, poles, radar or other instruments is important to coastal engineers to gain an understanding of the longer-term wave climate (years) or the short-term (storms and individual waves) characteristics of the waves in a certain region. As an example of information available for a certain engineering project, Fig. 3.5 shows the permanent (viz. 85 % of the time) wave-measuring locations in the Dutch North Sea that have provided directional wave data for over three decades.

In order to obtain wave information closer to the coast or at specific location, wave models can be used which use the measured wave information at the buoy location as boundary conditions. The buoys are located in relatively deep water, so that the waves are not influenced by the (changing) bed. The elevation data – sampled a few times per second – is translated to a radio signal and then transmitted to a post-processing centre where data analysis and derivation of wave parameters takes place.

For the Dutch coast usually a combination of sea and swell is present in the record. The swell can be recognised as the longer modulation in the record which becomes clear when the two signals are separated in the shorter and irregular sea and longer swell. A typical deep-water wave record from such a platform is given in Fig. 3.6. For most of the Dutch measuring locations, this type of elevation data is available since

[1]The local vertical land motions due to post-glacial rebound, tectonic effects, ground water or oil extraction can be of the same order as the average global or absolute rise, which over the last century is estimated at between 1 mm to 2 mm per year (IPCC, 2001, 2007)

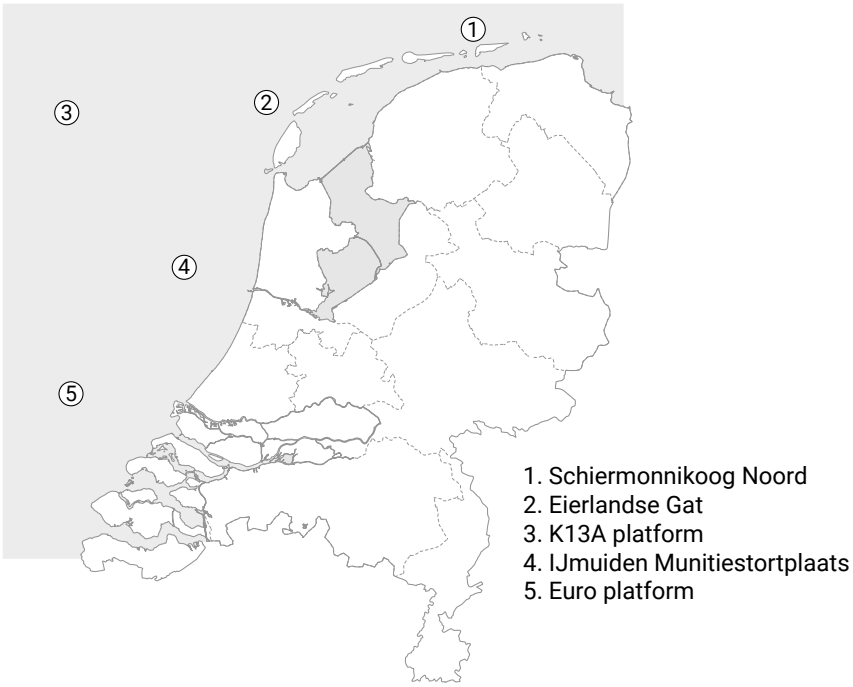

Figure 3.5: The five buoy locations in the Dutch North Sea area permanently providing directional wave data since at least 1989, two close to offshore platforms and the remaining ones at varying distances from the coast or outer delta. For more information see https://www.rijkswaterstaat.nl/water/waterdata-en-waterberichtgeving/waterdata & https://waterinfo.rws.nl, in Dutch.

1979. It can be used to arrive at short-term statistics and long-term wave climates. In the following section the techniques to do that will be explained.

3.4. Short-term wave statistics

3.4.1. Description of wave characteristics

Figure 3.6 already showed that real ocean wind waves have an irregular character (not-periodic, not repeating itself in time and space) as opposed to the single sinusoidal signal in Fig. 3.1. The waves are therefore called irregular or random waves. In spite of the seemingly unpredictable (random) way in which the signal fluctuates, if we describe the short-term variations in a statistical way by taking average parameters, it appears that the statistics can be considered constant in time (stationary). In order for the averages to be representative of the sea state, the record should be short enough to be statistically stationary (not changing in time). On the other hand the record should be long enough to get reliable averages. At sea 15 to 30 minutes is used, most commonly 20 minutes. On longer timescales the short-term mean values are variable due to variations in mean wind velocity, tidal elevation or tidal currents which change the wave characteristics. Thus wind waves are a random stationary process for timescales up to half an hour. In practice one recording of for instance 20 minutes is done every three hours. This record is thought to be representative for the entire

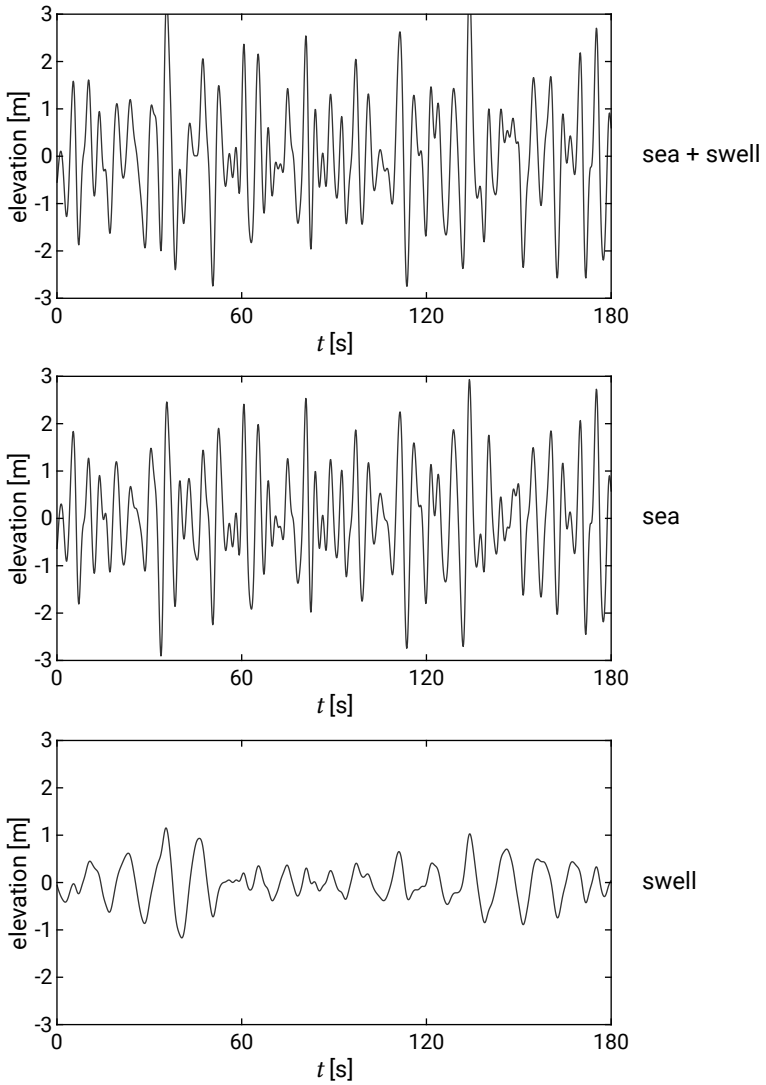

Figure 3.6: Example of a combined swell and sea time series (upper panel), separated in a sea component (middle panel) and a swell component (lower panel). The time series are generated from the spectra as shown in Fig. 3.7.

time period of three hours. The duration of a storm is generally 6 to 8 hours during which the conditions (mean wind speed) are more or less constant.

There are basically two ways to characterise a wave record in terms of its short-term statistics:

1. Based on direct analysis of the time series and regarding it as a sequence of individual waves, each with their own wave height and wave period (wave-by-wave analysis);
2. Through a spectral analysis using the fact that the surface can be seen as a summation of an infinite number of sine waves with different heights, periods and directions.

The short-term statistical analysis based on the time series is treated in Sect. 3.4.2. Spectral analysis is dealt with in Sect. 3.4.3. It appears that the short-term distribution of wave heights can be described by a Rayleigh distribution, as long as we are dealing with not too steep waves (wave slope ak small) in deep water. In these conditions the parameters as determined by the wave-by-wave analysis and by the spectral analysis can be related to each other by constant ratios. This is the topic of Sect. 3.4.4.

3.4.2. Analysis of the time series

The mean and the standard deviation are important statistical properties that can be derived from an arbitrary time series. For a stationary surface elevation signal the mean should be constant (zero for purely oscillatory signal), whereas the standard deviation σ is a vertical measure that can be related to the wave height, as we will see later. The *variance* of the[§1.2] ~~demeaned~~ [p102] surface elevation σ^2 is an important quantity in the statistical description of waves, since it is related to the mean wave energy per unit area E which is the sum of the potential and kinetic energy ($E = E_p + E_k$). The potential energy is $E_p = \frac{1}{2}\rho g \sigma^2$. In the linear approximation (valid for small-amplitude waves compared to the wavelength and water depth), the potential and kinetic energy are the same (or $E_p = E_k = \frac{1}{2}E$) and hence:

$$E = \rho g \sigma^2 \tag{3.6}$$

The difference between variance and energy therefore is just a factor ρg.

Alternatively, when the short-term time record (order 20 minutes) is considered as a series of individual waves with their own wave height and period, average parameters can be taken of the series of wave heights and periods in order to characterise the record. Remember that useful averages require a stationary record.

Before starting the wave-by-wave analysis, the mean water level should be subtracted from the record. We then have a purely oscillatory surface elevation signal about the mean. In the case of for instance a tidal variation it is possible that the record is not entirely stationary but that there is a slight variation in the mean water level. For a short record length, this trend will be approximately linear and can be determined by regression analysis and then subtracted from the signal so that the signal is stationary again.

When the [§1.2]~~signal is demeaned~~[§1.2]mean or trend is removed from the signal, individual waves can be defined[§1.2] ~~as having a wave height equal to the difference in elevation between the crest and the trough~~. The wavelength and wave period are the distance and period respectively between two subsequent downward or upward zero-crossings. [§1.2]The wave height of each individual wave is the difference in elevation between the crest and the trough. [p102] An advantage of using downward crossings is that it relates more directly to visual observations of wave heights. The reason is

that observers tend to define a wave as starting with the trough, such that the wave height is taken to be the height of the crest relative to the preceding trough.

Various average parameters can now be derived of which the most obvious probably is the mean wave height. Nevertheless, the mean wave height is not used that often. Of more practical use is the significant wave height H_s or $H_{1/3}$. The significant wave height is defined as the average height of the highest one third of the waves:

$$H_{1/3} = \frac{1}{N/3} \sum_{j=1}^{N/3} H_j \tag{3.7}$$

where H_j is the j-th wave (with $j = 1$ the largest wave, $j = 2$ the second largest etc.) and N is the total number of waves.

It is called significant wave height because it approximately corresponds to visual estimates of experienced observers at sea of a representative wave height. Apparently observers tend to bias their estimates to the higher waves in the record. Its correspondence with visual estimates and therefore easy quantification from ships and large databases makes it a useful measure for coastal engineers.

Another often used parameter is H_{rms}, the root-mean-square wave height, which is obtained by taking the square root of the mean of the wave heights squared:

$$H_{\mathrm{rms}} = \sqrt{\frac{1}{N} \sum_{i=1}^{N} H_i^2} \tag{3.8}$$

It can be seen as a wave energy measure, since the wave energy is related to the wave height squared (see also Sect. 3.4.4).

Other measures like $H_{1/10}$ and $H_{1/100}$ are also used and they are defined analogous to $H_{1/3}$ as the average of the highest 1/10 and 1/100 of the waves respectively.

The mean of all wave periods is called the mean wave period or zero-crossing wave period:

$$\overline{T_0} = \frac{1}{N} \sum_{i=1}^{N} T_i \tag{3.9}$$

Similar to $H_{1/3}$ the significant wave period is defined as the average wave period of the highest one-third of the waves. The significant wave period is not correlated to visual estimates and therefore has less physical meaning:

$$T_{1/3} = \frac{1}{N/3} \sum_{j=1}^{N/3} T_j \tag{3.10}$$

What values would typically be found at for instance the North Sea? For sea conditions significant wave heights range from order 1 m during quiet periods (with mean wave periods of order 5 s) to 10 m and more during storms (with mean periods of order 10 s). North Sea swell has wave heights of 0.5 m to 1 m and wave periods of around 10 s.

3.4.3. Spectral analysis

An alternative way of arriving at a statistical representation of the sea state uses the fact that the surface elevation at one location can be unravelled into various sine waves with different frequencies of which the amplitudes and phases can be determined by so-called Fourier analysis. Jean-Baptiste Fourier demonstrated that any signal can be described by a sum of harmonic components, a so-called Fourier series. Under the assumption of a stationary record, these sine waves have a constant amplitude and phase per component in time. For a time record with finite duration, the Fourier series can be written in terms of sine (or cosine) functions that fit an integer number of times in the record duration T_r.

The oscillatory surface elevation can be written as a Fourier series as follows:

$$\eta = \sum_{n=1}^{N} a_n \cos\left(2\pi f_n t + \alpha_n\right) \tag{3.11}$$

where

$$f_n = \frac{n}{T_r} \text{ for } n = 1, 2, \ldots$$

Although in nature the frequencies will be continuous, the frequencies in Eq. 3.11 are discrete by necessity, because in practice the length of the wave series is restricted to for instance 20 min ($^{\S 1.1}\Delta f = 1/T_r$ $^{\S 1.1}\Delta f_n = 1/T_r$) [p104]. The record length thus determines the smallest frequency (the longest wave) that can be determined from the record: $f_{\min} = 1/T_r$. Moreover, the time series is not continuous since the water level measurements are performed with a certain sampling interval. The sampling interval determines the highest frequency that can be determined from the record: $f_{\max} = \frac{1}{2\Delta t}$.

From the amplitudes of the various components the spectrum of wave energy over the range of wave periods or frequencies can be calculated. With a bit of trigonometry it can be found that for one harmonic component the variance is equal to $\frac{1}{2}a_n^2$. Then for a sum of harmonic components the corresponding variance is given by:

$$\sum_{n=1}^{N} \frac{1}{2} a_n^2 \tag{3.12}$$

The variance density spectrum gives the variance density per unit frequency interval for each frequency and is constant for $\Delta f \to 0$:

$$\lim_{\Delta f \to 0} \frac{1/2 a_n^2}{\Delta f} = E\left(f_n\right) \tag{3.13}$$

By taking the integral of the spectrum the total variance is recovered again:

$$\int_0^\infty E(f)\,\mathrm{d}f = \overline{\eta^2} = \sigma^2 \tag{3.14}$$

Two conclusions can be drawn. First, in the spectrum the variance density is the contribution of one component to the total variance. Second, the standard deviation σ of the surface elevation signal can be estimated from the area under the spectrum. Note further that from the variance density spectrum the energy density spectrum is readily obtained, since variance and energy are coupled through Eq. 3.6.

The so-computed spectrum describes the time series under consideration but is only an estimation of the spectrum representing the random process, since a next realisation under the same condition will give a slightly different surface elevation. To get a better estimate, averaging has to take place of spectra, either based on subdivisions of the time series or over frequency bins.

In Fig. 3.7 energy spectra are shown with the corresponding time series. In the middle and lower panels all energy is concentrated around the mid-frequencies. §1.2 The middle panel shows a spectrum for sea only. The narrower the spectrum, the more regular the waves are. For larger, longer waves the spectrum will be shifted towards the lower frequencies and contain more energy. For smaller, shorter waves the spectrum will be shifted towards the higher frequencies and be lower. §1.2 The lower panel shows a spectrum for swell only; it is narrower than the spectrum for sea, contains less energy and the energy is concentrated around lower frequencies. [p107] Sometimes one can distinguish between two adjacent or often partly overlapping parts of the spectrum. This means that two distinct wave fields are present: swell and sea (upper panel). If the mean frequencies of the two wave fields are close, then there will be so much overlap that the spectrum is broad, but otherwise looks like a spectrum with only one wave field.

What about the phases of the different components? The distribution of the phases over the frequencies is called a phase spectrum. Often the phase spectrum is not shown since in not too steep waves and in deep water the phases seem to be independent of each other and uniformly distributed between $-\pi$ and π. This means that the different components are not related through their phases and can be seen as individual waves moving independently through the signal, as if they were alone. This is the case for linear small-amplitude waves. So then only the amplitude or variance/energy spectrum remains to characterise the wave record.

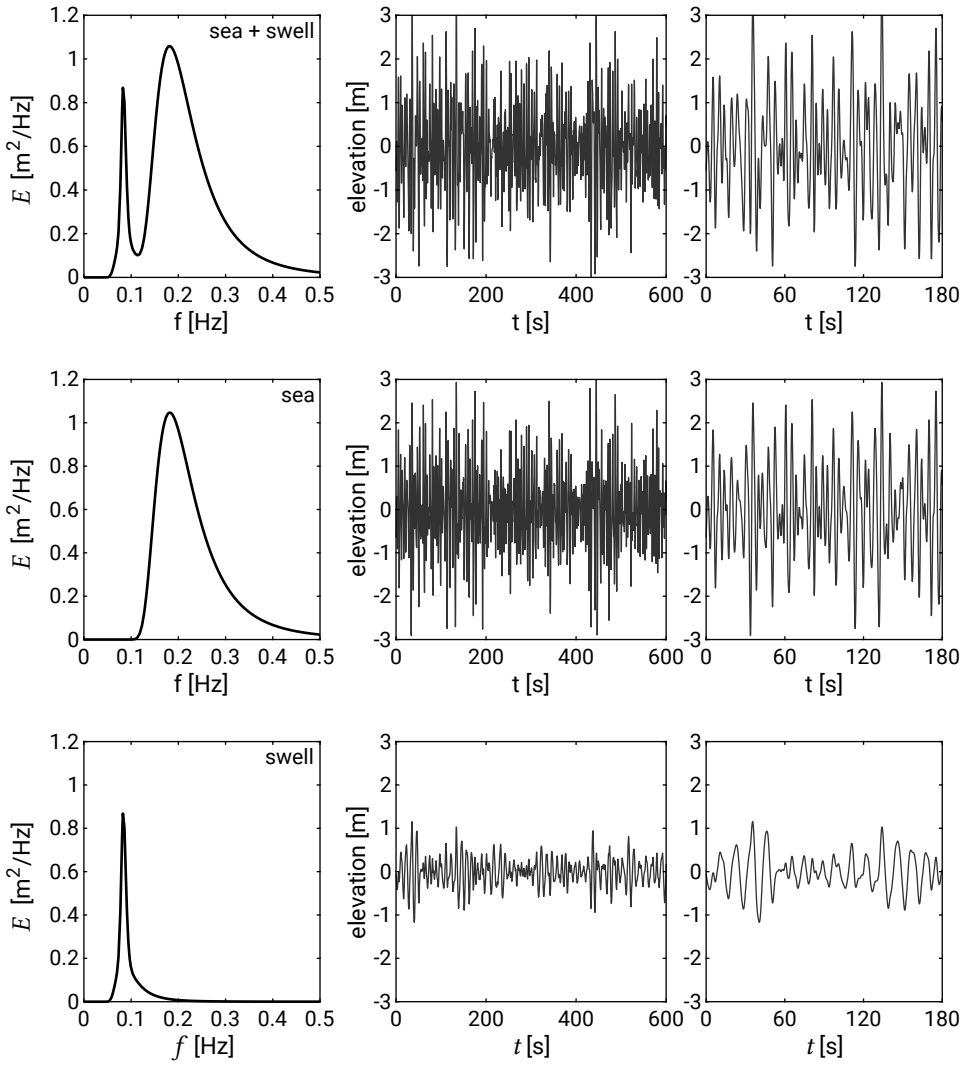

Figure 3.7: Surface elevation time series and corresponding spectra for sea and swell combined (upper panel), sea (middle panel) and swell (lower panel). To generate the sea component, a so-called JONSWAP spectrum (a typical spectrum for sea, see Sect. 3.5.1) is used with $H_S = 1.8\,\mathrm{m}$, $T_p = 5.5\,\mathrm{s}$ and a peak enhancement factor $\gamma = 1$ (see eq. (6.3.15) in Holthuijsen, 2007). For the swell component, $H_S = 0.5\,\mathrm{m}$, $T_p = 12\,\mathrm{s}$ and $\gamma = 5$ are used. For both sea and swell, the peak-width parameter is $\sigma = 0.07$ for $f \leq f_p$ and $\sigma = 0.09$ for $f > f_p$. The sea and swell spectra are combined in a bi-modal spectrum of swell and sea. The time series are generated from the spectra at a sampling frequency of 25 Hz assuming random phases. Note that the timeseries in the right panels correspond to Fig. 3.6.

Which parameters can be derived from the variance spectrum? First, the spectrum reveals the dominant frequencies in the wave record; most energy occurs at the spectral peak and the corresponding wave period is called the peak spectral period T_p. Other typical average parameters can be expressed in terms of spectral moments:

$$m_n = \int_0^\infty f^n E(f)\,\mathrm{d}f \qquad \text{for} \qquad n = \ldots, -3, -2, -1, 0, 1, 2, 3, \ldots \tag{3.15}$$

m_0 is the area under the spectrum. Since m_0 is the total variance integrated over all frequencies, the standard deviation is given by $\sigma = \sqrt{m_0}$ (see Eqs. 3.13 and 3.14). In Sect. 3.4.4 we will see how the zero-th moment m_0 and the second moment can be used to determine the zero-crossing period from the spectrum.

3.4.4. Short-term wave height distribution

In the previous section we have seen that in deep water and as long as the waves are not too steep, the surface elevation can be considered as the sum of a large number of components with random phases. In that case observations and theoretical considerations have shown that the wave heights can be described by a Rayleigh distribution. We will see below that by using the Rayleigh distribution, the parameters as determined by the wave-by-wave analysis and by the spectral analysis can be related to each other.

The short-term distribution of wave heights known as the Rayleigh distribution is:

$$p(H) = \frac{H}{4\sigma^2} e^{-\frac{H^2}{8\sigma^2}} \tag{3.16}$$

Although theoretically only valid for a narrow spectrum, observations have shown that also for broader spectra the wave heights more or less obey a Rayleigh distribution. In practice wave period variability is often ignored.

From the probability density function (Eq. 3.16) the probability can be derived that an individual wave height H' exceeds a specified wave height H:

$$P\left(H' > H\right) = 1 - P\left(H' < H\right) = 1 - \int_0^H p(H)\,\mathrm{d}H = e^{-\frac{H^2}{8\sigma^2}} \tag{3.17}$$

where the only parameter σ is the standard deviation and thus a wave height measure. As we have seen it can be estimated from either the time series or, since $\sigma = \sqrt{m_0}$, from the spectrum.

The wave height with a probability of exceedance P follows from Eq. 3.17:

$$H_P = 2\sigma\sqrt{2\ln(1/P)} \tag{3.18}$$

For instance, the height $H_{2\,\%}$ that is exceeded by 2 % of the waves is equal to §1.1 ~~$2\sigma\sqrt{2\ln(1/P)}$~~ §1.1 $2\sigma\sqrt{2\ln 50} = 5.59\sigma$ [p107] and $H_{1\,\%} = 6.07\sigma$.

In Sect. 3.4.3 $H_{1/3}$ was calculated from the time series. We can also use the Rayleigh distribution to calculate $H_{1/3}$. This can be shown to yield:

$$H_{1/3} = 4\sigma \tag{3.19}$$

The probability of exceedance of wave heights according to the Rayleigh distribution can now also be expressed in terms of significant wave height:

$$P\left(H' > H\right) = e^{-2\left(\frac{H}{H_s}\right)^2} \tag{3.20}$$

which is often graphically represented as in Fig. 3.8.

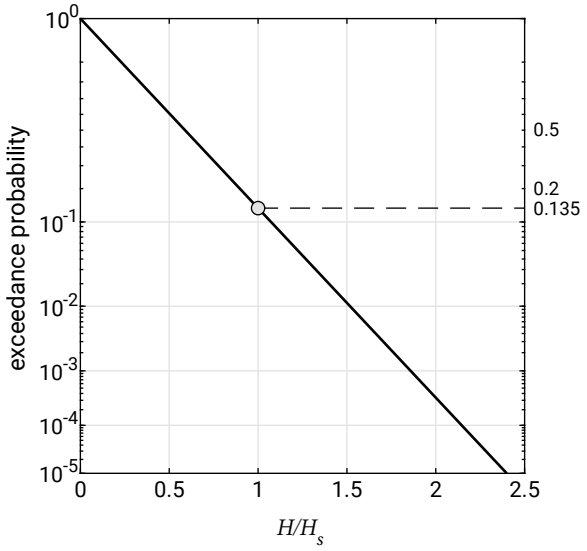

Figure 3.8: §1.2 ~~On Rayleigh paper (with a log-scale vertical axis) the Rayleigh distribution is represented by a straight line through the origin.~~ §1.2 The exceedance probability $P(H' > H)$ (Eq. 3.20) as a function of H/H_s shows as a straight line when plotted using a vertical scale with a spacing proportional to $\sqrt{-\ln P}$. [Figure is corrected] [p108]

§1.2 ~~The value of H_s can be read from the graph at the 13.5 % exceedance value (e^{-2}).~~ §1.2 The probability that an individual wave height is larger than H_s is 13.5 % (e^{-2}), which can be read from the graph or determined from Eq. 3.20. [p108] It also follows that 1 out of 100 waves will be higher than about 1.5 times H_s. The strength of the storm considered is apparently determined by just one value: H_s. A stronger storm would lead to a steeper distribution curve, which is again defined by a specific value of the significant wave height.

When irregular waves enter shallow water, the highest waves will start breaking due to the limited depth. This means that the Rayleigh distribution is no longer applicable for $H_s > 0.3h$ or so. Then, for the tail of the distribution, a Weibull distribution agrees better.

Based on Eq. 3.19 we define $H_{m_0} = 4\sqrt{m_0}$ as an alternative formula to calculate the significant wave height and use the subscript m_0 to indicate that the wave height is computed from the zeroth moment of the wave spectrum. By the way, from observations at sea it appears that a correction to this theoretical value gives $H_{1/3} \approx$ §1.1 $3.8\sqrt{m_0}$ [p108]. Summarizing, one can state that the short-term distribution of wave heights, i.e. the wave heights in a stationary sea state, exhibits some very typical relations:

Table 3.1: Typical wave heights (non-breaking waves)

Description	Notation	$H/\sqrt{m_0}$	H/H_s
RMS height	H_{rms}	$2\sqrt{2}$	0.707
Mean height	$\overline{H}$	$\sqrt{2\pi}$	0.63
Significant height	$H_s = H_{1/3}$	4.004	1
Average of 1/10 highest waves	$H_{1/10}$	5.09	1.27
Average of 1/100 highest waves	$H_{1/100}$	6.67	1.67

The maximum individual wave height in a wave record depends on the length of the record. Suppose we have a storm record with a duration of six hours. Suppose the mean wave period is $\overline{T} = 10\,\text{s}$, so on average we have $6 \times 60 \times 60/10 \approx 2000$ waves in the record. The maximum individual wave height can now be estimated by setting $P = 1/2000$ in Eq. 3.18. We then find that in a storm the maximum individual wave height $H_{\text{max}} \approx 2H_s$. This is handy method to quickly estimate H_s from a wave record with a certain number of waves.

For a regular wave, the energy content $E = {}^1\!/_2\rho g a^2 = {}^1\!/_8\rho g H^2$. Using Table 3.1 we have for an irregular wave field $E = \rho g m_0 = {}^1\!/_8\rho g H_{\text{rms}}^2$. Apparently, the root-mean-square wave height H_{rms} is the wave height representing the total energy content.

In a similar way, wave periods can be determined from the spectral moments. For instance the zero-crossing period:

$$T_2 = \sqrt{\frac{m_0}{m_2}} \tag{3.21}$$

Theoretically this is equal to the zero-crossing period $\overline{T_0}$ as determined from the time series. For narrow spectra such as for swell, T_2 and $T_{1/3}$ are approximately equal to the spectral peak period T_p. For a broader spectrum with a high frequency tail (a typical sea spectrum) $T_{1/3}$ is approximately equal to 0.9–0.95 T_p and T_2 is roughly equal to 0.7 T_p. However, the value of T_2 should be considered with care; because of the sensitivity of the higher moments for higher frequencies, T_2 will be sensitive to details in the measurements and data processing.

The wave climate for the North Sea is not very extreme. The significant wave height now and then reaches values of 8 metres in the northern part and 6 metres in the southern part (off the Dutch coast). The mean wave period under those conditions is around 10 seconds. The highest wave in the north is then approximately 15 metres high with a period of 15 to 20 seconds. Averaged over the year $H_s = 1\,\text{m}$ to $1.5\,\text{m}$ and $\overline{T} = 4$ to 5 seconds.

So far we have not taken the directionality of waves into account. In reality, however, the different harmonic components have different wave directions θ. That is why you

will sometimes also find information on a mean wave direction θ_m and the amount of spread around the mean.

3.5. Wind wave generation and dispersion

3.5.1. Locally-generated sea

Waves are generated by local wind fields. At the area of wave generation, these waves are relatively steep and short-crested. The latter means that there are no distinct wave fronts because the waves are irregular and directional. An example is given in Fig. 3.9. In this photo white-capping can also be seen, which is steepness-induced wave-breaking when the wave height becomes too large compared to the wavelength ($H/L > 0.14$).

The wave characteristics (height, period, propagation direction) and their duration depend on the characteristics of the wind field (speed, duration and direction), the fetch and the local water depth. Fetch is the maximum length of open water over which the wind blows, which is determined by meteorological and geographical conditions. Generally, the higher the wind speed and duration, the larger the wave height and period. But only for ideal cases, wave heights can be estimated on the basis of wind velocity, duration and fetch.

Although wind conditions cannot be predicted accurately long in advance, wind conditions can be described statistically. The wind climate consists of both velocity data and directional data. Velocities can be expressed by wind speed (when measured) or as a certain number on the Beaufort scale (when visually observed, see Intermezzo 3.2). These data can be found in meteorological yearbooks and in various atlases, for instance specific hydrographical atlases that contain data collected at sea.

Parameterised wave spectra have been formulated which relate the wind field to spectral density and can therefore be used to hindcast (estimate past events) wave parameters from known wind fields. An example is the Joint North Sea Wave Observation Project (JONSWAP) spectrum which is characteristic for (developing) wind sea in oceanic waters. A typical JONSWAP spectrum was shown in the middle panel of Fig. 3.7. It can be determined from the wind speed and the fetch. For a fully developed sea (not limited by either fetch or duration, which in reality will hardly ever happen) the so-called Pierson-Moskowitz spectrum is valid. This is a broader spectrum and only dependent on the wind speed.

Figure 3.9: Wind-generated gravity waves at sea, probably Beaufort 5. Photo from Rijkswaterstaat (‘Credits’ on page 579).

Intermezzo 3.2 Beaufort scale

The Beaufort wind speed scale (ranging from 0 to 12) relates wind speed to the local sea state using descriptors such as wave height, wavelength, white capping, amount of foam and spray. Beaufort, a British naval officer, introduced the Beaufort wind scale in 1805. For tactical reasons the scale was intended to exchange objective information between sailing vessels of the British Navy. The lower scales (2 to 4) refer to sailing speeds of the common naval vessel of that time (man-of-war) under full sail. The intermediate scales (5 to 9) refer to conditions that required reefing of sail. The higher scales (10 to 12) deal with survival of ship and crew. The Beaufort scale is summarised in Table 3.2 in the form that is used at present. Bold-printed expressions refer to the official terms of the §1.1 ~~(WMO)~~ §1.1 World Meteorological Organisation (WMO) [p111]. Pictures of typical sea states at various Beaufort wind speeds are available to assist observers on board of sea-going vessels (see also http://en.wikipedia.org/wiki/Beaufort_scale).

3.5.2. Wave dispersion

In principle the wave motion can be described by the continuity equation and the Navier-Stokes equations of motion. Difficulties arise however when attempts are undertaken to solve these equations. One of the complications is that the surface boundary condition is the surface elevation that we try to solve. If we linearise this surface boundary condition and assume a horizontal bottom, a simple solution to the equations is the single Fourier component that we described in Sect. 3.2. We then get the

Table 3.2: Beaufort scale

Beaufort No.	Wind speed		Phenomena observed on land	State of the sea surface	In Dutch as used by KNMI	Wave height
	m/s	kn				m
0	0 – 0.2	0 – 1	**Calm**: Still; smoke will rise vertically	Sea like mirror.	Windstil	0
1	0.3 – 1.5	1 – 3	**Light Air**: Rising smoke drifts; weather vane is inactive	Ripples with appearance of scales; no foam crests.	Zwakke wind	0.1 – 0.2
2	1.6 – 3.3	3 – 6.5	**Light Breeze**: Leaves rustle, people feel wind on skin; weather vane is inactive.	Small wavelets; crests of glassy appearance, not breaking.	Zwakke wind	0.3 – 0.5
3	3.4 – 5.4	6.5 – 11	Gentle Breeze: Leaves and twigs move around. Light-weight flags extend.	Large wavelets; crests begin to break; scattered whitecaps.	Zwak tot matige wind	0.6 – 1.0
4	5.5 – 7.9	11 – 16	**Moderate Breeze**: Moves thin branches, raises dust and paper.	Small waves, becoming longer; numerous whitecaps.	Matige wind	1.5
5	8 – 10.7	16 – 21	**Fresh Breeze**: Small trees begin to sway.	Moderate waves, taking longer form; many whitecaps; some spray.	Vrij krachtige wind	2
6	10.8 – 13.8	21 – 28	**Strong Breeze**: Large tree branches move, open wires (such as telegraph wires) begin to whistle, umbrellas are difficult to keep under control.	Larger waves forming; whitecaps everywhere; more spray.	Krachtige wind	3.5
7	13.9 – 17.1	28 – 34	**Near Gale**: Large trees begin to sway, noticeably difficult to walk.	Sea heaps up; white foam from breaking waves begins to be blown in streaks.	Harde wind	5
8	17.2 – 20.7	34 – 42	**Gale**: Twigs and small branches are broken from trees, walking into the wind is very difficult.	Moderately high waves of greater length; edges of crests begin to break into spindrift; foam is blown in well-marked streaks.	Stormachtig	7.5
9	20.8 – 24.4	42 – 49	**Strong Gale**: Slight damage occurs to buildings, shingles are blown off of roofs.	High waves; sea begins to roll; dense streaks of foam; spray may reduce visibility.	Storm	9.5
10	24.5 – 28.4	49 – 57	**Storm**: Large trees are uprooted, building damage is considerable.	Very high waves with overhanging crest; sea takes white appearance as foam is blown in very dense streaks; rolling is heavy and visibility is reduced.	Zware storm	12
11	28.5 – 32.6	57 – 65	**Violent Storm**: Extensive widespread damage. These typically occur at sea, rarely inland.	Exceptionally high waves; sea covered with white foam patches; visibility still more reduced.	Zeer zware storm	15
12	>32.7	>65	**Hurricane**: Extreme destruction.	Air filled with foam; sea completely white with driving spray; visibility greatly reduced.	Orkaan	>15

Airy wave theory (App. A). Neglecting non-linearities gives a good approximation for not too steep waves in deep water ($ak << 1$ for kh is large) or small-amplitude waves in shallow water ($a << h$ for kh is small). According to Airy wave theory, for a linear sine wave the relation between frequency ω and wavenumber k is given by:

$$\omega = \sqrt{gk \tanh kh} \tag{3.22}$$

and is called dispersion relation. It is a function of the local water depth and the restoring force g. The phase velocity $c = \omega/k$ is then given by:

$$c = \frac{gT}{2\pi} \tanh kh = c_0 \tanh kh \tag{3.23}$$

The phase velocity (speed) is the rate at which any phase of the wave (for instance the wave crest) propagates in space. It is also called propagation velocity (or speed) or wave celerity. The nature of the hyperbolic tangent is shown in Fig. 3.10.

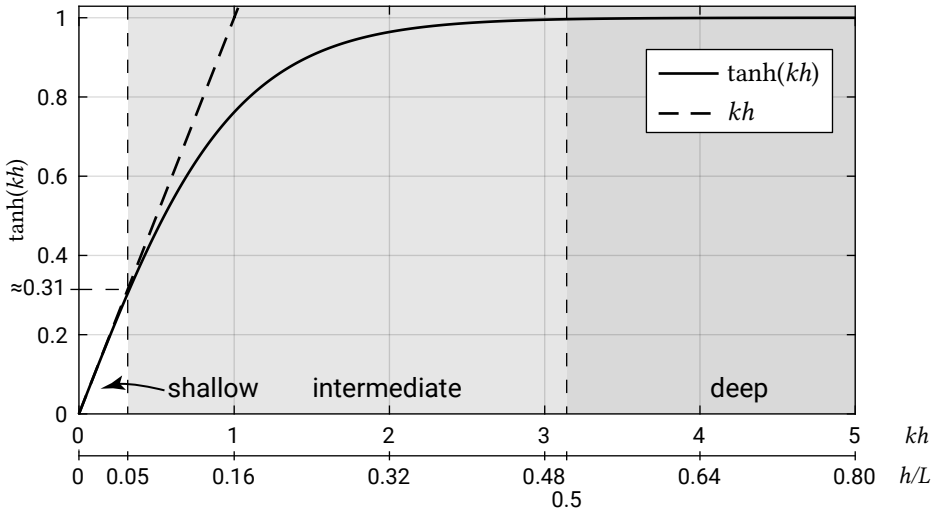

Figure 3.10: Nature of the hyperbolic tangent.

Given the fact that tanh kh equals 1 for $kh \gg 1$, c_0 represents the deep-water phase velocity $c_0 \approx 1.56T$ as function of T. The deep-water (or short-wave) approximation can be used without too many errors (order of 1 %) for $kh > \pi$ or $h/L > 0.5$. Wind waves in oceanic waters can be considered short waves, such that their phase velocity is linearly dependent on the wave period. Expressed in terms of the wavenumber in deep water the phase velocity $c_0 = \sqrt{gL_0/2\pi}$ and is therefore proportional to the square root of the deep-water wavelength. Hence, longer waves propagate faster than shorter waves. Independent harmonic components of a wind wave field can be expected to travel at different speeds. The separation of the different harmonic components due to their different propagation speeds is called frequency dispersion. Oceanic wind waves are highly dispersive.

Since $\tanh kh$ equals kh for $kh \to 0$, the dispersion relation reduces to $c = \sqrt{gh}$ for $kh \to 0$. Hence, if the wave is long enough ($kh < 0.31$ or $h/L < 1/20$), the wave celerity is only dependent on the local water depth. The shallower the water depth, the smaller the propagation speed. Since the wave celerity is independent of the wave period, the wave is called non-dispersive. This is the case for the tide and generally for tsunami waves as well. Wavelengths of tsunamis are easily 100 km or more[2] which is more than 20 times larger than the average water depth in the deep ocean, which is about 4000 m deep. A tsunami then propagates at a velocity of $c = \sqrt{9.81 \times 4000} = 200$ m/s or 700 km/h. As long as they do not dissipate their energy against a shore, tsunamis can travel at these high speeds for a long period of time and lose very little energy in the process.

If waves meet a current (in or against the wave propagation direction), the wavelength, propagation velocity and wave height will be affected. The propagation velocity and wavelength relative to a fixed reference frame will increase in the case of a current in the propagation direction. The wave height will decrease. In the case of an opposing current, it is the other way around.

3.5.3. Wave groups

Another interesting phenomenon in deep-water waves is that the wave crests move faster than the wave energy. Let us first consider a series of regular waves moving away from a disturbance into otherwise still water, such as a group of waves generated by a wave board in a wave flume and now moving away from the wave board. It can be seen that the wave front and the group of waves as a whole moves at a certain speed. This speed is called the group speed and is the speed with which the energy of the waves moves. The phase velocity, however, was defined as the velocity of a wave crest. When following a wave crest, we can see how it originates at the rear of the group, then moves forward through the group and finally disappears at the leading edge of the group. The phase velocity of the wave crest is therefore larger than the velocity of the wave front or the group (except in shallow water, where the group velocity is equal to the phase velocity).

Now look at irregular waves. They appear more or less in groups, so that we now have a series of groups as opposed to the one group as described above. The groupiness is caused by interference between waves of different wavelength. To demonstrate this, consider the limiting case of just two slightly different frequencies travelling in the same direction. We have a water depth of 20 m and two regular waves with an amplitude of 1.5 m each. The wave periods are 6.2 s and 7.0 s respectively. The two wave trains will interfere with each other as shown in Fig. 3.11. The length and period

[2] In Sect. 3.2, tsunami periods were said to range from 5 min to 60 min. As an exercise: use Table A.3 to compute the corresponding wavelengths at a depth of 4000 m. Also compute the wave period range for which this depth is classified as intermediate water.

of the groups can be computed from the differences in wavenumbers and frequencies respectively:

$$k_{\text{group}} = \Delta k = k_2 - k_1 \rightarrow L_{\text{group}} = \frac{2\pi}{\Delta k} \tag{3.24a}$$

$$\omega_{\text{group}} = \Delta\omega = \omega_2 - \omega_1 \rightarrow T_{\text{group}} = \frac{2\pi}{\Delta\omega} \tag{3.24b}$$

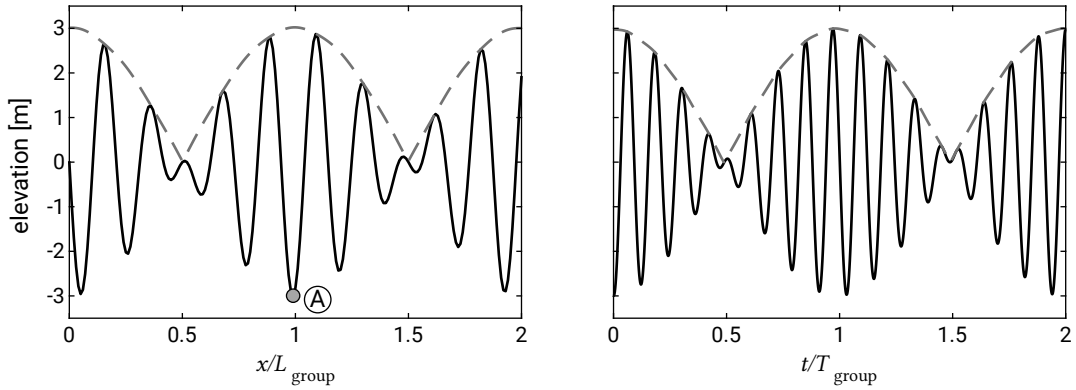

Figure 3.11: Wave grouping of two monochromatic (single-period) waves with a slightly different period. Either regular wave has an amplitude of 1.5 m, whereas the wave periods are 6.2 s and 7.0 s. The water depth is 20 m. The left panel shows the grouping in space at $t = 0$. The right panel shows the grouping in time at location A. As an exercise: compute the ratio between the number of waves in the group in time and the number of waves in the group in space and verify this ratio from the figure.

The broader the spectrum, the more irregular the waves are and the less clearly the groups can be distinguished. Because of the narrow spectrum, grouping is prominent in swell (see Sect. 3.5.4) and more pronounced if the swell is dispersed more. As in the case of disturbance, the energy of waves is carried in the group and not in each individual wave.

The ratio between the group velocity and the higher phase velocity is called n and reads according to Airy wave theory:

$$n = \frac{c_g}{c} = 0.5\left(1 + \frac{2kh}{\sinh 2kh}\right) \tag{3.25}$$

Figure 5.3 shows the dependency of n on the water depth and (deep-water) wavelength. For short waves in deep water n reduces to 0.5. The group velocity therefore is half of the propagation velocity of an individual wave crest. When calculating how long it will take for a group of swell waves to cover a certain distance, the group velocity needs to be taken into account. For long waves (or shallow water) n equals 1 such that the phase velocity is equal to the group velocity. The frequency dependency of the group velocity is comparable to that of the phase velocity. Hence, the fronts of longer-period waves travel faster.

In Sect. 3.4.4 we have already seen that the energy per square metre of water surface is $E = \frac{1}{8}\rho g H_{\text{rms}}^2$. This energy is propagated at the wave group speed c_g, thus causing an energy flux U, with

$$U = Ec_g = Enc \tag{3.26}$$

Based on energy conservation, offshore wave conditions can be translated to the nearshore. The energy balance therefore is an important concept in coastal engineering. It is discussed in detail in Ch. 5.

3.5.4. Sea versus swell waves

From Sect. 3.4 we know that an irregular wave train can be seen as a sum of sine waves with various periods. For not too long periods of time (maybe an hour and distances of tens of kilometres) and for small amplitudes, these sine waves have constant amplitudes and random phases. They travel in many different directions, all at their own velocity, given by the so-called dispersion relation according to Airy or linear wave theory.

Wave fields disperse (spread out) since the different harmonic components travel at different speeds that depend on their frequency. In Sect. 3.5.2 we referred to this phenomenon as frequency dispersion. From the dispersion relation it becomes clear that longer waves travel faster than shorter waves. Also, we have seen that the group velocity (the velocity of the front) is larger for longer-period waves.

At some distance from the storm centre, one would therefore first experience a long, fast-travelling swell and later an increasingly shorter wave period. At long distances from the storm centre the shorter waves are filtered out since dissipation processes (due to currents and white-capping) more strongly affect the shorter waves[3]. As a result only a long, and fairly regular (as the various components travel at different speeds) swell remains. Besides, the swell is uni-directional §1.1 or long-crested [p116], because only waves travelling in a particular direction end up at a certain location away from the storm centre. The spreading due to different directions of propagation is called direction dispersion. Due to frequency and direction dispersion, the spectrum of swell is narrow in frequency and direction respectively. As a result of spreading (and energy dissipation) swell is relatively low. Figure 3.12 shows swell waves arriving at the coast of Angola that have been generated in two different storms.

The characteristics of swell waves at a particular (coastal) location are determined by the characteristics of the storm and the distance to the storm. Swell can travel the oceans for thousands of kilometres. A 10 s swell wave travels at speed $c_0 \approx 1.56T =$

[3] In addition to dissipation and dispersion, non-linear wave transfer plays a role; energy is moved from the centre of the spectrum to both the higher and lower frequencies. The higher frequencies get subsequently dissipated, whereas the lower frequencies gain energy.

Figure 3.12: Swell waves arriving at the Atlantic coast of Angola from two distinct directions (southwest and northwest). This swell is generated by trade winds. Courtesy Stefanie Ross ('Credits' on page 579).

$1.56 \times 10 = 15.6\,\text{m/s} = 56\,\text{km/h}$. The group velocity will be about half that (in deep water). In Fig. 3.13 a graph is shown with wave height and period as a function of propagation distance from the storm centre.

In a first-order approximation,[§1.2]no [p117] mass transport is associated with short-wave propagation, such that the path of swell through the oceans is unaffected by the Coriolis effect. Swell therefore travels the globe along *great circles*, the shortest distance between two locations on a spherical object.

Some coasts around the world – for instance the west, east and south coasts of Australia – mainly experience swell waves, which have been generated in storms far away. A typical wave spectrum will then be narrow-banded. For other coasts, locally-generated storm waves dominate the wave climate, as is the case for the Dutch coast. The sea state then is irregular and short-crested. Most of the time, wave records off the Dutch coast show both swell waves generated in distant storms and locally-generated storm waves. Two distinct peaks can then be observed in the spectrum, see Fig. 3.14. The swell can only come from the north and is usually not older than a day or sometimes two days.

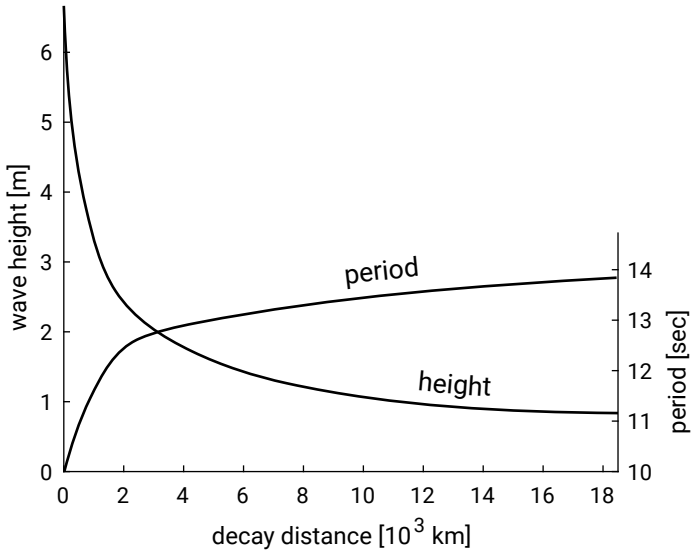

Figure 3.13: The effect of swell decay on wave period and wave height in the case of a 6.1 m high, 10-second wave according to J. L. Davies and Clayton (1980).

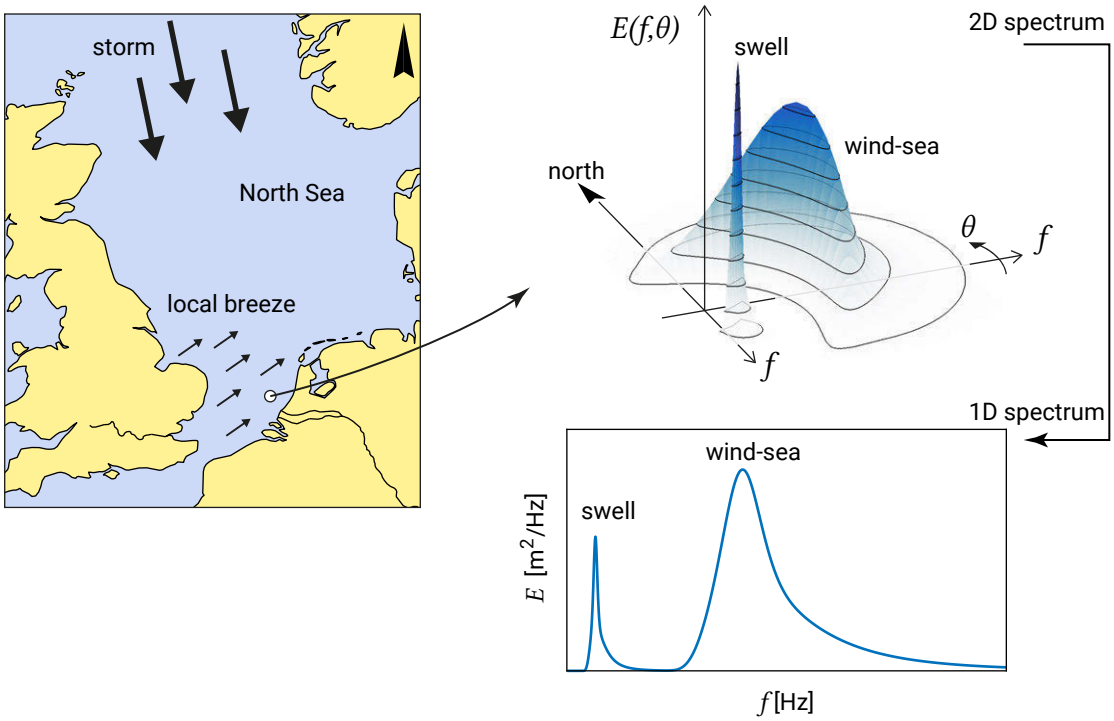

Figure 3.14: At a location off the Dutch coast, a northerly swell, generated by a storm off the Norwegian coast, meets a southwesterly sea generated by a local breeze (left). The 2D spectrum represents the spectral energy as a function of frequency and direction and is constructed by combining JONSWAP spectral shapes with Gaussian directional distributions. The 1D spectrum is obtained through integration over all directions. Even though in the 2D spectrum the swell peak is higher than the sea peak, the sea peak is the larger peak in the 1D spectrum because of the larger directional spreading for sea as compared to swell.

3.6. Long-term statistics and extreme values

As indicated above, waves are measured at regular intervals of 3 to 6 hours during a relatively short period during which the record can be considered stationary. This results in a series of wave observations with a sampling interval of 3 or 6 hours. If long enough (years or even decades, as in the case of the Dutch wave data), this series can in its turn be considered a set of random data representing the long-term wave climate of the location. Not only measured wave climates are used for this, but also hindcasts based on archived wind fields. Note that for periods of decades, conditions may not be stationary (due to for instance climate change impacts on wave climate).

For many engineering problems long-term statistics of average parameters are sufficient. The long-term data can be represented in various ways:

- Histograms of H_s present the percentage of occurrence of a certain significant wave height.
- Scatter plots of H_s versus wave period show the dependency of wave periods and wave heights.
- Tables can also include information on wave period and wave angle, for instance a table valid for a certain direction sector which gives the percentage of occurrence of H_s versus $\overline{T_0}$.
- Wave roses give the directional distribution of the wave heights.

Mostly, long-term distributions of significant wave heights are determined, which present H_s versus the percentage of exceedance. Long-term distributions of wave periods and wave angles can also be determined, but are often considered to be a function of the long-term wave height distribution. Sometimes the long-term distribution functions for H_s are calculated for different wave angle classes.

Since extreme conditions are not always part of observed data, extrapolation is sometimes needed. For extrapolation of the probabilities, several distributions can be used. The choice does not have a theoretical basis. Often used are the log-normal distribution and the Weibull distribution. These analyses will not give information on when an event will happen but it is possible to determine how often it is likely to happen.

The percentage of exceedance can also be expressed as a return period. The return period is defined as the average time between events with a (significant) wave height larger than a certain value.

For an engineering project the wave climate is generally known at some distance from the coastal site. We can then use a wave model to translate this offshore wave climate to a climate representative for the project site. However, a full wave climate consists of a multitude of wave conditions, which is often not practical. An example of a year-averaged wave climate based on a wave study is shown in Table 3.3 and Fig. 3.15. Instead of using all those conditions in morphodynamic computations, engineers often reduce such a climate to a representative set with fewer conditions. But what is

representative in this context? That depends on the problem under consideration. For an engineering problem which is governed by longshore sediment transport, a representative set of wave conditions means that at least the total longshore transport rate reproduced by the smaller set is identical to the rate based on the full climate. After such a wave climate schematisation, morphodynamic computations can be carried out for fewer conditions, which is therefore faster.

Table 3.3: Wave conditions for validation case. From Mol (2007)

condition	H_s [m]	dir [°N]	T_p [s]	duration [%]	days/yr
1	0.4	188	2.85	1.00	3.65
2	0.4	203	2.85	1.50	5.48
3	0.6	203	3.49	1.00	3.65
4	0.4	218	2.85	6.00	21.9
5	0.6	218	3.49	3.00	10.95
6	1.2	218	4.93	3.00	10.95
7	1.8	233	6.04	1.00	3.65
8	1.4	233	5.32	2.00	7.3
9	1.0	233	4.50	3.00	10.95
10	0.8	233	4.02	4.00	14.6
11	0.6	233	3.49	6.00	21.9
12	0.4	233	2.85	8.00	29.2
13	0.4	248	2.85	7.00	25.55
14	0.8	248	4.02	5.00	18.25
15	1.2	248	4.93	4.00	14.6
16	1.6	248	5.69	1.00	3.65
17	1.6	263	5.69	1.00	3.65
18	0.8	263	4.02	3.00	10.95
19	0.4	263	2.85	4.00	14.6
20	0.8	278	4.02	4.00	14.6
21	0.4	278	2.85	4.00	14.6
22	0.4	293	2.85	3.00	10.95
23	0.6	293	3.49	2.50	9.13
24	0.8	308	4.02	3.00	10.95
25	0.6	308	3.49	3.00	10.95
26	0.4	308	2.85	3.00	10.95
27	0.6	323	3.49	3.50	12.78
28	0.4	323	2.85	4.00	14.6
29	0.4	338	2.85	3.50	10.95
30	0.8	338	4.02	2.00	9.13
total				100	365

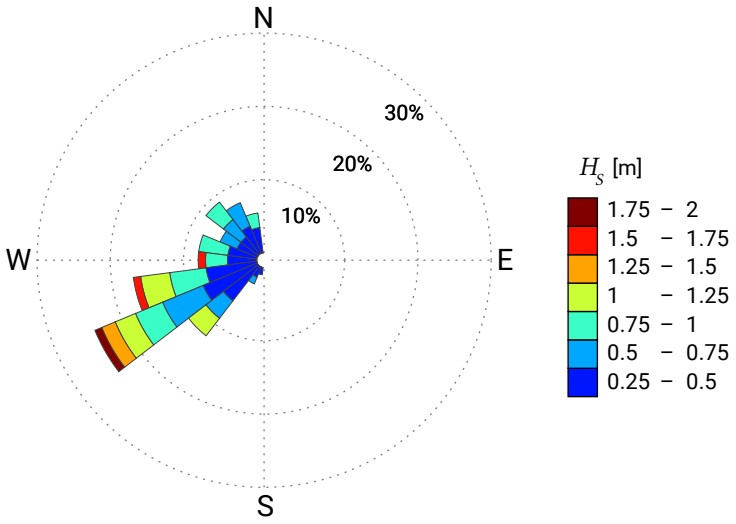

Figure 3.15: Wave climate for the validation case in Table 3.3 presented as a wave rose.

For applications like determining the height of a deck of a platform, the probabilities of individual wave heights are required. In such cases, the short-term and the long-term expectations must be combined to obtain the probability of exceedance of individual wave heights during a fixed period, for example the lifetime of the structure. This is also often close to a Weibull distribution.

Because in shallow water there is a direct relation between maximum breaking wave height and water depth, the wave height distribution is not independent of the occurrence of extreme water levels. Close to the shore, this could mean that the long-term distribution of wave heights coincides with the distribution of extreme water levels.

3.7. Generation of the tide

3.7.1. Equilibrium theory of the tide

At the coast, the tide is most easily observed as daily water level variations. At most places in the world, the tide is essentially semi-diurnal, i.e. having a period of approximately half a day. This means that two high waters and two low waters can be observed daily. The tidal range between high water and low water can be 10 metres or more depending on the location.

Isaac Newton was the first to explain the generation of the tide. After having identified the tide-generating forces, he assumed the ocean water to respond instantly to these forces. That is why his theory is called the equilibrium theory of tides. He also neglected the presence of continents and assumed the earth to be entirely covered by water. In the present section, we follow his theory to explain some well-known tidal phenomena. Subsequently, in Sect. 3.8 the effects of land masses and non-instantaneous response are discussed.

3.7.2. Gravitational pull

The tide-generating forces find their origin in the gravitational pull of the moon and the sun on the water in the oceans. The sun and the earth revolve around a common centre of mass. They attract each other by a force that is proportional to their respective masses and inversely proportional to the square of their mutual distance. Similarly, the moon and the earth revolve around their common centre of mass. Revolving about a common centre of mass implies that the attraction forces act as centripetal forces, so that the earth is constantly being accelerated towards the moon and the sun, as in free fall, the direction of the free fall being everywhere parallel to the line connecting the centres of mass. The difference in mass between the sun and the moon causes the common centre of mass of the earth-sun system to be located inside the sun, and of the earth-moon system within the earth. As a simplification, we can therefore say that the earth orbits the sun and that the moon orbits the earth (see Fig. 3.16).

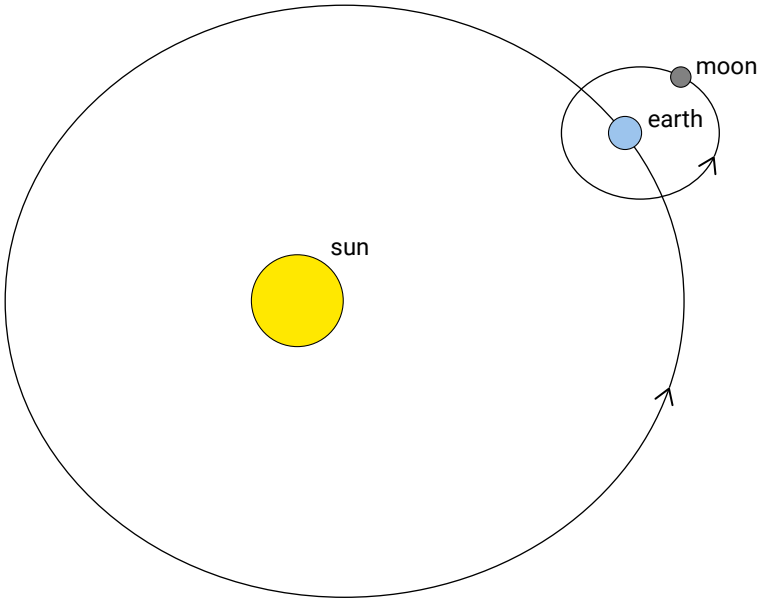

Figure 3.16: The orbit of the earth around the sun and the smaller orbit of the moon. The earth-moon system is orbiting the sun in the same direction as the moon is orbiting the earth.

At the same time, the earth rotates around its own axis in the same direction as the earth orbits the sun and the moon orbits the earth. The periods of these motions are explained in Intermezzo 3.3.

The gravitational pull of the sun on 1 kg of mass of the earth using the average distance between the sun and the earth of $d_s = 1.5 \times 10^{11}$ m is:

$$a_s = G\frac{M_s}{d_s^2} = 6.0 \times 10^{-4} g \tag{3.27}$$

where $G = 6.6 \times 10^{-11}$ N m^2/kg is the universal gravitational constant and $g = 9.81$ N/kg (or equivalently m/s^2) is the gravitational pull of the earth itself at the surface of the

Table 3.4: Main facts about the sun-earth and earth-moon systems (approximate figures).

mass of the sun	1.99×10^{30} kg
mass of the earth	5.98×10^{24} kg
mass of the moon	7.35×10^{22} kg
distance between (centres of) the sun and the earth	1.50×10^{8} km
distance between (centres of) the earth and the moon	3.84×10^{5} km
radius of the earth	6.37×10^{3} km

earth. Similarly, the gravitational pull of the moon on 1 kg of mass of the earth at an average distance of $d_m = 3.84 \times 10^8$ m is:

$$a_m = G\frac{M_m}{d_m^2} = 3.4 \times 10^{-6}\text{g} \tag{3.28}$$

Note that Eqs. 3.27 and 3.28 represent the gravitational acceleration (force per unit mass) for the centre of the earth. As such, they represent the attraction of the earth as a whole towards the sun and the moon (assuming the mass of the earth is concentrated at the earth's centre of mass).

For different locations at the earth's surface, the magnitude and direction of the gravitational acceleration slightly differ from each other and from the acceleration of the earth's centre, due to varying distances and angles to the centre of the attracting mass (see Fig. 3.17).

Summarizing, the gravitational attraction provides the centripetal acceleration that maintains the motion of the earth around the centre of mass of the earth-sun (earth-moon) system. For every point on earth, this centripetal acceleration of the earth in free fall towards the sun (moon) is directed parallel to the line connecting the centres of mass of the earth and the sun (moon). Its magnitude is determined by the gravitational acceleration a_s (a_m) of the sun (moon) on the earth's centre as given by Eq. 3.27 (Eq. 3.28). But nowhere at the surface of the earth is the gravitational acceleration exactly equal in magnitude and direction to the centripetal acceleration.

3.7.3. Differential pull or the tide-generating force

Equations 3.27 and 3.28 show that the sun's gravitational pull is two orders of magnitude larger than the moon's gravitational pull. This makes sense, since the earth orbits the sun and not the moon. Nevertheless, the sun contributes only about 30 % of the tidal amplitudes in the oceans; the moon is responsible for the remaining 70 %. The reason is that it is not the gravitational pull per se that is responsible for the tide-generating forces.

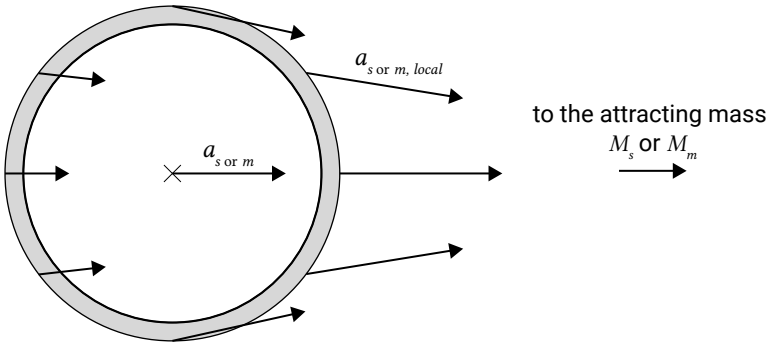

Figure 3.17: The gravitational acceleration towards the sun $a_{s,\text{local}}$ or moon $a_{m,\text{local}}$ depends on the distance to the attracting mass and on the angle to its centre. On the side of the earth closer to the attracting mass, the acceleration is greater than on the far side of the earth. The attraction of the earth as a whole towards the sun (moon) is found by considering the mass of the earth concentrated at the earth's centre of mass and is equal to a_s (a_m).

Above, we have seen that the gravitational attraction provides the centripetal acceleration that maintains the motion of the earth around the centre of mass of the earth-sun (earth-moon) system. With the gravitational attraction for the earth as a whole (Eqs. 3.27 and 3.28) accounted for[4], the tide is generated by a much subtler effect, i.e. the *difference* between the gravitational pull on ocean water masses that are located at different distances from the sun and the moon.

Consider 1 kg of mass on the near side of the earth which therefore is the earth's radius $R = 6.37 \times 10^6$ m closer to the sun than the centre of the earth is. The gravitational pull of the sun on 1 kg of mass on the near side of the earth is Δa_s greater than a_s, i.e.:

$$\begin{aligned} \Delta a_s = \quad a_{s,\text{near side}} - a_s \quad &= \quad G\frac{M_s}{\left(d_s - R\right)^2} - G\frac{M_s}{d_s^2} \quad \approx \\ 2G\frac{M_s R}{d_s^3} \quad &= \quad a_s \frac{2R}{d_s} \quad = \quad 0.515 \times 10^{-7} g \end{aligned} \tag{3.29}$$

This is known as *differential pull*. Note that the first-order approximation of [§1.1]Δa_s [p124] is inversely proportional to the cube of the distance. Similarly for the moon:

$$\Delta a_m \approx \quad 2G\frac{M_m R}{d_m^3} \quad = \quad a_m \frac{2R}{d_m} \quad = \quad 1.13 \times 10^{-7} \text{g} \tag{3.30}$$

[4] Alternative but equivalent explanations (as covered in TU Delft courses CTB2410 and CIE5317) take the moving earth as a reference frame and introduce 'fictitious' centrifugal forces (see also Intermezzo 3.1). Due to the revolution of the earth around the centre of mass of the earth-sun (earth-moon) system, there is an outward-directed centrifugal force that is the same at every point on the earth and directed parallel to the line of centres. The centrifugal acceleration (force per unit mass) balances the gravitational acceleration of the earth's centre towards the sun (moon).

The point furthest from the sun (moon) is in turn smaller than a_s (a_m) by the same amount Δa_s (Δa_m) which can be shown by a similar calculation. Carrying out the calculation for all places on the earth leads to a differential pull on the earth, as indicated schematically in Fig. 3.18 (compare with Fig. 3.17).

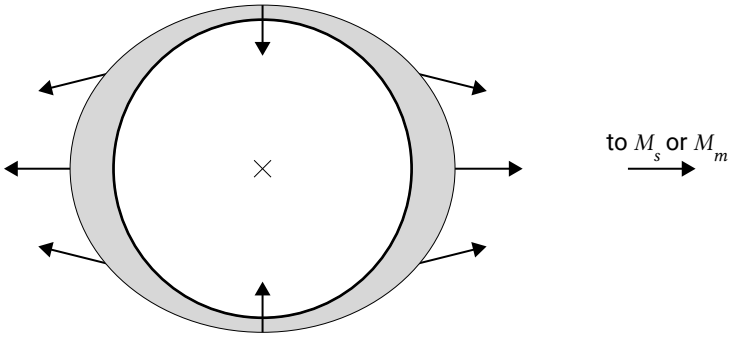

Figure 3.18: The direction and relative magnitudes of the differential gravitational pull at different locations on the earth's surface. At each location, it is given by the vector subtraction of $a_{s\,\mathrm{or}\,m,\mathrm{local}}$ and the part $a_{s\,\mathrm{or}\,m}$ that provides the centripetal acceleration. The depicted tidal bulges result from the tangential components of the differential pull (see Fig. 3.19).

The differential pull is responsible for the tidal generation and is therefore also referred to as *tidal force*. Since Δa is proportional to M/d^3, the solar differential pull Δa_s is only 0.46 times the lunar differential pull Δa_m. The moon is responsible for 69 % of the tidal mechanism, as $\Delta a_m/(\Delta a_m + \Delta a_s) = 69\,\%$.

The differential pull as sketched in Fig. 3.18 has components normal and tangential (or parallel) to the earth's surface. The normal components are many orders of magnitude smaller than the earth's own gravitational attraction. For example, for the point closest to the sun, the differential acceleration is normal to the earth surface and with a magnitude of $0.515 \times 10^{-7} g$ it is negligible compared to g. The tangential or 'horizontal' components are of the same order of magnitude as the normal components, but since they are perpendicular to the earth's gravity field, they cannot be neglected. The tangential forces are demonstrated in Fig. 3.19.

The effect of the tangential forces is to shift water to the side of the earth facing the sun (moon) and to the opposite side in tidal bulges (see Fig. 3.18). The piling up of water due to the tangential forces is balanced by pressure gradients in the opposite direction due to the sloping water surface. If the earth were completely covered by water, its equilibrium configuration would be an ellipsoid (rugby ball or egg).

The rapid diurnal rotation of the earth around its own axis makes the earth rotate underneath the tidal bulges, thus producing a semi-diurnal tide with two high and two low waters passing the same point on the earth every day. The period of the solar tide is exactly 12 h (our day is measured in terms of the sun, Intermezzo 3.3). The period of the lunar tide is governed by the period between the moon phases or the lunar day. The period of the semi-diurnal lunar tide is thus equal to half a lunar day = 12 hours and 25 minutes.

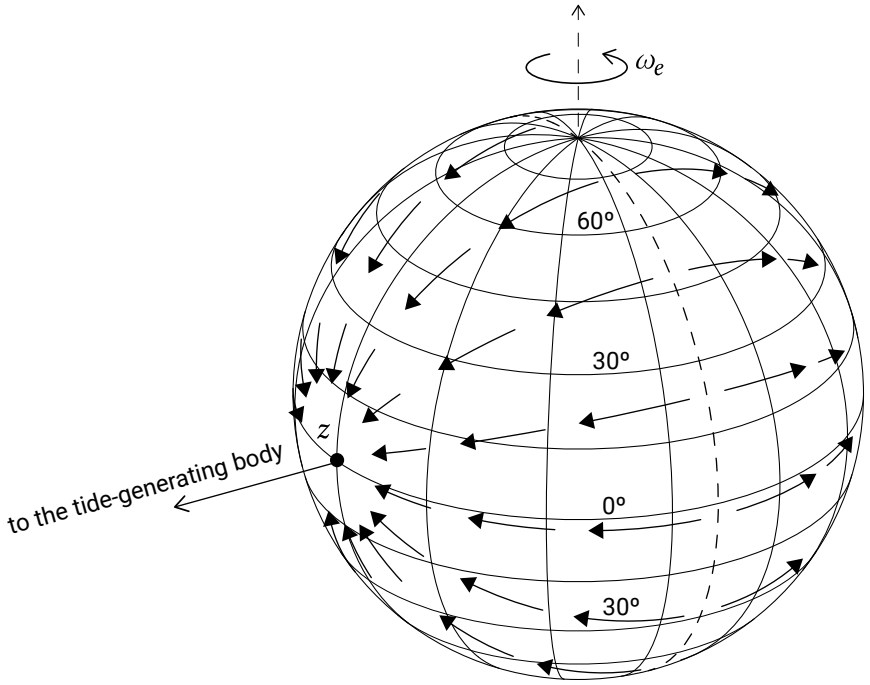

Figure 3.19: The horizontal component of the tidal force on the earth when the tide-generating body (the §1.1 ~~earth~~ §1.1 sun [p126] or the moon) is above the equator at z.

Intermezzo 3.3
Movements of the earth, earth-moon and earth-sun system

The earth circles the sun in 365.25 days. The earth rotates around its own axis in 23 hours and 56 minutes (sidereal day, relative to the stars) in the same direction in which the moon is revolving around the earth and the earth around the sun. While the earth completes one daily rotation, the earth also revolves with respect to the sun. As a result it is only after 24 hours or one (solar) day that the earth returns in the same position with respect to the sun as seen by an observer on the earth. A lunar day lasts even longer, viz. 24 hours and 50 minutes. This occurs because the moon progresses in its orbit around the earth during earth's daily rotation. The extra 50 minutes are required for the earth to 'catch up' with the moon, as will be explained below.

The period of the moon's revolution around the earth is 27.3 days (sidereal month). The moon takes 29.5 days to return to the same position relative to the sun as seen by an observer on the earth. Such a lunar month is the time between successive recurrences of the same phase; e.g., between full moon and full moon. During the 27.3 days of the sidereal month, the earth has moved along in its orbit around the sun and now the moon must 'catch up' to this new position. It takes 2.2 days to do so.

Furthermore, while the moon progresses in its orbit around the earth, the earth rotates around its own axis. The earth must rotate a bit more than a full rotation before any given location 'catches up' with the lunar bulge. During one rotation of the earth around its axis, the moon has covered 1/29.5th of its total orbit around the earth (with respect to the sun). Therefore, a lunar day is equal to $(1 + 1/29.5) \times 24\,\mathrm{h} = 24\,\mathrm{h}\ 50\,\mathrm{min}$. Figure 3.20 shows the required additional rotation of the earth to catch up with the moon.

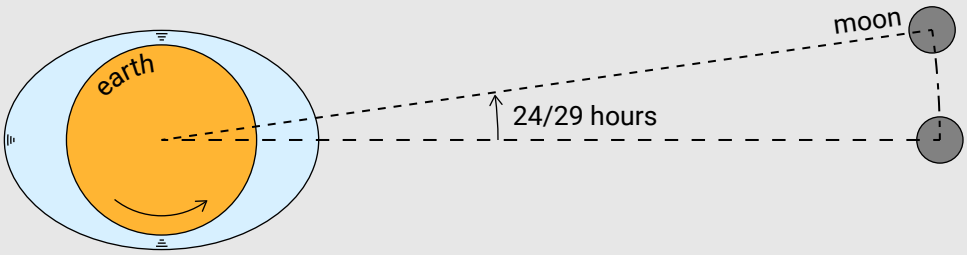

Figure 3.20: A lunar day (the time between successive transits of the moon for an observer on the earth) is 24 hours and 50 minutes.

3.7.4. Spring and neap tide

When the sun, the earth and the moon are in one line (at full and new moon), the solar and lunar tides reinforce each other. The ellipsoid becomes more pronounced and the tide gets a bigger amplitude; this is called *spring tide*. When the solar and lunar tides are 90° out of phase, their effects cancel each other (in the first and last quarter). The ellipsoid approaches a circle, and consequently the tide gets a smaller amplitude. This situation is called *neap tide* (Fig. 3.21). Figure 3.22 shows an example of these tidal variations.

The spring and neap tide cycle varies with moon phases and therefore with the lunar month of 29.5 days. The ratio of spring and neap tide amplitudes according to equilibrium theory can be estimated from Eqs. 3.29 and 3.30 as:

$$(0.515 + 1.13)/(1.13 - 0.515) = 2.7\ :\ 1 \tag{3.31}$$

This ratio is an approximation for the spring to neap tide ratio at open oceans. Anywhere else the ratio is affected by the presence of land masses (see Sect. 3.8).

3.7.5. Daily inequality

So far, we have either explicitly or implicitly assumed that the sun and the moon are directly above the equator of the earth (or in other words that the orbits of the moon and the earth lie in the equatorial plane). Under that assumption a certain place on the

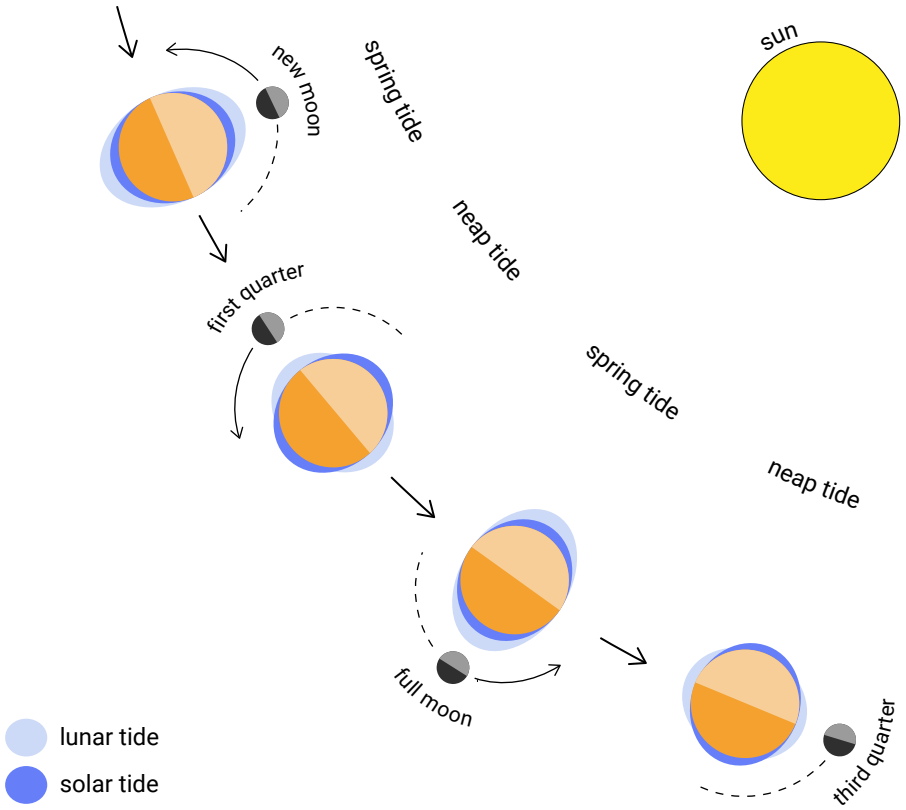

Figure 3.21: When the sun, the earth and the moon are in one line, the tidal forces of the sun and the moon reinforce each other and spring tides occur. Neap tides occur when the effect of the tidal forces of the sun and the moon on the tidal bulges cancel each other.

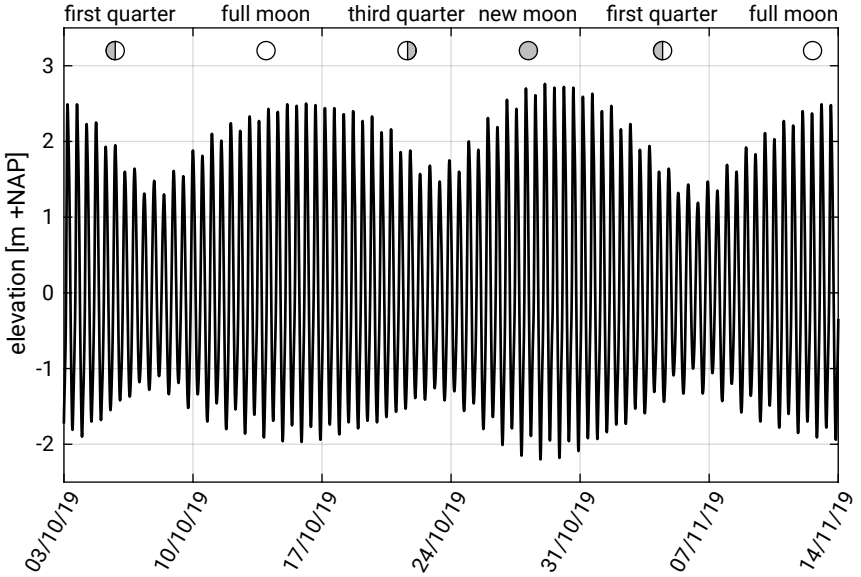

Figure 3.22: Tidal variation in Vlissingen during more than a month in 2019. Note the spring and neap tidal variation and the daily inequality (Sect. 3.7.5). Data from https://waterinfo.rws.nl.

earth experiences two high waters and low waters per day of equal height as can be seen from Fig. 3.23. The heights of those high waters and low waters depend on the latitude.

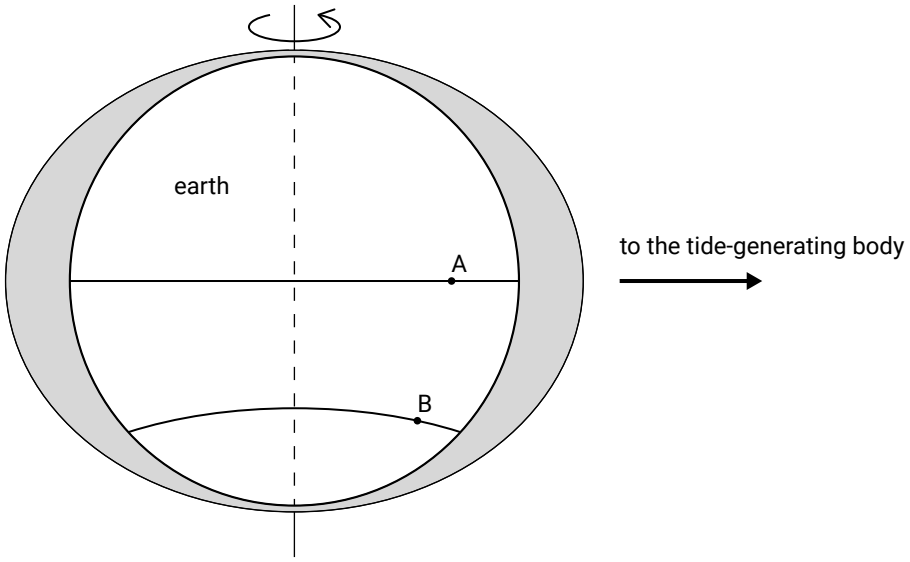

Figure 3.23: The tidal bulges for a tide-generating body above the equator. Observers A and B both experience two high and low waters a day of equal height. The heights depend on the latitude.

In reality, the orbits of the moon about the earth and of the earth about the sun are not in the equatorial plane, which complicates our simple picture of Fig. 3.23. While the moon's orbit and the earth's orbit are approximately in the same plane (5° difference), there is a time-varying declination angle between the equatorial plane and the earth-sun and earth-moon connection lines. As the tidal bulges tend to align themselves with the tide-generating body, the two high and low waters per day are not equal (see Fig. 3.24). This phenomenon is referred to as daily inequality. Apparently, the declination of the sun has a diurnal (daily) effect on the tides.

According to Fig. 3.24, the daily inequality is zero at the equator and increases with latitude[5]. At some higher latitudes, the daily inequality becomes so big that there is only one high and one low water (diurnal tide, see Sects. 3.7.6 and 4.4.1).

The earth's axis is tilted by 23.5° with respect to a line perpendicular to the plane of the earth's orbit around the sun. Due to the combination of this tilt and the orbiting of the earth around the sun, the declination of the sun varies seasonally. It is zero at the spring and autumn equinoxes (March 22 and September 22), positive during the Northern summer and negative during the Northern winter. The minimum declination of −23.5° (or 23.5° south) is reached on December 22 (Northern winter solstice) and the maximum of 23.5° on June 22 (Northern summer solstice). The daily inequality cycle of the solar tide therefore has a period of one year, with diurnal tides increasing

[5]Some areas around the equator experience a large daily inequality. This is related to the presence of land masses and will be further explained in Sect. 4.4.

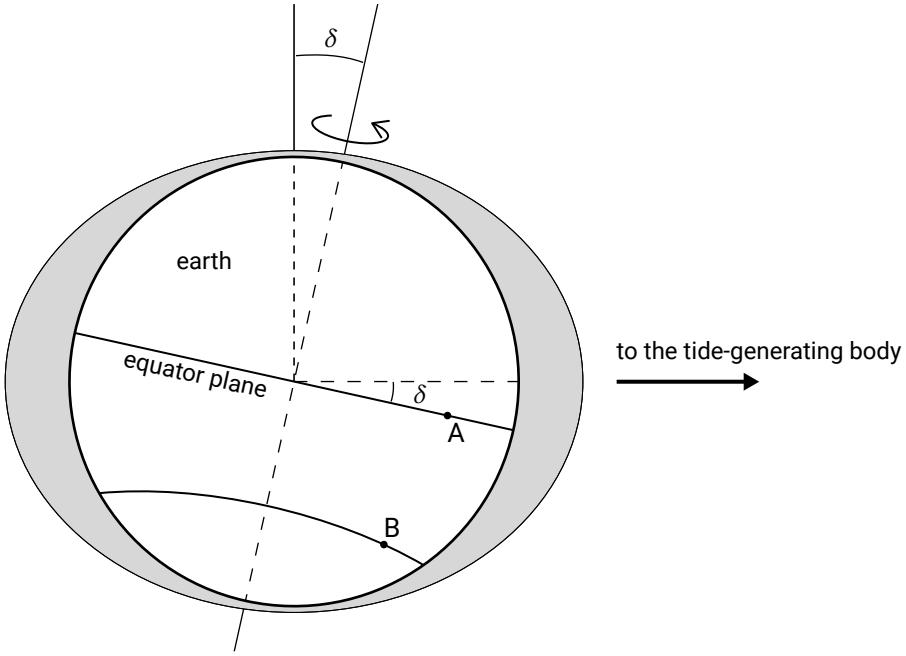

Figure 3.24: Daily inequality due to a non-zero declination angle δ between the equatorial plane and the line connecting the centres of the earth and the tide-generating body. For observer A the two high and low waters have the same height, but observer B experiences unequal heights in two successive high and low waters.

with increasing declination south or north and semi-diurnal tides maximum at zero declination. An interesting consequence of the latter is that spring tidal ranges around the equinoxes are usually higher than average spring tidal ranges (equinoctial tides).

The lunar daily inequality cycle has a period of 27.3 days. The north-south difference of the declination of the moon during the month is twice $23.5° \pm 5°$. The deviation of $5°$ has a cycle of 18.6 years and is a result of the $5°$ difference in moon's and earth's orbits. As with the sun, the largest daily inequalities correspond to the times that the moon is furthest south or north (minimum and maximum declination).

3.7.6. Tidal constituents

The principal tidal constituents are shown in Table 3.5. We have seen in Sect. 3.7.3 that the main lunar tide has a period of 12.42 h and the main solar tide a period of 12 h respectively. These *tidal constituents* (or tidal components) are called M2 and S2. The influence of the sun is characterised by the letter S, the influence of the moon by the letter M. The index 2 refers to phenomena that occur twice daily. The amplitudes and phases of these two constituents vary with the location on the earth.

The tidal variations are in the order of *decimetres only* in the open oceans. According to equilibrium theory, the amplitudes of M2 and S2 are 0.24 m and 0.11 m respectively. This gives a ratio of $S2/M2 = 0.46$, which could also be calculated using Eqs. 3.29 and 3.30 as $S2/M2 = 0.515/1.13 = 0.46$. The M2 and S2 signals have a slightly different

Table 3.5: Principal tidal constituents with equilibrium amplitudes from Apel (1987)

Tidal constituents	Name	Equilibrium Amplitude [m]	Period [h]
Semi-diurnal			
Principal lunar	M2	0.24	12.42
Principal solar	S2	0.11	12.00
Lunar elliptical	N2	0.046	12.66
Lunar-solar declinational	K2	0.031	11.97
Diurnal			
Lunar-solar declinational	K1	0.14	23.93
Principal lunar	O1	0.10	25.82
Principal solar	P1	0.047	24.07
Lunar elliptical	Q1	0.019	26.87
Long period			
Fortnightly	Mf	0.042	327.9
Monthly	Mm	0.022	661.3
Semi-annual	Ssa	0.019	4383

frequency, which gives a so-called beating of the two signals resulting in spring-neap tide variability: when the M2 and S2 components are in phase (the moon and the sun are aligned) it is spring tide and when they are out of phase it is neap tide, as discussed in Sect. 3.7.4. The beating of the two signals resulting in a variation of the amplitudes over the lunar month is comparable to the beating of two wave trains with slightly different frequencies, resulting in amplitude variation or modulation on a wave group scale as treated in Sect. 3.5.3. Intermezzo 3.4 treats this amplitude modulation in more detail.

The declination of the earth axis introduces semi-diurnal and diurnal tidal constituents K1, K2 and O1 and P1. Diurnal components carry a subscript 1. K1 with O1 expresses the effect of the moon's declination, K1 with P1 the sun's declination. K1, P1 and O1 account for diurnal inequality (see Intermezzo 3.4) and, at extremes, diurnal tides (where the semi-diurnal component has disappeared completely). The K2 constituent modulates the amplitude and frequency of M2 and S2 for the declinational effect of the moon and the sun, respectively. Other effects will generate other tidal constituents defined by an exact period, with their own amplitudes according to equilibrium theory and with their own phases with respect to each other. For instance, the moon's distance from the earth varies because the moon's orbit is elliptical and because the elliptical orbit is not fixed. This effect introduces semi-diurnal and diurnal constituents N2 and Q1. The longest period is 18.6 years, which is the period of the 5° variation of the lunar declination.

For practical purposes, the tide can be seen as a sinusoidal semi-diurnal water level variation modified with a fortnightly spring and neap tide amplitude variation and with a daily inequality that varies with latitude and with the monthly and annual cycle. In the extreme case the daily inequality is so large that the water level variation is only diurnal.

M2 and S2 are the main but not the only constituents with frequencies near twice per day (see Fig. 3.27). Note that the spectrum of equilibrium tides in Fig. 3.27 consists of discrete lines; tides have precise frequencies determined by the orbits of the earth and moon, and their spectrum is not continuous. We have seen before that ocean waves have all possible frequencies, and their spectrum is continuous.

Intermezzo 3.4 Astronomical constituents

Section 3.7.6 described the ocean tide as a sinusoidal semi-diurnal water level variation modified with a fortnightly spring and neap tide variation and with a daily inequality. The spring and neap tide variation is the result of the linear summation of principal components with a small differential frequency. Consider the M2 and S2 components. The linear combination of these two tidal components with a small difference in frequency results in an amplitude variation with a period determined by $\omega_{S2} - \omega_{M2}$, comparable to the beating of two short-wave trains with slightly different frequencies (see Sect. 3.5.3). This is shown in Fig. 3.25.

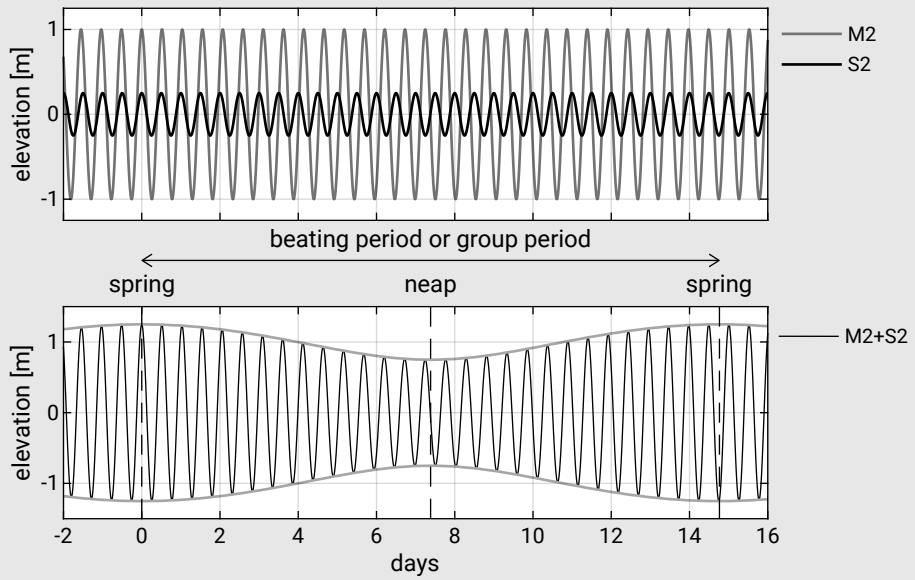

Figure 3.25: The interaction between M2 and S2 results in a spring and neap tide variation. Verify that the beating period of M2 and S2 is 14.77 days (cf. the group period for wind waves Eq. 3.24b).

The daily inequality for a predominantly semi-diurnal tide is the result of the summation of a semi-diurnal and a diurnal component and is demonstrated in Fig. 3.26

for M2 and K1. The result is the succession of two symmetrical tides with different tidal range (the difference between the elevations of the two successive high waters is called daily inequality).

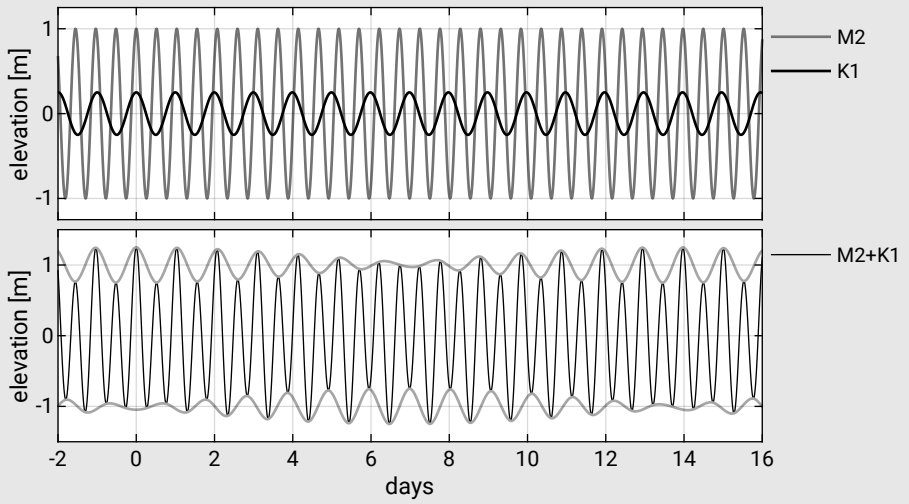

Figure 3.26: The interaction between M2 and K1 leads to daily inequality between two successive high waters and between two successive low waters. Also, a slower amplitude variation can be observed.

3.8. Propagation of the tide

3.8.1. Dynamic theory of tides

So far, the earth was schematised as if it were completely covered with water, with the earth rapidly turning through the slowly varying tide. For the semi-diurnal tide this is equivalent to a propagating tidal wave covering the entire circumference of the earth in one day. In reality, continents prevent the development of the tidal ellipsoid and the land masses do not move through the tide but move the water masses along with them. Furthermore, the limited water depth of the oceans prevents the development of an equilibrium tide. This becomes clear when considering the propagation properties of the tidal wave. The tidal wave is a long wave because the wavelength $L \gg h$ and has a small amplitude (order 1 m on an average ocean water depth of 4000 m). Therefore, and if friction can be neglected, the wave propagation speed follows from (see Sect. 3.5.2):

$$c = \sqrt{gh} \tag{3.32}$$

where:

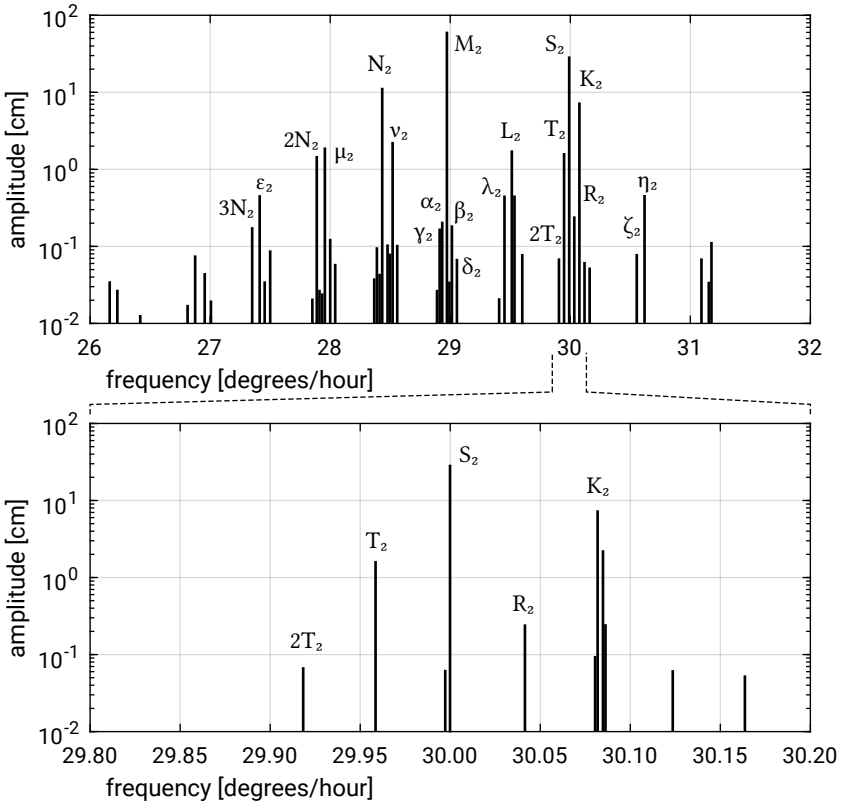

Figure 3.27: Spectrum of equilibrium tides with frequencies near twice per day. Upper: the spectrum is split into groups separated by a cycle per month (0.55 °/h). Lower: expanded spectrum of the S2 group, showing splitting at a cycle per year (0.04 °/h). The finest splitting in this figure is at a cycle per 8.847 years (0.0046 °/h). (From Richard Eanes, Center for Space Research, University of Texas in Stewart, 2008, see also https://github.com/introocean/introocean-en).

c	wave propagation speed	m/s
g	gravitation acceleration	m/s^2
h	water depth	m

Note that this phase velocity can also be derived directly on the basis of continuity and by balancing acceleration and pressure gradient, see Intermezzo 3.5.

For the development of the equilibrium tide, the semi-diurnal tide should cover half of the circumference of the earth in one period of 12 hours and 25 minutes. The circumference at the equator is $2\pi R = 2\pi \times 6.37 \times 10^3$ km $= 4.00 \times 10^4$ km and therefore the required propagation speed is $c = 4.00 \times 10^4$ km$/(2 \times 12.42$ h$) = 447$ m/s. This means that the tidal wave requires a water depth of 20 km – much more than the depth of the oceans – to travel fast enough (use Eq. 3.32). The travel distance reduces towards the poles and therefore the required propagation speed and water depth as well. The result is that the water depth becomes less of a limitation at higher latitudes.

Only in the Southern Hemisphere at a latitude of about 65°S, an equilibrium tide can more or less exist. To the south of Africa, South America and Australia the earth is circled by an uninterrupted band of water such that the tidal wave can travel around

the earth. Besides, at this latitude the water depth is not so much of a limitation for the propagation velocity, so that the original ellipsoid can develop.

From around 65°S the tidal wave propagates to the north into the Atlantic, Indian and Pacific Oceans. Because it takes time for the tidal wave to progress through the oceans, the tidal constituents at a particular location away from the area of tidal generation (around 65°S) lag behind the theoretical constituents from equilibrium theory. The further the location is away from the South Pole, the longer the time shift between the celestial event and its appearance in the form of the tide.

Assuming an average depth of the ocean of 4000 m, the propagation speed of the tidal wave is about 200 m/s and for $T = 12.42$ h the wavelength $L = 9000$ km. At a speed of 200 m/s (or 720 km/h) and if travelling in a more less straight line, it takes the tidal wave less than a day to travel from 65°S to say, Scotland. To reach the Netherlands, the tidal wave needs to cross the shallow North Sea basin. The latter takes another day or so, since the propagation speed strongly decreases in the shallow North Sea. This means that in the Netherlands spring and neap tide occur about two days after the corresponding moon configurations (see Fig. 3.22).

On its way, the tidal wave is distorted by local differences in water depth and – due to land masses – by restriction of the width or reflection. The period does not change, only the length of the wave changes via changes in propagation speed. The latter can be illustrated as follows. For the long tidal wave the wave celerity is proportional to the square root of the water depth. When the tidal waves reaches shallower water, the celerity will decrease which results in a concentration of energy and thus an increase in tidal amplitude (comparable to the shoaling effect of wind waves in shallow water; see Sect. 5.2.2). In shallower water along the ocean coasts and shallow seas like the North Sea, we have for instance a wavelength of $L = 450$ km (with $h = 10$ m and $c = 10$ m/s). Depending on the geometry of a bay, sea or ocean basin, resonance may occur, leading to amplification of the tidal amplitude at the coast (standing waves or – in combination with Coriolis – rotary standing waves, see Sect. 3.8.2).

In deep water, tidal current velocities are very small. For an ocean depth of 4000 m and a tidal amplitude of for instance 0.25 m, we get with Eq. 3.39 a tidal velocity amplitude of 1.2 cm/s. In shallower water this is quite different: tidal amplitude and tidal current velocities are larger. If $a = 1$ m and $h = 10$ m, the tidal current velocity is 1 m/s, hence two orders of magnitude larger.

Intermezzo 3.5 Tidal propagation in the open oceans

The tide can be described by the shallow-water equations (shallow-water approximation to the Navier-Stokes equations). For the tidal propagation in open oceans we can simplify these equations by neglecting advection, friction, horizontal diffusion and short-wave effects. We also assume a small tidal amplitude and bottom

slope. The resulting momentum equation is a balance between acceleration (inertia) and the pressure gradient:

$$\frac{\partial u}{\partial t} = -g\frac{\partial \eta}{\partial x} \tag{3.33}$$

where u is the horizontal velocity and η the oscillatory surface elevation. We further have the vertically integrated continuity equation:

$$\frac{\partial \eta}{\partial t} = -h\frac{\partial u}{\partial x} \tag{3.34}$$

where h is the water depth. Eqs. 3.33 and 3.34 together describe the tidal propagation.

Taking $\frac{\partial}{\partial t}$ of Eq. 3.34 and subtracting $h\frac{\partial}{\partial x}$ of Eq. 3.33 gives the classical wave equation:

$$\frac{\partial^2 \eta}{\partial t^2} = gh\frac{\partial^2 \eta}{\partial x^2} \tag{3.35}$$

Substitution of a progressive sine (or equivalently: cosine) wave $\eta = a\sin(\omega t - kx)$ into Eq. 3.35 yields:

$$\omega^2 = ghk^2 \tag{3.36}$$

and thus (only taking the positive solution for c):

$$c = \frac{\omega}{k} = \sqrt{gh} \tag{3.37}$$

The velocity is in phase with the surface elevation:

$$u = \frac{gak}{\omega}\sin(\omega t - kx) \tag{3.38}$$

Evidently, for progressive waves the maximum velocities are found under the crest of the wave. The velocity amplitude is:

$$\hat{u} = \frac{gak}{\omega} = \frac{a\omega}{kh} = a\sqrt{\frac{g}{h}} \tag{3.39}$$

Compare this expression for the velocity amplitude with the expression according to linear wave theory in the shallow-water approximation (see Eq. 5.23). As you can see, it is identical.

3.8.2. Amphidromic systems

The propagation of the tide is influenced by friction and resonances determined by the shapes and depths of the ocean basins and marginal seas. Because of the large scale of the tidal motion, the tidal propagation is also influenced by Coriolis acceleration (see Intermezzo 3.1). Generally we can neglect the effect of Coriolis for waves shorter than a few kilometres. In the previous section we found tidal wavelengths of the order of thousands of kilometres in the oceans and hundreds of kilometres in shallow seas.

Since the movement of the tides is deflected by Coriolis and blocked by land masses, rotary movements are formed in oceans basins, bays and seas that are counter-clockwise in the Northern Hemisphere and clockwise in the Southern Hemisphere. Such rotary systems are called amphidromic systems. In an amphidromic system the wave progresses about a node (no vertical displacement) with the antinodes (maximum vertical displacement) rotating about the basin's edges (see Figs. 3.28 and 3.29). The water can be seen to be sloshing around the basin. The node, where the amplitude of the vertical tide is zero, is called an amphidromic point.

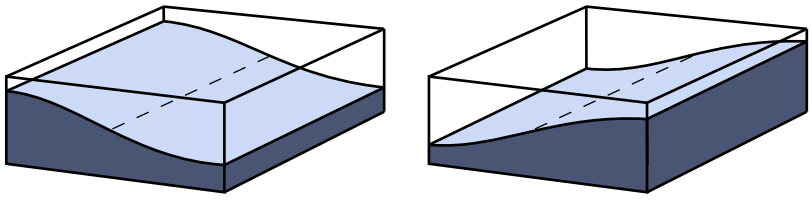

Figure 3.28: Normal standing wave.

It is possible to visualise the propagation of the tidal wave by mapping the lines of simultaneous high water (occurrence of High Water (HW) in sun hours after moon culmination) and the lines of equal tidal range (vertical distance between HW and Low Water (LW) in m). The lines of simultaneous HW are called co-tidal lines or, since these lines connect points of equal phase, co-phase lines. They often radiate away from a node and are not equally spaced, since the propagation speed depends on the water depth h. Co-range lines connect points experiencing the same tidal range. They often form irregular concentric circles about a node. This is illustrated in Fig. 3.30 and Fig. 3.31.

An amphidromic point is said to be degenerate when its centre appears to be located over land rather than water. Examples are found at the southern tip of Norway and

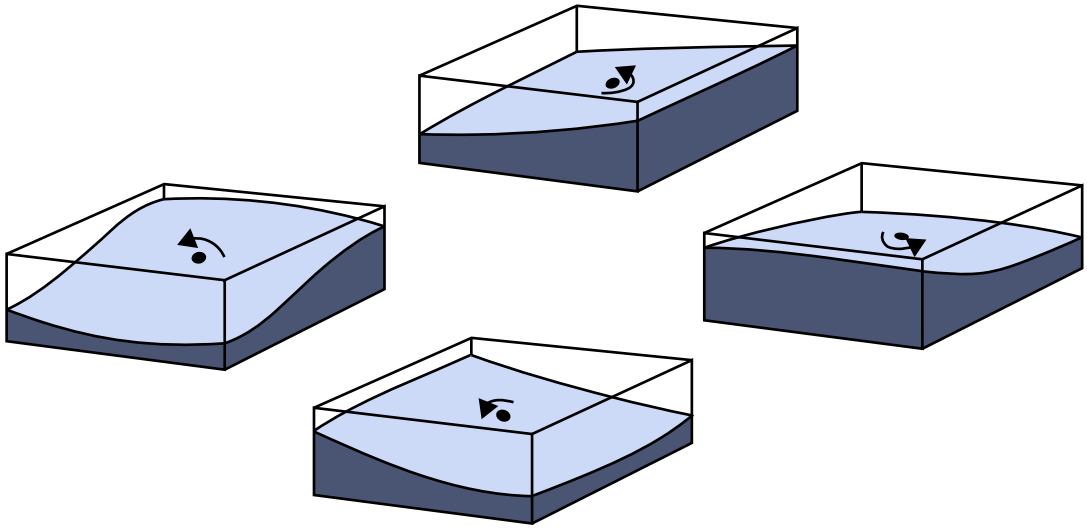

Figure 3.29: Tidal oscillation of a basin (Northern Hemisphere). The frequency of the oscillation is determined by the size of the basin and its depth.

northwest of Bournemouth (along the southwest coast of England, southeast of Bristol, see Fig. 3.31).

Evidently, the local tide at a coastal location is dependent on the size, shape and depth of the basin. Every place along the coasts of the world has its own specific tidal curve. If the tidal forcing is in resonance with an oscillation period for the sea or bay, the tidal range is amplified and can be enormous. At some locations, the difference between high and low water is up to 12 m (compare that to a few decimetres at the open oceans!).

3.8.3. Kelvin waves

As coastal engineers we are interested in the tidal propagation and the tidal range along the boundaries of oceans and seas. To better understand the propagation along closed coastal boundaries, we need a further understanding of the rotary wave forming the amphidromic system. These waves depend on the existence of a closed boundary. A definition sketch is given in Fig. 3.32. Wave propagation is in the positive y-direction in the Northern Hemisphere (NH), hence c is positive. Such a wave would deflect from this eastern boundary in the Southern Hemisphere (SH) because of Coriolis. Therefore, for the SH we expect a wave propagating in the negative y-direction (c negative).

As before, we assume a more or less horizontal bottom slope and a small tidal amplitude compared to the water depth. Balancing inertia, Coriolis, the pressure gradient and

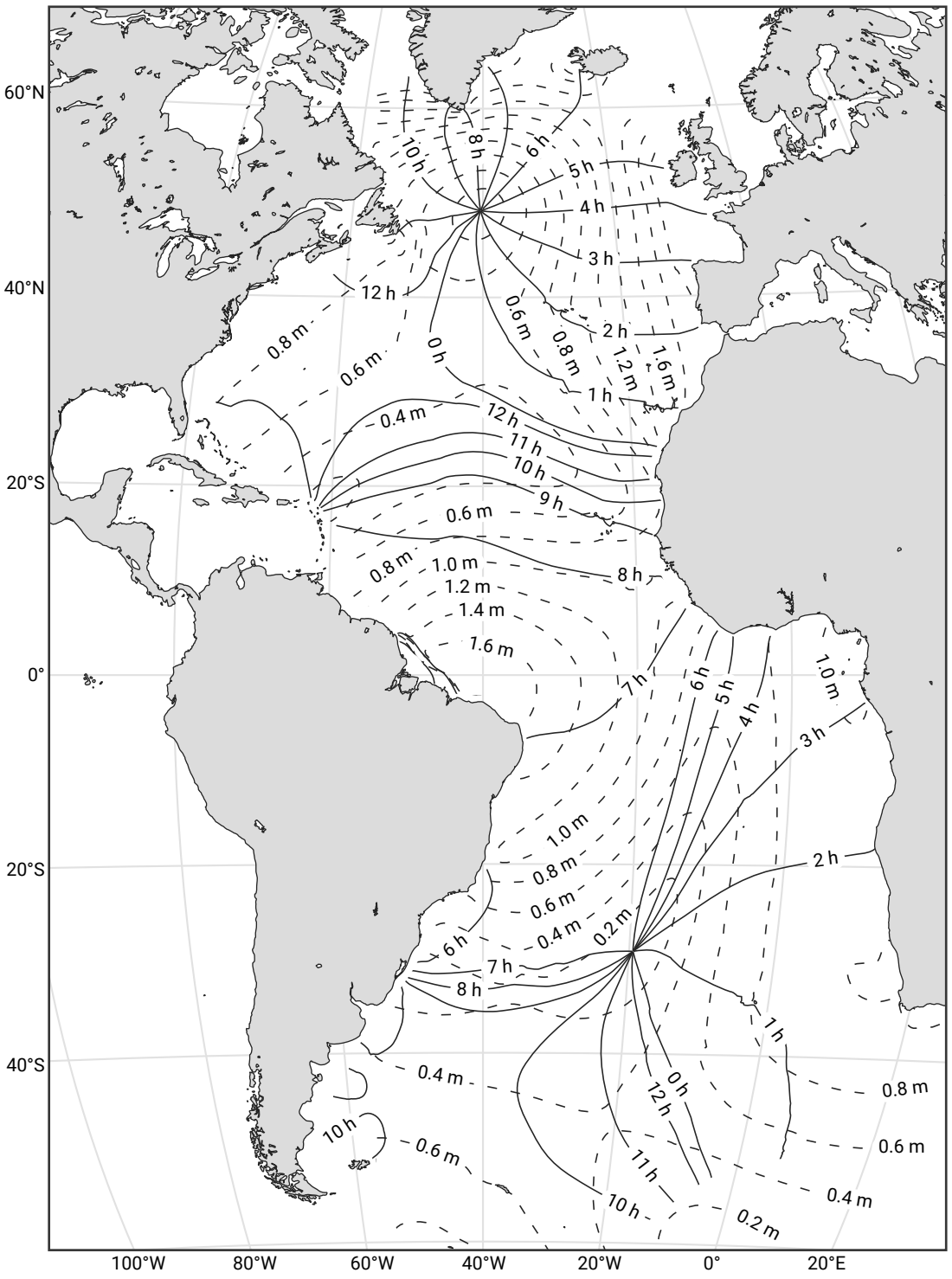

Figure 3.30: Propagation of the M2 tide in the Atlantic Ocean. The solid lines are co-tidal lines of simultaneous HW, the dashed lines are the co-range lines of equal tidal range. Model results obtained using the FES2014 tide model. FES2014 was produced by Noveltis, Legos and CLS and distributed by Aviso +, with support from CNES (https://www.aviso.altimetry.fr/).

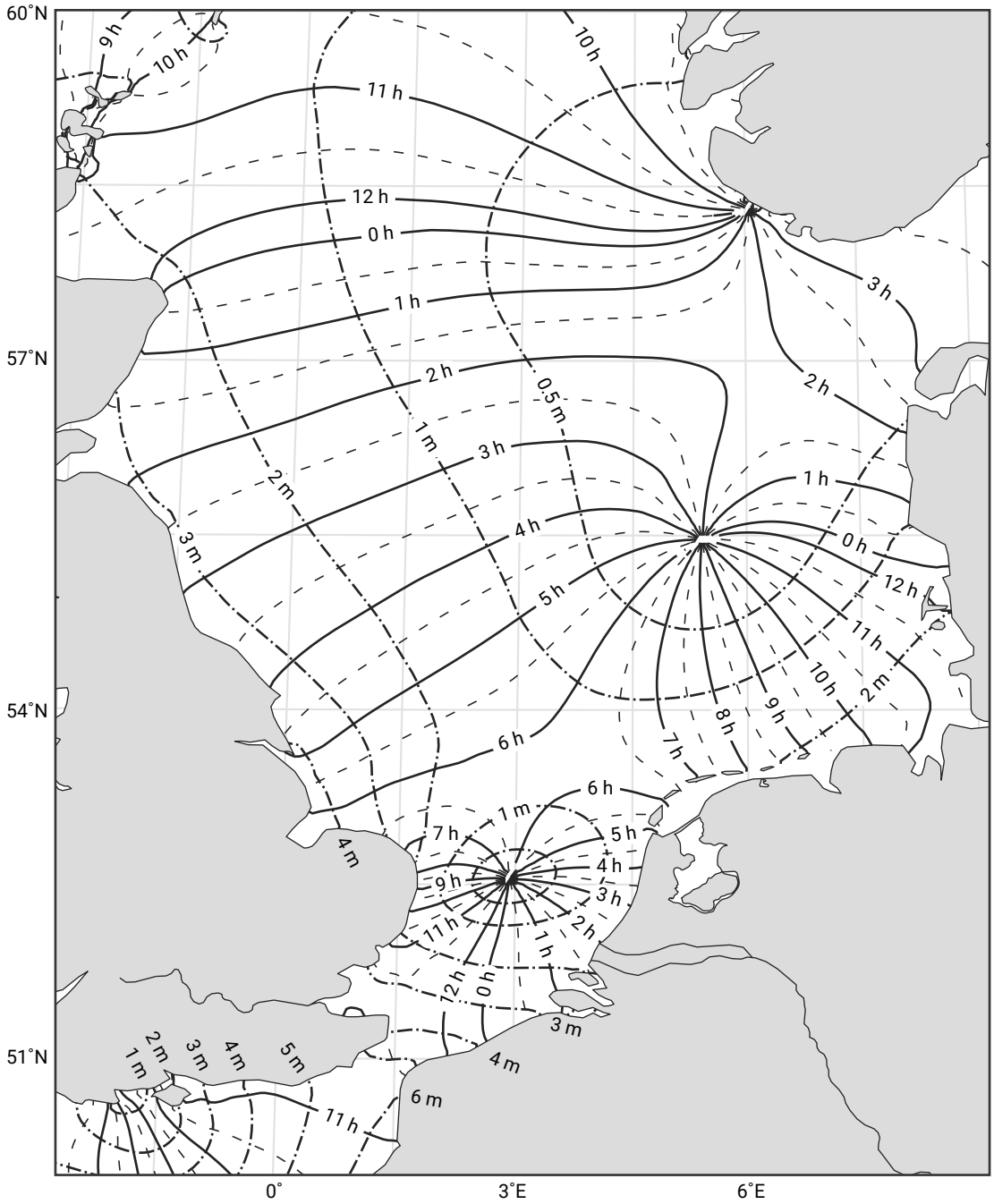

Figure 3.31: Propagation of the M2 tide in the North Sea with co-tidal lines radiating away from the amphidromic points and co-range lines encircling them. The co-tidal lines show that the phase increases counter-clockwise around the amphidromic point (typical of NH amphidromes). The co-range lines show the tidal range increasing away from the node. Model results obtained using the FES2014 tide model. FES2014 was produced by Noveltis, Legos and CLS and distributed by Aviso+, with support from CNES (https://www.aviso.altimetry.fr/).

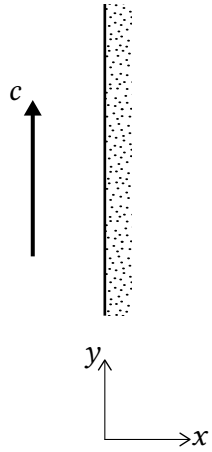

Figure 3.32: Closed eastern boundary with direction of tidal wave propagation (NH).

bed friction leads to the following reduced shallow-water equations in two horizontal dimensions:

$$\frac{\partial u}{\partial t} - fv = -g\frac{\partial \eta}{\partial x} - \frac{\tau_{b,x}}{\rho h} \tag{3.40a}$$

$$\frac{\partial v}{\partial t} + fu = -g\frac{\partial \eta}{\partial y} - \frac{\tau_{b,y}}{\rho h} \tag{3.40b}$$

where:

u, v	velocity in x-, y-direction	m/s
f	$2\omega_e \sin\varphi$ is the Coriolis parameter with the earth's angular velocity $\omega_e = 72.9 \times 10^{-6}$ rad/s and the latitude φ positive in the NH and negative in the SH	1/s
η	oscillatory water level variation	m
$\tau_{b,x}$	bottom shear stress in x-direction	N/m^2
$\tau_{b,y}$	bottom shear stress in §1.1 ~~x~~ §1.1 y-direction [p141]	N/m^2
ρ	water density	kg/m^3
h	water depth	m

The Coriolis acceleration has been introduced in the above equations of motion in such a way that it makes a right angle with the particle velocity and acts towards the right (to starboard side) in the NH and towards the left (to port) in the SH (see Intermezzo 3.1). Check for yourself the signs of the Coriolis terms in Eqs. 3.40a and 3.40b. In doing so, note that the latitude φ and hence the Coriolis parameter f are assumed to have positive values in the NH and negative values in the SH.

Continuity requires:

$$\frac{\partial \eta}{\partial t} + h\left(\frac{\partial u}{\partial x} + \frac{\partial v}{\partial y}\right) = 0 \tag{3.41}$$

If we neglect friction and take into account that the velocity u at the closed boundary (the coastline) is zero, the balance equations reduce to:

$$-fv = -g\frac{\partial \eta}{\partial x} \tag{3.42a}$$

$$\frac{\partial v}{\partial t} = -g\frac{\partial \eta}{\partial y} \tag{3.42b}$$

$$h\frac{\partial v}{\partial y} = -\frac{\partial \eta}{\partial t} \tag{3.42c}$$

Note that the cross-shore (x) momentum balance (Eq. 3.42a) is geostrophic: there is a balance between Coriolis force and the pressure gradient due to water level differences. This is comparable to the influence of Coriolis on the flow in a confined channel (see Intermezzo 3.6). The alongshore momentum balance, Eq. 3.42b, is the same as that for shallow-water gravity waves (the progressive tidal waves from Intermezzo 3.5). Equation 3.42b combined with the reduced continuity equation Eq. 3.42c yields a set of equations that §1.1 ~~it~~ §1.1 is [p142] equivalent to Eqs. 3.33 and 3.34 and thus has an equivalent solution. Now substitute this solution $\eta = \hat{\eta}\cos(\omega t - ky)$ and $v = g/c\ \eta$ with $c = \pm\sqrt{gh}$ in the geostrophic flow equation, Eq. 3.42a. The resulting equation now gives a solution known as a Kelvin wave:

$$\eta(x, y, t) = \eta_0 e^{\left(\frac{fx}{c}\right)}\cos(\omega t - ky) \tag{3.43a}$$

$$v(x, y, t) = \frac{c}{h}\eta_0 e^{\left(\frac{fx}{c}\right)}\cos(\omega t - ky) \tag{3.43b}$$

The Kelvin wave propagates along the coast (in the y-direction) at the shallow-water speed. The alongshore velocity is in phase with the water level (as for the propagating wave of Intermezzo 3.5). The amplitude is maximum at the coast (η_0) and then decays with distance from the coast (in the negative x-direction). The scale of the decay is c/f in which the variables are the latitude and the water depth:

$$\frac{c}{f} = \sqrt{gh}\frac{1}{1.46 \times 10^{-4} \times \sin\varphi} = 21453\frac{\sqrt{h}}{\sin\varphi} \tag{3.44}$$

At 45° latitude this amounts to about 1900 km for the deep oceans, with an average water depth of 4000 m, and about 200 km for a shallow sea with a typical water depth of 50 m.

The value of c/f cannot be negative, since this would make the sea level grow exponentially offshore. This implies, as expected, that the Kelvin wave propagates in the positive y-direction in the NH (where f is positive) and in the negative y-direction in the SH (where f is negative).

Intermezzo 3.6 Geostrophic momentum balance

If the flow takes place in a confined conduit or channel that prevents a deviation of the course (i.e. a steady current), the Coriolis acceleration causes a pressure gradient across the conduit:

$$\frac{1}{\rho}\frac{\partial p}{\partial n} = 2\omega_e V \sin\varphi \tag{3.45}$$

where:

ρ	water density	$\mathrm{kg/m^3}$
p	water pressure	$\mathrm{N/m^2}$
n	normal to and directed to starboard of the current V	–

In open channel flow, the pressure gradient becomes visible as a gradient of the water surface:

$$\frac{1}{\rho}\frac{\partial p}{\partial n} = g\frac{\partial \eta}{\partial n} \tag{3.46}$$

Note: upon comparing the above two equations (Eqs. 3.45 and 3.46) with the full depth-integrated shallow-water equations, it can be seen that only the pressure gradient due to the water level surface and the Coriolis acceleration are retained.

As an example, we compute the sea level difference across the Strait of Florida. The Florida Current is located at latitude 26°N; the current velocity is about 1 m/s; the width of the Strait of Florida is about 80 km.

$$\frac{1}{\rho}\frac{\partial p}{\partial n} = 2 \cdot 0.729 \times 10^4 \cdot \sin 26^\circ \cdot 1 = 6.4 \times 10^{-5}\ \mathrm{m/s^2} \tag{3.47}$$

The elevation difference over 80 km is computed as follows:

$$\Delta\eta = \frac{1}{\rho}\frac{\partial p}{\partial n}\frac{\Delta x}{g} = \frac{6.4 \times 10^{-5}}{9.81} \cdot 80 \times 10^3 = 0.52\ \mathrm{m} \tag{3.48}$$

The observed value is 0.45 m, which is close to our estimate. (Similar computations can be made for e.g. the Western Scheldt, the British Channel or the Dutch Texel Inlet).

The Kelvin wave is a coastally trapped wave; it needs a coastline. In the NH, the wave propagates poleward along an eastern boundary and equatorward along a western boundary with its maximum amplitude at the boundary. It thus forms a wave trapped to the boundary and rotating counter-clockwise around an amphidromic point (like a standing wave, but now rotating). The rotation is clockwise in the SH.

In the North Sea multiple amphidromic points can be observed (see Fig. 3.31). The Kelvin wave enters the North Sea basin from the north. Some of the energy is dissipated in the basin and some is reflected from the shallow areas in the southern part of the North Sea. This reflected wave forms its own amphidromic system.

For the ideal Kelvin wave, friction is not taken into account. Neglecting friction can be a good approximation for deeper water. Near the coast inertia is relatively unimportant, but bottom friction needs to be taken into account. The velocity is then governed by the balance between the bottom friction and the alongshore water level gradient. This will be treated in more detail in Ch. 5.

3.9. Tidal analysis and prediction

Because the tide is caused by regular astronomical phenomena, it can be predicted accurately a long time ahead (although not including meteorological effects such as storm surges). The method used for tide prediction is harmonic analysis. Analogous to the treatment of wind waves, the water level at a certain location as a function of time is expressed by the following formula:

$$\eta(t) = a_0 + \sum_{n=1}^{N} a_n \cos\left(\omega_n t - \alpha_n\right) \tag{3.49}$$

where:

η_t	measured (or predicted) tidal level with reference to a fixed level	m
a_0	mean level	m
a_n	amplitude of component number n	m
ω_n	angular velocity of component number n	1/h
a_n	phase angle of component number n	–
t	time	h
N	number of harmonic components	–

Contrary to the traditional harmonic analysis, the frequencies ω_n are known here, having been derived from astronomical considerations. The phase angles α_n have to be derived from observations as they are extremely site-specific. This applies to the amplitudes a_n as well. Tidal analysis for a certain location therefore is the determination

of amplitudes and phases. Note that the phase angles are a function of the adopted time origin.

The length of the analysed water level record determines the number of constituents that can be determined. A year's length can unravel the main constituents, except for the constituent with the period of 18.6 yr. The effect of this can be introduced by adjusting amplitudes and phases according to the position in that long-term cycle. Instead of Eq. 3.49 we then get:

$$\eta(t) = a_0 + \sum_{n=1}^{N} f_n a_n \cos\left(\omega_n t - \alpha_n + \beta_n\right) \tag{3.50}$$

Here f_n is the so-called nodal factor that captures the effect of the 18.6 yr-cycle on the tidal amplitudes. The correction to the phase is given by β_n. The nodal modulation can also be used to reduce the number of constituents in a tidal analysis; since the tidal constituents are gathered in groups with similar frequencies (see Fig. 3.27), the effect of smaller amplitude constituents in a group can be taken into account via corrections to the amplitude and phase of the main, larger amplitude constituent in the group.

When the tidal constituents are known for a certain location, they can be used to predict future tides. For many ports in the world, the tidal constituents are known and publicly available. If for a project local tidal constituents are not known, two solutions can be chosen. The first is to collect local data for a short period (for instance a month) from which the most important constituents can be determined. Another possibility is to use data from a nearby station and use a model for tidal propagation to determine the amplitudes and phases for the project site.

An example of the result of a harmonic analysis for some ports along the Dutch coast is presented in Table 3.6. This table shows the main harmonic components used for prediction of the astronomic tide. Each component has an internationally agreed abbreviation. The most important constituents have already been discussed in Sect. 3.7.6. Besides those principal constituents, each constituent may also have higher harmonics, generated by non-linearities. Higher-order components carry a subscript 3, 4 or higher. From the table one can see that the ratio of the effects of the sun and the moon is approximately 1 to 4 along the Dutch coast (ratio S2/M2 $\approx$ $^1/_4$).

Nota bene: in Table 3.6, the mean level is denoted by A_0 and gives the mean difference between *Normaal Amsterdams Peil* (NAP) – the fixed reference level for height in the Netherlands – and MSL. MSL is the mean sea level as determined from measurements and is the level without tides and averaged meteorological effects. Close to the coast this difference can be neglected; but if one looks at a river farther upstream, the river gradient influences the mean sea level. The difference between NAP and MSL changes a little during the year, as can be seen from the small amplitude of component SA. The angular velocity of this component (0.041) leads to a period of 365 d.

Contrary to the Dutch tide tables, in other such tables A_0 represents the difference between a Chart Datum and MSL. Chart Datum is then defined as a low level that is exceeded rarely, for instance Lowest Astronomical Tide (LAT) or Mean Lower Low Water (MLLW). LAT is defined as the lowest tide level which can be predicted to occur under average meteorological conditions and under any combination of astronomical conditions. MLLW is the average height of the lower of the two daily low waters over a long period of time. When only one low water occurs on a day, this is taken as the lower low water.

Because of this site-specific definition of the Datum level, the Datum plane is not necessarily horizontal. Utmost care is required when performing hydraulic calculations in this case (see also App. C). The Datum level used by different countries for the same waterway can also be different, which leads to different depth figures for the same location. This is the case for the Western Scheldt, where Dutch and Belgian charts show such differences.

Tidal levels like MLLW are long-term averaged tidal levels based on measurements and therefore include averaged meteorological influences on the water level. The period of averaging is preferably 18.6 years, so that the tidal component with this duration is properly taken into account. Commonly used long-term averaged tidal levels are for instance Mean Low Water (MLW) and Mean High Water (MHW). Other tidal levels are defined in App. C.

The tidal range can be defined using different tidal levels. The normal tidal range is defined as MHW – MLW. But also the spring tidal range (Mean High Water Spring (MHWS) – Mean Low Water Spring (MLWS)) or neap tidal range (Mean High Water Neap (MHWN) – Mean Low Water Neap (MLWN)) can be used.

In morphodynamic modelling preferably a complete spring-neap tide cycle is taken into account. This is, however, computationally demanding. To reduce computational costs, a so-called morphological representative tide can be used. This is a single tidal cycle that is expected to have a similar effect on the morphology as the total spring-neap tidal cycle.

Table 3.6: Main constituents of the tide at several places in the Netherlands. Amplitude (cm) and phase lag in ° ref. to CET (UTC+1)

Component	Angular Velocity in °/h	Vlissingen 51°27′N 3°36′E		Euro Platform 52°0′N 3°17′E		H. of Holland 51°59′N 4°7′E		Rotterdam 51°55′N 4°30′E		IJmuiden 52°28′N 4°35′E		Delfzijl 53°20′N 6°56′E	
A_0	ref. to NAP in cm	−1		0		7		24		2		7	
		a [cm]	φ [°]	a [cm]	φ [°]	a [cm]	φ [°]	a [cm]	φ [°]	a [cm]	φ [°]	a [cm]	φ [°]
SA	0.041	7	216	9	213	8	222	7	241	10	220	9	219
SM	1.016	4	33	3	31	3	32	3	43	3	22	4	32
Q1	13.399	3	133	4	126	3	131	3	148	4	133	3	179
O1	13.943	11	195	11	188	11	191	9	209	11	193	9	247
P1	14.959	3	353	3	340	3	346	2	11	3	346	3	48
K1	15.041	7	10	8	358	8	359	6	17	8	358	8	43
3MS2	26.952	3	281	2	288	2	312	2	344	2	338	4	167
MNS2	27.424	3	143	1	154	2	182	2	211	2	210	3	33
NLK2	27.886	4	354	2	1	2	26	2	58	2	54	4	245
μ2	27.968	13	161	6	174	8	200	8	232	9	227	15	55
N2	28.440	29	35	12	26	12	59	10	95	10	108	21	310
NU2	28.513	9	26	4	25	5	52	5	86	4	88	8	288
MPS2	28.943	3	110	1	107	1	170	1	206	2	205	5	27
M2	28.984	175	59	74	54	79	86	72	121	68	129	136	333
λ2	29.456	6	76	3	80	3	110	3	144	3	142	5	348
2MN2	29.528	13	257	6	261	7	290	7	325	7	323	12	168
S2	30.000	48	117	18	111	19	147	17	184	17	198	34	46
K2	30.082	14	117	5	111	6	147	5	184	5	198	10	43
2S M2	31.016	4	348	2	358	2	25	2	61	3	54	4	270
2M K3	42.927	3	162	1	141	1	191	1	225	1	263	1	120
MK3	44.025	2	316	1	281	1	288	1	349	0	279	1	278
3MS4	56.952	2	196	1	193	2	235	2	303	3	268	4	216
MN4	57.424	4	94	4	105	6	137	5	204	7	157	5	118
M4	57.968	13	120	10	130	17	165	15	230	20	186	17	145
MS4	58.984	9	181	7	185	11	222	9	291	12	246	10	224
MK4	59.066	2	178	2	184	3	221	3	290	4	244	3	222
2MN6	86.408	5	82	2	64	2	95	2	211	2	269	4	321
M6	86.952	9	109	4	92	5	128	4	243	4	290	7	352
2MS6	87.968	9	161	4	146	4	188	4	302	5	343	7	61
M8	115.936	3	115	1	142	2	230	1	358	3	330	1	217
3MS8	116.952	5	166	2	194	4	281	2	51	4	23	2	276

4

Global wave and tidal environments

4.1. Introduction

In this chapter we look into the global variation in the main processes that shape the coast: wind, waves and tides. Based on large-scale observations such as the latitude and the continent, a general idea of the wave, wind and tidal conditions at a project site can be obtained. Questions that can be answered are for instance:

- What is the wind system we are dealing with at this latitude and what is the dominant direction?
- Are locally generated waves important or are we mainly dealing with swell waves?
- What wave heights can we expect?
- Does the wave climate exhibit seasonality?
- Can we expect a large tidal range in this part of the world?
- Is there a diurnal or a semi-diurnal tide?

This chapter starts with a treatment of the zonal wind systems (Sect. 4.2). Knowledge of these global wind patterns is helpful in identifying the prevailing wind conditions for a project site, as well as the wave climate. In Sect. 4.3, the global wave climate is discussed and some generalisations are made about the coastal impact of different wave conditions. Subsequently, global tidal environments and coastal characteristics are discussed in Sect. 4.4. Here it is emphasised, moreover, that it is the *relative* effect of waves and tides rather than the absolute tidal ranges and wave heights that determines the coastal character.

Please bear in mind that wind, waves and tides vary not only globally, but also regionally and locally. An example of variation due to regional geographic variation is the sheltering of the southern part of the Florida coastline from waves due to the presence of the Bahamas. On a local scale, the location of a land reclamation project

may be chosen such that persistent swell cannot arrive at the site. These smaller-scale variations are considered from Ch. 5 onwards.

4.2. Zonal wind systems and ocean circulation

4.2.1. Solar radiation and temperature distribution

Winds and ocean currents develop as a consequence of uneven distribution of heat over the earth's surface. This heat imbalance is largely explained by the fact that different parts of the earth's surface receive different amounts of solar radiation.

The main source of thermal energy for the earth is the electro-magnetic radiation emitted by the sun. As the radiation passes through the earth's atmosphere, it is depleted by reflection from the top of clouds and absorption by clouds and atmospheric gases. The incoming radiation that actually reaches the earth's surface may be absorbed there, be transmitted downwards if it encounters a material which is transparent to it, or be reflected. The absorption of radiation leads to heating. The heat may be transmitted downwards by conduction or, in the case of fluids, by convection.

The earth in turn emits electro-magnetic radiation into space. The low-frequent terrestrial radiation is readily absorbed by gases in the atmosphere such as water vapour, carbon dioxide and ozone. These gases in turn emit long-wave radiation in all directions. As a result, they act as a layer of insulation around the earth analogous to the glass of a greenhouse; their effect on earth temperatures has been called the greenhouse effect. Human-induced emissions of greenhouse gases may increase the ability of the atmosphere to absorb radiation and lead to a gradual warming of the earth and atmosphere. This is referred to as global warming.

Ignoring any change in the earth's mean annual temperature from one year to the next and taking mean annual values, a balance must exist between incoming solar radiation and outgoing terrestrial radiation. However, the amount of incoming radiation is strongly dependent on the latitude. The total annual incoming radiation is greatest at the equator and decreases towards the poles. Figure 4.1 shows the long-term averaged incoming and outgoing radiation intensity as a function of the latitude. At high latitudes the incoming radiation is less than the outgoing radiation: a net loss of heat by radiation is found. Near the equator there is a net gain. The changeover from a surplus to a deficit in the net annual radiation balance occurs at about 37° latitude N and S. The uneven distribution of heat over the earth's surface requires transfer (advection) of heat. For that reason, both winds (Sect. 4.2.2) and ocean currents (Sect. 4.2.3) are generated that are responsible for advective heat transport. About 60 % of the advective heat transport can be attributed to the movement of air and the remaining 40 % to ocean currents.

The amount of incoming solar radiation is determined by factors such as the average distance between the sun and the earth, the daily sunlight duration, the transparency

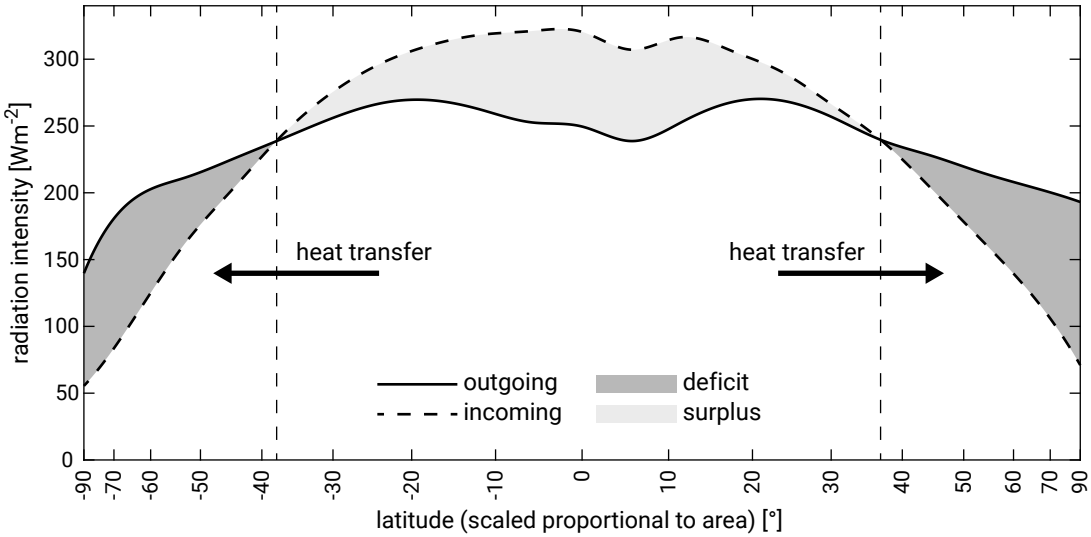

Figure 4.1: Zonal mean incoming and outgoing top-of-the-atmosphere radiation from CERES satellite radiation measurements in the period 2001–2014.

of the atmosphere and the angles at which the sun's rays strike the earth. These factors vary not only with latitude but have a seasonal component as well. Another factor governing the heat distribution is the fact that different surfaces absorb and store energy at different rates. Land surfaces heat rapidly during the day and cool down fast during the night, whereas an ocean responds more slowly to changes in incoming radiation. This is because:

- in water, the solar radiation penetrates further than in land;
- water has a roughly four times greater specific heat capacity than land (four times more energy is required to raise the temperature of water);
- water has a big storage possibility for heat by the process of mixing and evaporation.

Figure 4.2 shows the effect of the seasons and the differential warming of the oceans and the land on the air temperature distribution over the earth surface. The figure shows the temperature distribution in January (Northern winter, Southern summer) and July (Northern summer, Southern winter), which for most places on earth represent the extreme conditions. In winter the oceans remain warmer than the land and in summer the land heats up more than the oceans. As a result, in January the isotherms over the NH oceans bend towards the North Pole and the isotherms over the SH oceans bend towards the equator. In July this situation is reversed. In winter the isotherms are more closely spaced (larger thermal gradients) than in summer. Furthermore, isotherms are more closely spaced over land masses than over open oceans.

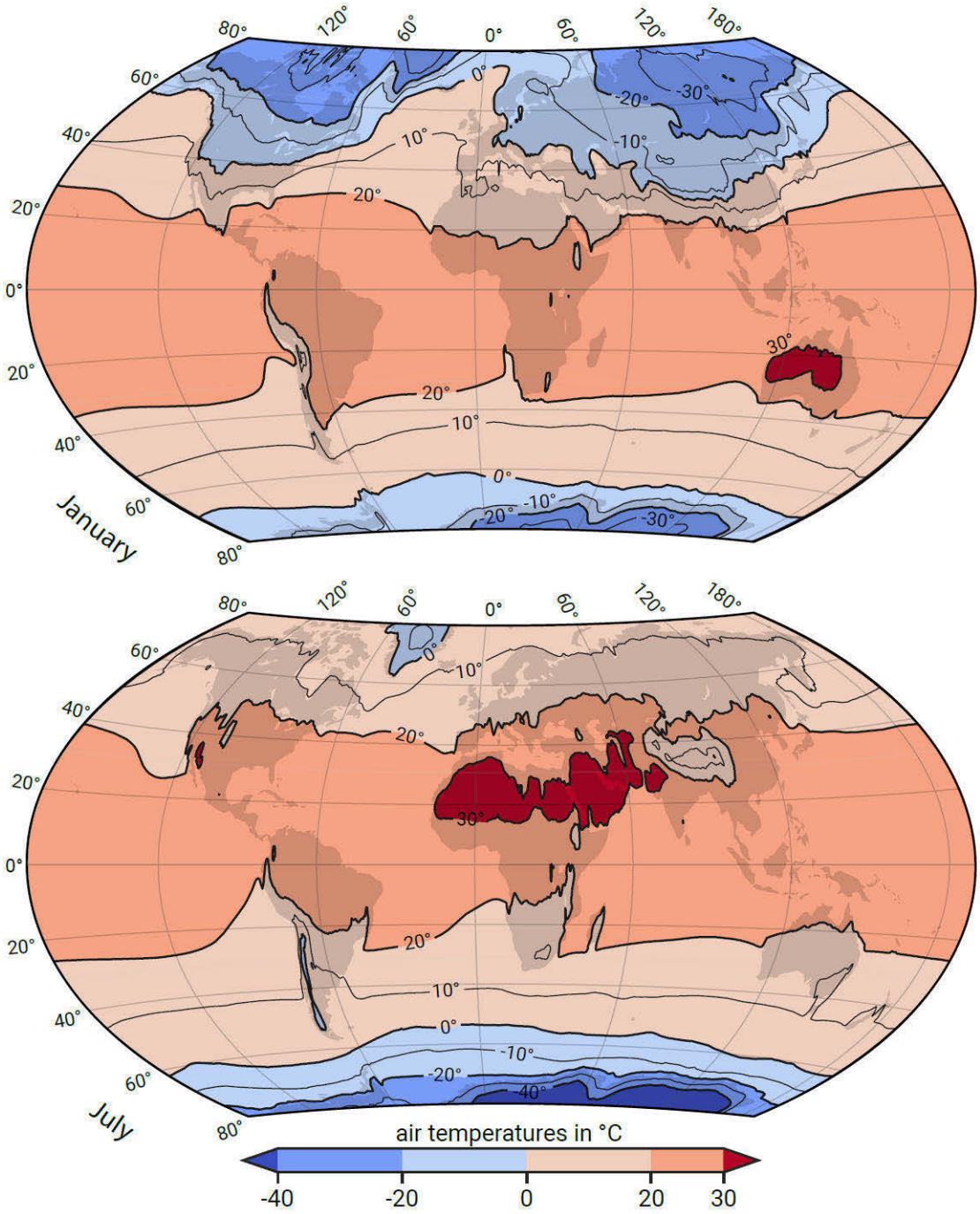

Figure 4.2: Air temperatures at $h = 2$ m above the surface in January (upper plot) and July (lower plot). Isotherms join places with similar temperature conditions. Generally, the isotherms follow the latitudes, but isotherms over the oceans bend towards the equator in summer and towards the poles in winter. Data from the ECMWF ERA5 model reanalysis dataset (ECMWF, n.d., and https://apps.ecmwf.int/codes/grib/param-db/?id=167).

4.2.2. Atmospheric circulation and wind patterns

Near the equator, where the average solar radiation is greatest, the air is warmed at the surface and rises. It attains a maximum vertical altitude of about 14 kilometres (top of the troposphere[1]) and then begins flowing horizontally to the North and South Poles. This creates the band of low air pressure known as the Intertropical Convergence Zone (ITCZ). Because air moves from high surface pressure toward low surface pressure, the ITCZ draws in surface air from higher latitudes, resulting in surface winds towards the equator.

If the earth did not rotate, and if its surface would be entirely uniform with respect to transparency to solar radiation, heat capacity and thermal conductivity, then we might expect a simple convection cell circulation to exist within the troposphere in each hemisphere (Fig. 4.3). Each cell would have a horizontal dimension of the order of 10^4 km, with a vertical dimension of only some 10 km.

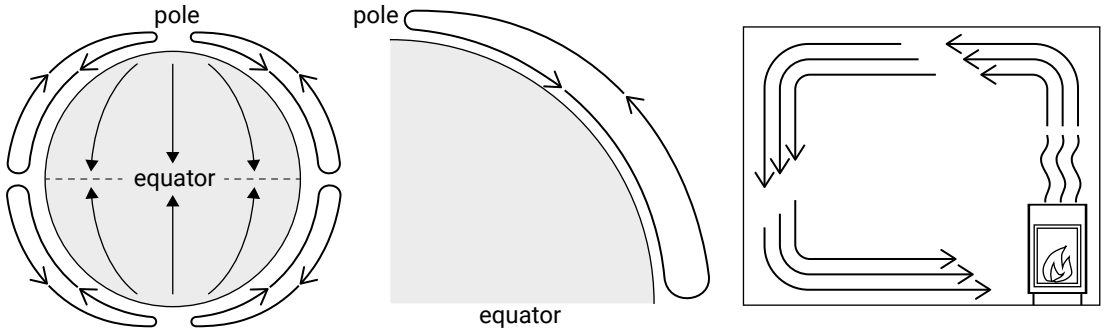

Figure 4.3: Convection cell circulation on a non-rotating uniform earth. The left and middle panels show the one cell per hemisphere circulation pattern when only solar radiation is taken into account. The right panel shows the analogy with a fire heating the air and creating a circulation cell in the room.

In reality, due to the rotation of the earth, the cells on the Northern and Southern Hemispheres break up in three smaller cells each (Fig. 4.4).

The earth rotation results in the so-called Coriolis effect (see Intermezzo 3.1). It causes currents and atmospheric flows to deviate to the right (starboard side) on the NH and to the left (port side) on the SH. Due to the Coriolis effect, the air in the upper atmosphere is deflected when moving away from the equator.

At about 30° of latitude (north and south) the air begins to flow from west to east (this is the subtropical jet stream), causing an accumulation of air in the upper atmosphere. To compensate for this accumulation, some of the air in the upper atmosphere sinks back to the surface, creating the subtropical high pressure zone.

From this zone, the surface air travels in two directions:

[1]Troposphere is the upper part of the atmosphere, where the temperature decreases with increasing altitude.

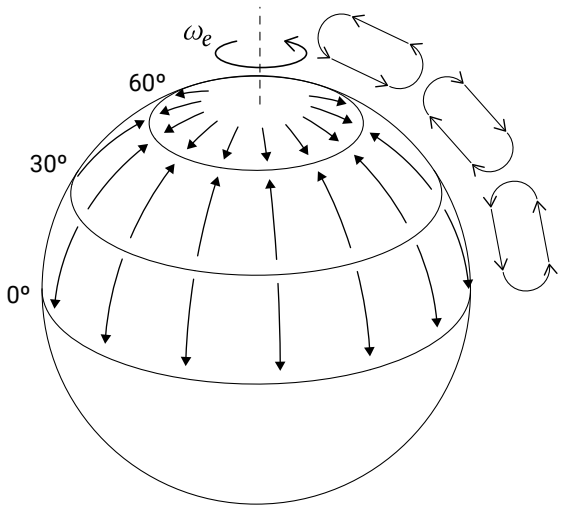

Figure 4.4: Convection cell circulation on a rotating uniform earth. Due to the rotation of the earth, the cells on the Northern and Southern Hemispheres break up in three smaller cells each.

1. Back towards the equator, creating the trade winds or tropical easterlies (Fig. 4.5). These trade winds are deflected by the Coriolis effect, resulting in the northeast trades (NH, right deflection) and the southeast trades (SH, left deflection);
2. Towards the poles, producing the westerlies that are also deflected by Coriolis.

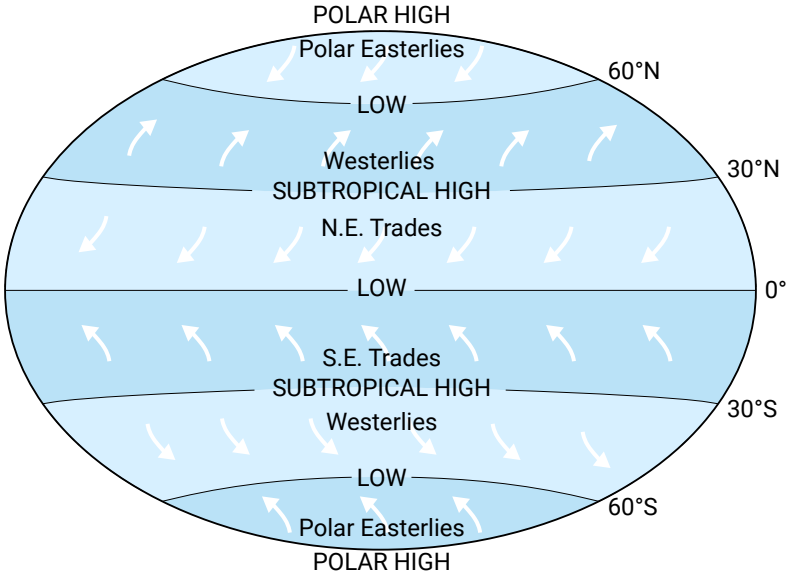

Figure 4.5: Schematic presentation of pressure belts and prevailing wind systems at the earth's surface. The earth is encircled by several broad prevailing wind belts, which are separated by narrower regions of either subsidence (highs: poles and about 30°N and S) or ascents (lows: ITCZ and about 60° N and S). The direction and location of these wind belts are determined by solar radiation and the rotation of the earth.

Roughly at 60° north and south latitude, the subtropical westerlies collide with cold air travelling from the poles (polar easterlies). This collision results in the uplift of air and the creation of subpolar low pressure zones (and associated mid-latitude cyclones).

After it reaches the top of the troposphere, part of this lifted air is directed towards the polar highs and part is directed towards lower latitudes.

In Fig. 4.5 we can thus clearly distinguish regions with mainly westerly winds at latitudes between 30° and 60°, which we know extremely well in the Netherlands. These are strong and variable winds. Also the regions with mainly NE and SE trade winds between the equator and 30° are clearly visible. Trade winds are moderate but persistent throughout the year. They mainly occur over the oceans, since near the continents they are generally overruled by tropical and subtropical seasonal winds called monsoons (see below). The polar easterlies are moderate as well and blow over land (Antarctica) or ice (Arctic area) for the larger part of the year. The area near the ITCZ where the wind climate is predominantly calm is called *doldrums*. However, the tropics can experience tropical storms which develop over sea and ocean areas with high surface temperatures. Depending on the location, these tropical storms are called hurricanes (near the Americas), cyclones (near India and Africa) or typhoons (near SE-Asia and Australia). The storms follow a path which is only partly predictable, and stop only after crossing into a continent. Another cyclonic source are the east coast cyclones that form off the east coasts of USA, Australia, Brazil and Africa between 25° and 35° N and S.

When the non-uniformity of the earth's surface is introduced, the situation becomes considerably more complex. Due to the presence of land masses, the large-scale pressure belts are broken up into several areas of low and high pressure (see Fig. 4.6). Both the topography of a certain area (mountains affect the pressure distribution) and the differential warming of the oceans and the land play a role. The resulting typical wind patterns for the months of January and July are also shown in Fig. 4.6. We can recognise westerlies and trade winds as well as seasonally reversing winds called monsoons.

The westerlies are the strongest winds, especially around 50° to 60° N and S. Their seasonality is largest in the Northern Hemisphere where the differential warming of oceans and continents strongly influences the location of Highs and Lows (due to the larger presence of land masses in the NH). Especially the Asian land mass causes significant deviations from the large-scale pressure and wind belts (compare Fig. 4.5 and in Fig. 4.6).

It can , moreover, be clearly observed that some tropical areas are dominated by trade winds (blowing in the same direction throughout the year), whereas other areas in the tropics and subtropics are dominated by seasonally reversing monsoons. These moderate but persistent winds are the result of the larger amplitude of the seasonal cycle of land temperature compared to that of nearby oceans. This is evident in for instance SE Asia, where the Asian continent warms up in July, thus creating a Low above China, causing a SW wind blowing from the sea to the land. In January, when the water of the Indian Ocean maintains a higher temperature than the continent, the situation is reversed, causing a NE wind. The SW summer monsoon (blowing from the sea to the land) is warm and humid and the NE winter monsoon (blowing from the

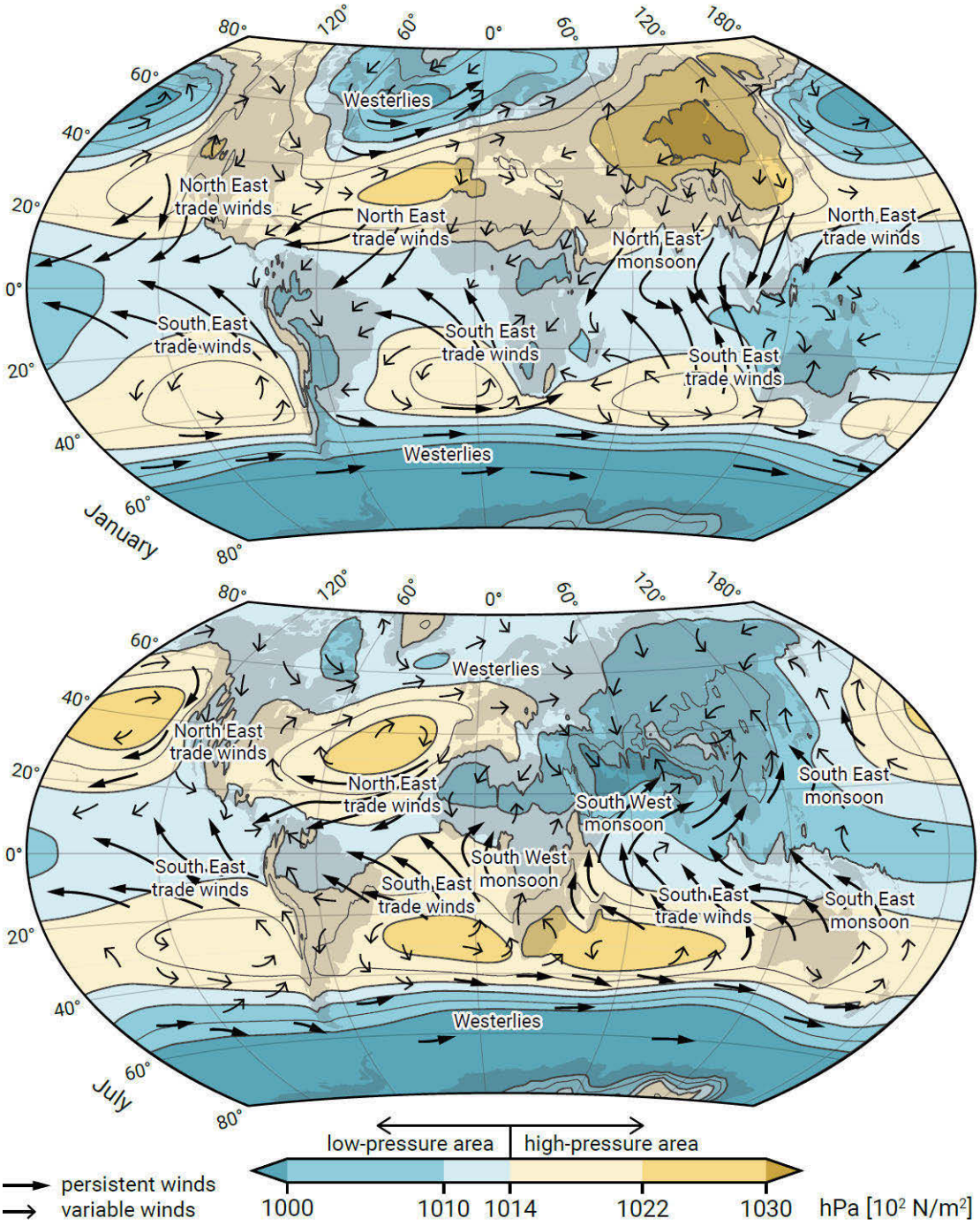

Figure 4.6: The air pressure at mean sea level and the global wind patterns, in January (top panel) and July (bottom panel), indicating the main wind systems. Pressure data from the ECMWF ERA5 model reanalysis dataset (ECMWF, n.d., and https://apps.ecmwf.int/codes/grib/param-db/?id=151).

land towards the sea) is relatively cold and dry[2]. The above holds for large continental land masses (like Asia), but also N and S America and Africa have a monsoon. For minor land masses onshore winds may be experienced in winter.

Summarising, the zonal wind systems are determined by large-scale pressure belts as a result of latitude-dependent heating of the earth. We can distinguish between:

- Polar easterlies at high latitudes (>70°);
- Strong westerlies at mid-latitudes (30°–70°);
- Extensive, but moderate trade winds in the subtropics (10°–30°);
- Quieter doldrums around the equator (10°N–10°S).

These winds blow in the same direction throughout the year, but vary spatially and temporally with the seasons. The trade winds and in particular the westerlies are the most important in supplying energy to the coastal system. Although the trade winds are not as strong as the westerlies, they blow over large areas throughout the year.

Regional and local effects are:

- Seasonally reversing monsoons due to changes in heating of continents and oceans;
- Cyclones (tropical and east coast cyclones);
- Land and sea breezes that arise from differences in temperature of land and sea

4.2.3. Oceanic circulation

Besides atmospheric circulation, ocean water circulation also contributes to the continuous re-distribution of excess heat from the equatorial zone. This thermohaline ocean circulation is density-driven and redistributes not only heat, but salt and dissolved gases as well. It is sometimes called the great or ocean conveyor belt. In a simplistic view of the great conveyor belt (see Fig. 4.7), warm, salty surface water is chilled in the North Atlantic and eventually sinks to flow south towards Antarctica. There, it is cooled further to flow outward at the bottom of the oceans into the Atlantic, Indian, and Pacific basins. After upwelling primarily in the Pacific and Indian Oceans, the water returns as surface flow to the North Atlantic, again supplying heat to the polar zones. The surface flow is primarily wind-driven and is confined to a layer of typically 50 m to 100 m of well-mixed water.

[2]Similarly, differences between day and night land-sea temperatures can locally generate an onshore breeze during the day (sea breeze) and an offshore breeze (land breeze) at night.

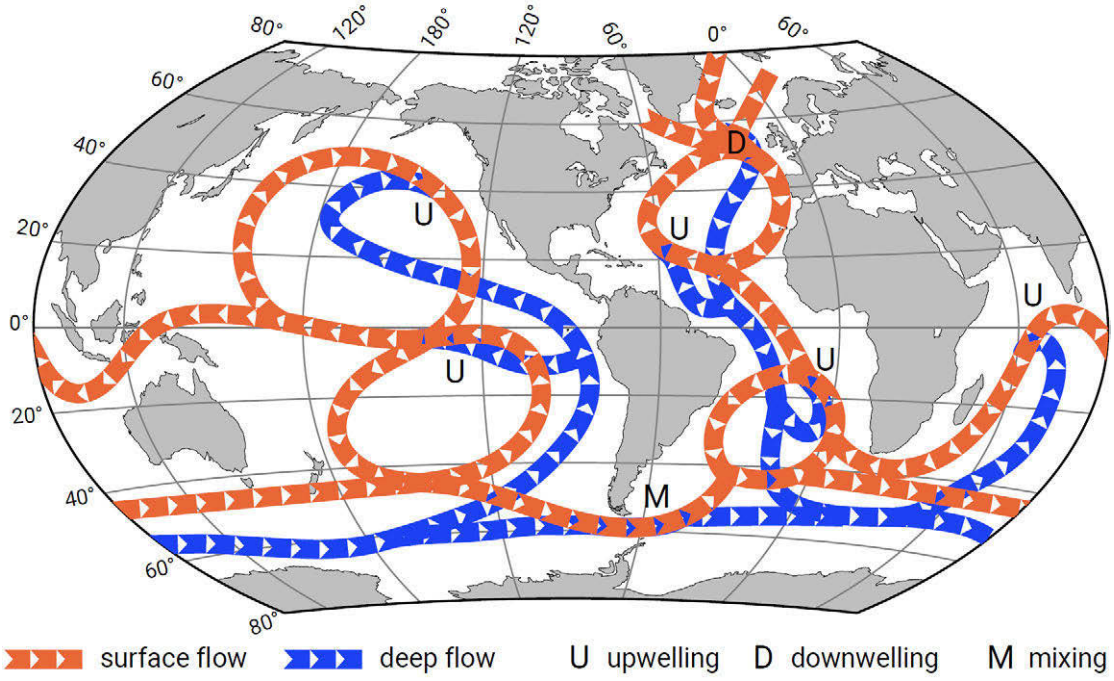

Figure 4.7: The global current patterns ('great conveyor belt') consisting of a wind-driven surface flow (red) and the density-driven deep ocean currents (blue). Indicated are locations of upwelling (U), downwelling (D) and mixing (M).

4.3. Large-scale variation in wave environments

4.3.1. Wave height variation

Ocean waves are generated by wind. It can therefore be expected that the global wind systems (Sect. 4.2.2) determine the global wave environments. Global wave environments are those zones of the seas and the oceans that have similar general wave characteristics, such as similar year-averaged significant wave heights and similar seasonality. Besides, the shape and orientation of the oceans determine the fetch and hence influence the propagation of waves.

Figure 4.8 shows annual mean values for the significant wave height, as well as monthly means for January and July. For this analysis, mean significant wave heights were used obtained by visual observation of individual waves from ships for the period of 1958 to 1997. The significant wave heights vary mostly between 1 m and 5 m.

From Fig. 4.5, Fig. 4.6 and Fig. 4.8, the following general conclusions can be drawn:

- Wave heights are highest at mid-latitudes (north and south). This is the result of the westerlies, which are the strongest winds. These winds (and embedded mid-latitude cyclones) are the source of relatively large waves;
- The mid-latitude wave climate in the North Pacific and North Atlantic is especially seasonal, with much larger wave heights in the Northern winter than in the summer. This is the result of the strong seasonality in the NH westerlies,

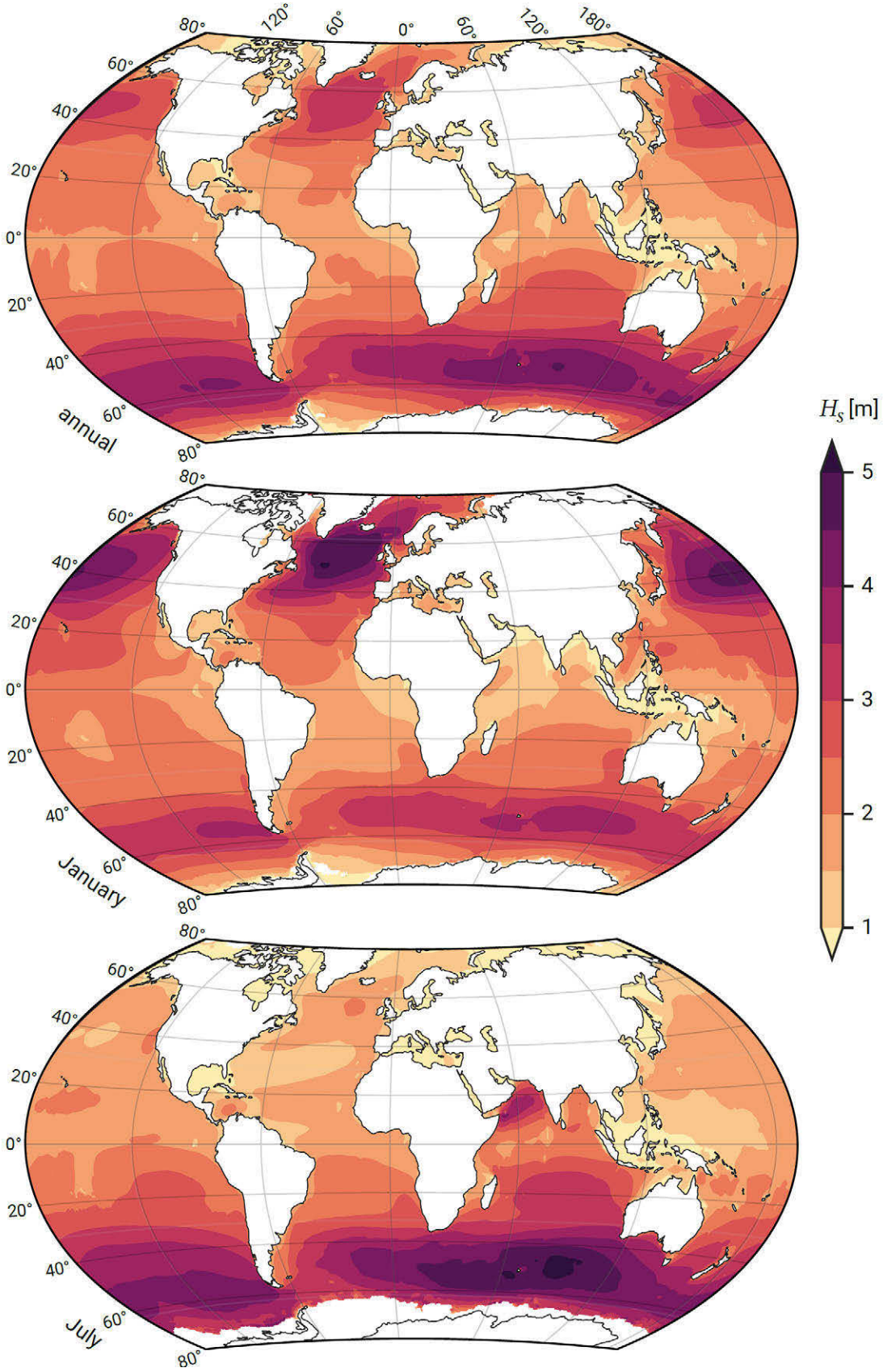

Figure 4.8: World-wide significant wave height of combined wind waves and swell (in m) based on model reanalysis data for the period 1979–2019 (ECMWF, n.d.).Top: annual mean values. Middle: monthly mean values for January. Bottom: monthly mean values for July.

due to the presence of land masses, especially the large Asian land mass (see Sect. 4.2.2);
- The Southern Ocean is characterised by an almost unlimited fetch and vast regions with high waves. Although the waves are highest in the Southern winter, the seasonality is much smaller than for the Northern Hemisphere (as a result of the smaller seasonality of the westerlies in the absence of vast land masses);
- Wave heights in the subtropics associated with the gentle trade winds are moderate;
- In the tropics and subtropics, sources of larger waves are either swell propagating from higher latitudes (originating from the westerlies), or seasonal winds (e.g. monsoons and tropical storms);
- Monsoons have a regional impact. It appears that the highest wave heights in the Arabian Sea coincide with the SW monsoon (summer). This is because the SW monsoon blows from sea to land. The NE monsoon blows from the land, except for the Malaysian Peninsula, which is exposed during the NE monsoon;
- Tropical and east coast cyclones can generate large waves but are limited in extent and too seasonal to greatly impact longer-term wave climates.

The wave climate (in terms of wave height) is generally characterised by the mean significant wave height H_s on a yearly average basis:

- Low wave energy $H_s < 0.6\,\mathrm{m}$;
- Medium wave energy $0.6\,\mathrm{m} < H_s < 1.5\,\mathrm{m}$;
- High wave energy $H_s > 1.5\,\mathrm{m}$.

4.3.2. Wave environments

J. L. Davies and Clayton (1980) identified four major deep-water wave environments (Fig. 4.9):

- Storm wave environments;
- West coast swell environments;
- East coast swell environments;
- Protected sea environments.

Besides, they identified trade and monsoon influences and tropical cyclone influences.

The global wave environments are strongly linked to the zonal wind systems (Sect. 4.2) and have the following characteristics (see also Short, 2005):

Storm wave climate

- The most energetic wave environment;
- Locally generated by westerlies and associated mid-latitude cyclones;
- Located between 40° and 60° N and S;

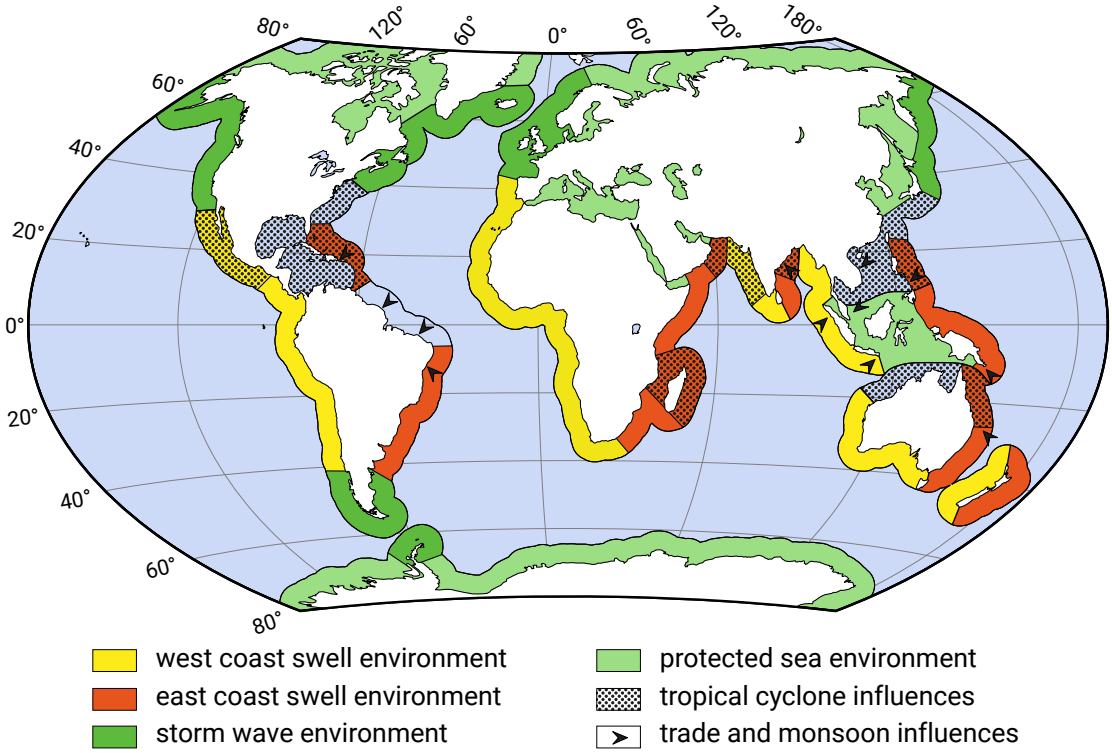

Figure 4.9: World-wide distribution of wave environments. Classification according to J. L. Davies and Clayton (1980).

- Operates year-round in the Southern Hemisphere and in winter in the Northern Hemisphere;
- Generally a combination of sea and swell is present at a certain location;
- Waves are steep, short-crested, irregular and multi-directional (sea);
- Direction is predominantly westerly (to southwesterly in the Northern Hemisphere) impacting west-facing and south-facing (NH) coasts;
- Deep water significant wave heights are 5 m to 6 m 10 % of the time. The Southern Ocean has the most persistent higher waves with heights of 2 m to 3 m 90 % of the time;
- Wave periods are about 5 s, longer during storms

West coast swell climate

- Stems from storm waves generated by westerlies in the Northern and Southern storm wave belt (highest and most persistent is the westerly swell generated at 55°S). Note that swell in the Northern Hemisphere can be generated in the Southern storm wave belt and vice versa;
- Located between 0° to 40° N and S;
- Year-round in the Southern Hemisphere, seasonal (in winter) in the Northern Hemisphere (like the storm waves from which they originate);
- West coast swell reaches west coast of Americas, Africa, Australia and New Zealand;

- Swell tends to arrive mostly from the northwest when generated in the Northern storm wave belt and from southwest when generated in the Southern Hemisphere;
- Consists of persistent and long-period waves (typical period of 10 s);
- Waves are uniform in direction, shape and size and wave heights are moderate to high (typical wave heights are for instance 1 m to 2 m off swell-dominated coasts);
- There is not much variation in wave heights around the mean (only as a result of tropical storms occurring for instance once a month in Queensland, Australia);
- In the tropics (for instance Angola, see Fig. 3.12) swell can also stem from trade winds.

East coast swell climate

The east coast swell climate has many of the characteristics of west coast swell. East coast swell originates from storms in the same storm wave belts as the west coast swell, but is directed such that it reaches east-facing coasts. They are generally lower than west coast swell and arrive less frequently than west coast swell.

Protected wave environments

Protected wave environments are areas protected from the arrival of swell and with irregular, low-amplitude waves from local winds. These are areas shielded by ice (in the polar zones), reefs (in the tropics), island archipelagos or land masses. An example of the latter are enclosed or semi-enclosed seas such as the Mediterranean.

4.3.3. Coastal impact of different wave conditions

The world-wide distribution of wave characteristics has strong implications for coastal engineering. The wave climate at a particular site is dependent on regional and local factors such as basin characteristics and local geometry. It is therefore almost impossible to classify coasts on the basis of the global wave climates. Nevertheless, the following broad generalisations can be made for a wave-dominated coastal system (see also Mangor, 2004):

- On open coasts, a *storm wave climate* is characterised by waves which are highly variable in height, period and direction. The waves are continuously reshaping the coastal profile, which results in a dynamic, sandy coastal profile with bars and wide sandy beaches backed by dunes. The profile often has an offshore storm bar, which is formed by offshore transport by the larger waves associated with storms, which in the NH mostly occur in winter. These larger waves break at relatively deep water, so the littoral zone (the active coastal zone, Fig. 1.14) extends to relatively large water depths. Since the slope of the profiles tends to be

flatter for steeper waves, the result is a wide littoral zone. Since the wave influence decreases offshore, there is an offshore fining of sediments. The breaking waves tend to be of the spilling type (see Sect. 5.2.5);

- Since *swell waves* are relatively low and long (low steepness) and have a more or less constant wave height year-round, a swell climate gives a relatively narrow sandy littoral zone. The breaking waves tend to be of the plunging type rather than the spilling type (see Sect. 5.2.5). The transition from coarser sandy sediment in shallower waters to finer sediments in deeper waters is quite abrupt. The gently sloping outer part of the littoral zone is dominated by finer sediments. The low and long waves tend to move sand onshore;
- The *monsoon climate* of Southeast Asia gives a seasonal wave climate with the highest waves in summer under the influence of the SW monsoon. The summer waves are moderate in height and relatively constant in direction and height. The corresponding profiles therefore are similar to the swell climate profiles: a fairly narrow sandy inner littoral zone, shifting to a gently sloping outer part of the littoral zone dominated by finer sediments;
- *Cyclones* give rise to very high waves and storm surge. When they hit, they greatly impact the coastal profile, causing erosion and storm bars. But because of their relatively low frequency of occurrence (for instance one or two per year that make landfall at a particular location), the coastal morphology will first and foremost be determined by the normal wave climate (either a monsoon or swell climate).

4.4. Large-scale variation in tidal characteristics

4.4.1. Global tidal environments

Not only wave characteristics, but tidal characteristics also vary globally. The two main variables on the basis of which tidal environments can be classified are:

- Magnitude of the tide, which can be characterized by the tidal range, i.e. the vertical distance covered by the tide;
- Tidal character, which can be determined by the importance of diurnal versus semi-diurnal components.

As we have seen in Sect. 3.8 the tidal wave is distorted by local differences in water depth (and thus influenced by the slope and width of the continental shelf) and by the location and shape of land masses and large embayments. This results in a global variation in tidal range controlled by the large-scale coastal configuration and indicated in Fig. 4.10. The categories that form the basis of this figure are:

- Micro-tidal regime: mean spring tidal range < 2 m;
- Meso-tidal regime: mean spring tidal range 2 m to 4 m;
- Macro-tidal regime: mean spring tidal range > 4 m.

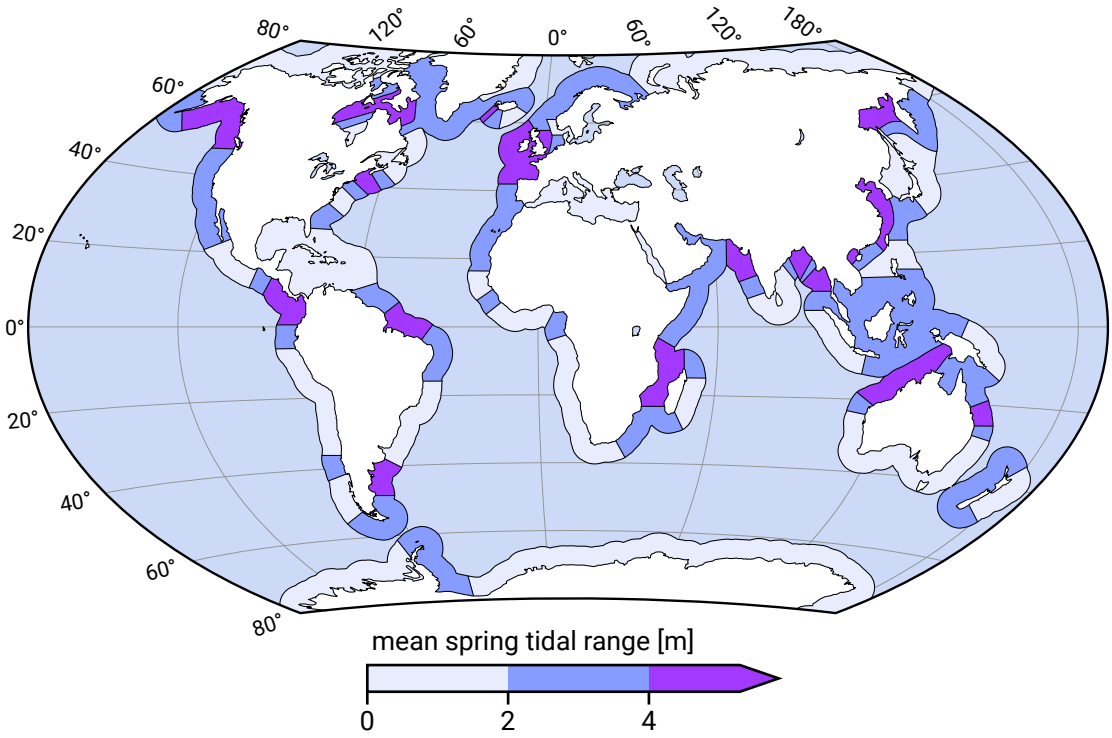

Figure 4.10: World distribution of mean spring tidal range (MHWS – MLWS). Tidal classification according to J. L. Davies and Clayton (1980).

Figure 4.10 shows that semi-enclosed seas possibly enhance tidal amplification (see Sect. 3.8.2) and therefore often experience a macro-tidal range. For open coasts and fully enclosed seas a micro-tidal regime can generally be observed.

The tidal character is defined by the form factor F. The form factor is determined as the ratio of the amplitudes of the sum of the two main diurnal components K1 and O1 and the sum of the two main semi-diurnal components M2 and S2:

$$F = \left(\mathrm{K}_1 + \mathrm{O}_1\right) / \left(\mathrm{M}_2 + \mathrm{S}_2\right) \tag{4.1}$$

with the symbols of the constituents in this case indicating their respective amplitudes.

Based on the form factor, four categories are distinguished (see Table 4.1). Examples of tidal curves per category are given in Fig. 4.11.

Table 4.1: The tidal character expressed by the form factor F

Category	Value of F		
Semi-diurnal	0	–	0.25
Mixed, mainly semi-diurnal	0.25	–	1.5
Mixed, mainly diurnal	1.5	–	3
Diurnal		>	3

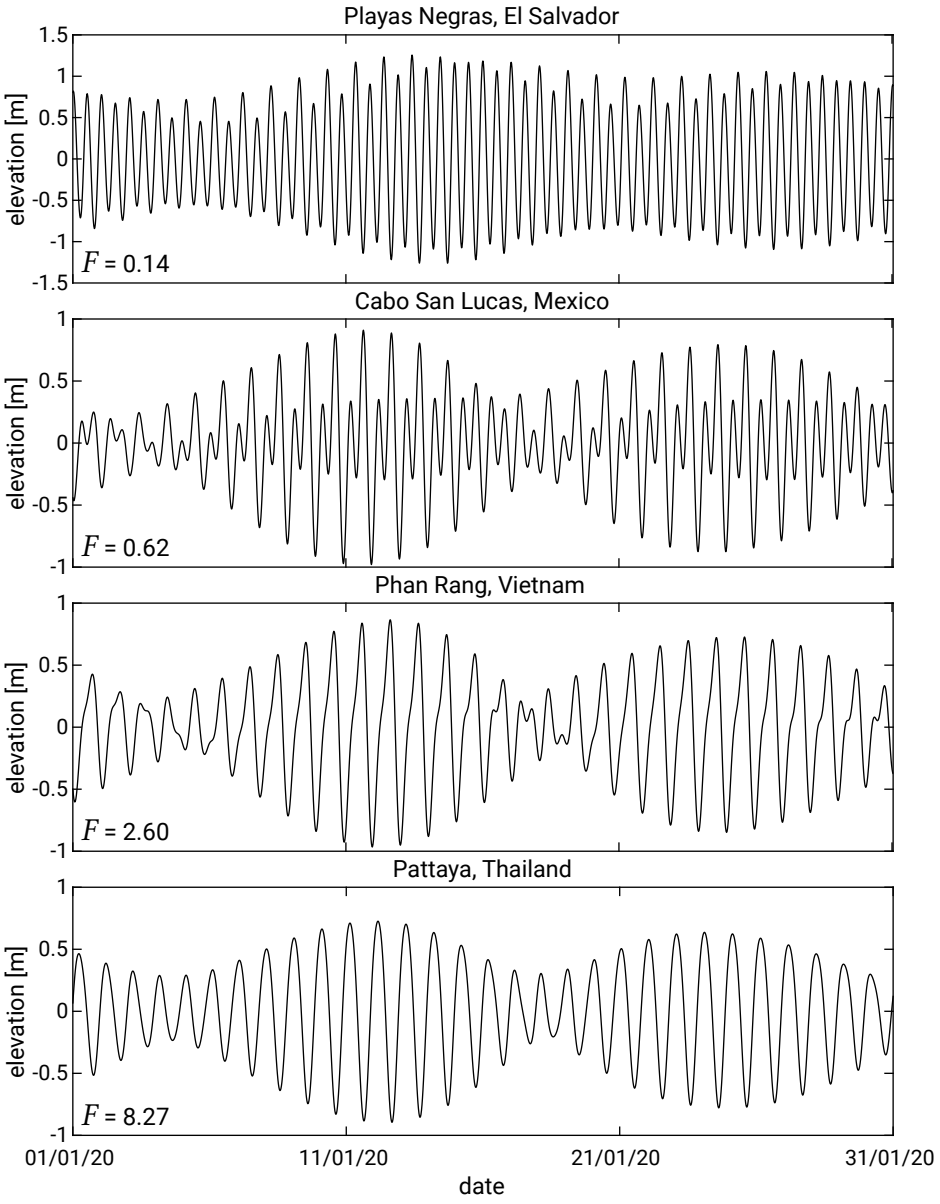

Figure 4.11: Examples of tidal curves illustrating all four different tidal characters. The time series, at offshore locations indicated by the nearest large city, were generated by accessing the TPXO7.2 model created by Oregon State University (OSU) (Egbert & Erofeeva, 2002) using the Tide Model Driver (TMD) toolbox provided by Earth and Space Research (ESR) (Erofeeva et al., 2020).

Global variations in the form factor arise due to a combination of geography and latitude. As explained in Sect. 3.7.5, diurnal components are introduced due to the declination of the earth axis. The combination of diurnal and semi-diurnal components manifests itself as daily inequality (one high water is higher than the other). The daily inequality increases with latitude and is further influenced by the presence of land masses which can locally magnify the larger tide. The latter may occur when the diurnal tidal component excites one of the resonance modes of the basin or bay. Due to

this resonance phenomenon, many areas around the equator (e.g. Vietnam) experience a mainly diurnal tidal regime, in spite of their low latitude.

The world's distribution of the tidal character is shown in Fig. 4.12. The figure shows that most of the world's coastlines experience either semi-diurnal or mainly semi-diurnal mixed tides. Nevertheless the extent of the areas with diurnal and mainly diurnal mixed tides is still significant. When comparing Fig. 4.10 and Fig. 4.12, it can be seen that many of the areas where diurnal tides dominate have a micro-tidal regime and none a macro-tidal regime. Apparently, areas with diurnal and mainly diurnal mixed tides tend to have smaller tidal ranges than semi-diurnal systems.

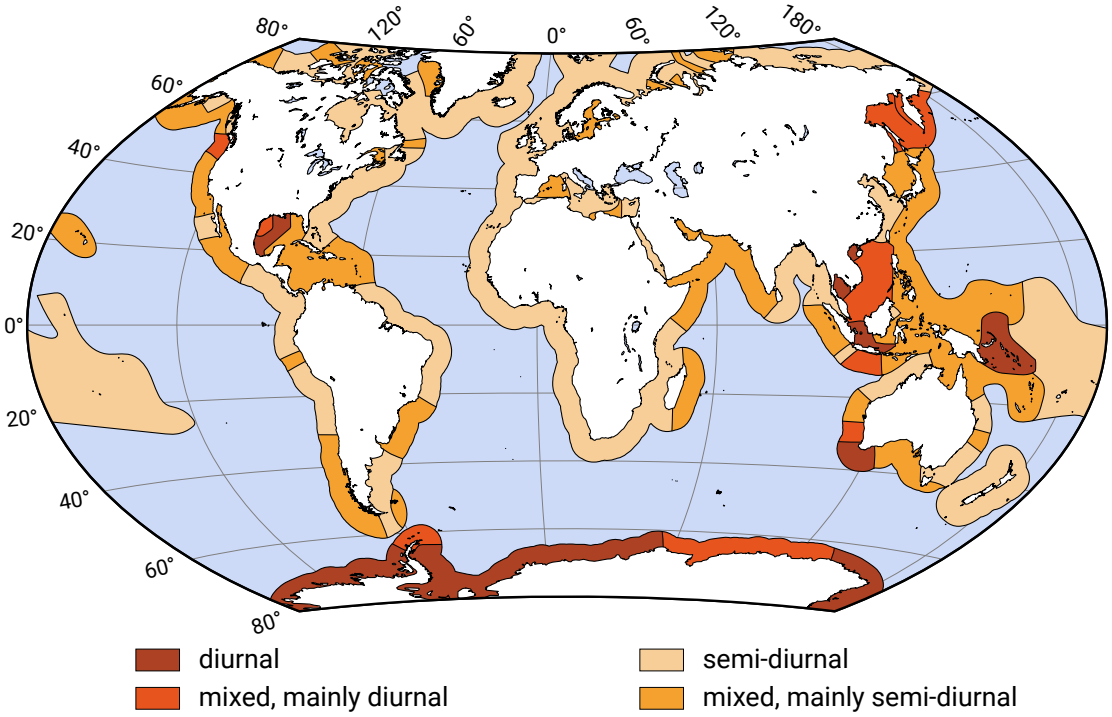

Figure 4.12: Tidal environments of the world. Note that the transitions between the tidal types are progressive and not abrupt. The attribution of the tidal type follows J. L. Davies and Clayton (1980).

4.4.2. Coastal impact of tide and classification

The semi-diurnal or diurnal rise and fall of the water level creates a so-called intertidal zone that is exposed during low water and submerged during high water. In the absence of waves (or with only very low wave energy), tide-dominated coasts develop wide, low-gradient tidal flats (see for example Fig. 2.11) in the intertidal zone and subtidal zone (the area only infrequently exposed, during extreme low tides). Tidal currents in combination with horizontal translation of the water line determine the morphology of these tidal flats. Due to the low-energy conditions, tide-dominated coasts generally consist of relatively fine sediments. The sediment distribution patterns are exactly opposite to those on wave-dominated coasts: since tidal currents increase in

strength for larger water depths, the finest sediments occur on the often muddy flats and in the wetlands of the upper intertidal zone. The coarser sandy sediments occur in the lower intertidal zone and further seawards. From the upper part of the intertidal zone to the supratidal zone (only submerged during spring tides or storm surges) salt marshes are well developed. In tropical to subtropical regions, mangroves occupy the intertidal zone.

Tide-dominated flats occur for large tidal ranges and small wave heights. This is the case for macro-tidal coasts, but tide-dominated coasts can also be found for micro-tidal regimes, as long as the wave energy is very low (for instance in an estuary). It is rather the relative importance of tide and waves than the absolute tidal range that determines the coastal character. Hayes (1979) and Davis Jr. and Hayes (1984) distinguish five classes, based on a combination of tidal range and wave energy classification (Fig. 4.13).

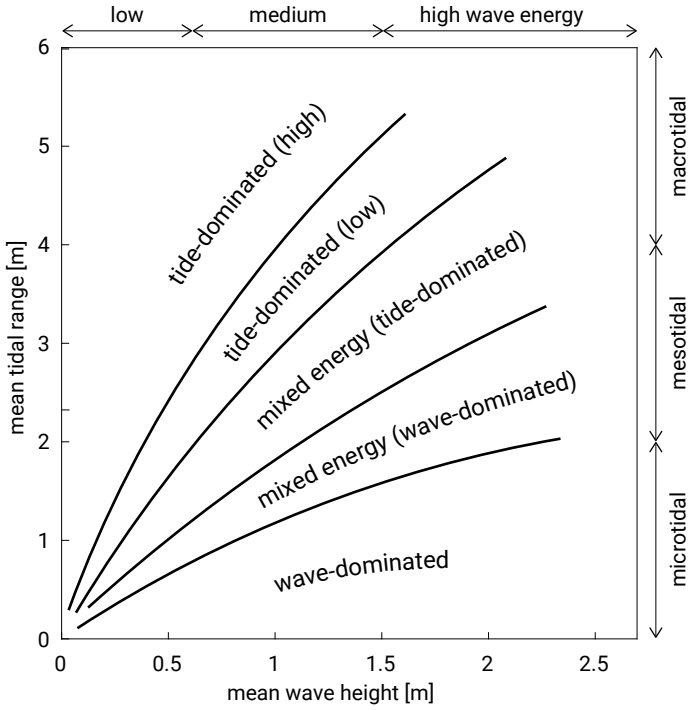

Figure 4.13: Relationship between mean tidal range and wave height according to Davis Jr. and Hayes (1984) and Hayes (1979), delineating different fields of wave and tide dominance. Note that the convergence of the fields for low wave and tidal energy means that very small differences in tide or waves may result on a different dominance and corresponding morphology.

A useful parameter to distinguish between wave and tide influence is the relative tidal range RTR as introduced by Masselink and Short (1993):

$$RTR = MSTR/H_b \tag{4.2}$$

where $MSTR$ is the mean spring tidal range and H_b is the wave height just before breaking. For $RTR < 3$ we find the wave-dominated beaches as described in Sect. 4.4.2. For $RTR > 15$ the beaches gradually approach the pure tidal flat situation. For the

intermediate range, we find beaches shaped by waves with some distinct tidal characteristics, such as a wide intertidal zone. The effect of the tide is that the zone of wave attack shifts with the tidal phase. This means that there is not enough time for wave-dominated bar morphology to develop. In other words: tides flatten out the beach morphology. Tides develop wide, low-amplitude parallel or sub-parallel bars (tidal ridges) on the intertidal beach, especially for macro-tidal regimes. During storms, waves flatten these ridges out. Tide-dominated coastal features are treated more extensively in Ch. 9.

5

Coastal hydrodynamics

5.1. Introduction

This chapter deals with the nearshore hydrodynamics that are important for sediment transport. It treats mean and oscillatory water levels and currents induced by waves, wind and tides. Quite a lot of attention is paid to waves and wave-induced currents because of their effectiveness in transporting sediment in the surf zone.

The following aspects of waves are described:

- Linear wave propagation effects in shoaling waves (until wave-breaking): increasing wave heights, decreasing wavelengths and refraction towards normal incidence (Sect. 5.2);
- Non-linear transformation of wave shapes from initially symmetric, sinusoidal profiles, to the asymmetric, pitched-forward profiles typical for near-breaking waves (Sect. 5.3);
- Wave dissipation in the wave boundary layer and its effect on wave-orbital velocities, bed shear stress and net wave-induced flow (called Longuet-Higgins streaming) close to the bed (Sect. 5.4);
- Wave-induced water level changes in breaking waves such as set-up (raising of the water level) at the coast, and wave-induced flow in breaking waves: a circulation current in the cross-shore direction (with, in the lower part of the water column, an offshore-directed undertow) as well as a longshore current along the coast (Sect. 5.5).

Subsequently §1.1~~Sect. 5.5~~§1.1Sect. 5.6 [p169] describes wind-generated set-up and currents. Section 5.7 is dedicated to tidal propagation in coastal waters. Last, Sect. 5.8 discusses some other long-wave phenomena in coastal waters, viz. seiches and surf beat.

5.2. Wave transformation

5.2.1. Energy balance

When waves propagate from deep into intermediate and shallow water, the waves transform, i.e. wave height, length and direction change until the waves finally break and lose their energy. Wave transformation takes place because the waves are affected by the seabed through processes such as *refraction*, *shoaling*, *bottom friction* and *wave-breaking*.

When the water depth becomes less than about half the wavelength (see Sect. 3.5.2 for deep- and shallow-water criteria), the waves start to be affected by the bottom and slow down. A certain harmonic component retains its frequency, but the propagation speed c decreases through Eq. 3.23 and the wavelength L decreases correspondingly. The effect on the wave height can be imagined as follows: as the first wave in a wave train is slowed down due to decreasing water depth, the following wave is still in slightly deeper water and is thus moving at a higher speed. This wave tends to 'catch up' with the wave in front of it, which is being slowed. This results in a concentration of wave energy and an increase in wave height. This process is called *shoaling* (Sect. 5.2.2). Changes in water depth and thus propagation speed can also occur *along* a wave crest. This forces an obliquely incident wave (at an angle with the coastline) to bend toward normal incidence (*refraction*, Sect. 5.2.3). *Diffraction* is wave transformation due to sheltering by obstructions like islands or breakwaters.

Various software packages are available to translate offshore wave conditions to wave conditions in the nearshore. The effects of shoaling, refraction, bottom friction and wind can be incorporated in these models. Examples are HISWA and SWAN, both developed at Delft University of Technology. The simpler packages are based on for instance a spectrally integrated energy balance. Numerically (or analytically) solving the energy balance yields information on the wave transformation (i.e. the changes in H, L, c and wave direction θ) of a wave field, while the waves approach the shore. In the presence of a current, energy is not conserved any longer, since transfer of energy between waves and currents is possible. In that case another wave quantity, wave action E/ω, will be conserved and the wave action balance rather than the energy balance should be solved. In the absence of a current, the wave action balance reduces to the energy balance. Since in this book the focus is on conceptual understanding, we will only consider the energy balance and treat a few simplified situations in which wave transformation is separated into the processes of shoaling, refraction, diffraction and breaking.

Integrating over all frequencies and directions in an irregular wave field, the following energy conservation equation can be composed:

$$\underbrace{\frac{\partial E}{\partial t}}_{\text{change of energy}} + \underbrace{\frac{\partial}{\partial x}\left(Ec_g \cos\theta\right)}_{\text{import of energy in } x\text{-direction}} + \underbrace{\frac{\partial}{\partial y}\left(Ec_g \sin\theta\right)}_{\text{and in } y\text{-direction}} = \underbrace{S - D}_{\text{gain of energy}} \tag{5.1}$$

In this equation, θ is the wave direction with respect to the x-axis (see Fig. 5.1), S is the generation term and D is the dissipation term. Underlying the spectral integration are the assumptions that: 1) the irregular wave field at one location can be represented by a single value for θ; and 2) that the total energy $E = {}^1/_8 \rho g H_{rms}^2$ is propagated at the wave group speed c_g (see Eq. 3.26). This only holds for a narrow-banded spectrum, and therefore not for a wide spectrum or a spectrum of combined swell and storm. For wave action conservation to reduce to energy conservation, we must assume a spatially constant peak period.

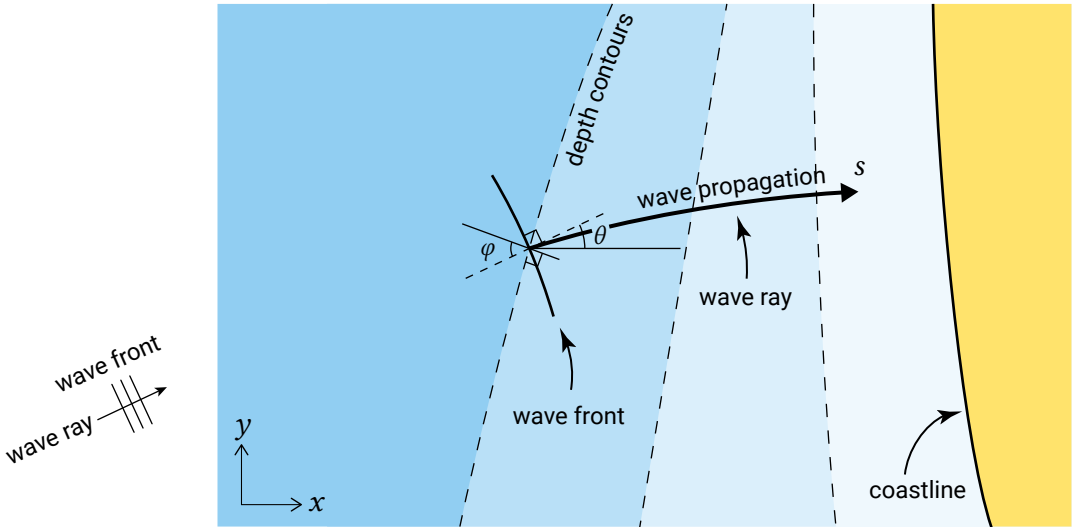

Figure 5.1: Definition of wave angles for a wave propagating along a wave ray s. The wave direction θ is the angle with the x-axis. It generally differs from the (local) angle of incidence φ with respect to the depth contours. For a uniform coastline with the x-axis perpendicular to the coast we have $\theta = \varphi$.

The deep-water group velocity is independent of location and can therefore be pulled out of the derivative. In intermediate and shallow water, the group velocity is dependent on the location (the water depth) and can therefore not be pulled out of the derivative. S can be additional input of energy due to wind, which we generally neglect for the relatively small nearshore zone. Dissipation of wave energy D results in a decrease of wave height while waves approach the shore. Various processes can contribute to the dissipation term on the right-hand side. The most efficient wave energy dissipation mechanism is wave breaking. This occurs mainly in the surf zone, but also in deeper water (where it is called white-capping). Other mechanisms include bottom

friction – especially over large areas with shallow water – and interaction with vegetation (mangroves, salt marshes). D (and S) are not known well and all sorts of empirical formulas exist which allow for the equation to be solved.

If we assume that the wave conditions are stationary (do not change in time), the term $\partial E/\partial t$ on the left-hand side equals zero and the energy balance in the coastal zone can be written as:

$$\boxed{\frac{\partial}{\partial x}\left(Ec_g \cos\theta\right) + \frac{\partial}{\partial y}\left(Ec_g \sin\theta\right) = -D_f - D_w} \tag{5.2}$$

with the total wave energy $E = {}^1/_8 \rho g H_{rms}^2$ being propagated at the wave group speed c_g in the wave propagation direction θ. Wave dissipation due to wave-breaking is denoted D_w, and wave dissipation due to bottom friction is denoted D_f. The direction θ can change and we therefore need information on θ to find a solution. For simple cases (alongshore uniform coast), Snell's law gives this information (see Sect. 5.2.3). Eq. 5.2 can also be written along a wave ray s:

$$\boxed{\frac{d}{ds}\left(Ec_g\right) = -D_f - D_w} \tag{5.3}$$

Be aware that the wave ray is not a straight line due to θ variations (see Fig. 5.1).

In order to close the equation, expressions for D_f and D_w need to be formulated. D_f is a function of the shear stress due to (mainly) wave orbital motion near the bed (see Sect. 5.4.3) and is relatively small. Battjes and Janssen (1978) express D_w based on an analogy with a bore model from the observation that after breaking, waves behave like a bore or a moving hydraulic jump.

5.2.2. Shoaling

Consider a linear (single-harmonic) long-crested wave propagating in water that becomes gradually shallower (an alongshore uniform, sandy coast with parallel depth contours). The wave is normally incident, viz. the wave crest is parallel to the depth contours, Fig. 5.2.

The wave propagation speed will be affected by the bottom when the water depth becomes less than about half the wavelength. A decreasing water depth yields a decreasing wave speed and wavelength, according to the dispersion relation as introduced in Sect. 3.5.2. Figure 5.3 shows c/c_0 and L/L_0 – where the subscript 0 refers to deep-water conditions – as a function of local water depth h divided by L_0. To find a relation between the wave height H and the water depth h we have to examine

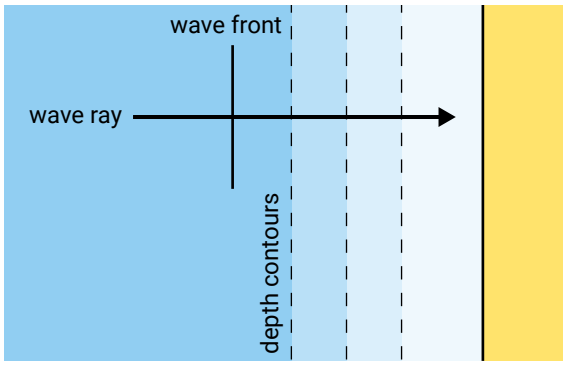

Figure 5.2: Normally incident waves with parallel depth contours ($\varphi = \theta = \text{constant} = 0$).

the energy balance. Outside the breaker zone the dissipation is approximately zero (neglecting bottom friction and white-capping) and integration of Eq. 5.3 yields:

$$U = Ec_g = Enc = \text{constant} \tag{5.4}$$

where:

U	wave power or energy flux per unit wave crest width (see also Eq. 3.26)	J/(m s)
E	wave energy per unit surface area	J/m^2
c_g	wave group velocity	m/s
c	wave celerity	m/s
n	ratio c_g to c	–

Eq. 3.25 and Fig. 5.3 show the dependency of n on the water depth and (deep water) wavelength. The energy flux U is also called the wave power and is the rate at which energy is transmitted in the direction of wave propagation across a vertical plane perpendicular to the direction of wave propagation and extending over the entire depth.

Since $E = {}^1\!/\!_8 \rho g H^2$, Eq. 5.4 can be used to relate the wave heights at two arbitrary locations (locations 1 and 2):

$$U_2 = U_1 \rightarrow E_2 n_2 c_2 = E_1 n_1 c_1 \rightarrow H_2^2 n_2 c_2 = H_1^2 n_1 c_1 \tag{5.5}$$

or:

$$\frac{H_2}{H_1} = \sqrt{\frac{c_1}{c_2}\frac{n_1}{n_2}} \tag{5.6}$$

where the subscripts indicate the location at which the parameters are evaluated.

If we choose location 1 in deep water where the wave properties are more easily evaluated ($n_1 = n_0 = {}^1/_2$), we find the following formula for the wave height (subscripts 2 are dropped):

$$\frac{H}{H_0} = \sqrt{\frac{1}{\tanh kh}\frac{1}{2n}} = K_{sh} \tag{5.7}$$

The parameter K_{sh} is called the shoaling factor and is purely a function of kh (n is a function of kh only). In Fig. 5.3 it is shown as a function of h/L_0. It is 1.0 in deep water, then decreases slightly with water depth to 0.91 and subsequently rises to infinity. In reality the wave height increase in the shoaling zone is limited by dissipation due to wave-breaking. Breaking and the limits of breaking are discussed further on in this chapter (Sect. 5.2.5). Note that the theory of shoaling is equally valid for decreasing as for increasing water depth. This means that a wave that passes over a local shoal resumes its original height, as long as no breaking has occurred.

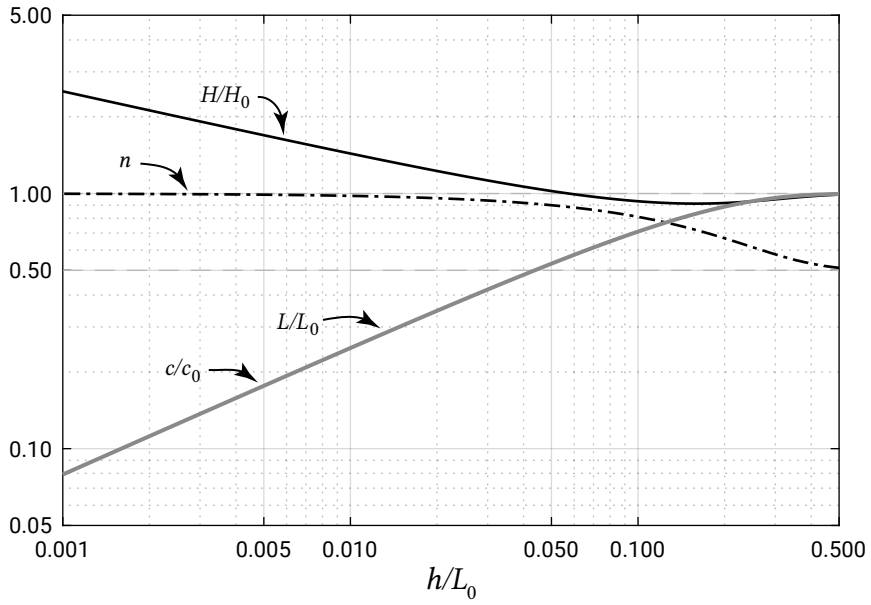

Figure 5.3: The shoaling factor $K_{sh} = H/H_0$ (Eq. 5.7), n (Eq. 3.25) and $c/c_0 = L/L_0 = \tanh kh$ (see Eq. 3.22) as a function of h/L_0.

In order to determine the shoaling coefficient, it may be helpful to use standard tables containing the values of the hyperbolic functions. These tables can be found in, for instance, the CEM (see Sect. 1.7.3). An extract of these tables is given in App. A.

Shoaling of tides and tsunamis

The phenomenon of shoaling has been explained in this section for wind waves. However, the intermediate- and shallow-water propagation of other waves such as tsunamis and tides is affected by depth variations as well[1]. For example, at sea the wave heights of a tsunami are only of the order of a metre. When tsunamis travel into progressively shallower water, however, their energy is concentrated by shoaling and possibly tunnelling[2], causing them to steepen and rise to many metres in height.

5.2.3. Refraction

Instead of a normally incident wave, consider now an obliquely incident linear wave approaching at a deep-water angle φ_0 to the shore. The wave is again long-crested and the bottom contours are essentially straight and parallel as shown in Fig. 5.4. The wave is in the shoaling region outside the breaker zone.

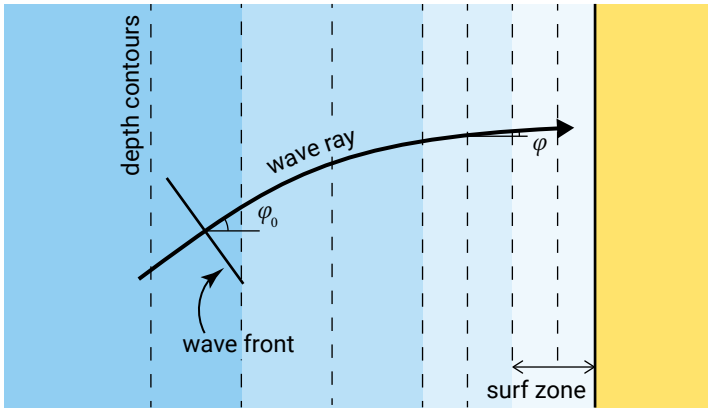

Figure 5.4: Obliquely incident waves propagating on alongshore uniform depth contours.

When a wave approaches underwater contours at an angle, it is evident that the sections of the crest in the deeper parts travel faster than those in the shallower sectors. This causes the wave crest to turn towards the depth contour. This bending effect is called refraction, and is analogous to similar phenomena in physics (light, sound). The effect is shown in Fig. 5.5. It takes place in addition to the effects of shoaling and continues up to the shoreline.

In analogy with refraction of light, the direction of the wave rays changes proportionally to the wave propagation speed according to Snell's law[3]:

$$\frac{\sin\varphi_2}{c_2} = \frac{\sin\varphi_1}{c_1} \tag{5.8}$$

[1] Note that shallow water is a relative measure depending on the wavelength of the wave; in Sect. 3.8.1 for instance, it was demonstrated that the oceans already constitute shallow water for the tidal wave.
[2] Tunnelling is the concentration of energy due to width restriction. See also Sect. 3.8.1 and Sect. 5.7 for examples.
[3] Named after the Dutch astronomer Willebrord Snellius (born Willebrord Snel van Royen, 1580–1626).

Thus, along the wave ray, $\sin\varphi/c$ is constant and equal to its deep-water value $\sin\varphi_0/c_0$. Eq. 5.8 holds for breaking as well as non-breaking waves, but for straight, parallel depth contours only.

By applying Snell's law, it is possible to construct a field of wave rays over a given bottom configuration for a given wave direction and wave period. The wave angle can thus be considered known in the energy balance, Eq. 5.2.

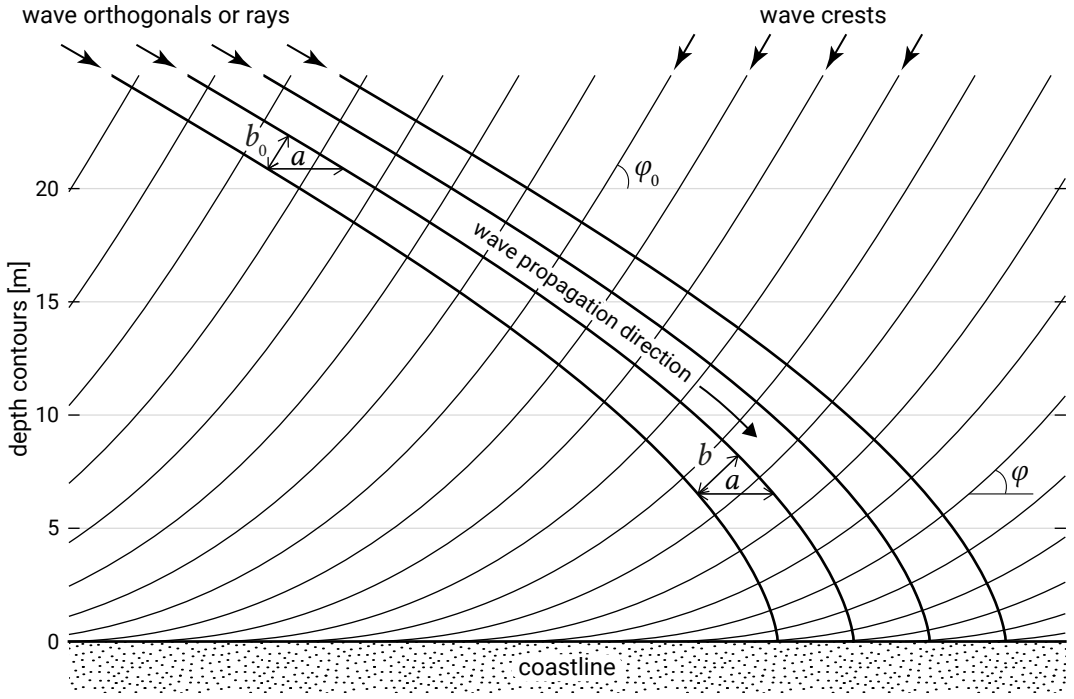

Figure 5.5: Wave refraction over straight and parallel depth contours (i.e. at a uniform coast), showing every second wave crest. The waves refract from $\varphi_0 = 60°$ offshore towards shore-normal according to Snell's law (Eq. 5.8). The wave celerity as a function of the water depth is computed using the dispersion relation (Eq. 3.22) and $T = 6\,\mathrm{s}$.

Figure 5.5 shows that the distance b between the wave rays varies. If we assume that for long-crested waves no wave energy moves laterally along the wave crest and thus that the energy remains constant between wave rays (normal to the wave crest), energy conservation between two wave rays requires that (cf. Eq. 5.3):

$$Encb = \text{const} \rightarrow H_2^2 n_2 c_2 b_2 = H_1^2 n_1 c_1 b_1 \tag{5.9}$$

The wave height at two locations therefore relates as:

$$\frac{H_2}{H_1} = \sqrt{\frac{c_1}{c_2}\frac{n_1}{n_2}}\sqrt{\frac{b_1}{b_2}} \tag{5.10}$$

Using $n_0 = 1/2$ (valid in deep water) the wave height H at any location can be related to the wave height in deep water:

$$\frac{H}{H_0} = \sqrt{\frac{1}{2n}\frac{c_0}{c}\frac{b_0}{b}} = K_{sh}K_r \tag{5.11}$$

where K_{sh} is the shoaling coefficient according to Eq. 5.7 and

$$K_r = \sqrt{\frac{b_0}{b}} \tag{5.12}$$

is the refraction coefficient used to calculate the change in wave height when a wave approaches at an angle to the shore. Since, for parallel depth contours, every wave ray refracts in the same way, the distance between given wave rays, measured parallel to the depth contours, remains constant (distance a in Fig. 5.5) and is equal to:

$$a = \frac{b}{\cos\varphi} = \text{const} \tag{5.13}$$

and thus:

$$K_r = \sqrt{\frac{\cos\varphi_0}{\cos\varphi}} \tag{5.14}$$

This result for the wave height variation in the case of parallel depth contours may also be found directly from Eq. 5.2. Assuming an alongshore uniform situation (y-derivative equal to zero) outside the surf zone (dissipation negligible), integration yields:

$$Enc\cos\varphi = \text{ const} \tag{5.15}$$

which directly results in Eq. 5.10.

The effect of refraction on the wave height in the present example is to reduce the increase in wave height due to shoaling. In a real-life situation with a more complicated pattern of depth contours, two basic calculating techniques are available for refraction patterns: graphically and numerically (see above). A description of the first method is given in the CEM (see Sect. 1.7.3). Fundamentally, all methods of refraction analysis are based on Snell's law and conservation of wave energy. A refraction diagram is given in Fig. 5.6 as an example of the results of a refraction study. If the wave rays converge, there is an accumulation of energy and relatively high wave heights can be expected. In contrast, if wave rays diverge, the energy is spread over a larger part of the wave crest, so the wave height is reduced.

Depth refraction in obliquely incident shoaling waves was explained from differences in water depth and hence wave celerity along a wave crest. Refraction may also occur due to mean currents, in which case it is called *current refraction*. When short waves interact with a current, amongst others the celerity of the waves is affected. Current refraction takes place if the current velocity varies along a wave crest, e.g. in tidal entrances (Sect. 9.4.1), in major ocean currents, or in harbour entrance channels.

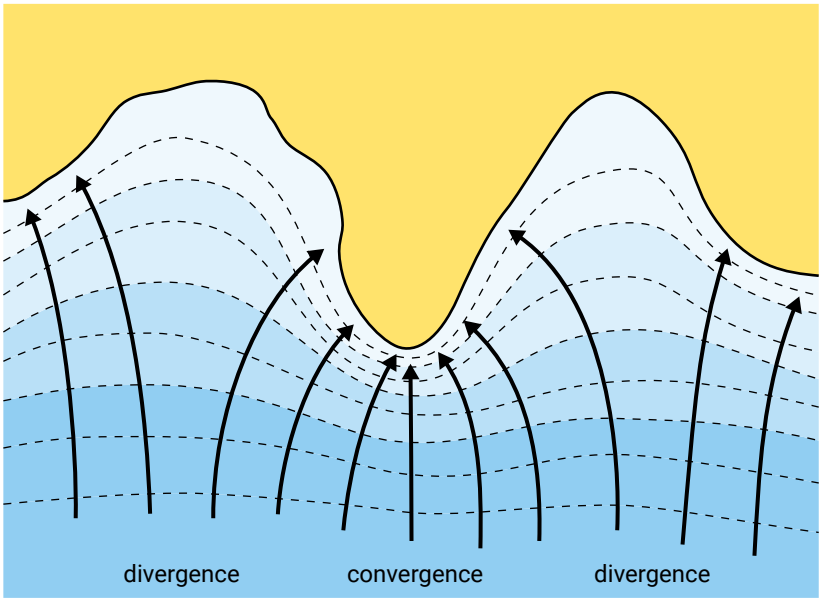

Figure 5.6: Wave refraction diagram. Wave energy converges in the case of convex depth contours (as seen from the sea) and diverges in the case of concave depth contours.

5.2.4. Diffraction

If obstructions to the wave propagation (an offshore island, a breakwater, a headland) or abrupt changes in the bottom contours are present, there is a large (initial) variation of wave energy along a wave crest, which leads to transfer of energy along the wave crests. This phenomenon is called diffraction. Figure 5.7 shows the diffraction of an incident wave train in case there are no depth changes. A part of the wave front is blocked by the breakwater and is reflected seaward. The remainder of the wave front will bend around the obstacle and thus penetrate into the zone in the lee of the obstacle (shadow zone). The diffracted wave crests will form concentric circular arcs with the wave height decreasing along the crest of each wave.

Figure 5.7 also shows the wave ray that separates the shadow or diffraction zone from the wave zone. Due to the lateral transfer of wave energy into the shadow zone, the wave height along this ray is lower than the incident wave height; in the case of constant depth (and thus constant celerity), the wave height is 50 % of the original wave height according to linear theory and about 70 % for irregular directional waves. The wave heights decrease deeper into the shadow zone. Further from the breakwater into the wave zone, the wave height gradually approaches the incident wave height.

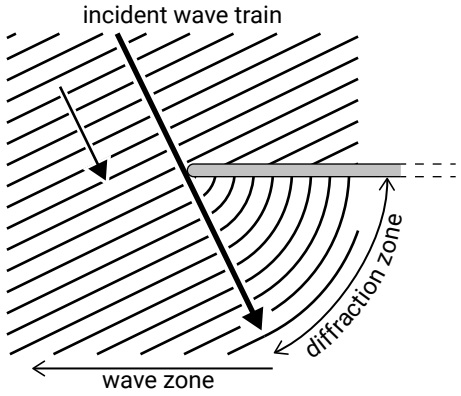

Figure 5.7: Diffraction of an incident wave train.

The extent of energy penetration in the area landward of an obstacle depends on the ratio of a typical lateral dimension of the obstacle, e.g., the length of a single detached breakwater λ to the wavelength L. When a thin pile is located in waves with a large wavelength, $\lambda/L \ll 1$, wave energy spreads behind the entire pile. In the case of a long, detached breakwater, $\lambda/L \gg 1$, diffraction occurs around each breakwater head, but wave energy will not spread in the entire zone behind the breakwater.

Figure 5.8 shows waves passing through a gap between two detached breakwaters. Diffraction occurs in the lee of the breakwaters on both sides of the gap. For large enough gap lengths (relative to the wavelength), these diffraction patterns are independent. Interaction of the two patterns may occur for smaller gap lengths.

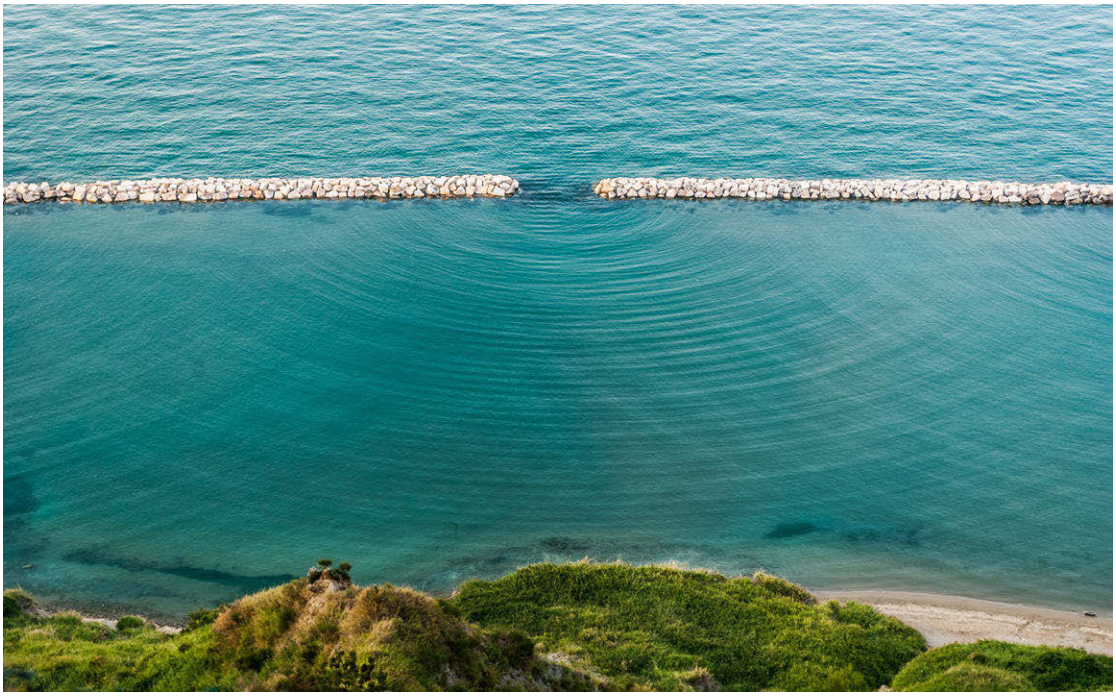

Figure 5.8: Typical diffraction pattern through a gap between two detached breakwaters in Pesaro, Italy. Photo by Roberto Lo Savio ('Credits' on page 579).

The theory of wave diffraction is solved mathematically by application of the 'Cornu spiral' (see for instance Battjes (2006)). This graphical method yields spatially varying diffraction coefficients, defined as the ratio of the diffracted wave height to the incident wave height, assuming that the latter is not disturbed by the obstacle. The CEM Chapter II-7 and (in more detail) the Shore Protection Manual Volume I Chapter 2 present diffraction coefficients as a function of position (relative to a semi-infinite rigid impermeable breakwater) and as a function of the breakwater gap width.

The disadvantage of the above methods is that they assume a constant water depth. In reality there will generally be a sloping bottom or an uneven bed and the results will therefore be influenced by this bottom. Numerical models can take into account shoaling, diffraction, refraction, reflection (and breaking) simultaneously.

5.2.5. Wave-breaking

Section 5.2.2 demonstrated how shoaling would increase the wave height until infinity, at least in the absence of a physical limit to the steepness of waves. A wave crest becomes unstable and starts breaking when the particle velocity exceeds the velocity of the wave crest (the wave celerity). This breaking condition corresponds to a crest angle of about 120° (see Fig. 5.9).

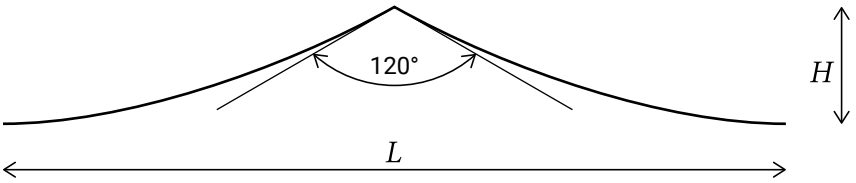

Figure 5.9: Maximum crest angle.

Miche breaking criterion and breaker index

Miche (1944) expressed the limiting wave steepness based on the Stokes wave theory (a non-linear expansion of the linear Airy theory that better describes steeper waves, see Intermezzo 5.1):

$$\left[\frac{H}{L}\right]_{\max} = 0.142 \tanh(kh) \tag{5.16}$$

In deep water Eq. 5.16 reduces to:

$$\left[\frac{H_0}{L_0}\right]_{\max} = 0.142 \approx \frac{1}{7} \tag{5.17}$$

When the deep-water steepness exceeds this limit, steepness-induced wave-breaking (called white-capping) occurs. Only a limited part of the wave energy is dissipated through white-capping. The steepness $H_s/L_{0,p}$ of wind waves is often less than 0.05.

Note that §1.1 $L_{0,p}$ [p180] is the deep-water wavelength corresponding to the peak period. Consider for example a deep-water wave height $H_s = 1.5$ m and a wave period of $T_p = 5$ s. These are average conditions for the Dutch coast. We find $L_{0,p} = 1.56T_p^2 = 39$ m and $H_s/L_{0,p} = 1.5/39 = 0.04$. Under these conditions, even for the higher waves in the record, little white-capping is expected.

In shallow water Eq. 5.16 becomes:

$$\left[\frac{H}{L}\right]_{\max} = 0.142\frac{2\pi h}{L} \approx 0.88\frac{h}{L} \tag{5.18}$$

This is equivalent to:

$$\gamma = \left[\frac{H}{h}\right]_{\max} = \frac{H_b}{h_b} \approx 0.88 \tag{5.19}$$

with γ is the breaker index, H_b is the breaking wave height and h_b is the water depth at the breaking point. Using solitary wave theory – a non-linear wave theory valid for shallow water – gives a slightly different value $\gamma \approx 0.78$.

The breaker index shows that in the shallow nearshore zone wave-breaking of individual waves starts when the wave height becomes greater than a certain fraction of the water depth. This is called depth-induced breaking, since the limiting wave height is governed by a water depth limitation.

The water depth limitation can be explained as follows. The decrease in water depth and the increase in wave heights due to shoaling result in a significant increase in horizontal particle velocities with respect to the wave celerity. When waves approach the shore, the wave celerity is reduced. In addition, we have seen that the wave height increases due to shoaling and the orbital motion within the waves is also changing (see also Sect. 5.4): although the orbit in deep water is a circle, in shallow water the orbit becomes an ellipse with a horizontal axis longer than the vertical axis. The vertical axis of the orbit at the water surface is equal to the wave height. Since shoaling causes an increase in the wave height, the vertical motion of the water particles at the surface must also increase. In addition to this, the horizontal movements grow in relation to the vertical movements, which means that there must be a significant increase of the particle velocity near the surface, until the horizontal particle velocity exceeds the wave celerity.

The Rayleigh distribution demonstrated that the maximum wave height $H_{\max}$ in a wave record is equal to $2H_s$. The maximum value of H_s/h for which the largest waves are breaking is therefore half of the value of the breaker indices. Hence $H_s/h \approx 0.4-0.5$ based on the Miche criterion.

The breaking parameters are shown in Fig. 5.10. The point where the wave height suddenly decreases because the largest wave in the wave field starts breaking is called the breaker point.

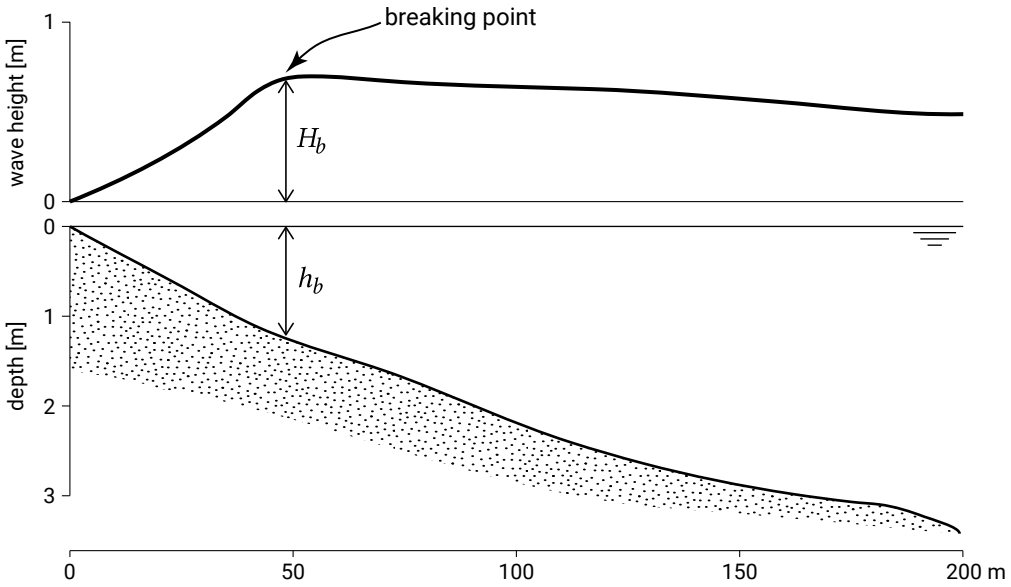

Figure 5.10: Wave-breaking parameters H_b and h_b.

The above wave-breaking criteria have been derived for a horizontal bottom. In reality the bottom will be sloping, which will affect the breaker index. Before we look at the dependency of the breaker index on the angle of the slope, we first consider the process of breaking on a slope.

Effect of bed slope on breaking process

Depending on the wave properties and the angle of the bed slope, the process of breaking takes place in various different ways. Battjes (1974) showed that the Iribarren parameter guides this process. It is defined as follows:

$$\xi = \frac{\tan\alpha}{\sqrt{H_0/L_0}} \tag{5.20}$$

where:

$\tan\alpha$	steepness of the beach	–
L_0	wavelength in deep water	m

The Iribarren parameter ξ represents the ratio of the slope steepness $\tan\alpha$ and the wave steepness. The latter is represented by the deep-water steepness instead of the steepness at the breaker point. In irregular waves the Iribarren parameter is often computed with H_s and L_0 based on T_p. A distinction is made between spilling, plunging and surging breakers, depending on the value of ξ (Fig. 5.11). The transition from surging to plunging breakers is often referred to as collapsing breakers. The typical

value of the Iribarren parameter ξ for the breaker type is also given in the figure. These values are indicative and the transition between the various breaker types is gradual.

Spilling breakers are usually found along flat beaches. These waves begin breaking at a relatively great distance from shore and break gradually (over a distance of 6 to 7 wavelengths) as they approach progressively shallower water. During breaking, a foam line develops at the crest and leaves a thin layer of foam over a considerable distance. There is very little reflection of wave energy back towards the sea. Practically all wave energy is dissipated in the breaking process.

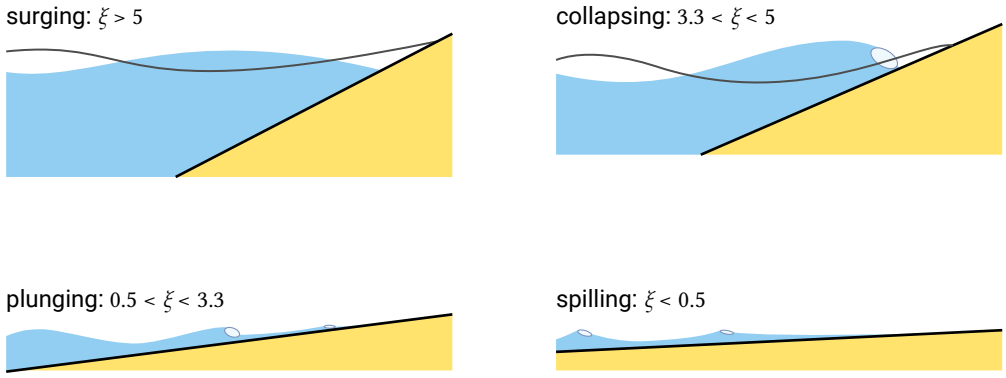

Figure 5.11: Breaker types.

A plunging breaker is a type that is found on moderately-sloped beaches. The curling top is typical of such a wave. When the curling top breaks over the lower part of the wave, a lot of energy is dissipated into turbulence. Some energy is reflected back to the sea, and some is transmitted towards the coast, while forming a 'new' wave.

Surging breakers occur along rather steep shores for relatively long swell waves. The waves surge up and down the slope with minor air entrainment. The breaker zone is very narrow and more than half of the energy is reflected back into deeper water. The breakers form like plunging breakers, but the toe of each wave surges upon the beach before the crest can curl over and fall. It is debated whether surging breakers are actually breakers or rather standing waves (caused by interference of the incoming and reflected wave).

A collapsing breaker is between a plunging and a surging breaker and thus in between breaking and non-breaking.

The parameter ξ indicates that, for a slope, the notions 'steep' and 'gentle' are relative. A beach slope of 1:100 is usually thought to be gentle, at least for a wind wave with a period of a few seconds. For this beach slope, the wave conditions discussed above – a deep-water wave height $H_s = 1.5$ m and a wave period of $T_p = 5$ s – lead to $\xi = 0.05$. The breakers are thus of the spilling type. For a tidal wave, however, such a beach slope is rather steep; a tidal wave on a beach does not break and is completely reflected.

How does the bottom slope influence the breaker index γ? Experimental results and theoretical considerations suggest that waves need time to break, so that at steeper

slopes they will break at smaller water depths, which results in a larger breaker index. This means that γ increases with increasing ξ from ca. 0.6 to 0.8 for spilling breakers to 0.8 to 1.2 for plunging breakers. The average value is ca. 0.8, corresponding to the values found for a horizontal bottom, see e.g. Eq. 5.19. Battjes and Janssen (1978) therefore adapted the Miche equation (Eq. 5.16) to account for the influence of bottom slope.

Surface roller

Breaking waves generate a layer of air-water mixture, which moves in a landward direction in the upper parts over the water column. This so-called surface roller is thought to act as a temporary storage of energy and momentum. Instead of being dissipated immediately after the breakpoint, organised wave energy is converted into turbulent kinetic energy first (which can be seen from the development of a roller at the face of a breaking wave), before being dissipated ultimately via the production of turbulence. To take this into account, sometimes an additional energy balance equation is used: the roller balance equation. The roller energy E_r represents the amount of kinetic energy in a roller propagating at the shallow-water speed $c = \sqrt{gh}$.

5.3. Wave asymmetry and skewness

In the previous sections, linear wave propagation from deep to shallow water was discussed. We considered the propagation and conservation of a bulk quantity, the energy, in the shoaling region and breaker zone, without considering any exchange of energy (or momentum) between different wave components due to non-linear interactions. The local wave characteristics were described by linear wave theory.

However, waves propagating towards the shore become more and more asymmetric, until the point of wave-breaking. Apart from an increase in wave height, the shoaling process is typically characterised by:

- gradual peaking of the wave crest and a flattening of the trough (this asymmetry relative to the horizontal axis is called skewness);
- relative steepening of the face until breaking occurs, resulting in a pitched-forward wave shape (this asymmetry relative to the vertical axis is often simply called asymmetry).

These non-linear effects cannot be described by linear theory, and the closer we come to the shore the more apparent the deviations from linear theory become. Numerous non-linear theories (Stokes theory, cnoidal wave theory, Boussinesq equations; see Intermezzo 5.1 for an overview) have been developed to take into account these complicated non-linear processes. The non-linear effects are crucial in determining the magnitude of the wave-induced transport (see Ch. 7). In the following we will therefore subsequently consider skewness and asymmetry.

Skewness

Figure 5.12 shows a wave with a long, flat trough and narrow, peaked crest, as can be observed in shallow water.

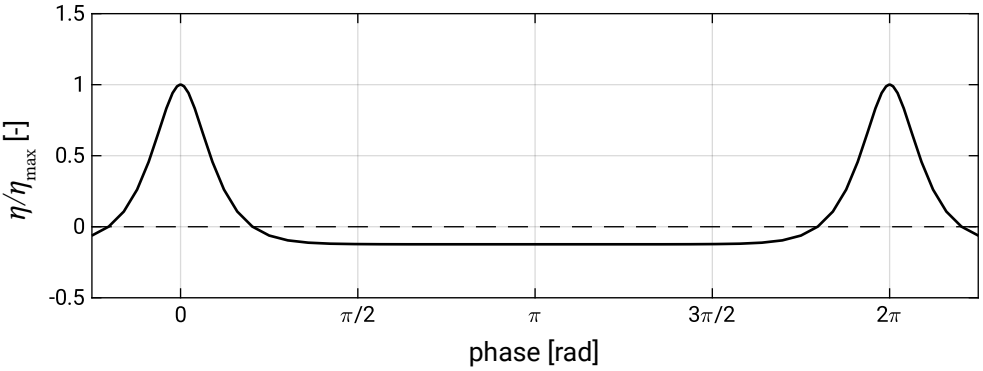

Figure 5.12: A skewed wave ($H/h = 0.5$ and $L/h = 30$) with on the horizontal axis the phase $S(x,t) = \omega t - kx$. The shallow-water wave is computed using fifth-order cnoidal wave theory (Intermezzo 5.1). Alternatively, it can be computed using a Fourier approximation, for which 20 harmonic components are required to converge towards the cnoidal solution (see Fig. 5.18). Produced using software by Fenton (https://johndfenton.com/Steady-waves/Fourier.html).

This asymmetric profile (relative to the horizontal axis) can only be described by a sum of sinusoidal waves with higher harmonics (frequencies that are a multiple of the basis frequency: $\cos S$, $\cos 2S$ etc. with $S = \omega t - kx$). Let us illustrate this using Stokes second-order theory. The second-order equation for the surface elevation can be written as:

$$\eta = \hat{\eta}_1 \cos(\omega t - kx) + \hat{\eta}_2 \cos 2(\omega t - kx) \tag{5.21}$$

The amplitude of the second-order correction is small compared to the first-order component (as long as $\hat{\eta}_1 = a$ is sufficiently small). The Stokes wave is sketched in Fig. 5.13.

It can be seen that the resulting Stokes wave profile $\eta_1 + \eta_2$ has crests which are narrower and more peaked than those of a cosine profile and troughs that are wider and flatter; the profile is skewed. The second term η_2 represents the Stokes second-order wave travelling at the same speed as the first-order wave η_1 (hence, it does not obey the linear dispersion relation). Since the two components travel at the same speed, the wave form does not change; it has a permanent form. Similarly in energy spectra of shoaling waves, one can find harmonics of the spectral peak which are coherent in phase with the spectral peak. Note that taking into account higher-order terms in Eq. 5.21 will make the profile approach the profile of Fig. 5.12 more and more (see also Fig. 5.18).

Since the higher harmonics remain phase-locked and in phase with the primary harmonic, Stokes waves have a permanent form. This is different from the deep-water situation we described in Ch. 3. There we considered the irregular sea state at a certain

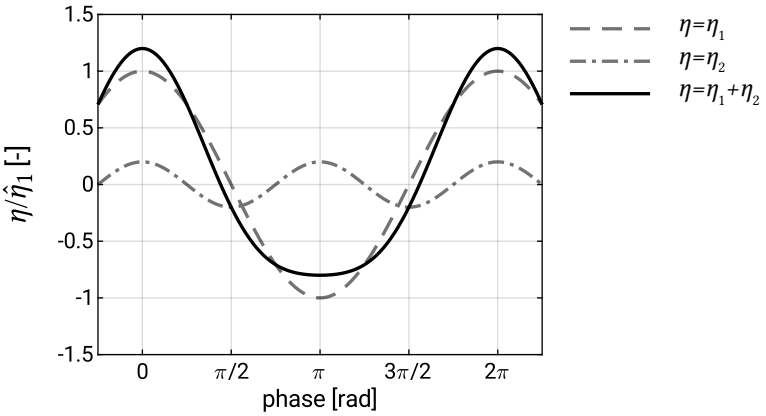

Figure 5.13: A second-order Stokes wave (solid line) is composed of a first-order (dashed line) and a second-order (dashed-dotted line) component, according to Eq. 5.21 with $\hat{\eta}_2/\hat{\eta}_1 = 0.2$. The phase on the horizontal axis is the phase $S = \omega t - kx$ of the primary harmonic. For more background on Stokes theory see Section 5.6.2 in Holthuijsen (2007).

location to be the sum of linear, freely moving waves with random phases. Because of the different phase speeds of the different components (satisfying the linear dispersion relation), we cannot have a permanent form.

A statistical indicator for the skewness is the normalised cube of the surface elevation $\langle \eta^3 \rangle / \sigma^3$: the time-averaged value of the cube of surface elevation normalised with the cube of the standard deviation σ^3. The brackets denote time-averaging. Figure 5.14 shows the quantity η^3 for a sinusoidal wave and for a second-order Stokes wave. It can be seen that for a linear wave[4] the time-averaged value $\langle \eta^3 \rangle$ is zero, while for a Stokes wave it is not, since the crests weigh more heavily than the troughs. The sign defines the ratio of crests to troughs. If it is positive – as is the case for the Stokes wave – then the crests are bigger than the troughs. Note that Stokes type wave forms have positive values of skewness, but zero asymmetry (around the vertical axis), since they are not pitched forward.

Linear theory could be used to estimate the variance (energy density) of nearshore waves. However, it cannot be used to estimate skewness, since a linear superposition of random waves has by definition zero skewness over the ensemble.

Of course not only the surface elevation, but also the orbital velocities become skewed; the orbital velocities in the direction of wave movement ('onshore') become higher, and the orbital velocities against the wave direction ('offshore') become smaller. This naturally means that the duration of the onshore-directed orbital motion becomes smaller and the duration of the offshore-directed orbital signal becomes larger.

[4]Similarly, in an irregular wave field approximated by a linear superposition of freely moving waves, the skewness value is zero.

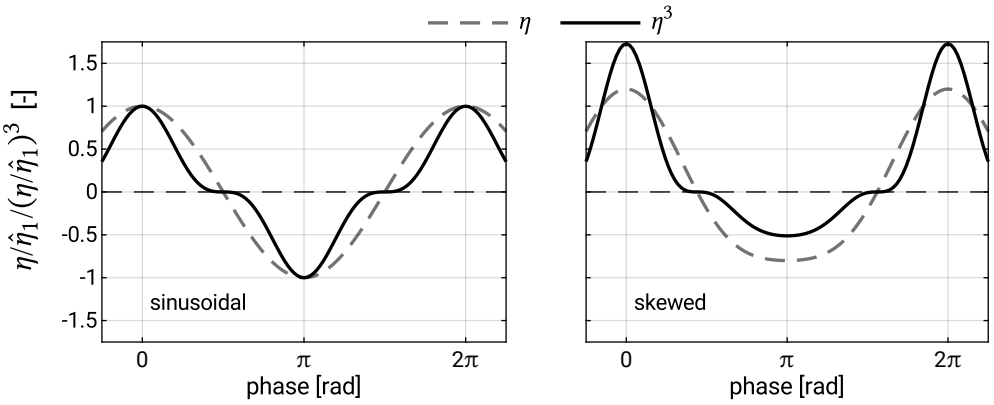

Figure 5.14: Quantity of $\eta^3/\hat{\eta}_1^3$ compared to $\eta/\hat{\eta}_1$ for a sinusoidal wave (left) and a second-order Stokes wave (right) as a function of the phase $S = \omega t - kx$ of the first or primary harmonic. Note that for the sinusoidal wave, the time-average $\langle \eta^3 \rangle = 0$, whereas for the second-order Stokes wave $\langle \eta^3 \rangle > 0$.

Asymmetry

The pitched-forward wave shape is the result of the fact that in shallow water the wave crest moves faster than the wave trough. This is clear because the propagation speed of non-linear shallow-water waves $c = \sqrt{g(h+\eta)}$. Note that for small-amplitude shallow-water waves this reduces to $c = \sqrt{gh}$ (see Intermezzo 3.5). The wave crest of a harmonic wave with amplitude a has a higher propagation velocity $c_{\text{crest}} = \sqrt{g(h+a)}$ than the trough which propagates with $c_{\text{trough}} = \sqrt{g(h-a)}$. This leads to a pitched-forward profile or relative steepening of the face of a wave that can be represented by the inclusion of a second harmonic that is forward phase-shifted with respect to the primary harmonic (see the left panel of Fig. 5.15). A Stokes wave train cannot exhibit wave asymmetry; because of the small amplitude approximation of the Stokes theory, the higher harmonic remains phase-locked to the primary harmonic. The right panel of Fig. 5.15 shows a time series of a pitched-forward (sawtooth-like) wave at one location, namely location A ($x/L = 0$) in the left panel of Fig. 5.15.

The left panel of Fig. 5.15 shows a rapidly rising and slowly falling surface elevation. Note that for the sawtooth-like wave of Fig. 5.15, the phase shift between the first and the second harmonic is such that the asymmetry is maximum and the skewness is zero. The sawtooth-like wave of Fig. 5.15 can also be depicted as a function of $S = \omega t - kx$. This results in Fig. 5.16. Compare this figure to the skewed wave of Fig. 5.13.

Figure 5.17 compares the quantity η^3 for a skewed wave and an asymmetric wave as a function of the phase $S = \omega t - kx$ of the first or primary harmonic. It can be seen that for the asymmetric wave the time-averaged value $\langle \eta^3 \rangle$ is zero, while for the skewed wave it is not, since the crests weigh more heavily than the troughs.

Shoaling waves first become gradually more skewed while remaining reasonably symmetric about the vertical axis – as an example see the flume measurements of Fig. B.2

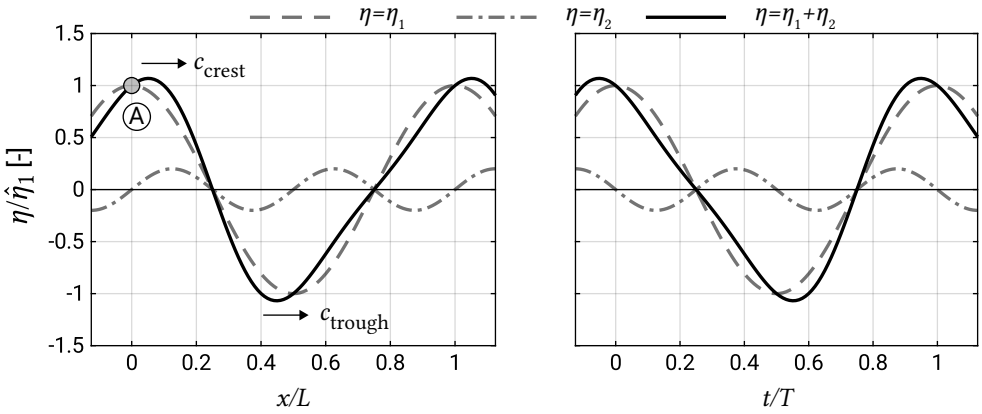

Figure 5.15: Asymmetric wave (solid black line), computed as the superposition of a first-order (dashed line) and a 90° forward phase-shifted second-order signal (dashed-dotted line). The phase on the horizontal axis is the phase $S = \omega t - kx$ of the first-order component (or primary harmonic). The left figure shows the spatial variation at $t = 0$ and the right figure shows the temporal variation of the water surface elevation at A ($x/L = 0$).

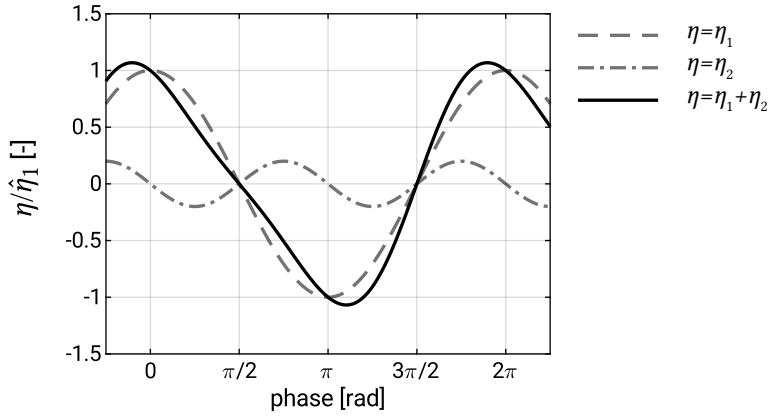

Figure 5.16: A second-order asymmetric wave, generated using two harmonic components, of which the second one is 90° forward phase-shifted.

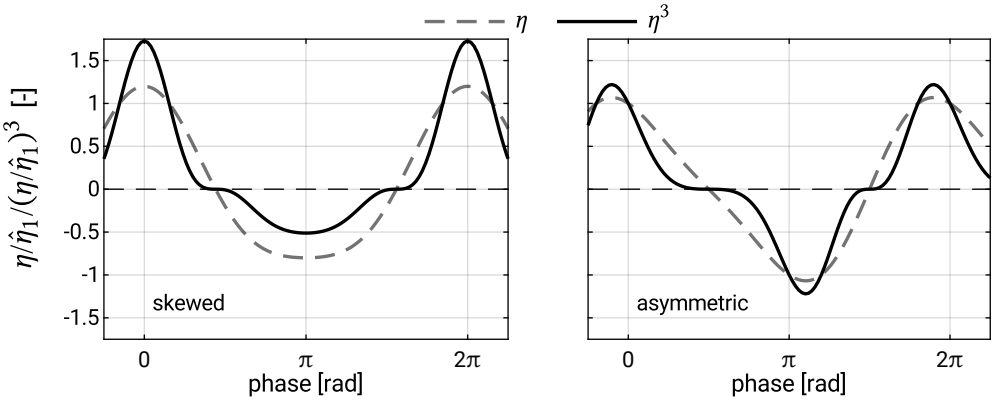

Figure 5.17: Quantity of $\eta^3/\hat{\eta}_1^3$ compared to $\eta/\hat{\eta}_1$ for a skewed wave (left) and an asymmetric wave (right). Note that for the skewed wave, the time-average $\langle \eta^3 \rangle > 0$, whereas for the asymmetric wave $\langle \eta^3 \rangle = 0$.

in App. B. Closer to the surf zone, phase-shifting of the harmonic(s) leads to an increase in wave asymmetry and – eventually – to a decrease in wave skewness as well. Ultimately the pitching forward results in wave-breaking.

The Ursell parameter $U = HL^2/H^3$ can be used as an indicator for skewness and asymmetry. Doering and Bowen (1995) presented parameterisations of velocity skewness and asymmetry based on the Ursell parameter. They mainly focused on the skewness and asymmetry of the orbital velocities, because of their importance for sediment transport.

Intermezzo 5.1 Non-linear wave theories

Linear wave theory is obtained by linearising the free-surface boundary conditions; the boundary conditions are applied to the mean water surface $z = 0$, instead of the instantaneous water surface η. Non-linearities can be neglected for not too steep waves in deep water ($ak \ll 1$ for kh is large) or small-amplitude waves in shallow water ($a \ll h$ for kh is small).

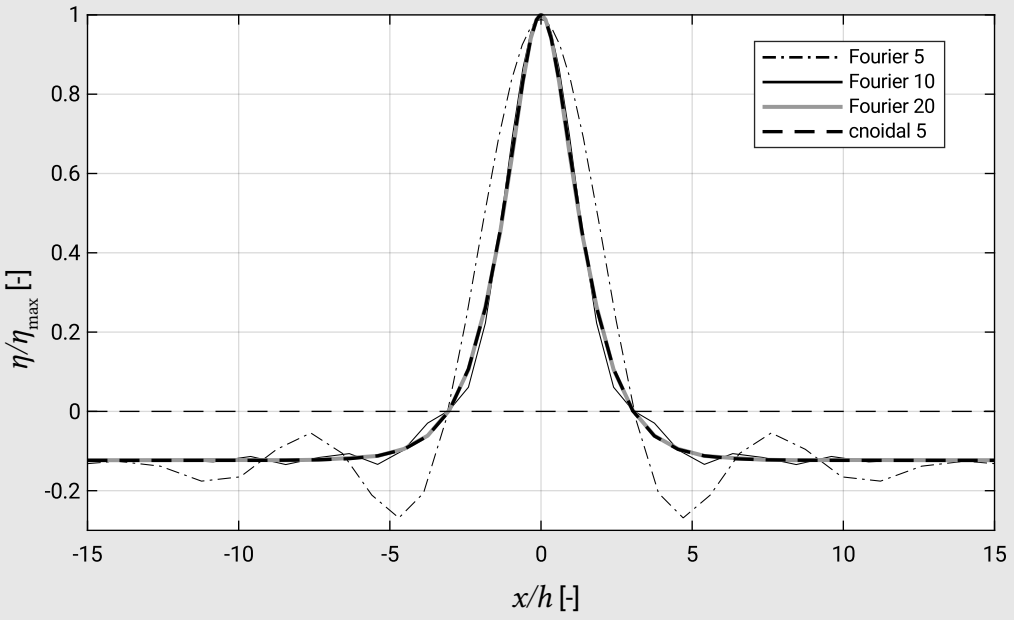

Figure 5.18: Surface elevation records generated for $H/h = 0.5$ and $L/h = 30$, which amounts to $T\sqrt{g/h} = 26.29$ or $h/(gT^2) = 1.45 \times 10^{-3}$ and $H/gT^2 = 7.23 \times 10^{-4}$ in Fig. 5.19. Both fifth-order cnoidal wave theory and a numerical Fourier approximation method (with 5, 10 and 20 harmonic components) are used. About 20 harmonic components are required for the Fourier approximation to converge towards the cnoidal solution. Produced using software by Fenton (https://johndfenton.com/Steady-waves/Fourier.html).

For a non-linear solution, the free-surface boundary conditions have to be applied at the free surface η. The complication is that η is unknown. Amongst others, the following non-linear theories have been developed:

- Stokes series expansion. Stokes used the result of the linear theory to find a first approximation to the neglected non-linear terms. This results in a second-order correction to the first (linear) approximation of the solution. Note that the second-order correction can be used to obtain a third-order correction and so on. Non-linear terms consist of quadratic terms, so instead of the linear solution $a \cos S$ (with the phase $S = \omega t - kx$), the second-order solution has an additional term proportional to $a^2 \cos^2 S$ that results in a term proportional to $a^2 \cos 2S$, a harmonic with half the period of the linear solution. A Stokes series thus has the form $\eta = \hat{\eta}_1 \cos S + \hat{\eta}_2 \cos 2S + \hat{\eta}_3 \cos 3S + \ldots$ in which the first term is the linear solution. For convergence, every next coefficient should be small compared to the lower-order coefficient, which will only be the case for sufficiently small amplitudes $\hat{\eta}_1 = a$. Stokes theory does not converge in shallow water; if the Ursell parameter $U = HL^2/h^3$ is too large, the series diverges.
- The stream function theory is an alternative to the Stokes theory. It also adds higher harmonics to the linear solution.

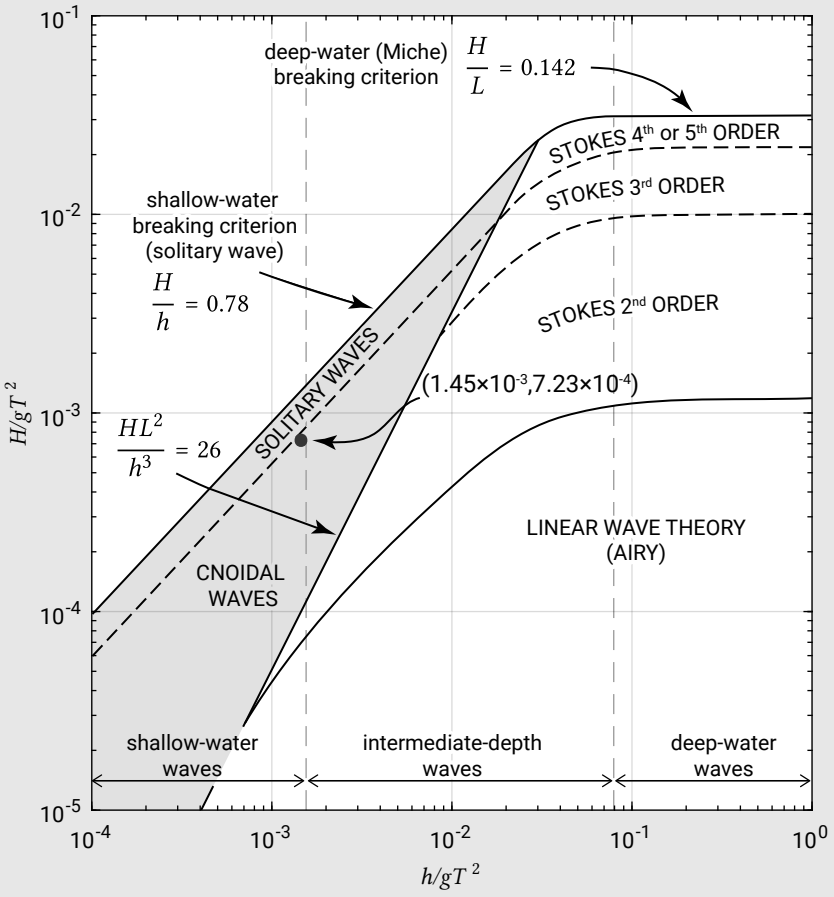

Figure 5.19: The relative depth on the horizontal axis and the wave steepness on the vertical axis delineate the validity of various waves theories. The black dot indicates the wave of Fig. 5.18. (Based on Kamphuis, 2000; Le Méhauté, 1976).

- Applicable in shallow water is the cnoidal wave theory. Solutions are given in terms of elliptic integrals of the first kind; the solution in deep water is identical with linear wave theory and in shallow water to solitary wave theory. The latter is a single wave without a trough and a mass of water above mean water level moving entirely in the wave propagation direction.
- Boussinesq models can be seen as an extension of the shallow-water equations (see for instance TU Delft course CTB3350/CIE3310-09). The shallow-water equations describe non-linear waves that all travel at the same speed $c = \sqrt{g(h+\eta)}$. Orbital velocities are depth-uniform and the pressure is hydrostatic. Since there is no vertical variation of the wave field, the vertical does not have to be resolved. Boussinesq models account – to some extent – for the non-hydrostatic pressure distribution and depth-dependency of orbital velocities. The advantage over the shallow-water equations is that Boussinesq models include frequency dispersion. Since the equations can still be integrated over the vertical, the equations are computationally efficient.

A review of the validity of various wave theories (until wave-breaking) is given by Le Méhauté (1976). See also Fig. 5.19.

5.4. Wave orbital velocity, pressure and bed shear stress

5.4.1. Wave orbital velocities

So far we have focused on the wave surface elevation. Underneath the wave surface, there is a fluid motion associated with the motion of the water surface; the fluid particles describe an orbital path. To first order (within the limitations of Airy small-amplitude wave theory), the orbits are closed[5] circles in deep water and closed ellipsoids in water of finite depth, with the ellipsoids becoming flatter near the bottom. At the bottom vertical velocities are zero per definition. The further from the surface, the smaller the orbital diameter becomes. In deep water the orbital diameter has been reduced to only 4 % of the value at the surface at a depth of half a wavelength. In the case of shallow water, the water particles under a propagating wave of *finite* amplitude describe an elliptical orbit. From the surface down to the bottom, the vertical displacement of the water particles reduces to zero, while the horizontal displacement remains almost constant (Fig. 5.20).

[5] At second order, particle paths are no longer closed orbits and there is a drift or mass transport in the direction of wave propagation (Sect. 5.5.1).

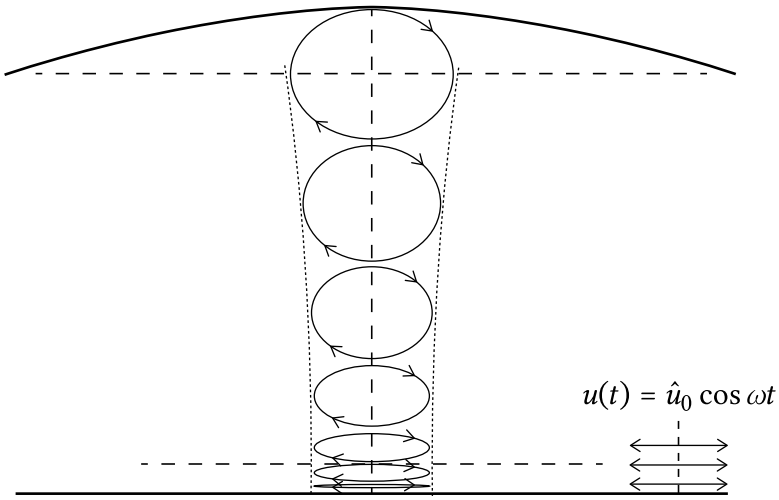

Figure 5.20: Water particle movement in finite-amplitude wave in intermediate to shallow water depth.

Now consider waves of infinitesimal amplitudes. According to linear theory, the horizontal orbital velocity varies harmonically with an amplitude $\hat{u}$ equal to:

$$\hat{u}(z) = \omega a \frac{\cosh k(h+z)}{\sinh kh} \tag{5.22}$$

where:[§1.1] [Units of ω and k are edited] [p192]

ω	angular frequency $(2\pi/T)$	rad/s
a	wave amplitude	m
k	wavenumber $(2\pi/L)$	rad/m
L	wavelength	m

The z-axis is defined positive upward with $z = 0$ at the surface and $z = -h$ at the bottom. The velocity u is in the wave propagation direction. Using the $\cosh kh$ and $\sinh kh$ approximations for shallow and deep water (App. A), the horizontal velocity profiles can be drawn schematically as in Fig. 5.21.

In shallow water ($kh \ll 1$; in practice $kh < \pi/10$ or $h/L > 1/20$), the depth-uniform velocity amplitude is given by (cf. Eq. 3.39):

$$\boxed{\hat{u} = \frac{\omega a}{kh} = c\frac{a}{h} = \sqrt{gh}\frac{H}{2h}} \tag{5.23}$$

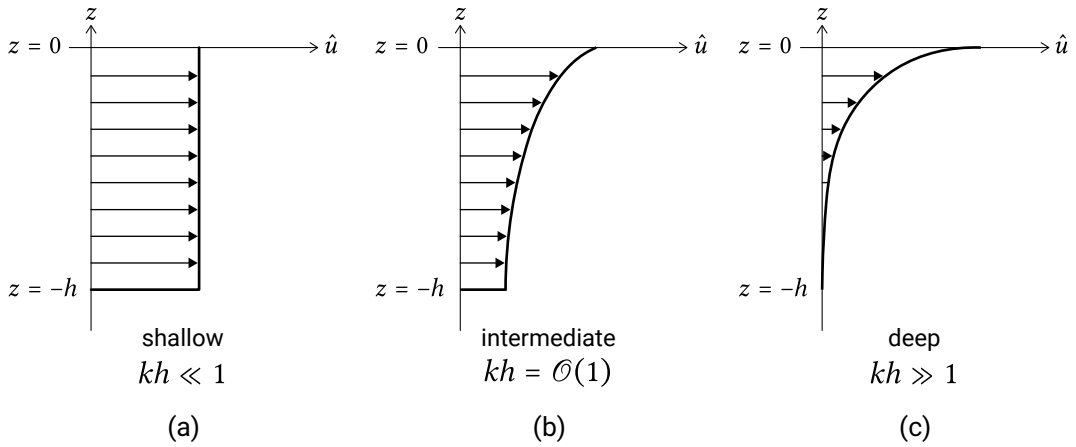

Figure 5.21: Schematic drawing of vertical profiles of the velocity amplitude $\hat{u}$.

The particle excursions (i.e. the horizontal and vertical displacements of the particles) are the time integrals of the oscillatory horizontal and vertical flow velocities respectively. This means that the amplitude of the horizontal particle excursion is given by:

$$\hat{\xi} = \frac{\hat{u}}{\omega} \tag{5.24}$$

Note that Sect. 5.3 described how in shoaling waves the surface elevation becomes gradually more skewed and asymmetric. Of course the wave orbital velocities near the bed will also become skewed and asymmetric. Although the linear approximation will not describe the changing wave form, the orbital velocity magnitude can be estimated reasonably well using linear wave theory.

5.4.2. Dynamic pressure

Pressure gradients in coastal waters are mainly due to mean water level variations (hydrostatic pressure) and fluctuations of pressure due to waves. The hydrostatic pressure due to mean water level variation is $p_0 = -\rho g z$ and hence linearly increases from zero at the water surface §1.1~~$z =$~~ §1.1$z = 0$ [p193] to $p_0 = \rho g h$ at the bottom $z = -h$. In the case of waves, the total pressure is the sum of this hydrostatic pressure p_0 (from $z = -h$ to §1.2~~$z = \eta$~~ §1.2$z = 0$ [p193]) plus the wave-induced or dynamic pressure p_{wave} (from $z = -h$ to $z = \eta$). Wave-induced pressure oscillations are different under wave crest and wave trough and – in intermediate and deep water – reduce with depth below the free surface (Fig. 5.22a).

According to linear theory, the wave-induced pressure varies harmonically (in phase with the surface elevation η) with amplitude:

$$\hat{p} = \frac{\rho g H}{2} \frac{\cosh k(h+z)}{\cosh kh} \tag{5.25}$$

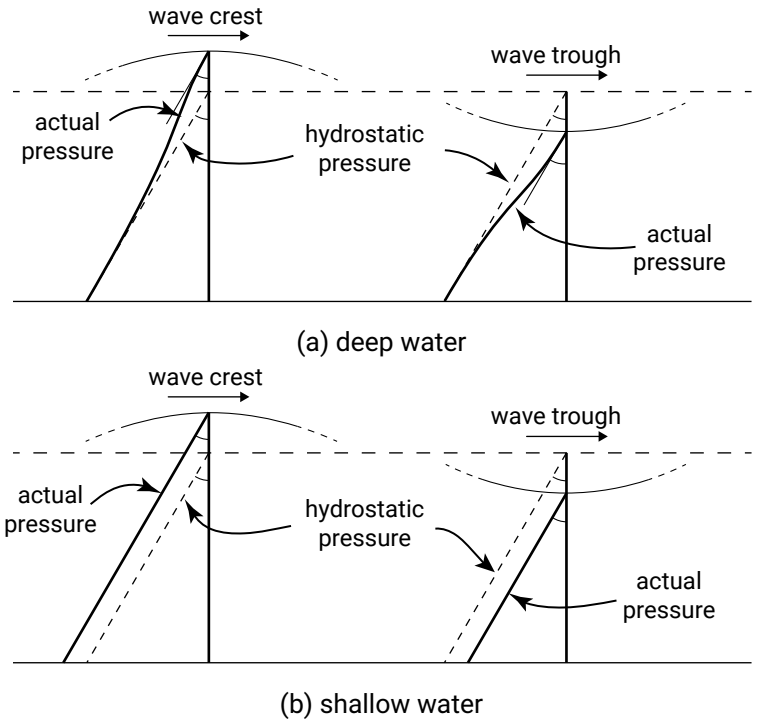

Figure 5.22: Wave-induced pressure oscillations combined with the hydrostatic pressure in still water give the actual pressure.

which reduces in shallow water to:

$$\hat{p} = \frac{\rho g H}{2} \tag{5.26}$$

Hence, in shallow water the hydrostatic dynamic pressure varies linearly with the free-surface elevation $p_{\text{wave}} = \tilde{p} = \rho g \eta$ (Fig. 5.22b). The tilde indicates the purely oscillatory character.

To derive Eq. 5.25 the amplitude was assumed to be very small in order to linearise the free-surface boundary condition. It is therefore not valid in the region between the trough and the crest elevation. We can, however, assume that the dynamic pressure is hydrostatic between wave trough and wave crest: $\tilde{p} = \rho g \eta$.

5.4.3. Wave boundary layer

Most wave theories are valid from the water level to a small distance from the bed (Fig. 5.23), where the flow still is unaffected by the boundary. Closer to the bed, in a thin layer called the wave boundary layer, vorticity (rotation) can be generated, which is not included in linear wave theory or in most other (irrotational) wave theories for that matter. The distance denoted as δ in Fig. 5.23 is the thickness of the wave boundary layer, the transition layer between the bed and the layer of 'normal' oscillating flow. The thickness is generally between 1 cm and 10 cm for short-period waves ($T < 10$ s).

The reason for this small thickness is that there is not sufficient time for the layer to grow out in the vertical direction, because the current regularly reverses.

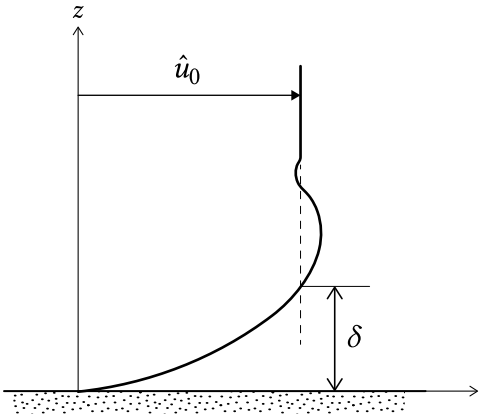

Figure 5.23: The velocity at the boundary is zero. At some distance above the boundary, the velocity reaches a constant value, $\hat{u}_0$ called the free stream velocity. The region of velocity variation in the vertical or *shear* is called the boundary layer. The height or thickness of the boundary layer is δ.

It is typical for oscillating boundary layers that the maximum flow velocity near the bed is somewhat larger (a few percent) than the so-called free stream velocity. The free-stream velocity amplitude $\hat{u}_0$ according to linear theory is given by Eq. 5.22 for $z = -h$:

$$\hat{u}_0 = \frac{\omega a}{\sinh kh} \tag{5.27}$$

The flow in the wave boundary layer is generally turbulent due to the presence of roughness elements on the bed. The water moving along the bed incurs a shear stress on the bed. This becomes clear when imagining that – as a result of viscosity and turbulence – the flow sticks to the wall (no-slip condition). Hence, the orbital velocity increases from zero at the bed to the undisturbed free-stream velocity at the top of the wave boundary layer $z = \delta$. Because of the thin boundary layer, the velocity gradients perpendicular to the bed are large and give rise to large stresses in the wave boundary layer. The friction in the wave boundary layer results in dissipation of wave energy.

In coastal waters, turbulent stresses – arising from turbulent fluctuations of the velocity – are much larger than viscous stresses arising from small-scale erratic movements of molecules. Now think of the total horizontal velocity u and vertical velocity w to be composed of a mean, a wave and a turbulent part, hence $u = U + \tilde{u} + u'$ and $w = W + \tilde{w} + w'$. Turbulent shear stress is defined as the stress introduced when averaging over the turbulent motion:

$$\tau(z) = \rho\overline{u'w'} \tag{5.28}$$

The detailed modelling of the wave boundary layer is a complex research field. It involves the modelling of the turbulence in the wave boundary layer that is induced by roughness of the bed. Such a wave boundary layer model gives the detailed time-dependent velocity distribution over the wave boundary layer. Besides a purely oscillatory flow, a non-zero wave-averaged horizontal flow – called streaming – is found. It was first explained by Longuet-Higgins (1953) who demonstrated that for linear waves the streaming is directed in the wave propagation direction (see Fig. 5.26). It is therefore potentially important for transporting sediment onshore. The disturbance of the wave motion due to the wave boundary layer leads to additional stresses in the wave boundary layer when averaging over the organised wave motion. In analogy with Eq. 5.28, these stresses are given by $\rho\overline{\tilde{u}\tilde{w}}$ (the overbar now represents averaging over the short-wave motion). Above the wave boundary layer, this term can generally be neglected. In Intermezzo 5.5 it is shown that the term in the wave-averaged horizontal momentum equation responsible for the streaming is (proportional to) $\partial\overline{\tilde{u}\tilde{w}}/\partial z$. It acts as a (depth-varying) force in the wave boundary layer, pushing the flow forward. The formula found by Longuet-Higgins for the mean streaming velocity at the top of the boundary layer is:

$$U_0 = \frac{3}{4}\frac{\hat{u}_0^2}{c} \tag{5.29}$$

For practical purposes it is generally enough to consider the following aspects of the wave boundary layer:

- The water moving along the bed incurs a shear stress on the bed. The orbital motion under waves, even without the presence of a uniform current, gives a time-varying shear stress at the bed, which can set sediment grains into motion (see Ch. 6);
- Due to bed friction, the wave boundary layer dissipates energy from the flow above (this is the term D_f in Eq. 5.2);
- The wave-induced streaming (Eq. 5.29) should be taken into account for net-sediment transport computations.

In Sect. 5.5.6 it is briefly indicated how the vertical structure of the mean flow (including the wave boundary layer) can be resolved using a relatively simple eddy viscosity turbulence model. Until then, we will only consider depth-integrated momentum equations that hence contain depth-invariant quantities. For instance, we consider the bed shear stress in a simple parameterised way, so that we do not have to bother with distributions of the shear stress over the depth.

Bed shear stress

If we refrain from turbulence modelling, (bed) friction is a major unknown that has to be determined using (empirical) friction laws. This introduces coefficients that need to be calibrated, which makes the calibration of these models important.

To determine the bed shear stress, Jonsson (1967) introduced the concept of a wave friction factor in analogy with the current friction factor (see Intermezzo 5.2). The current friction factor relates the bed shear stress to the depth-averaged current velocity, whereas the wave friction factor relates the bed shear stress to the free stream velocity. For a current only, the *magnitude* of the bed shear stress is $\tau_c = c_f \rho U^2$ (with flow aligned with x-axis, see Intermezzo 5.2). Under waves, the bed shear stress varies in time and reverses with the direction of the orbital velocities.

For linear waves with a free stream velocity $u = \hat{u}_0 \cos \omega t$, Jonsson defined the friction factor f_w through the following formula for the magnitude of the *maximum* bed shear stress:

$$\hat{\tau}_w = 0.5 \rho f_w \hat{u}_0^2 \tag{5.30}$$

For a rough bed and turbulent flow, it is not easy to determine the friction coefficient as it cannot be measured directly. The friction coefficient will generally depend on the bed material and the bed forms (e.g. ripples). The following variables can be found in expressions for f_w for rough turbulent flow:

- the bed roughness k_s (Nikuradse roughness) or r of the wall; the bed roughness represents the size of the roughness elements, for instance the grains;
- the particle excursion amplitude close to the bed $\hat{\xi}_0 = \hat{u}_0/\omega$ (see Eq. 5.24 and App. A).

Intermezzo 5.2 Current-only bed shear stress

Assume a current-only situation with the depth-mean flow velocity $\vec{U} = (U, V)$ in the (x, y)-direction. The bottom shear stress acts in the direction of the current and can be described by a quadratic friction law:

$$\tau_b = \rho c_f |\vec{U}| \vec{U} \tag{5.31}$$

The friction factor c_f is a dimensionless coefficient relating the bed shear stress to the square of the velocity. Linear friction laws are rarely used since they have no physical justification.

c_f can be expected to depend on the bed material and bed forms (bed roughness). For uniform flow in a canal driven by a small slope of the mean water surface, Chézy derived theoretically a Chézy coefficient $C = 18 \log 12h/r$, where r is the bottom roughness and h is the water depth. The Chézy coefficient C relates to c_f as follows:

$$c_f = \frac{g}{C^2} \tag{5.32}$$

Alternatives are to prescribe a Nikuradse roughness height k_N or an empirical Manning value n. The Nikuradse roughness and the Manning value can be related to c_f. The choice between these methods affects the depth dependency of c_f and can therefore have important consequences for computed flow fields.

Let us consider two cases in which $\hat{u}_0$ is the same, but T differs. For the case with a large value for T, the value of $\hat{\xi}_0$ is larger than in the case with the lower value for T. Assuming an equal value for r, this means that the case with the larger value for the wave period gives lower values for the wave friction factor. This can be understood by considering that the boundary layer thickness varies with time. In case of a larger wave period, more time is available to develop the boundary layer, which therefore reaches a larger maximum thickness. Consequently, the velocity gradients in the boundary layer are smaller, leading to a smaller maximum shear stress and friction factor.

A frequently applied formula for f_w is that of Jonsson (1967), rewritten by Swart (1974) into:

$$f_w = \exp\left[-5.977 + 5.213\left(\frac{\hat{\xi}_0}{r}\right)^{-0.194}\right] \tag{5.33a}$$

$$f_w = 0.30 \qquad \text{for } \left(\frac{\hat{\xi}_0}{r}\right) < 1.59 \tag{5.33b}$$

Many simpler formulas exist, such as (Soulsby, 1994):

$$f_w = 1.39\left(\frac{\hat{\xi}_0}{r/30}\right)^{-0.52} \tag{5.34a}$$

$$f_{w,\max} = 0.3 \tag{5.34b}$$

For the roughness value r the so-called Nikuradse roughness k_s is often used, which is normally set as a function of the grain size.

Equation 5.33 is shown graphically in Fig. 5.24 and compared to the simpler formulation of Eq. 5.34. As expected, the friction factor f_w increases if $\hat{\xi}_0/r$ decreases. The upper limit of f_w has been questioned by various researchers: some suggest that there is no upper limit and that the friction factor remains proportional to $\hat{\xi}_0/r$.

In case of irregular waves, the near-bed orbital velocity amplitude in the above formulas should be based on the root-mean-square wave height and the wave orbital excursion parameter near the bed on the root-mean-square wave height and peak period. Example 5.1 presents an example of a bed shear stress computation.

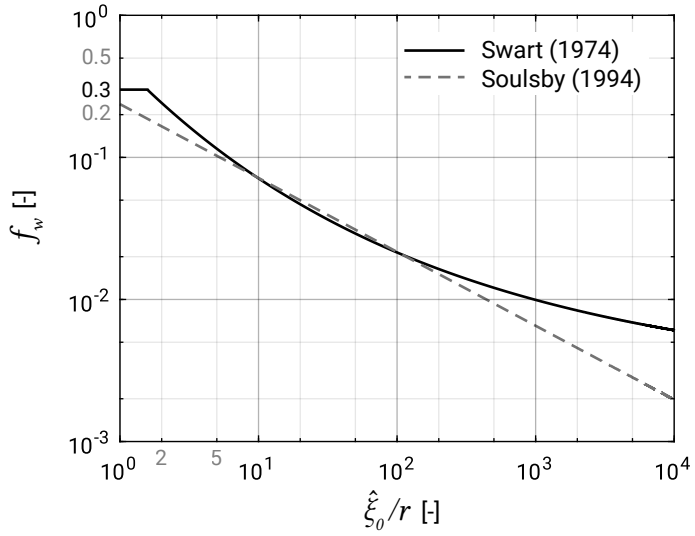

Figure 5.24: Friction factor f_w as a function of the particle excursion at the bed $\hat{\xi}_0$ divided by the bed roughness $r = k_s$. Equation 5.33 (after Swart, 1974, black solid line) is compared to the simpler Eq. 5.34 (after Soulsby, 1994, gray dashed line).

Example 5.1 Bottom shear stress under waves only

Input parameters

Water depth	h	=	3	m
Roughness height	r	=	0.06	m
Wave height	H	=	1.18	m
Wave period	T	=	8	s

Required Bottom shear stress

Output The amplitude of the velocity near the bed can be found from linear wave theory:

$$\hat{u}_0 = \frac{\omega H}{2}\frac{1}{\sinh kh} = 1\,\mathrm{m/s} \quad \text{and} \quad \hat{\xi}_0 = \frac{\hat{u}_0 T}{2\pi} = 1.27\,\mathrm{m} \tag{5.35}$$

For a value of $\hat{\xi}_0/r > 1.59$ the friction factor equals:

$$f_w = \exp\left[-5.977 + 5.213\left(\hat{\xi}_0/r\right)^{-0.194}\right] = 0.045 \tag{5.36}$$

The maximum bottom shear stress follows from:

$$\hat{\tau}_w = \frac{1}{2}\rho f_w \hat{u}_0^2 = 22.5\,\mathrm{N/m^2} \tag{5.37}$$

Discussion For a maximum near-bed orbital velocity of 1 m/s, the bottom shear stress due to waves equals 22.5 $\mathrm{N/m^2}$. Now consider the situation of a mean current of 1 m/s. Assume that the roughness height and water depth are the same as above. Using $C = 18 \log 12h/r = 50\,\mathrm{m^{1/2}/s}$ we find:

$$\tau_c = \rho \frac{g}{C^2} U^2 = 3.9\,\mathrm{N/m^2} \tag{5.38}$$

The bed shear stress due to waves with a maximum near bed orbital velocity of 1 m/s is almost 6 times the value for the bed shear stress due to an average current velocity of 1 m/s. This is a direct consequence of differences in boundary layer thickness and hence near-bed velocity gradients. The wave boundary layer is limited in thickness, whereas the current boundary layer generally occupies the entire water column.

5.5. Wave-induced set-up and currents

5.5.1. Wave-induced mass flux or momentum

Propagating waves not only carry energy across the ocean surface, but momentum as well. Momentum is defined as the product of mass and velocity. It can be thought of as mass in motion or a mass transport or flux: a water particle has a mass, and if the particle is moving, it has momentum. Momentum per unit volume can thus be written as the product of the mass density ρ and the velocity $\vec{u} = (u_x, u_y, w)$ of the water particles. Momentum (per unit volume) $\rho\vec{u} = (\rho u_x, \rho u_y, \rho w)$ is a vector quantity, a quantity which is fully described by both magnitude and direction. The direction of the momentum vector is the same as the direction of the velocity vector.

The total amount of wave momentum per unit surface area in §1.1 ~~wave propagating direction~~ §1.1 the direction of wave propagation [p200] is obtained by integration over the depth. Averaged over time this gives (with u the horizontal orbital velocity in the wave propagation direction):

$$q = \overline{\int_{-h}^{\eta} \rho u \, dz} \tag{5.39}$$

There is only a contribution to the momentum from the wave trough level to the wave crest level, since below the wave trough the velocity varies harmonically in time (see Sect. 5.4.1), giving a zero time-averaged result. If we measure the velocity at some point above MSL, we will only record velocities during *part* of the wave period and all of the recordings will be positive (and in the wave propagation direction). Between the wave trough level and MSL, we will record velocities for a larger part of the wave period and, although a part of the recording will be negative, the wave-averaged mean velocity will still be positive. The momentum q can thus be interpreted as a net flux of mass between wave trough and wave crest associated with wave propagation.

We can compute the integral of Eq. 5.39 for a single harmonic component (non-breaking) by substituting the velocity according to linear wave theory (see Eq. 5.22) at $z = 0$ and integrating from $z = 0$ to the instantaneous surface elevation $\eta = a\cos\omega t$. We then find, for the mean momentum in a plane perpendicular to the wave propagation direction per unit surface area:

$$q_{\text{non-breaking}} = \overline{\int_0^{a\cos\omega t} \rho \frac{a\omega}{\tanh kh} \cos\omega t \, dz} = \overline{a\cos\omega t \rho \frac{a\omega}{\tanh kh} \cos\omega t} = \frac{\rho a^2 \omega}{2\tanh kh} = \frac{\rho g a^2}{2c} = \frac{E}{c} \tag{5.40}$$

This formula shows that q is a non-linear quantity in the amplitude a. The result is second-order accurate in the amplitude (linear wave theory is first-order accurate). Apparently, wave-induced mass flux occurs even for a perfect sinusoidal orbital motion, but is a second-order effect. In the linear, small-amplitude approximation, q is zero and wave propagation is merely a matter of movement of the wave form, not of mass. In relation to net mass flux associated with wave propagation, the term Stokes drift is often used (see Intermezzo 5.3).

Equation 5.40 is valid outside the surf zone. In the surf zone the mass flux is substantially larger than outside the surf zone. It is assumed to consist of two parts, one due to the progressive character of the waves (Eq. 5.40) and the other due to the surface roller in breaking waves:

$$q_{\text{drift}} = q_{\text{non-breaking}} + q_{\text{roller}} = \frac{E}{c} + \frac{\alpha E_r}{c} \tag{5.41}$$

In this equation, E_r is the roller energy. The first part of the right-hand side is the mass flux for non-breaking waves, whereas the second part accounts for the contribution of the mass of the surface roller. Various authors have argued values for the factor α in Eq. 5.41 to be in the range of 0.22 to 2 (Nairn et al., 1990; Roelvink & Stive, 1989). Their arguments are too complex to discuss here, so we assume that α is in the order of 1.

In the case of a closed boundary, like a coastline, there is a zero net mass transport through the vertical, as otherwise water would increasingly pile up against the coast. This means that there must be a net velocity below the wave trough level to compensate for the flux above the wave trough level: a return current. The cross-shore depth-mean velocity below the wave trough level must compensate for the mass flux perpendicular to the shore and is therefore given by:

$$U_{\text{below trough}} = -\frac{q_{\text{drift},x}}{\rho h} = -\frac{q_{\text{drift}} \cos\theta}{\rho h} \tag{5.42}$$

In breaking waves, the mass transport towards the coast between wave crest and wave trough may be quite large, resulting in rather large seaward-directed velocities under the wave trough level (see Fig. 5.25). The large return current in the surf zone is called undertow.

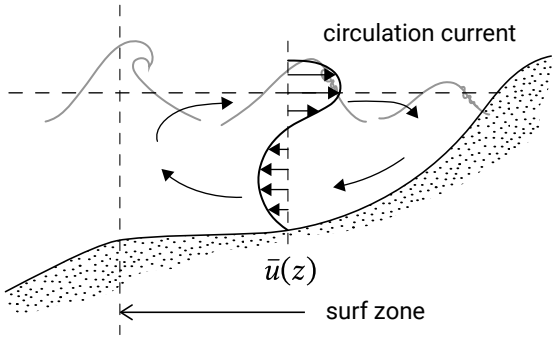

Figure 5.25: The undertow is a return current below the wave trough level to compensate for the onshore mass flux in the surf zone.

Also in the two-dimensional case of a laboratory wave flume, the same mass of water has to return to the 'sea' again. In the lower part of the water column, this gives a return flow (see Fig. 5.26). The figure also shows Longuet-Higgins streaming close to the bed (see Sect. 5.4.3). In Fig. 5.25, we have assumed that in the surf zone the steady Longuet-Higgins streaming may well be overridden by the undertow. The distribution over the depth of the return current or undertow (and the streaming) can be solved using a horizontal momentum equation (not depth-averaged!), see Sect. 5.5.6.

Appendix B provides an example of wave flume experiments of periodic and random waves on a gently sloping beach (Stive, 1985). Figure B.2 shows the measurements of return currents in shoaling and breaking periodic waves. In non-breaking waves there is relatively small return current. In breaking waves, the mass transport towards the coast between wave crest and wave trough may be quite large, resulting in rather large seaward-directed time-averaged velocities under the wave trough level.

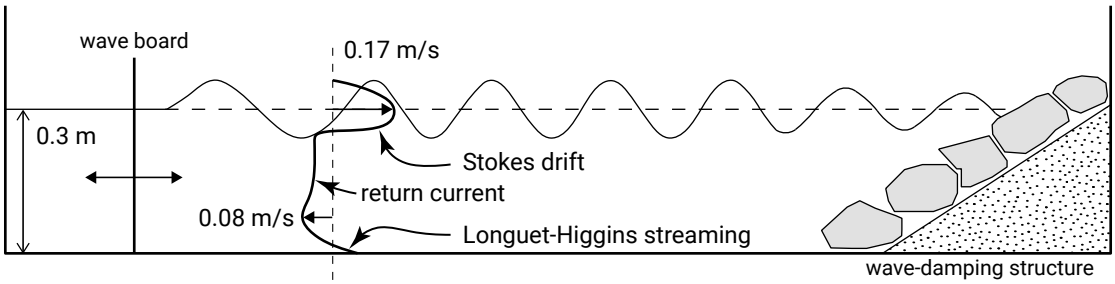

Figure 5.26: Velocities averaged over a wave cycle under propagating waves in a wave flume. Even in this case of *non-breaking* waves, there is a small return current. Note that the term 'undertow' is only used for the larger return current under *breaking* waves.

Intermezzo 5.3 Stokes drift

We explained mass transport from an Eulerian point of view in the text above (by placing a measuring pole in a fixed cross-section and concluding that above the wave trough level the recorded velocity has a non-zero time-averaged result in the wave propagation direction). It can also be explained from a Lagrangian point of view, viz. by following a water particle moving in its orbital motion (see Fig. 5.20). Since the horizontal movement is in general smaller closer to the bed (see Eq. 5.22 and Fig. 5.21), the water particle moves faster in the wave propagation direction when it is located under the wave crest, and then it runs backward when under the trough of the wave. As a result, particle paths are not entirely closed orbits and there is a residual motion in the wave propagation direction over one wave period. This residual motion is referred to as Stokes drift and gives rise to a net mass transport in the direction of wave propagation. When we integrate the Lagrangian mass transport over the vertical, we get the same result as the Eulerian mass transport above the wave trough level.

The undertow is important for seaward sediment transport, because of the relatively high offshore-directed velocity in the lower and middle part of the water column in a zone with relatively high sediment concentrations (due to wave-breaking). The undertow is thought to be responsible for the severe beach erosion during heavy storms. Sediment transport due to return currents is also important for shallow areas that have a deeper area between them and the coast. Examples are shallow areas on the ebb-tidal deltas of coastal inlet systems, where the mass flux is not (entirely) compensated by undertow, as the water can flow away at the back of these flats (where often tidal channels are present). This is further discussed in Sect. 9.4.1.

5.5.2. Radiation stress

Newton's second law states that the rate of change of momentum of a fluid element equals the forces on the element. Waves can change the momentum through net 'inflow' or 'outflow' of momentum, either by net inflow or outflow of momentum with the particle velocity or via a net wave-induced pressure force. *Radiation stress* is the name given to the depth-integrated and wave-averaged flow (or flux) of momentum due to waves. It was first defined by Longuet-Higgins and Stewart (1964) as the excess momentum flux due to the presence of waves.

If there is change in wave-induced momentum flux (radiation stress) from one location to another, wave forces act on the fluid, impacting mean water motion and levels. These wave forces are responsible for:

- lowering the mean water level in the shoaling zone (set-down);
- raising the mean water level in the surf zone (set-up);
- driving a longshore current in the case of waves obliquely approaching the shore (1 m/s under some conditions).

Definition of radiation stress components

The wave-induced horizontal flux of momentum through a vertical plane at a given location consists of:

- the transfer of momentum $\rho\vec{u}$ through that plane, with the particle velocity normal to that plane;
- the wave-induced pressure force acting on the plane due to the wave-induced pressure p_{wave} in the water.

First assume that the plane under consideration is perpendicular to the wave propagation (Fig. 5.27). The wave-induced pressure p_{wave} acts by definition normal to the plane. Besides, at every height above the bed, the particle velocity u transports momentum ρu through the plane (per unit crest length).

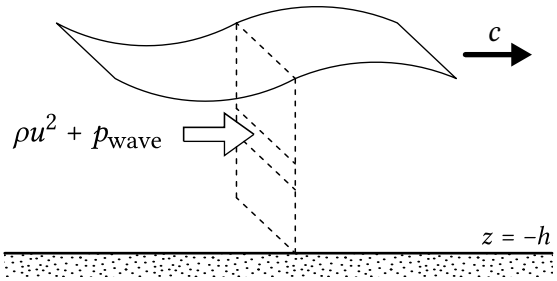

Figure 5.27: Horizontal transport of wave-induced momentum through a vertical plane of unit width perpendicular to the wave propagation direction.

Now consider a coordinate system according to Fig. 5.28. The wave propagates at an angle with the x-axis. The particle velocity has a component u_x in the x-direction

and a component u_y in the y-direction. The particle velocity u_x transports both x-momentum ρu_x and y-momentum ρu_y. The transport of x-momentum by the particle velocity u_x through a vertical plane perpendicular to the x-axis (per unit time and per unit area) is $(\rho u_x)u_x$ and the transport of y-momentum through the plane is $(\rho u_y)u_x$. The momentum fluxes can be seen in the left part of Fig. 5.29.

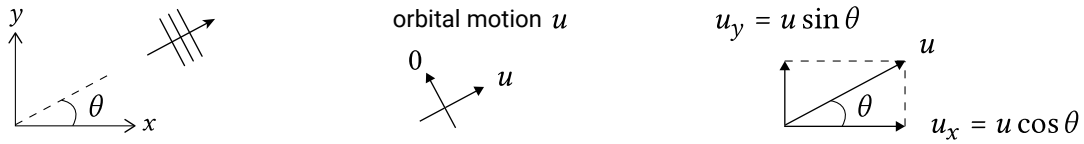

Figure 5.28: Coordinate system and velocity vector.

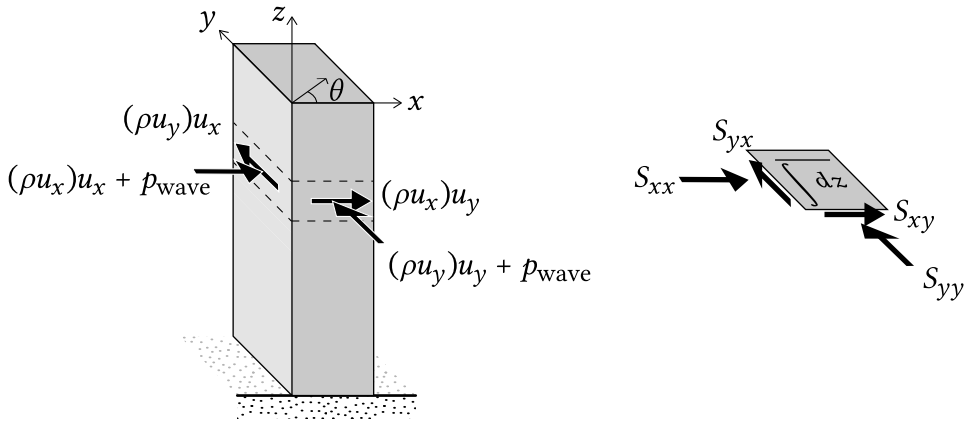

Figure 5.29: Schematic of the momentum transport and radiation stress components at a certain point in x, y-space for obliquely incident waves. The radiation stresses are obtained by integration of the momentum transport over the water column and averaging over time.

Figure 5.29 visualises the momentum transport and radiation stress components in x-direction and y-direction at a certain point in x, y-space. The momentum transport through the entire plane per unit crest length is obtained by integration over the depth from bottom to instantaneous water surface. Time-averaging yields, for the total wave-averaged transport of x-momentum in the x-direction or the radiation stress S_{xx}:

$$S_{xx} = \underbrace{\overline{\int_{-h_0}^{\eta} (\rho u_x)\, u_x \, dz}}_{\substack{\text{part due to advection by} \\ \text{horizontal particle velocity}}} + \underbrace{\overline{\int_{-h_0}^{\eta} p_{\text{wave}} \, dz}}_{\text{pressure part}} \tag{5.43}$$

S_{xx} acts normal to the considered plane and is therefore a normal component of the radiation stress. It is equivalent to a normal stress acting in the x-direction.

The radiation stress component S_{xy} (the shear component of the radiation stress) is defined as the transport of x-momentum in the y-direction. It acts as a shear stress

on the plane (it is directed in the x-direction, and works on the plane normal to the y-direction) and is given by:

$$S_{xy} = \overline{\int_{-h_0}^{\eta} \left(\rho u_x\right) u_y + \tau_{xy}\, dz} \tag{5.44}$$

The shear stress due to waves is zero for an irrotational ideal fluid, so that we have:

$$S_{xy} = \overline{\int_{-h_0}^{\eta} \left(\rho u_x\right) u_y\, dz} \tag{5.45}$$

It consists of a contribution due to advection by the horizontal orbital velocity only. Note that for the special case of normally incident waves, the x-direction is the wave propagation direction, and u_y and hence S_{xy} are zero.

Considering a plane normal to the y-direction, we find for the momentum fluxes in the y-direction, the normal component:

$$S_{yy} = \underbrace{\overline{\int_{-h_0}^{\eta} \left(\rho u_y\right) u_y\, dz}}_{\substack{\text{part due to advection by} \\ \text{horizontal particle velocity}}} + \underbrace{\overline{\int_{-h_0}^{\eta} p_{\text{wave}}\, dz}}_{\text{pressure part}} \tag{5.46}$$

and the shear component:

$$S_{yx} = \overline{\int_{-h_0}^{\eta} \left(\rho u_y\right) u_x\, dz} \tag{5.47}$$

In the special case that the x-direction is the wave propagation direction $u_y = 0$, S_{yy} reduces to the pressure part and $S_{yx} = S_{xy} = 0$.

Radiation stress formulas using linear wave theory

By using linear (first-order) wave theory, formulas for the radiation stress can be obtained that are valid to second order. The complete derivation can be found in Holthuijsen (2007). Intermezzo 5.4 gives an excerpt of this derivation.

Intermezzo 5.4
Derivation of (normal) radiation stress from linear wave theory

It is easiest to start from a wave propagating in positive x-direction so that $u_x = u$ and $u_y = 0$. If we substitute $u = \hat{u}\cos(\omega t - kx)$, with $\hat{u}$ according to Sect. 5.4.1,

in the particle velocity part of Eq. 5.43, we find (see Holthuijsen (2007) for the derivation):

$$S_{xx,\text{ horizontal particle velocity}} = \overline{\int_{-h_0}^{\bar{\eta}} \left(\rho u^2\right) dz} \approx \int_{-h_0}^{0} \rho \overline{u^2}\, dz = nE \tag{5.48}$$

where:

$S_{xx,\text{ hor. part. vel.}}$	radiation stress in the wave propagation direction due to advection of momentum by the horizontal orbital motion	N/m
n	ratio of group velocity and phase velocity	–
E	wave energy in the water column per m^2	J/m^2

In the case of irregular waves, this equation can be applied using $E = {}^1\!/\!_8 \rho g H_{rms}^2$. For the mass flux, we found a zero contribution for every level below the wave trough because $\overline{u} = 0$. The momentum flux, however, is non-zero for the entire water depth, since $\overline{u^2} \neq 0$. It varies in principle over the depth. Only in shallow water, where the horizontal orbital velocity is uniformly distributed, the particle velocity part of the radiation stress is uniformly distributed.

The pressure for any level below the trough would give a zero time-averaged result according to linear theory. There is, however, a contribution to the time-averaged wave-induced pressure $\overline{p_{\text{wave}}}$ due to the vertical flux of momentum by the vertical fluid motion. This may be thought of as the vertical oscillatory fluid motion, helping carry the weight of the water column, and is given by $-\rho\overline{w^2}$, in which w is the vertical orbital velocity. The contribution to the radiation stress can be found by substituting the linear equation for w and integrating to the mean water level. We find:

$$S_{xx,\text{ pressure, 1}} = -\overline{\int_{-h_0}^{\bar{\eta}} \rho w^2\, dz} \approx -\int_{-h_0}^{0} \rho \overline{w^2}\, dz = (n-1)E \tag{5.49}$$

Furthermore, there is a contribution to the radiation stress due to the pressure fluctuations between wave trough and wave crest level. In Sect. 5.4.2 we assumed that the pressure between wave trough and crest level fluctuates as $\tilde{p} = \rho g \eta$. This gives the following net contribution to the radiation stress:

$$S_{xx,\text{ pressure,2}} = \overline{\int_{0}^{\bar{\eta}} \rho g \eta\, dz} = \frac{1}{2}\rho g \overline{\eta^2} = \frac{1}{2}E \tag{5.50}$$

This gives for the pressure part of the radiation stresses:

$$S_{xx,\text{ pressure}} = \underbrace{(n-1)E}_{\substack{\text{contribution due to (depth-varying)}\\ \text{vertical momentum flux}}} + \underbrace{{}^1\!/_2 E}_{\substack{\text{contribution at top}\\ \text{of water column}}} = \left(n - {}^1\!/_2\right) E \tag{5.51}$$

The term $\overline{w^2}$ varies in principle with the water depth, whereas the other part (from Eq. 5.50) is located at the top of the water column. In shallow water ($n = 1$) the vertical orbital velocities are zero and the pressure part of the radiation stresses reduces to a contribution $S_{xx,\text{pressure}} = {}^1\!/_2 E$ at the top of the water column. In deep water, where $n = {}^1\!/_2$, the pressure component to the radiation stress is $(n - {}^1\!/_2)E$.

The total radiation stress in the wave propagation direction (x-direction) is now:

$$S_{xx} = S_{xx,\text{ pressure}} + S_{xx,\text{ horizontal particle velocity}} = (n - {}^1\!/_2)E + nE \tag{5.52}$$

The stresses normal to the wave propagation direction S_{yy} consist of the pressure part $(n - {}^1\!/_2)E$ only. The shear stresses are zero.

From Intermezzo 5.4 – or more specifically from Eq. 5.52 – we conclude that:

1. The pressure part of the radiation stress is equal to $(n - {}^1\!/_2)E$. Since pressure is a scalar, this term is part of radiation *normal* stresses in all directions.
2. The magnitude of the advective part of the radiation stress, the part due to transport of momentum by the particle velocity, is nE. It is by definition in the wave propagation direction.

With this result, we can now deduce the more general formulas for the radiation stress components for waves travelling in a direction θ relative to the positive x-direction (see Fig. 5.28). If the x-axis is not the propagation direction we have $\vec{u} = (u_x, u_y) = (u\cos\theta, u\sin\theta)$ and with Eqs. 5.43, 5.45 and 5.47, we find:

$$S_{xx} = \left(n - \frac{1}{2} + n\cos^2\theta\right) E \tag{5.53a}$$

$$S_{yy} = \left(n - \frac{1}{2} + n\sin^2\theta\right) E \tag{5.53b}$$

$$S_{xy} = S_{yx} = n\cos\theta\sin\theta E \tag{5.53c}$$

In the situation of an alongshore uniform coast, the positive x-direction is generally taken as the shore-normal direction and the positive y-direction is parallel to the coastline. The angle of incidence of the wave φ with respect to the depth contours is now

equal to the angle θ with the positive x-axis. For that situation, the radiation stress components are sketched in Fig. 5.30.

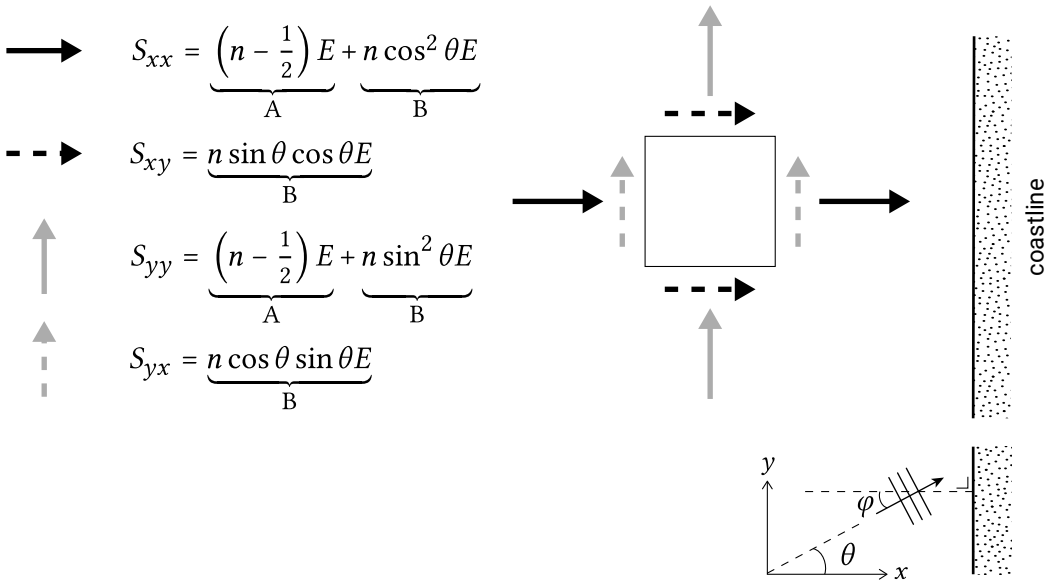

Figure 5.30: Radiation stress components according to linear wave theory. Situation sketch for alongshore uniform coast with depth contours parallel to y-axis. 'A' indicates the pressure part, 'B' indicates the part due to advection by the horizontal particle velocity.

Note that if the x-axis coincides with the wave propagation direction ($^{\S 1.1}\not{=}\ 0^{\S 1.1}\theta = 0$ [p209]), the above Eqs. 5.53a to 5.53c reduce to:

$$S_{xx} = \left(2n - {}^1\!/_2\right) E \tag{5.54a}$$

$$S_{yy} = \left(n - {}^1\!/_2\right) E \qquad \text{for waves propagating in the } x\text{-direction} \tag{5.54b}$$

$$S_{xy} = S_{yx} = 0 \tag{5.54c}$$

This is in accordance with the earlier findings that:

- The normal stresses perpendicular to the direction of wave propagation consist of the pressure part $(n - {}^1\!/_2)E$ only;
- The normal stresses in the direction of wave propagation consist of the pressure part $(n - {}^1\!/_2)E$ plus the part due to momentum transfer by the horizontal orbital motion nE;
- The shear stresses are zero if the x-direction is the direction of wave propagation.

In *deep* water, where $n = {}^1\!/_2$, the pressure component to the radiation stress is $(n - {}^1\!/_2)E = 0$ and the fluid particle part becomes $nE = {}^1\!/_2E$ in the direction of wave propagation. Thus, in the case of wave propagation in the x-direction, we find $S_{xx} = {}^1\!/_2E$, and $S_{yy} = 0$. In *shallow* water, on the other hand, where $n = 1$, it follows that $S_{xx} = {}^3\!/_2E$, and $S_{yy} = {}^1\!/_2E$. Here both contributions add to the total radiation stress S_{xx} and S_{yy}

is equal to the pressure part. The radiation (normal) stress in shallow water is clearly larger than in deep water. Moreover, it has two components in shallow water: parallel and perpendicular to the direction of wave propagation.

Radiation stress in breaking waves

In *breaking surf zone waves*, the effect of the surface roller will be to delay the momentum release from the wave-breaking. In practice this means that the equations for the radiation stresses will contain a term due to roller energy too. Different models exist for this term, enhancing either the pressure part or advection part of the radiation stress or both. Svendsen (1984) proposes an additional contribution to the radiation stress in the propagation direction due to the velocity in the roller by an amount $q_{\text{roller}}c = \alpha E_r$ (see Eq. 5.41). This contribution is concentrated near the water surface, where the wave-breaking takes place. Under the assumption of shallow water, the radiation stress below the wave trough level is dominated by the part due to advection of momentum by the horizontal orbital motion (verify this from Intermezzo 5.4). Since in shallow water the horizontal orbital velocity is uniformly distributed, the advective part of the radiation stress is uniformly distributed as well.

5.5.3. Wave-induced forces

The above equations describe the wave radiation stresses acting in a vertical plane of water. Horizontal gradients in the radiation stresses give rise to a net wave-induced *force* on the water in a particular direction.

The net force in the x-direction is described by (Fig. 5.31):

$$F_x = -\left(\frac{\partial S_{xx}}{\partial x} + \frac{\partial S_{xy}}{\partial y}\right) \tag{5.55}$$

where the first term represents the effect of variations in the x-directed radiation normal stresses and the second term the effect of variations in the y-direction of the x-directed radiation shear stress.

In coastal engineering practice, it is common to work with alongshore and cross-shore orientated axes. The y-axis is defined parallel to the shoreline, while the x-axis is perpendicular to the shoreline. F_x is thus the force in the cross-shore direction.

The second (shear) term in Eq. 5.55 is zero for an alongshore uniform coastline (no gradients in the y-direction). We then have:

$$F_x = -\frac{dS_{xx}}{dx} \qquad \text{for an alongshore uniform coast} \tag{5.56}$$

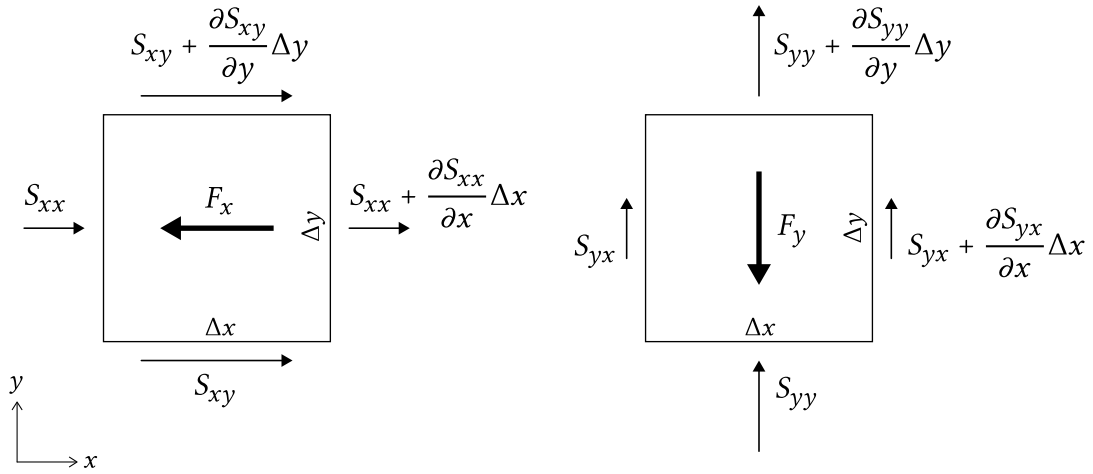

Figure 5.31: Wave-induced forces. An increase of momentum transport (increase in radiation stress) in x- or y-direction is equivalent to a loss of momentum, hence, to exerting an opposite force on the water body.

In the alongshore direction the force is:

$$F_y = -\left(\frac{\partial S_{yy}}{\partial y} + \frac{\partial S_{yx}}{\partial x}\right) \tag{5.57}$$

The first term in Eq. 5.57 can be non-zero if gradients in wave height occur along the coast. For an alongshore uniform coast this term is zero such that Eq. 5.57 reduces to:

$$F_y = -\frac{dS_{yx}}{dx} \qquad \text{for an alongshore uniform coast} \tag{5.58}$$

Remember that S_{yx} – the radiation shear stress on a plane perpendicular to the x-axis – represents the transport of y-momentum in the x-direction. A cross-shore gradient herein gives a net force in the y-direction.

Variations in the radiation stresses occur due to changes in n, E or θ . Further offshore, the wave-induced forces are relatively small, but in the nearshore zone large forces occur due to wave transformation as a result of large gradients in water depth.

In the shoaling region, the wave height and hence wave energy increase up to the edge of the surf zone, from where the wave height and wave energy decrease again. In the shoaling region the value of n gradually increases from its deep-water value $n = 1/2$, to its shallow-water value $n = 1$. The wave angle θ gradually decreases from deep water to shallow water. The combined result is a positive gradient of $\partial S_{xx}/\partial x$ and an offshore-directed force in the shoaling region, and a negative gradient of $\partial S_{xx}/\partial x$ and an onshore-directed force in the surf zone. Section 5.5.4 shows how this results in wave set-down in the shoaling region and wave set-up in the surf zone. We will further see that the force in the y-direction is zero outside the surf zone but non-zero

in the surf zone, where it drives a longshore current. It is of course only present in situations where the waves approach the coastline under a certain angle (such that there is a component of wave orbital velocity in the alongshore direction).

We have expressed the depth-integrated wave forces in terms of the radiation stresses, which is quite common in coastal engineering applications. Other equivalent expressions can also be found in model descriptions (Intermezzo 5.5).

Intermezzo 5.5 Wave forces in momentum equations

In momentum equations that are averaged over the wave motion, wave forces appear. These wave forces have two contributions: due to pressure fluctuations and due to momentum transfer by the particle velocity. They may be formulated in terms of radiation stresses (as in Eq. 5.55-Eq. 5.58) or they may equivalently be expressed in terms of the wave orbital motion and wave-induced pressure. In the latter case the wave forces in three dimensions may be expressed as:

$$\frac{R_x}{\rho} = -\frac{\partial \left\langle \tilde{u}_x \tilde{u}_x \right\rangle}{\partial x} - \frac{\partial \left\langle \tilde{u}_y \tilde{u}_x \right\rangle}{\partial y} - \frac{\partial \left\langle \tilde{w} \tilde{u}_x \right\rangle}{\partial z} - \frac{1}{\rho}\frac{\partial \left\langle p_{\text{wave}} \right\rangle}{\partial x} \tag{5.59a}$$

$$\frac{R_y}{\rho} = -\frac{\partial \left\langle \tilde{u}_x \tilde{u}_y \right\rangle}{\partial x} - \frac{\partial \left\langle \tilde{u}_y \tilde{u}_y \right\rangle}{\partial y} - \frac{\partial \left\langle \tilde{w} \tilde{u}_y \right\rangle}{\partial z} - \frac{1}{\rho}\frac{\partial \left\langle p_{\text{wave}} \right\rangle}{\partial y} \tag{5.59b}$$

$$\frac{R_z}{\rho} = -\frac{\partial \left\langle \tilde{u}_x \tilde{w} \right\rangle}{\partial x} - \frac{\partial \left\langle \tilde{u}_y \tilde{w} \right\rangle}{\partial y} - \frac{\partial \langle \tilde{w} \tilde{w} \rangle}{\partial z} - \frac{1}{\rho}\frac{\partial \left\langle p_{\text{wave}} \right\rangle}{\partial z} \tag{5.59c}$$

Note that the wave forces R_i are not integrated over the depth. The brackets $\langle\ \rangle$ denote time-averaging over the short-wave period. The wave orbital motion is now denoted with $(\tilde{u}_x, \tilde{u}_y, \tilde{w})$, with the tilde to distinguish the wave motion from the mean motion. Note the pressure contribution due to the non-zero time-averaged wave pressure and the horizontal momentum transfer terms in R_x and R_y that are directly related to the radiation stresses. In R_z we recognise the term $-\rho\overline{\tilde{w}^2}$ that contributed to Eq. 5.49. We can also recognise the term $\partial\langle\tilde{u}\tilde{w}\rangle/\partial z$ that was said to act, in the wave boundary layer, as a horizontal force pushing the flow forward (causing streaming, Sect. 5.4.3).

5.5.4. Cross-shore balance: wave set-up and set-down

Wave forces have an effect on the mean flow; they induce mean water level variations (set-down, set-up) and mean currents (a longshore current in the case of waves obliquely approaching the shore).

First we consider the wave force in the cross-shore direction (given by Eq. 5.55). For illustration purposes, we consider the simplified situation of a long-crested wave normally incident to straight and parallel depth contours (parallel to the y-axis, $\theta = \varphi = 0$). This means that there are no gradients in the alongshore direction: the situation is alongshore uniform (all y-derivatives are zero) and the wave force reduces to Eq. 5.56.

Cross-shore mass balance (alongshore uniform coast)

In a stationary case, the *cross-shore current averaged over the entire water column* must be zero (since water neither piles up higher and higher against the coast nor flows towards deeper water). At every point in the cross-shore profile, the onshore- directed mass flux near the water surface is therefore compensated by an offshore-directed return current at lower elevations, such that the net depth-averaged flow through each cross-section is zero (see Fig. 5.25). The offshore-directed depth-mean velocity under the wave trough level can be found from Eq. 5.42.

Cross-shore momentum balance (alongshore uniform coast)

The wave force is determined by the cross-shore gradient of S_{xx}. The magnitude of the radiation stress $S_{xx} = (2n - {}^1\!/_2)E$ in the wave propagation direction depends on the wave height, the water depth and the wavelength. Based on energy conservation, Sect. 5.2.2 showed that the wave energy (wave heights) tends to increase when the waves approach the surf zone (after a small initial decrease). Since n increases in intermediate water depths, S_{xx} increases in the shoaling region. Further offshore in really deep water, the radiation stress S_{xx} is constant. An increasing S_{xx} in the landward direction means that, at a water column, a resulting force due to radiation stresses is acting in the seaward direction (see Figs. 5.31 and 5.32). A (small) difference in water level at both sides of the water column (lower towards the coast) ensures that equilibrium of forces is achieved again. This phenomenon is called wave set-down, which means that outside the breaker zone in intermediate water depths, the water level at the landward side of a water column is a bit lower than at the seaward side (see Figs. 5.32 and 5.33, top figure). Inside the surf zone, the magnitude of S_{xx} decreases rapidly due to wave-breaking while moving towards the waterline. The decrease in S_{xx} is equivalent to a force in the landward direction (see Fig. 5.32). To achieve equilibrium again, the water level at the landward side of the column should be higher than at the seaward side (wave set-up, see Fig. 5.32) creating a seaward-directed pressure force (see Fig. 5.33, upper plot).

The lower figure of Fig. 5.33 illustrates the cross-shore balance of momentum between two (arbitrary) points 1 and 2. The net pressure force (per unit alongshore distance) is $P_x\,\Delta x = -\rho g h\, d\overline{\eta}/dx\,\Delta x$. It consists of:

- the hydrostatic force ${}^1\!/_2\rho g h^2$ at point 1; minus
- the hydrostatic force ${}^1\!/_2\rho g(h + dh/dx\,\Delta x)^2 \approx {}^1\!/_2\rho g h^2 + \rho g h\, dh/dx\,\Delta x$ at point 2; minus

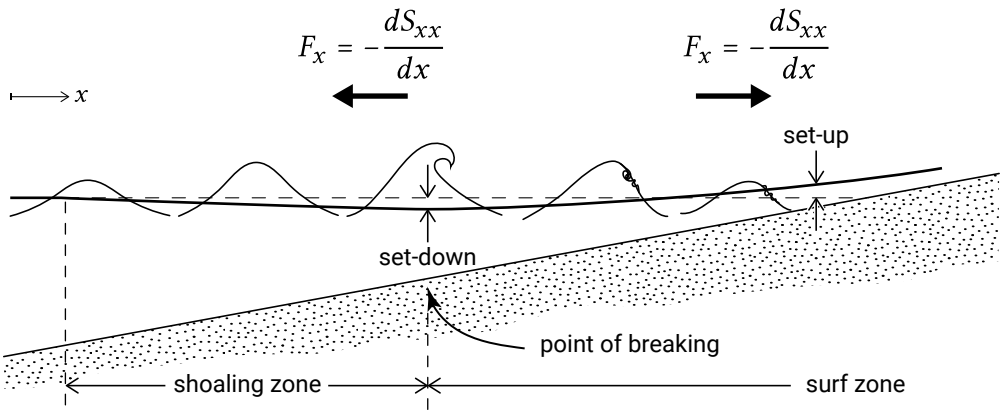

Figure 5.32: In the shoaling zone, S_{xx} increases in landward direction, resulting in a wave force acting in seaward direction and a lowering of the mean water level towards the breaking point. Wave-breaking in the surf §1.2zone [p213] causes S_{xx} to decrease in landward direction, such that an onshore wave forces raises the water level towards the shore (set-up).

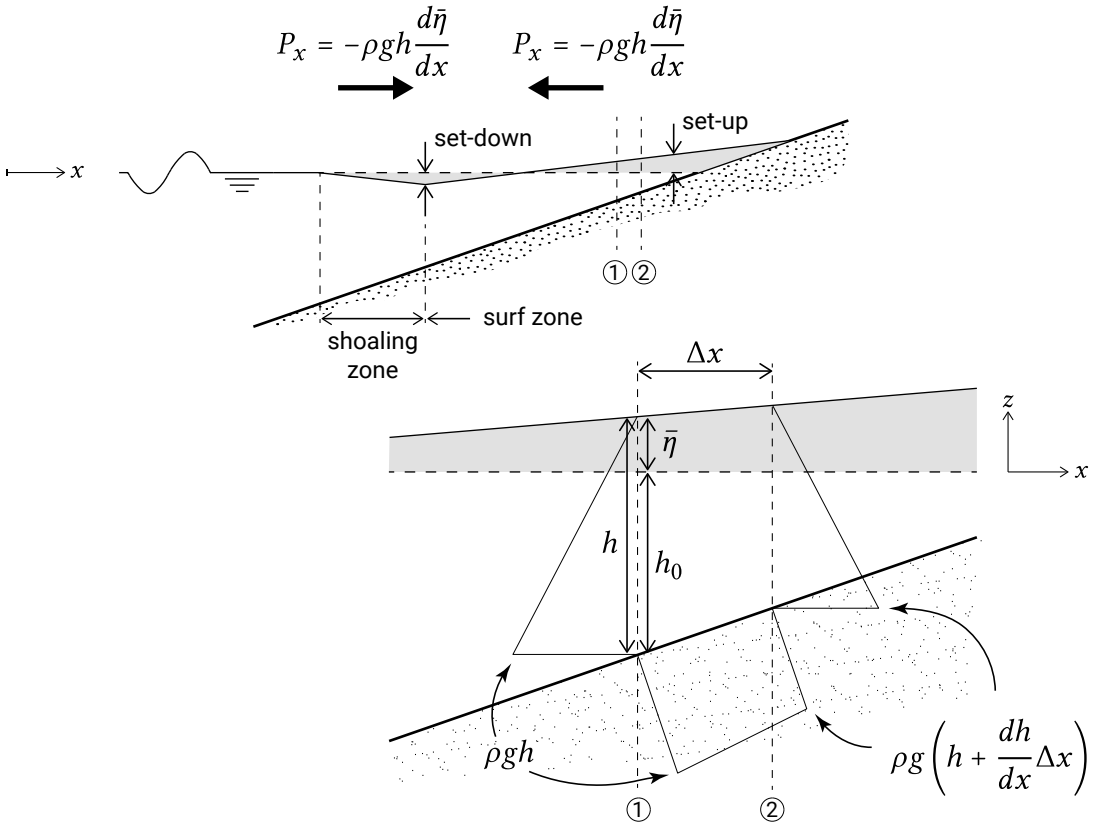

Figure 5.33: The control volume for a simple cross-shore momentum balance between two locations 1 and 2. The radiation stress is $S_{xx,1}$ at location 1 and $S_{xx,2}$ at location 2. The triangles and quadrangle indicate the pressure forces. If locations 1 and 2 are in the surf zone, the onshore-directed wave force (onshore since $S_{xx,1} > S_{xx,2}$) is balanced by a net offshore pressure force (through a raising of the water level towards the coast).

- the *horizontal* component $\approx \rho g h (dh_0/dx\ \Delta x)$ of the hydrostatic force along the bottom.

The equilibrium between the radiation stress gradient and pressure term due to the water level slope (see Fig. 5.34) yields the following first-order differential equation:

$$\boxed{F_x = -\frac{dS_{xx}}{dx} = \rho g h \frac{d\bar{\eta}}{dx} = \rho g \left(h_0 + \bar{\eta}\right) \frac{d\bar{\eta}}{dx}} \tag{5.60}$$

where:

x	co-ordinate axis pointing from land to sea	m
h_0	still-water depth at point x (in absence of waves)	m
$\bar{\eta}$	wave-induced water level set-up at point x	m

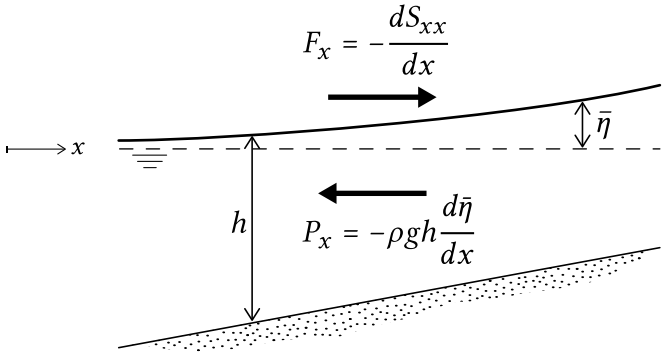

Figure 5.34: The force balance between wave force and pressure force reads $F_x + P_x = 0$. In the surf zone F_x is positive (landward-directed) and P_x is negative (seaward-directed).

Eq. 5.60 is the depth-integrated cross-shore momentum equation for a stationary alongshore uniform situation. This balance in the cross-shore direction holds both for obliquely and normally incident waves. We have not included bottom friction in this equation, because it is generally assumed to be an order of magnitude smaller than the other terms in the equation[6]. Furthermore, the Coriolis term is assumed to be small compared to the wave forcing. The equation is valid inside and outside the surf zone under the conditions listed above.

Note that inside (outside) the surf zone the term §1.1 ~~$dSxx/dx$~~ §1.1 dS_{xx}/dx [p215] is negative (positive) yielding a positive (negative) water level gradient ($d\bar{\eta}/dx$), see Figs. 5.32 and 5.34. Therefore, the still water surface becomes lower in the shoaling region (set-down). Moving inside the surf zone towards the waterline, the still water surface becomes higher (set-up). In order to calculate the wave set-up (and set-down), we

[6] Apotsos et al. (2007) showed that this assumption may result in underprediction of the set-up. For simplicity, however, bottom stress is often neglected, also in this book.

need to assess the radiation stress terms inside and outside the surf zone and integrate Eq. 5.60 with respect to x.

With Eq. 5.53a we can write Eq. 5.60 as:

$$-\frac{d}{dx}\left[\left(n-\frac{1}{2}+n\cos^2\theta\right)E\right]=\rho g h\frac{d\bar{\eta}}{dx} \tag{5.61}$$

The spatial wave energy variation must be solved from the conservation of energy, Eq. 5.2, which reduces to $d(Ec_g\cos\theta)/dx=-D_w$ under the present assumptions.

Simple model for wave set-down in the case of normally incident waves

For waves normally incident to an alongshore uniform coast ($\theta=\varphi=0$) and under the assumption of shallow water ($n=1$), the momentum balance Eq. 5.61 can be written as:

$$-\frac{d}{dx}\left(\frac{3}{2}E\right)=\rho g h\frac{d\bar{\eta}}{dx} \tag{5.62}$$

Section 5.2.2 gave us the following energy balance for a normally incident shoaling wave:

$$\frac{H_2}{H_1}=\sqrt{\frac{\S1.1 c_{g,1}\,\S1.1 c_{g,1}}{c_{g,2}}}\,[\text{p216}] \tag{5.63}$$

Amongst others, Longuet-Higgins and Stewart (1962) derived a formula for the set-down for regular waves by integration of Eq. 5.62 using the energy balance of shoaling waves Eq. 5.63. The integration constant is determined from $\bar{\eta}=0$ in deep water. It can be shown that, in the shallow-water approximation, the set-down then equals:

$$\bar{\eta}=-\frac{1}{16}\frac{H^2}{h} \tag{5.64}$$

For waves propagating without dissipation towards the shore, the wave height increases and the water depth decreases. Hence, the set-down gradually increases in magnitude to a maximum just outside the breaker zone, at the point where the waves start breaking. At the breaker point the set-down equals:

$$\overline{\eta_b}=-\frac{1}{16}\frac{H_b^2}{h_b}=-\frac{1}{16}\gamma H_b \tag{5.65}$$

where:

$\overline{\eta_b}$	water level change at the point of wave-breaking	m
γ	wave-breaking index (H_b/h_b)	–
H_b	wave height at point of breaking	m
h_b	still water depth at point of breaking	m

Thus, with γ put equal to 0.8 the set-down at the point of breaking is 4 % of the local water depth.

Analytical model for set-up in the case of normally incident waves

Inside the surf zone, the dissipation due to wave-breaking needs to be included in the energy balance. In the following, an analytical equation for wave set-up is derived using a very simple dissipation model and assuming normally incident waves. The derivation considers equilibrium of forces for the entire breaker or surf zone (see Fig. 5.35).

A simple model for the energy dissipation due to wave-breaking assumes that the wave height everywhere in the surf zone is proportional to the local water depth: everywhere in the surf zone $H = \gamma h$ (see Eq. 5.19). If we further use the shallow-water approximation ($n = 1$), then it follows that $S_{xx} = {}^3\!/_2 E$ is decreasing from the breaker line towards the coastline. Following similar reasoning as in the previous section, this causes landward-directed resulting forces acting on a water column. This will be balanced by a water level increase (in the landward direction) over the water column. If we substitute $S_{xx} = {}^3\!/_2 E = {}^3\!/_{16}\rho g H^2 = {}^3\!/_{16}\rho g \gamma^2 h^2$ in Eq. 5.62, we find the following balance:

$$-\frac{d}{dx}\left[{}^3\!/_{16}\gamma^2 h^2\right] = h\frac{d\bar{\eta}}{dx} \tag{5.66}$$

and thus:

$$\frac{d\bar{\eta}}{dx} = -{}^3\!/_8\gamma^2\frac{dh}{dx} \tag{5.67}$$

Substituting $h = h_0 + \bar{\eta}$ in Eq. 5.67 gives:

$$\frac{d\bar{\eta}}{dx} = -\frac{{}^3\!/_8\gamma^2}{\left(1 + {}^3\!/_8\gamma^2\right)}\frac{dh_0}{dx} \tag{5.68}$$

Hence, because the water depth decreases in the surf zone ($dh_0/dx < 0$), the set-up increases ($d\overline{\eta}/dx > 0$). With a constant bottom slope and a constant breaker index, the water level slope inside the breaker zone is constant.

Equation 5.67 – or equivalently Eq. 5.68, which gives a bit more complex math – can be integrated from the breaker point to the water line to get the wave set-up throughout the surf zone (using $\bar{\eta} = \bar{\eta}_b$ for $h = h_b$ to find the integration constant C):

$$\bar{\eta} = -\frac{3}{8}\gamma^2 h + C = \bar{\eta}_b + {}^3\!/_8\gamma^2 \left(h_b - h\right) \tag{5.69}$$

At the shoreline, the water depth h is zero and we find for the set-up at the water line:

$$\bar{\eta}_{\text{shore}} = \bar{\eta}_b + {}^3\!/_8\gamma^2 h_b = \bar{\eta}_b + {}^3\!/_8\gamma H_b \tag{5.70}$$

The water level §1.1 ~~$\Delta\bar{\eta}$ difference~~ §1.1 difference $\Delta\bar{\eta}$ [p218] between the breaker line and the point of maximum water level rise (wave set-up) equals:

$$\Delta\bar{\eta} = \frac{3}{8}\gamma H_b \tag{5.71}$$

With $\gamma = 0.8$ this amounts to $0.3H_b$. Wave set-up can thus be quite significant, as is further illustrated in Example 5.2. Since the maximum set-down at the breaker line is ${}^1\!/_{16}\gamma H_b$, the maximum wave set-up relative to the still water level is ${}^5\!/_{16}\gamma H_b$ (see Fig. 5.35).

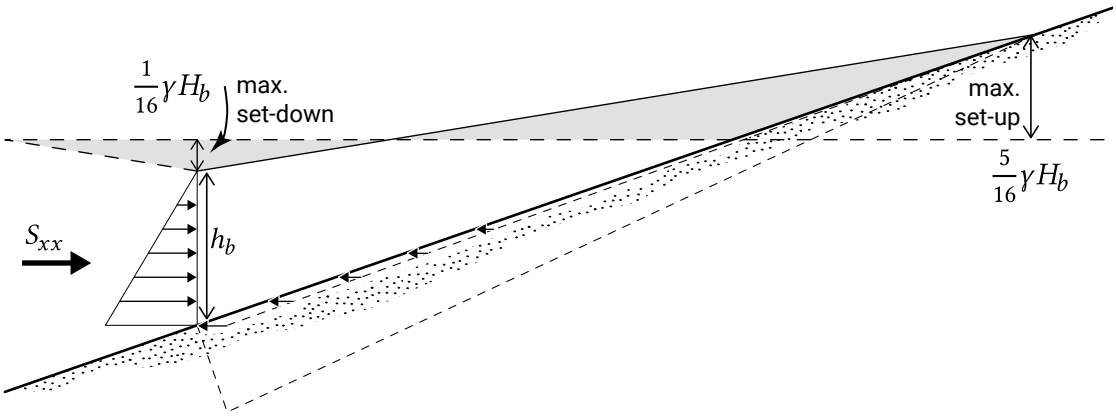

Figure 5.35: Set-down and set-up and equilibrium of forces in the entire breaker zone.

Example 5.2 Maximum wave set-up relative to still water level

Input parameters

Offshore wave height	H_0	=	5	m
Wave period	T	=	12	s
Offshore wave direction	φ_0	=	0°	(normally incident)
Breaker index	γ	=	0.7	

Required Maximum wave set-up relative to the still water level

Output The first step is to compute the wave height at the breaker line. H_b depends on shoaling and (though not in this case) refraction. Computer programs can be used, or linear wave theory using the following iterative steps (for an arbitrary wave angle):

1. Guess a breaker depth, h_b and compute h_b/L_0
2. Use Table A.3 in App. A to determine the shoaling coefficient K_{sh} and the ratio of wave speeds c/c_0
3. Determine the angle φ using $\sin\varphi = c/c_0 \sin\varphi_0$
4. Compute the wave height at water depth h_b from ~~$H = H_0 K_{sh} (\cos\varphi_0 / \cos\varphi)$~~ $H = H_0 K_{sh} \sqrt{(\cos\varphi_0 / \cos\varphi)}$ [p219]
5. Check whether $H/h_b = \gamma = 0.7$. If yes: o.k.; if no: return to step 1 with a better guess of h_b.

In this case of normally incident waves, step 3 can be omitted. It follows that ~~Hb~~ H_b = 5.5 m [p219]. The maximum wave set-up then becomes $^5/_{16}\gamma H_b$ = 1.2 m above still water level.

Conclusion If we assume an average beach slope of 1:50, then almost 60 m of beach width is 'lost' by the effect of wave set-up.

Summary

- In the shoaling zone, S_{xx} increases in the positive x-direction (the cross-shore direction); the positive gradient in S_{xx} ($\partial S_{xx}/\partial x > 0$) is equivalent to a force F_x directed in the offshore direction. This is compensated for by an onshore-directed pressure force due to a set-down (lowering of the water level). The set-down can be approximated as $^1/_{16}\gamma H_b$;
- In the surf zone, S_{xx} decreases in the positive x-direction; the resulting negative gradient in S_{xx} ($\partial S_{xx}/\partial x < 0$) is equivalent to a force F_x directed in the onshore direction. This is balanced by an offshore-directed pressure force due to wave set-up (raising of the water level towards the water line). The maximum wave set-up relative to the still water level is $^5/_{16}\gamma H_b$.

Concluding remarks

- The wave height increase in the shoaling zone as well as the wave height decay in the surf zone can be predicted reasonably well using a wave action or energy balance. When assuming (as we did) that inside the surf zone local wave height and local water depth are directly related, the build up of the wave set-up starts

at the (first) point of breaking. In reality, there is a delay in the transfer of momentum from the wave motion to the mean flow. This means that the set-up (and also the start of the build-up of the longshore current) is shifted in the landward direction. The delay may be caused by the temporary storage of energy and momentum in surface rollers of breaking waves. In this way the dissipation process is delayed, shifting the region of wave set-up in the shoreward direction. This temporary storage can be modelled using a roller model and a roller energy balance;

- Waves are irregular. For the computation of the wave set-up for irregular waves, the root-mean-square wave height H_{rms} is generally applied;
- In an irregular wave field, wave heights vary at the wave group scale (Sect. 5.8.2). That means that the magnitude of the radiation stress varies on the wave group scale as well. This time-varying force generates water level fluctuations with a timescale much longer than the wave period (long waves);
- Waves generally approach the coastline under a (small) angle that decreases in smaller water depths. Therefore S_{xx}, the cross-shore gradients of S_{xx} and the set-up are smaller than for normally incident waves.

5.5.5. Alongshore balance: longshore current

In the alongshore direction, the transfer of momentum from the wave motion to the mean flow gives rise to a longshore current. Note that besides this wave-induced (due to wave dissipation in the breaker zone) current, tidal and wind forces can also generate a current along the coast. These are discussed in Sect. 5.6 and Sect. 5.7.2.

The longshore current (velocity magnitude and cross-shore distribution) is an important input parameter in longshore sediment transport computations.

Alongshore momentum balance (straight, parallel depth contours)

We consider again the 2D situation (see Fig. 5.4) of a long-crested wave obliquely incident to an alongshore uniform coast ($\theta = \varphi$ and all y-derivatives are zero). The cross-shore rate of variation of the shear component of the radiation stress S_{yx} acts as a driving force (Eq. 5.58). In the cross-shore direction, the balancing force was supplied by a hydraulic pressure gradient. However, for an infinitely long uninterrupted coastline, no such hydraulic pressure gradient can develop in the alongshore direction. The counterforce, which restores the equilibrium, therefore must be supplied by bed shear stresses that develop when a longshore current is generated. The bottom shear stress restrains the current and is non-zero only in the presence of a current. Note that in the cross-shore direction the bed shear stress associated with the mean current was assumed to be small, as compared to the pressure force.

We only consider the stationary situation. The alongshore component of the momentum balance for a steady state and alongshore uniformity can be written as:

$$\boxed{F_y = -\frac{dS_{yx}}{dx} = \overline{\tau}_{b,y}} \tag{5.72}$$

The balance between the driving force and the resisting or retarding force is shown in Fig. 5.36.

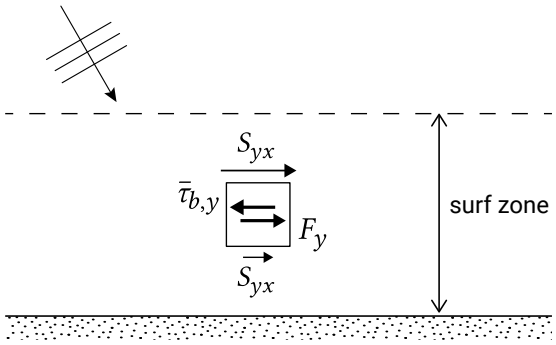

Figure 5.36: Forces acting on the water column (plan view). The longshore current direction is from left to right in the figure.

Wave force in alongshore uniform situation

Let us first assess $F_y = -dS_{yx}/dx$ in deeper water, i.e. outside the breaker zone. In Sect. 5.5.2 we found $S_{yx} = En \sin\varphi \cos\varphi$. The wave angle changes as a function of x, but does not vary with y. The latter implies that Snell's law for regular waves is valid (Eq. 5.8): $\sin\varphi/c = \text{constant}$. Conservation of energy (Eq. 5.2) requires $d(Ec_g \cos\varphi)/dx = -D_w$ under the present assumptions. For linear waves we can now write the wave force Eq. 5.58 as:

$$F_y = -\frac{dS_{yx}}{dx} = -\frac{\sin\varphi}{c}\frac{d}{dx}Ec_g \cos\varphi = \frac{D_w}{c_0}\sin\varphi_0 \tag{5.73}$$

Apparently the alongshore driving force is a function of the dissipation of the wave energy. Outside the surf zone, the dissipation of wave energy can be neglected and hence the energy flux $Ec_g = (Ec_g \cos\varphi, Ec_g \sin\varphi)$ is constant. We have in the absence of dissipation: S_{yx} §1.1 is constant [p221] and $F_y = 0$. So, although outside the surf zone the wave conditions change with x (wave height due to shoaling; wave direction due to refraction), the radiation shear stress is constant. Therefore, since the alongshore forcing is only present when the waves are breaking, the longshore current is confined to the surf zone (see also Intermezzo 5.6).

Intermezzo 5.6 Energy dissipation and mean currents

The finding that a mean current is only driven in the case of energy dissipation is universally valid, also in less simplified situations. The wave force consists of two parts:

- A part in the wave propagation direction that is related to the energy dissipation. This term is concentrated near the water surface, where the dissipation actually takes place. This D/c part is rotational and can therefore induce mean currents or circulation currents in the case of a closed boundary. It is a result of the vorticity generated by wave-breaking and stems from the effect of both velocity and pressure variation on the momentum flux;
- An irrotational part that is depth-invariant. This implies that there is no vertical imbalance. Thus, this part can be balanced by set-up and set down without driving currents. It only affects the wave-induced current indirectly, through its effect on the mean depth. In the surf zone, the latter influence on the mean current is small compared with that of the dissipation.

Analytical model for alongshore wave force in the surf zone

To find an easy analytical equation for the §1.1 ~~longshore current~~ §1.1 alongshore wave force [p222], we assume again the simple model for wave dissipation due to breaking that relates the wave height to the local water depth: $H = \gamma h$ for every water depth in the surf zone. An alternative would be solving the energy balance numerically. Snell's law and the simple dissipation model result in:

$$F_y = -\frac{\sin\varphi}{c}\frac{d}{dx}Ec_g\cos\varphi = -\frac{\sin\varphi_0}{c_0}\frac{d}{dx}{}^1\!/\!_8\rho g\gamma^2h^2c_g\cos\varphi \tag{5.74}$$

In shallow water $c_g = c = \sqrt{gh}$ and since, due to refraction, φ is small (generally around 10° to 15°), we assume $\cos\varphi \approx 1$. We now have:

$$F_y \approx -\frac{\sin\varphi_0}{c_0}{}^1\!/\!_8\rho g^{3/2}\gamma^2\frac{d}{dx}h^{5/2} = -\frac{5}{16}\frac{\sin\varphi_0}{c_0}\rho(gh)^{3/2}\gamma^2\frac{dh}{dx} \tag{5.75}$$

As mentioned above, the radiation shear stress S_{yx} is constant seaward of the border of the breaker zone (thus the wave force is zero). It decreases inside the breaker zone to zero at the waterline (see Fig. 5.37).

For many day to day wave conditions, this gradient in S_{yx} causes alongshore stresses (forces) which are in the same order of magnitude as the bottom shear stress in rivers: in the order of 1 N/m^2 to 10 N/m^2. The cross-shore gradient in the alongshore radiation stress S_{yx} is therefore an important driving force in the littoral zone.

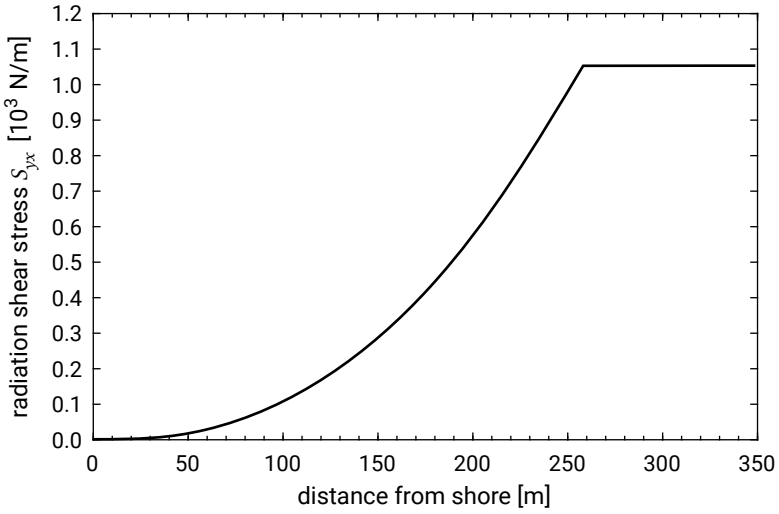

Figure 5.37: Radiation shear stress S_{yx} for $H_0 = 2\,\text{m}$, $T = 7\,\text{s}$, $\varphi_0 = 30°$, constant bottom slope 1:100 and a breaker index $\gamma = 0.8$.

Quadratic friction law for bed shear stress

The next step §1.2in determining an analytical equation for the alongshore current [p222] is the formulation of the bed shear stress. In Sect. 5.4.3 we have already discussed the quadratic friction law for wave- and current-only situations. For currents the turbulence is present in the entire water column. The turbulence due to waves is present in the wave boundary layer only and significantly increases the bed shear stress. This is not only due to the significant increase in friction factors, but also due to the velocity being generally higher in the wave motion. For the vertical profile of the longshore current, we need a quadratic resistance law of combined current and wave action. Such a law is non-trivial since:

- Due to the quadratic friction law, the addition of the effects of waves and current is non-linear. Due to the non-linear addition, the combined shear stress averaged over the wave period is generally larger than the linear summation of the current-only and wave-only bed shear stress;
- The waves and currents may not have the same direction. The waves are incident with a certain angle, whereas the longshore current is parallel to the coast. As a result, the direction and magnitude of the bed-shear stress during the wave cycle varies continuously. The time-averaged bed shear stress depends on the angle between the waves and current;
- As discussed earlier, for currents the turbulence is present in the entire water column and for waves in the wave boundary layer only. It therefore makes sense to relate the bed shear stress due to currents to a depth-mean velocity and due to waves to the free-stream velocity outside the wave boundary layer. This raises a question, however: the velocity at which height should be chosen for the combined wave current motion?

- Note that the above descriptions deal with the time-averaged bottom shear stress; they disregard the momentary (or intra-wave) shear stresses that may occur within the wave period. This seems reasonable when determining the wave-induced currents. However, the intra-wave velocity fluctuations may be important for the net (wave-averaged) sediment transport (see also Chs. 6 and 7).

For the reasons mentioned above, many different models exist for the bed shear stress under waves and currents. Depending on the model, the relative contributions of waves and currents to the bed shear stress vary. Some models describe the time-averaged bed shear stress, others the instantaneous bed shear stress. The description of the sediment transport requires an accurate formulation of bed shear stress (intra-wave or time-averaged, depending on the sediment transport model). Therefore in Sect. 6.5 bed shear stress is treated in more detail.

For the determination of the time-averaged bed shear stress in the alongshore direction, necessary to compute the longshore current, we take a fairly simple approach:

- The wave motion is described by shallow-water theory (constant orbital amplitude outside the wave boundary layer);
- The angle of incidence is very small, such that for the wave motion $(u_x, u_y) = (\hat{u}\cos\omega t, 0)$;
- The bed friction vector is related to the *depth-averaged* velocity vector. The latter is the sum of the depth-averaged longshore current velocity and the wave orbital motion: $\vec{u} = (\hat{u}\cos\omega t, V)$, see Fig. 5.38;
- The time-varying bed friction is written as:

$$\vec{\tau}_b = \rho c_f |\vec{u}|\vec{u} \tag{5.76}$$

- The enhancement of the friction factor (compared to a current-only situation) due to the small height of the wave boundary layer as compared to the current boundary layer is not further specified.

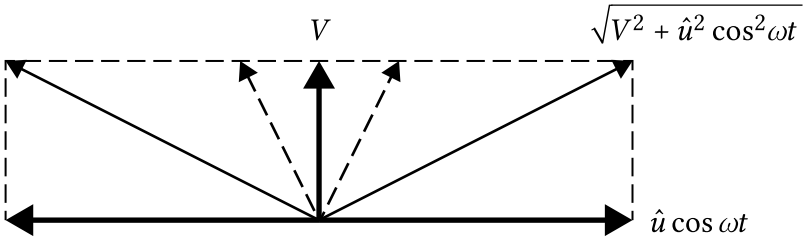

Figure 5.38: The magnitude of the instantaneous velocity vector in the surf zone, with §1.1V§1.1V the longshore current velocity and §1.1$\hat{u}\cos\omega t$ [p224] the orbital velocity (in the cross-shore direction).

In the cross-shore direction, the time-averaged (not the instantaneous) bed shear stress is zero. With the above approximations, the time-averaged bed shear stress in the alongshore direction reads:

$$\overline{\tau}_{b,y} = \overline{\rho c_f |\vec{u}| V} = \rho c_f \overline{\sqrt{V^2 + \hat{u}^2 \cos^2 \omega t}} \overline{\sqrt{V^2 + \hat{u}^2 \cos^2 \omega t}} V \quad (5.77)$$

If we further assume that $V \ll \hat{u}$, this can be simplified to:

$$\overline{\tau}_{b,y} = \frac{2}{\pi} \rho c_f \hat{u} V \quad (5.78)$$

With $\hat{u}$ in shallow water given by Eq. 5.23 and with a constant ratio of wave height over water depth across the entire surf zone we find:

$$\overline{\tau}_{b,y} = \frac{1}{\pi} \rho c_f \sqrt{gh} \frac{H}{h} V \quad (5.79)$$

Analytical model for longshore current (no lateral dispersion)

For steady conditions, the alongshore velocity follows from the balance between the driving force and the resisting friction force (Eq. 5.72). This yields with Eq. 5.73 and Eq. 5.79:

$$\frac{D_w}{c_0} \sin \varphi_0 = \frac{1}{\pi} \rho c_f \sqrt{gh} \frac{H}{h} V \quad \Leftrightarrow \quad V(x) = \frac{\pi}{c_f \rho \sqrt{g}} \frac{\sin \varphi_0}{c_0} \frac{D_w(x)}{H(x)} \sqrt{h(x)} \quad (5.80)$$

The magnitude of the depth-averaged longshore current velocity varies in the surf zone as a function of the dissipation, wave height and water depth. The dissipation and wave heights can be modelled using a wave model (with roller model). In our simple dissipation model $\gamma = H/h =$ constant and we can write the force balance (Eq. 5.72) as:

$$-\frac{5}{16} \frac{\sin \varphi_0}{c_0} \rho (gh)^{3/2} \gamma^2 \frac{dh}{dx} = \frac{1}{\pi} \rho c_f \overline{\sqrt{gh\gamma V}} \overline{\sqrt{gh\gamma}} V \quad (5.81)$$

which leads to:

$$V(x) = -\frac{5}{16} \pi \frac{\gamma}{c_f} g \frac{\sin \varphi_0}{c_0} h \frac{dh}{dx} \quad (5.82)$$

For a constant beach slope $\tan\alpha = -dh_0/dx$ and for $dh/dx \approx dh_0/dx$, the current velocity is proportional to the depth with a maximum at the breaker line (where $h = h_b$):

$$V(x) = \frac{5}{16}\pi\frac{H_b}{c_f}g\frac{\sin\varphi_0}{c_0}\frac{h}{h_b}\tan\alpha \tag{5.83}$$

A longshore current profile according to Eq. 5.83 is shown in Fig. 5.39. The larger the wave height H_b at breaking, the larger the maximum longshore current velocity and the wider the littoral zone; a factor 2 larger wave height would then result in a factor 8 larger discharge in the surf zone. Eq. 5.83 also allows us to get an idea of the effect of the beach slope $\tan\alpha$. A steeper slope, on the one hand, results in (linearly) higher velocities. On the other hand, the width of the surf zone becomes linearly smaller. The discharge through the entire surf zone is then constant to a first approximation (we have, amongst other factors, neglected the effect of the beach slope on the breaking parameter, Sect. 5.2.5). If the wave angle is small, the longshore current velocity at a specific water depth within the surf zone becomes a linear function of φ_0 (since: $\sin\varphi_0 = \varphi_0$ for small φ_0).

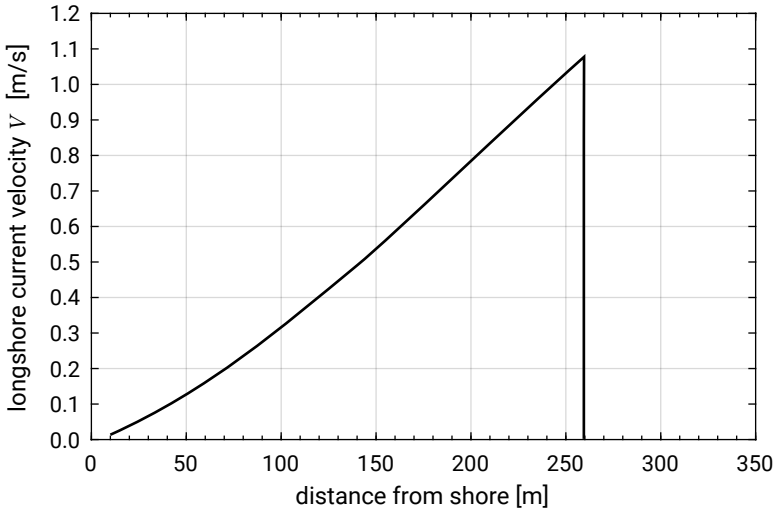

Figure 5.39: Alongshore velocity distribution (regular wave field, $H_0 = 2\,\text{m}$, $T = 7\,\text{s}$, $\varphi_0 = 30°$, bottom slope 1:100, $\gamma = 0.8$, roughness height $r = 0.06\,\text{m}$). The deviation from the linear distribution stems from cross-shore variation in friction factors. The current velocity is zero outside the surf zone.

Turbulent forces redistributing momentum

So far, the effect of lateral dispersion of momentum by turbulence has been ignored. Including turbulence in the momentum equation tends to smooth out velocity gradients (including the unrealistic velocity gradient at the breaker point).

Let us first look at turbulence and turbulence modelling in a bit more detail. In Sect. 5.4.3, the total velocity vector was said to be composed of a mean, a wave and a turbulent

part. The turbulent shear stress was subsequently defined as the stress introduced when averaging over the turbulent motion. In analogy with the modelling of viscous stresses, in a turbulent flow the shear stress is generally related to velocity gradients through a turbulent or eddy viscosity ν_T. The molecular viscosity ν seems to make water sticky and resist flowing and may be thought of as a measure of viscous fluid friction. Similarly ν_T is a measure of turbulent fluid friction (in coastal waters $\nu_T \gg \nu$). The eddy viscosity ν_T [m^2/s] depends on a characteristic spatial scale and on a characteristic velocity. In the littoral zone, both are related to wave motion. The wave orbital motion, for instance, can be regarded as a measure for the characteristic velocity. For vertical mixing, the characteristic (mixing) length is the depth. Horizontal mixing is not restricted by water depth. For that reason, in nearshore modelling the horizontal eddy viscosity §1.1~~$\nu_{T,H}$~~§1.1$\nu_{T,H}$ [p226] is often taken much larger than ν_T for vertical mixing. Typical values for the eddy viscosity ν_T are 10^{-2} m^2/s.

We have seen that the driving force for the longshore current is §1.1~~$\partial S_{yx}/\partial x$~~§1.1$\partial S_{yx}/\partial x$ [p227]. The shear component of the radiation stress S_{yx} was defined through Eq. 5.47, in which the velocity components are due to the orbital motion. In analogy with Eq. 5.47, we can write for the turbulent force:

$$S'_{yx} = \overline{\int_{-k_0}^{\eta} \left(\rho u'_y u'_x\right)\, dz} \tag{5.84}$$

where the overbar now represents averaging over the turbulent motion (indicated with primes). This shear stress or friction force per unit surface area, acts on a surface parallel to the coast. It can be modelled as:

$$S'_{yx} \cong h\rho\nu_{T,H}\frac{dV}{dx} \tag{5.85}$$

The eddy viscosity §1.1~~ν_T~~§1.1$\nu_{T,H}$ [p227] [m^2/s] is also referred to as horizontal diffusivity.

The momentum equation in the alongshore direction now reads:

$$\boxed{\frac{D_w}{c_0}\sin\varphi_0 + \frac{d}{dx}\left(h\rho\nu_{T,H}\frac{dV}{dx}\right) = \overline{\tau}_{b,y}} \tag{5.86}$$

The effect of turbulent forces, smoothing the longshore current profile, is indicated in Fig. 5.40. Since the largest velocity gradient occurs at the breaker line, the maximum transfer of horizontal momentum will occur here. This leads to a reduction in the maximum velocity, a landward shift of the position of maximum velocity and to a situation where, also outside the breaker zone, longshore current velocities occur. The cross-shore distribution of the eddy viscosity now also determines the velocity distribution.

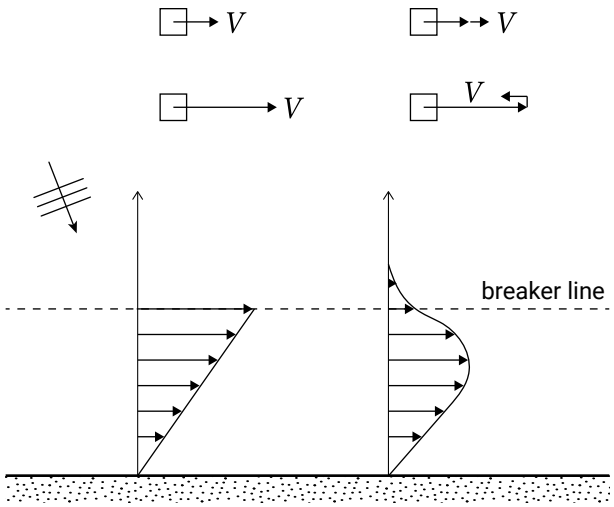

Figure 5.40: Effect of turbulence on the velocity profile.

Roller momentum

Section 5.5.4 discussed that the measured onset of set-up occurs closer to the shore than predicted. This spatial lag was attributed to the roller momentum, which had not been taken into account. Similarly longshore current velocity profiles show an onshore shift in the maximum longshore current velocity. This can be modelled by including the roller contribution in the alongshore momentum equation.

Irregular waves

Until now we have only considered regular waves. In reality, of course, waves are irregular and there is no sharply defined breaker line. The effect of wave irregularity is therefore to smooth out the velocity distribution, very similar to the effect of turbulence, giving a wider and less sharply peaked velocity distribution. This is also illustrated in Fig. 5.41, which shows the output of a computation with the computer model Unibest-CL+.

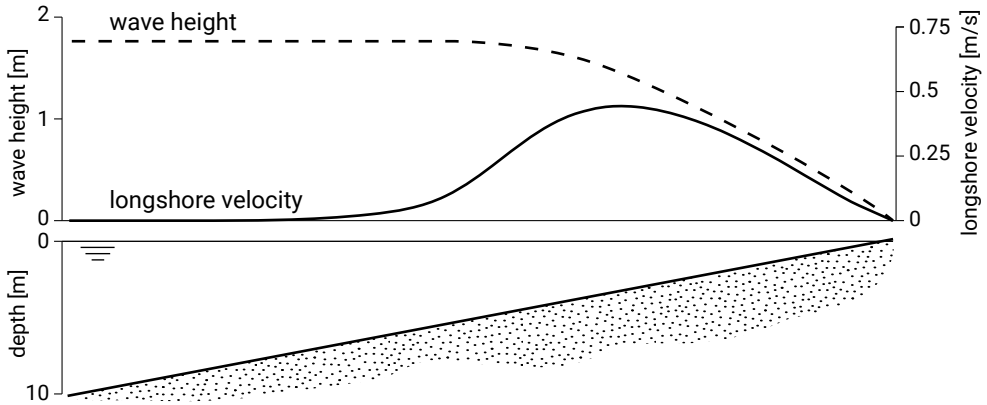

Figure 5.41: Wave-driven velocity computed with the computer model Unibest-CL+ (https://www.deltares.nl/en/software/unibest-cl) using as model input: $H_{s,0} = 2\,\text{m}$; $\gamma = 0.7$; $\varphi_0 = 30°$; $T_p = 8\,\text{s}$).

Profile with breaker bar

If we have a coastal profile with a breaker bar, then the determination of the velocity distribution becomes more complicated. In a simplified approach, we can distinguish between a breaker zone at the seaward side of the breaker bar (if waves indeed break at the corresponding water depths) and a breaker zone near the shoreline where the remaining wave energy is dissipated. This simplification would lead to a zero longshore current velocity in the deeper section between both breaker zones. Also in such a situation, both lateral transfer of horizontal momentum and the irregularity of the waves will smooth out the velocity distribution. An example of the longshore current distribution is given in Fig. 5.42. Wave-breaking tends to concentrate on the bars and at these locations a longshore current exists. For the highest wave condition, wave-breaking already occurs at the outermost bar, whereas for the lowest wave condition wave-breaking occurs only at the innermost bar and close to the shoreline.

5.5.6. Vertical structure of the wave-induced currents

The previous sections explained that in an alongshore uniform situation, the (depth-integrated) cross-shore radiation stress balances the wave set-up. The alongshore radiation stress gradient, on the other hand, was seen to be balanced by a time mean bed shear stress associated with a longshore current. Since the wave forces were vertically integrated, depth-dependent variation was not considered. However, due to the vertical non-uniformity of the driving forces in the nearshore zone, secondary currents are driven. The imbalance between the cross-shore wave radiation stress gradient and the pressure gradient due to the set-up drives a 2D-vertical (2DV) circulation current inside the breaker zone, with a surface current running towards the coast (mass flux) and a seaward current below the wave trough level (the undertow).

The formula for the depth-mean value of the undertow under wave trough level was already determined in Sect. 5.5.1 based on a computation of the mass flux above the wave trough level and continuity considerations. The vertical imbalance between the forces (per unit mass) is indicated in Fig. 5.43.

The pressure gradient due to set-up, the $g\partial\overline{\eta}/\partial x$ term, is the same at all levels, whereas the radiation stress term $\partial s_{xx}(z)/\partial x$ is not evenly distributed over the water column. Instead it is particularly large near the water surface due to the strong pressure and velocity variations above wave trough level (in the surface roller of breaking waves). A fluid particle below mean trough level will therefore experience a net force averaged over the wave period which is directed seaward.

To determine the velocity distribution of the cross-shore circulation current and the longshore current, the horizontal momentum balances without integration over the vertical need to be solved. To avoid computationally demanding 3D computations, a quasi-3D approach can be taken. This involves solving the depth-averaged horizontal momentum equations to obtain the depth-averaged quantities, and subsequently at

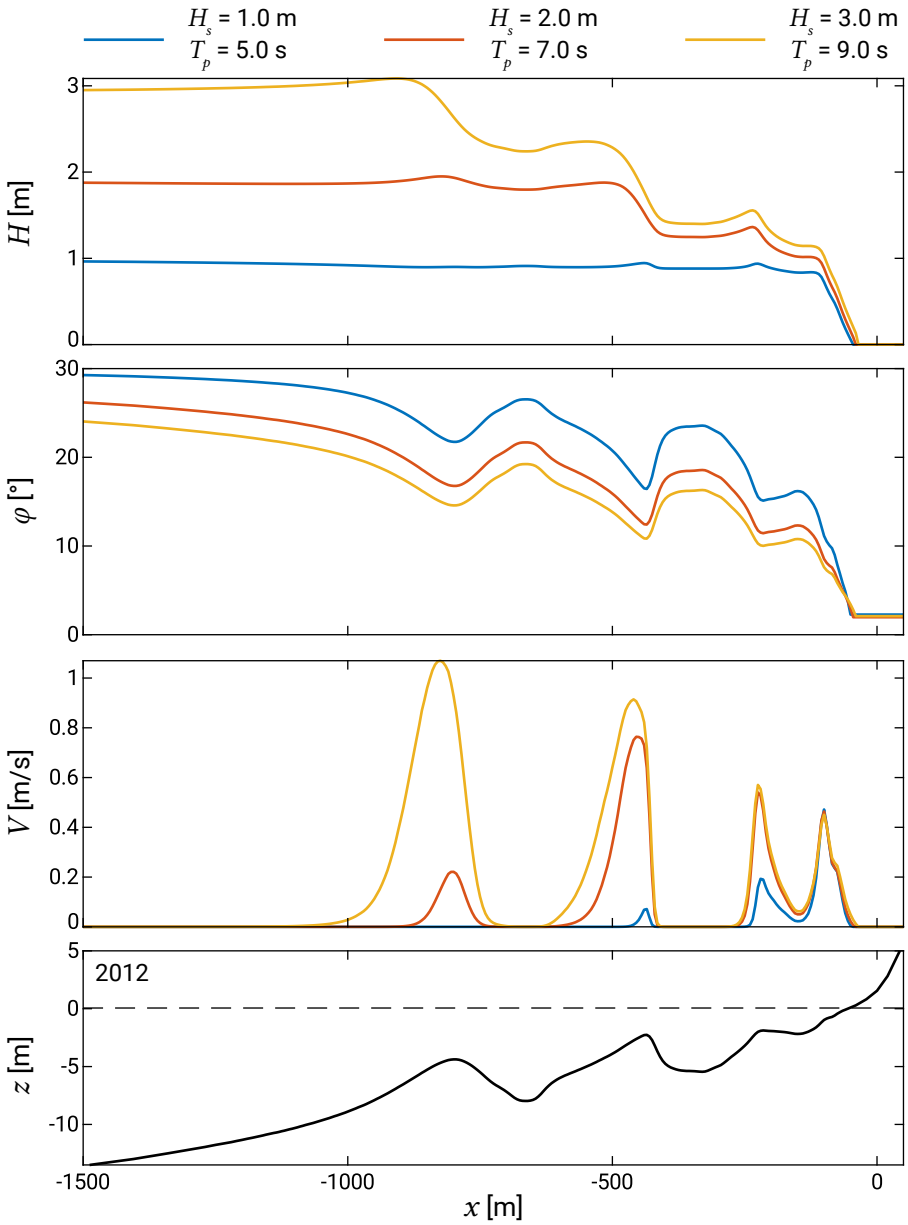

Figure 5.42: Longshore current profiles, calculated with the Unibest-CL+ (https://www.deltares.nl/en/software/unibest-cl), for Jarkus transect 7003850 (JARKUS, n.d.), which is near Egmond, the Netherlands. The profile was measured in 2012 and shows the effect of both the autonomous bar cycle (Sect. 7.3.4) and – in deeper water – shoreface nourishments. Three different deep-water wave conditions are used: $H_s = 3\,\mathrm{m}$ and $T_p = 9\,\mathrm{s}$ (breaking occurs on all bars), $H_s = 2\,\mathrm{m}$ and $T_p = 7\,\mathrm{s}$ (no substantial breaking takes place at the outermost bar), $H_s = 1\,\mathrm{m}$ and $T_p = 5\,\mathrm{s}$ (breaking takes mainly place at the innermost bar and close to the shoreline). In all cases $\varphi = 30°$ in deep water.

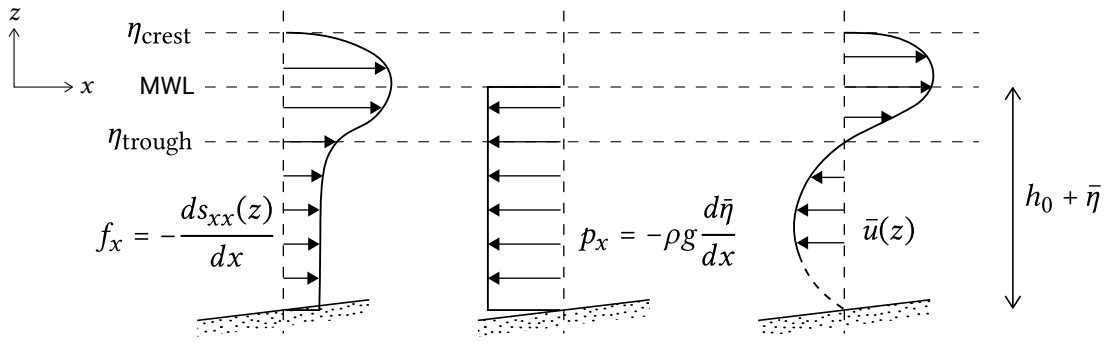

Figure 5.43: Vertical distribution of stresses in undertow. The imbalance in the vertical between the radiation stresses (left figure) and pressure (middle figure) drives a circulation current in the surf zone (right figure).

every position solving a momentum balance that resolves the vertical, but neglects spatial gradients. By neglecting the advective terms, locally a horizontal bottom is assumed. The computation is simplified by only considering the area below the wave trough level. In a steady situation, the locally applied momentum balance in the i-direction, $i = x$ or y then is of the form:

$$\frac{\partial \tau_i}{\partial z} = R_i \tag{5.87}$$

where R_i (see Intermezzo 5.5) is the forcing that below the wave trough level is dominated by the pressure gradient. The trough-to-crest layer, containing the moving water surface, is accounted for via an effective shear stress at the trough level, compensating for the momentum decay above it, and via the condition that the net mean flow below trough level must compensate for the mass flux in the surface layer. The modelling of the surface layer is thus reduced to the formulation of the effective shear stress and the mass flux. The effects of wind can be added by applying a surface shear stress due to wind (see also Sect. 5.6). If the appropriate forcing term - related to the dissipation in the wave boundary layer - is taken into account, the near-bottom streaming in the wave boundary layer will be resolved as well (Sect. 5.4.3).

The shear stress can be related to the velocity gradients by:

$$\tau_i = \rho \nu_T \frac{\partial u_i}{\partial z} \tag{5.88}$$

The eddy viscosity ν_T represents the turbulence in the water column. Often a parabolic distribution of the eddy viscosity is used; for a slope-driven current the turbulence is restricted by the bed and the surface and is largest in the middle of the water column. Furthermore, turbulence from different sources (wind-driven current, wave-breaking and increased turbulence in the wave boundary layer) can be taken into account. For wind-induced- and wave-breaking-induced turbulence, a maximum can be expected near the surface (which can be modelled by for instance a half-parabolic distribution).

Integration of Eq. 5.88 using an appropriate eddy viscosity distribution yields the velocity distribution over the vertical. For a parabolic eddy viscosity, we find a logarithmic velocity distribution.

Up to this point, we have considered the undertow and alongshore current in isolation. In reality, the wave-induced current has a 3D structure, as can be seen in Fig. 5.44.

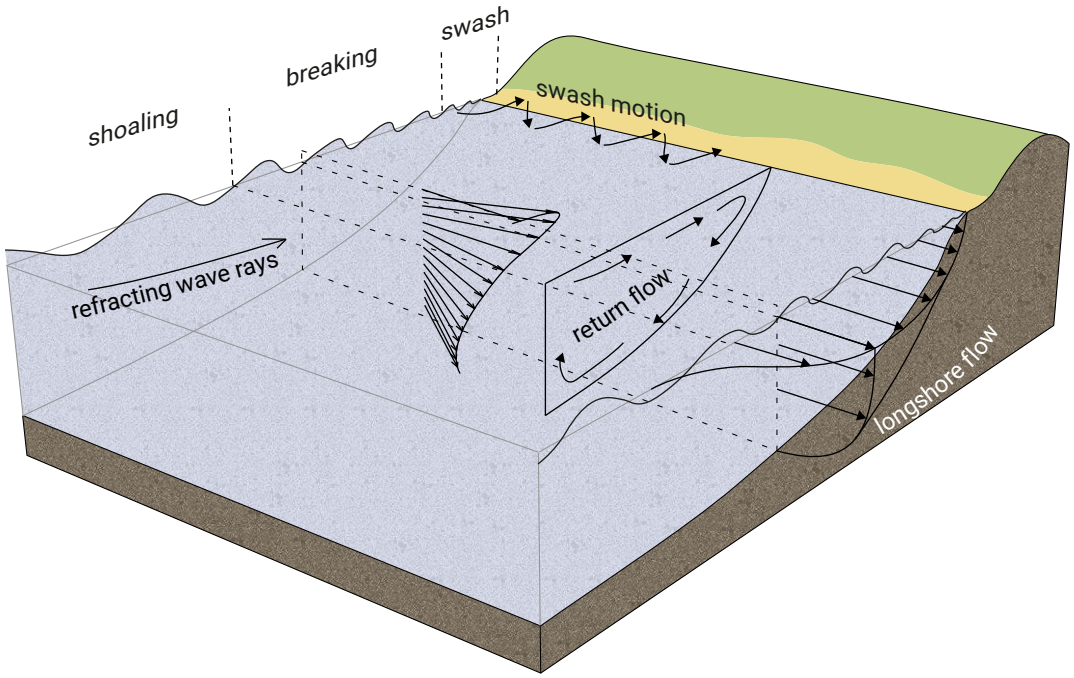

Figure 5.44: 3D structure of the wave-induced current profile in the surf zone, composed of the undertow and the alongshore current.

5.5.7. 3D effects

So far, we considered situations without alongshore variations. For various reasons however, wave conditions can vary along a certain stretch of coast; for instance due to wave refraction on a non-uniform nearshore region or due to wave diffraction in the lee side of structures. Wave-induced forces will vary according to changes in the wave conditions and the terms §1.1 $\partial S_{xx}/\partial y$ §1.1 $\partial S_{yy}/\partial y$ [p231] and $\partial S_{xy}/\partial y$ may be non-zero in Eqs. 5.55 and 5.57. Variations in wave height along a coastline create variations in cross-shore wave forces along the coast and hence in wave set-ups. Consequently, pressure gradients $\rho g h \, \partial\bar{\eta}/\partial y$ occur along the coast and 3D current patterns are the result. We will briefly discuss the following situations:

- Eddy formation in the shadow zone of structures;
- Creation of rip currents;
- 3D current patterns around shoals.

Eddy formation in the shadow zone of structures

In the case of wave sheltering due to for instance groynes or detached breakwaters, wave set-up can be expected to be less in the sheltered area than in the unsheltered region. This generates local nearshore currents towards the sheltered area. Figure 5.45 shows a situation at a groyne. In the shadow zone of the groyne, due to set-up differences a current runs towards the groyne, until it is diverted outward along the structure, creating an eddy.

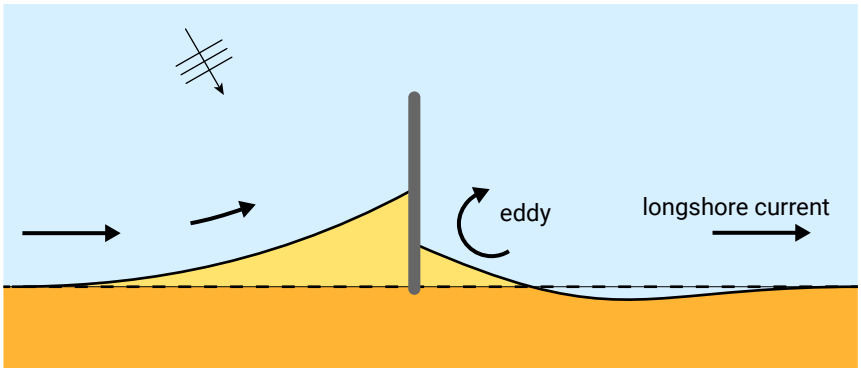

Figure 5.45: Current pattern in lee side of groyne (eddy formation). Note also that upstream (or updrift) of the breakwater, the longshore current diminishes slowly because of the decreasing angle of incidence.

In Fig. 5.46 set-up differences create nearshore currents towards the sheltered zone from both sides of the detached (emerged) breakwater. Continuity requires that water leaves the area as well. Therefore, a return flow will be present in deeper water, resulting in the development of two eddies. A characteristic flow pattern is generated (see Fig. 5.46).

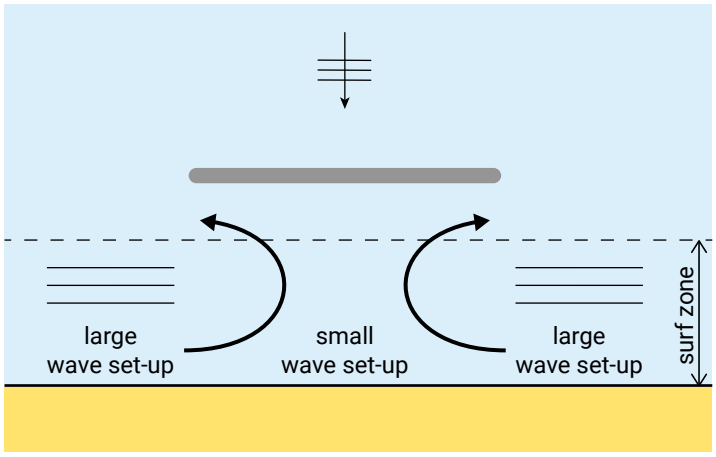

Figure 5.46: Current patterns behind a detached, emerged breakwater.

Rip currents due to convergence or divergence of wave energy

Rip currents are strong, narrow currents that flow seaward from the surf zone. They are fed by longshore-directed surf zone currents that turn seaward to form a rip current. The longshore currents are generated by set-up differences and run from the position of the highest set-up towards the position of the lowest set-up. The alongshore variation in wave set-up can be generated by convergence and divergence of wave energy due to depth refraction or sheltering effects due to for instance headlands. An undulating coastline gives concentration of wave energy towards the undulations due to depth refraction (Fig. 5.47b). The longshore currents run from the position of the highest waves and hence highest set-up to the position of the lowest waves. In this way, a rhythmic pattern of rip currents is generated. Such a situation will only be able to develop for nearly normal incidence; in the case of obliquely incident waves, a longshore current driven by gradients in radiation shear stress (Fig. 5.47a) will overshadow the more subtle effects of set-up differences. A combination of the two effects may occur for slightly oblique wave incidence (Fig. 5.47c).

Wave-induced currents around shoals (and submerged breakwaters)

In case of a complex topography with interrupted breaking, the pattern of wave-induced currents is more complicated. A still relatively simple example concerns a shoal on which waves are breaking (Fig. 5.48). Due to refraction, the waves will tend to converge toward the top of the shoal. As the waves break on the seaward slope of the shoal, they generate a dissipation-related wave force. At the top of the shoal, there is no closed boundary that requires a zero mean flow. Instead, the water will flow over the shoal in the direction of the force. The water flows over the shoal until it reaches the channel behind the shoal, where water level gradients will deflect it and drive it to the sides of the shoal. There it has room to flow seawards again, thus closing the circulation. In tidal inlets systems the wave-driven currents around shoals on the outer delta can be so strong that they dominate the tidal residual currents (see Sect. 9.4.1).

In a similar fashion, the interruption of wave-breaking can generate rip currents along a stretch of coast. Non-homogeneous wave-breaking can occur in the case of a non-homogeneous alongshore bar system or a (series of) submerged breakwater(s) on which waves break, see Fig. 5.49. (Partial) wave-breaking on the bar induces a set-up over the bar as well as an onshore flow. Water level gradients and continuity force the flow to deflect to the sides and return seaward in between the breakwaters or bars in a concentrated rip current.

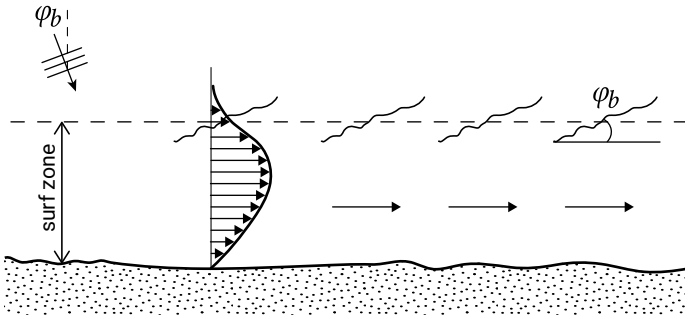

(a) typical longshore current distribution in case of obliquely incident waves

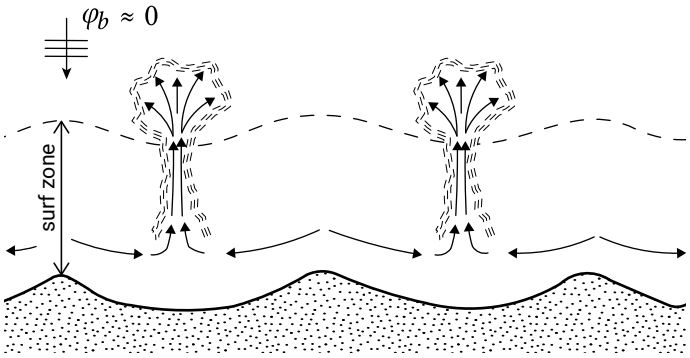

(b) rip current pattern for undulating coastline in case of approximately normal incidence

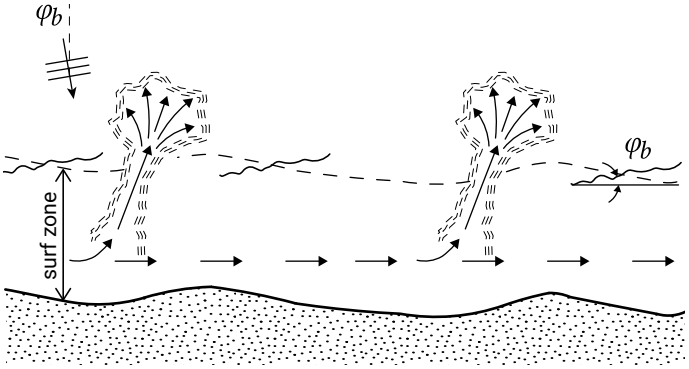

(c) combination of previous two cases for slightly oblique waves

Figure 5.47: Nearshore circulation patterns for different angles of wave incidence φ_b.

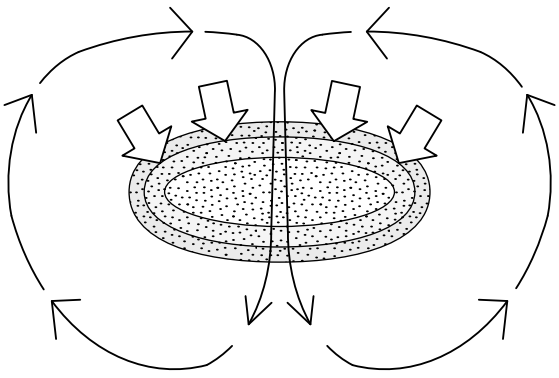

Figure 5.48: Wave-induced forces (white wider arrows) and currents (dark thinner arrows) around a shoal.

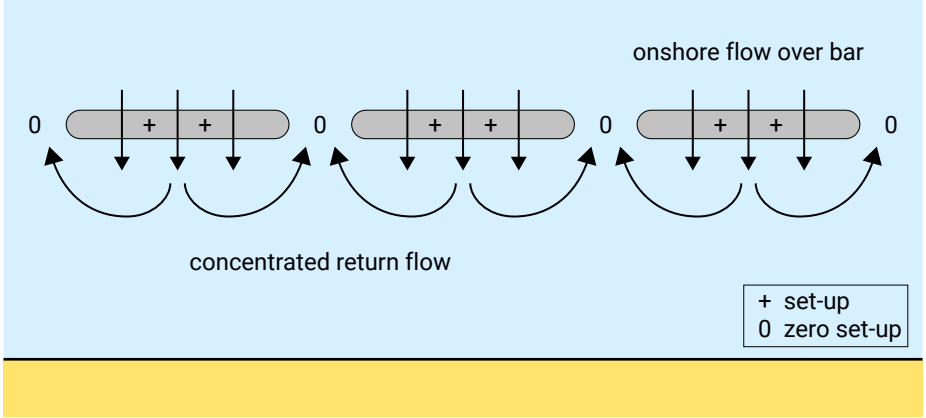

Figure 5.49: Rip currents in case of submerged breakwaters (or an interrupted bar system).

5.6. Wind-induced set-up and currents

Moving air exerts a shear stress τ on the water surface that can be modelled by, again, a quadratic friction law:

$$\tau_{\text{wind}} = C_d \rho_a W^2 \tag{5.89}$$

where:

τ_{wind}	wind shear stress	N/m^2
C_d	drag coefficient depending on wind velocity: $C_d = (0.63 + 0.066W) \times 10^{-3}$ for $2 < W < 21$ (Smith & Banke, 1975)	–
ρ_a	density of air ($1.25\,\text{kg/m}^3$)	kg/m^3
W	wind velocity at the water surface	m/s

Due to this wind shear stress, the upper parts of the water layers will start to move more or less in the same direction as the wind direction. When the wind is seaward directed, a seaward-directed current is generated in the upper water layers, the velocity of which is determined by the duration of the particular wind condition and its force. Similarly, a landward-directed wind will induce a landward current in the upper layers. However, a coastline forms a barrier for this landward current and in an equilibrium situation the mean onshore directed flow should be zero (just as with wave-induced flow). Therefore, to compensate for the landward- (or seaward-) directed water mass movement in the upper layers, an opposite-directed water mass transport follows in the lower water layers. In addition to these 'compensation currents', a water level set-up or set-down develops near the coast to balance the wind-induced shear stresses (see Fig. 5.50)

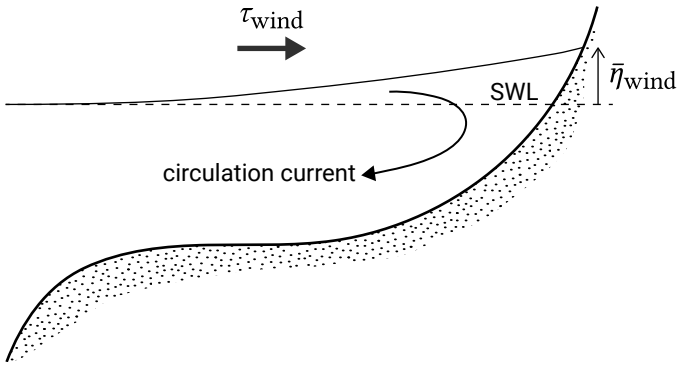

Figure 5.50: Wind set-up balancing wind shear stress in the case of onshore wind on a shelf. In the deep ocean, the water set into motion in the upper layers can easily spread out. Vertical exchange of water makes this possible. On the shelf there is no escape due to limited water depth and the surface water is driven ashore.

The equilibrium condition is given by:

$$\rho g h \frac{d\bar{\eta}}{dx} = \tau_{\text{wind},x} \tag{5.90}$$

Equation 5.90 shows that the wind set-up is inversely proportional to the water depth. Hence, in the shallow coastal zone (up to the shelf break) water can pile up to great heights (storm surge).

When the wind is directed parallel to a (long) coast, a longshore current is generated. It takes some time (order of magnitude one day) for the wind-driven current to develop completely. In the equilibrium situation and in the absence of other driving forces, the wind shear stress and the bed shear stress are equal, as was the case for the wave-induced longshore current.

The vertical distribution of the wind-generated current differs substantially from the current generated by a water level gradient (Fig. 5.51). The highest flow velocities occur at the water surface, with usually a rapid decrease in the downward direction (much more than with the logarithmic velocity profile).

During storms, the wind stress may have an important effect on the residual longshore current. Often, however, the effect of wind stress on the longshore current in the littoral zone can be neglected. Furthermore, the morphological impact is limited due to the relatively small velocities near the bottom, where the highest sediment concentrations occur.

Wind-driven currents are of greater importance in, for instance, coastal lagoons. The Dutch Wadden Sea is an example of a series of tidal basins in which wind-driven currents may play an important role. With dominant SW winds, a significant volume of water and sediment can be transported towards the east. This may lead to a gradual, but over the years continuing, shift of the watersheds between the barrier islands and

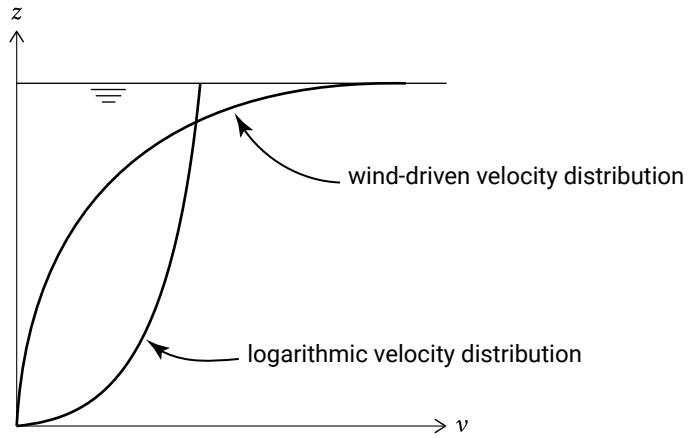

Figure 5.51: Typical velocity distribution for wind-driven current.

the mainland. FitzGerald and Penland (1987) hypothesise that this primarily wind-generated transport is the main force behind inlet migration in the German Wadden Sea.

In Sect. 1.4.6, the phenomenon of storm surge was introduced. A storm surge is like a raised dome of water due to the combination of strong onshore winds (causing the wind set-up described above) and lowered atmospheric pressure in a storm centre. The lower atmospheric pressure also raises the water level. The coastal topography of the North Sea (shallow and funnel-shaped) and its predominantly westerly winds make it very susceptible to storm surges. The severity of a storm surge depends on its timing relative to the tidal cycle and the duration of the storm system. A storm system with a long duration (a few days) coinciding with spring tide can result in severe flooding of coastal areas. For example, the storm surge height in the southern North Sea, resulting in the 1953 flood event, was 2.9 m and the storm duration was more than two days. In contrast, storm surges in the Bay of Bengal build up from tropical cyclones. Bangladesh experienced storm surge heights of around 9 m in 1970. Due to the lack of appropriate coastal protection, this surge resulted in a very large number of casualties (500 000).

5.7. Tidal propagation in coastal waters

5.7.1. Definitions

The vertical rise and fall of the water level is called the vertical tide or simply tide. High tide means high water levels, whereas low tide means low water levels (see Fig. 5.52). The rising period is the time it takes for the water level to get from the lowest elevation to the highest elevation, the falling period is the time it subsequently takes to reach the lowest level. The associated horizontal movement back and forward is the horizontal tide or tidal current. We speak about flood currents if the current velocity is in the

tidal wave propagation direction. Ebb currents are directed against the propagation direction.

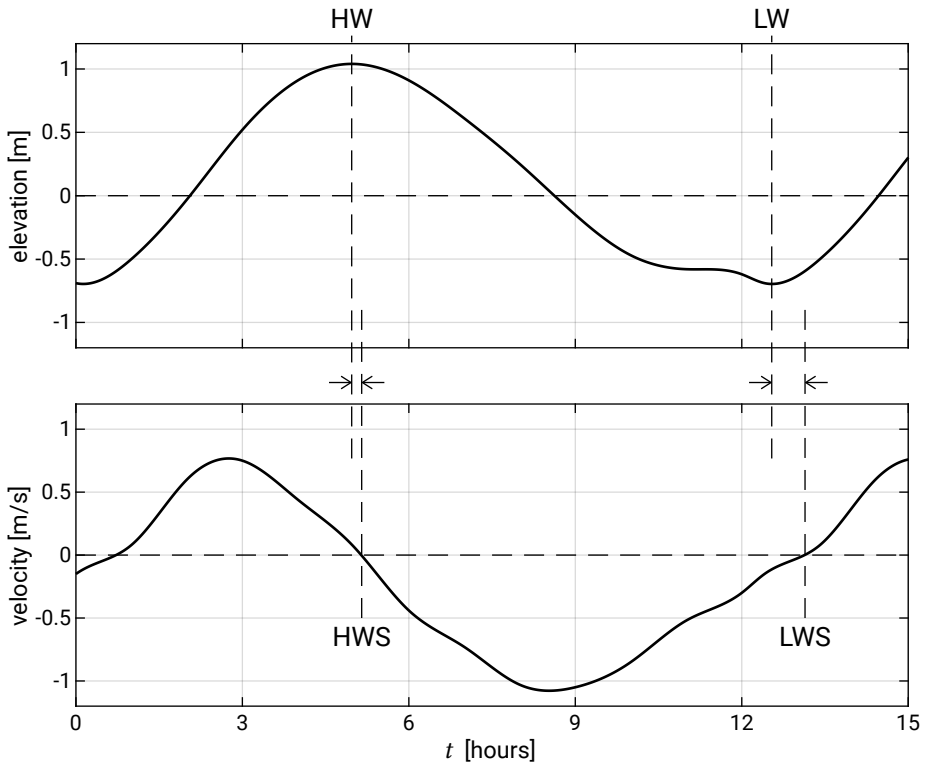

Figure 5.52: Vertical and horizontal tide in Rotterdam, where High Water Slack (HWS, flow reversal from flood to ebb) occurs shortly after HW, and Low Water Slack (LWS, flow reversal from ebb to flood) follows LW with a slightly larger time difference.

Although this seems clear, there is the danger of confusion. *Ebb* or ebb tide or ebb period may be used to indicate falling water levels as well as ebb currents. Due to the complex phase relationship between vertical and horizontal tide (see Sect. 5.7.2 and further), a falling tide does not necessarily coincide with ebb currents. To avoid any confusion, we use the words ebb and flood solely to refer to the *horizontal tide*.

Slack water is the name used for tidal flow reversal. We will see in Sect. 5.7.2 that the velocity generally leads the surface elevation in shallow water. As a consequence, flow reversal from ebb to flood occurs around low water and is therefore called Low Water Slack (LWS), see Fig. 5.52. High Water Slack (HWS) around high water occurs for flow reversal from flood to ebb. The term slack water *period* refers to the duration of slack water (i.e. the period of time during which current velocities are below some threshold)

5.7.2. Tidal propagation along the shore

Figure 5.53 shows measured water level (vertical tide), current velocity (horizontal tide) and current directions for a location a few kilometres off the Dutch coast.

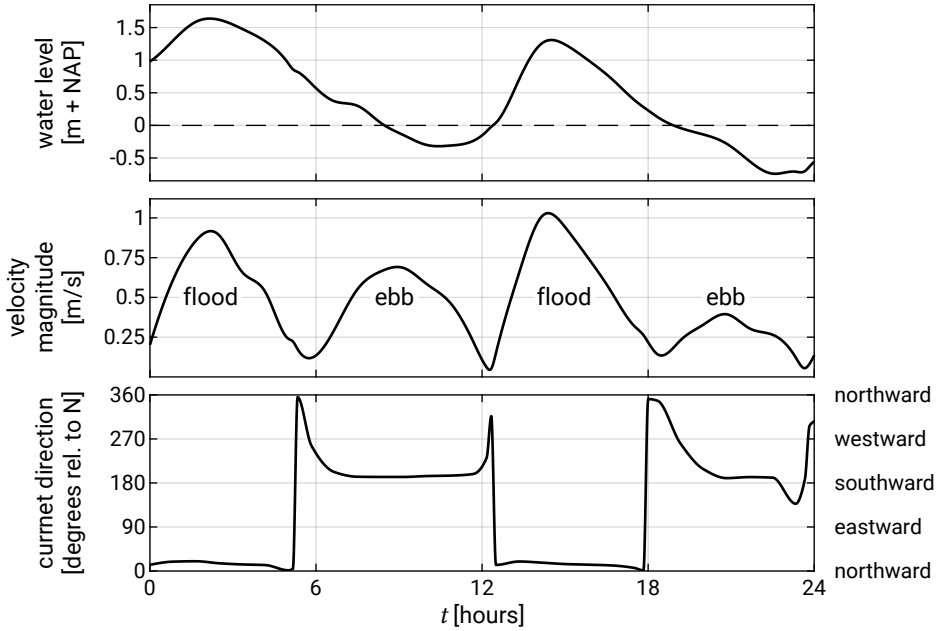

Figure 5.53: Water level (top panel), current velocity (middle panel) and current direction (lower panel) at the measuring location 'Stroommeetpaal IJmuiden' on the 21st of February 2020 (data source: https://waterinfo.rws.nl/). The location is about 500 m offshore from the entrance of the IJmuiden harbour.

The flood-tidal current runs in the northward direction along the Dutch coast and the ebb current runs southward, in accordance with the direction of the rotary wave in the ocean basins and seas in the Northern Hemisphere (Sect. 3.2). The flood and ebb velocities are at a maximum around high and low water respectively. The latter is typical of the propagation of the tide in relatively deep water, where bed friction has relatively little effect on the propagation. As explained in Sect. 3.8, under those circumstances, the tidal wave has a progressive character and water level and velocity are in phase (just as for wind waves). Figure 5.53 further shows that the tidal record deviates from an ideal symmetrical oscillation, which will be discussed later on in this section.

The effect of bottom friction

As previously, an alongshore uniform coast is considered with the y-axis defined parallel to the shoreline and the x-axis perpendicular to the shoreline. If the tidal elevation at lowest order is equal to $\eta(t) = a\cos(\omega t - ky)$, the alongshore tidal velocity can be written as $v(t) = V\cos(\omega t - ky - \varphi)$. For the M2 tide $\omega \approx 1.4 \times 10^{-4}\,\mathrm{s}^{-1}$.

For the Kelvin wave we found $\varphi = 0$ for the propagation alongshore (Sect. 3.8). With the flood velocity defined as positive, $\varphi = 0$ means that velocity and elevation are in phase (progressive wave). The Kelvin wave was found by solving the momentum balance in the x- and y-directions, Eqs. 3.42a and 3.42b, and the continuity equation Eq. 3.42c. We assumed that friction was very small compared to inertia.

In coastal engineering applications, we generally consider the tidal flow in a zone relatively close to the coast (order 10 km). In that case we cannot neglect friction. If we neglect the inertia term $\partial v/\partial t$ in Eq. 3.42b, but add a friction term, the momentum equation (in the alongshore y-direction) becomes:

$$\cancel{\frac{\partial v}{\partial t}} = \underbrace{-g\frac{\partial \eta}{\partial y}}_{\text{alongshore water level gradient}} \underbrace{-\frac{\tau_{by}}{\rho h}}_{\text{friction}} \tag{5.91}$$

inertia (local acceleration)

In this equation the alongshore pressure gradient $\partial\eta/\partial y$ is constant in the cross-shore direction (for the narrow coastal strip under consideration). Although a quadratic friction law is more appropriate, for simplicity we assume that the friction is linearly dependent on the alongshore tidal velocity: $\tau_{by} = \rho c_f v|v| \approx \rho r v$. Eq. 5.91 now reads:

$$g\frac{\partial \eta}{\partial y} = -\frac{r}{h}v \tag{5.92}$$

This equation suggests that the local nearshore water level gradient in a certain tidal phase is balanced by (linear) bed friction. Hence, the tidal velocity is not in phase with the tidal elevation, but with the negative alongshore water level gradient. Or, to put it simply: at any point in time the water flows from a location with high water to a location with low water (not different from river flow, with the difference that the tide reverses direction). In this example the phase difference $\varphi = -\pi/2$.

Figure 5.54 shows that for $\varphi = -\pi/2 = -90^\circ$ the velocity leads the elevation by a quarter period or about 3 hours for the M2 tide. Figure 5.54 shows also that for the special case of $\varphi = -\pi/2$:

- during the entire time it takes for the water to reach the lowest elevation (the falling period), the velocities are negative (ebb current);
- during the time it takes to reach the highest elevation (the rising period), the velocities are positive (flood current).

Thus: in case that the velocity leads the surface elevation by 90°, the falling period coincides with the ebb duration and the rising period with the flood duration.

In general, the phase relationship between vertical and horizontal tide is very complex. Not only friction but also (partial) reflections of the tidal wave introduce phase differences between velocity and elevation. Generally, the phase difference φ in coastal waters and basins varies between zero and $\varphi = -\pi/2$. If there is a phase difference between velocity and tidal elevation, it will be such that the velocity peaks before the tidal elevation.

The effect of friction is not only to introduce a phase difference between elevation and velocity, but to reduce their magnitudes as well, compared to the same frictionless

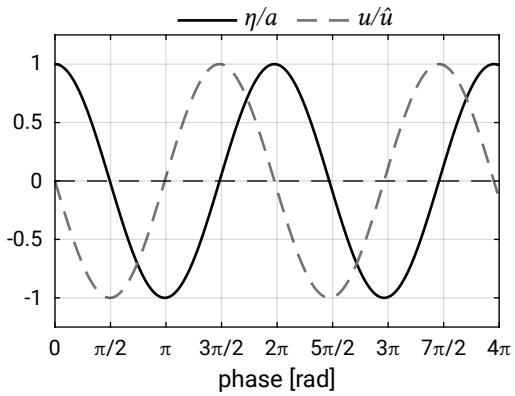

Figure 5.54: Tidal elevation and tidal velocity divided by their respective amplitudes. With flood velocities defined as positive, $\varphi = -\pi/2 = -90°$ means that the velocity leads the elevation by about 3 hours in the case of the M2 tide.

wave. In Sect. 5.7.3, the effects of friction and reflection are examined in more detail for the propagation into tidal basins.

Alongshore differences

Along the Dutch coast the tidal wave propagates northwards. We saw that at lowest order the tidal elevation and velocity along the coast (y-direction) can be described by $\eta = a\cos(\omega t - ky)$ and $v = V\cos(\omega t - ky - \varphi)$. This means that the phase ky of the tide increases (or in other words: the wave form is delayed) from the delta area in the south towards the Wadden area in the north. This can be seen from Fig. 5.55.

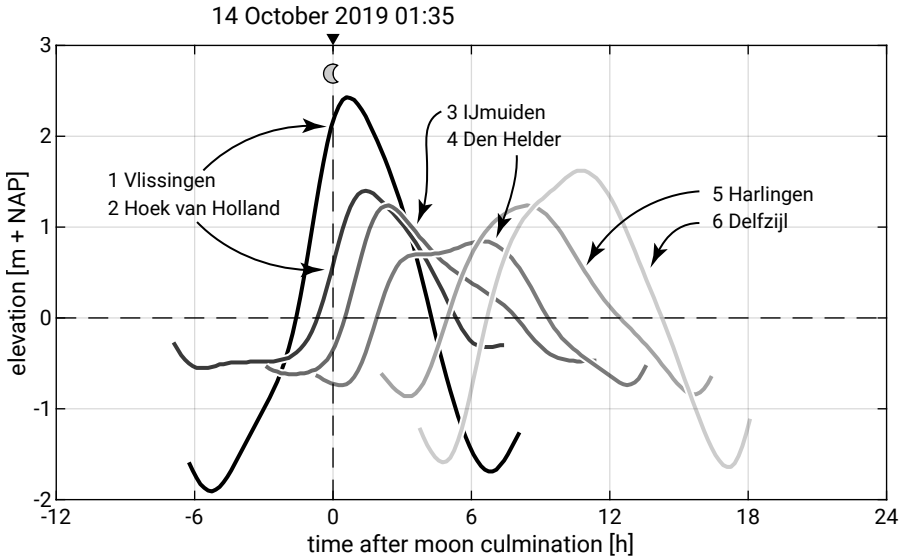

Figure 5.55: Tidal curves at six stations along the Dutch coast (data source: https://waterinfo.rws.nl/). The station numbers rise from south to north. The time in hours on the horizontal axis is relative to the moon culmination on October 14th 2019 01:35 (calculated using https://www.mooncalc.org). §1.2Note that MSL is approximately equal to NAP; current MSL is less than 0.1 m above NAP. [p242]

The figure shows that not only the phase ky differs along the coast, but the shapes and amplitudes as well. Figure 5.56 clearly shows that the tidal range is largest at Vlissingen (on average 3.8 m) and smallest around Den Helder (on average 1.3 m). Along the Holland coast, the central part of the Dutch coast, the average tidal range is 2 m at most[7]. Nevertheless, this tidal range is significantly larger than the tidal range from equilibrium theory. The alongshore differences are related to the position of the amphidromic points in the North Sea (see Fig. 3.31).

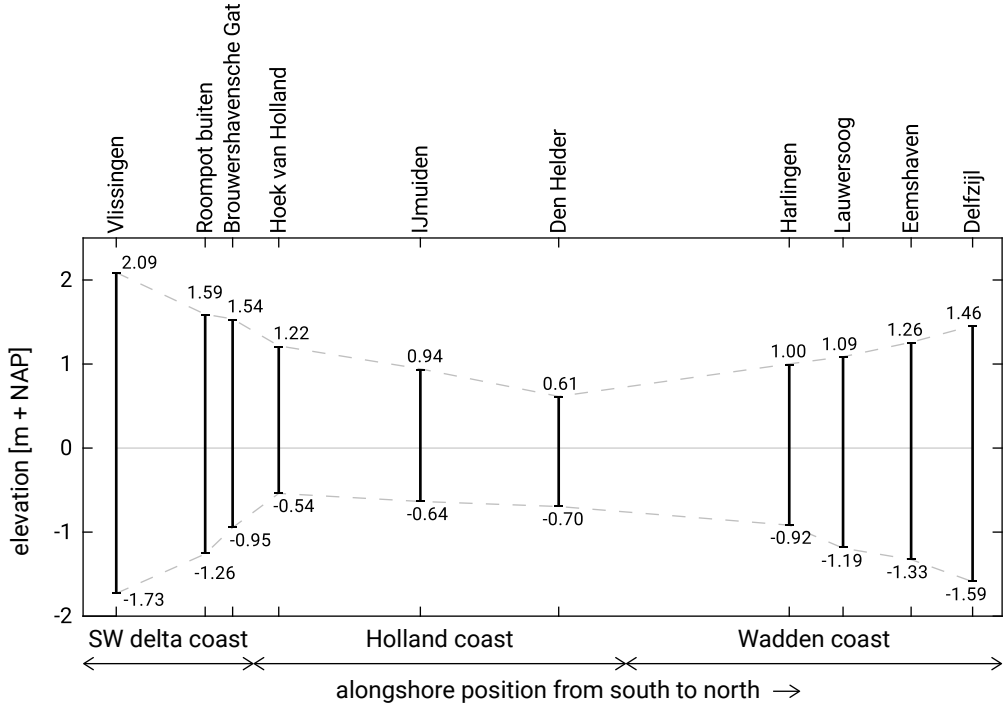

Figure 5.56: Average tidal range along the Dutch coastline. MHW and MLW are computed for each station as the yearly average of all recorded high waters and low waters in 2019 (data source: waterinfo.rws.nl). The x-axis denotes the alongshore position north of Vlissingen.

As opposed to the stochastic wind waves, the tidal motion is deterministic, viz. independent of weather or climatic conditions. Once the tidal constituents (amplitudes and phases) are known at certain measurement locations, the tide can be forecast. Using a model based on momentum and continuity equations and data from measurements made simultaneously at different points along the coast, the tide at locations different from the measurement locations can be forecast as well.

Skewness and asymmetry

Figures 5.55 and 5.56 indicate that the tidal curves deviate from an ideal symmetrical tide. We see that:

- §1.2 ~~High~~ §1.2 At some of the locations, high [p243] water is further above the mean than low water is below it; this also implies a shorter duration of positive water

[7] The *spring* tidal range, however, is everywhere at least 2 m. Therefore, the Dutch coast qualifies as a meso-tidal regime, see Sect. 4.4.1.

levels than negative water levels; this type of asymmetry is equivalent to the skewed wind waves in the shoaling zone, with long, flat troughs and narrow, peaked crests (see Sect. 5.3). In Vlissingen the skewness of the tidal elevation is positive and in Den Helder negative.
- the time it takes for the water to reach the lowest elevation (the falling period) is not equal to the time it takes to reach the highest elevation (the rising period). The resulting shape of the tidal curve is asymmetric about the vertical axis, comparable with the asymmetry in wind waves just before breaking.

Figure 5.57 shows in more detail an average tidal curve for Vlissingen. It shows a falling period of 6.28 h and a rising period of 5.57 h. Although the exact ratios vary, for all stations along the Dutch coast the falling period is longer than the rising period. For instance, in IJmuiden the falling period and rising period are 8.03 h and 4.22 h respectively. This phenomenon is often referred to as *tidal asymmetry*.

The longer falling period can be explained from the phase velocity for shallow water $c = \sqrt{g(h+\eta)}$. For high tide (η positive), the propagation velocity is larger than for low tide (η negative). Since the high tide (the wave crest) propagates faster than the low tide (the trough), the rising period is smaller than the falling period. This generally holds for the open coast, but in basins this may be different.

When it is said that the (vertical) tide is flood-dominant, this refers to a shorter rising than falling period. Vice versa, ebb dominance indicates a shorter falling period. For the reasons mentioned in Sect. 5.7.1, the terms flood and ebb dominance in relation to the vertical tide may be confusing. We will therefore use flood (or ebb) dominance only to indicate the direction of *net sediment transport* (see Sect. 9.7) as a result of asymmetries of the *horizontal tide*.

Like the vertical tide, the horizontal tide may display both skewness and asymmetry:

- the average peak flood current may be stronger than the average peak ebb current, which leads to a shorter flood duration than ebb duration (or vice versa);
- the velocity signal may be asymmetric around the vertical, which means that the rate at which the velocity changes around slack water (i.e. flow reversal) is different when changing from ebb to flood than when changing from flood to ebb (see for instance Fig. 5.52).

Figure 5.53 shows that if the horizontal and vertical tide are in phase, the skewed and asymmetric tidal elevation directly translates to similar characteristics for the tidal velocity. In basins the relationship between the vertical and horizontal tide can be more complex. Tidal asymmetry will be discussed in more detail in Sect. 5.7.4.

Cross-shore distribution of the tidal velocity

Surface waves refract towards the coast and generate a longshore current along the coast. Tidal propagation tends to be along a coast or channel. Hence, both wave-induced longshore currents and tidal currents are mainly parallel to the coast (see

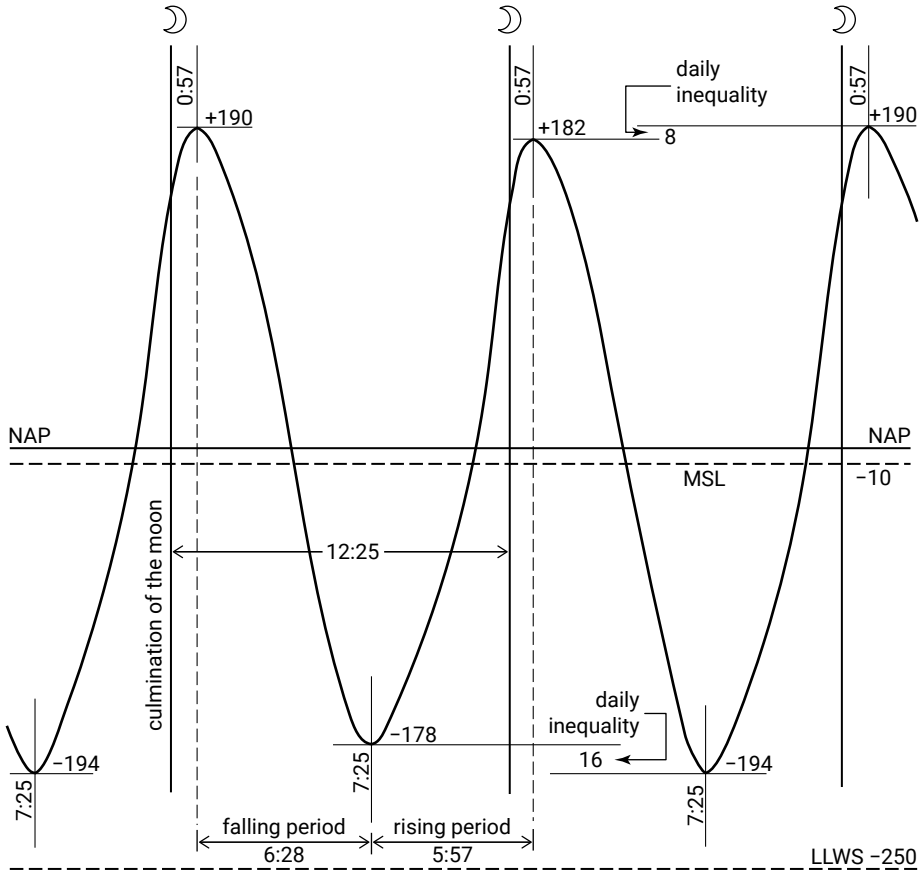

Figure 5.57: Average tidal curve in Vlissingen (adapted from Rijkswaterstaat, 1949). Time (horizontal axis) in hours and height (vertical axis) in cm. Note that MSL is shown as being below NAP, which is nowadays not the case any longer.

Fig. 5.58). The direction of the tidal current reverses during the tidal cycle. Alongshore tidal velocities in shallow water can be anything from a few decimetres per second to several metres per second.

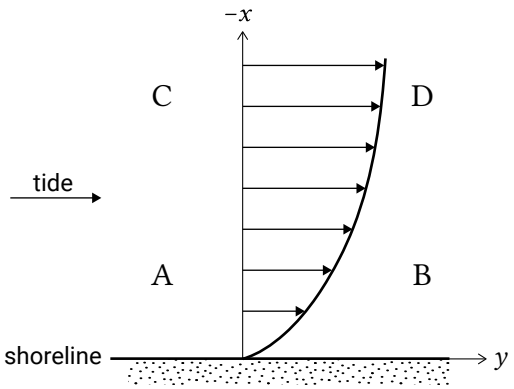

Figure 5.58: Tidal current along the shore. The negative $x-$axis and positive $y-$axis are indicated.

In very shallow water, the inertia effect is small and the velocity at any moment in the tide is governed by the balance between alongshore water level gradient and friction.

According to Eq. 5.92, the velocity magnitude is, at every moment of the tidal phase, linearly dependent on the water depth and the alongshore water level gradient. If we use a quadratic friction law with a constant friction factor, the velocity magnitude is proportional to the square root of the product of water depth and alongshore water level gradient:

$$v \propto \sqrt{h\frac{\partial \eta}{\partial y}} \tag{5.93}$$

If the tidal velocity at one particular water depth is known, for instance from measurements, then a very practical method for finding the cross-shore distribution of the velocities is by using Eq. 5.93. This leads to:

$$v_2 = v_1\sqrt{\frac{h_2}{h_1}} \tag{5.94}$$

where:

$v_{1,2}$	tidal current velocities at cross-shore positions 1 and 2	m/s
$h_{1,2}$	still water depth at points 1 and 2	m

Note that in this approach it is assumed that the alongshore water level gradient does not vary in the cross-shore direction (the water level difference between D and C in Fig. 5.58 is equal to the difference between B and A). Following this simple approach, a tidal alongshore velocity of 0.7 m/s at a water depth of 10 m yields a tidal velocity of 0.3 m/s at a water depth of only 2 m. In this shallow region, with 2 m water depth, waves can be very effective in increasing bed shear stress (the wave boundary layer acts as an extra resistance for the flow). Consequently, the tidal velocities in the wave-influenced littoral zone will even be smaller.

Effect of tide on wave-generated longshore current

The tide influences the wave-generated longshore current in the breaker zone. One complicating factor here is that the direction of the tidal velocity changes twice during one tidal cycle. The appropriate way to include the effect of tides is first to combine the driving forces (during ebb and flood periods) and then to calculate the velocity. Simply adding the tidal velocity to the wave-induced longshore current is not correct (that would only be possible if the velocity is a linear function of the driving force, which is not the case).

Figure 5.59 shows the velocity distribution for the combination of wave-generated currents with ebb and flood tidal velocities. The maximum tidal velocity occurs outside the breaker zone, but the effect inside the breaker zone can be quite substantial. If the

tidal force is in the same direction as the wave-driven current, the maximum alongshore flow velocity increases (and shifts towards the breaker line). If the tidal force is in the opposite direction, the maximum velocity decreases (and shifts towards the shoreline). The longshore current in the breaker zone, although reduced in velocity, might then be in the opposite direction as the tidal current present further seawards.

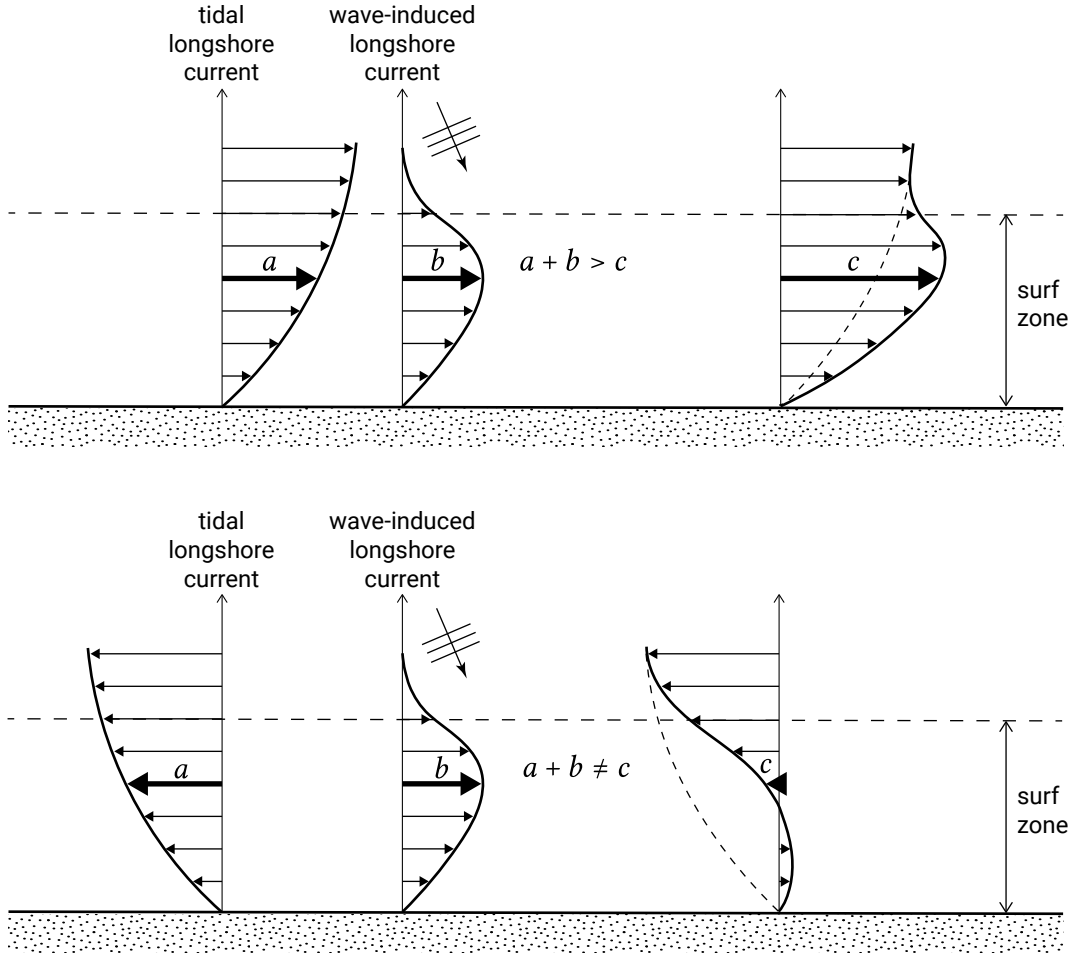

Figure 5.59: Combination of wave-induced and tidal longshore currents at two different phases of the tide: (a) tidal current; (b) wave-induced longshore current and (c) combination of the two. In order to compute the combination, the driving forces rather than the velocities must be added.

If the wave-induced alongshore driving forces are large enough relative to the tidal forces, the tidal current in the breaker zone may be overshadowed by the wave-induced longshore current. Flow reversal with the tide may not occur.

Tidal currents may significantly complicate the determination of the longshore current in the breaker zone. In practical cases, like for instance for the Dutch coast, it will be necessary to establish the longshore current throughout the entire tidal cycle. Only in areas with weak tidal forces (for instance the Mediterranean) the effect of tides on the water movement in the breaker zone can be neglected.

Tidal currents around structures

Structures tend to divert the tidal flow especially when they extend far seaward. The harbour moles of IJmuiden, the sea port of Amsterdam, were extended to approximately 2500 m in the period 1962 to 1968. The convergence of the tidal flow (contraction of the streamlines) around this breakwater led to relatively high velocities in front of the harbour entrance, where subsequently a scour hole developed. Another example is the long dam that was constructed at the Dutch Wadden island of Texel in 1995.

Figure 5.60 schematically shows the deflection of tidal currents by IJmuiden harbour. Due to the tidal variation, the flow field is not stationary. The depicted flow field represents the ebb flow. Near the harbour entrance a flow contraction can be noticed, while downstream from the harbour moles, an eddy is visible. A simple rule of thumb states that the alongshore length of the eddy should be – in a stationary situation – around six times the length of the harbour mole. Due to the tide reversal, however, the growth of the eddy is restricted. The flow patterns have implications for the sediment transport and resulting morphology.

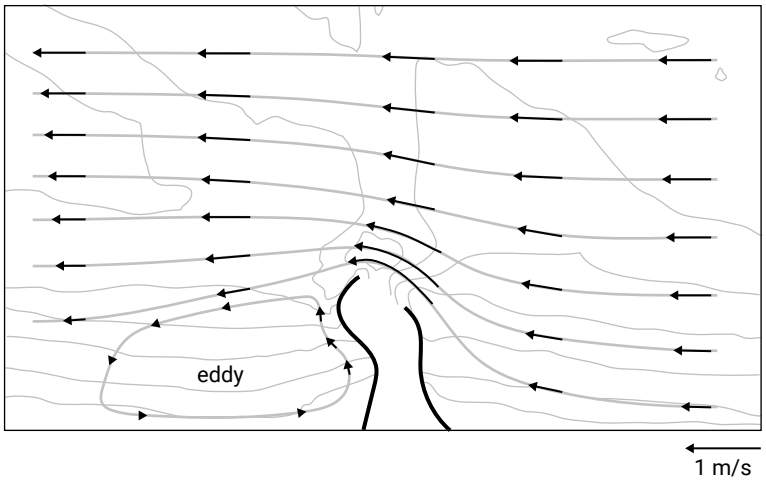

Figure 5.60: Schematic representation of the ebb flow field in the vicinity of IJmuiden harbour.

§1.1 ~~In this study the harbour basin itself was not included in the computation.~~ §1.1 In the computation that this schematic was based on, the harbour basin itself was not included [p247]. The tidal flow passing the harbour entrance can drive an eddy in the harbour basin. This can lead to an exchange of water and sediment between the harbour and the area outside.

5.7.3. Tidal propagation into basins

In tidal basins we generally find a main channel, which transports the majority of the ebb and flood discharge. It is along this main channel that the tidal wave is primarily

propagated. If we choose to align the x-axis with the channel-axis, we may approximate the tidal propagation with a set of one-dimensional equations. These are the balance equations for mass and momentum in the x-direction.

To derive these equations, we schematise the cross-section $A(x,t)$ of the basin with a width b into two parts. One part represents the flow carrying part of the cross-section, discharging all the flow; the other part is the storage part, which only stores water without discharging, see Fig. 5.61. The storage part represents the tidal flats that are covered during higher water and are exposed during lower water.

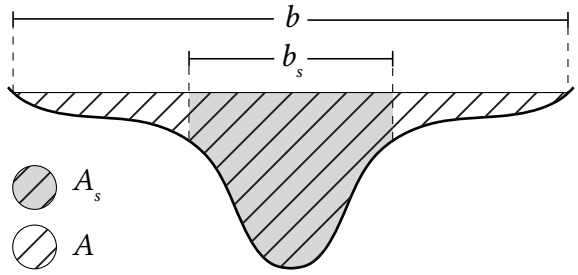

Figure 5.61: Definition of cross-sectional parameters.

The flow-carrying cross-section has an area $A_s(x,t)$, which is the product of a flow-carrying width $b_s(x,t)$ and a representative instantaneous depth $h(x,t)$. This depth $h(x,t)$ is the sum of the representative flow-carrying water depth $h_0(x,t)$ relative to a horizontal mean water level and the tidal level $\eta(x,t)$. The mean flow velocity in the flow-carrying cross-section (averaged over the total cross-section) is indicated as $u_s(x,t)$. The flow-carrying cross-section can be written as $A_s = b_s h = b_s(h_0 + \eta)$. The tidal discharge through this cross-section is $Q = A_s u_s$.

The one-dimensional balance equations are derived for an infinitesimal short section in the basin. The mass balance (continuity equation) yields:

$$\underbrace{\frac{\partial}{\partial x}\left(A_s u_s\right)}_{\substack{\text{volume change}\\ \text{due to in- and}\\ \text{outgoing transport}}} + \underbrace{b\frac{\partial \eta}{\partial t}}_{\substack{\text{volume change}\\ \text{due to water}\\ \text{level change}}} = 0 \quad \Leftrightarrow \quad \frac{1}{b}\frac{\partial}{\partial x}\left(b_s h u_s\right) + \frac{\partial \eta}{\partial t} = 0 \tag{5.95}$$

The mass balance equation can be simplified with $b = b_s$ (no intertidal storage areas), and under the assumption of a prismatic channel (cross-sectional shape and size and bottom slope are constant along the channel, hence b is independent of x). This gives:

$$\S1.1\ \frac{\partial}{\partial x}(\cancel{hu}) = \frac{\partial \eta}{\partial t} = \cancel{0}\ \S1.1\ \frac{\partial}{\partial x}(hu) + \frac{\partial \eta}{\partial t} = 0\,[\text{p249}] \tag{5.96}$$

Note that for convenience we have dropped the subscript s for u. The total water depth can be taken outside of the x-derivative for a small ratio of tidal amplitude over water depth and a prismatic channel. Compare this equation to Eq. 3.41.

The momentum balance reads:

$$\underbrace{\frac{\partial}{\partial t}\left(A_s u_s\right)}_{\substack{\text{momentum}\\ \text{change}}} + \underbrace{\frac{\partial}{\partial x}\left(A_s u_s^2\right)}_{\substack{\text{in- and outflow}\\ \text{of momentum}}} + \underbrace{g A_s \frac{\partial \eta}{\partial x}}_{\substack{\text{pressure}\\ \text{gradient}}} + \underbrace{\frac{b_s}{\rho}\tau_b}_{\substack{\text{bottom}\\ \text{friction}}} = 0 \tag{5.97}$$

With $b = b_s$ and under the assumption of a prismatic channel (so that A_s does not vary with x), we find the 1D shallow water tidal propagation equation:

$$\frac{\partial u}{\partial t} + u\frac{\partial u}{\partial x} + g\frac{\partial \eta}{\partial x} + \frac{\tau_b}{\rho h} = 0 \tag{5.98}$$

Here, we have again dropped the subscript s for u.

By conducting a scale analysis, it can be shown under what conditions which terms are of similar order of magnitude and which terms may be neglected. For typical orders of magnitude of the tidal amplitude to water depth ratio $a/h = \mathcal{O}(10^{-1})$ and $h \approx \mathcal{O}(10\,\mathrm{m})$ the advective (second) term on the left-hand side can be neglected.

For simplicity we assume a linear friction law $\tau_b = \rho c_f |u| u \approx \rho r u$. We get:

$$\frac{\partial u}{\partial t} + g\frac{\partial \eta}{\partial x} + \frac{r}{h}u = 0 \tag{5.99}$$

Compare the above equation to Eqs. 3.40a and 3.40b and Eq. 5.91.

As in Intermezzo 3.5, we take the $\partial/\partial t$ of the continuity equation (Eq. 5.96) and [§1.2]subtract [§1.2]$h\partial/\partial x$ [p249] of the momentum equation (Eq. 5.99). For a small tide (a/h small) this leads to:

$$\frac{\partial^2 \eta}{\partial t^2} - gh\frac{\partial^2 \eta}{\partial x^2} + \frac{r}{h}\frac{\partial \eta}{\partial t} = 0 \tag{5.100}$$

This equation has elements of the classical wave equation (Eq. 3.35) and of a diffusion equation (last two terms of the left-hand side).

We can implement further simplifications depending on the relative magnitude of the inertia (local acceleration) and friction term. In many shallow tidal basins, the flow is friction-dominated. The inertia term may then be neglected to a first approximation.

Friction-dominated flow

Consider a shallow estuary for which friction dominates inertia. The basin is long, i.e. all tidal energy is dissipated in the basin before the tide reaches the end of the basin.

In a straight basin Eq. 5.100 is valid. For friction-dominated flow, Eq. 5.100 reduces to a diffusion equation (the last two terms remain):

$$\frac{\partial \eta}{\partial t} = D\frac{\partial^2 \eta}{\partial x^2} \tag{5.101}$$

in which $D = gh^2/r$ is the tidal diffusion coefficient. The solution to this equation can be shown to be:

$$\eta(x,t) = ae^{-kx}\cos(\omega t - kx) \quad \text{with} \quad k = \sqrt{\frac{\omega}{2D}} \tag{5.102}$$

From substitution in the continuity equation, Eq. 5.96, we get:

$$u(x,t) = \frac{a}{h}\sqrt{\omega D}e^{-kx}\cos(\omega t - kx + \pi/4) \tag{5.103}$$

The amplitudes of the horizontal and vertical tide are progressively damped with distance x from the inlet. Furthermore, the velocity leads the surface elevation by 45°. The phase speed $c = \omega/k$ is given by $c = \omega/k = \sqrt{2\omega D}$. Note that this differs from the phase speed of a linear progressive wave $c = \omega/k = \sqrt{gh}$.

Note that with a quadratic friction law (instead of the simple linear approximation) the tidal diffusion coefficient is dependent on the flow magnitude and therefore varies strongly over the tidal period. This non-linear character implies that the basin deforms the tidal wave during diffusion and it loses its sinusoidal character. The symmetry between ebb and flood is broken.

Around slack water the flow will not be described correctly by the tidal diffusion equation; during the slack waters friction is not dominant. The tide then propagates approximately as an undamped wave (see the progressive wave solution of the classical wave equation of Intermezzo 3.5).

The Dutch former Zuiderzee is an example of a tidal basin of such length that the tidal wave at the end of the basin was nearly damped out. The tidal wave entering through the Texel Inlet or Marsdiep and the Vlie Inlet was largely damped out at Amsterdam and the Veluwe banks. In tidal rivers (where the river flow velocity and the tidal flow velocity are of similar order) we also find slowly-damping propagating tidal waves, e.g. the Lek and the Waal in the Netherlands and the St. Lawrence river in Canada. In these tidal rivers, the reflected tidal wave is negligibly small, so that the tide has the character of an inland-diffusing wave. See Fig. 5.62.

Inertia-dominated flow

Let us now consider the (mostly unrealistic) case of negligible friction. Eq. 5.100 reduces to the classical second-order wave equation. We have already seen this equation

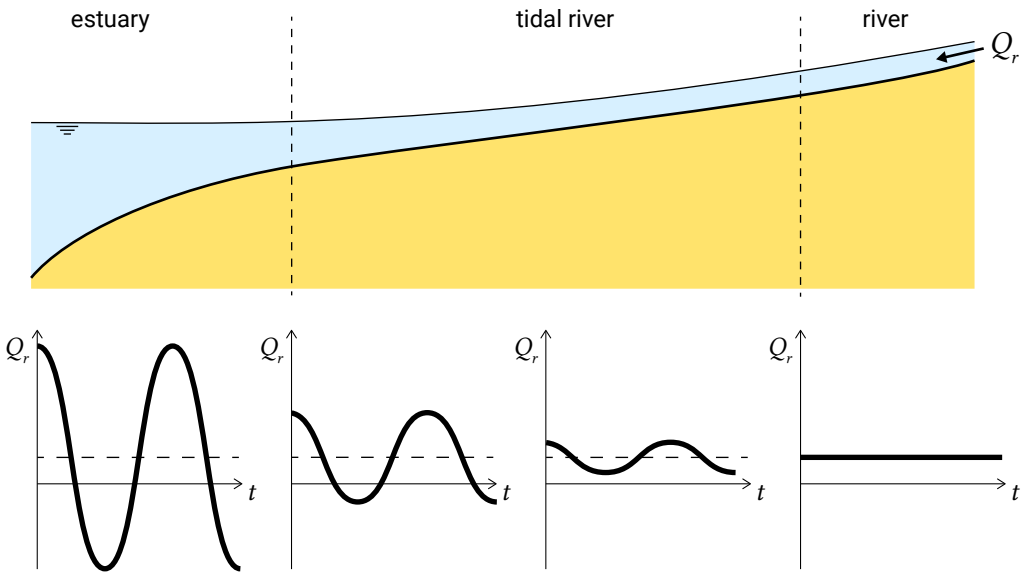

Figure 5.62: In a tidal river, the river and tidal discharge are of the same order of magnitude.

when discussing tidal propagation in seas and ocean basins (Eq. 3.35). This equation allows wave propagation in two directions (in positive and negative direction along the channel axis). Since the incident tidal wave is not damped by friction, it is reflected at the basin end $x = L_b$. The surface elevation at the inlet $x = 0$ must be equal to a sinusoidal open sea or ocean tide $\eta(0,t) = a\cos\omega t$. This results in a standing tidal wave:

$$\eta(x,t) = \frac{1}{2}\frac{a}{\cos kL_b}[\underbrace{\cos\left(\omega t - k\left(x - L_b\right)\right)}_{\text{incident wave}} + \underbrace{\cos\left(\omega t + k\left(x - L_b\right)\right)}_{\text{reflected wave}}] =$$

$$= a\frac{\cos\left(k\left(L_b - x\right)\right)}{\cos kL_b}\cos\omega t \tag{5.104a}$$

$$u(x,t) = \frac{1}{2}\frac{ac}{h\cos kL_b}\left[\cos\left(\omega t - k\left(x - L_b\right)\right) - \cos\left(k\left(x - L_b\right) + \omega t\right)\right] =$$

$$= -\frac{ac}{h}\frac{\sin\left(k\left(L_b - x\right)\right)}{\cos kL_b}\sin\omega t \tag{5.104b}$$

In Eq. 5.104b, c is the phase speed and $c = \sqrt{gh}$. Water level and flow velocity are 90° out of phase, as can be seen from the terms $\cos\omega t$ and $\sin\omega t$ in Eqs. 5.104a and 5.104b respectively. This is an important characteristic of a standing wave pattern.

The amplitudes along a basin are sketched in Fig. 5.63. The amplitude of the tidal elevation along the estuary varies according to $\cos(k(L_b - x)) = 0$. Hence, the standing wave has a maximum amplitude (or antinode) in the surface elevation §1.1 ~~at~~ §1.1 for

$k(L_b - x) = 0$ [p252], i.e. at the landward end $x = L_b$. The tidal amplitude at the landward end is therefore larger than that at the seaward end. The antinode in the surface elevation corresponds to a minimum (or node) in the velocity amplitude; at the landward end the velocity is zero. This can be seen from the term $\sin(k(L_b - x))$[§1.1] ~~$= \pi/2$~~ [p252] in Eq. 5.104b.

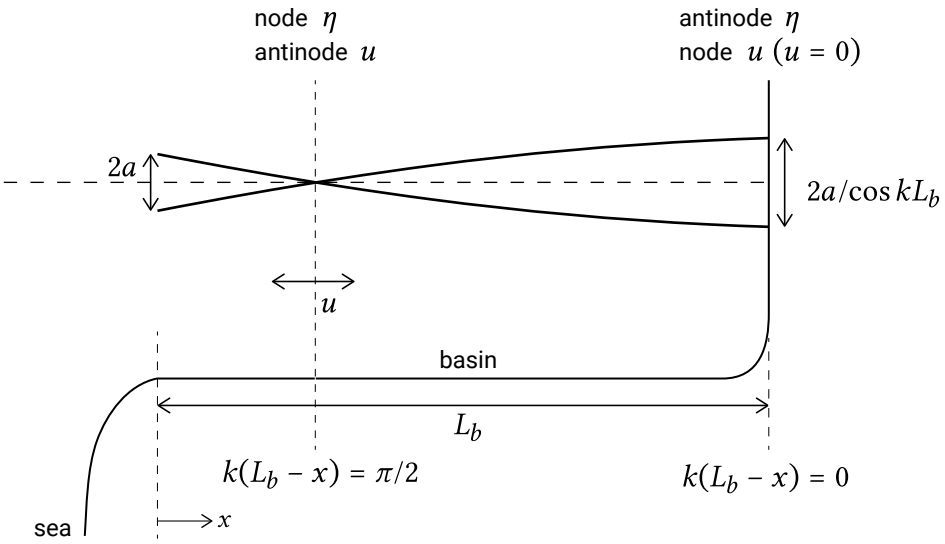

Figure 5.63: Standing wave pattern in a tidal basin.

If the basin is long enough, a node in the elevation (zero amplitude) and an antinode in the velocity (maximum amplitude) will occur for $k(L_b - x) = \pi/2$. The longer the basin, the more nodes and antinodes it can accommodate.

The amplitudes of both the vertical and horizontal tide are inversely proportional to $\cos kL_b$. If $kL_b = \pi/2, 3\pi/2, \ldots$, then $\cos kL_b = 0$ which means that the amplitudes of η and u become infinitely large. Note that $kL_b = \pi/2$ is equivalent to $L_b = {}^1\!/_4 L$. So, resonance occurs for basins with a basin length equal to a quarter of the tidal wavelength L or an uneven multiple of a quarter wavelength.

Resonance occurs because for $kL_b = \pi/2$ the incident and reflected wave cancel each other at the mouth, or, in other words, we have a node of the surface elevation at the mouth. The amplitude of the vertical tide at the mouth is therefore zero relative to the amplitude in the basin. At the same time we had the condition that the tide at the mouth was equal to the ocean tide $\eta(0, t) = a \cos \omega t$. Since this must be zero relative to the tide in the basin, the amplitude in the basin must go to infinity. In reality, this would not occur, since bed friction would dampen the amplitudes.

So far, we considered a sinusoidal tidal motion and thus a single tidal frequency. In reality, more tidal constituents are present. If the natural period of a basin is close to the period of one of the tidal constituents, that constituent will be amplified by resonance more than others.

Combination of friction and inertia

In most tidal basins both friction and inertia play a role. The tidal wave can be described as the superposition of an incoming and a reflected damped wave. Without friction a standing wave pattern will result. With friction, the incoming (and reflected) wave is partly damped, so that the result is a total surface elevation pattern that has a partly propagating and partly standing character.

Figure 5.64 shows the ratio of the amplitude of a harmonic tidal component at the end of the basin over the amplitude at the mouth. Depicted is the solution of the 1D tidal propagation in a prismatic basin for various values of $s_1 = r/h\omega$. Check from Eq. 5.100 that s_1 is the ratio between the friction term and the local acceleration term. For $s_1 = r/h\omega = 0$, we recognise the frictionless situation with resonance for $L_b = {}^1\!/_4 L$ and ${}^3\!/_4 L$. For large values of s_1, the damping of the tide due to friction can be recognised. The values in between are a combination of both effects.

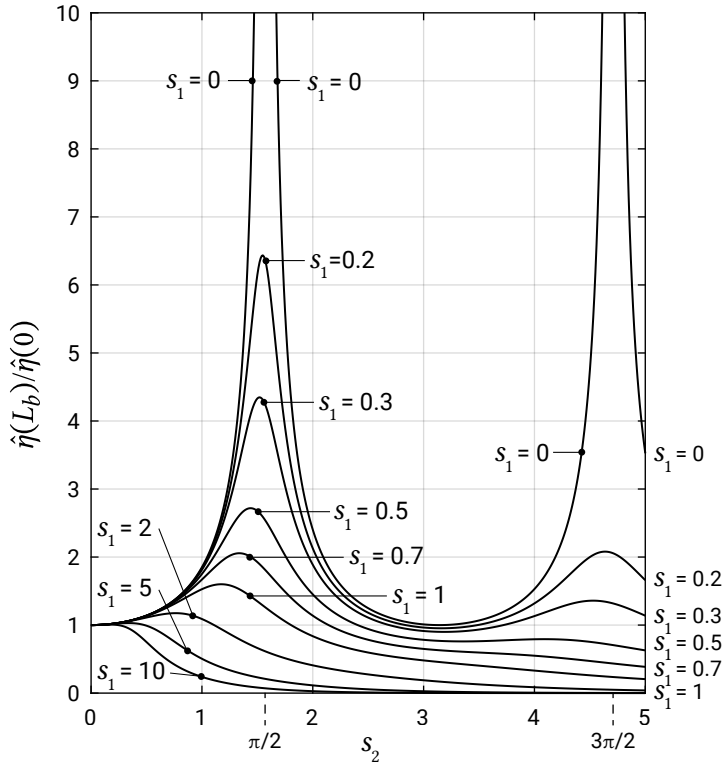

Figure 5.64: Tidal propagation in a prismatic basin (linear solution). The variable on the horizontal axis is the basin length in terms of $s_2 = \omega L_b/\sqrt{gh} = k_{r=0} L_b$ with $k_{r=0}$ the wavenumber for the frictionless situation. The amplification factor on the vertical axis is the tidal amplitude at the basin end over the tidal amplitude at the mouth. The amplification factors are shown for different values of $s_1 = r/(h\omega)$. Note that $s_2 = \pi/2$ and $s_2 = 3\pi/2$ are equivalent to $L_b = {}^1\!/_4 L_{r=0}$ and ${}^3\!/_4 L_{r=0}$, respectively, with $L_{r=0}$ the tidal wavelength for the frictionless situation. These are the conditions for resonance found in the previous paragraph on inertia-dominated flow.

Width convergence and shoaling

So far we have only considered prismatic basins. In such basins, dissipation of energy due to friction inevitably dampens the tidal amplitude.

In the case of a funnel-shaped estuary, the cross-section is largest at the inlet and then gets progressively smaller. This gives a convergence of tidal energy that increases the tidal amplitude along the channel axis. The balance between the counteracting effects of energy loss due to friction and energy convergence due to width restriction determines whether the tidal amplitudes increase or decrease along the channel axis. Note that a rapid convergence of energy for the incident wave implies a rapid divergence of energy for a reflected wave.

Progressive shallowing of a basin gives a similar concentration of wave energy counteracting the dampening by friction. The reason is that the propagation speed becomes smaller in smaller water depths. This is identical to the phenomenon of shoaling in wind waves (see Sect. 5.2.2).

In the case of gradual changes in width and depth (no reflection on the sides or on a sill) and, in the absence of friction, the energy is conserved along the channel axis. Analogous to Eq. 5.9 we have:

$$Encb_s = \text{constant} \rightarrow \hat{\eta}^2\sqrt{gh}b_s = \text{constant} \rightarrow \frac{\hat{\eta}_2}{\hat{\eta}_1} \propto \left(\frac{h_1}{h_2}\right)^{1/4}\left(\frac{b_{s1}}{b_{s2}}\right)^{1/2} \tag{5.105}$$

According to this equation, width reduction has a stronger effect on the tidal amplitude than depth reduction.

Storage considerations and short basins

A short basin has a length that is short relative to the tidal wavelength: $L_b \ll {}^1/_4 L$, say $L_b < {}^1/_{10} L$ or $L_b < {}^1/_{20} L$. For such a short basin we can find a solution for the tidal elevation and velocity based on the continuity equation alone. Let us first look at the general continuity equation Eq. 5.95. It can be written as:

$$-\frac{\partial Q}{\partial x} = b\frac{\partial \eta}{\partial t} \tag{5.106}$$

Integration along the channel axis from a location x to the end of the basin gives:

$$Q(t,x) = \int_x^{L_b} b\frac{\partial \eta}{\partial t}\, dx \tag{5.107}$$

This equation shows that the tidal discharge in a certain cross-section depends on the amount of water needed to fill the basin landward of the cross-section under consideration. This volume of water (excluding any fresh water) that has to flow in and

out through the inlet during one tidal cycle is called the tidal prism. It thus makes sense that the tidal prism has empirically been found to determine the equilibrium, or minimal stable cross-sectional channel area of a cross-section (Sect. 9.5.2).

In a short basin this situation can be simplified, since we can expect the water level in the basin to immediately follow the water level in the sea. There is no variation in the tidal amplitude along the channel axis: $\partial\eta/\partial x = 0$. For a sinusoidal tide at the seaward boundary, the entire basin thus oscillates in exactly the same way as the first harmonic. Eq. 5.107 then yields:

$$Q(t,x) = A_s u_s = \frac{\partial \eta_0}{\partial t} \int_x^{L_b} b \, dx = \frac{\partial \eta_0}{\partial t} A_b \Leftrightarrow \tag{5.108}$$

$$\boxed{u_s(x,t) = \frac{\partial \eta_0}{\partial t} \frac{A_b}{A_s}} \tag{5.109}$$

in which A_b is the basin surface area upstream of x and A_s is the channel cross-sectional area at x. At the time of high water in the sea, everywhere in the basin the water levels are maximum. Low water also occurs everywhere at the same time. Therefore the velocities are zero at high and low water. At the time of mean water level, the ebb and flood currents are maximum. This corresponds with a velocity that leads the surface elevation (by $\varphi = -\pi/2 = -90°$). The velocities in a cross-section are larger if a larger upstream surface area needs to be filled. Due to the uniformly oscillating water level, this situation is referred to as pumping mode.

In the case of a narrow gorge to the small basin, friction can reduce the amplitude inside the short basin and change the phase relationships.

5.7.4. Tidal asymmetry

In Sect. 5.3 it was described how wind waves propagating towards the shore become more and more asymmetric until the point of wave-breaking. We had seen that this shoaling process was characterised by:

- increase in amplitudes;
- peaking of the wave crest and a flattening of the trough, and;
- relative steepening of the face resulting in a pitched-forward wave shape.

Comparable effects occur for tidal propagation in basins. This is illustrated in Fig. 5.65 for a number of tidal basins in the Netherlands.

As the tide propagates up the estuary, the water depth and basin width change. The shoaling and narrowing of the estuary slows the progress of the tidal wave, increasing its amplitude along the channel axis. Friction, on the other hand, will reduce the amplitudes. The net effect depends on the situation. Furthermore, tidal asymmetry

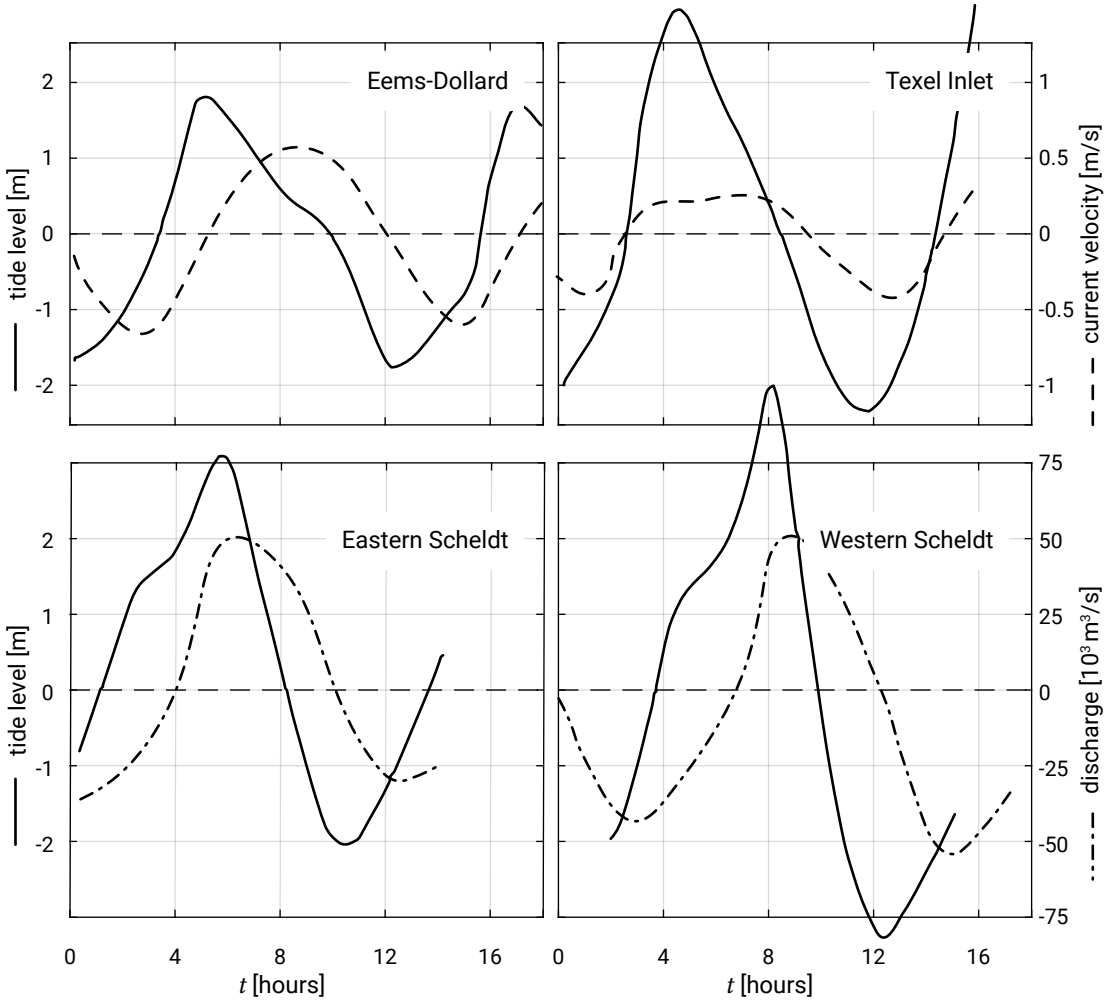

Figure 5.65: Tidal curves for water level, flow velocity and discharge for several Dutch basins. (Data from Dronkers, 1986).

develops. As a result, in most tidal basins the tidal curves for water level and flow velocity (or discharge) strongly differ from a sinusoidal curve.

First consider the situation of a prismatic tidal river or basin without intertidal storage areas. We also neglect reflection from the head. In the absence of friction, the propagation velocity is given by $c = \sqrt{gh} = \sqrt{g(h_0 + \eta)}$. We can also write the propagation velocity as $c = \sqrt{gA_s/b}$. Without intertidal storage areas, the high and low tide use the same channels and the propagation velocity of the high tide $c = \sqrt{g(h_0 + a)}$ is larger than that of the low tide $c = \sqrt{g(h_0 - a)}$. We can thus expect the rising period to be shorter than the falling period (see Fig. 5.66). Hence, the tidal wave becomes distorted, with a steep vertical face.

In extreme cases, as a result of certain bathymetric conditions, the steep vertical face can take on the form of a wall of water travelling up the basin. This causes an almost instantaneous rise of the water level as the water wall passes (see Fig. 5.66). This

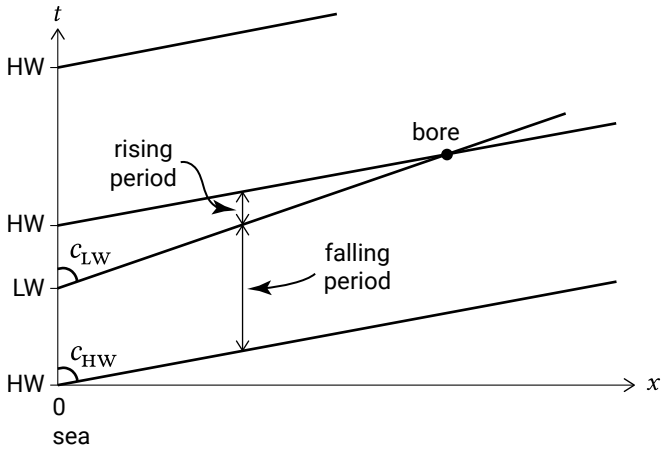

Figure 5.66: Tidal propagation along a basin (x-axis) in the case of a faster propagation of High Water (HW) with respect to the propagation of Low Water (LW). The rising period becomes increasingly smaller than the falling period. A bore develops when the rising period is reduced to zero (or when high water 'catches up' with low water).

phenomenon is called a *tidal bore* (see Intermezzo 5.7). In the modelling of the surface in breaking waves, an analogy with a bore is often made.

Friction gives an additional slowing down of the low tide with respect to the high tide, since the low tide 'feels' the bottom more. In tidal rivers this effect is even larger; since the river flow velocity and the tidal flow velocity are of similar order, the flow velocity and hence the friction is much larger at maximum ebb than at maximum flood.

Friction also causes damping of the amplitude that is stronger during ebb around LW than during flood around HW. The preferential damping of the LW is depicted in Fig. 5.67. It results in an asymmetry of the surface elevation about the horizontal axis (a positively skewed signal).

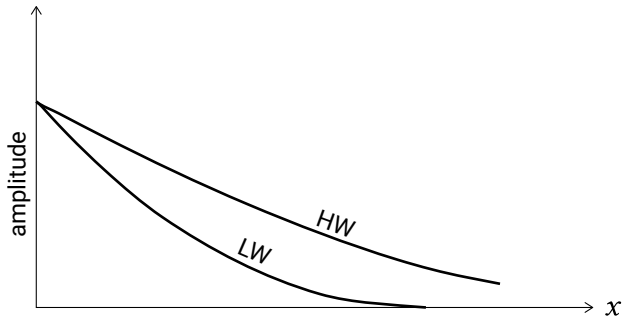

Figure 5.67: §1.2 ~~Tidal~~ §1.2 Amplitudes of HW and LW for tidal propagation along a basin (x-axis) §1.2 ~~showing a faster propagation of HW with respect to the propagation of LW. HW is damped less by friction than LW~~. §1.2 In this case, HW is damped less by friction than LW, and, consequently, HW propagates faster than LW. [p257] This is particularly true if, due to river discharge, the flow velocity at ebb is much higher than at flood.

Intermezzo 5.7 Tidal bore

Some rivers located at the landward end of an estuary experience an extreme tide-dependent condition - a tidal bore, an abrupt and migrating rise in the water level (Figs. 5.68 and 5.69). Tidal bores can cause great inconvenience to ship traffic. In those cases port authorities try and eradicate the bore by changing the shape and depth of the estuary.

Figure 5.68: Spectators watching the tidal bore in the Qiantang Estuary, China. Photo by Marcel J.F. Stive ('Credits' on page 579).

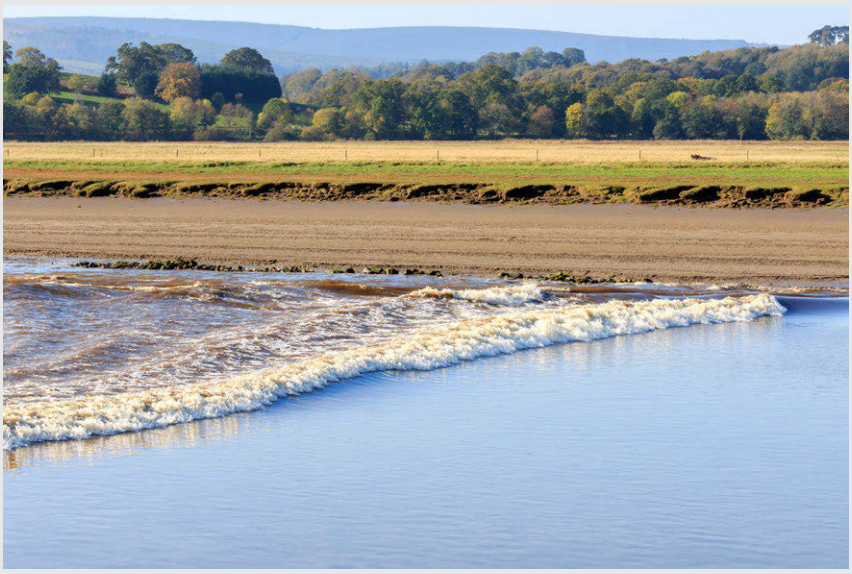

Figure 5.69: Tidal bore on the Nith River, Scotland. Photo by Richard P. Long ('Credits' on page 579).

Bores are uncommon, forming only in special circumstances that depend on tidal conditions and the morphology of the estuary. The bore in the Salmon river near

Truro at the head of the Bay of Fundy is typically only about half a metre high. In the Bay of St. Malo on the northern coast of France, a bay with the world's second largest tidal range, the bore rarely exceeds a metre in height. Large tidal bores occur in the Araguari River in the Amazon system and in the Qiantang estuary in China. The bore reaches 5 m in the Araguari River and nearly the same height in the Qiantang. In the Brazilian Amazon, tidal bores are known as *pororoca*.

Flood and ebb dominance

In the frictionless case and without reflection from the head, the vertical and horizontal tides are in phase. As a result, the horizontal tide displays similar sawtooth asymmetry as the vertical tide. The flood duration is identical to the ebb duration and the ebb velocities are equal to the flood velocities.

Due to the effect of friction, we can expect a phase shift between vertical and horizontal tide that increases inland. In the extreme case of the horizontal tide leading the vertical tide by a phase difference of $\pi/2$ (see Fig. 5.54), a shorter rising period directly corresponds to a shorter flood duration than ebb duration. In the absence of other non-tidal forcing or river discharge, the net tide-averaged discharge should be zero, even though the tidal current is asymmetric. Therefore, a shorter flood duration means that the maximum flood velocities are higher than the maximum ebb velocities.

Systems in which the maximum flood velocities are higher than the maximum ebb velocities are called flood-dominant. If the maximum ebb velocities are higher, we speak about ebb dominance. Flood dominance can be expected for a large tide (or more precisely a large ratio of tidal amplitude over water depth a/h). In that case, the propagation of high water is faster than of low water and thus the rising period is shorter than the falling period. The result is floods with a higher velocity and a shorter duration. This effect increases for longer basins.

Flood dominance can be counteracted by the presence of a river flow that increases the seaward-directed velocities (see Fig. 5.72). For negligible river flow, the presence of intertidal storage areas counteracts flood dominance. In many tidal basins, intertidal flats are present, which fall dry and are flooded again during the tidal cycle. The small water depths on these intertidal marshes and flats cause the high tide to propagate slower than the low tide. This is sometimes indicated by the ratio of intertidal storage volume over channel volume V_s/V_c (Friedrichs & Aubrey, 1988). Dronkers (1986, 2005) uses another indicator, viz. the wet surface area at HW over the wet surface area at LW: §1.1 ~~S_{HW}/S_{LW}~~ §1.1 $A_{b,\mathrm{HW}}/A_{b,\mathrm{LW}}$ §1.1 (see Fig. 9.34) [p260].

Ebb dominance is further enhanced by the fact that the water level averaged over the flood period is generally higher than that averaged over the ebb period. Since during ebb the discharge is similar to the discharge during flood, the ebb velocities must on

average be larger because of the smaller cross-section for the flow (for the same flood and ebb durations).

Summarizing, ebb dominance means that the ebb has higher maximum velocities and a shorter duration than the flood, whereas flood dominance refers to floods with a higher velocity and shorter duration. A large tidal amplitude and shallow channels enhance flood dominance. A large intertidal storage volume (as compared to channel volume) enhances ebb dominance. This shows that the basin geometry controls the tidal distortion.

Sawtooth asymmetry of the horizontal tide

So far we mainly mentioned skewness (flood or ebb dominance) of the horizontal tide. The horizontal tide can also display sawtooth asymmetry. In case of a short basin (length much smaller than a quarter of the tidal length, with the amplitudes of the incoming and reflected tidal wave of the same order), this will be the dominant form of asymmetry.

In a short basin, the tidal phase difference between seaward and landward end is negligible. Further, in a short basin η and u are out of phase; LWS (flow reversal from ebb to flood) occurs at LW, and HWS (flow reversal from flood to ebb) occurs at HW. At slack water, $d\eta/dt = 0$. The rate of change of the velocity du/dt around slack water is proportional to the landward basin area A_b and inversely proportional to the channel cross-section A_s (this can be found using Eq. 5.108).

Consider a short basin with shallow channels and little storage-offering flats. The channel cross-section A_s is much larger around HW than at LW. As a consequence, the rate of velocity change at HWS is smaller; the HWS duration is longer than the §1.1 ~~L_W slack~~ §1.1 LWS [p261] duration.

On the other hand, in a basin with vast storage-offering tidal flats and deep channels, §1.1 ~~Ab~~ §1.1 A_b [p261] is much larger around HW than around LW. As a result the variation of the flow velocity around HWS is much larger than around LWS; the HWS duration is shorter than the LWS duration.

Impact of the tide at sea

The asymmetry of the velocity variation in a tidal basin will strongly depend on the water level variation of the tide at sea. This holds especially for short basins, and to a lesser degree also for longer basins. A faster water level rise than fall at sea causes higher flood flow velocities than ebb flow velocities in the basin and vice versa. A long duration of HW at sea causes a long HWS duration and a short duration of HW at sea a short HWS duration. This holds in the same way for low water.

Deformation of the tidal wave along the coast has an impact on the ebb-flood asymmetry in the adjacent tidal basins and hence on the net inward or seaward sediment

transport and the morphological evolution. Fig. 5.70 illustrates the tidal variation for the Dutch coast and the adjacent tidal basins; this shows how the sea-borne tidal asymmetry is transferred into the basins.

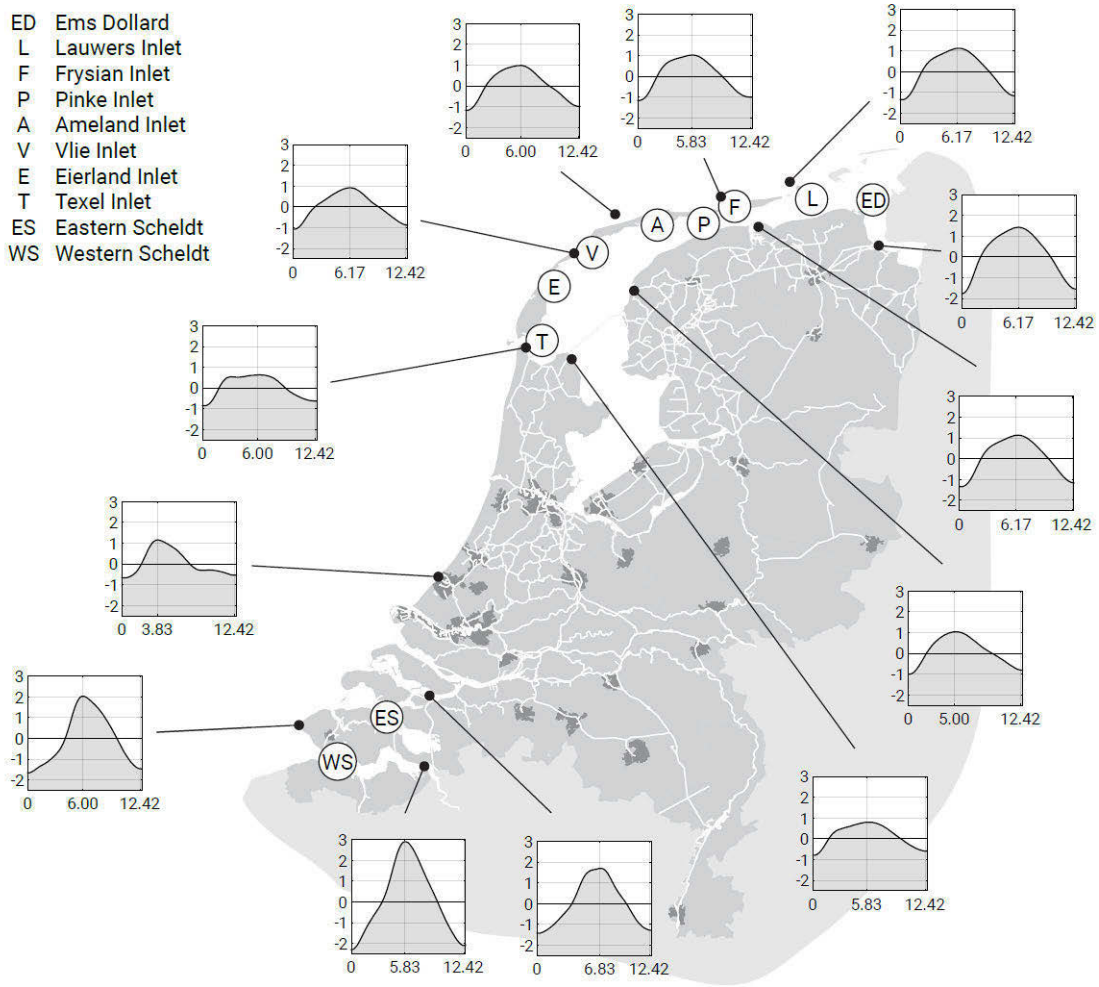

Figure 5.70: Tidal variation of the water levels along the Dutch coast and in the adjacent basins (data from https://waterinfo.rws.nl/). The reference time for each station corresponds to the first LW on 3 October 2019. Note that a shorter rising period than falling period at sea causes higher flood than ebb velocities in the basins. A shorter falling period has the opposite effect.

Relevance to sediment transport

The asymmetries of the horizontal tide are of extreme importance for the net sediment transport. The first type of asymmetry, skewness or asymmetry about the horizontal, is important for residual (net) sediment transport in tide-dominated areas (mainly tidal inlet systems). For instance, if the maximum flood velocity exceeds the [§1.2 maximum [p261]] ebb velocity, a residual sediment transport in the flood direction is likely to happen, since sediment transport responds non-linearly to the velocity. Hence, flood dominance implies a residual transport in the flood direction. For medium to coarse sediment this is the dominant effect. Note that in the same way, short-wave skewness

in the nearshore (see Fig. 5.14) leads to a net transport in the wave propagation direction. Chapters 6, 7 and 9 will discuss transport due to skewness of the velocity signal in both wave- and tide-dominated environments in more detail.

Flood-dominant systems tend to import sediment (assuming the transport is a power function of the velocity, see Sect. 9.7.2). As a consequence, they tend to become shallower and their channels tend to infill. Ebb dominance, on the other hand, results in a net seaward transport, which tends to keep channels deep. Ebb-dominant behaviour is an important driver for the formation of a tidal basin in coastal lowlands after a barrier breach. This is further treated in Sect. 9.7.2.

The second type of asymmetry (around the vertical) affects the residual transport for fine sediment in inlets and basins. This is because fines need time to settle; they are allowed to deposit if the slack duration is long enough. For asymmetries around the vertical, slack durations are not equal; if for instance the duration of HWS (before ebb) is longer than the duration of LWS (before flood), stronger sedimentation occurs just before flow reversal to ebb. We will see in Sect. 9.7.3 that this leads to a net transport of fines in the flood direction.

5.7.5. Overtides

Mathematically, tidal distortion and asymmetry can be described by the inclusion of higher harmonics, that is, tidal periods that do not originate from a tidal forcing period but are integer fractions ($1/2$, $1/3$, etc.) of the period of the basic astronomical constituents generated by the attraction forces of earth, moon and sun. For that reason they are named *overtides*. Since these higher harmonics are generated as a result of non-linear effects in shallowing coastal waters and tidal basins (compare with wind waves, Sect. 5.5), they are also called shallow-water tides. The phase relationships between the tidal constituents determine whether the tidal elevation and velocity curves are asymmetric about the horizontal or about the vertical axis.

Two important sources for non-linearity in the tidal propagation equations are bottom friction and continuity. The continuity equation Eq. 5.96 or Eq. 5.95 leads to $c = \sqrt{gh}$ or $c = \sqrt{gA_s/b}$. Different celerities of the high and low tide were seen to introduce tidal asymmetry. The resulting distortion of the surface elevation profile can be approximated with a second harmonic: a wave with twice the frequency of the basic harmonic. Equivalently, non-linear tidal propagation in shallow water thus generates a M4 tide from the M2 tide with a period that is $1/2$ the M2 period. In the same way, additional higher harmonics can be generated (M8, etc.). The higher harmonics to S2 are S4, S8, etc. If the different tidal components interact, interaction tides can be generated, e.g., M2 and S2 can generate MS4 (see Table 3.6). This explains why Table 3.6 is so much longer than Table 3.5!

The second source of higher harmonics is the quadratic (and hence non-linear) bottom friction term $\tau_b = \rho c_f u|u| \propto \cos\omega t|\cos\omega t|$. A Fourier expansion of this term can be

shown to give tidal constituents with a frequency that is three times as high as the basic frequency. Friction thus generates an M6 tide from the M2 tide, with a period that is 1/3 of the M2 period. Similarly, from S2 the S6 tide is generated. In the denominator of the friction term in Eq. 5.98 we have the water depth h, which varies with the tidal stage. This will introduce second harmonics (M4 etc.).

Figure 5.71 demonstrates the effect of the summation of M2 (semi-diurnal, 12.42 h period) and M4 (quarter-diurnal, 6.21 h period) with amplitudes of §1.1 ~~$a_{M4} = 1$ m~~ §1.1 $a_{\mathrm{M2}} = 1$ m and §1.1 ~~$a_{M2} = 0.2$ m~~ §1.1 $a_{\mathrm{M4}} = 0.2$ m [p263] respectively. The surface elevation is given by:

$$\eta(t) = a_{\mathrm{M2}} \cos\left(\omega_{\mathrm{M2}} t - \varphi_{\mathrm{M2}}\right) + a_{\mathrm{M4}} \cos\left(\omega_{\mathrm{M4}} t - \varphi_{\mathrm{M4}}\right) \tag{5.110}$$

Since $\omega_{\mathrm{M4}} = 2\omega_{\mathrm{M2}}$ and with $t' = t - \varphi_{\mathrm{M2}}/\omega_{\mathrm{M2}}$, this can be written as:

$$\eta(t) = a_{\mathrm{M2}} \cos\left(\omega_{\mathrm{M2}} t'\right) + a_{\mathrm{M4}} \cos\left(2\omega_{\mathrm{M2}} t' - \left(\varphi_{\mathrm{M4}} - 2\varphi_{\mathrm{M2}}\right)\right) \tag{5.111}$$

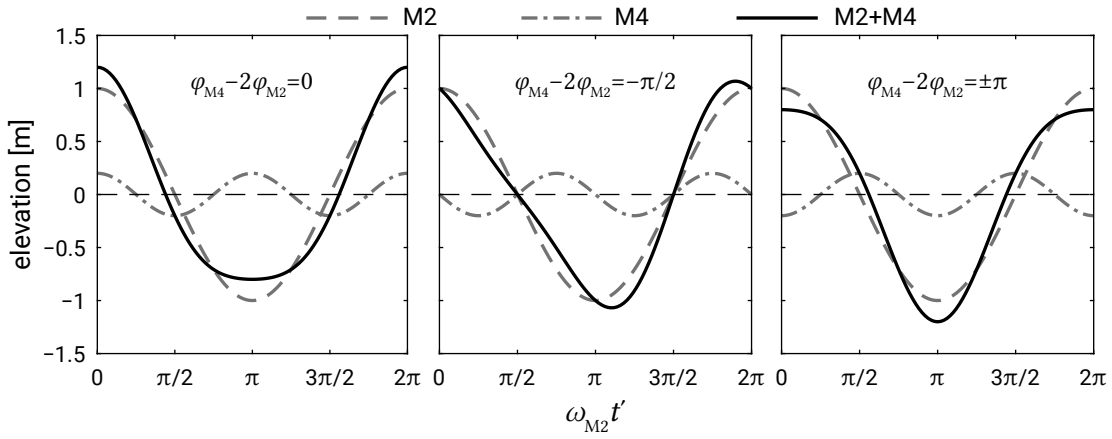

Figure 5.71: Influence of the relative phase difference between the M2 and M4 tide on the asymmetry about the horizontal axis and vertical axis. The combined signal becomes positively skewed when the two are in phase (left panel), asymmetric (w.r.t. the vertical axis, i.e., leaning forward in space, hence backward in time) when the phase shift $\varphi_{\mathrm{M4}} - 2\varphi_{\mathrm{M2}} = -\pi/2$ (middle panel), and negatively skewed when the two are out of phase (i.e., $\varphi_{\mathrm{M4}} - 2\varphi_{\mathrm{M2}} = \pm\pi$, right panel). Note that not depicted is §1.1 ~~$\varphi_{\mathrm{M2}} - 2\varphi_{\mathrm{M2}} = \pi/2$~~ §1.1 $\varphi_{\mathrm{M4}} - 2\varphi_{\mathrm{M2}} = \pi/2$ [p264], which would result in a backward-leaning signal in space and forward-leaning signal in time.

On the x-axis of Fig. 5.71 we have $\omega_{\mathrm{M2}} t'$ in radians. The phase lag between M2 and M4 is $\varphi_{\mathrm{M4}} - 2\varphi_{\mathrm{M2}}$. If the phase lag is 0° or ±180°, the result is an asymmetry about the horizontal (either a positive or negative skewness). For $\varphi_{\mathrm{M4}} - 2\varphi_{\mathrm{M2}} = 0°$ the signal is positively skewed (left panel), for $\varphi_{\mathrm{M4}} - 2\varphi_{\mathrm{M2}} = \pm 180°$ it is negatively skewed (right panel). If $\varphi_{\mathrm{M4}} - 2\varphi_{\mathrm{M2}} = \pm 90°$, the result is an asymmetry about the vertical axis (a longer falling period than rising period or vice versa). Shown in the figure is the situation that the falling period is longer than the rising period (middle panel). For

relative phase differences other than the special cases of 0°, ±90° and ±180°, the two types of asymmetry will be combined.

Sediment transport as a result of asymmetry of the horizontal tide is explained in Sect. 9.7 in connection with the overtides.

5.7.6. Residual currents

River discharge is the most obvious source of a net tide-averaged flow velocity and discharge (see Fig. 5.72).

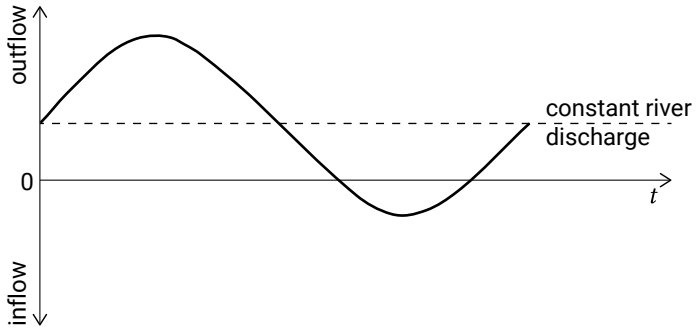

Figure 5.72: Combined effect of tidal flow and river discharge.

In the absence of river discharge or other nontidal forcing (e.g. wind), the net tide-averaged discharge should be zero. Nevertheless, vertical or horizontal circulation currents and residual currents may exist. For instance, an irregular coastline or a headland can induce residual currents, in pretty much the same way as the §1.2~~long dam~~§1.2harbour moles [p264] in Sect. 5.7.2. Other processes and mechanisms are treated below.

The relevance of these residual currents and secondary flows to the sediment transport and the bed topography is described in Ch. 9.

Tidal residual current pattern in an inlet gorge

An important physical mechanism to bear in mind when interpreting tidal currents is inertia. The tidal flow in an inlet gorge has so much momentum that it cannot spread out fast enough when leaving the gorge: it forms a *tidal jet*. The length of such a tidal jet is a few hundred times the water depth, so a few kilometres. On the other hand, the water flowing into the gorge has to accelerate and is therefore inertia-dominated, i.e. close to potential flow. This means that the highest velocities coincide with the shortest path through the gorge, i.e. just around the tips of the islands (Fig. 5.73). The tidal residual current pattern in this highly schematised situation boils down to a quadruplet of gyres, two at either side of the inlet (Fig. 5.74).

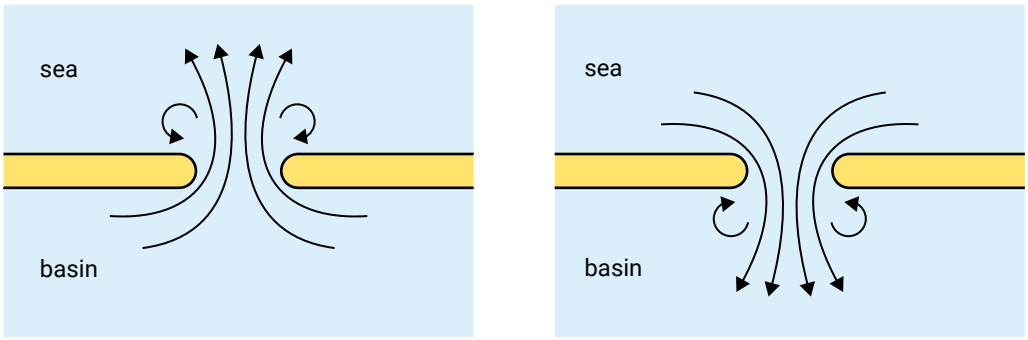

(a) (b)

Figure 5.73: Outgoing tidal jet (a) and ingoing tidal jet (b).

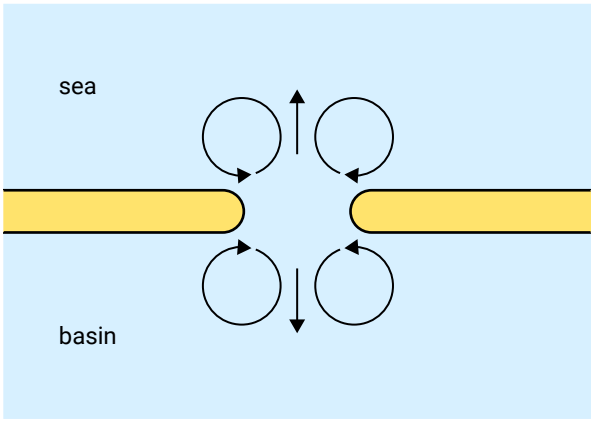

Figure 5.74: Schematised tidal residual currents around an inlet.

Stokes drift

As for wind waves (Sect. 5.5.1), a Stokes drift or mass flux is associated with tidal propagation of an at least partly progressive tidal wave. A Stokes drift in the direction of tidal propagation will occur if more than half of the flood tide coincides with water levels above the tidal cycle mean water level. The corresponding inflow of water must, for a closed basin, be compensated by an opposing outgoing flow, much like the undertow (Sect. 5.5.1).

The magnitude is dependent on the phase coupling between the horizontal and the vertical tide. Suppose u is the tidal current velocity in a 1D channel, h the mean water depth and η the water surface elevation above mean sea level, and let u and η be given by:

$$\eta = a\sin(\omega t - kx) \text{ and } u = \hat{u}\sin(\omega t - kx - \varphi) \tag{5.112}$$

The tidal residual flux of *water* is then given by (compare with Eq. 5.40):

$$q_{res} = \hat{u}a\frac{1}{T}\int_0^T \sin(\omega t - kx - \varphi)\sin(\omega t - kx)\,dt = \frac{1}{2}\hat{u}a\cos\varphi \tag{5.113}$$

Thus, if the horizontal tide (u) and the vertical tide (η) are 90° out of phase ($\varphi = -\pi/2$), there is no residual flux. But if they are more or less in phase ($\varphi \approx 0°$), there can be a considerable residual current.

Bathymetry-induced residual current

If the cross-section of a channel consists of deeper and shallower sections, the residual flow in the deeper channels is usually in the ebb direction, whereas in the shallower parts it is in the flood direction. This leads to a net (averaged over the tidal cycle) flood current in the shallower section and a net ebb current in the deeper sections, as indicated schematically in Fig. 5.75.

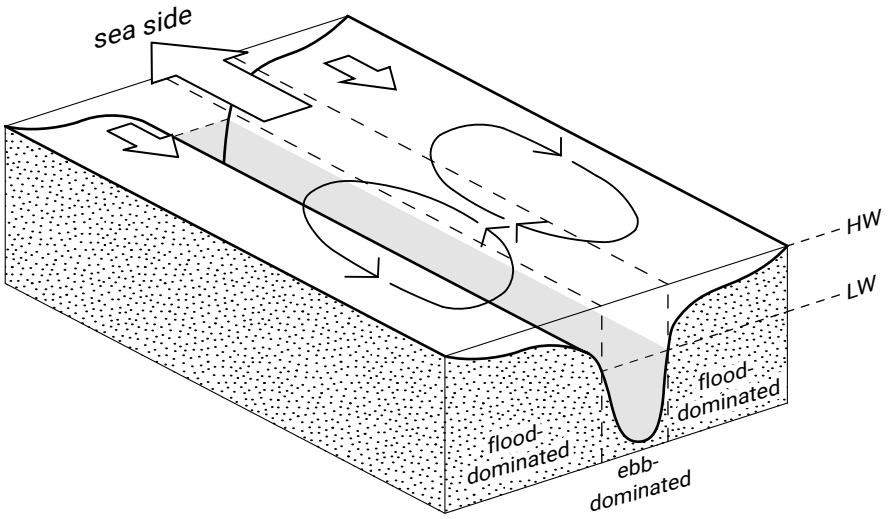

Figure 5.75: Bathymetry-induced circulation.

Coriolis-induced residual current and secondary flow

Due to Coriolis, the flood and ebb flow in a basin tend to be concentrated along opposite banks: the flood flow more along the right bank, viewed from the flood flow direction, and the ebb flow more along the right bank, viewed from the ebb flow direction (in a Northern Hemisphere basin). Averaged over the tide, this may give rise to residual flood and ebb currents. In a confined channel that prevents a deviation of the course, the Coriolis force is balanced, in a depth-averaged sense, by a water level (pressure) gradient (see Intermezzo 3.6). Compare this with the cross-shore force balance between a water level gradient due to set-up and the wave forces in the surf zone (Sect. 5.5.4). As in the cross-shore profile, the channel prevents a depth-mean transversal velocity. The depth distribution of the Coriolis force is determined by the velocity profile (e.g. logarithmic) along the channel axis (see Eq. 5.114). Thus, the depth distribution of the Coriolis and pressure forces are different (compare Fig. 5.43), resulting in a secondary circulation in the channel cross-section (hence in the vertical plane). Since the Coriolis force changes sign at ebb and flood, the effect is neutral in a tide-averaged sense.

Curvature-induced and Coriolis-induced secondary flow

In river bends, a secondary circulation occurs perpendicular to the main flow direction. Closer to the bottom it is directed towards the inner bend and closer to the surface towards the outer bend. In tidal channels a similar curvature-induced circulation can be found. The curvature-induced secondary flow pattern is the result of different depth distributions of pressure and curvature-induced centrifugal forces, analogous to the Coriolis-induced circulation described above. The curvature-induced flow, however, does not change sign as the tide turns. In the following, we will combine both effects.

A simple description is obtained when the assumption is adopted that the flow (both ebb and flood) has adapted to the channel bend under the influence of bottom friction and mean surface slope (pressure gradient) and that both the channel and flow structure are angle-independent in a cylindrical coordinate system. The transversal (perpendicular to the mean flow) force balance then reads:

$$\underbrace{-\frac{u^2}{R}}_{\text{centrifugal force}} + \underbrace{fu}_{\text{Coriolis}} + \underbrace{\frac{1}{\rho}\frac{\partial p}{\partial y}}_{\text{pressure gradient}} - \underbrace{\frac{\partial}{\partial z}\nu_T\frac{\partial v}{\partial z}}_{\text{turbulent viscosity}} = 0 \tag{5.114}$$

where:

R	radius of the channel bend (assumed to be much larger than the channel width)	m
u	local velocity along the channel axis	m/s
z	vertical coordinate; bottom: $z = -h$, surface $z = \eta$	m
v	transversal velocity	m/s
y	transversal coordinate	m
ν_T	eddy viscosity	m^2/s

If stratification (density differences) is neglected, the transversal pressure gradient $\partial p/\partial y = \rho g\, \partial\eta/\partial y$ is due to the water level slope, counteracting the centrifugal and Coriolis forces. The equation describes the evolution of a transversal circulation current v due to the vertical shear in the lateral channel flow u. The bend radius R is an important factor in determining the relative importance of the centrifugal force and the Coriolis force. The Coriolis contribution changes sign at ebb and flood; the centrifugal force exerts its influence at ebb and flood in the same direction.

In a depth-averaged sense, and neglecting the bed shear stress due to the transversal circulation, the centrifugal forces and Coriolis force are balanced by a water level gradient. As above, a circulation current arises, since the depth distribution of the various forces is different (see the first two terms in Eq. 5.114 that are determined by the velocity profile along the channel axis).

By twice integrating the force balance Eq. 5.114 over depth, it is possible to derive a formula for the transversal circulation current. Near the bottom this circulation

is towards the inner bend (tide-averaged, see Fig. 5.76). The Coriolis acceleration strengthens the transversal circulation, when from the perspective of the main flow the channel outer bend is a right bank (i.e. at ebb and flood this implies opposite bends, and this holds for the Northern Hemisphere). The transversal circulation gives the tidal flow a spiralling character.

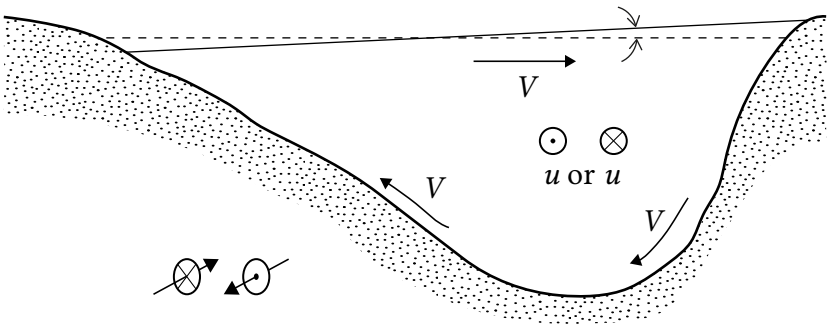

Figure 5.76: Cross-section of a channel bend showing tide-averaged transversal circulation. The Coriolis contribution changes sign at ebb and flood; the centrifugal force exerts its influence at ebb and flood in the same direction. Near the bed, the transversal circulation in a tide-averaged sense therefore runs from the outer bend to the inner bend. The water level is higher in the outer bend.

5.8. §1.1~~Curvature-induced and Coriolis-induced secondary flow~~§1.1Long-wave phenomena in coastal waters

[p268]

5.8.1. Seiches

Seiches are free oscillations that occur in basins of moderate size (harbour, lake, bay or even sea). They are standing waves with a frequency equal to the resonance frequency of the basin in which they occur. The oscillations may be caused by sudden changes in wind conditions. After generation, the water sloshes back and forth until the wave motion is dampened out by friction. Seiches generally have half-lives of only a few periods, but may be frequently regenerated. The difference between seiches and the tidal resonance phenomena in basins as discussed above is that the latter are not free oscillations, but forced at a certain tidal frequency.

Seiches can have periods ranging from a few minutes up to several hours. They can cause havoc in a harbour by setting up reversing currents at the entrance or by rocking ships free of their moorings. They can also abruptly surge onto piers and beaches and sweep people away. The Great Lakes of North America and some of the large lakes in Switzerland are especially prone to seiches, because they are enclosed basins with large fetches and strong winds.

As seiches are a resonance phenomenon, it is obvious that the basin size in relation to the wavelength is an important factor. Therefore, measures against the generation of seiches are usually based on size restrictions of a harbour or other basins, and on the use of irregularly shaped basins.

Seiches can oscillate in a semi-enclosed (Fig. 5.77, right) and closed mode (Fig. 5.77, left) or in a combination of these two modes if the open end is somewhat restricted. In simple cases the wavelength is twice or four times the basin length (or a certain fraction thereof).

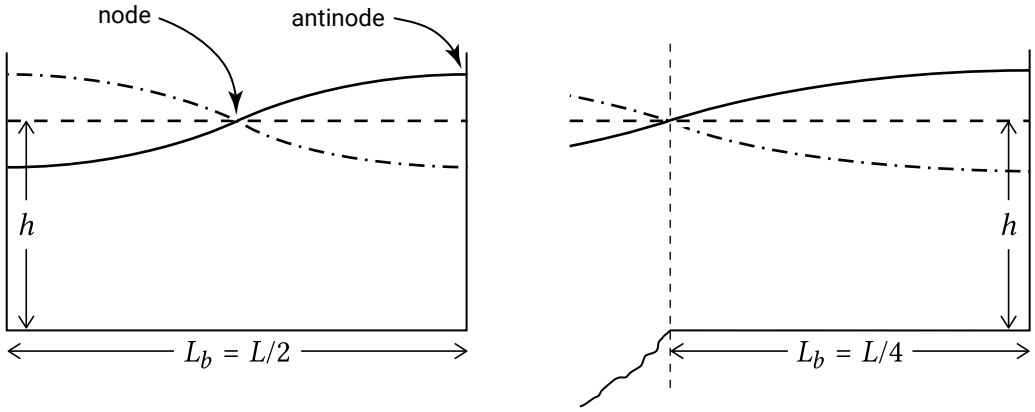

Figure 5.77: Standing wave in a closed body of water and in a semi-enclosed body of water. Basin length L_b and wavelength L

Usually, the vertical amplitude of a seiche, even at an antinode, is small. However, especially at a node, the horizontal displacement of the water can be significant. This can cause mooring difficulties for ships. Another related influence on large ships is the effect of the water surface slope.

In the port of Rotterdam, a seiche was observed in the morning of 1 March 1990. It appeared first as a minor fluctuation of around 10 cm at light island Goeree (an observation post some kilometres offshore) at 0:00 hours. Then, at about 01:30 hours, it appeared as a huge standing wave of 1.75 m at Rozenburg lock, a navigation lock some 15 km inland. Figure 5.78 shows a smaller seiche at the same locations observed on 27 August 2001.

5.8.2. Bound long waves and surf beat

The concept of wave radiation stresses and wave-induced forces considered in this chapter did not include temporal variations created by individual waves or wave groups, because radiation stress was calculated as the resultant integrated over the wave period and any wave groups. As we have seen in Sect. 3.5.3, waves generally travel in groups of higher and smaller waves. Due to the wave height variation in the groups, the radiation stresses vary as well, being highest under the highest waves. This results in a time-varying set-down in the shoaling zone, with the largest depression under the

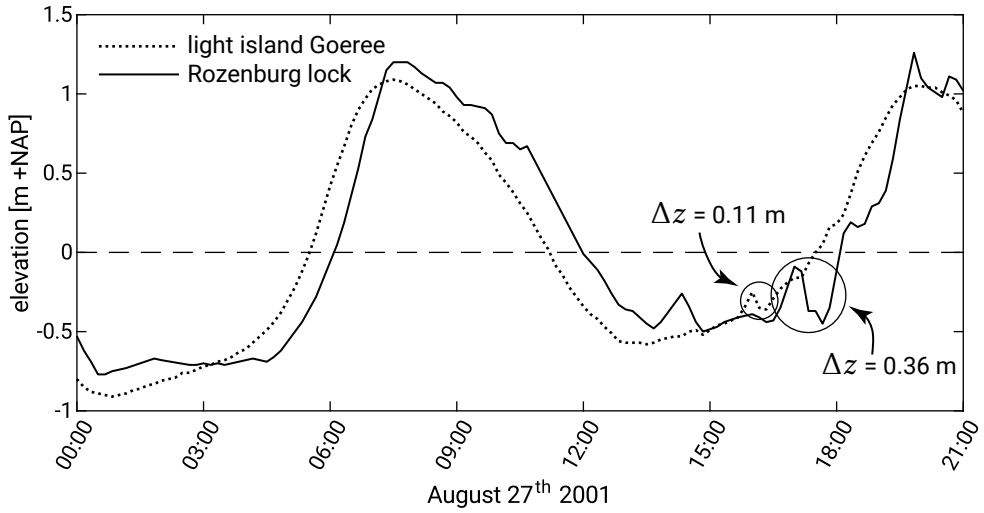

Figure 5.78: Seiche in the port of Rotterdam (data from https://waterinfo.rws.nl/). At the light island Goeree, the seiche can be observed as a disturbance of 0.11 m (grey line) and, as it propagates up the Rotterdam waterway, the disturbance grows to 0.36 m by the time it reaches the Rozenburg lock (black line) after approximately one hour.

highest waves. The effect of this is a long wave motion on the wave group scale. The long wave is forced; it has the length and frequency of the group and the phase speed is not that of a free gravity wave, but it travels with the group at the wave group speed. This phenomenon is referred to as the bound long wave associated with the group.

For a perfect bound long wave, the phase shift between the long wave and the short-wave envelope (enveloping the maxima and minima of the individual waves) equals $-\pi$ (it is 180° out of phase with the group, meaning that the wave trough of the bound long waves coincides with the maximum of the wave envelope, see Fig. 5.79).

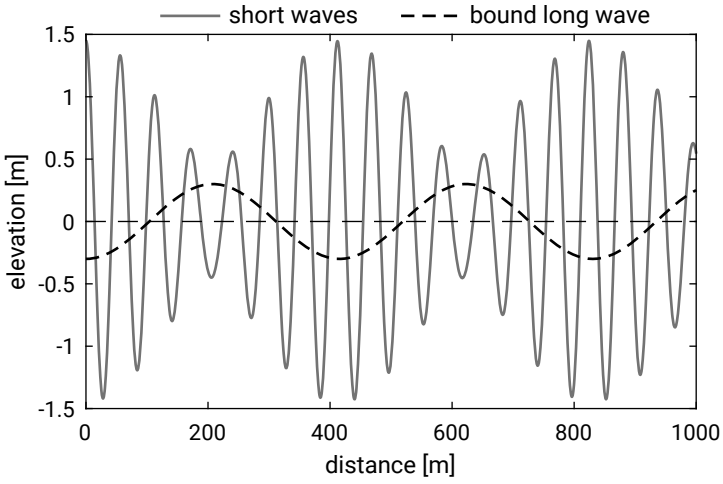

Figure 5.79: A bound long wave, perfectly out of phase (π rad) with the wave group. Note that the troughs of the bound long wave coincide with the maxima of the wave group envelope. The bichromatic wave consists of two waves: $a_1 = 0.5$ m, $T_1 = 5.75$ s and $a_2 = 1.0$ m, $T_2 = 6.15$ s, travelling in a water depth of 30 m. The group length $L_g = 420$ m.

In reality, however, it appears that the correlation between the long-wave motion and the group is smaller (but still negative as long as we stay offshore from the surf zone), and that it changes into a positive correlation as we enter the surf zone. The change in the correlation indicates that the long waves are no longer moving at the speed of the group. It is said that the bound long wave is released from the group after breaking. As we will see in Ch. 7, the correlation is important for the magnitude and direction of sediment transport by the long wave.

Due to the variations of wave height in a group, wave-breaking can occur intermittently within a group for waves that exceed a certain height. This generates a time-varying set-up and therefore oscillations of the water level near the shore. A general name for low-frequency water level oscillation near the shore is surf beat. The exact generation mechanisms of surf beat are still uncertain and, besides the present explanation, many alternative and sometimes conflicting explanations have been proposed in the literature.

Surf beats occurring near port entrances can have a negative impact on mooring conditions in harbour basins.

6

Sediment transport

6.1. Introduction

Changes in coastal morphology are the consequence of spatial gradients in net sediment transport rates (compare Sect. 1.4.3 and Eq. 1.1). Therefore, this chapter discusses sediment transport mechanisms and prediction methods. Unfortunately, the interaction between hydrodynamics and sediment is very complex and poorly understood. A famous anecdote says that when Albert Einstein's son started researching sediment transport, his father warned him strongly of the difficulties in dealing with sediment transport processes (see e.g. Vollmers (1989)). Whether this actually happened is questionable (Gyr & Hoyer, 2006), but the anecdote illustrates the frustration that coastal engineers and scientists must sometimes feel when trying to understand and model sediment transport. In view of the above, the modelling of sediment transport is largely based on empiricism.

Sediment transport can be defined as the movement of sediment particles through a well-defined plane over a certain period of time. The movement of sediment particles depends on the characteristics of the transported material (grain size, fall velocity). These sediment properties are discussed in Sect. 6.2. Next, in Sect. 6.3, initiation of motion is considered. It is shown that sediment particles will start moving when a so-called critical velocity (or critical shear stress) is exceeded. This bed shear stress is the result of the combined wave-current motion. Section 6.4 discusses the various transport regimes and modes. Generally, two transport modes are distinguished: bed load and suspended load. If the particles are moved in bed load mode, they roll, shift or make small jumps over the seabed, but stay close to the bed. Transport in suspended load mode, on the other hand, implies that grains are lifted from the seabed at flows above the critical flow velocity and transported in suspension by the (moving) water. Below a certain flow velocity, the grains settle down again. General bed load and suspended load transport formulations are treated in Sects. 6.5 and 6.6 respectively. In

Sect. 6.7 the so-called energetics approach to bed load and suspended load transport is discussed. This approach gives us an easy method to unravel sediment transport into the separate contributions of waves and currents. Section 6.8 deals with some of the additional complications that can be expected when dealing with fine sediment (mud and finer sand fractions). Section 6.9 discusses the choice between various transport models and schematisations that can be made for specific situations.

6.2. Sediment properties

6.2.1. General

In the coastal zone we find sediments like quartz (SiO_2), carbonates and clay minerals (sheets of silicates, see Intermezzo 2.3). Depending on the particle size we distinguish silt and clay, sand, gravel, and cobbles (see Sect. 2.6.2). Clay particles are very small with a large surface area compared to their volumes. This surface area is chemically active, which, especially when wet, leads to the typical cohesive characteristics of its bulk form. Quartz and carbonate sands on the other hand are non-cohesive; the grains do not stick together. A handful of pure sand cannot be picked up by hand in the way a piece of clay can be picked up. In these lecture notes the main focus is on sand.

6.2.2. Grain size, density and bulk properties

Two important parameters for sediment transport are the median particle diameter D_{50} and the grading, for example, D_{90}/D_{10}. D_x is defined as the sediment particle diameter (in metres) for which x% by weight is finer. In American literature, a ϕ scale is often used to identify the particle dimensions:

$$\phi = -\log_2 D \tag{6.1}$$

where:

D	sand grain diameter	mm

§1.2For every ϕ, the diameter D [mm] can be found with $D = 2^{-\phi}$. Classifications of sediments on the basis of size are found in Table 2.2. [p274] Sediment is called well-sorted if D_{90}/D_{10} is small (say < 1.5, although there is no formal classification); for large values of D_{90}/D_{10} (for instance > 3) we speak of poorly sorted or well-graded sediment.

Besides grain size, other properties of either the grains or the bulk material are important for sand transport, such as grain shape (the grains are not perfect spheres), grain density, fall velocity, angle of repose, porosity and sediment concentration:

- The grain density ρ_s depends on the mineral composition of the sand. Most of the world's beach sands consist of quartz (feldspar is the second most common mineral), with a mass density of 2650 kg/m^3. Other minerals are often referred to as heavy minerals, since their mass density is usually greater than §1.2~~27 000 kg/m^3~~§1.2 2700 kg/m^3 [p275];
- Relative density s is defined as the ratio of sediment density over water density ρ_s/ρ. For natural sediments, s will be normally around 2.65;
- The fall velocity depends on the grain characteristics as well as on the fluid characteristics (such as water density and viscosity). This is further discussed in Sect. 6.2.3. Roughly speaking, the fall velocity of medium-sized sand particles (0.1 mm $< D <$ 0.5 mm) in water varies from 0.01 m/s to 0.05 m/s;
- When (dry) sand is poured onto a flat surface, it will form a mound. The surface of the mound has a slope tan φ_r (with φ_r is the angle of repose) which depends mainly on the grain size;
- The porosity p is defined as the ratio of pore space (voids) to the whole sediment volume. Natural sands have porosities in the range of 0.25 to 0.50; a frequently applied figure is 0.40 (or 40 %);
- The sediment concentration c can be defined in two ways: mass concentration and volume concentration. The mass concentration is the mass of the solid particles per volume (c in kg/m^3 or equivalently g/L) and is often used when measuring sediment concentrations. Volume concentration is defined as the ratio of the volume of solid particles to the whole volume (c in m^3/m^3 or in %). Sediment in a sediment bed has a volume concentration of $n = 1 - p$. For sediment in suspension, the volume concentration c indicates the volume of sediment per volume of the mixture. If the sediment in such a mixture settles to the bed, 1 m^3 of solid particles will occupy $1/(1-p)$ (p: porosity) m^3 at the bed. Volume concentrations are obtained from mass concentrations by multiplication by $1/\rho_s$;
- Contrary to the grain density (ρ_s) as mentioned above, bulk density is the mass of a unit volume of e.g. a mixture of particles and air or water. The **dry** bulk density is defined as $n\rho_s$. If the whole pore volume is filled with water (density ρ), then we obtain the **saturated** bulk density, which is defined as $n\rho_s + p\rho$. A typical figure for the dry bulk density is 1600 kg/m^3, and for the saturated bulk density 2000 kg/m^3.

6.2.3. Fall velocity

When a particle falls in still and clear water, it accelerates until it reaches a constant vertical velocity that is called fall velocity or settling velocity. This velocity can be assessed from the balance between the downward-directed gravity force F_G (minus the effect of buoyancy) and the upward-directed (retarding) drag force F_D as indicated in Fig. 6.1.

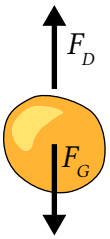

Figure 6.1: Forces on a 'sphere' in clear water.

Basic equation

The downward-directed gravity force F_G on a sphere combined with the upward buoyancy effect is given by the so-called underwater weight of the sphere, viz. by the weight of the sphere minus the weight of the displaced volume of water. With weight equal to mass times acceleration due to gravity, we have for a perfect sphere:

$$F_G = (\rho_s - \rho)\, g \left(\frac{\pi}{6} D^3\right) \tag{6.2}$$

where:

ρ_s	mass density of the particle	kg/m^3
ρ	mass density of the surrounding fluid	kg/m^3
D	particle diameter	m
g	acceleration of gravity	m/s^2

In this equation, the second term between brackets is the volume of the sphere.

The upward-directed force is equal to the so-called drag force denoted by:

$$F_D = \frac{1}{2} C_D \rho w_s^2 \left(\frac{\pi}{4} D^2\right) \tag{6.3}$$

where:

C_D	drag coefficient	–
w_s	particle fall velocity	m/s

The second term between brackets refers to the cross-section of the sphere. The drag force is non-zero only if $w_s > 0$.

In equilibrium, both forces are in balance and the fall velocity w_s (in m/s) is given by:

$$w_s = \sqrt{\frac{4(s-1)gD}{3C_D}} \tag{6.4}$$

in which s is the relative density (see Sect. 6.2.2).

A particle's fall velocity depends on its size, its density and the magnitude of the drag coefficient C_D. This drag coefficient depends on the shape of the particle and its roughness, but mainly on the grain's Reynolds number:

$$\mathrm{Re} = w_s D/\nu \tag{6.5}$$

where:

ν	kinematic viscosity coefficient	m^2/s

The kinematic viscosity is defined as the dynamic viscosity divided by the water density: $\nu = \mu/\rho$. A characteristic value for ν is $10^{-6}\,\mathrm{m}^2/\mathrm{s}$. The dynamic viscosity represents the fluid's internal resistance to flow ('thickness') and is a function of the temperature and to a smaller extent of the density.

Dependence on Reynolds number

For low grain Reynolds numbers ($\mathrm{Re} < 0.1$ to 0.5) in the so-called Stokes range, the drag coefficient can be described by (see Fig. 6.2):

$$C_D = 24/\mathrm{Re} \tag{6.6}$$

yielding:

$$w_s = \frac{(s-1)gD^2}{18\nu} \tag{6.7}$$

In this range, the fall velocity depends on the square of the grain diameter, the relative density and the kinematic viscosity coefficient.

For high grain Reynolds numbers ($400 < Re < 2 \times 10^5$), in the so-called Newton range, the drag coefficient becomes a constant ($C_D \approx 0.5$). In that case it follows from Eq. 6.4:

$$w_s = 1.6\sqrt{gD(s-1)} \tag{6.8}$$

In this range, the fall velocity depends on the square root of the grain diameter and the relative density and is independent of the kinematic viscosity coefficient. This is also the case for extremely high Reynolds numbers ($Re > 2 \times 10^5$), where the drag coefficient is (constant) around 0.2.

For quartz spheres falling in still water, a Reynolds number of 0.5 corresponds roughly to a particle diameter of 0.08 mm, while a Reynolds number of 400 corresponds to a

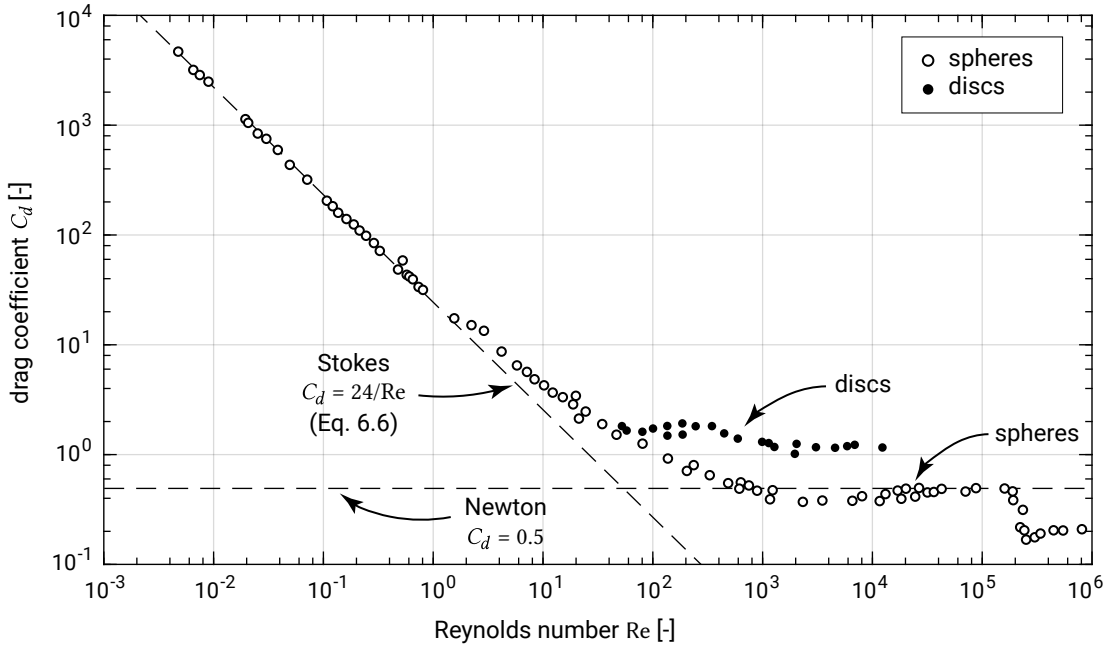

Figure 6.2: Drag coefficient as a function of Reynolds Number (Vanoni, 1975).

diameter of about 1.9 mm. Since most beach sediments fall in the range of 0.08 mm to 1.9 mm, in most practical cases neither the Stokes approximation nor the Newton approximation can be used.

For very small particles (silt, clay) the fall velocity is proportional to D^2; for gravel size particles the fall velocity is proportional to $\sqrt{D}$. For sand, the fall velocity falls in the transition range between a D^2 dependency and a $\sqrt{D}$ dependency. By lack of a simple expression for the drag coefficient in this range, it is common practice to use empirical formulas for the fall velocity. In literature, many formulas can be found (e.g. Van Rijn (1984b) and Ahrens (2000)). As an example, in Fig. 6.3, for two formulas the fall velocity as a function of the grain diameter is plotted.

Hindered settling

In high-concentration mixtures, the fall velocity of a single particle is reduced due to the presence of other particles. This can be explained as follows: with each downward grain movement, a similar fluid volume must flow upward; this upward flow slows down the other grains. In order to account for this hindered settling effect, the fall velocity in a fluid-sediment mixture should be determined as a function of the sediment concentration c and the particle fall velocity w_s. An often-used formula for the effective fall velocity in a mixture is:

$$w_e = (1 - c)^{\alpha} w_s \tag{6.9}$$

where:

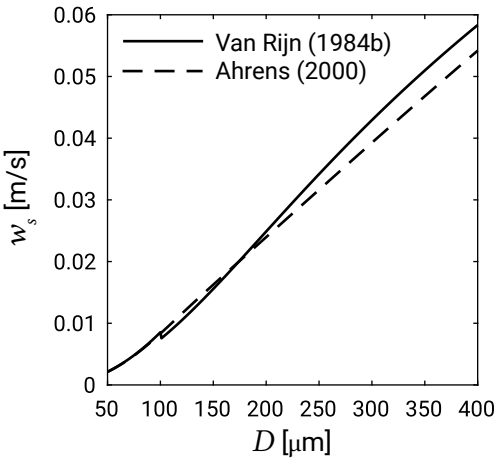

Figure 6.3: Sediment fall velocity as a function of the grain size in fresh water with a temperature of 18 °C ($\rho_w = 1000\,\mathrm{kg/m^3}$, $\rho_s = 2650\,\mathrm{kg/m^3}$ and $\nu = 1.05 \times 10^{-6}\,\mathrm{m^2/s}$). Comparison between Van Rijn (1984b) and Ahrens (2000).

w_e	effective fall velocity	m/s
w_s	fall velocity of one grain in clear water in rest	m/s
c	sediment concentration (volumetric %, volume of solid sediment particles in volume of water-sediment mixture)	–
α	coefficient (ranging from 4.6 at low Reynolds numbers to 2.3 at high Reynolds numbers)	–

In many engineering cases related to sediment transport, the sediment concentration can be as high as approximately 1 vol.% ($2.65\,\mathrm{kg/m^3}$), meaning that the effect of sediment concentration on the fall velocity is small. This is not the case in sheet flow conditions (see Sect. 6.4.2) and in very silty environments, where sediment concentrations can be significantly higher.

6.3. Initiation of motion

6.3.1. Forces on a single grain

Sediment can only be transported if the water movement exerts a large enough shear stress τ_b on the grains. The so-called critical shear stress $\tau_{b,cr}$ describes the point of initiation of motion. If this condition is exceeded, grains move, roll or are brought into suspension. Note that instead of the term *bed shear stress* one may find the term *shear velocity* (u_*), which is related to the bed shear stress through $\tau_b = \rho u_* |u_*|$.

In order to assess the critical condition of initiation of motion, the various forces acting on an individual grain have to be taken into account (see Fig. 6.4). These forces can be divided into forces which tend to move the grain – the drag force F_D (Fig. 6.4a) and

the lift force F_L (Fig. 6.4b) – and a force which tries to keep the grain in its place; the gravity force F_G (Fig. 6.4c).

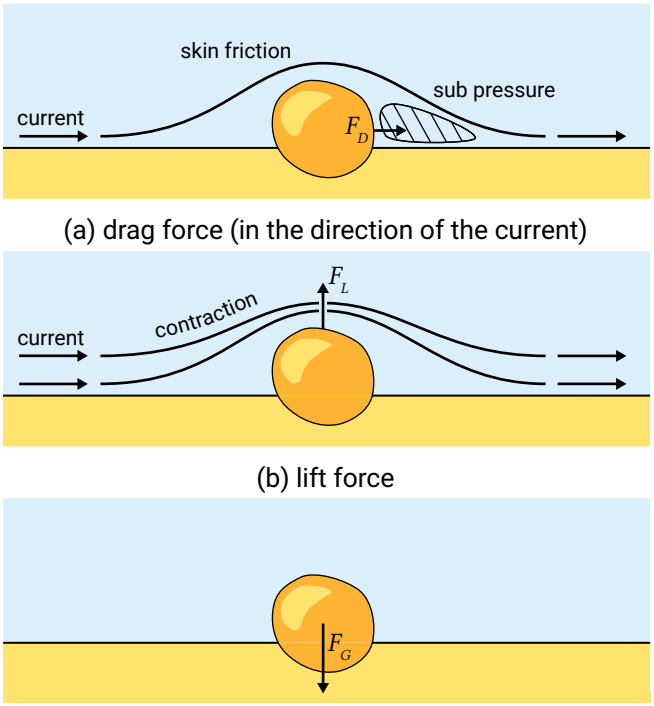

Figure 6.4: Forces on an individual grain in a stationary situation.

The *drag force* is a combination of skin friction acting on the surface of the grain and a pressure difference on the up- and downstream sides of the grain because of flow separation at the downstream end of the particle. Analogous to Eq. 6.3, the drag force is proportional to:

- the square u^2 of a typical upstream horizontal flow velocity;
- the particle's surface area and hence for spheres to D^2;
- the water density ρ.

The *lift force* results from the flow separation, as well as from the flow contraction above the grain. A higher local flow velocity results in a lower local pressure (Bernoulli law). The difference in vertical pressure causes an upward-directed lift force. Similarly to the drag force, the lift force is proportional to the particle's surface area (and thus to D^2 in the case of a sphere) and to u^2.

The total driving force (drag and lift combined) is therefore proportional to $\rho u^2 D^2$. The resisting *gravity force* is proportional to $(\rho_s - \rho) g D^3$ (see Eq. 6.2). Equilibrium of forces, whether horizontal, vertical or rotational, therefore, is expressed through a formula of the following type:

$$\left(\rho_s - \rho\right) g D^3 \propto \rho u_{cr}^2 D^2 \tag{6.10}$$

in which u_{cr} is the critical velocity of the water at which grains start moving. Since the bed shear stress is proportional to the velocity squared times the water density, we could also write:

$$\left(\rho_s - \rho\right) g D^3 \propto \rho \tau_{b,cr} D^2 \tag{6.11}$$

Here, $\tau_{b,cr} = \rho u_{*,cr}^2$ is the critical bottom shear stress (critical in the sense that higher bottom shear stresses lead to the initiation of motion).

From the proportionality Eq. 6.11, the so-called critical Shields parameter θ_{cr} can be deduced:

$$\boxed{\theta_{cr} = \frac{\tau_{b,cr}}{\left(\rho_s - \rho\right) g D} = C} \tag{6.12}$$

The constant C has to be determined experimentally. The experiments of Shields, performed on a flat bed, are the most widely used. He defined the critical bed shear stress as the bed shear stress at which the (extrapolated) measured transport rates were just zero. For sand placed smoothly on this flat bed, C was found to be around 0.05. Appendix D points out the similarities between Eq. 6.12 and stone stability and structural damage approaches for slopes of loose rock and of breakwater elements.

6.3.2. Shields curve

Shields found experimentally that the 'constant' [§1.1] $C \approx 0.05$ [p281] is a weak function of the grain Reynolds number defined as:

$$\mathrm{Re}_* = \frac{u_* D}{\nu} \tag{6.13}$$

where:

u_*	shear velocity	m/s
D	diameter of grains	m
ν	kinematic viscosity coefficient	m^2/s

The subscript $*$ is used to indicate that the Reynolds number is based on u_*.

Figure 6.5 shows measured values of C as a function of Re_*. The shaded band separates two zones: movement of sediment particles was observed in the zone above this shaded band, whereas no movement was observed in the zone underneath the shaded band. The shaded band therefore indicates initiation of motion. Sometimes, the shaded band is represented by a single line, which is then referred to as the Shields curve. The average value can be seen to be approximately 0.05.

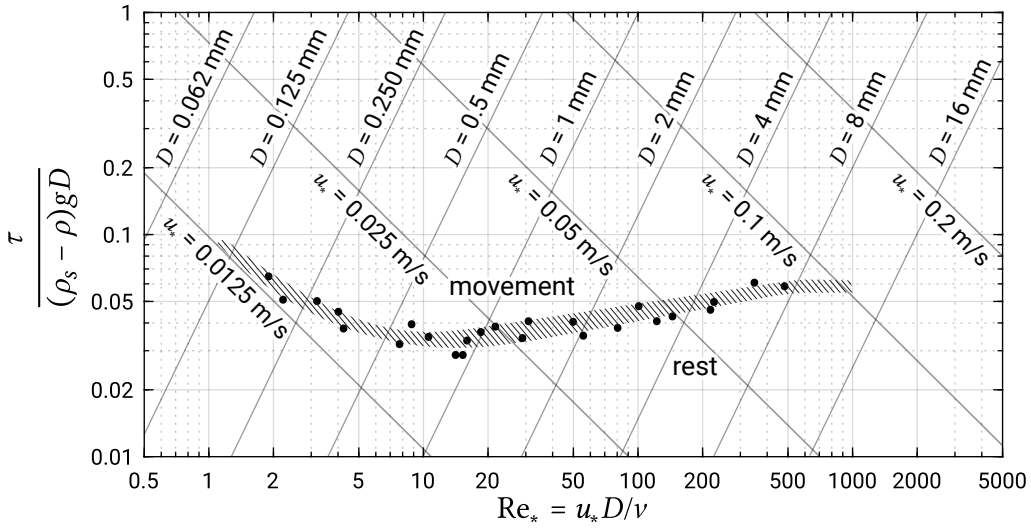

Figure 6.5: Shields curve (Shields, 1936). Note that the axes are drawn on a log-log scale. The lines of constant D and u_* do not originate from Shields and are valid for constant density $\rho_s = 2650\,\mathrm{kg/m^3}$ and kinematic viscosity $\nu = 1.25 \times 10^{-6}\,\mathrm{m^2/s}$ at a water temperature of 12 °C.

Unfortunately, reality is more complex. Reasons for this include:

- The Shields curve is valid for uniform flow on a flat bed. The effect of bed ripples and the effect of the combination of unidirectional and oscillatory flow on initiation of motion are largely unknown;
- Gradation of the bed material may play a role, especially for poorly sorted sediment ($D_{90}/D_{10} > 3$). In these cases, the smaller particles will be hidden in the voids between the larger particles, while the larger particles are more exposed. After exposed smaller particles are washed out, a top layer of coarser particles (with higher critical flow velocities) remains and prevents movement of the underlying smaller particles. This is called *bed armouring*;
- For a sloping bed in the flow direction, it can be argued that the critical flow velocity will be somewhat smaller for downward-sloping beds and somewhat higher for upward-sloping beds;
- Cohesive forces between the grains – due to the presence of cohesive sediment in the bed – may drastically increase resistance against erosion (see also Sect. 6.8). Biological activity and consolidation may be important in this respect as well.

Notwithstanding these complications, many practical sediment transport formulas use the critical Shields parameter θ_{cr} (Eq. 6.12) and the Shields curve to define initiation of motion. Amongst others, Van Rijn (1984a) represented the Shields curve as a function of a non-dimensional grain size D_*:

$$D_* = D_{\mathrm{so}} \left(\frac{g(s-1)}{\nu^2} \right)^{1/3} \tag{6.14}$$

The Shields curve can be represented in terms of D_*, since every grain diameter has a corresponding $u_{*,cr}$ as can be seen in Fig. 6.5. With $\theta_{cr} = f(D_*)$, no iteration is necessary to obtain the critical shear stress, as would be the case when applying the Shields curve. In addition, the threshold parameter can be corrected to account for the effect of the bed slope $\tan\alpha$ on the threshold of motion. This formulation results in an increase of the critical shear stress for upslope movement and a decrease of the critical shear stress for downslope movement. We then have a formula of the type:

$$\theta_{cr} = f\left(D_*, \tan\alpha\right) \tag{6.15}$$

6.4. Basic principles of transport modelling

6.4.1. Definitions

Sediment transport can be defined as the movement of sediment particles over a certain period of time through a well-defined plane. The vertical extent of such a plane is generally from the bed to the water level. In the horizontal direction the plane may extend from the edge of the surf zone to the water line. In that case the total wave-induced longshore transport integrated over the surf zone is considered. Often, however, the transport rates are expressed per metre width.

Since coastal engineers are interested in *volumes* of accretion and erosion, it is common practice to express the sediment transport rates S in $m^3/s/m$ (volumes of sand per second per metre width). These sediment volumes may be expressed in terms of *volumes of solid grains*. Other sediment transport formulas directly yield the *deposited volumes* of sand (per second and metre width). Deposited volumes of sand include the pores between the grains and are a factor $1/(1-p)$ larger than the volumes of solid grains (see Sect. 6.2.2). In the mass balance Eq. 1.1, it was assumed that the volumetric sediment transport rates include the pores. If transport rates of solid grains are considered instead, the mass balance reads (with zero local gains or losses):

$$(1-p)\frac{\partial z_b}{\partial t} + \frac{\partial S_x}{\partial x} + \frac{\partial S_y}{\partial y} = 0 \tag{6.16}$$

where:

$z_b(x,t)$	bed level above a certain horizontal datum	m
$S_x(x,y,t)$	sediment transport rate in the x-direction (volume of solid grains per second and per m width)	$m^3/m/s$
$S_y(x,y,t)$	transport rate in the y-direction	$m^3/m/s$
p	porosity	–

Instead of volumetric transport rates, sometimes mass transport rates are given. This generally does not concern the *dry* mass of the sediment (with density ρ_s), but the immersed (underwater) mass of the sediment. The relation between the volumetric transport rate S (of deposited material, hence including pores) and the immersed mass transport rate I_m is:

$$I_m = \left(\rho_s - \rho\right)(1-p)S \tag{6.17}$$

where:

I_m	immersed mass transport rate	kg/m/s
S	volume transport rates of deposited material	m^3/m/s

Other transport formulas are expressed in terms of immersed weight $I = gI_m$.

The above-mentioned transport rates can be instantaneous transport rates, but also transport rates averaged over various hydrodynamic conditions (a wave group, a storm, a year). The latter is of most interest to coastal engineers.

Bed load versus suspended load

Different transport modes can be distinguished:

Bed load transport the transport of sediment particles in a thin layer close to the bed. The particles are in more or less continuous contact with the bed. Bed load transport at low shear stresses is shown in Fig. 6.6a. At higher shear stresses, an entire layer of sediment is moving on a plane bed (Fig. 6.6b). This is called *sheet flow* and is often considered bed load, since grain-grain interactions play a role.

Suspended load transport the transport of particles suspended in the water without any contact with the bed. The particles are supported by turbulent diffusive forces. Figure 6.6c shows this transport mode.

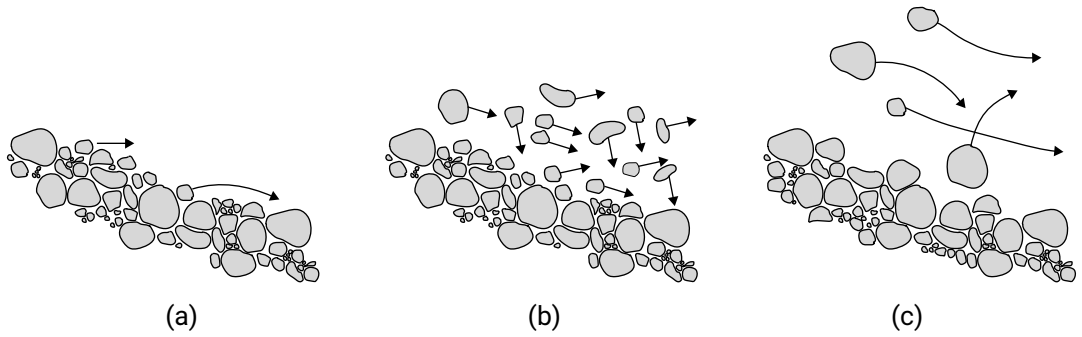

Figure 6.6: Different modes of sediment transport:(a) bed load at small shear stresses; (b) sheet flow (often considered as bed load at higher shear stresses); (c) suspended load.

The sum of bed load and suspended load is called total load. In addition, a third category exists that is named *wash load*. Wash load consists of very fine particles that

will only settle in still water and are not found in the bed. Since these particles do not contribute to bed level changes, wash load is not taken into account into the total load transport.

Bed load transport at low shear stresses

As soon as the bed shear stress exceeds a critical value (Shields parameter between 0.03 and 0.06, see Sect. 6.3), sediment particles start rolling or sliding over the bed. If the bed shear stress increases further, the sediment particles move across the bed by making small jumps, which are called saltations. As long as the jump lengths of the saltations are limited to, say, a few times the particle diameter, this type of motion is considered part of the bed load transport. Close to initiation of motion, the bed remains flat, but for somewhat larger bed shear stresses the bed load occurs primarily via the migration of small-scale bed forms. When the jumps become larger, the particles lose contact with the bottom and become suspended.

Sheet flow transport

At higher shear stresses (Shields parameters higher than about 0.8–1.0), the particles closer to the bed start moving in multiple layers, instead of rolling and jumping in a single layer. In a wave tunnel with reversing flow (see Fig. 6.8), this process can be observed very clearly; the top layer of the bed moves back and forth as a sheet of sand over a flat immobile bed. If the thickness of the sheet flow layer is defined as the distance between the non-moving bed and the level where the time-averaged sediment concentration becomes lower than a volume concentration of 8 vol.% (see Dohmen-Janssen et al., 2001), the thickness of the sheet flow layer is in the order of centimetres. For 8 vol.% the distance between particles is on average equal to the grain diameter. This means that intergranular forces and grain-water interactions are important. Bagnold (1956) defined bed load as that part of the total load that is supported by intergranular forces. According to this definition, sheet flow transport can be considered bed load transport at high shear stresses.

Suspended load transport

Above the bed load layer or sheet flow layer, sediment may be in suspension. Particles in suspension do not immediately return to the bed under the influence of their settling velocity, but are kept in suspension by fluid turbulence. Suspended particles present in a certain vertical plane can be assumed to move horizontally across the plane with the water particles and thus at the same speed as the water particles. The particles are suspended in the flow at relatively low concentrations (less than 1 vol.%), so that intergranular forces are not important.

As mentioned above, in the sheet flow regime (Shields parameters above 0.8–1.0) an entire layer of sediment is moving on a plane bed. Because the bed is plane, the assumption seems reasonable that the suspended load *above* the sheet flow layer is supported by fluid turbulence (or in other words: that the vertical transport of sediment is governed by turbulent diffusive processes). Suspended transport supported by fluid turbulence is further treated in Sect. 6.6.

At lower Shields parameters (below 0.8–1.0), however, the bed will not remain plane. Instead smaller and larger bed forms occur under the influence of currents and the wave orbital motion. Orbital ripples have a length in the order of the free stream orbital velocity amplitude $\hat{u}_0$ (see Sect. 5.4.3 and Eq. 5.27), whereas anorbital ripples are much smaller and scale with the grain size. In the case of a rippled bed, the bed roughness is related to the ripple geometry rather than the grain diameter, as was the case for a plane bed. Furthermore, the flow separates behind the ripple crest and an organised pattern of vortices is formed near the bed (see Fig. 6.7).

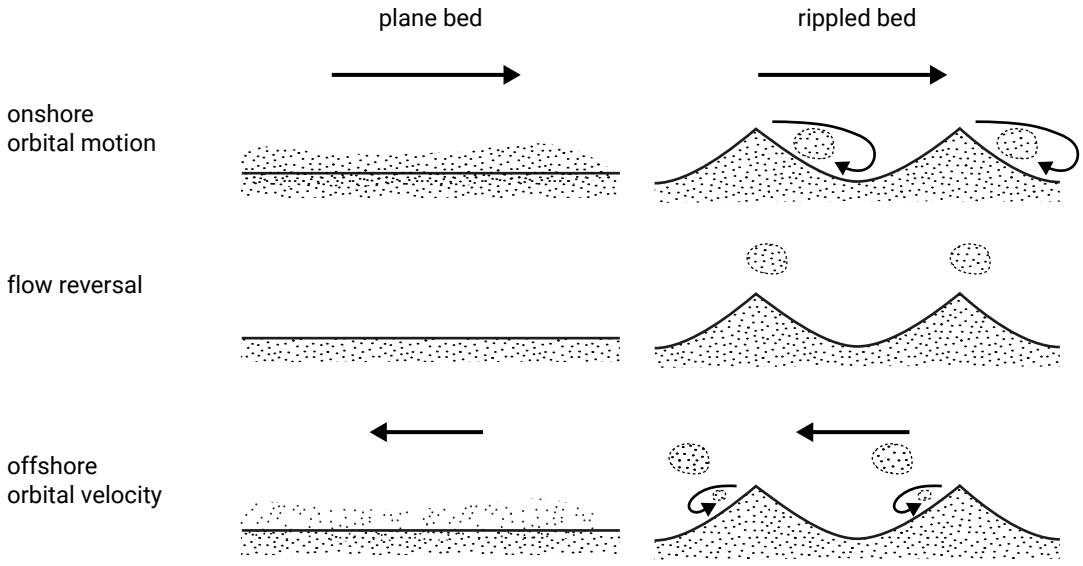

Figure 6.7: Velocity field near a rippled bed in oscillatory flow. The sediment-laden vortices formed by the larger onshore orbital motion are transported in offshore direction by the offshore orbital motion, resulting in a wave-averaged offshore transport.

These vortices are capable of bringing large amounts of sediment into suspension. The timing of these suspension events within the wave cycle is crucial for the magnitude (and the direction, see Sect. 6.6.1 and Intermezzo 6.1) of the resulting wave-averaged sediment transport. Whereas in the plane bed case, it is normally assumed that turbulent diffusive forces keep the sediments in suspension; for a rippled bed, a different approach should be taken, because the upward transport of sediment is now the result of an organised motion. This complicates the computation of $c(z,t)$ as well as of $\nu(z,t)$ considerably and is not explicitly considered in this book.

Intermezzo 6.1 Intra-wave sediment concentration

In a coastal environment, both the velocity and the concentration exhibit large variations within a wave period. Unfortunately, our understanding of $c(z,t)$ especially is very poor. Even in a relatively simple laboratory case of a wave tunnel (Fig. 6.8), the relation between flow kinematics and sediment concentration is far from unambiguous. This can be seen from Fig. 6.9 where nearly a hundred different records of $c(t)$ are shown, all measured at a constant near-bed elevation and under identical regular wave conditions. The scatter in the measuring results is very large. Nevertheless, we can see the following qualitative behaviour:

- A peak in the sediment concentration just after the maximum onshore and offshore velocity ($t/T = 0.25$);
- Two secondary peaks in sediment concentration just after flow reversal (associated with vortices developing over a rippled bed).

The behaviour of $c(z,t)$ in irregular progressive and breaking waves is even less well understood and very difficult to model with reasonable accuracy. This has serious implications for the accuracy of calculations of the intra-wave sediment flux $c(z,t) \cdot u(z,t)$. Besides, due to the oscillatory behaviour of $u(z,t)$, its average value is close to zero, making the computations very sensitive to errors.

Measurements in wave flumes (as opposed to tunnels) show the presence of suspended sediment particles from the bed up to the (instantaneous) water surface. The largest concentrations are found close to the bed, where the diffusivity is large due to ripple-generated eddies. Further away from the bed, the sediment concentrations decrease rapidly because the eddies dissolve rather rapidly travelling upwards.

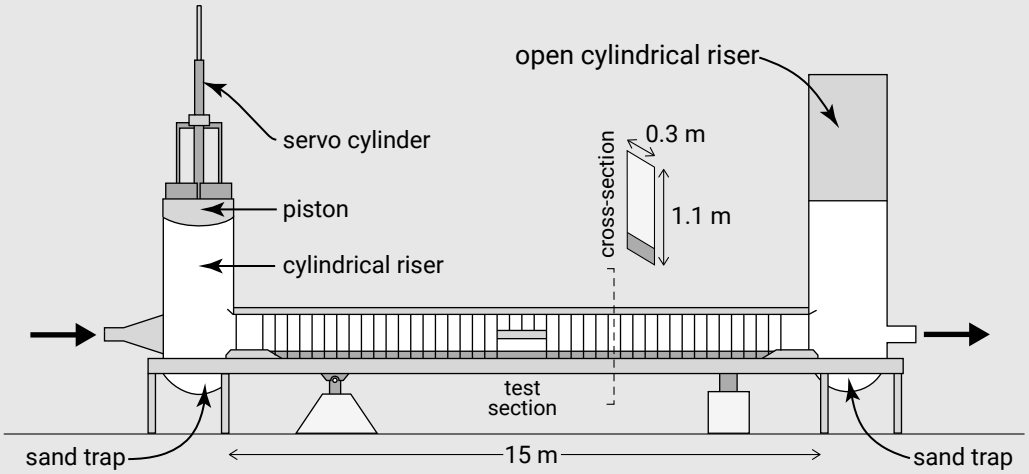

Figure 6.8: Schematic representation of the Large Oscillating Water Tunnel (LOWT) used in the Netherlands to study intra-wave sediment transport phenomena under controlled simulated wave conditions at full scale. The system basically consists of a vertical U-tube with one open leg. The other leg is provided with a piston. At the bottom of the test section, a sediment bed may be installed. The generated oscillatory flow is purely horizontal; as opposed to the case of progressive waves, vertical velocities and horizontal gradients, and thus wave-induced streaming, are absent.

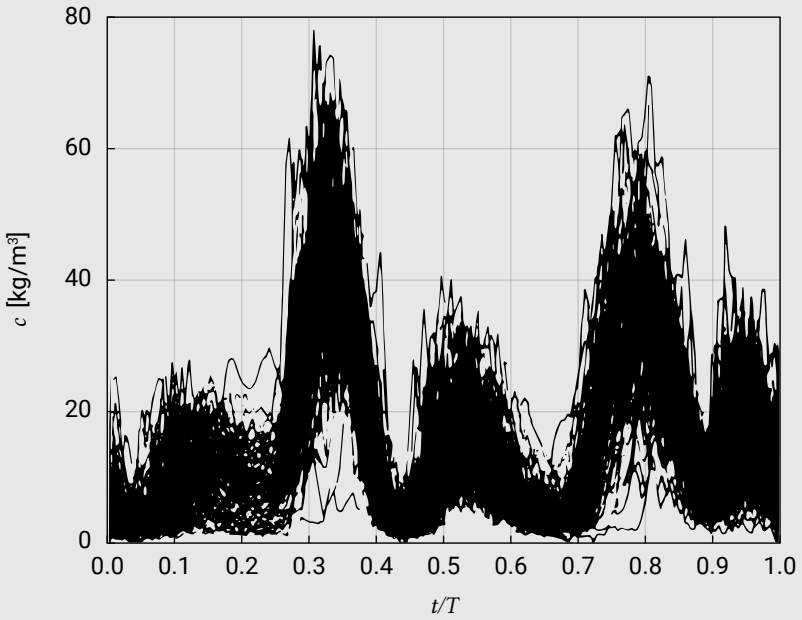

Figure 6.9: Sediment concentrations as a function of time (99 individual records) (Bosman, 1982). On the x-axis: time t relative to wave period T. On the y-axis: sediment concentration in kg/m^3 ($= \mathrm{g/l}$). Sinusoidal water motion $\hat{u}_0 = 0.3\,\mathrm{m/s}$ and $T = 1\,\mathrm{s}$, measured at ripple crest position.

6.4.2. Practical modelling of sediment transport

The mechanisms behind bed load and suspended load are quite different. It is therefore common practice to use separate transport formulas for the two modes of transport.

Bed load transport is almost exclusively determined by the bed shear stress acting on the sediment particles that roll, slide and jump along the bed. Hence, bed load formulas are often expressed in terms of bed shear stress due to currents and waves, often supplemented with a criterion that describes initiation of motion. These formulas are based on either a time-averaged or an instantaneous bed shear stress (Sect. 6.5). In the latter case the sediment is normally assumed to respond *instantaneously* (without delay) to the *intra-wave* (within the wave period) shear stress variation. This is a so-called *quasi-steady* approach to bed load transport. It assumes that inertia (resistance to accelerations and decelerations) plays a minor role only. This is probably a valid assumption for particles smaller than a few millimetres. Generally, the coefficients in the formulas are empirically derived. In practical applications, bed load transport formulas are assumed to predict sheet flow transport rates when used for large Shields parameters.

Suspended load transport takes place above the bed load layer. This is depicted in Fig. 6.10. The suspended sediment *flux* at a certain height above the bed is often modelled as the product of the sediment concentration c and the horizontal velocity u of the water that is transporting the sediment. The suspended sediment *transport* can be computed by integrating the suspended sediment flux uc from the top of the bed load layer to the water level. In order to compute the sediment concentration c, it is generally assumed that turbulent diffusive forces are responsible for transporting the sediment upwards in the water column, against the downward movement with the fall velocity. This approach is treated in detail in Sect. 6.6.

Since sediment particles are allowed time to settle, suspended load does *not* respond instantaneously to hydrodynamic conditions. At the top of the bed load layer, a boundary condition needs to be supplied, for instance a prescribed concentration at $z = a$ (called *reference concentration*) or a prescribed pick-up rate from the bed. Since the bed load transport is determined by the excess shear stress (above a critical value), the reference concentration should be a function of this as well. The exact distinction between the bed load and suspended load is quite arbitrary.

In the coastal zone, where waves play an important role in water motion, both the water velocity u and the sediment concentration c usually vary strongly as a function of time, on a scale comparable to the wave period. However, in engineering applications often only the wave-averaged velocity distribution $U(z)$ and wave-averaged concentration $C(z)$ are used (as shown in Fig. 6.10). The validity of this approach is discussed later.

As mentioned before, the diffusion approach to suspended load transport only makes real sense in case of a plane bed. In the case of a rippled bed, vortices shed off the

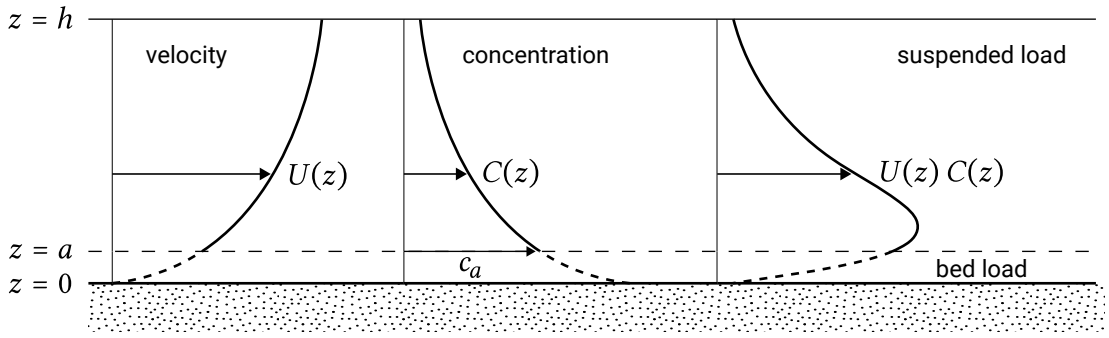

Figure 6.10: Bed load transport takes place in a thin bed load layer close to the bed (between $z = 0$ and $z = a$). The suspended load transport takes place in the upper layer. Note that the z-coordinate is still vertically upward but now the bed is $z = 0$ and the mean water level at $z = h$.

rippled bed bring sediment into suspension. This is an organised rather than a turbulent motion. In practical situations, the presence of ripples can be taken into account by a larger pick-up rate and diffusivity of sediment (Sect. 6.6).

An entirely different approach to bed load and suspended sediment transport is the energetics approach (Bagnold, 1962, 1963, 1966; Bailard, 1981; Bailard & Inman, 1981; Bowen, 1980). It assumes that a certain portion of the fluid energy is expended to keep the sediment, in both bed load and suspended load, in motion. This results in quasi-steady formulas that relate the bed load and suspended load transport to the instantaneous intra-wave velocity at a certain height above the bed. The energetics approach will be treated in Sect. 6.7.

The sum of the bed load transport rate S_b and suspended transport rate S_s equals the total transport rate S_t:

$$S_t = S_b + S_s \tag{6.18}$$

Here S_b and S_t can denote the instantaneous or averaged (over sufficient wave periods) sediment transport. Instead of separately modelling bed load and suspended load transport, sometimes a *total load* formula is used that is assumed to predict the total transport. Such a total load formula could for instance be a function of the time-averaged bed shear stress.

6.5. Bed load based on the Shields parameter

6.5.1. Importance of the Shields parameter

Bed load transport occurs when the bed shear stress or the §1.2 ~~bed shear stress velocity~~ §1.2 shear velocity [p290] $u_* = \sqrt{\tau_b/\rho}$ exceeds a critical value (initiation of motion, Sect. 6.3). In

the bed load layer, turbulent mixing is often assumed to be still small (due to the presence of the bed), so that it only slightly influences the motion of sediment particles. Gravity limits vertical particle movement. We can then assume that the bed load transport responds instantaneously (without delay) to the bed shear stresses.

Many approaches for bed load transport are based on this reasoning and take the sediment transport to be a direct function of the shear stress on the grains. In such formulas the dimensionless sediment transport is invariably a function of a Shields parameter θ (dimensionless shear stress). Many formulas used in coastal engineering practice have been based on already existing formulas used in river engineering. In Fig. 6.11 a comparison is made between various bed load transport formulas developed for rivers.

Although the formulas seem quite different at first glance, Fig. 6.11 demonstrates that they all represent dimensionless transport as a function of a Shields parameter. Further note that the predicted transport rates for a certain value of the Shields parameter vary by up to an order of magnitude. This is (unfortunately) quite common for sediment transport predictions and underlines the fact that calibration of the transport formulas for the locations and conditions under consideration is crucial.

6.5.2. Including waves

For nearshore applications the influence of waves needs to be included into the Shields parameter. This can be done in two ways, either by using the time-averaged (wave-averaged) bed shear stress for the combined wave-current motion or by using the instantaneous bed shear stress (varying during the wave motion). Both approaches will be explained below.

The instantaneous bed load transport vector S_b for waves and currents combined can be written in a dimensionless form as:

$$\Phi_b(t) = \frac{S_b(t)}{\sqrt{(s-1)gD_{50}^3}} \tag{6.19}$$

This dimensionless formulation was proposed by Einstein (1942, 1950) based on theoretical considerations. The denominator is the square root of a parameter representing the specific underwater weight of sand grains. Further, S_b is the bed load transport rate in volume per unit time and width. In applying a certain formula, one should check whether S_b is defined *including* pores or *excluding* pores.

Based on the above, we may expect that instantaneous dimensionless bed load transport $\Phi_b(t)$ responds quasi-steadily to instantaneous bed shear stress (above the threshold for motion, in other words, the critical level of bed shear stress). Hence,

$$\Phi_b(t) = f\left(\theta'(t), \theta_{cr}\right) \tag{6.20}$$

in which f is an algebraic operator and θ_{cr} is defined by Eq. 6.12. The instantaneous dimensionless effective shear stress $\theta'(t)$ due to currents and waves is given by:

$$\theta'(t) = \frac{\tau_b'}{\left(\rho_s - \rho\right) g D_{50}} \tag{6.21}$$

The Shields parameter θ' is a measure of the *forcing* on the sediment grains (drag and lift) relative to the resisting force (see Sect. 6.3.1). The effective bed shear stress τ_b' is that part of the total bed shear stress which is transferred directly to the grains in the bed as skin friction. The form drag induced by *bed forms* is not effective in relation to bed load transportation. One way to compute skin friction is to use a roughness height related to the grain size, not to the bed form size. Also, so-called efficiency or ripple factors μ can be used that represent the fraction of the total bed shear stress that can be attributed to skin friction. The latter approach was followed in Fig. 6.11.

The non-dimensional critical shear stress parameter θ_{cr} represents the threshold of motion of sand grains. It can be computed using the classical Shields curve (Fig. 6.5) or an explicit approximation of the form Eq. 6.15.

Time-averaging Eq. 6.20 gives a time-averaged bed load sediment transport:

$$\boxed{\left\langle \Phi_b(t) \right\rangle = \left\langle f\left(\theta'(t), \theta_{cr}\right) \right\rangle} \tag{6.22}$$

The brackets $\langle\ \rangle$ denote time-averaging.

Some time-averaged formulas for bed load transport relate the time-averaged bed load transport directly to a time-averaged bed shear stress magnitude (averaged over the wave motion) rather than an instantaneous bed shear stress:

$$\boxed{\left\langle \Phi_b(t) \right\rangle = f\left(\left\langle \left|\theta'(t)\right| \right\rangle, \theta_{cr}\right)} \tag{6.23}$$

Note the differences between Eqs. 6.22 and 6.23.

By correlation of the non-dimensional parameters in Eqs. 6.22 and 6.23, using a range of data sets for sediment transport, a general bed load transport formula can be obtained. Many of these exist, based on different data sets and correlating different parameters.

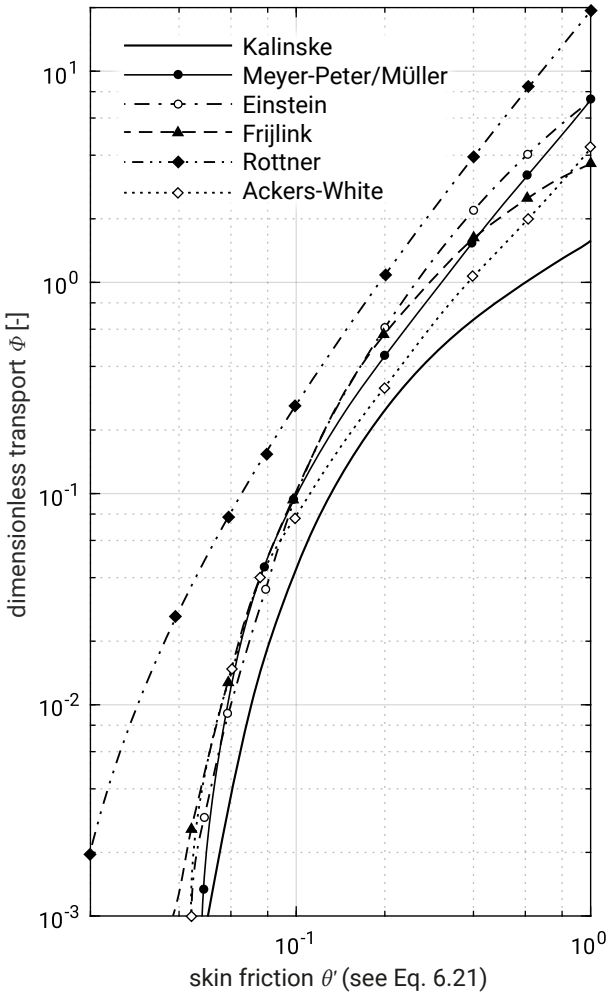

Figure 6.11: Comparison of various bed-load transport formulas developed for rivers. On the y-axis is the dimensionless transport Φ in the case of steady flow (cf. Eq. 6.19), on the x-axis a Shields parameter based on skin friction (cf. Eq. 6.21). Note that $\Delta = (\rho_s - \rho)/\rho$ and the subscript 0 to the shear stress refers to the bed shear stress. Adapted from Breusers (1983).

6.5.3. Instantaneous bed load transport

As an example of a bed load transport formula of the form of Eq. 6.20, we mention the quasi-steady bed load transport formula according to Ribberink (1998). The author assumed that the sand transport rate is a function of the difference between the actual time-dependent non-dimensional bed shear stress and the critical bed shear stress:

$$\Phi_b(t) = \frac{S_b(t)}{\sqrt{(s-1)gD_{50}^3}} = 9.1\frac{\beta_s}{(1-p)}\left\{\left|\theta'(t)\right| - \theta_{cr}\right\}^{1.8}\frac{\theta'(t)}{\left|\theta'(t)\right|} \tag{6.24}$$

The values of the coefficients in this equation were derived using various datasets of sediment transport in oscillatory flow over horizontal beds. Therefore, the formulation is supplemented with a correction β_s to account for slope effects on the transport (see Intermezzo 6.2). The modulus is used to obtain the correct *direction* of transport, i.e.

in the direction of the instantaneous bed shear stress. The transport *magnitude* is dependent on the shear stress magnitude to the power 1.8. The transport rate $^{\S 1.1}S_b(t)$ [p294] is given in volumes, per unit time and width, of deposited material (see the factor $(1-p)$ in Eq. 6.24).

Intermezzo 6.2 Slope effect

An often-neglected transport component is the one due to gravitation along a sloping bed. In case of a sloping bed, not only the effects of slope on the initiation of motion (see Eq. 6.15) have to be taken into account, but also the transport directly induced by gravity when the grains have been set in motion. The bed load formulas are mostly derived from data sets for a horizontal bed and do not automatically include the effect of slope. Nevertheless, we expect moving grains to rather go downhill than uphill. This gives an additional transport component which is directed downhill. Therefore, sometimes a slope correction parameter is introduced (after Bagnold, see also Sect. 6.7.2) which increases the transport rates for downslope transport and decreases the transport rates for upslope transport.

The downhill gravitational transport component has a smoothing effect on the bed topography. This effect is of great importance for the morphological stability of the bed and for the equilibrium state to which the bed topography tends (but which it probably never reaches, since this state is a function of the ever-changing input conditions).

To calculate $S_b(t)$, we need to compute the instantaneous dimensionless bed shear stress (Eq. 6.21). As already indicated in Ch. 5, the computation of time-averaged – let alone instantaneous – bed shear stress under a combined wave-current motion is not straightforward at all. Without detailed modelling of the vertical velocity structure and turbulence, the computation of $\theta'(t)$ is most easily done using a quadratic friction law (see Sects. 5.4.3 and 5.5.5).

Grant and Madsen (1979) suggested expressing bed shear stress as a quadratic function of the combined wave-current velocity at some height z above the bed. With the velocity $u_0(t)$ at the top of the wave boundary layer ($z=\delta$), we have:

$$\tau_b(t) = {}^1\!/_2 \rho f'_{cw} \left|u_0(t)\right| u_0(t) \tag{6.25}$$

in which f'_{cw} is a (skin) friction factor for the combined wave-current motion and u_0 is the time-dependent (intra-wave, that is: within the wave period) near-bottom horizontal velocity vector of the combined wave-current motion. Compare Eq. 6.25 with Eqs. 5.30 and 5.76. In principle the problem is 2DH, since waves and currents may interact under an arbitrary angle. The bed shear stress τ_b and near-bed velocity u_0 are vectors in the same direction with varying magnitudes and varying directions during the wave cycle.

The velocity u_0 should be representative for irregular wave groups and therefore contain contributions due to wave skewness and asymmetry, wave group-related amplitude modulation and bound long waves. These contributions to $u_0(t)$ were described in detail in Ch. 5 and follow from an appropriate wave theory. In addition, the mean flow at the top of the wave boundary layer must be taken into account, for instance by solving the mean flow in the vertical. Wave-induced contributions to the near-bed mean velocity are Longuet-Higgins streaming, undertow and longshore current, as already discussed in Ch. 5. The near-bed velocity vector is then computed as the vector addition of the near-bed oscillatory velocity signal and the time-averaged velocity at the same height.

We then have for the time-dependent $\theta'(t)$:

$$\theta'(t) = \frac{{}^1\!/_2 \rho f'_{cw} \left|u_0(t)\right| u_0(t)}{\left(\rho_s - \rho\right) g D_{50}} \tag{6.26}$$

We have now reduced the problem to the determination of the skin friction factor f'_{cw}. This is the major unknown and therefore the bottleneck in many transport computations. It is dependent on amongst others the bed roughness, which is highly variable in nature and not easily measured in practical applications. This is why results from laboratory experiments are still widely used to find a relationship between the friction factor and the bed roughness.

Note that, since the friction factor f'_{cw} is a skin friction factor (related to grains only and not to bed forms), we need to use roughness heights related to the grain size and not the height of bed forms.

Grant and Madsen determine the friction coefficient f'_{cw} for currents and waves in combination by first computing the (skin) friction factors for 'waves alone' and 'currents in the presence of waves'. This can be done using formulas as presented in Sect. 5.4.3 (but with f'_c evaluated using the mean velocity at the top of wave boundary layer). Note furthermore that currents in the presence of waves experience an increased roughness due to the wave boundary layer. Next, f'_{cw} is calculated by weighting f'_w and f'_c linearly with the relative strength of the near-bed net current and oscillatory velocity amplitude. Others propose different models, resulting in different relative contributions of waves and currents to bed shear stress.

The net wave-averaged bed load transport rate can be obtained by averaging of the time-dependent transport vector $S_b(t)$ over the duration of the imposed near-bottom velocity time series. It includes the transport by the mean current as well as the net transport as a result of the oscillatory wave motion. Due to the non-linear relation between velocity and shear stress, the latter contribution will be zero only for a completely symmetric velocity signal.

At small shear stresses, this bed load transport formulation represents the transport occurring as individual particles moving over a rippled bed, while at higher shear stresses

the formulation represents the sheet flow phenomenon where particles move as bed load in several layers (sheets) over a plane bed.

6.5.4. Bed load transport based on time-averaged shear stress

Considerably simpler are the bed load formulas in which, instead of the instantaneous bed shear stress, the time-averaged bed shear stress is used. Bijker (1967) was the first to present such a model (of the type of Eq. 6.23) for the combination of waves and currents. As a starting point he used the Kalinske-Frijlink bed load transport formula for currents only. This empirical formula had been used extensively for river applications. Bijker adjusted this formula for the combined-wave current situation, by assuming that the effect of waves is to enhance the stirring of sediment, which is consequently transported by the mean current. Later we will explain in some detail that this assumption is especially valid for longshore sediment transport calculations (oscillatory movement approximately perpendicular to the current). The Bijker formula (1967) is given here as an example of a transport formula for time-averaged bed load transport:

$$S_b = BD_{50} \underbrace{\frac{U}{C}\sqrt{g}}_{\substack{\text{current only}\\ \text{transports}\\ \text{the sediment}}} \exp \underbrace{\left[\frac{-0.27(s-1)D_{50}\rho g}{\mu \left\langle |\tau_{cw}| \right\rangle}\right]}_{\substack{\text{wave-current shear stress}\\ \text{stirs up the sediment}}} \tag{6.27}$$

where:

B	Bijker coefficient (= 5)	–
D_{50}	representative particle diameter	m
U	current velocity (e.g. longshore current)	m/s
s	relative density ρ_s/ρ	–
C	Chézy coefficient (see Intermezzo 5.2)	$m^{½}/s$
μ	ripple coefficient: part of the total bed shear that is available for transporting material	–
$\left\langle \lvert\tau_{cw}\rvert \right\rangle$	time-averaged shear stress magnitude for the combined wave-current motion	N/m^2

The value of the Bijker coefficient B has been subject to much discussion. It has been suggested that the value of B should vary from 2 well outside the breaker zone to 5 inside the breaker zone. The main difference with the original Kalinske-Frijlink formula is the use of the time-averaged wave-current shear stress magnitude $\left\langle |\tau_{cw}| \right\rangle$ instead of the time-averaged current-only bed shear stress. We can interpret Eq. 6.27 as the product of the transporting mean velocity times the sediment load stirred up by the combination of waves and currents: $S = U \times$ 'sediment load'. In shallow water the contribution of the wave motion to the bed shear stress magnitude (and therefore to

the stirring of sediment) is often more important than the contribution by the mean current. Therefore, it is often said that waves stir up the sediment, while currents transport it.

Bijker reasoned that at every moment in time, the bed shear *magnitude* determines the stirring of sediment, irrespective of the direction of this shear stress. Therefore, the bed load transport is dependent on $\langle|\tau_{cw}|\rangle$ instead of, for instance, the time-averaged bed shear stress $\langle\tau_{cw}\rangle$. The difference between the two becomes clear when considering a sinusoidal wave only, for which the bed shear oscillates symmetrically as well. The time-averaged bed shear stress $\langle\tau_{cw}\rangle$ is zero. Nevertheless, the waves are able to stir up sediment when the absolute value of the bed shear $|\tau_{cw}|$ is larger than zero (no threshold of motion criterion is considered). Similarly, for the combination of waves and currents, the sediment load is determined by the shear stress *magnitudes*.

Bijker developed generalised formulas for the bed shear stress τ_{cw} for waves at an arbitrary angle with the current. In Sect. 5.5.5 we have already seen that we cannot simply add up the shear stress due to currents and waves; due to the non-linear relationship between velocity and shear stress, we need to add the velocities instead (see Fig. 6.14).

Bijker started with a time series of (linear) waves plus current at a certain height z_t above the bed, from which he derived – using an analytical turbulence model – approximate formulas for not only the mean bed shear stress in the direction of the current τ_m but also for the mean shear stress magnitude $\langle|\tau_{cw}|\rangle$. Bijker's formula for the mean value of the bed shear stress magnitude under combined waves and currents reads:

$$\langle|\tau_{cw}|\rangle = \tau_c \left[1 + \frac{1}{2}\left\{\xi\frac{\hat{u}_0}{U}\right\}^2\right] \tag{6.28}$$

where:

$\hat{u}_0$	maximum orbital velocity at top of wave boundary layer	m/s
U	depth-averaged velocity	m/s
ξ	combination of various parameters $\xi = \sqrt{\frac{1}{2}\frac{f_w}{f_c}} = C\sqrt{\frac{f_w}{2g}}$	–

This formula is dependent on the waves-only friction factor f_w (Eq. 5.33) and the current-only friction factor f_c (Eq. 5.32). It represents the average length of the vector $\langle|\tau_{cw}|\rangle$ of Fig. 6.14 and is independent of the angle between waves and current.

For a typical surf zone situation with approximately normally incident waves (perpendicular to the longshore current velocity V) and under the assumption of $\xi\frac{\hat{u}_0}{V} \gg 1$, Bijker's formula for the mean bed shear stress τ_m in the current direction reduces to a formula identical to Eq. 5.77.

Bijker's model for wave-current shear stress is just one of many wave-current interaction models that can be used in morphodynamic models. Soulsby et al. (1993)

compared various wave-current interaction models, ranging from the Bijker model to sophisticated wave boundary layer models, and analysed how waves and currents in a combined wave-current motion contribute to bed shear stress (see Intermezzo 6.3).

Intermezzo 6.3 Parameterisation of wave-current interaction models

The two parameters that were considered in the intercomparison were the time-averaged bed shear stress in the direction of the current (denoted τ_m) and the maximum bed shear stress (denoted $\tau_{\max}$). See also Fig. 6.12. The choice for these parameters is based on the fact that τ_m is generally required for the computation of the mean current profile in wave-current motion, whereas the parameter $\tau_{\max}$ is important to determine the threshold of motion and the entrainment of sediment. Both the maximum shear stress during a wave cycle and the mean shear stress in the current directionare related to shear stresses that would occur if the wave- and current-only shear stresses could be summed linearly.

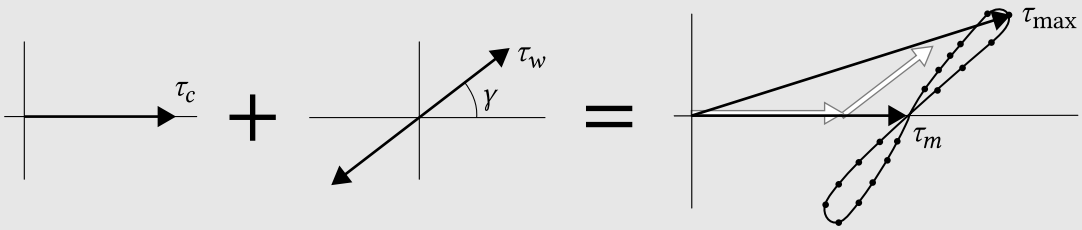

Figure 6.12: Schematic for bed shear stresses with wave-current interaction. The current-alone stress (τ_c, left), and the wave-alone stress (with amplitude $\tau_{w,middle}$) combine non-linearly to give stresses having mean τ_m and maximum $\tau_{\max}$ (right). After Soulsby et al. (1993). The orbital velocity makes an angle γ with the mean current.

Figure 6.13 shows a result of this intercomparison. The lower figure shows that mean bed shear stress goes to zero for waves only and to the current-only shear stress for currents only. For the combination of waves and currents, all models show the expected non-linear enhancement of the bed shear stress when currents and waves are combined; the dotted line in both the upper and lower figure shows the result for a linear addition of the effect of waves and current (shear stress due to waves and currents simply added up). The models differ in the relative effect of waves and currents, with the Bijker model overestimating the effect of waves. This is caused by the fact that the Bijker model does not take into account that the mean flow near the bed is reduced (and the shear stress enlarged) due to the extra resistance introduced by the wave boundary layer. In Fig. 6.12 it was already demonstrated that the angle between waves and current is important. Soulsby et al. (1993) showed that the non-linear enhancement decreased for angles γ going from 0° (waves and current aligned) to 90° (waves and current perpendicular).

The majority of the compared models require extensive computations for the prediction of the time-averaged bed shear stress. Soulsby et al. (1993) parameterised

the models, so that they can be used in a computationally efficient way in morphodynamic models. The models are derived for monochromatic waves (a single harmonic). When applying the models to irregular waves, the orbital excursion amplitude should be based on the H_{rms} (the root-mean-square wave height, Sect. 3.4.2).

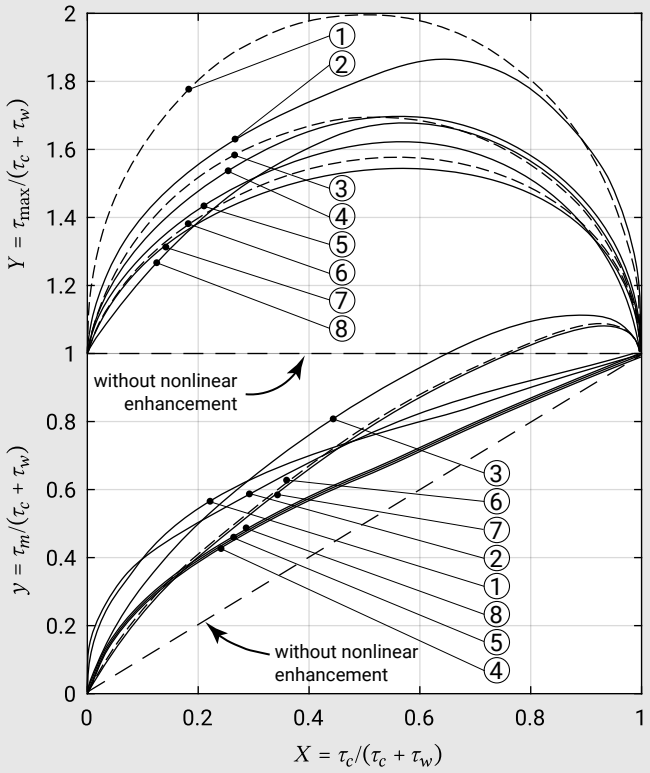

Figure 6.13: Intercomparison of various wave-current interaction models for an angle γ of 0° between waves and currents and for given values of z_0/h and $\hat{\xi}_0/z_0$ where $\hat{\xi}_0 = \hat{u}_0/\omega$ is the particle excursion amplitude (see Eq. 5.24) close to the bed and $z_0 = k_s/30$ with k_s is the Nikuradse roughness height. Adapted from Soulsby et al. (1993).

6.5.5. Summary and concluding remarks

Some theoretical and many (semi-)empirical bed load formulas have been proposed in the literature. Many formulas were originally developed for rivers, and later applied to coastal environments by using a bed shear stress due to waves and currents in the original formulas (Meyer-Peter Müller, Kalinske et cetera). These formulas can normally be written in the form Eq. 6.23.

Unfortunately, there is a massive difference in the results of the different (bed load) formulas, making the uncertainty in sediment transport computations rather large.

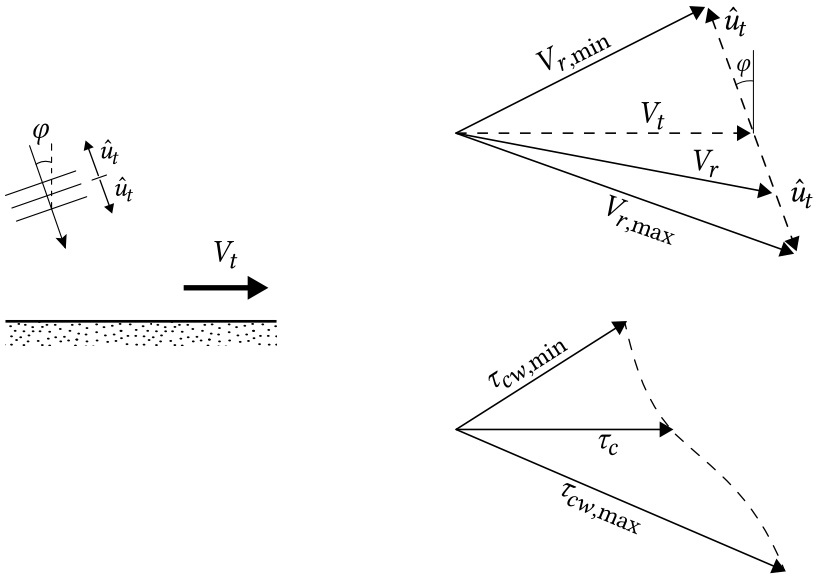

Figure 6.14: Left: plan view of velocity components u_t and V_t at a certain elevation z_t above the bed. Top right: the resultant velocity is V_r and varies in magnitude and direction during the wave cycle (between $V_{r,\min}$ and $V_{r,\max}$). Bottom right: bed shear stress components during the wave cycle. Since $\tau_{cw} \propto |V_r| V_r$, the larger velocities contribute relatively more to the bed shear stress.

Transport formulas can only be used with enough confidence if they have been properly calibrated, preferably with data for the considered site and for representative hydrodynamic conditions.

A common attribute in bed load formulas is that the shear stress is raised to a certain power, say 1.5 to 2. In Eq. 6.24, for instance, at any moment in time, the transport is in the *direction* of the intra-wave velocity and has a *magnitude* proportional to the shear stress magnitude to the power 1.8. Since the shear stress itself is related quadratically to the velocity signal, we may simply state that the magnitude of the instantaneous bed load transport depends on the modulus of the near-bed velocity raised to a power $n = 3$ to 4. As expected, the velocity *direction* does not influence the sediment load. Since the transport is in the direction of the instantaneous velocity, we have $S(t) \propto \text{sign}(u)\,|u|^n$ or equivalently $S(t) \propto u\,|u|^{n-1}$. The latter function may be interpreted as the product of a transporting velocity u and the sediment load stirred by waves and currents proportional to $|u|^{n-1}$. This concept we already encountered in Sect. 6.5.4 for the more specific case of transport dominated by a mean current. Averaged over time, for instance over the short-wave period or the tidal period, we have $\langle S \rangle \propto \left\langle u\,|u|^{n-1} \right\rangle$, with brackets denoting time-averaging. Intermezzo 6.4 demonstrates that even a purely oscillatory motion may give rise to a net (time-averaged) sediment transport.

Intermezzo 6.4 Net sediment transport due to an oscillatory motion?

An oscillatory velocity signal may, under certain circumstances, result in a wave-averaged sediment transport. First imagine a velocity signal $u(t)$ that is purely

symmetric about the horizontal axis (a sine or sawtooth wave). In that case $u|u|^{n-1}$ is also symmetric and it follows that the wave-averaged transport $\langle S \rangle = 0$ (check this by sketching u, $|u|^2$ and $u|u|^2$ as a function of time). The symmetrical orbital motion simply moves an amount of sediment back and forth without a net wave-averaged transport. Now consider a positively skewed velocity signal, typical for shoaling waves (Sect. 5.3) or a flood-dominant tide (Sect. 5.7.4), with larger peak velocities in the wave propagation direction than in the opposite direction. Even though $\langle u \rangle = 0$, we now find $\langle S \rangle \neq 0$. This is because the sediment load responds non-linearly to the velocity, such that more sediment is stirred up during the part of the wave cycle with velocities in the propagation direction (again draw $u|u|^2$). The result is a net (bed load) transport in the propagation direction. Similarly, a net current superimposed on a sinusoidal velocity signal introduces asymmetry about the horizontal axis, leading to a net sediment transport (in the current direction) that is larger than the transport for the current alone situation. Verify this!

6.6. Diffusion approach for suspended transport

6.6.1. General formulation

When the actual bed shear stress is (much) larger than the critical bed shear stress, the particles will be lifted from the bed. If this lift is beyond a certain level, then the turbulent upward forces may be larger than the submerged weight of the particles. In that case, the particles go into suspension, which means that they lose contact with the bottom for some time.

For not too high sediment concentrations and not too heavy particles (so that they follow the water motion), we can assume that at every height the particles move through a vertical plane with the horizontal water velocity. The sediment flux can then be computed from the vertical distribution of fluid velocities and sediment concentrations, as follows:

$$q_s^{\S 1.1}(z,t) = c(z,t)u(z,t) \text{[p301]} \tag{6.29}$$

where:

q	sediment flux	$m^3/s/m^2$
c	local instantaneous sediment concentration at height z above bed	m^3/m^3
u	local instantaneous fluid velocity at height z above bed	m/s

The instantaneous suspended transport rate S_s is found by integrating the sediment flux (Eq. 6.29) from the top of the bed load layer ($z = a$, Fig. 6.10) to the instantaneous water level $h = h_0 + \eta$:

$$S_s(t) = \int_{\S1.1\ z=a}^{h} c(z,t)u(z,t)\,dz \text{[p302]} \tag{6.30}$$

The suspended sediment transport is in the direction of the water velocity. Time-averaging over a representative period gives the time-averaged suspended sediment transport (*exclusive of pores*).

The instantaneous velocity and concentration at a certain height consists of a mean part and an oscillatory part, which is fluctuating on the wave scale but has a zero time mean. Hence:

$$u = U + \tilde{u} \quad \text{and} \quad c = C + \tilde{c} \tag{6.31}$$

in which:

U	time-averaged fluid velocity at height z	m/s
C	time-averaged concentration at height z	m^3/m^3
$\tilde{u}$	oscillating fluid component	m/s
$\tilde{c}$	oscillating concentration component	m^3/m^3

Substituting Eq. 6.31 into Eq. 6.30 and time-averaging yields:

$$\underbrace{\langle S_s \rangle}_{\substack{\text{time-averaged} \\ \text{sediment transport rate}}} = \underbrace{\int_a^h UC\,dz}_{\substack{\text{current-related} \\ \text{part}}} + \underbrace{\int_a^h \overline{\tilde{u}\tilde{c}}\,dz}_{\substack{\text{wave-related} \\ \text{part}}} \tag{6.32}$$

Time-averaging is indicated by the brackets and the overbar. In order to express the transport rate in terms of deposited volumes, we need to multiply Eqs. 6.30 and 6.32 with $1/(1-p)$, with p the porosity of the deposited material.

The first part of the right-hand side of Eq. 6.32 is the so-called *current-related suspended sediment transport*: the transport of sediment particles by the time-averaged current velocities. In the coastal zone, the transporting currents are often wave-induced, for instance rip currents and longshore currents. Furthermore, secondary currents can give rise to a net current-related sediment transport, even though the depth-averaged mean current velocity is zero, see Intermezzo 6.5. An example is the undertow, below the wave trough level, which is responsible for an offshore-directed suspended sediment transport under breaking waves. The time-averaged sediment concentrations are affected by the wave motion. Considerable amounts of sediment are brought into

suspension by turbulence, generated at the surface under breaking waves and in the wave boundary layer near the bed.

The second part of the right-hand side is the *wave-related suspended sediment transport*: the transport of sediment particles by the oscillatory water motion. As for the bed load transport, skewness of the oscillatory velocity signal can result in a net wave-related suspended sediment transport (see Intermezzo 6.4). It is however complex and (computer) time-consuming to compute the wave-related suspended sediment transport by solving the intra-wave velocities and concentrations. Moreover, very little is known about the intra-wave concentrations and such a computation would be very uncertain. The exact phase relationship between velocity and concentration at every height above the bed is crucial in determining the magnitude and direction of the wave-related suspended sediment transport. In the case of a plane bed, one may expect a wave-related suspended sediment transport in the wave propagation direction. But in the case of a rippled bed (where the concentrations are largest around flow reversal, see Intermezzo 6.1) this may lead to an offshore-directed wave-related suspended load transport! The latter could be the case if more sediment is brought into suspension at flow reversal from onshore to offshore.

The wave-related part of the suspended sediment transport is often assumed to be smaller than the current-related part. This simplifies the modelling significantly. In practical models it is therefore often assumed that the suspended load transport is dominated by the transport by the mean current; the suspended sediment flux is computed as the product of the wave-averaged current and concentration profiles (using e.g. formulations according to Van Rijn (1989, 1993, 2000) and Soulsby and Van Rijn (Soulsby, 1997).

$$\underbrace{\langle S_s \rangle}_{\substack{\text{time-averaged} \\ \text{sediment transport rate}}} \simeq \underbrace{\int_a^h UC\, dz}_{\substack{\text{current-related} \\ \text{part}}} \tag{6.33}$$

The contribution of the oscillatory velocity to the sediment transport is then thought to be taken into account in bed load transport computations. The mean (wave-induced) current profile can be computed as explained in Sect. 5.5.6. In order to compute the time-averaged concentration, an advection-diffusion equation is often used. This will be treated below.

Note that even with a zero depth-averaged velocity – as in the case of a circulation current – a net current-related sediment transport can occur (see Intermezzo 6.5).

By using a bed load transport formula of the form as in Eq. 6.22 and a suspended load transport according to Eq. 6.33, it is possible that bed load and suspended load transport are in opposite directions. Let us first consider cross-shore sediment transport. In the surf zone, the bed load transport will generally be directed onshore (due to short-wave

skewness) and the suspended transport offshore as a result of the undertow. This is further discussed in Sect. 7.5. In the alongshore direction, further simplifications may be made. Since, due to refraction, the oscillatory wave motion is almost perpendicular to the coast, the transport in the alongshore direction is governed by the slowly varying longshore current (wave- or tide-induced). The role of waves in longshore transport is merely to stir up sediment that is consequently predominantly transported along the coast by the current (cf. Sect. 6.5.4). Specific longshore sediment transport formulas are treated in Sect. 8.2.

Intermezzo 6.5
Net suspended sediment transport due to secondary flows

The combination of suspended load transport with secondary flows can give a net sediment transport, even though the depth-averaged velocity is zero. This is the result of the non-uniform distribution of the sediment concentration over the vertical: most of the sediment is concentrated in the lower part of the water column. An example is the cross-shore secondary flow under breaking waves discussed above, that gives a net transport component against the direction of wave propagation; the sediment concentrations are largest in the lower layers of the water column, where the velocity is offshore-directed (undertow). Under non-breaking waves, wave-induced streaming close to the bed may result in an onshore directed transport. In the same way, secondary flows in a tidal basin can have a net effect on the transport direction. The curvature-induced secondary flow in a channel bend (Sect. 5.7.6), for instance, will give a net transport component towards the centre of curvature (from the outer bend to the inner bend). Another potentially important contribution of this type is associated with the deformation of the velocity profile as the flow moves up or down a steep slope (see Fig. 6.15). When averaged over the tide, this gives a net upslope transport. This may explain why the steep banks of tidal channels can be stable.

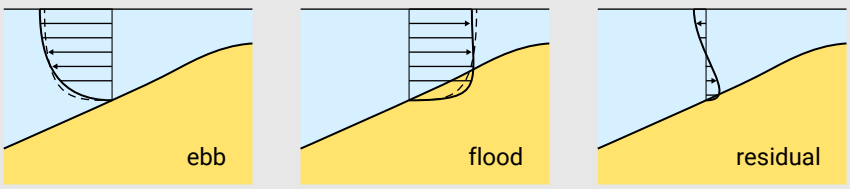

Figure 6.15: Residual tide-averaged velocity profile resulting in a net upslope transport.

6.6.2. Sediment continuity

In order to obtain the sediment concentration, a mass balance equation for the sediment needs to be solved. The general conservation statement for the sediment reads:

$$\underbrace{\frac{\partial c}{\partial t}}_{\substack{\text{change in}\\ \text{sediment}\\ \text{concentration}}} \underbrace{+\frac{\partial uc}{\partial x}+\frac{\partial vc}{\partial y}}_{\substack{\text{net import of sediment}\\ \text{by the horizontal}\\ \text{fluid velocity}}} \underbrace{+\frac{\partial wc}{\partial z}}_{\substack{\text{net upward transport}\\ \text{of sediment by the}\\ \text{vertical fluid velocity}}} \underbrace{-\frac{\partial w_s c}{\partial z}}_{\substack{\text{net downward transport}\\ \text{with the fall velocity}}} = 0 \tag{6.34}$$

or using the continuity equation for the fluid:

$$\frac{\partial c}{\partial t}+u\frac{\partial c}{\partial x}+v\frac{\partial c}{\partial y}+w\frac{\partial c}{\partial z}-\frac{\partial w_s c}{\partial z}=0 \tag{6.35}$$

Please note that in Eqs. 6.34 and 6.35 the velocity and the concentration are the *total signals consisting of a mean, an oscillatory and a turbulent part.*

The horizontal advective terms are often (but not always) smaller than the vertical advective terms (see Intermezzo 6.6). Let us for simplicity neglect the horizontal advective terms of Eq. 6.34, so we are left with:

$$\frac{\partial c}{\partial t}+\frac{\partial wc}{\partial z}-\frac{\partial w_s c}{\partial z}=0 \tag{6.36}$$

Intermezzo 6.6 Drift of suspended sediment

Similarly to the drift of water (Stokes drift, Sect. 5.5.1), there is also a drift of suspended sediment. Under the wave crest the suspended sediment concentration is stretched out, whereas under the trough it is compressed. Stokes drift was explained by the fact that water levels are higher during the forward orbital motion than during the backward motion. Analogously, a suspended sediment drift occurs. This drift is only taken into account when the horizontal advective terms are included in the advection-diffusion equation.

As said previously, the velocity and the concentration consist of a mean, an oscillatory and a turbulent part. Hence, $w = W + \tilde{w} + w'$ and $c = C + \tilde{c} + c'$. We are certainly not going to resolve the turbulent motion and would like to average over that motion. This is called Reynolds averaging. If we average Eq. 6.36 over the turbulence scale, most terms with turbulent fluctuations average out, except for one term, viz. $\partial\langle c'w'\rangle/\partial z$. Here the brackets denote averaging over the turbulence timescale and $\langle c'w'\rangle$ is the (upward) sediment flux by turbulence. Further, the Reynolds averaged vertical water

velocity can be assumed to be negligible compared to the fall velocity of the sediment. With the simplification of a constant fall velocity (in reality the fall velocity depends on the concentration, see Sect. 6.2.3), we end up with the following often-used form of the advection-diffusion equation:

$$\frac{\partial c}{\partial t} \underbrace{- w_s \frac{\partial c}{\partial z}}_{\substack{\text{sediment net going downward} \\ \text{with its fall velocity}}} \underbrace{+ \frac{\partial \langle c' w' \rangle}{\partial z}}_{\substack{\text{sediment net going upward} \\ \text{with fluid turbulence}}} = 0 \tag{6.37}$$

Please note that in this equation the concentration c now denotes the turbulence-averaged concentration: $c = C + \tilde{c}$.

In order to model the sediment flux due to turbulence, we make a similar assumption that upward transport of sediment is due to turbulent diffusion, as we did for the fluid (see for instance Eqs. 5.85 and 5.88):

$$-\langle c' w' \rangle = \nu_{t,s} \frac{\delta c}{\delta z} \tag{6.38}$$

in which $\nu_{t,s}$ is the turbulent diffusivity of sediment mass in m^2/s and c is now defined as *volume concentration* (see Sect. 6.2.2). This upward transport by turbulent diffusion can be understood as follows. Turbulent exchange makes sure that a sediment-laden fluid parcel goes upward to a level with a lower sediment concentration. A sediment parcel going downward contains less sediment than the average parcel at the level where it arrives. Since more sediment particles are carried upward than downward, the net effect is upward transport.

Sometimes the turbulent diffusivity $\nu_{t,s}$ of sediment mass is taken to be equal to the turbulent viscosity ν_t of the water. However, it can also be argued that the mixing of water and sediment are two different things. Whatever approach is taken, normally the damping of turbulence due to high sediment concentrations is taken into account. This refers to the influence that sediment particles have on the turbulence structure of the fluid. This effect becomes increasingly important for high sediment concentrations that result in stratification and hence damping of turbulence. This affects both the water motion and the sediment distribution. Empirical formulations are sometimes used, which reduce the eddy viscosity dependent on the sediment concentration.

The non-steady advection-diffusion equation now reads:

$$\boxed{\frac{\partial c}{\partial t} - w_s \frac{\partial c}{\partial z} - \frac{\partial}{\partial z} \nu_{t,s} \frac{\delta c}{\delta z} = 0} \tag{6.39}$$

As a bottom boundary condition, a sediment concentration at a certain level near the bed is prescribed, the so-called reference concentration. This concentration is prescribed at a certain reference level, for instance $z_a = 2D_{50}$, also depending on the bed

load formula. The reference concentration is often assumed to be a function of the bed shear stress (much like the bed load transport formulas). Hence, at the bed the response is quasi-steady, whereas higher in the vertical, the sediment concentration lags behind the shear stress at the bed. An alternative boundary condition is a pick-up function that prescribes the vertical concentration gradient instead of the concentration.

Detailed models that also resolve the wave boundary layer (Sect. 5.4.3) resolve the time-dependent concentration in the vertical, in order to model sheet flow transport and suspended load transport. The time-dependent suspended sediment concentration can be determined with an unsteady advection-diffusion equation such as Eq. 6.39. This approach involves the modelling of the turbulence, which increases and decreases during a wave period; this is difficult and time-consuming (see also Intermezzo 6.1).

6.6.3. Time-averaged concentration distribution

In a steady situation $\partial c/\partial t = 0$ and $c = C$. A balance must exist between the upward transport by turbulence and the downward transport with the fall velocity. Integration of Eq. 6.39 over the depth (with a zero vertical flux at the water surface) leads to:

$$w_s C(z) + \nu_{t,s}(z)\frac{dC(z)}{dz} = 0 \tag{6.40}$$

This equation indicates an equilibrium between the downward transport with the fall velocity $w_s C(z)$ and the net upward movement of grains by turbulence.

As mentioned above, local turbulence in the water column leads to an upward and a downward exchange of sediment-laden fluid parcels. Since the sediment concentration is larger close to the bed, more grains will be transported in the upward direction than in the downward direction. This leads to a turbulent transport of sediment, which depends on the gradient in concentration over the vertical. This is why it is referred to as a gradient-type transport. On average, turbulence transports sediment from levels of high concentration to levels of lower concentration, i.e. from lower levels in the water column to higher levels.

Generally the suspended sediment is somewhat finer than the bed material. Hence, in order to compute the constant fall velocity, a smaller grain diameter is often used than in the computation of the bed load transport.

The assumption of upward transport due to turbulent diffusion seems reasonable for a plane bed. In case of a rippled bed however, it can be expected that upward transport is by eddies generated by the ripples (see Intermezzo 6.1). These are coherent fluid motions that bring the sediment upward by convection. In that case, the whole concept of upward transport proportional to a concentration gradient does not hold

anymore. Sometimes, the diffusion concept is stretched a bit by assuming that the sediment diffusivity accounts for the convection processes also.

It makes sense to relate the turbulent diffusivity $\nu_{t,s}$ of sediment mass to the eddy viscosity of the fluid through a factor β: $\nu_{t,s} = \beta\nu_t$. A value of $\beta < 1$ reflects that the sediment particles cannot respond fully to the turbulent fluid velocity fluctuations (inertia). On the other hand $\beta > 1$ (supported by laboratory experiments) indicates a more effective mixing for sediment particles than for water particles. It has been argued that this is the result of larger centrifugal forces on sediment particles in eddies than on fluid particles (because of their higher density). In the following $\beta = 1$ is used.

With an appropriate distribution for $\nu_{t,s}$ (for which many options are discussed in literature!) and a bottom boundary condition, Eq. 6.40 can be integrated either numerically or analytically. Analytical solutions are possible for simple diffusivity distributions.

The integration is performed from a near-bed reference level a to the water surface. At the reference level a, a concentration-type boundary condition can be used. Since in principle $z = a$ corresponds to the top of the bed load layer, the reference concentration must be somehow related to the bed load transport rate, for instance via:

$$C_a = \frac{S_b}{ua} \tag{6.41}$$

where:

S_b	bed load transport	$m^3/m/s$
u	average fluid velocity in the bottom layer	m/s
a	thickness of the bottom layer (order of magnitude of the bottom roughness r)	m

The reference concentration is often formulated as a function of the time-averaged bed shear stress and should take the enhanced stirring by waves into account.

The most general solution of Eq. 6.40 is:

$$C(z) = C_a \exp\left[-\int_{z=a}^{z} \frac{w_s}{\nu_{t,s}(z)} dz\right] \tag{6.42}$$

where:

C_a	time-averaged concentration at level $z = a$	–
w_s	fall velocity	m/s
z	height above the bed	m

Einstein (1942, 1950) and Rouse (1937) suggested a parabolic distribution of the diffusion coefficient over the water depth:

$$\nu_{t,s}(z) = \kappa u_* \frac{z}{h}(h - z) \tag{6.43}$$

where:

κ	Von Karman constant $= 0.4$	–

A parabolic sediment diffusivity is in accordance with the generally assumed parabolic eddy viscosity in the water column (increasing from zero at the 'walls' to a maximum away from the walls, see Eq. 5.88 and the text below it).

This results in the following concentration distribution (see Fig. 6.16):

$$C(z) = C_a \left[\frac{h - z}{z} \frac{a}{h - a} \right]^{z_*} \tag{6.44}$$

where:

a	thickness of the bottom layer	m
C_a	concentration at reference level $z = a$	–
z_*	Rouse number defined as $z_* = \frac{w_s}{\kappa u_*}$	–

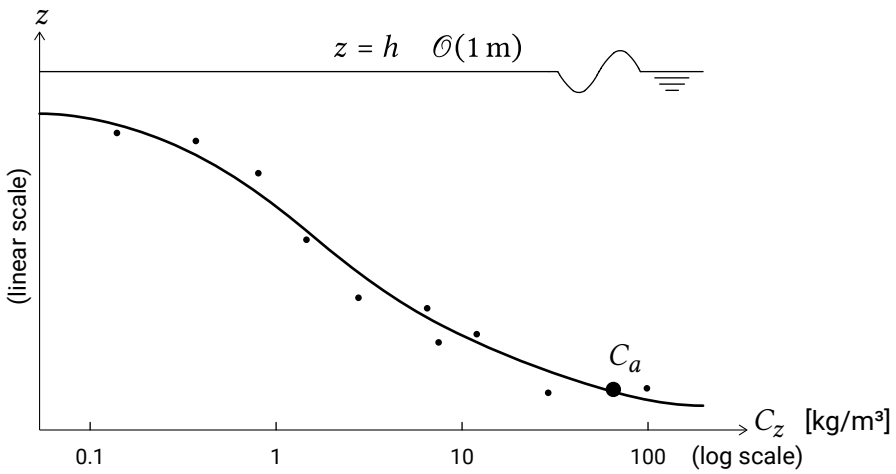

Figure 6.16: Sediment concentration distribution over water depth (parabolic mixing coefficient). Concentration magnitude and distribution over depth are representative for wave or wave-current situations, as for instance in the surf zone.

The Rouse number is a non-dimensional number that not only defines the sediment concentration profile, but also determines the mode of transport. It is the ratio between the downward sediment fall velocity and the upwards velocity on the grain represented by κu_*. For Rouse numbers larger than, say, 2.5 (or $w_s/u_* > 1$) all transport is bed

load transport. For a Rouse number smaller than, say, 0.8, we have only wash load. Between these extremes, sediment suspension occurs. If $w_s/u_* > 1$ we may say that the sediment is coarse and responds quasi-steadily to the flow field. For $w_s/u_* < 1$ ('fine' sand in suspension) non-instantaneous sediment responses start playing a role.

6.7. Energetics approach

6.7.1. Introduction

The energetics approach to bed load and suspended load transport is a more integrated approach to bed load and suspended load transport and was first developed by Bagnold (1963, 1966) for rivers. The underlying idea is that a certain amount of energy is needed to keep the bed load moving and the suspended load at a certain height above the bed. The sediment transport formula of Bagnold is therefore proportional to the rate of energy dissipation of the stream. It also includes an efficiency factor for bed load and suspended load that determines how efficiently the energy is used for the sediment transport. Besides, the effect of downward transport by gravity is included. In this section the energetics transport model is discussed in general terms. In Sect. 7.5, we apply the model to unravel the various contributions to cross-shore sediment transport as well as treat model applications to obtain equilibrium beach profiles.

6.7.2. Energetics approach for combination of waves and currents

Bagnold derives formulas for the immersed weight suspended load I_s and bed load transport I_b (see text below Eq. 6.17 for the definition of immersed weight transport rates) for uni-directional flow. In his derivations, it was hypothesised that the fluid acts as a machine expending energy at a prescribed efficiency rate to offset the work done in transporting sediment. His reasoning is briefly demonstrated here for bed load transport.

The immersed weight of a mass of bed load m_b is given by $W = \left(\rho_s - \rho\right)/\rho_s \, g m_b$. The component of this perpendicular to the sloping bed – with bed slope $\tan\alpha$ – is $W\cos\alpha$, whereas the component parallel to the bed is $W\sin\alpha$. Hence, the frictional resistance for downslope transport is equal to $W\left(\mu\cos\alpha - \sin\alpha\right)$. Here, the friction coefficient $\mu = \tan\varphi_r$ with φ_r is the angle of repose (Sect. 6.2). 'Work' is defined by the exerted force times the distance travelled in the direction of the force. Therefore, the work done (per unit time) in maintaining bed load in motion is equal to the force required to overcome frictional resistance times the mean speed U_b at which the grains travel. Further, since $U_b\cos\alpha$ is the horizontal component of the grain velocity in a vertical

section, the immersed weight transport rate through a vertical section is defined as $I_b = WU_b \cos\alpha$. We can now write:

$$\text{work done per unit time } = W\left(\mu\cos\alpha - \sin\alpha\right)U_b = I_b\left(\tan\varphi_r - \tan\alpha\right) \tag{6.45}$$

Some fraction ε_b of the dissipated fluid power ω is expended to offset the work done in maintaining the bed load.

Hence:

$$I_b = \frac{\varepsilon_b\omega}{\left(\tan\varphi_r - \tan\alpha\right)} \tag{6.46}$$

A similar derivation for suspended load leads to:

$$I_s = \frac{\varepsilon_s\omega}{\left(w_s/U_s - \tan\alpha\right)} \tag{6.47}$$

Eqs. 6.46 and 6.47 apply to uni-directional flow along a downsloping bed. Bowen (1980) rewrites these equations for a cross-shore situation with normally incident waves. The formulas for the instantaneous transport rates then read:

$$I_b = \frac{\varepsilon_b\rho c_f u^3}{\tan\varphi_r - u/|u|\tan\alpha} \tag{6.48a}$$

$$I_s = \frac{\varepsilon_s c_f \rho u^3|u|}{w_s - u\tan\alpha} \tag{6.48b}$$

where:

$\varepsilon_b, \varepsilon_s$	efficiencies for bed and suspended load	–
c_f	friction coefficient	–
w_s	sediment fall velocity	m/s
$\tan\varphi_r$	tangent of angle of repose of the sediment	–
$\tan\alpha$	bed slope	–
ρ	water density	kg/m^3

The time-dependent velocity u is defined as positive seawards, the direction of x positive. The bed load and suspended load velocity of the grains (U_b and U_s) are represented by u. Further, the dissipated fluid power ω (work done per unit time) is computed as the energy dissipation rate D_f, due to bottom friction. D_f is given by the product of bed shear stress τ and the near-bottom time-varying flow u. The bed shear

stress is assumed to be described by a quadratic friction law $\tau_b = \rho c_f |u| u$, so that $\omega = D_f = \rho c_f u^2 |u|$. Note that in this way only the dissipation in the wave boundary layer is taken into account. For applications in the surf zone, Roelvink and Stive (1989) add to this the energy dissipation due to turbulence near the bottom induced by wave breaking. The modulus signs in Eqs. 6.48a and 6.48b are chosen such as to properly account for the direction of transport in terms of velocity and slope. Hence, for seaward transport (u positive) the denominators are reduced; material is therefore more easily transported downslope.

The bed slope is limited by the following two conditions:

$$\tan\alpha \to \tan\varphi_r \qquad \text{giving avalanching or slumping} \tag{6.49a}$$

$$\tan\alpha \to w_s/u \qquad \text{giving autosuspension} \tag{6.49b}$$

Autosuspension refers to the fact that for a certain bed slope (and hence a certain amount of gravitational energy) the sediment 'suspends itself'. Bailard (1981) argued that the condition in Eq. 6.49b needs to be supplied with an efficiency factor as well (such that $\varepsilon_s u$ instead of u should be used).

Note that the model lacks an initiation of transport condition like the critical Shields parameter and that both the bed load and the suspended sediment transport respond instantaneously to the flow field (as opposed to the diffusion approach of Sect. 6.6).

In a parallel development, Bailard (Bailard, 1981, 1982; Bailard & Inman, 1981) generalised the Bagnold model to a total load model of time-varying sediment transport over a plane, sloping bed. In the Bailard formulation both the bed load and suspended load transport rate vectors are composed of a velocity-induced component directed parallel to the instantaneous velocity vector and a gravity-induced component directed downslope. Now alongshore and onshore-offshore currents as well as oscillatory wave-induced orbital motion with a local angle of incidence are considered.

Here we will not go into the details of the derivation and the final formulas, but follow Roelvink and Stive (1989), who write the Bailard formula in general terms (for the simplified case of the velocity aligned with the local bed slope):

$$S(t) = \underbrace{C_1 u(t) \left|u(t)\right|^{n-1}}_{\text{quasi-steady response to time-varying flow}} + \underbrace{C_2 \left|u(t)\right|^{m} \tan\alpha}_{\text{response to downslope gravity force}} \tag{6.50}$$

Here $\tan\alpha$ is the local bed slope and $u(t)$ is the near-bottom time-varying cross-shore flow. For bed load, the powers are $n = m = 3$, and for suspended load the powers are $n = 4$ and $m = 5$. After time-averaging (indicated by brackets) we find that:

- the bed load transport $\langle S_b \rangle$ is proportional to the odd moment $\left\langle u|u|^2 \right\rangle$ and the even moment $\left\langle |u|^3 \right\rangle$; and

- the suspended load transport $\langle S_s \rangle$ is proportional to the odd moment $\langle u|u|^3 \rangle$ and the even moment $\langle |u|^5 \rangle$.

Note that for the *even* moments, the terms within brackets (i.e. before time-averaging) are positive for every moment in time, whereas for the *odd* moments these terms have the same sign as the instantaneous velocity. The transport terms containing the odd moments $\langle u|u|^2 \rangle$ and $\langle u|u|^3 \rangle$ reflect the quasi-steady bed load and suspended sediment load transport respectively, due to the time-varying flow. The terms containing the even moments $\langle |u|^3 \rangle$ and $\langle |u|^5 \rangle$ reflect the downslope-directed, gravity-driven transport and are usually an order of magnitude smaller than the terms containing the odd velocity moments.

We could therefore make the following approximate statement:

$$\langle S_b \rangle \propto \langle u|u|^2 \rangle \tag{6.51a}$$

$$\langle S_s \rangle \propto \langle u|u|^3 \rangle \tag{6.51b}$$

Note that in Sect. 6.5.5, we found similar dependencies for bed load transport, viz. $\langle S_b \rangle \propto \langle u|u|^{n-1} \rangle$ with $n = 3$ to 4. There we also found that net sediment transport is either due to net currents or due to skewed oscillatory velocity signals. This distinction is comparable to the distinction between current-related and wave-related suspended sediment transport, as discussed in Sect. 6.6.1. We will further explore these different transport contributions in Sect. 7.5 (for cross-shore sediment transport) and in Sect. 9.7.2 (for tide-induced sediment transport).

As said before, a criterion for initiation of motion was not taken into account in the energetics approach discussed above. This can be expected to increase the asymmetry in sediment stirring. Another simplification is the assumed quasi-steady approach for suspended load transport. Coarse sediment responds more or less instantaneously to the flow velocity, but for finer material this may not be the case. Fine material in this respect is defined as having a diameter such that $u_*/w_s > 1$, where u_* is the shear velocity and w_s is the fall velocity (see also Sect. 6.6.3). The larger this parameter, the more time the suspended particles need to settle. As a result of these time-lags in the vertical sediment distribution, the transport rates may be reduced (since the maximum concentrations no longer coincide with the maximum velocities at every height above the bed). An example of a sediment transport formula in which such time-lag effects are taken into account is given by Dibajnia and Watanabe (1993).

6.8. Some aspects of (very) fine sediment transport

6.8.1. Memory effects

Suspended load transport is a quite common condition in the coastal environment, maybe even more common than pure bed load. From a morphological modelling point of view, we must distinguish two types of suspended load: one which is determined entirely by the hydrodynamic conditions and the sediment properties at the point of consideration, and one which includes a 'memory effect' and responds to the conditions in all points it has come through in the past. The former type can be modelled with a sediment transport formula (e.g. the Bijker or the Bailard formula), or with an intra-wave model which describes the suspension process during a wave cycle (see Sect. 6.6).

The §1.2depth-averaged [p314] sediment concentration associated with the second type of suspended load transport is described by an advection/diffusion equation of the type Eq. 6.52, as given by, amongst others, Katopodi and Ribberink (1992) for tidal currents, and Wang and Ribberink (1986) for nearshore applications:

$$T_A \frac{\partial c}{\partial t} + L_A \left[\frac{u}{u_{\text{tot}}} \frac{\partial c}{\partial x} + \frac{v}{u_{\text{tot}}} \frac{\partial c}{\partial y} \right] = c_{\S 1.2_e \S 1.2_{eq}} - c \text{[p314]} \tag{6.52}$$

§1.2Eq. 6.52 describes the adjustment of the depth-averaged concentration c to its equilibrium value c_{eq} according to a relaxation process. The parameters T_A and L_A represent the characteristic scales of this adjustment process.§1.2~~in which~~ §1.2The adaptation time T_A is a timescale of the order of magnitude h/w_s and §1.2the adaptation length L_A is a length scale of the order of magnitude $u_{\text{tot}} h/$§1.1~~ws~~§1.1w_s [p314]. The adaptation time- and length scales increase for finer sediment (smaller settling velocity). The equilibrium concentration, $c_{\S 1.2_e \S 1.2_{eq}}$ [p314], corresponds to the spatially uniform situation and is usually derived from a sediment transport formula, or from a simpler model which applies to uniform situations.

Note that Eq. 6.52 can also be considered a decay equation of the type:

$$\frac{Dc}{Dt} + \frac{c}{T_A} = \frac{c_{\S 1.2_e \S 1.2_{eq}}}{T_A} \text{[p314]} \tag{6.53}$$

in which D/Dt stands for the material derivative, i.e. moving along with the sediment flow. If the concentration at $t = 0$ is given, the general solution can be written as:

$$c(t) = c(0) e^{-t/T_A} + \int_0^t \S 1.2 \frac{1}{T_A} c_{\S 1.2_e \S 1.2_{eq}}(\tau) e^{-(t-\tau)/T_A} \, d\tau \text{[p314]} \tag{6.54}$$

in which τ is a formal time variable which runs from 0 to the actual time t. Apparently, all values of the equilibrium condition encountered in the time interval between 0 and

t contribute to the forcing term (i.e. the second term in the right-hand part of the equation), but their contributions become smaller as they occurred longer ago. This shows that the memory of the system is not infinite, but has a certain timescale T_A.

The memory effect of the suspended load concentration can be rather important in a tidal inlet system, with its strong spatial variations of the bed topography and the hydrodynamic conditions (see Sect. 9.7.3).

§1.2Note that for constant c_{eq}, Eq. 6.54 reduces to $c(t) - c_{eq} = (c(0) - c_{eq})e^{-t/T_A}$. This can be rewritten as $c(t) = c(0) + (c_{eq} - c(0))(1 - e^{-t/T_A})$, which is similar in form to Eq. 1.2. [p314]

6.8.2. Critical shear stress and settling velocity

Sand, silt and clay particles are continuously entrained, transported and deposited in the coastal system by currents and waves. Due to the difference in grain size and cohesiveness, the sediment transport characteristics of sand and mud are different. In general, sand is transported as bed load (at the bed-water interface) and as suspended load (higher in the water column). For low sediment concentrations, silt and clay are only transported in suspension. For high concentrations, silt and clay can also be transported as fluid mud in a layer near the bed. In that case, the fluid mud will act as a viscous layer on top of the bed, blocking the exchange of sand between the bed and the water column.

We have seen that the fall velocity is an important parameter determining the vertical distribution of suspended sediment (see for instance Eq. 6.40). The fall velocity depends on the size, shape and specific density of the particles and of the water temperature and the sediment concentration. As a guideline, an individual silt particle of 10 µm has a fall velocity in still water of about 0.1 mm/s. For sand, the particle properties are relatively independent of time (because the quartz crystals are chemically hard and stable, it takes years to change the size of a sand grain). But, as we have seen in Sect. 2.6.2, the size and shape of mud can change quite easily. As a result of flocculation, the size of individual mud particles increases. With this increase, particles become heavier, which will speed up the settling of the particles. On the other hand, due to the increase in size, the drag force – the resistance the particle 'feels' when settling – will also increase. This will slow down the particle and can eventually cause deflocculation.

Another factor influencing the sediment transport is the exchange between the bottom layer and the water column. The upward sediment flux from the bed into the water column strongly depends on the bed composition. From laboratory experiments it was concluded that two regimes can be distinguished: a non-cohesive and a cohesive regime (Van Ledden & Wang, 2001). The clay content (the weight percentage of particles with a grain size smaller than 4 µm) of the bed material is the governing parameter for the transition between both regimes. For clay content of less than 5 % to 10 % the bed

behaves more or less non-cohesively. Sand and mud are eroded more or less independently, so the 'normal' formulations for the bed erosion can be used. For clay content exceeding 5 % to 10 % the bed behaves cohesively. The sand and mud particles are eroded simultaneously. Figure 6.17 gives the critical velocities as a function of mud (clay and silt) content in the bottom material.

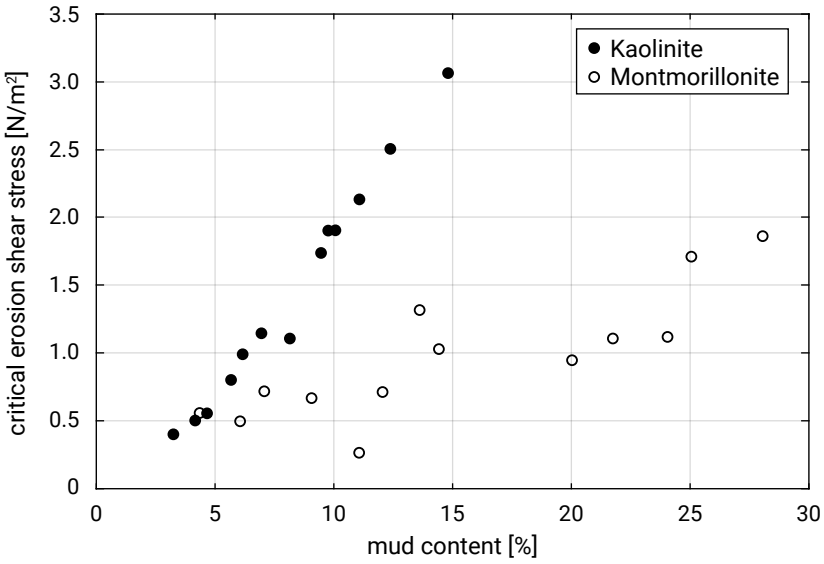

Figure 6.17: Effect of mud content on the critical erosion shear stress for two different sand-mud mixtures (data from Torfs, 1995). Mud content on the horizontal axis represents the percentage of fines smaller than 63 µm, hence including silt and clay fractions.

In sediment transport modelling, the exchange processes between water column and bottom layer are often assumed to be governed by the critical bed shear stress of the bottom material and the actual occurring bed shear stresses (Sect. 6.3).

For actual bed shear stresses larger than the critical bed shear stress of the bed material, the grains can be eroded, whereas for actual bed shear stresses smaller than the critical bed shear stress of the bed material, the grains can settle:

$$\tau_{b,\text{actual}} > \tau_{b,cr} \qquad \rightarrow \text{erosion} \tag{6.55a}$$

$$\tau_{b,\text{actual}} < \tau_{b,cr} \qquad \rightarrow \text{sedimentation} \tag{6.55b}$$

For non-cohesive material, the critical bed shear stress $\tau_{b,cr}$ for erosion is equal to the critical bed shear stress for sedimentation. For cohesive material, where there is a strong binding force between the particles, this is not the case. The critical bed shear stress for erosion is *larger* than the critical bed shear stress for sedimentation. This

implies that for a range of actual bed shear stresses, there is no exchange with the bottom layer in the case of cohesive sediments:

$$\tau_{b,\text{actual}} > \tau_{b,cr,er} \quad \rightarrow \text{erosion} \tag{6.56a}$$

$$\tau_{b,cr,sed} < \tau_{b,\text{actual}} < \tau_{b,cr,er} \quad \rightarrow \text{no exchange with bottom layer} \tag{6.56b}$$

$$\tau_{b,\text{actual}} < \tau_{b,cr,sed} \quad \rightarrow \text{sedimentation} \tag{6.56c}$$

The exact formulations for sediment transport of mixtures of sand and mud are still a subject of research.

6.8.3. Environmental issues

Due to the chemical constitution of mud and especially clay, the particles are easily bound together, as we have seen in Sect. 2.6.2. Organic matter is also easily bound to mud particles. This is one of the main reasons why delta areas are so fertile and thus one of the main reasons why people settle in these low-lying, rather dangerous areas. The fertile coastal areas are also good habitats for flora and fauna.

Unfortunately, contaminants are also easily bound by mud particles. At certain low concentrations, naturally occurring elements (i.e. copper and zinc) may have beneficial effects. But with increasing concentration, contaminants can become toxic and cause damage to the natural environment. An increase in concentration can occur due to fluvial inputs in the coastal system, but also as a result of a disturbance of a contaminated bed caused by, for example, dredging.

During dredging operations, extremely dangerous contaminants such as heavy metals and PCBs may be part of the dredged material. Highly contaminated mud has to be treated as chemical waste. This can have serious consequences for the costs of a dredging project in a harbour. The dredged material must be transported to special depots, for example the 'Slufter' near the Port of Rotterdam (see Fig. 6.18) and isolated from the environment.

For the construction of large land reclamation projects, huge volumes of sand are required. These volumes are often dredged at the sea bottom as close as possible to the construction site, in a very vulnerable area, close to the coast. Let us assume that for a very large project 500 million m^3 of sand is required. The sand can be dredged in the open sea, but the bottom contains 2 % silt (a quite normal content for natural seabeds). During the dredging operation with hopper dredges, the bed material is pumped into the hopper. The sand remains in the hopper; the fines (silt) return to the sea with the overflow. Dredging 500 million m^3 for the land reclamation means that about 10 million m^3 of silt is mobilised in a relatively short period of time. This might result

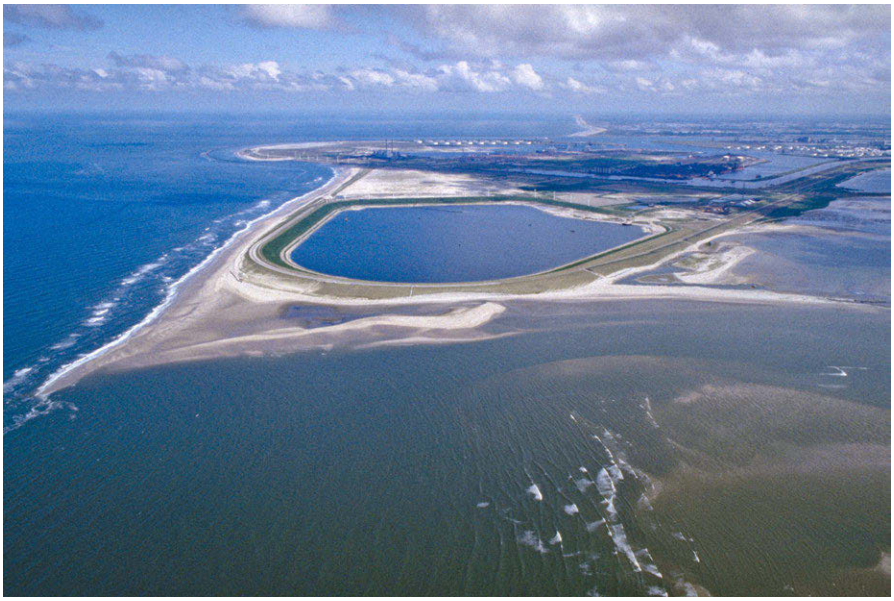

Figure 6.18: The Slufter after the Maasvlakte Extension 1 in 1972 (Rotterdam, the Netherlands). From Rijkswaterstaat ('Credits' on page 579).

in a heavy additional silt burden for the receiving sea system. Detrimental effects are likely.

6.9. Discussion

6.9.1. Choice of models

The quantitative description of sediment transport is still largely empirical (e.g. Fredsøe and Deigaard (1992) and Van Rijn (1989)). There is a variety of transport formulas and models, each with its own strengths and weaknesses. Note that all the models discussed in this chapter are geared towards describing sub-aqueous ('underwater') transport. Aeolian transport (by wind) and transport in the swash zone around the water line are not considered. They can, however, be important for the sediment balance.

Results of sediment transport computations often show large discrepancies compared with actual measurements. A factor 2 to 5 too large or too small is certainly not exceptional. Many researchers are trying to improve the results, for instance by proposing better and more reliable descriptions of the various elements in a formula. For practical problems in coastal engineering, however, the simpler models – e.g. Bijker (Sect. 6.5.4) and Bailard (Sect. 6.7.2) – are still the ones to beat.

A. G. Davies et al. (2002) present a very interesting intercomparison study of various research and practical sand transport models. They summarise their study as follows:

> "A series of model intercomparisons, and model comparisons with field data, was carried out as part of the EU MASTIII SEDMOC Project (1998–2001). Initially, seven 'research' models were intercompared over a wide range of wave and current conditions, corresponding to both plane and rippled sandbeds. These models included both one-dimensional vertical (1DV) formulations, varying in complexity from eddy viscosity and mixing length models to a full two-phase flow formulation, and two-dimensional vertical (2DV) formulations capable of representing vortex shedding above sand ripples. The model results showed greatest convergence for cases involving plane beds, with predicted sand transport rates agreeing to well within an order of magnitude, and greatest divergence for cases involving rippled beds. A similar intercomparison involving (mainly) practical sand transport models, carried out over wide wave and current parameter ranges, also showed greatest variability for cases involving rippled beds. Finally, (mainly) practical models were compared with field data obtained at five contrasting field sites. The results showed that suspended sand concentrations in the bottom metre of the flow were predicted within a factor of 2 of the measured values in 13 % to 48 % of the cases considered, and within a factor of 10 in 70 % to 83 % of the cases, depending upon the model used. Estimates of the measured alongshore component of suspended sand transport yielded agreement to within a factor of 2 in 22 % to 66 % of cases, and within a factor of 10 in 77 % to 100 % of cases. *The results suggest that, at the present stage of research, considerable uncertainty should be expected if untuned models are used to make absolute predictions for field conditions. The availability of some measurements on site still appears to be a necessary requirement for high-accuracy sand transport predictions. However, for morphological modellers, the results may be viewed as more encouraging, since many of the present models exhibit agreement in their relative behaviour over wide ranges of wave and current conditions, which is a prerequisite to obtaining correct morphodynamic predictions.*"

6.9.2. Specific situations

In this chapter we have discussed the topic of sediment transport in quite general terms. In the next three chapters, sediment transport is considered for specific situations, as is the resulting morphodynamic response of the system.

Chapters 7 and 8 are devoted to wave-dominated coastal systems: uninterrupted coastal stretches, pocket beaches and wave-dominated deltaic coastlines. We make a distinction between cross-shore (Ch. 7) and longshore (Ch. 8) sediment transport (Fig. 6.19).

Such a distinction may seem artificial at first glance, but is often made because of the following differences:

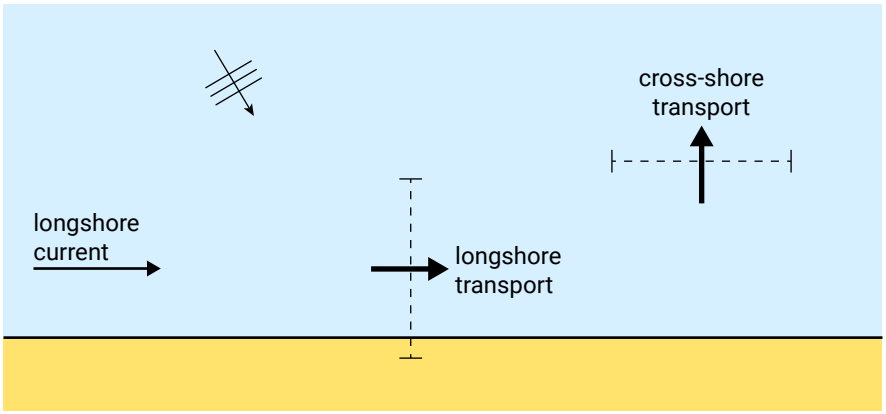

Figure 6.19: Distinction between longshore transport parallel to the shoreline and cross-shore transport transverse to the shoreline.

- Long-term changes in the coastline are often the result of gradients in longshore transport. They are easily observed near disturbances, such as breakwaters or river mouths. Cross-shore transport is responsible for short-term variations, such as changes in the position and size of breaker bars and dune erosion during storms. Long-term changes due to cross-shore transport (for instance a long-term loss to deeper water) may also occur, but are harder to detect (and may be difficult to distinguish from long-term changes due to alongshore processes);
- Where coastline change as a result of human-induced changes is concerned, alongshore and cross-shore effects are either of equal importance (on low wave energy coasts, e.g. the Mediterranean) or alongshore effects dominate (on high-wave energy coasts, e.g. the Dutch North Sea coast). This may explain why cross-shore impacting structures – such as offshore breakwaters and perched beaches (see Ch. 10) – perform better on low-energy coasts than on high-energy coasts;
- The wave orbital motion is very important in transporting material in the cross-shore direction, but not in the alongshore direction. The wave orbital motion is approximately cross-shore directed in the nearshore. Since every wave in principle moves sand back and forth, gross cross-shore transports (per m width) are large and much larger than longshore transport rates (per m width). For wave-dominated coasts not influenced or interrupted by coastal inlets, wave-induced surf zone longshore flow is the main driving agent. The direction and magnitude of the wave-induced longshore transport is determined by the wave conditions (wave height, period and direction). Net cross-shore transport rates, however, are generally an order of magnitude smaller than longshore transport rates.

In Ch. 9, the specifics of tide-dominated systems (tidal basins) and tide- and wave-dominated coastal inlets are considered. The sediment exchange between coast and basins is also discussed. Dynamics of fine sediment transport are very important in tidal basins; coarser sediment (quartz and carbonate sands) is predominantly found in

seaside regions, while the finer sediment (silt and clay) settles in the more protected landward regions.

7

Cross-shore transport and profile development

7.1. Introduction

In this chapter we consider the hydrodynamic, sediment transport and morphodynamic processes in the cross-shore direction that determine the coastal profile shape. In the first instance, we will disregard any structural losses both due to longer-term cross-shore effects like sea level rise, shoreface feeding and aeolian losses (discussed later in this chapter), and due to longshore sediment transport gradients (discussed in Ch. 8) that lead to structural changes in the mean shoreline position.

Let us first define what the coastal profile is. On a long timescale, say decades to millennia, the coastal profile or shoreface extends from the shelf to the sub-aerial ('under the air', i.e. exposed to the air) beach and dune system (see Figs. 7.1 and 7.2). In this zone we observe generally parallel or nearly parallel depth contours, while the profile slopes are generally steeper than 1 in 1000. We conjecture that this depth contour configuration is mainly caused by cross-shore processes and that these processes are dominated by wave action. On the shelf (see Fig. 7.1) we may observe three-dimensional morphologies (sand banks, sand ridges and shoreface-connected sand ridges) that are commonly a result of tidal action and generally have only secondary impacts on the coastal profile. Shelf slopes are generally smaller than 1 in 1000.

The response of the coastal profile to wave action is extremely depth-dependent, i.e. the shallower the depth, the faster the response. We therefore introduce a rough zoning, viz. the lower shoreface, the upper shoreface (Fig. 1.14) and the backshore (the coastal plain in Figs. 1.15 and 7.4). As stated above, at this moment we ignore longer-term cross-shore and alongshore effects and concentrate on shorter-term cross-shore effects. We assume that the backshore is simply a dune or cliff (as in Fig. 7.2), high enough to prevent overwash and without alongshore gradients. In this particular case

the lower shoreface (large depths) responds slowly to wave action, while the upper shoreface and the dune or cliff backshore (shallow depths) respond fast.

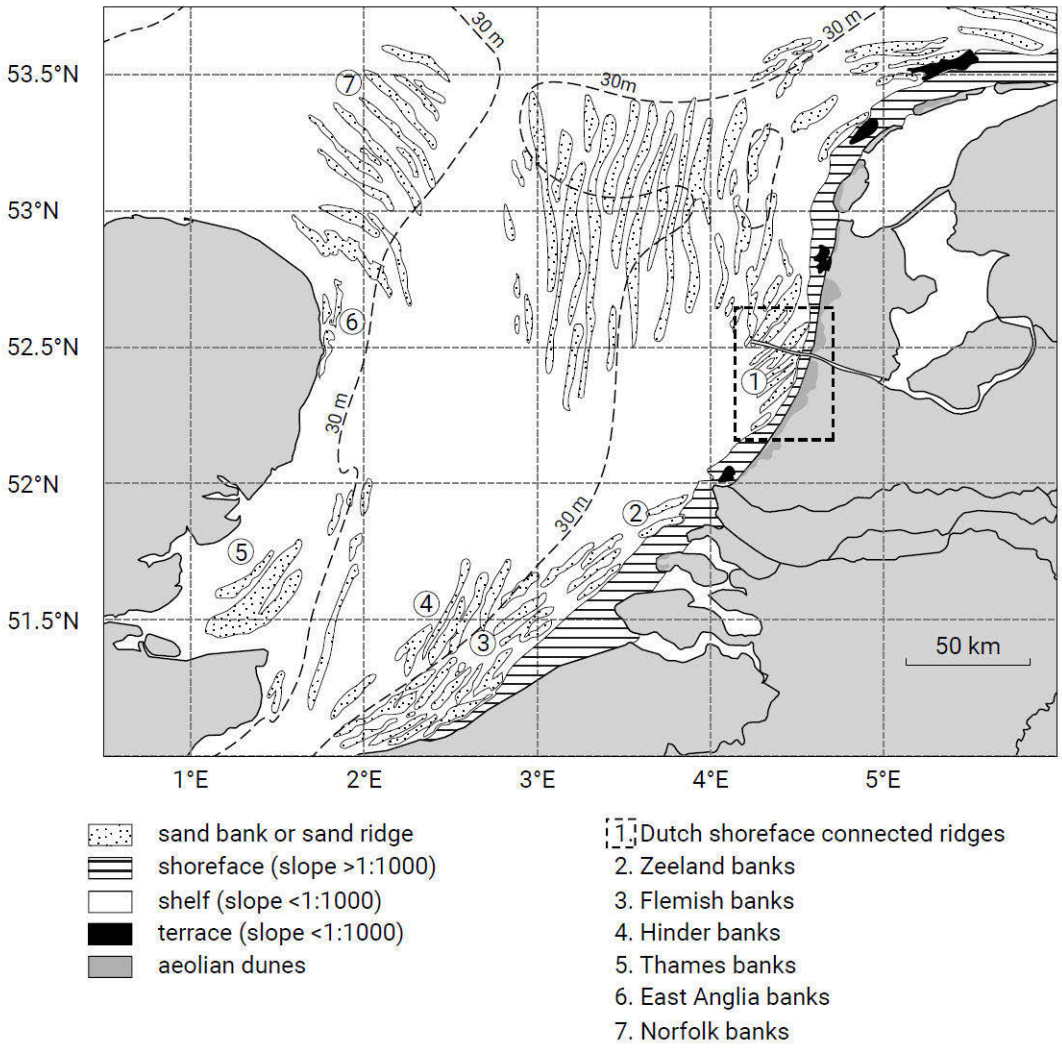

Figure 7.1: The shoreface (horizontal lines) and the shelf (white) in the southern part of the North Sea with linear sand banks or ridges on the shelf and along the central Dutch coast or Holland coast connected to the shoreface (dashed box) (adapted from Van de Meene & Van Rijn, 2000). In front of the Southwest Delta and Wadden coasts, the bed slope flattens from $\sim 1:100$ to $\sim 1:1000$ at water depths of about 20 m, whereas in front of the Holland coast the transition occurs at a water depth of about 16 m (see also Intermezzo 7.1).

We define the upper shoreface as consisting of the surf zone, the beach and the first dune row or cliff face. This zone responds nearly instantaneously to wave action, which we may notice on the shoreline if disturbed by human interference, such as a sand castle. Also in the surf zone we observe that surf zone bars – if present – respond on the timescale of events, i.e. storm events may move surf zone bars offshore, while more moderate wave action may move them onshore (Sect. 7.5). Under more extreme conditions, when the water level rises due to a storm surge, the upper beach or even the dune or cliff face will respond. The upper beach may develop a scarp (a nearly

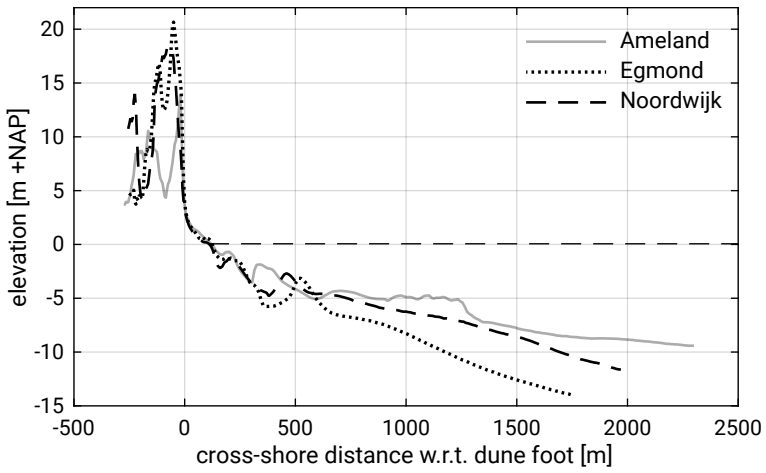

Figure 7.2: Three instantaneous cross-shore profiles along the Dutch coast at the three locations indicated in the map of Fig. 7.3. The cross-shore distance is relative to the dune foot, here defined as MSL +3 m. Note the flat coastal profile of Ameland as compared to the steeper Holland or central Dutch coast (i.e. Egmond and Noordwijk). (Data from JARKUS, n.d.)

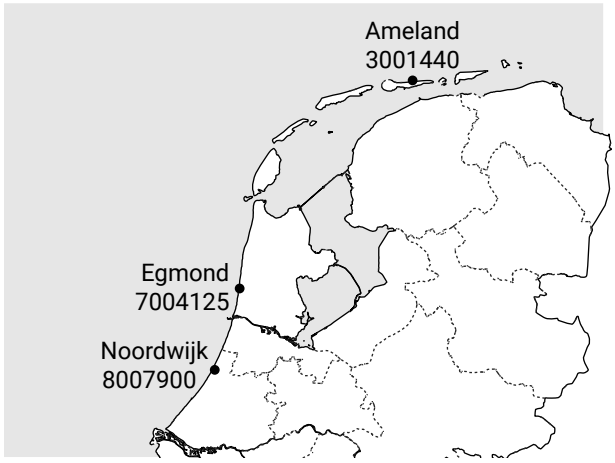

Figure 7.3: The location of the three instantaneous cross-shore profiles along the Dutch coast shown in Fig. 7.2. The JARKUS transect numbers refer to the number of the coastal section or, in Dutch, *kustvak* (first digit), and the last digits refer to the alongshore distance with regard to a reference transect which differs for each coastal section. For example, the transect near Egmond is in coastal section 7, 41.25 km south of Den Helder (which is the first transect in coastal section 7).

vertical slope along the beach as a result of erosion) under moderate surge, while the dune or cliff face under a high surge level reaching the dune or cliff face may undergo surge erosion. We will treat these extreme events at a later stage.

On longer timescales, say many decades to millennia, the whole shoreface profile is morphodynamically active (cf. (Stive & De Vriend, 1995)). However, on shorter timescales, say hours to a few decades (engineering scales), the lower shoreface shows negligible activity compared to the upper shoreface. In the field of coastal engineering it is therefore often assumed that the *morphologically active zone* extends from the first

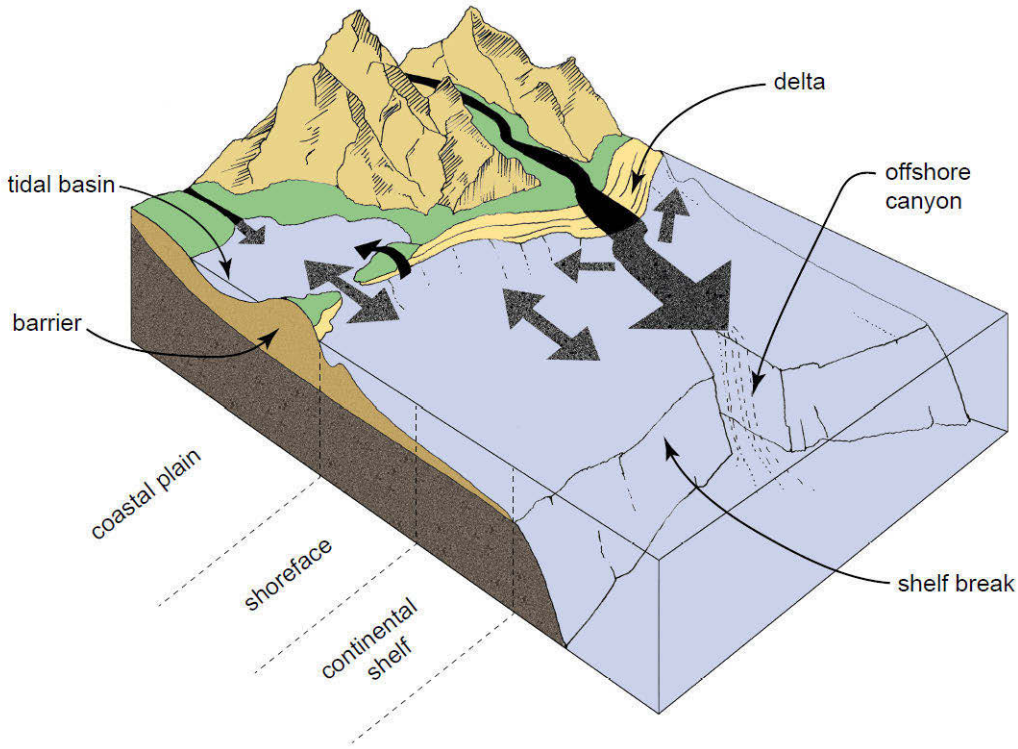

Figure 7.4: The shoreface is the §1.2 ~~active~~ zone between the shore and the continental shelf. §1.2 On larger timescales the entire shoreface is influenced by wave action and morphodynamically active. The shelf extends to the shelf break.

dune or cliff face to just a little offshore the surf zone at the upper part of the lower shoreface at a depth (relative to MSL) of about twice the wave height extreme, which is exceeded, for example, for twelve hours per year§1.2 (see also Sect. 7.2.3) [p324]. A second coastal engineering assumption is that – although the active zone may display profile variability in response to instantaneous, episodic or seasonal forcing – the active profile shape remains at a dynamic equilibrium when averaged over time (say years to decades) and alongshore space (say 100 m to 1000 m). Unless alongshore sediment transport gradients exist, it is a third common coastal engineering assumption that the amount of sediment in the active zone remains unchanged, which implies that there is no structural loss. The above three assumptions form the basis for the modelling of the year- to decade-averaged shoreline changes treated in Ch. 8.

However, there exist a number of arguments to also pay attention to the morphodynamic behaviour of the upper shoreface on timescales shorter than a year. Amongst these arguments is the necessity to gain insight into the profile and plan form variation of the upper shoreface for infrastructure design and beach use purposes.

With the above in mind, we will therefore treat the following topics. In Sect. 7.2 we discuss the concept of a dynamic equilibrium shoreface profile, which ignores profile and plan form dynamics on scales shorter than years. This concept is instrumental in the modelling of year- to decade-averaged shoreline changes and in the design of upper shoreface nourishments. Subsequently, in Sect. 7.3, we treat the dynamic variations

of the upper shoreface profile and plan form on timescales shorter than a year, including surge-induced dune erosion. This gives insight into the upper shoreface profile variations on shorter timescales, which is relevant for the safety of nearshore infrastructure and for recreational beach use. Section 7.4 then considers structural changes to the position of the upper shoreface profile on longer – say decades to millennia – timescales, when the assumption that the amount of sediment in the active zone remains unchanged is violated. Finally, in Sect. 7.5 we discuss cross-shore sediment transport processes that are relevant for both the dynamic equilibrium profile and the inter-annual variations therein.

Intermezzo 7.1 The Dutch shoreface

§1.2 ~~The shoreface is the active zone between the shore and the continental shelf.~~ §1.2 The shoreface is the zone between the shore and the continental shelf. It is morphodynamically active on decadal to millennial timescales. On annual to decadal timescales, morphodynamic activity involves mainly the upper shoreface. The upper shoreface is the zone with regular and dominant wave action, whereas on the lower shoreface wave action only occurs during larger storm events. The Dutch upper shoreface is the beach and surf zone with breaking waves and breaker bars between the waterline and approximately the NAP −8 m depth contour, with mean bed slopes varying between 1:50 to 1:200. The Dutch lower shoreface is the zone between approximately the NAP −8 m and NAP −20 m depth contours with typical bed slopes between 1:200 and 1:1000, where sand ridges may be present. Offshore the shoreface merges with the continental shelf where the slope is generally less than 1:1000; tidal sand waves and sand banks may be present here.

7.2. Equilibrium shoreface profile

7.2.1. The concept

Consider a coastal stretch that has no alongshore sediment transport gradients. If we adopt the coastal engineering assumption that the amount of sediment in the upper shoreface remains constant, the shoreline position will remain the same when averaged over several years. Figure 7.5 shows the Ameland, Egmond and Noordwijk shoreface profiles (Fig. 7.3) from 1965–2019 (from the JARKUS (n.d.) database with yearly measurements along the Dutch coast). The cross-shore distance is relative to the relevant local beach pole or *Rijksstrandpaal* (RSP) in Dutch. In order to cancel any structural gains or losses, the profiles have been shifted to the same duneface location (Fig. 7.6).

We observe that the various profiles show a dynamic variation that is clearly related to the position of the bar(s). We will discuss bars further on. We also observe that the profile variations remain in an envelope that seems stable over the years. One may

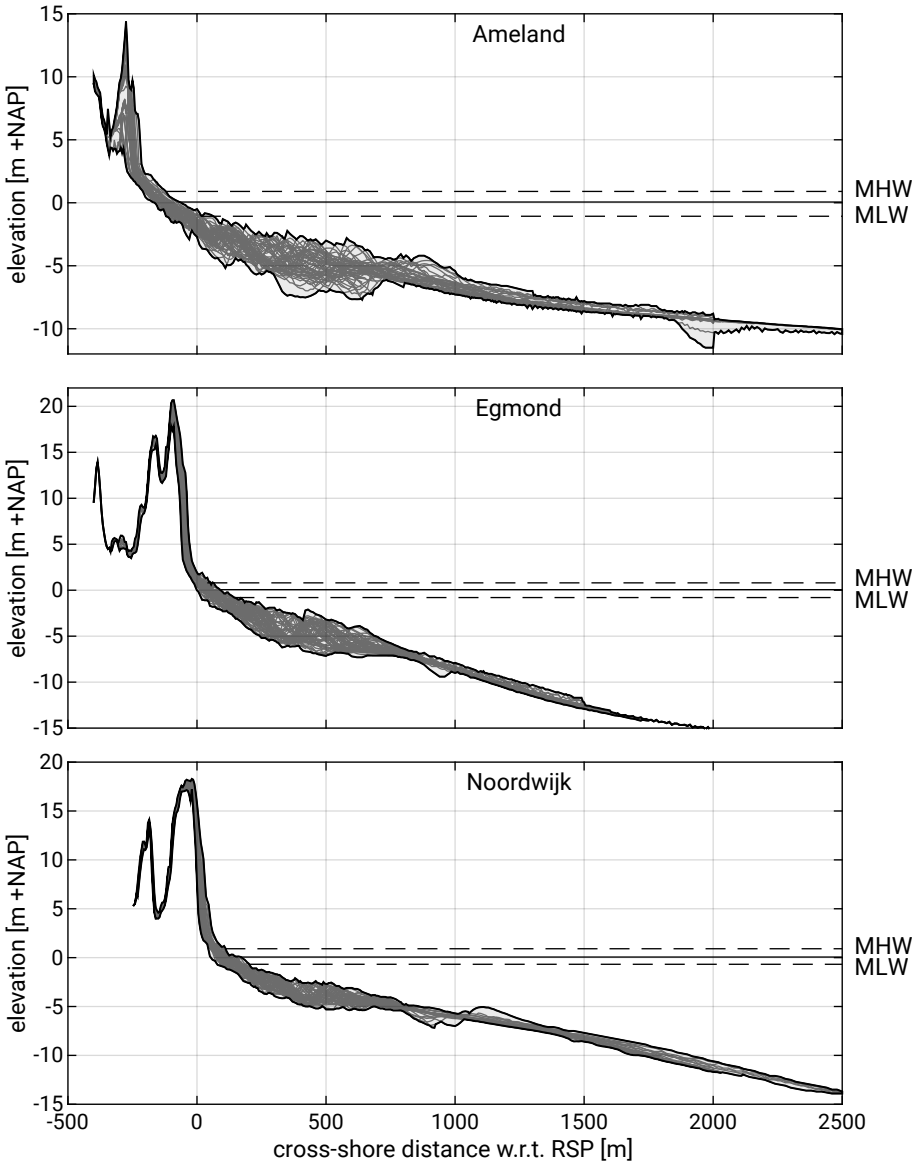

Figure 7.5: Upper shoreface profile variation for Ameland (upper panel), Egmond (middle panel) and Noordwijk (lower panel) over the period 1965–2019. The cross-shore distance is relative to the relevant local beach poles or *Rijksstrandpaal* (RSP). The average HW and LW lines are also indicated. Note the significantly stronger variability of Ameland's dune and nearshore profile as compared to the other two locations. (Data from JARKUS, n.d.).

therefore speak of the existence of a dynamic equilibrium profile (e.g. as follows from a best fit through the profile data).

It is commonly assumed that if one exposes, e.g. in the laboratory, a beach profile to constant wave forcing at a fixed water level, a stable equilibrium profile (cross-shore profile of constant shape) will be reached after a sufficiently long time. Is there a relation between this stable equilibrium profile and the dynamic equilibrium profile as found in the field? The answer is partly yes and partly no. We may expect that a shore profile in the field will respond to a constant forcing condition and that it will also

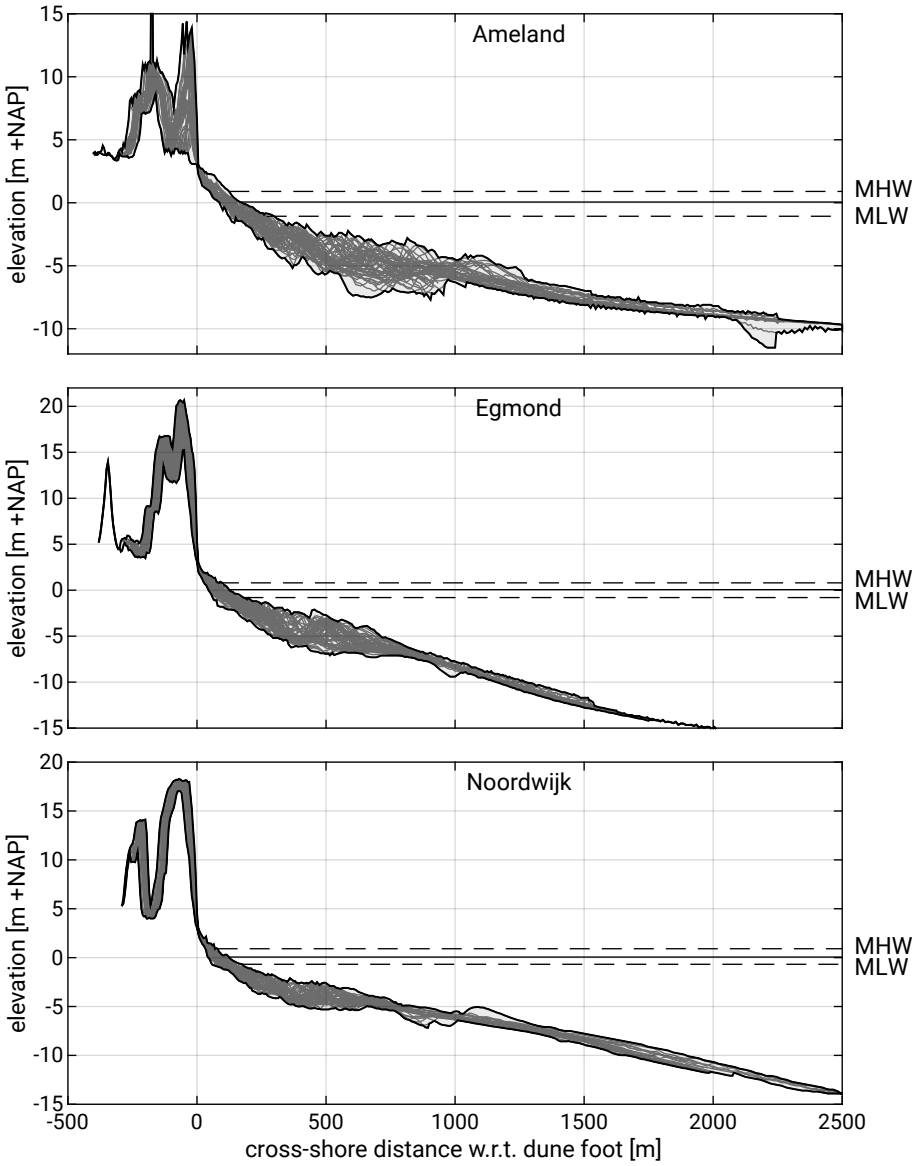

Figure 7.6: Upper shoreface profile variation for Ameland (upper panel), Egmond (middle panel) and Noordwijk (lower panel) over the period 1965–2019. The profiles have been shifted to the same duneface location (MSL +3 m), so any structural gains or losses are cancelled out. The average HW and LW lines are also indicated. (Data from JARKUS, n.d.).

search for an equilibrium form to that forcing. However, in nature the forcing (waves and water levels) is far from constant and varies so rapidly that a stable equilibrium is never reached. It is for this reason that the shoreface profile continuously oscillates in response to the varying forcing. However, interestingly, these oscillations are confined to a steady envelope, the mean position of which we define as a dynamic equilibrium profile.

In the following sections we will first describe empirical and semi-empirical approaches to generalise the best profile fit for arbitrary upper shoreface profiles (Sect. 7.2.2).

Secondly, in Sect. 7.2.3, we will discuss the engineering applications of the dynamic equilibrium concept.

7.2.2. (Semi-)empirical derivations

Bruun

Bruun (1954) was one of the first coastal engineers to introduce the existence of a dynamic equilibrium profile. He proposed an empirical equation for the equilibrium beach profile based on an analysis of beach profiles along the Danish North Sea coast and the California coast. The equation consists of a simple power law relating the water depth h to the offshore distance x' (where $x' = 0$ is around the mean waterline and is positive in the offshore direction), as follows:

$$h = A(x')^m \tag{7.1}$$

where:

m	exponent equal to $m = {}^2/_3$	–
h	water depth	m

Interestingly, the value of $m = {}^2/_3$ corresponds to the theoretical derivation of Bowen (1980), see Eq. 7.24. The dimensional constant A (the dimension of which depends on the magnitude of the exponent m; with $m = {}^2/_3$ the dimension of A is $m^{1/3}$) is a so-called shape factor that depends on the "stability characteristics of the bed material" (what this actually means is somewhat unclear). Bruun found that $A = 0.135m^{1/3}$ provided the best correlation for North Sea beaches in the Thyborøn area in Denmark. Hughes and Chiu (1978) show that $A = 0.10m^{1/3}$ provides the best correlation for beaches along the coast of Florida. The larger A is, the steeper the profile. So, apparently North Sea beaches are somewhat steeper than Florida beaches. Whether this can be explained physically will be discussed next.

Dean

The Bruun equation – a simple power law – was supported by Dean (1977) on semi-empirical grounds by reasoning that for a certain grain size, nature strives towards a uniform energy dissipation $\varepsilon\left(D_{50}\right) = D/h$ (loss in wave power) per unit volume of water across the surf zone (in W/m^3). The reasoning behind this is that the energy dissipation per unit volume is a measure for the "destructive forces" (causing offshore

sediment transport) acting on a sediment particle. With Dean's equilibrium assumption and for waves normally incident to an alongshore uniform coast $\theta = \varphi = 0$, the energy balance Eq. 5.2 can be written as:

$$\frac{d\left(Ec_g\right)}{dx} = -D = -h\varepsilon\left(D_{50}\right) \tag{7.2}$$

where:

E	wave energy per unit sea area	J/m^2
c_g	group velocity	m/s

We again use the simple dissipation model for the surf zone $H = \gamma h$ (see Ch. 5). If we further assume shallow water ($c_g = c = \sqrt{gh}$), Eq. 7.2 leads to:

$$\begin{aligned} \frac{d}{dx}\left(1/8\rho g\gamma^2 h^2\sqrt{gh}\right) = -h\varepsilon\left(D_{50}\right) \Rightarrow \\ \varepsilon\left(D_{50}\right) = -\frac{1}{h}\frac{d}{dx}\left(1/8\rho g\gamma^2 h^{5/2}\sqrt{g}\right) = \\ = \frac{5}{16}\rho g^{3/2}\gamma^2\sqrt{h}\frac{dh}{dx'} \end{aligned} \tag{7.3}$$

Note that in the last step of this equation we have reverted to the cross-shore coordinate x' which is positive offshore. The depth is the only parameter that varies with x'. If we integrate Eq. 7.3 we get:

$$h\left(x'\right) = \left(\frac{24\varepsilon\left(D_{50}\right)}{5\rho g^{3/2}\gamma^2}\right)^{2/3}\left(x'\right)^{2/3} \tag{7.4}$$

Apparently, based on monochromatic waves and a constant breaker index across the surf zone $\gamma = H/h$, the magnitude of the exponent m in Eq. 7.1 can be derived and is found to be ⅔, in agreement with Bruun's suggestion. Furthermore, the dimensional shape factor A (in $m^{1/3}$) is given by:

$$A = \left(\frac{24\varepsilon\left(D_{50}\right)}{5\rho g^{3/2}\gamma^2}\right)^{2/3} \tag{7.5}$$

in which the equilibrium energy dissipation rate $\varepsilon\left(D_{50}\right)$, in W/m^3, depends on the particle diameter. Hence, in Dean's approach the shape factor A is some function of the particle diameter. Assuming that the breaker index does not vary with the wave conditions, A is independent of the deep-water wave conditions. The magnitude of A is seen to vary from $0.079\,m^{1/3}$ to $0.398\,m^{1/3}$ (Dean, 1977).

The shape parameter A was empirically related to the median grain size by Moore (1982), showing that a coarser grain size implies a larger value of §1.1 A [p329], and thus a steeper cross-shore profile. Dean (1987) showed that this relation could be transformed to a relation using the fall velocity w_s (in cm/s) as a parameter, viz.:

$$A = 0.067 w_s^{0.44} \tag{7.6}$$

Or for w_s in m/s:

$$A = 0.5 w_s^{0.44} \tag{7.7}$$

If this result is accurate and universally valid, we have a powerful tool. Once we know the fall velocity of the sediment (which depends largely on the grain size, Sect. 6.2.3), we can predict the equilibrium profile after for instance nourishment with borrow material of a different grain size than the native material (see also Sect. 10.7.2). Qualitatively, this result is in line with the finding that coarser beaches are generally steeper than finer beaches.

7.2.3. Engineering applications

Before discussing the importance of the dynamic equilibrium concept for engineering applications, we need to know how accurate the predictive ability is. We therefore apply a parabolic fit to the three typical profiles along the Dutch coast described above (Fig. 7.5), knowing that these profiles differ considerably (see Figs. 7.7 and 7.8). Two profiles are from the Holland coast, one in the southern section and one in the northern section and one from the Wadden Sea coast (in all cases D_{50} = approximately 200 µm). The fits were made to match the average profile over the 55 yearly measurements. Note that the formula $h = A(x)^m$ results in a vertical slope of the beach profile at the waterline ($x' = 0$). This is not realistic. In practical applications it should be considered to position this point at a level somewhere above the waterline (1 m in our example). This results in more reasonable slopes at the waterline. Furthermore, we need to define the offshore extent of the profile fit, for which one may adopt the active zone concept as defined by Hallermeier (1978), who introduced the concept of depth of closure (§1.2 ~~Fig. 1.14~~ §1.2 Sect. 1.5.1). §1.2 ~~In his definition the active zone corresponds to the surf zone width for extreme conditions exceeded for twelve hours per year.~~ §1.2 Hallermeier's inner closure depth (see Fig. 1.14) corresponds to the surf zone width for extreme conditions which are exceeded for twelve hours per year. It marks the seaward limit of the upper shoreface, where the majority of the bed dynamics takes place. Since $h_b = H_b/\gamma$, the depth of closure is more than twice the wave height extreme. [p330]

Even though the mean grain diameter is the same for all three locations, the optimal values of A with fixed power $m = 2/3$ (see Fig. 7.7 and Table 7.1) differ by a factor of

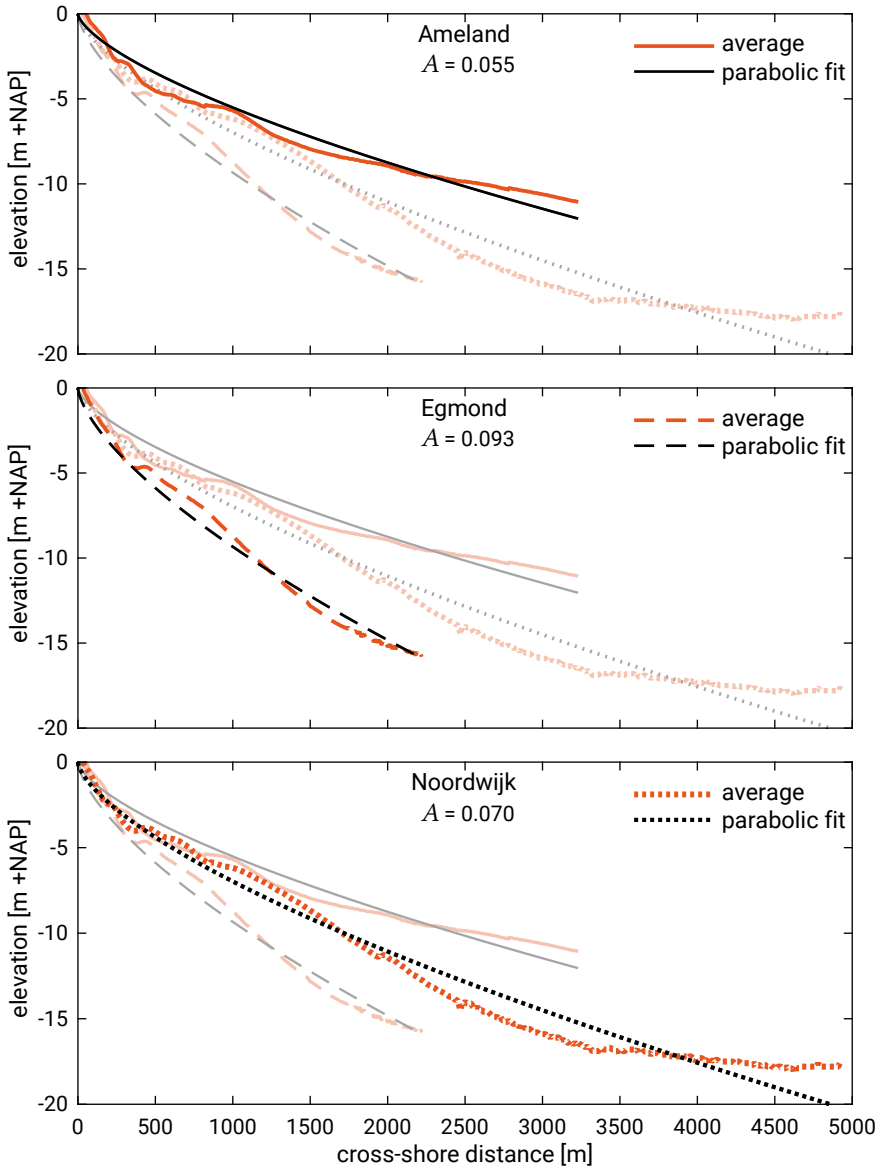

Figure 7.7: Parabolic fits (black lines) to the long-term-averaged (1965–2019) profiles (blue lines) of Ameland (top panel), Egmond (middle panel) and Noordwijk (bottom panel) according to Eq. 7.1 with A as a free parameter and $m = 2/3$. Note that each panel also shows the profiles of the other two locations.

almost 2! According to Eq. 7.7, the value of A should be 0.10 (based on a fall velocity $w_s = 0.0256\,\mathrm{m/s}$). These results indicate that the predictive ability of Eq. 7.1 is limited. We hypothesise that the value of A is not only dependent on the fall velocity, but also on several other variables, like wave climate, tide and surge water level variations and coastal currents. Hence, we must be hesitant to use Eq. 7.1 for engineering applications, given its limited predictive ability. Obviously, a fit with two free parameters improves the fit somewhat (Fig. 7.8), but the variation in the values of A is even larger and the theoretical foundation is lacking.

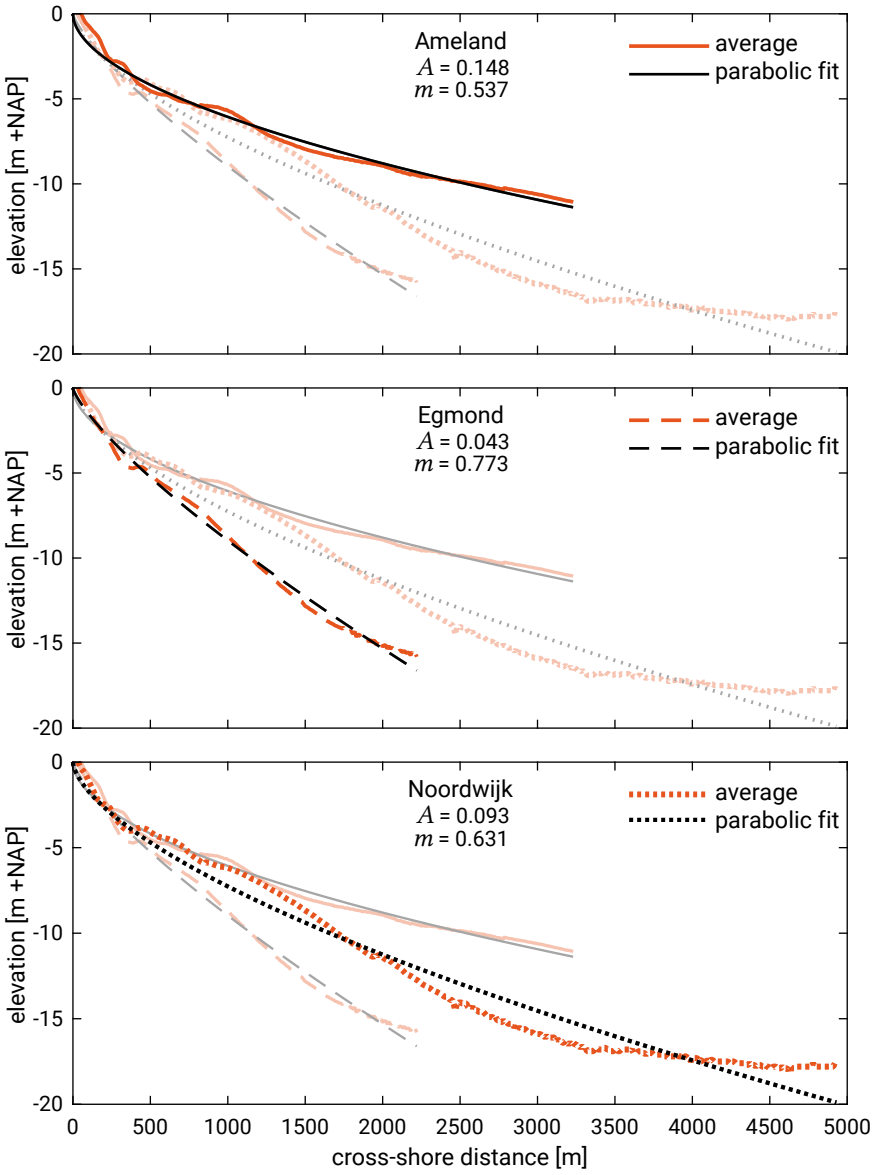

Figure 7.8: Parabolic fits (black lines) to the long-term (1965–2019) averaged profiles (blue lines) of Ameland (top panel), Egmond (middle panel) and Noordwijk (bottom panel) according to Eq. 7.1 with A and m as free parameters. Note that each panel also shows the profiles of the other two locations.

Nonetheless, the dynamic equilibrium concept is one of the few tools that a coastal engineer has available to make a prediction of the expected profile of a new land reclamation or a newly constructed offshore island. A particularly useful application concerns the expected changes in the dynamic equilibrium profile when a coast is nourished with borrow sediment sizes that differ from the native sediment size. Dean (2002) discusses this application at length.

Table 7.1: Optimal values for A for Eq. 7.1 with fixed power $m = 2/3$.

A (Eq. 7.7)	A (Ameland)	A (Egmond)	A (Noordwijk)
0.10	0.055	0.093	0.070

7.3. Morphodynamics of the upper shoreface

7.3.1. Introduction

In the previous section we have focused on the dynamic equilibrium profile of the upper shoreface, temporally averaged over years and alongshore spatially averaged over about a kilometre. We assumed that a cross-shore profile will evolve towards a (stable) equilibrium, corresponding to the concurrent forcing, and that disequilibrium implies that not enough time has been available to achieve equilibrium. In such an approach, the focus is on the order and regularity in the profile evolution.

On timescales shorter than a year and especially on the timescale of episodic events, we may observe highly dynamic variations of the upper shoreface profile and plan form. In this section, the emphasis is on variability and diversity instead of order and regularity. We will first discuss the high dynamic variability of the intertidal beach and the surf zone on the timescale of events (Sect. 7.3.2). Next, we introduce the typical seasonal variations that are common on many beaches worldwide (Sect. 7.3.3). Cyclic behaviour of bars on the timescale of years is discussed in Sect. 7.3.4. Last, we focus on the impact of episodic events on a dune-backed shoreface (Sect. 7.3.5). These issues are considered relevant for the safety of nearshore infrastructure and for recreational beach use.

7.3.2. Beach states

Let us first investigate morphologic features that we may encounter on the upper shoreface on the timescale of wave events (short-term variation). Remember that we defined the upper shoreface to range from the surf zone at its furthest offshore reach (i.e. the active depth as defined by Hallermeier) to the first dune or cliff face. Parts of the upper shoreface are the beach (normally sub-aerial) and the intertidal zone, which is the zone between low water and high water, at the transition between the surf zone and the beach.

Looking at the intertidal zone, we observe strongly three-dimensional morphology, probably the strongest in the upper shoreface. An example is shown in Fig. 7.9, where we observe a ridge-runnel structure on the intertidal beach. Although it impacts beach recreation and use, the importance of ridge-runnel structures in terms of shoreface behaviour is limited. We expect that the surf zone morphological structure has a larger impact on upper shoreface behaviour. On many beaches worldwide we may observe one, two and sometimes more surf zone bars, while in the intertidal zone a bar may

also be present. In the examples presented on the Holland coast (a so-called dissipative beach, see later on in this section) we observe one surf zone bar and an intertidal bar. The bars determine the locations and rates of energy dissipation due to wave-breaking and may thus dictate the morphological response. Further on, we will discuss the behaviour of the surf zone bars averaged over many years, which determines their cross-shore location (Sect. 7.3.4).

Figure 7.9: Ridge (intertidal bar) runnel (drainage channel) structure at low water at the northern flank of the Sand Engine on 16 February 2016. Photo by Jurriaan Brobbel, Rijkswaterstaat ('Credits' on page 579).

On the timescale of wave events, we may observe highly dynamic variations of the upper shoreface profile and plan form. In the literature, the various morphodynamic regimes (also called beach states) have been classified according to their overall appearance, which is often related to previous weather conditions on daily to monthly timescales. Wright and Short (1984) distinguished a series of six beach states, ranked hierarchically from the highest state, dissipative, to the lowest state, reflective. In between the two end states, four intermediate beach states can be discerned. They based their analysis on observed behaviour at Australian beaches. Dissipative and reflective beaches are relatively two-dimensional, although reflective beaches usually have pronounced arc-shaped shoreline formations that are called beach cusps. Due to their small alongshore variability, the dissipative and reflective end states can be characterised by their cross-shore profile. The cross-shore profiles of reflective and dissipative beaches correspond roughly to 'summer' and 'winter' beaches, respectively (see Fig. 1.3 and Sect. 7.3.3). They can be described as follows:

Reflective beaches are characterised by a relatively steep and narrow beachface with a berm and a narrow surf zone without bars. Nearshore and beach slopes are between 0.10 and 0.20. The sandy material is relatively coarse (see Sect. 7.2.2). For these beaches a large Iribarren parameter (Eq. 5.20) can be expected (say

larger than 2). Collapsing or surging breakers are common on reflective beaches. The corresponding waves have a low steepness (long, small-amplitude waves). Thus, reflective beaches are the result of a period of mild wave conditions that transport sediment onshore. Reflective beaches are often found in swell and monsoon wave climates (see Sects. 4.3.2 and 4.3.3). Since in these climates the conditions have a low variability, the resulting morphodynamic behaviour is less dynamic than is the case for storm wave climates that are characterised by a higher variability.

Dissipative beaches – at the other end of the spectrum – are characterised by a wide and flat sandy coastal zone with one or multiple linear bars and with dunes backing a wide beach. The nearshore slope is about 0.01 and the beach slope about 0.03. The sandy material is relatively fine. The corresponding Iribarren numbers are small (around 0.2 to 0.3, corresponding to spilling breakers). A dissipative beach is the result of high-energy waves that start breaking far offshore (in a wide surf zone, say up to 500 m wide). These high-energy, short waves are typical for a storm wave climate and the associated variability results in a highly dynamic coastal profile.

The four intermediate beach states are all strongly three-dimensional. Whereas rip currents (Sect. 5.5.7) and corresponding rip channels are generally absent on pure dissipative and reflective beaches, they are an important attribute of intermediate beach morphologies. For intermediate beach states, plunging waves tend to occur.

Instead of the Iribarren number, another more or less equivalent parameter is often used to indicate the beach state, viz. the dimensionless fall velocity:

$$\Omega = \frac{H_b}{w_s T} \tag{7.8}$$

where H_b is the wave height at breaking, T is the wave period and w_s is the fall velocity. The reflective beaches at one end of the spectrum typically have $\Omega < 1$, whereas for dissipative beaches at the other end of the spectrum we have $\Omega > 6$. For values in between, intermediate beach states are found.

Klein et al. (2005) used the distinction between dissipative, intermediate and reflective beach states, as explained above, to classify southern Brazilian beaches (Fig. 7.10). Their work is very illustrative in showing the dependency on grain size and beachface slope.

The beach state at a certain location is not invariable; beaches can move through a series of beach states. Wright and Short (1984) use the dimensionless fall velocity to explain whether the response will be slow (low energy, reflective) or fast (high energy, dissipative) and whether erosion or accretion will occur. Mild wave conditions slowly force a beach towards a reflective beach state through onshore sediment transport, whereas storm waves are responsible for fast offshore movement of sediment,

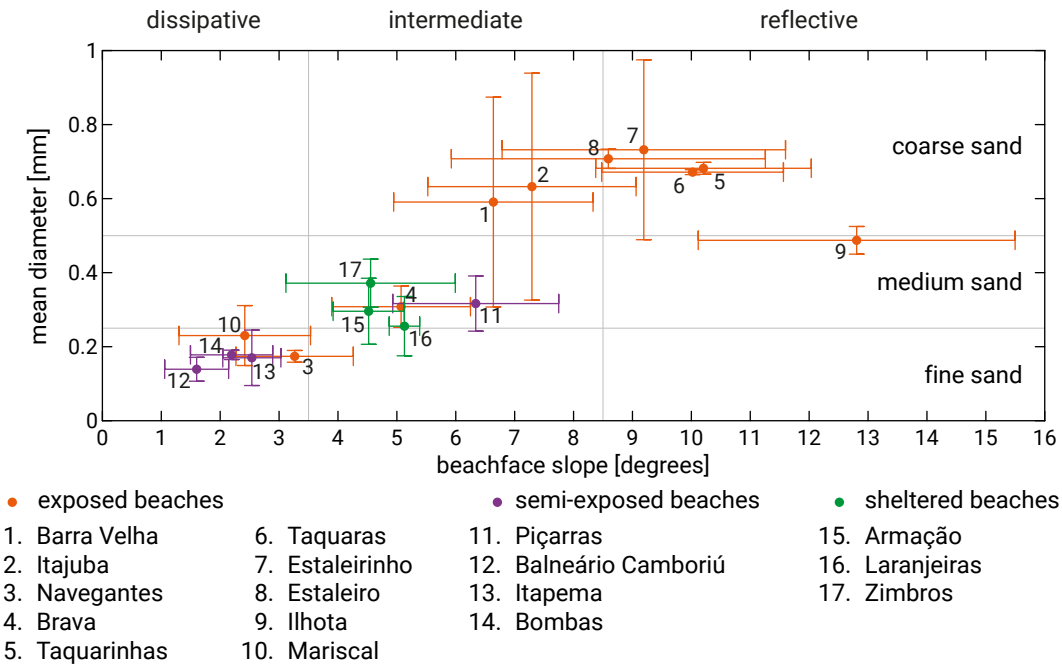

Figure 7.10: Relationship between sedimentary grain size and slope of the beachface indicates the importance of morphodynamic stages and energy level (data from Klein, 2003).

resulting in a dissipative beach state. Hence, wave conditions which move a beach toward a higher state (the dissipative state being the highest in rank) cause erosion; wave conditions which move a beach downstate[1] cause accretion.

Based on ARGUS video imaging techniques, Lippmann and Holman (1990) and Ranasinghe et al. (2004) gained detailed insight into intermediate beach state dynamics at two different single-barred beaches: Duck, North Carolina, USA, and Palm Beach, Sydney, Australia, respectively. These studies showed that beaches continuously cycle through the four intermediate beach states in response to changing wave conditions. The three-dimensional structure of the morphology can be wiped out by an episodic event (a *reset event*, a high-energy event that resets the three-dimensional character to an alongshore uniform bar position typical for the highest beach state). In conclusion, we may encounter high three-dimensional variability, which may turn into two-dimensional variability (alongshore uniform morphology) after a reset event (Stive & Reniers, 2003), see also Fig. 7.11). The progression from alongshore uniform morphology to the reflective beach takes place in weeks or months.

Depending on the beach state, rhythmicity can be observed in for instance beach cusps and rip channels[2]. Scientists have long tried to couple the spatial scales of these rhythmic features to certain length scales in the hydrodynamic forcing or geological constraints. However, in the last two decades or so, the focus has been more and more

[1]Downstate implies consecutive beach states under gradually more moderate energy forcing.

[2]Rip channels are found in between shore-connected transverse bars or as cross-shore depressions in a shore-parallel bar. The latter bars are also called surf zone crescentic bars systems in literature: surf zone sand bars with alongshore undulations in height and cross-shore position of the bar crest.

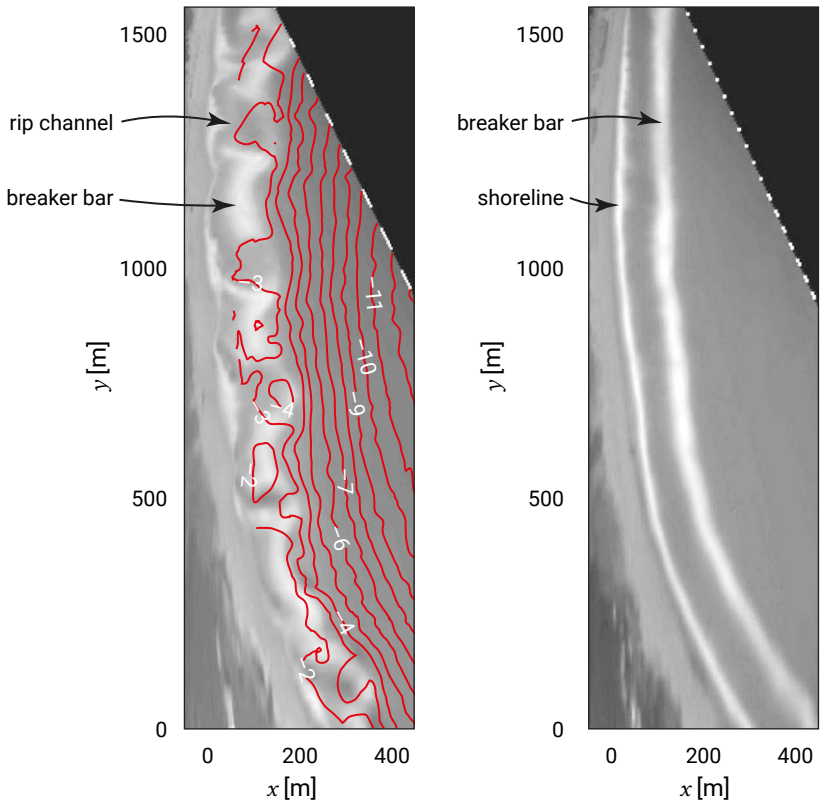

Figure 7.11: ARGUS imagery is used to obtain photographic images of incident wave-breaking. Waves break over shallow bars, where the foam of the breaking waves shows up as an area of high light intensity. Left panel: Example of a time exposure of Palm Beach, Australia, and superposed bottom contours displaying a complex pattern of shallow shoals (light areas corresponding to intense wave-breaking) cut by deep rip channels (dark areas without wave-breaking). The beach is located on the left. Right panel: Another example of a time exposure at the same beach showing intense wave-breaking on a linear bar and additional breaking at the shoreline (Argus images courtesy of Graham Symonds).

on *self-organisation* (see e.g. Coco and Murray (2007)). Self-organisation means that certain spatial patterns are associated with internal dynamics rather than with external forcings. These two contrasting approaches are further explained in Intermezzo 7.2.

Obviously, we have discussed interesting notions about intertidal and surf zone variability due to antecedent and concurrent forcing conditions. With timescales of antecedent forcing conditions of days to months, these observations are of importance for the beach state and its suitability for recreation and beach use, but are of limited importance on longer timescales.

Intermezzo 7.2
Spatial scales: governed by external forcing or internal dynamics?

Traditionally, it has been assumed that the spatial structures in the forcing (called *forcing templates*) become imprinted in the sediment bed. Observed length scales

in the resulting morphology would then correspond directly to length scales in the forcing. A complicating factor is that the morphodynamic response is not always instantaneous. This implies that some time is required for the spatial scales of the morphological patterns to evolve towards the scales of the forcing. Due to natural variability in the forcing, not enough time may be available to get to that point. Hence, the morphology of the system generally reflects the mix of the antecedent and concurrent hydrodynamics (thus a history of wave height, period and direction combinations). Predictability of the morphological length scales then strongly depends on knowledge about the entire history of the forcing and – if only the concurrent forcing is known – on the relative importance of antecedent and concurrent forcing. Note that due to the stochastic nature of the hydrodynamic forcing conditions, future forcing is at best known in statistical terms!

In a self-organisation approach it is assumed that rhythmic features are initiated by positive feedbacks between hydrodynamics and morphology (leading to divergent behaviour) and are stabilised by negative feedbacks (leading to convergent behaviour), see Sect. 1.5.2. This implies that the observed length scales in the coastal morphology do not necessarily correspond to the length scales of the initial forcing processes. Only after a feedback process between forcing and morphology do certain length scales predominate. To differentiate it from *forced behaviour*, self-organisation has also been termed *free behaviour*.

Note that although the *length scales* of the morphodynamic features do not match those of the external forcing, self-organisation approaches assume the system to respond to (changing) hydrodynamic forcing. This is in accordance with observations that when hydrodynamic conditions change, bars and other features respond. The self-organisational processes, in which certain length scales prevail, need sufficient time for the dominant length scales to appear (hence the concurrent forcing should last sufficiently long).

Let us consider the example of rip-channel spacings in alongshore non-uniform surf zone bars (generally in the order of 100s of metres). A once-popular explanation of the fact that rip channel spacing is related to length scales in the forcing, was forcing due to edge waves. Edge waves are waves trapped against a shoaling beach. They are the wind-wave equivalent of coastally trapped tidal Kelvin waves (Sect. 3.8.3). Just as with Kelvin waves, the amplitude of edge waves varies sinusoidally along the shore and diminishes rapidly seawards from the shoreline. Whereas Coriolis is the mechanism behind the Kelvin waves, the trapped-wave phenomenon of edge waves has been attributed to wave refraction near the shore as a result of the variable water depth. The standing edge-wave patterns are presumed to become imprinted on the underwater sediment bed resulting in rip-channel systems. Although it has been argued that rip-channel spacings are correlated to length scales of edge waves (e.g. Bowen and Inman (1971) and Holman and

Bowen (1982)), observed patterns could not be correlated with concurrent or antecedent (one week) hydrodynamic forcing (Holman et al., 2006; Turner et al., 2007). Later (modelling) work could not verify these relationships either (e.g. Caballeria et al., 2002; Reniers et al., 2004). Wave groups are another possible forcing mechanism for rip currents (e.g. Reniers et al. (2004)). This is discussed further in the TU Delft course Coastal Dynamics II (CIE4309).

According to the self-organisation hypothesis, rip channels are thought to develop as a response to small, initial disturbances of the seabed that grow due to positive feedback. Where the water depth is locally smaller due to seabed disturbance, wave-breaking is enhanced, as is the resulting wave set-up and onshore flow, leading to a 2D circulation pattern (cf. Sect. 5.5.7). Furthermore, since sediment concentrations decrease from the breaking point to the shoreline, at locations where the water depth is smaller than average, the onshore sediment transport decreases shoreward. This transport convergence leads to deposition that further decreases the water depth. Where the water depth is locally larger, the flow is offshore-directed and the offshore sediment transport increases in the seaward direction (hence transport divergence). The resulting erosion leads to the progressive carving out of rip channels.

The testing of self-organisation hypotheses has been undertaken using process-based models as well as more abstract models. Such self-organisation approaches have suggested that rip channel spacings increase with an increase in hydrodynamic energy and depend on the antecedent morphology as well (for a review see Coco and Murray (2007) and Smit (2010)). Field observations, however, do not always convincingly support these relationships (e.g. Ranasinghe et al. (1999) and Turner et al. (2007)).

What are the implications of self-organisation for modelling efforts? As stated earlier, in the self-organisation hypothesis, small disturbances may grow to finite-amplitude shapes as a result of a feedback process. Theoretically, a model in which the governing internal dynamics are correctly represented can therefore be expected to properly represent the scale of the evolving morphodynamic features under known forcing. However, in practice, numerical models have only shown very limited success. Also, the exact positioning of the features (e.g. the rips) is very sensitive to small variations in the initial conditions[a]. Since the 'true' initial conditions (the positioning of the disturbances in nature) are not known precisely, it is not possible to predict the exact positioning.

[a] This sensitivity to initial conditions is typical for chaotic dynamics and is often popularly referred to as the butterfly effect.

7.3.3. Storm and seasonal changes

In the previous section we treated the beach state, which is a result of everyday morphological response to the antecedent and concurrent forcing. Here, we look at the response of the upper shoreface profile due to storm events with low surge heights and – largely in line with this – to the summer-winter response of the upper shoreface.

The cross-shore profile responds differently to summer and winter conditions, leading to a seasonal behaviour and profile characterisation as shown in Fig. 1.3. In response to the milder summer wave conditions, the offshore bars of the 'winter' profile move onshore and finally attach to the shore and rebuild the wider berm associated with the 'summer' profile. Hence, in summer the beach is 'rich' in sediment (a high beach profile; slope high) and in winter it is 'poor' in sediment (a low beach profile; slope gentle). In the classification of Wright and Short (1994), typical summer profiles resemble reflective beaches and winter profiles dissipative beaches (Sect. 7.3.2).

The summer-winter seasonality is strongest for the Northern Hemisphere storm wave climate, which exhibits a large seasonality (Sect. 4.3). Note that situations also exist in which the seasonal behaviour is reversed. For instance, the beaches in the Rhone delta on the Mediterranean coast show the reverse behaviour due to the summer mistral.

The summer-winter behaviour can also occur when a relatively calm period is interrupted by a storm event (Fig. 7.12). This behaviour was recorded by List and Farris (1999) along a stretch of the eastern USA coast (see Fig. 7.13).

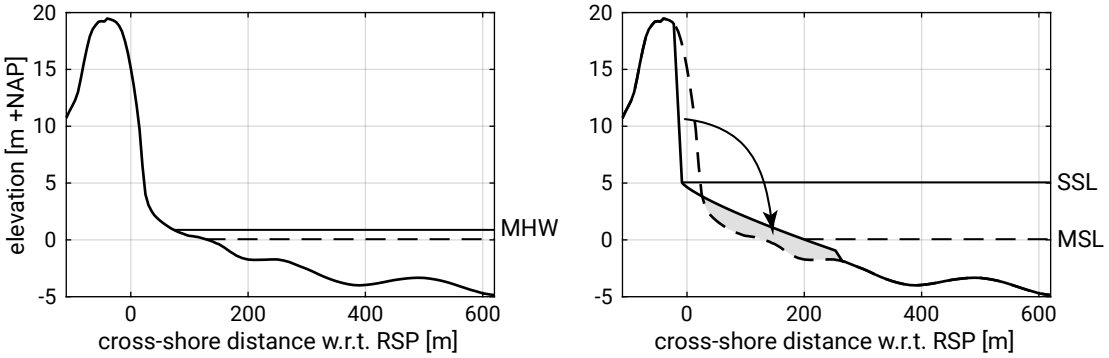

Figure 7.12: Left: profile during a calm period with normal water level and wave conditions ('summer' profile, see Fig. 1.13 for details). Right: profile as a result of storm wave height and surge conditions ('winter profile'). The post-storm profile is computed according to Vellinga, see Fig. 7.18 for further info on the Vellinga profile and the storm conditions considered here.

Figure 7.13 shows that after a calm period a 'summer' beach is present which turns into a 'winter' beach during a storm (note the relatively low storm surge heights). After the storm the beach nearly completely returns to its summer state: the beach breathes, so to speak. Interestingly, there is a large variation in the degree of breathing. The average recession/accretion is 10 m but some locations show much less variation, while others reach 15 m to 20 m. The latter locations are also known as 'hotspots', locations with more erosion than their surroundings. The reasons for this are not well-known,

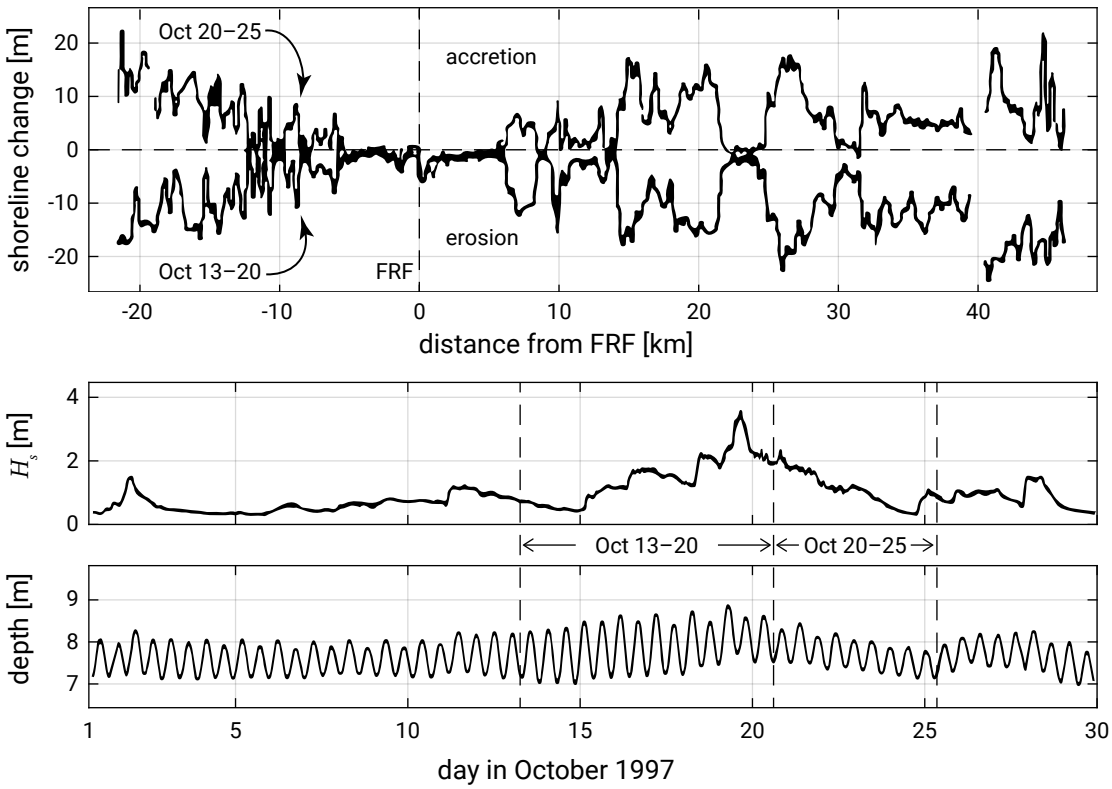

Figure 7.13: Upper figure: shoreline change between October 13 and 20 and between October 20 and 25 along a stretch of coast that is approximately 80 km long. FRF is the location of the Field Research Facility of the Army Corps of Engineers. Lower figures: the significant wave height at 8 m depth and tidal variation in time. The three vertical lines in the lower figures indicate October 13, 20 and 25 respectively. Note that surge is included in the tidal level variation. (Adapted from List et al., 2005; List & Farris, 1999).

but it is likely that a variable offshore bathymetry may cause wave energy focusing (see Sect. 5.2.3 and specifically Fig. 5.6) and that the position and height of dissipative bars play a role.

7.3.4. Bar cycles over years

In Sect. 7.3.2 on beach states, we have discussed the three-dimensional behaviour of bars under antecedent and concurrent wave forcing conditions. This behaviour is either forced or self-organisational behaviour of the bar around its mean position of that particular instant. However, that mean position varies over time, as we will discuss here.

If we study the behaviour of bars on longer timescales, i.e. years, we observe that bars generally and on average move offshore under more energetic conditions and may move a little back onshore during less energetic but skewed waves. The net offshore movement generally shows cyclic behaviour; the initial bar formation is in the intertidal zone, after which the bars move offshore and grow in size until a maximum is

reached somewhere around the initiation of the surf zone, after which they gradually decrease in size and amplitude and finally disappear at the end of the active shoreface profile. Along the Holland coast, this cycle varies between 4 to 5 years at the South Holland coast and around 15 years at the North Holland coast. The cyclic behaviour is indicated in Figs. 7.14 and 7.15 for the North Holland and South Holland coast, respectively.

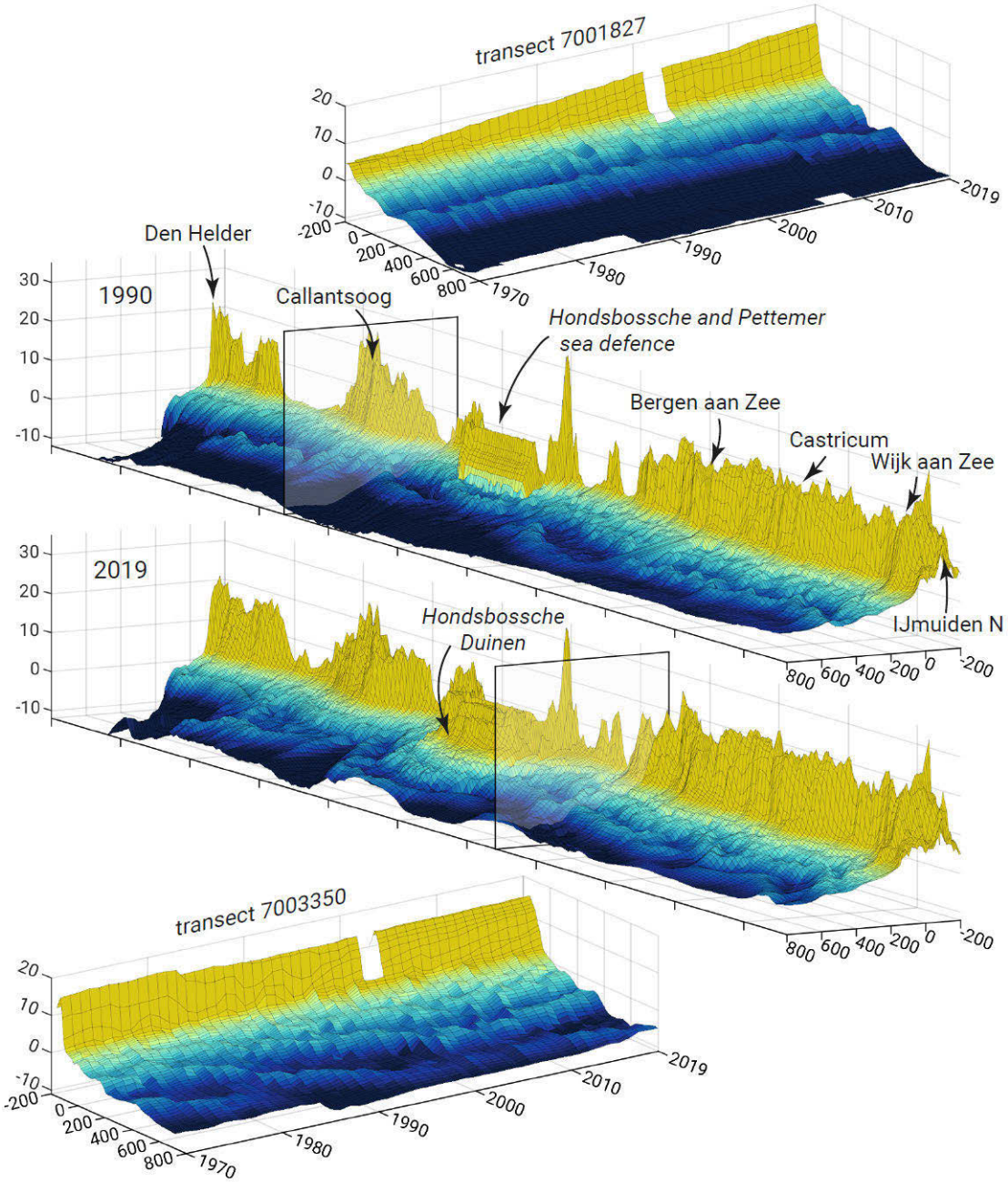

Figure 7.14: 3D image of the coast of North Holland from Den Helder (transect 7000150) to IJmuiden (transect 7005450) in 1990 and 2019, as well as the time evolution in two transects indicated by the transparent panels in the 3D images. (Data from JARKUS, n.d.).After completion of the sandy reinforcement of the Hondsbossche and Pettemer sea defence in 2018, it was renamed 'Hondsbossche Dunes' ('Hondsbossche Duinen' in Dutch).

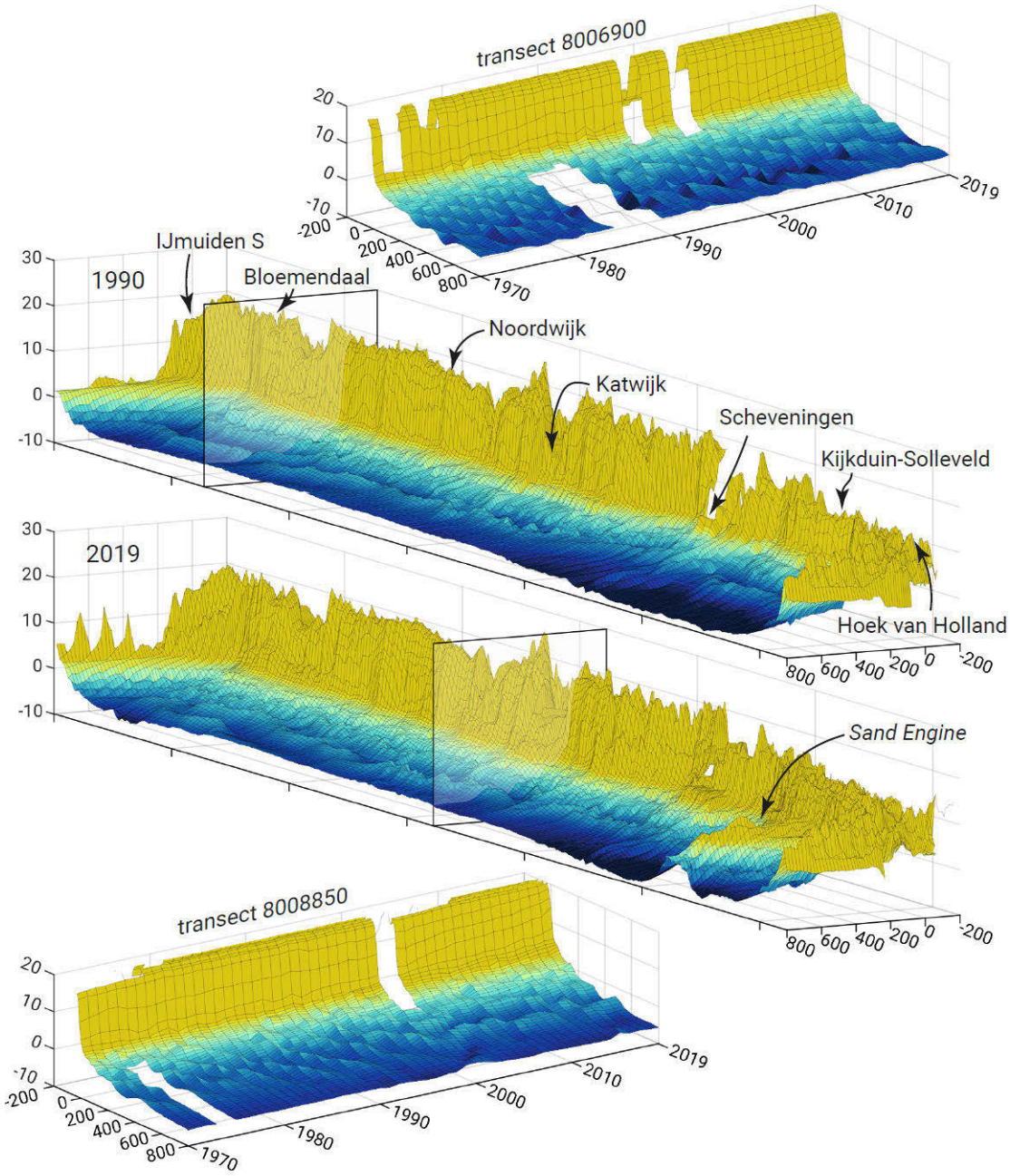

Figure 7.15: 3D image of the coast of South Holland from IJmuiden (transect 7005600) to Hoek van Holland (transect 9011900) in 1990 and 2019, as well as the time evolution in two transects indicated by the transparent panels in the 3D images. (Data from JARKUS, n.d.).

The difference in cycle time between North Holland and South Holland is most probably explained by the fact that the shoreface slope is steeper and the bars are larger on the NH coast (see Fig. 7.5), so that more energy is needed to induce sufficient sediment transport. The importance of this behaviour is most probably that the bar's position will influence the energy dissipation that energetic waves will undergo. This may lead to regional differences in shoreline response (see List and Farris results in Sect. 7.3.3).

The North Holland transect 7001827 between Callantsoog and Petten demonstrates an undisturbed, stationary bar movement (Fig. 7.14, top right). On the contrary, near Bergen aan Zee (transect 7003350) the initial 15-year bar cycle stagnated around 2000 (Fig. 7.14, bottom left). When comparing the 3D images of 1990 and 2019 (Fig. 7.14, middle) the sandy reinforcement of the Hondsbossche and Pettemer sea defence – completed in 2018 – is clearly visible.

The South Holland transect 8006900, just south of Zandvoort, exhibits an initially rapid offshore bar migration (4-year cycle) that gradually slowed down to a 5-year cycle from 1990–2010 and a still longer cycle since 2010 (Fig. 7.15, top right). Near Katwijk (transect 8008850) the initial rapid offshore bar migration (5-year cycle) stagnated around 2000 (Fig. 7.15, bottom left). The 3D images (Fig. 7.15, middle) clearly show the nourishment intervention known as the Sand Engine, comprising an unprecedented 21.5 Mm^3 §1.1 ~~unit commands~~ [p343] concentrated mega-nourishment, which was implemented in the summer of 2011 (Sect. 10.7.6).

We believe that the changes to the autonomous bar cycle in both North Holland and South Holland are §1.1 ~~the cause of~~ §1.1 the result of [p343] the Dutch coastline preservation strategy, which consists of frequent sand nourishments on the beach and shoreface to maintain the coastline in its 1990 position.

7.3.5. Episodic changes (dune erosion)

Dune erosion in the Netherlands and more generally along the southwest North Sea coasts takes place during storm surges, when the mean water level increases and waves can reach the dune face and impact it (Fig. 7.16). Sand eroded from the dunes (by a kind of episodic avalanching process) is transported offshore by a strong undertow. The combination of a strong undertow and high concentrations of suspended sediment in the proximity of the dunes, leads to a large offshore transport capacity. Further seaward the transport capacity of the flow decreases and the sediment starts to settle forming a new coastal profile that better fits the storm surge conditions. The newly developed foreshore is more efficient in dissipating the energy associated with the incoming waves and consequently dune erosion rates decrease as the storm progresses.

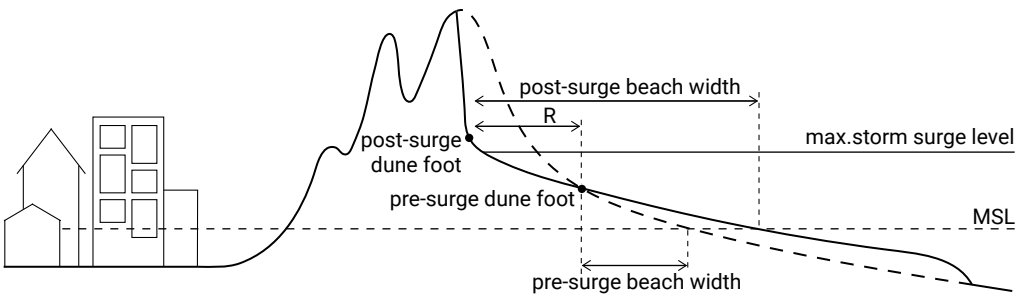

Figure 7.16: Typical storm surge dune erosion when the surge level reaches the dune face.

Existing design rules in the Netherlands allow for erosion rates of 80 m to 100 m of dune retreat during design storm conditions (Fig. 7.17). [§1.1]Design conditions are usually extreme conditions with a specified return period used in the design of coastal works. [p344] During a severe storm surge, with design conditions of offshore water levels approximately 5 m to 6 m above MSL and with severe wave conditions (wave heights $H_s \approx 7$ m to 9 m and peak periods $T_p \approx 12$ s to 18 s), the dunes will erode quickly and fiercely. Figure 7.17 presents retreat rates for lower design conditions as well.

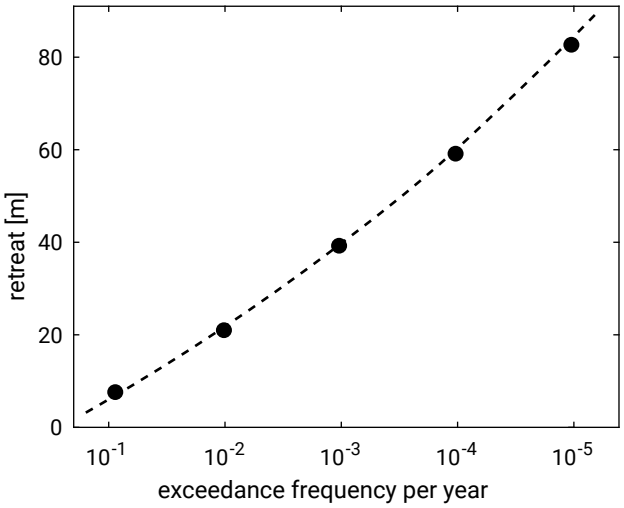

Figure 7.17: Retreat rates as a function of different design conditions (frequency of exceedance).

Figure 7.16 suggests that a new equilibrium profile is formed that fits the extreme conditions. Indeed this was the basis of the 'erosion profile' approach of Vellinga (1986), who extended earlier work of Van de Graaff (1977). The difference with the dynamic equilibrium profile methods of Bruun and Dean is that the timescale is different. This erosion profile method is presently still used for the basic assessment of the safety of the Dutch dunes (ENW, 2007).

For sediments with a D_{50} between 90 µm and 225 µm, Vellinga conducted a comprehensive set of experiments on different scales, and derived a scale relation showing the effect of grain size on the erosion profile shape:

$$\frac{n_l}{n_h} = \left(\frac{n_h}{n_w^2}\right)^{0.28} \tag{7.9}$$

where n_x represents the ratio between two cases with different scales of a variable x. If a small-scale physical model is made to represent reality (the 'prototype'), this scale relation can be used to derive the physical model dimensions and grain diameter. Note that in a scale series, the prototype can be a larger-scale model.

The following scales are specified in Eq. 7.9:

n_l	ratio between a horizontal distance in prototype and the equivalent distance in the model	–
n_h	ratio between water depth in prototype and the water depth in the model	–
n_w	ratio between fall velocity of bottom material in prototype and fall velocity of bottom material in model	–

Using the scale relation Eq. 7.9, Vellinga derived for the shape of the erosion profile (the post-storm profile):

$$h = A(x')^{0.78} \tag{7.10}$$

This equation relates the water depth h to the offshore distance x' through a dimensional shape factor A, which can also be derived from Eq. 7.9:

$$A = 0.39 w_s^{0.44} \tag{7.11}$$

where w_s is in m/s. The position of $x' = 0$ in Eq. 7.10 is now defined by the storm surge level instead of by the MSL. Based on a fall velocity of $w_s = 0.0256\,\mathrm{m/s}$, we find that the erosion profile is described by $h = 0.078(x')^{0.78}$. Clearly, the shape of the erosion profile is affected by grain size, with coarser material resulting in steeper slopes.

Note the similarity between Eqs. 7.10 and 7.11 on the one hand and Eqs. 7.1 and 7.7 on the other hand, but also note the different power and the different coefficient used in determining the shape parameter.

An interesting empirical finding by Vellinga concerns the extent of the sedimentation zone (see Fig. 7.18). This zone was found to reach a depth of approximately 75 % of the offshore significant wave height relative to the surge level. Equations 7.10 and 7.11 thus describe the erosion profile down to a depth of 75 % of the significant wave height. The horizontal position of the erosion profile is defined by the conservation of sediment in the cross-shore profile.

We can now make a rough estimate of the dune retreat. For simplicity, we assume that the erosion profile and the pre-storm equilibrium profile have the same shape, but that the erosion profile is shifted upward to the elevation of the storm surge level instead of the MSL. A landward translation (retreat) of the profile is required to ensure conservation of sediment. Since we have assumed a shape-invariant profile, the required dune retreat distance can be estimated using Bruun's rule (see Sect. 2.5.2 and Sect. 7.4). Following Bruun's rule, the volume of sediment eroded from the upper profile balances the deposited volume in deeper water for a retreat distance equal to (cf. Eq. 7.13):

$$R_{SS} = SSL(L/^{\S 1.2}\cancel{D}^{\S 1.2}d)[\text{p347}] \tag{7.12}$$

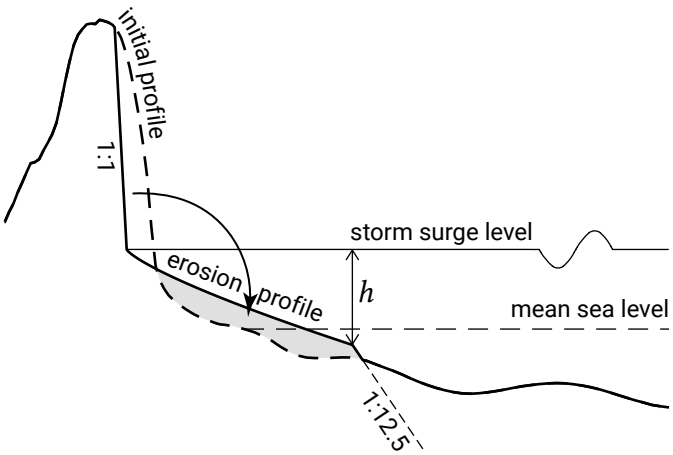

Figure 7.18: Extent of the sedimentation zone to a depth h equal to approximately 75 % of the offshore (significant) wave height $H_s = 8\,\mathrm{m}$. The 'erosion profile' or post-storm profile (after Vellinga, 1986) has a prescribed shape (Eq. 7.10 with $A = 0.078$) and its location is determined by balancing the volumes of erosion (higher in the profile) and accretion (lower in the profile). The vertical and horizontal scale are not the same (the 1:1 slope is a 45° slope in reality). The initial profile matches Fig. 1.13 and $SSL = 5\,\mathrm{m}$.

where SSL is the storm surge level above MSL, L the length over which the erosion and sedimentation takes place and §1.2 ~~d~~ §1.2 d) [p347] the corresponding height.

We assume that the dune height above MSL is 10 m. Let us take the same design storm conditions as given before, i.e. a storm surge level of approximately 5 m to 6 m above MSL and wave heights of $H_s \approx 7\,\mathrm{m}$ to 9 m. From Vellinga's finding that the sedimentation reaches a depth relative to the surge level of 75 % of the offshore significant wave height, we find that this depth is of the same order of magnitude as the storm surge level (viz. 5 m to 6 m). Hence, the region of sedimentation extends seawards until the point where the seabed is approximately at MSL, so that the height over which the sedimentation and erosion take place is equal to the dune height above MSL and $d = 10\,\mathrm{m}$ in Eq. 7.12. The length L over which the changes take place can be estimated from the erosion profile, which we assume to be determined by Eqs. 7.10 and 7.11. Using $w_s = 0.0256\,\mathrm{m/s}$, we have $h = 0.078(x')^{0.78}$ or $0.75H_s \approx 0.078L^{0.78}$ and thus $L = 220\,\mathrm{m}$ to 300 m. From Eq. 7.12, we obtain a dune retreat distance of 110 m to 180 m. This is (somewhat) larger than the design rule outcome of 80 m to 100 m.

We will get a significantly closer estimate using a dune erosion prediction model such as DUROS-plus, which was largely developed from a prediction model that was proposed by Vellinga, which in essence is not very different from our crude hand computation. As in the above, the depth to which the erosion profile reaches is computed as 75 % of the offshore significant wave height. The initial profile, however, is not necessarily identical in shape to the erosion profile. Furthermore, the shape of the erosion profile now is a function of both the sediment fall velocity and the offshore significant wave height and has a 1:1 slope above storm surge level. Again the position of

the erosion profile must be determined by a horizontal translation, until erosion and sedimentation volumes are balanced.

More refined methods to assess dune erosion exist, especially as a function of the specific storm surge conditions and duration, including variation over the tide. With these, the evolution in time of the erosion and sedimentation can be mimicked, which is necessary when the final 'equilibrium erosion profile' is not reached. These methods are commonly used for advanced designs.

After a storm surge, the beach width has become substantially wider (Fig. 7.16) and the coastal profile is not in equilibrium with the post-surge hydrodynamic conditions. Waves, tide and wind reshape the foreshore and the dunes gain eroded sand back gradually. In a situation without alongshore sediment transport gradients, the dunes recover to pre-storm volume. However, the timescale of dune recovery is considerably larger than that of erosion.

7.4. Structural losses or gains

In the previous sections we have assumed that while the beach and surf zone may breathe and may display three-dimensionality or simply two-dimensionality under cross-shore wave forcing, the amount of sediment in the active zone remains constant. On engineering scales (1 to 100 years) a number of processes exist that violate these assumptions. A prime one is alongshore transport gradients, treated in Ch. 8. Shoreline orientations and hence alongshore transport rates will vary, which will lead to either shoreline advance or retreat, while the upper shoreface profile will remain in profile equilibrium. On these engineering scales, aeolian (transport by wind) sand loss from the beach to the dunes and nearshore offshore canyons may be important as well. They can be accounted for as sinks.

A further 'sink', which is virtual because no sediment is lost, is due to relative sea level rise. This effect was first described by Bruun (1962). As explained in Sect. 2.5.2, Bruun argued that the response of the upper shoreface to an increased MSL is so fast that the equilibrium upper shoreface profile will adjust to the same profile, but relative to the new MSL (Figs. 2.22 and 7.19b). Hence, even though no sediment is lost from the profile, the shoreline retreats.

The retreat distance R follows from sediment continuity considerations. The new equilibrium profile requires that the shoreline retreats to supply sediment to the lower surf zone in order to maintain the equilibrium profile. Horizontal retreat R leads to a sediment yield of $R \times d$, where d is the height over which erosion and sedimentation takes place (viz. the closure depth plus dune crest height). Relative Sea Level Rise (RSLR)

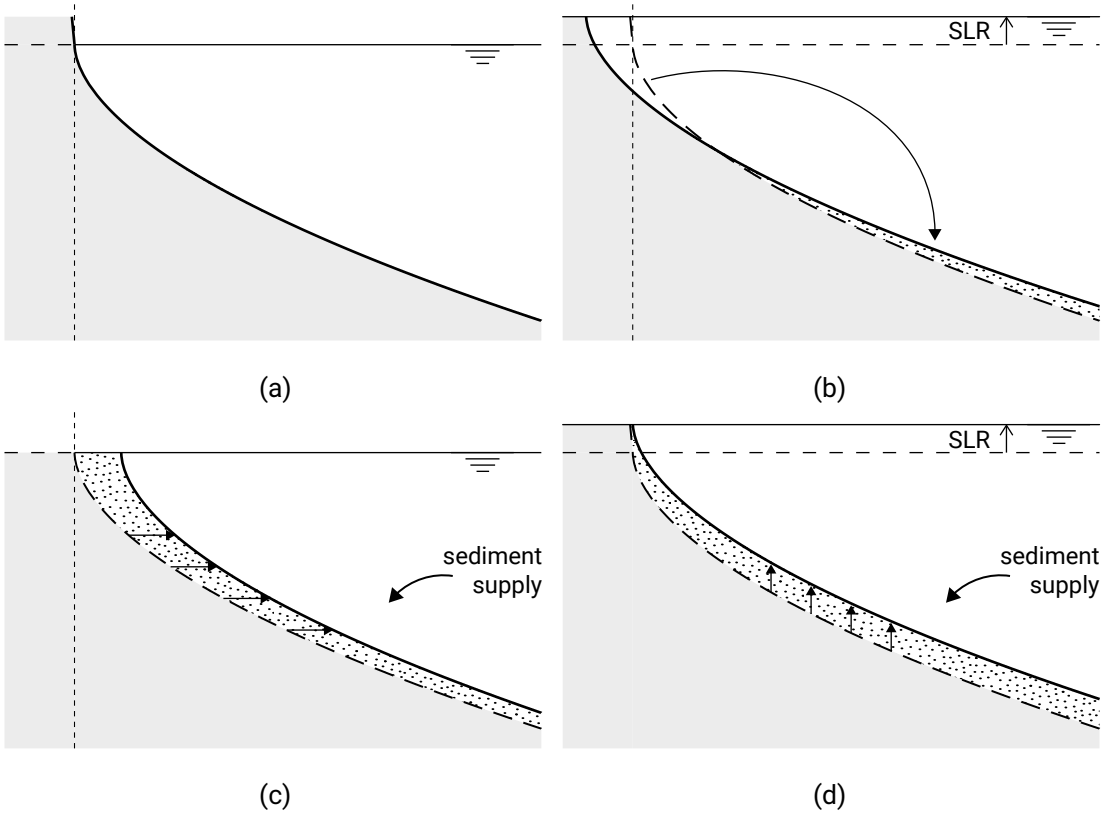

Figure 7.19: Equilibrium shoreface response to sea level rise and sediment supply: (a) the equilibrium profile before sea level rise; (b) shoreline retreat and shoreface erosion due to sea level rise (Bruun rule); (c) coastal progradation in the case of sediment supply; (d) balance between sea level rise and sediment supply.

leads to a demand of sand of $L \times \mathrm{RLSR}$, where L is the length over which the erosion and sedimentation takes place. Balancing the two (no net loss or gain) gives:

$$R_{\mathrm{RSLR}} = \mathrm{RSLR}(L/d) \tag{7.13}$$

where RSLR is the rise of relative sea level[§1.1] ~~above MSL~~ [p348], L the length over which the erosion and sedimentation takes place and d the corresponding height. In practice the ratio L/d is of the order 50 to 150 (Zhang et al., 2004).

Sediment supply may counteract the effect of shoreline retreat. Fig. 7.19c assumes a horizontal shift of the profile in the case of a sediment source. If the rate of sediment supply keeps up with the rate of sea level rise, the accommodation space created by the sea level rise is filled by incoming sediments (Fig. 7.19d) and the profile moves upward only; the position of the shoreline remains unchanged.

Quite often the Bruun rule is used to assess possible future effects of sea level rise. Although it gives qualitative insight into profile response to sea level changes, it is not a valid model approach in general due to oversimplifications (see e.g. Ranasinghe and Stive (2009)). One of the problems with the application of the Bruun rule – for instance

when considering shore nourishment to counteract the effects of sea level rise – is that time is required for equilibrium to be established. Often this point is not considered by coastal engineers. Rapid sea level rise induces rapid coastal response. However, the timescale on which present sea level rise influences coastal evolution in general and coastal erosion in particular, is relatively large. Present coastal evolution on smaller time- and spatial scales is dominated by other causes.

7.5. Cross-shore sediment transport

7.5.1. Introduction

The research field of cross-shore hydrodynamics, sediment transport dynamics and resulting bed profile dynamics is highly topical and very complex, and simple, analytical treatments do hardly exist. The reason is that over the whole of the shoreface the constituent processes vary strongly. In the upper shoreface, say the surf zone, under normal conditions we encounter a mix of bed and suspended load transport due to undertow, bound and free long waves, short-wave skewness in combination with breaking-induced turbulence (Bailard, 1981; Roelvink & Stive, 1989). In this zone, during extreme conditions the undertow is dominant (Steetzel, 1993), although long-wave effects (bound and free long waves) cannot be ignored (Van Thiel de Vries, 2009). On the middle and lower shoreface, again a mix of bed and suspended load transport is encountered, but here wave boundary layer streaming, bound long waves and short-wave skewness are relevant. Also, upwelling and downwelling due to stratification and Ekman currents may play a role here (but are outside the scope of this book).

For calculating bed profile dynamics of the upper shoreface (under storm surge and non-storm surge conditions), process-based, numerical models have been developed. These models describe sediment transport as a function of the wave evolution in the surf zone, which requires a largely empirical description of the highly variable wave energy dissipation and related flow variations. For the middle and lower shoreface, analytical approaches are available due to Bowen (1980), who derived formulas for equilibrium profiles by balancing onshore and offshore transport components.

In Sect. 7.5.2, the cross-shore sediment transport rates are decomposed into contributions due to undertow, short-wave skewness and bound and free long waves associated with wave groups. This gives new insight into the relevance of the various flow components to net sediment transport. In Sect. 7.5.3, we reproduce some of the analytical approaches for the middle and lower shoreface as introduced by Bowen.

7.5.2. Decomposition of the transport rate

As explained in Ch. 5, the velocity u close to the bed can be assumed to consist of a wave group-averaged component $\bar{u}$, a short-wave-averaged oscillatory component u_{lo} and a short-wave component u_{hi}:

$$u = \underbrace{\bar{u}}_{\substack{\text{time-averaged component} \\ \text{(streaming outside surf zone,} \\ \text{undertow in surf zone)}}} + \underbrace{u_{lo}}_{\substack{\text{low-frequency motion} \\ \text{at wave group scale}}} + \underbrace{u_{hi}}_{\substack{\text{oscillatory motion} \\ \text{at short-wave scale}}} \tag{7.14}$$

We are now interested in the relative contributions of these components of the time-varying flow to the net sediment transport (*net* meaning averaged over the wave group). Let us for simplicity focus on the third odd velocity moment that determines the bed load transport (see Eq. 6.51). By assuming that $\bar{u} \ll u_{lo} \ll u_{hi}$ and using a Taylor expansion (see Intermezzo 7.3), Roelvink and Stive (1989) showed that the most important contributions to the third odd velocity moment are given by:

$$\left\langle u|u|^2 \right\rangle = \underbrace{3\left\langle \bar{u}\left|u_{hi}\right|^2 \right\rangle}_{1} + \underbrace{\left\langle u_{hi}\left|u_{hi}\right|^2 \right\rangle}_{2} + \underbrace{3\left\langle u_{lo}\left|u_{hi}\right|^2 \right\rangle}_{3} + \ldots \tag{7.15}$$

The term $|u_{hi}|^2$ in all three terms reflects that the sediment load is stirred by short waves. The first term on the right-hand side of Eq. 7.15 is related to the subsequent transport by the mean current. The mean current could be the onshore-directed wave-induced near bed streaming in non-breaking waves (Sect. 5.4.3) or the offshore-directed undertow in the surf zone (Sect. 5.5). The second and third term represent the contribution to the velocity moment (and hence the net transport) of the oscillatory part of the instantaneous velocity; the second term is related to the short-wave skewness, whereas the third term is associated with the interaction between the long-wave velocity and the short-wave velocity variance (the latter will change periodically on the timescale of short-wave groups).

The second term is zero for a completely symmetrical oscillating velocity signal. However, in shoaling waves the velocity signal becomes asymmetric about the horizontal axis (positively skewed, meaning $\left\langle u^3 \right\rangle > 0$, see Sect. 5.3). As a result the second term is non-zero and onshore-directed. In Intermezzo 6.5, we explained this transport contribution as follows: the larger onshore peak velocities under the wave crests are more effective in stirring up sediment than the smaller offshore velocities under the wave troughs. The relation between the amount of sediment stirring and velocity is non-linear; a twice as high velocity stirs up (in this case) four times more sediment. The result is an onshore transport.

The third term is non-zero as long as there is a correlation between the slowly varying short-wave velocity variance (the short-wave envelope) and the long wave forced by

the wave group. Outside the surf zone this correlation is negative (where the bound long wave is not yet 'released from the group'); the mean water surface decrease (trough of the bound long wave) is found under the larger amplitude waves in the group (Fig. 7.20).

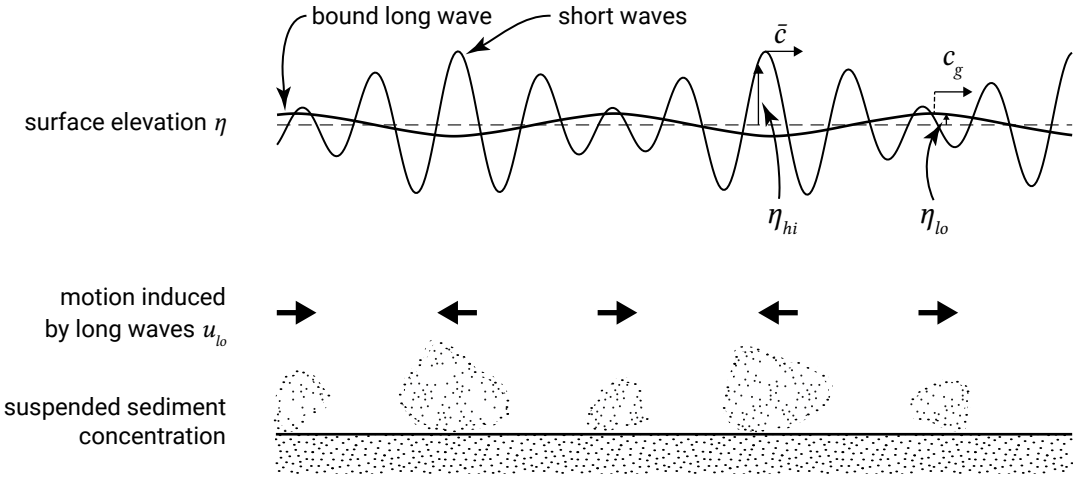

Figure 7.20: Offshore (suspended) sediment transport under a bound long wave (outside the surf zone). The sediment suspended by the highest waves is transported offshore by the out of phase long-wave motion. The effect is a net offshore transport.

As long as the trough of the bound long wave coincides with the highest velocities in the group, most sediment is stirred up while the long-wave velocities are offshore-directed. The net transport by the bound long wave motion is therefore offshore-directed (Fig. 7.20 shows this for suspended sediment transport). If the phase relationship between the short-wave envelope and the long wave changes, this situation may change. The main reason why the phase relationship may change is that bound long waves become released during breaking of the short waves.

Roelvink and Stive (1989) analysed the decomposition of the velocity moments using laboratory measurements in a large (full-scale) wave flume. Calculated and measured total third and fourth odd flow moments (important for bed load and suspended load transport respectively) are compared in Fig. 7.21. The figure clearly shows the onshore-directed component due to short-wave skewness. It increases in shoaling waves and decreases again in the surf zone (Sect. 5.3). The undertow component is offshore-directed in the entire surf zone. The long-wave contribution is offshore-directed until the correlation between the short-wave variance and long wave becomes positive somewhere in the surf zone.

From Fig. 7.21 it also becomes clear that gross cross-shore transports are much higher than net cross-shore transports. This makes accurate cross-shore transport predictions very difficult.

As mentioned in Sect. 7.5.1, during extreme conditions the transport contribution due to undertow is dominant. This explains that under higher and longer waves, as

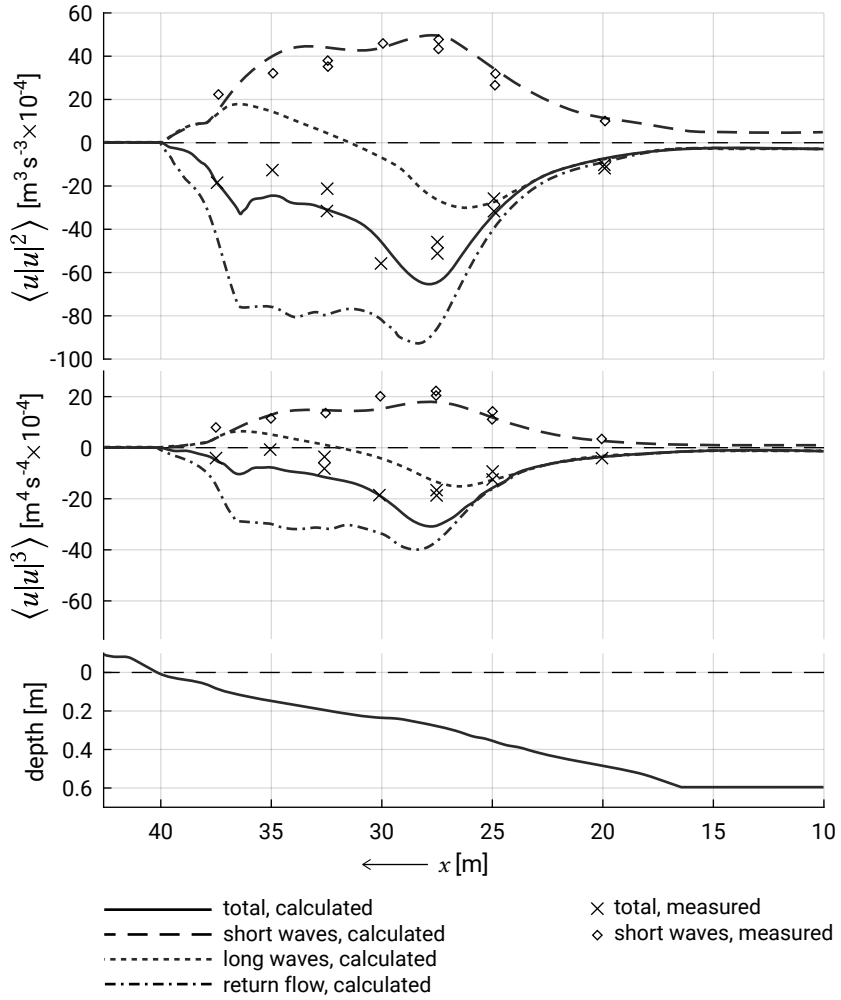

Figure 7.21: Total third ($n = 3$) and fourth ($n = 4$) odd flow moments and their constituent components (i.e. for the third odd moment, the terms 1, 2 and 3 on the right-hand side of Eq. 7.15); wave flume measurements (symbols) and model predictions (lines). This situation – with a dominant transport component due to undertow and a net offshore transport – represents storm wave conditions. For milder conditions the onshore transport components are relatively more important. From Roelvink and Stive (1989).

present during storms, a net offshore transport is observed, leading to a 'winter' profile (Sect. 7.3.3). By contrast, milder waves build up the profile to a 'summer' profile via onshore transport, due to predominantly short-wave skewness.

A similar decomposition of the transport rates can be made for the situation in which tidal flow dominates the velocity u. For this we refer to Sect. 9.7.2.

7.5.3. Analytical solutions for the middle and lower shoreface

Bowen (1980) derives formulas for the equilibrium shape of the middle and lower shoreface based on balancing onshore and offshore transport terms. He discusses the contribution of the main process of oscillatory orbital motion in combination with a mean

flow, a higher harmonic orbital motion (asymmetry[3]) and a long wave motion, for instance a bound long wave. Because of the non-linear coupling of these contributions in sediment transport, their interactions are important. His analytical approach gives a good insight into these process interactions, and we note that the model efforts of Bailard (1981), Bailard and Inman (1981), Roelvink and Stive (1989) and Stive and De Vriend (1995) are very much inspired by this.

In this section, we present an abstracted form of certain parts of Bowen's landmark paper.

Bowen starts by stating that:

> "Any understanding of the relationship between the incident waves and the topography of a beach is greatly complicated by the beach being rarely, if ever, in equilibrium with the existing wave field. The morphology depends on some complex integral of past wave conditions, an integral heavily weighted towards periods of high waves. (...) The real situation is perhaps too complex for parameters to be developed without some guidance as to the relative importance of various possible processes. Simple theoretical models are particularly useful in defining these possibilities. (...) The purpose of the present paper is to develop a consistent model for onshore-offshore sediment transport under the influence of waves, currents and gravity. (...) The model is, however, neither unique nor necessarily correct (...), but a doubtful model is clearly preferable to no model. (...) The most important aspect of the present approach is the rigorous development of a theory, starting from any given model of sediment transport."

Note that he speaks of a beach, but in what follows he concentrates rather on the middle and lower shoreface, not on the surf zone. The probable reason is that we lack straightforward analytical descriptions of the interactions between undertow, asymmetric oscillatory flow motion, breaking-induced turbulence and the bound and free long waves on the upper shoreface.

He explains the existence of a beach as follows:

> "If a beach was exposed to waves having an exactly symmetrical, orbital velocity, all the sediment would slide down the slope and out to sea. The existence of the beach depends on small departures from symmetry in the velocity field, balancing this tendency for gravity to move material offshore. (...) The development of the theory assumes as a basic hypothesis that the orbital motion of the incoming waves is the dominant motion."

[3] In this section – as opposed to elsewhere in the book – we follow the wording of Bowen and use the word asymmetry for a skewed wave that is asymmetric about the *vertical* axis.

Hence, the basic idea is that the velocity u consists of two interacting components, the symmetrical orbital velocity $U_0 = u_0 \cos(\omega t)$ and a perturbation U_1, where:

$$u = U_0 + U_1, \quad \text{with generally} \quad U_0 \gg U_1 \tag{7.16}$$

The perturbation §1.1U_1 of the primary symmetrical harmonic §1.1U_0 [p354] can take many forms; cases of particular interest are:

1. A constant, steady current: $U_1 = u_1$;
2. The velocity field associated with a higher harmonic of the incoming wave: $U_1 = u_m \cos(m\omega t + \theta_m)$, with $m = 2, 3, 4, \ldots$;
3. A perturbation due to a wave with a frequency ω_t unrelated to ω: $U_1 = u_t \cos(\omega_t t)$.

Note that in principle the steady current can be any current. Especially relevant for the shoreface is undertow in the surf zone and boundary layer streaming, further offshore. The higher harmonics are relevant in the surf zone, with forward pitching or even sawtooth waves and θ_m is non-zero, while further offshore we have only skewed or peaked waves (symmetrical around the vertical), where θ_m is zero. The third item (a wave with a frequency unrelated to the primary harmonic) is not discussed in this book.

Bowen adopts Bagnold's transport description for uniform flow and transforms it for non-linear oscillatory motion, resulting in Eqs. 6.48a and 6.48b. According to Bowen, Bagnold's energetics model is the simplest available model that includes the basic properties that are necessary to describe cross-shore sediment transport. He especially stresses the explicit inclusion of the gravitational effect of a sloping bed.

Bowen also discusses the limitations of the energetics model:

> "First, and perhaps most serious, the transport in this model depends only on the immediate flow conditions, adjusting instantaneously to changes without any time lag. Second, the theory applies to fully developed flow and does not describe initiation of movement; it does not apply to large particles that may move only intermittently at peak flows."

First Bowen looked at suspended sediment transport and then at bed load transport both on the middle and lower shoreface. We will only repeat his suspended sediment transport derivations, because Stive and De Vriend (1995) showed by evaluating the transport terms for a typical shoreface situation that this transport mechanism is dominant on the middle and lower shoreface.

From Eq. 6.48b, the suspended load transport can be expressed as:

$$I_s = \frac{\varepsilon_s c_f \rho}{w_s} \frac{u^3 |u|}{(1 - \gamma u)} \quad \text{with} \quad \gamma = \frac{\tan \alpha}{w_s} \tag{7.17}$$

For normal transport conditions $\gamma u < 1$. If γu approaches 1, I_s goes to infinity and autosuspension effects (avalanching, i.e. the slope is so steep that all particles go into suspension) totally dominate the transport.

Bowen now expands Eq. 7.17, using the Taylor series as in Intermezzo 7.3, and takes a time average (denoted by the overbar), arriving at a net transport $\langle I_s \rangle$ over a number of wave periods. If we consider normal transport conditions, the expansion involves the small quantities U_1/U_0 and γU_0. To second order, Bowen's transport formula reads:

$$\begin{aligned}\langle I_s \rangle = &\frac{\varepsilon_s c_f \rho}{w_s} \Big[\overline{U_0^3 |U_0|} + {}^{\S 1.1}4 \overline{{}^{\S 1.1}4 U_1 U_0^2 |U_0|} + {}^{\S 1.1}6 \overline{{}^{\S 1.1}6 U_1^2 U_0 |U_0|} + \\ &\gamma \left(\overline{U_0^4 |U_0|} + {}^{\S 1.1}5 \overline{{}^{\S 1.1}5 U_1 U_0^3 |U_0|} \right) + \gamma^2 \overline{U_0^5 |U_0|} + \ldots \Big] \text{ [p355]}\end{aligned} \tag{7.18}$$

Terms of the form $U_0^n |U_0|$ vanish if n is odd, since U_0 is assumed to be a symmetric oscillation.

Now, to first order, the equation reduces to:

$$\langle I_s \rangle = \frac{\varepsilon_s c_f \rho}{w_s} \left[{}^{\S 1.1}4 \overline{{}^{\S 1.1}4 U_1 U_0^2 |U_0|} + \gamma \overline{U_0^4 |U_0|} + \ldots \right] \text{ [p356]} \tag{7.19}$$

The first term describes the transport, onshore or offshore, due to a perturbation of the flow field U_1. The second term involves the slope $\tan\alpha$ and is generally positive, representing the tendency for downslope transport.

Bowen continues by evaluating the transport equations for the first form of the perturbation U_1, viz. $U_1 = u_1$ is a constant in time. Using Eq. 7.19, this yields to first order:

$$\langle I_s \rangle = \frac{\varepsilon_s c_f \rho}{w_s} \left[\frac{16}{3\pi} u_1 u_0^3 + \frac{16}{15\pi} \gamma u_0^5 \right] \tag{7.20}$$

Equation 7.20 is a general result for any distribution of a steady flow $U_1(x)$. One could consider undertow, upwelling or downwelling but Bowen chooses to continue with boundary layer streaming as the relevant effect, which we support for the middle and lower shoreface.

An equilibrium profile, purely in suspended load, exists if the gravitational effects balance the influence of the steady current everywhere and $\langle I_s \rangle$ vanishes. From Eq. 7.20, when $\langle I_s \rangle = 0$:

$$\gamma = \frac{\tan\alpha}{w_s} = -\frac{5u_1}{u_0^2} \tag{7.21}$$

This equation essentially contains no free parameters, which is an attractive feature of Bagnold's model.

The second-order, Eulerian mean velocity due to boundary layer streaming is of the order $-u_0^2/c$ (Eq. 5.29), where c is the wave phase speed (Eq. 3.23), so that:

$$\tan\alpha \simeq \frac{5w_s}{c} = \frac{5w_s\omega}{g\tanh kh} \tag{7.22}$$

where k is the local wavenumber, h the water depth. This yields a formula for the equilibrium slope in terms of $w_s\omega/g$, a dimensionless parameter also used by Dean (1973).

If sediment of a given grain size is in equilibrium with the local slope, so that $\langle I_s \rangle$ vanishes for this grain size, any coarser material with a larger fall velocity has a smaller value of γ. The term involving gravity is reduced, the onshore term remains constant, coarser material therefore moves onshore; similarly, finer material moves offshore as observed. As can be observed from Eq. 7.22, profiles of coarser material are steeper, and any material that finds itself on a beach that is 'too steep' moves seawards. This leads to a new null hypothesis that is in far better agreement with observations than classical models.

In shallow water c tends to $\sqrt{gh}$ and Eq. 7.22 is readily integrated:

$$\tan\alpha = \frac{dh}{dx} \simeq 5w_s/\sqrt{gh} \Rightarrow h^3 \simeq \left(7.5w_s x\right)^2/g \tag{7.23}$$

And thus the equilibrium profile is described by:

$$\boxed{h \simeq \left(7.5w_s\right)^{2/3}/g^{1/3}x^{2/3}} \tag{7.24}$$

Intriguingly, this result accurately resembles the results earlier presented for the equilibrium shoreface profiles of Bruun and Dean (Eq. 7.1). The profile shape factor A according to Eq. 7.24 is for $w_s = 0.0256\,\mathrm{m/s}$:

$$A = \left(7.5w_s\right)^{2/3}/g^{1/3} = 0.16 \tag{7.25}$$

This result is reasonably close to $A = 0.10$ for the same fall velocity according to Eq. 7.7.

Next, Bowen considered the role of the higher harmonics associated with the incoming wave field (thus, wave asymmetry). The perturbation U_1 is now a higher harmonic of $U_0 = u_0\cos(\omega t)$, viz. $U_1 = u_m\cos(m\omega t + \theta_m)$.

The effect of wave asymmetry on the transport is derived from the first-order equation Eq. 7.19. The first-order term §1.1 $4U_1U_0^2|U_0|$ §1.1 $\overline{4U_1U_0^2|U_0|}$ [p357] vanishes if m is odd. We

therefore only have to take even harmonics into account, the second harmonic ($m = 2$) being the most important. For the second harmonic we have:

$$\overline{4U_1|U_0^2|U_0} \overline{4U_1U_0^2|U_0|} = -\frac{16}{5\pi}u_0^3 u_2 \cos\theta_2 \tag{7.26}$$

The term arising from Eq. 7.26 is not an alternative to the contribution due to the Longuet-Higgins boundary layer streaming, but an additional factor. We therefore add the term from Eq. 7.26 to Eq. 7.20 and find:

$$\langle I_s \rangle = \frac{\varepsilon_s c_f \rho}{w_s}\frac{16}{15\pi}u_0^3\left[5u_1 - 3u_2\cos\theta_2 + \gamma u_0^2\right] \tag{7.27}$$

Again, an equilibrium profile for suspended load is found for $\langle I_s \rangle = 0$:

$$\gamma = \frac{\tan\alpha}{w_s} = -\frac{5u_1}{u_0^2} + \frac{3u_2\cos\theta_2}{u_0^2} \tag{7.28}$$

To evaluate this equation, Bowen assumed $\theta_2 = 0$ and used the second-order Stokes solution (see Intermezzo 5.1) to estimate u_2. Herewith he derived that:

$$\tan\alpha \simeq \frac{9}{4}\frac{w_s}{c}\left[2 + (\sinh kh)^{-2}\right] \tag{7.29}$$

The term in brackets is shown in Fig. 7.22. In deep water, the effect of wave asymmetry is negligible compared to that of the wave boundary layer streaming. As the waves shoal, the wave harmonics become increasingly important. Since in very shallow water the Stokes solution is not necessarily a good approximation, the trend is indicated by a dashed line. At some point, the waves break and the form of u_2 is only known from very limited empirical data.

According to Eq. 7.29, wave asymmetry becomes as important as drift when:

$$\sinh kh \sim 2^{-1/2} \tag{7.30a}$$

$$h \sim 0.01 g T^2 \tag{7.30b}$$

where T is the wave period. Equation 7.30 suggests that the extent of the nearshore area in which wave asymmetry is the dominant effect is strongly dependent on the period of the incoming waves. On the west coast of North America, which is generally exposed to waves of much longer periods, wave asymmetry should have a much more significant effect than on the east coast.

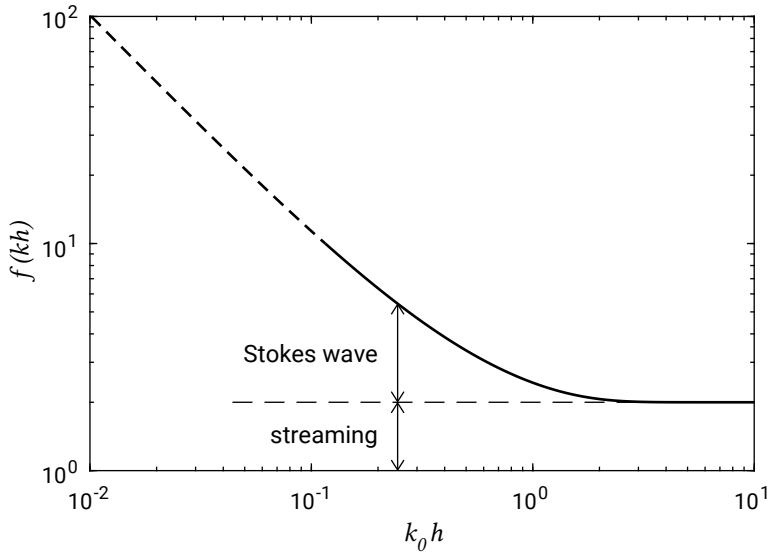

Figure 7.22: The term $f(kh) = 2 + (\sinh kh)^{-2}$ (see Eq. 7.29), plotted as a function of the nondimensional depth $k_0 h$, where $k_0 = \omega^2/g$ is the deep-water wavenumber.

As kh becomes small, then from Eq. 7.29 a formula for the equilibrium profile due to asymmetry can be derived, comparable to Eq. 7.24:

$$h^5 \sim \left(\frac{5.7 w_s x}{\omega^2}\right)^2 g \tag{7.31}$$

Bowen's landmark paper contains many more interesting analytical derivations and again we note that these analytical ideas have been at the basis of many numerical process-based model efforts. It is a paper worth studying if one is interested in solving the cross-shore morphology problem.

Intermezzo 7.3 Taylor series expansion of velocity moments

Bowen (1980) outlined a Taylor series expansion of the velocity moment $u^n|u|$. He assumed the velocity u to consist of two interacting components, viz. U_0 and a perturbation U_1, hence $u = U_0 + U_1$. Under the assumption that U_0 is much larger than U_1, the Taylor series expansion reads:

$$u^n|u| = U_0^n \left|U_0\right| + (n+1) U_1 U_0^{n-1} \left|U_0\right| + \frac{n(n+1)}{2} U_1^2 U_0^{n-2} \left|U_0\right| + \ldots \tag{7.32}$$

In practice, U_0 is the wave orbital velocity $U_0 = u_0 \cos(\omega t)$ which vanishes during the orbital cycle, and the assumption that U_1 is small compared to U_0 is not justified during the stages of the orbital velocity when U_0 is small. The approximation is really that $U_1 \ll u_0$, the maximum orbital velocity, and that the significant periods

for transport are when U_0 is large. This is probably a reasonable assumption, as the transport is proportional to the third or fourth power of the total velocity.

8

Longshore transport and coastline changes

8.1. Introduction

The purpose of this chapter is to illustrate how alongshore sediment transport contributes to shaping our coasts. The insight gained in the previous chapters, describing the water and sediment movements along coasts, will now be combined to provide the necessary explanations.

The main principle behind coastal change has already been indicated in Chs. 1 and 7: *coastal change occurs where there are spatial sediment transport gradients and/or sediment sinks or sources.* In this chapter we specifically look at gradients in mainly wave-driven longshore transport or, in other words, *littoral* transport. Consider an infinitely long, straight sandy coast with parallel depth contours, as sketched in Fig. 5.4. If waves approach this coast at a uniform angle along its entire length, and there are no other current-driving forces such as tides and wind, then there will be a constant, uniform transport of sand along this coast. What, then, causes erosion or deposition? This is caused by *changes (gradients)* in transport rates along a coast. This change may result from changing any of the factors influencing the longshore sediment transport rate, such as nearshore wave height and angle of wave incidence.

Various methods to compute longshore sediment transport are treated in Sect. 8.2. The calculation of shoreline position is described in Sect. 8.3. Section 8.4 discusses the various coastal shapes and characteristics that can be explained from longshore sediment transport gradients.

In Sect. 6.9.2 it was mentioned that coastline change is dominated by alongshore effects in the case of human-induced changes on high-wave energy coasts (e.g. the Dutch North Sea coast). In Sects. 8.3 and 8.4, we therefore mainly focus on typical time and spatial scales for engineering or coastal maintenance (years to decades and 1 km

to 100 km, see Sect. 1.5.3) and implicitly assume dominance of alongshore transport processes.

8.2. Longshore transport formulas

8.2.1. General transport formulas

Longshore sediment transport is the net movement of sediment particles through a fixed vertical plane perpendicular to the shoreline. The direction of this transport is parallel to the shoreline and the depth contour lines. Without further specifications it is often meant to be the total or *bulk* transport in the alongshore direction (e.g. the total transport along a coast in the entire active zone).

Wave-driven longshore sediment transport depends, amongst other factors, on the hydrodynamics in the breaker zone (see Ch. 5) and on the sediment properties (see Sect. 6.2). However, regardless of the strength of the transport-generating hydraulic forces, sediment transport will only occur if moveable sediment is available in a certain area, either in the bed or in the water column through supply from an adjacent area. If the seabed is fixed (for instance by bottom protection, biochemical processes or vegetation or in the case of absence of sediment), erosion is prevented and the *actual transport* may be smaller than the local *transport capacity* based on the hydrodynamics. The sediment transport formulas presented in this section all reflect the *longshore transport capacity* assuming that the material is actually present and available for transport.

The computation of the sediment transport parallel to the coast can, in principle, be handled with any of the general sediment transport models introduced in Ch. 6. When these models are applied to compute longshore sediment transport rates, we can simplify the problem by assuming that transport in the alongshore direction is by a time-invariant longshore current.

Let us, for instance, consider the (suspended) sediment transport description based on velocity multiplied by concentration, Eq. 6.30. In principle the current velocity in the alongshore direction $v(z,t)$ at a certain position in the surf zone is a function of z and t. It consists of a mean and oscillatory component: $v(z,t) = V(z)+\tilde{v}(z,t)$. The short-wave motion acts mainly in the cross-shore direction (φ is small due to refraction) and thus nearly perpendicular to the sediment transport direction. In practice it is therefore often assumed that the alongshore oscillatory velocity $\tilde{v}(z,t)$ is small and that during a period with no significant change in the offshore wave conditions, a relatively time-invariant current velocity $v(z,t) \approx V(z)$ is present. This assumption implies that the mean water motion is the main contributor to longshore sediment transport. Note that the sediment concentration, in principle, fluctuates on the timescale of the waves and can – just as the velocity – be seen as the sum of a mean component and an oscillatory component, viz. §1.1 ~~$c(z,t) = C(z)+ \approx (z,t)$~~ §1.1 $c(z,t) = C(z) + \tilde{c}(z,t)$ [p362].

The purely oscillatory component of the sediment concentration, however, will not give rise to a net transport since $V(z) \cdot \tilde{c}(z,t)$ is purely oscillatory and therefore has a time average equal to zero. Hence, (suspended load) transport models based on solving the velocity and concentration distribution can be reduced to the current-related part only (cf. Eqs. 6.32 and 6.33):

$$\left\langle s_y \right\rangle = \int_a^h V(z) \cdot C(z) dz \tag{8.1}$$

where:

s_y	net longshore sediment transport excl. pores	$m^3/m/s$
$V(z)$	longshore current velocity at height z above the bottom	m/s
$C(z)$	time-averaged sediment concentration at height z	m^3/m^3
a	thickness of bed load layer	m
h	local (still) water depth	m

Note that such a computation yields the longshore (suspended) sediment transport at a certain cross-shore location. If we like to quantify the total transport in e.g. the surf zone, we must integrate the outcome of the equation over the width of the surf zone.

The longshore current velocity $V(z)$ can have many different driving forces, but for most beaches this current is driven predominantly by breaking waves which approach the coast at an angle. The longshore current is concentrated more or less in the surf zone and occurs regardless of whether there is sediment transport or not. Methods to compute this longshore current were outlined in Sect. 5.5.5.

We have concluded that the role of the oscillatory wave motion in *transporting* the sediment in the alongshore direction is limited. What then is the role of waves – besides generating the longshore current – in longshore sediment transport? Their role is to enhance the amount of sediment in suspension $C(z)$. As a result of turbulence, generated in the wave boundary layer and at the surface under breaking waves, considerable amounts of sediment are brought into suspension:

1. Due to the orbital motion (in mainly the cross-shore direction), the magnitude of the bed shear stress varies over the wave cycle and peaks twice every wave cycle. Especially during these peaks a lot of sediment is mobilised and entrained;
2. Breaking waves strongly increase the turbulence in the water column and therefore relatively easily bring suspended sediments into the upper part of the flow.

Summarizing, since the wave motion in the breaker zone is nearly perpendicular to the resulting current, the major influence of waves is to stir more material loose from the beach and keep it in suspension, thereby increasing the sediment concentration. It is the (wave-induced) longshore current (and not the oscillatory wave motion) that is mainly responsible for the net movement of material along the coast.

We can also demonstrate these findings using a transport formula of the form Eq. 6.24 or Eq. 6.51. With the orbital motion approximately cross-shore and the bed shear stress according to Eq. 5.76, we have:

$$\left\langle s_y \right\rangle = m_1 \left\langle \left|\vec{\tau}_b\right|^{(n-1)/2} \right\rangle V = m_2 \left\langle |\vec{u}|^{n-1} \right\rangle V \tag{8.2}$$

where:

s_y	longshore sediment transport (per unit width)	$m^3/m/s$
V	longshore current velocity at some level above the bed (e.g. depth mean velocity)	m/s
$\left\|\vec{\tau}_b\right\|$	magnitude of the bed shear stress vector due to combined wave-current motion	N/m^2
$\left\|\vec{u}\right\|$	magnitude of the combined wave-current velocity vector	m/s
m_1, m_2	(dimensional) coefficients	–
n	power (typically 3 to 5)	–

In Eq. 8.2, $m_1\left|\vec{\tau}_b\right|^{(n-1)/2} = m_2\left|\vec{u}\right|^{n-1}$ describes the sediment load that is transported by the longshore current velocity V. The sediment load is stirred up by the combination of longshore current and wave orbital motion (see Fig. 6.13 for the non-linear enhancement of the bed shear stress in the combined wave-current motion). Especially the wave orbital motion is important because of the small boundary layer thickness and hence large shear stresses (see Sect. 5.4.3). Substitution of $\left|\vec{u}\right| = \sqrt{u^2 + V^2}$ (see Fig. 5.38), with $u = \hat{u}\cos\omega t$ the cross-shore time-varying orbital motion, yields for $n = 3$:

$$\left\langle s_y \right\rangle = \underbrace{m_2 \left\langle u^2 + V^2 \right\rangle}_{\substack{\text{sediment load stirred by} \\ \text{wave-current motion}}} \underbrace{V}_{\substack{\text{longshore current} \\ \text{responsible for transport}}} = \frac{1}{2} m_2 \hat{u}^2 V + m_2 V^3 \tag{8.3}$$

Assuming the stirring due to the short-wave motion is dominant, the longshore transport is approximately proportional to $\left\langle s_y \right\rangle \propto \hat{u}^2 V$. This again reflects that the effect of short waves is to mobilise the material which is consequently transported by the longshore current. In Sect. 8.2.3, specifically in Intermezzo 8.1, we will see that commonly used bulk longshore transport formulas can be interpreted in a similar way.

8.2.2. Cross-shore distribution of longshore transport

The cross-shore distribution of longshore sediment transport is, of course, strongly determined by the cross-shore distribution of the longshore current. The longshore current distribution on a barred beach for different wave conditions (Fig. 5.42) is repeated in Fig. 8.1a. Furthermore, Fig. 8.1 shows the longshore transport rates as calculated with the longshore sediment transport model Unibest-CL+. Comparing the upper and

middle panel of Fig. 8.1a while keeping Eqs. 8.1 and 8.3 in mind, we may conclude that most of the sediment stirring takes place in a relatively narrow zone on the seaward flanks of the breaker bars, where most of the wave-breaking takes place. Also note the non-linear dependency of the transport on the velocity. Figure 8.1b demonstrates that the outcomes of uncalibrated transport formulas may differ substantially.

Bayram et al. (2001) analyse the cross-shore distribution of longshore sediment transport according to a few well-known predictive formulas and field measurements at Duck, North Carolina. Measured hydrodynamics were used as much as possible as input for the transport models. The transport models were used with standard coefficient values without further calibration. Figure 8.2 gives the result for one specific condition ($H_{rms} = 3.18\,\text{m}$, $T_p = 12.8\,\text{s}$) representative for a large transport on a barred sandy profile during a storm. The mean longshore current velocity in the surf zone was 0.6 m/s. The water depth at the most offshore measurement point was 8.6 m. The peak in the transport rate was observed some distance shoreward of the bar crest, whereas the formulas predicted the peak to occur more seaward (i.e., close to the bar crest).

For this specific run, most formulas overpredict the sediment transport. Furthermore, the differences between the various models are rather large. The formulas used differ particularly in the way the influence of the waves is taken into account. Besides, sensitivities to certain input parameters vary between the formulas. This could be seen from runs under different conditions that showed a different relative behaviour of the various formulas. Total transports between the various transport formulas can easily differ by up to a factor ten! This illustrates the need for calibration of the formulas before results from computer computations can be used in specific coastal engineering cases. The data used for calibration should be representative for the specific site and hydrodynamics conditions. Examples of such calibration data are observed coastline changes following a certain 'event' (such as the construction of a new harbour along a coastline, or the damming of a river and the subsequent erosion of the shoreline of the river delta).

8.2.3. Bulk longshore transport formulas

The general transport formulas, which were compared in the previous section, were developed from the early seventies onwards (Bijker was the first to include the effect of waves in a general transport formula, see Eq. 6.27). Before that time only bulk formulas were available. These bulk longshore transport formulas did not give the distribution over the surf zone, but only the total transport over the entire width of the littoral zone. Note however that, although general formulas may resolve the cross-shore distribution over the surf zone, they are not necessarily better in predicting bulk transport rates, considering the large uncertainties involved in transport computations. Clear advantages of bulk transport formulas are that they are robust and easy to calibrate and apply.

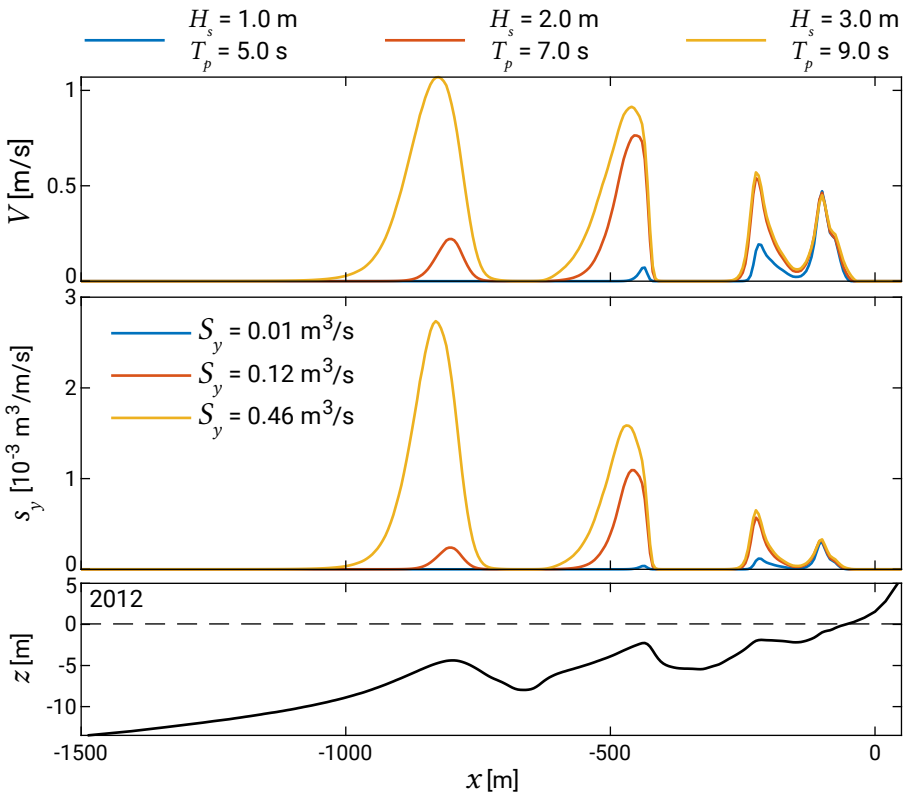

(a) longshore current velocity, sediment transport rates (with the Bijker transport formula in deposited volumes) and coastal profile using three different deep-water wave conditions: $H_s = 3\,\text{m}$ and $T_p = 9\,\text{s}$, $H_s = 2\,\text{m}$ and $T_p = 7\,\text{s}$ and $H_s = 1\,\text{m}$ and $T_p = 5\,\text{s}$ and $\varphi = 30°$ in deep water

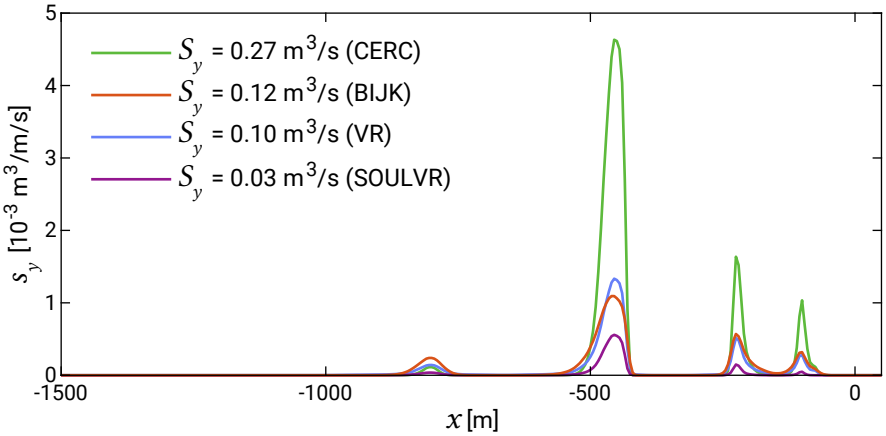

(b) sediment transport rates (deposited volumes) for $H_s = 2\,\text{m}$ and $T_p = 7\,\text{s}$ using four different transport formulas (CERC, Bijker (BIJK), Van Rijn (VR) and Soulsby Van Rijn (SOULVR)) with default settings (uncalibrated)

Figure 8.1: Example of model results (longshore current velocity $V(x)$, longshore transport rates $s_y(x)$ and transport integrated over the cross-shore S_y) computed with Unibest-CL+ (https://www.deltares.nl/en/software/unibest-cl) for a profile measured in 2012 near Egmond (transect 7003850 from JARKUS, n.d.) using $D_{50} = 200\,\mu\text{m}$ and $D_{90} = 300\,\mu\text{m}$. §1.1The cross-shore distribution of the CERC transport is determined by assuming that the transport is proportional to the third power of the longshore current velocity $V(x)^3$. [p366]

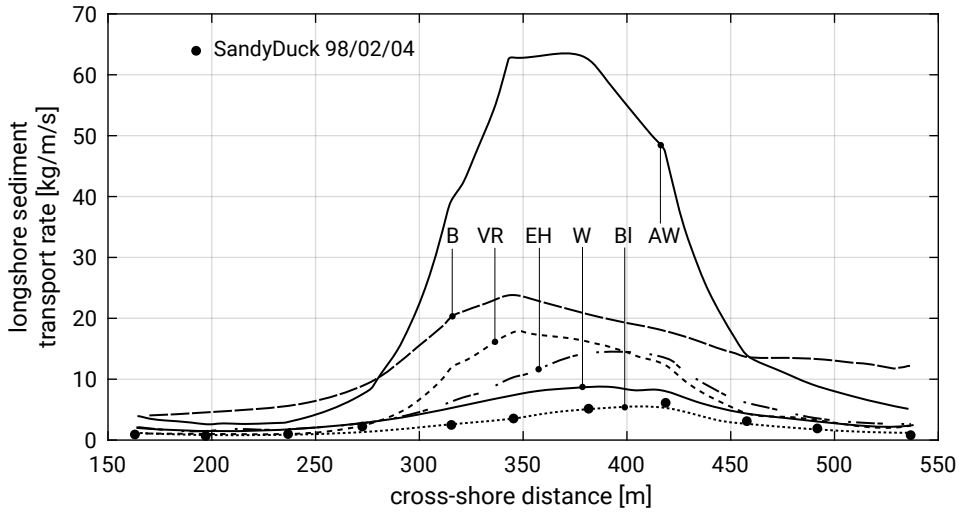

Figure 8.2: Comparison between calculated and measured cross-shore distribution of longshore sediment transport rate for one run of the SandyDuck experiment (98/02/04). Adapted from Bayram et al. (2001). The letters indicate different models, amongst them B: Bijker (Eq. 6.27), BI: Bailard-Inman (Sect. 6.7.2), VR: Van Rijn (Eq. 6.33 for suspended load plus separate bed load formula).

In this section, three bulk formulas are presented: 1) the Coastal Engineering Research Council (CERC) formula; 2) a formula according to Kamphuis (1991); and 3) a formula according to Bayram et al. (2007).

The CERC formula

Although one of the oldest longshore transport formulas, the CERC formula is still widely used. It was developed by the Coastal Engineering Research Council (CERC) of the American Society of Civil Engineers (ASCE). The development of this formula took place in the late 1940s, well before longshore current theory was developed. The formula was calibrated using a large number of prototype and laboratory measurements.

The CERC formula gives the bulk longshore sediment transport – the total longshore sediment transport over the breaker zone – due to the action of waves approaching the coast at an angle. Hence, only the effect of the wave-generated longshore currents is included; tidal currents or other alongshore currents are not considered. If the longshore current is exclusively driven by waves, one can imagine that both the sediment concentration and longshore current velocity can be related in some way to the incident wave conditions. This is reflected in the CERC formula which reads in its most general form:

$$S = \frac{I}{\rho g(s-1)(1-p)} = \frac{K}{\rho g(s-1)(1-p)}(Enc)_b \cos\varphi_b \sin\varphi_b \tag{8.4}$$

where:

I	the immersed (underwater) weight of sediment transported, cf. Eq. 6.17	N/s
S	the deposited volume of sediment transported	m^3/s
ρ	density of the water	kg/m^3
s	the relative density of the sediment ρ_s/ρ	–
p	porosity	–
g	gravitational acceleration	m/s^2
K	coefficient	–
E	wave energy	J/m^2
c	the wave phase velocity	m/s
n	the ratio between group and phase velocity	–
φ	the wave angle of incidence	–
b	subscript referring to conditions determined at the outer edge of the breaker zone	–

Equation 8.4 is a dimensionally correct form of the CERC formula as presented by Komar and Inman (1970). The original CERC formula had a dimensional coefficient (such that the coefficient was dependent on the units used) and was formulated in terms of US Customary Units. The Komar and Inman form does not have this problem.

According to Eq. 8.4 the bulk longshore sediment transport rate S is a function of the product of the energy flux $(Enc)_b$ at the point of breaking (see also Eq. 5.4) and $\cos\varphi_b \sin\varphi_b$. This term $P = (Enc)_b \cos\varphi_b \sin\varphi_b$ was named 'longshore component of wave power' and its physical interpretation has been the topic of many discussions over the years. It was not until 1972 – years after the original presentation of the CERC value – that Longuet-Higgins related P to the then new concept of radiation stresses (Sect. 5.5.2). From Eq. 5.53c and Fig. 5.30 it becomes clear that P is the shear component of the radiation stress at the breaker point, multiplied by c at the breaker point: $P = S_{yx,b}c_b$. We know that the cross-shore gradient in radiation shear stress is responsible for driving the longshore current (Eq. 5.72). The radiation shear stress at the point of breaking can therefore be seen as this driving force integrated over the surf zone. But that still does not explain how the product of $S_{yx,b}$ and c_b should be interpreted. The CERC formula was probably rather intuitively derived. Inman and Bagnold (1963) derived a bulk longshore transport formula in a more fundamental way, namely based on an energetics approach, and found a formula similar in form to the CERC equation. This is demonstrated in Intermezzo 8.1.

Often the CERC equation is rewritten in terms of wave height parameters by substituting $E = \frac{1}{8}\rho g H_b^2$. Shallow-water wave-breaking is assumed, such that n_b can be taken equal to 1 and $^{\S1.1}e^{\S1.1}c_b \approx \sqrt{gh_b}$ [p368] in which h_b is replaced with H_b/γ. For the breaker index $^{\S1.1}\gamma$ [p368], a value of 0.78 is often assumed. (Sect. 5.2.5). Using

the double-angle formula $2\cos\varphi_b \sin\varphi_b = \sin 2\varphi_b$, the CERC formula Eq. 8.4 can be expressed as:

$$S = \frac{K}{16(s-1)(1-p)}\sqrt{\frac{g}{\gamma}}\sin 2\varphi_b H_b^{2.5} \tag{8.5}$$

For irregular waves, the value of the coefficient K depends on whether, for the wave height at breaking H_b, the root-mean-square wave height H_{rms} or the significant wave height H_s is used. A value of $K_{\text{for } H_{rms}} = 0.77$ was derived from a field study by Komar and Inman (1970) corresponding to H_{rms}. This is the value commonly seen in longshore transport rate computations. In the Shore Protection Manual §1.1(now CEM) [p369], the US Army Corps of Engineers mentions a value of $K_{\text{for } H_{rms}} = 0.92$. In more recent studies, Schoonees and Theron (1993, 1996) suggested a significantly lower value of the coefficient, namely about 0.5, based on a re-examination of available field data. For a specific project, it is best to determine the coefficient by calibration. Engineers often prefer to use, for H_b, the significant wave height H_s at breaking. In that case the value of the coefficient $K_{\text{for } H_s}$ is smaller, viz. $K_{\text{for } H_s} = \left(\frac{1}{\sqrt{2}}\right)^{5/2} K_{\text{for } H_{rms}} \approx 0.4 K_{\text{for } H_{rms}}$ (since for a Rayleigh distribution: $H_s = \sqrt{2}H_{rms}$, see Table 3.1).

Intermezzo 8.1
Bulk longshore transport based on the energetics approach

Inman and Bagnold (1963) applied the energetics concept of Bagnold (1963), as explained in Sect. 6.7.2, to the littoral zone. In the surf zone, the wave oscillatory motion, with angle of incidence φ, is thought to set an amount of sediment into motion without resulting in a net transport. The sediment supported by the wave action (with a total immersed weight W) is passively advected with a representative longshore current velocity V, such that the bulk immersed weight longshore transport rate is given by $I = WV$.

Per unit crest width, the wave power (rate of transport of energy) that is available for dissipation in the entire surf zone is equal to $(Ec_g)_b$, see Eq. 5.3, with b referring to the values at the breaker line. The crucial assumption now is that a proportion ε of the wave power is dissipated by means of bottom friction and used in transporting sediment as bed load. The mean frictional force applied to the whole of the sediment bed per unit crest width is proportional to $(Ec_g)_b/\hat{u}_b$, where $\hat{u}_b$ is mean frictional velocity relative to the bed within the surf zone and is assumed to be proportional to the orbital velocity near the bottom just before wave-breaking. Per unit shoreline, the frictional force is proportional to $(Ec_g)_b \cos\varphi_b/\hat{u}_b$.

The frictional resistance of the sediment is equal to μW, in which the friction coefficient $\mu = \tan\varphi_r$ is the tangent of the internal angle of repose indicated by φ_r.

Equating the frictional force on the bed and the resisting force leads to $W = \varepsilon(Ec_g)_b \cos\varphi_b/(\mu\hat{u}_b)$. Hence, according to Inman and Bagnold:

$$I = WV = \varepsilon \times \frac{\left(Ec_g\right)_b \cos\varphi_b}{\mu\hat{u}_b} V \tag{8.6}$$

Let us now rewrite the analytical result for the longshore current velocity (Eqs. 5.82 and 5.83) using the shallow-water approximation Eq. 5.23 for the orbital velocity. This gives for the maximum longshore current velocity at the breaker line (a representative longshore current velocity V at a mid-surf zone location would have half this maximum value):

$$V_b = \frac{5}{8}\pi \frac{\tan\beta}{c_f} \hat{u}_b \sin\varphi_b \tag{8.7}$$

Substitution in Eq. 8.6 yields:

$$I = \text{ constant } \times \frac{\tan\beta}{c_f \mu} (Enc)_b \cos\varphi_b \sin\varphi_b \tag{8.8}$$

Neglecting dependencies on the beach slope and the physical properties of the sand yields:

$$I = \text{ constant } \times (Enc)_b \cos\varphi_b \sin\varphi_b \tag{8.9}$$

This is identical in form to the CERC equation Eq. 8.4. We have however not been totally consistent, since in the derivation of Eq. 8.7 we assumed $\cos\varphi_b \approx 1$.

Equation 8.5 is a very practical form of the CERC equation. It shows that, *as long as the other parameters are constant*, the transport magnitude increases with increasing wave angle at the breaker point until a maximum is reached at $\varphi_b = \pm 45°$ (in practice §1.1 φ_b [p370] will be in the range $-20°$ to $20°$ due to refraction). Interesting is also that the longshore transport is proportional to the wave height to the power of 2.5. This can be interpreted, using Intermezzo 8.1, as a sediment load proportional to E_b and hence to H_b^2, that is transported with a velocity proportional to $\hat{u} = \frac{1}{2}\sqrt{g\gamma H_b}$ and hence to $\sqrt{H_b}$. The breaking parameter is often taken as a constant (0.78). However, from Sect. 5.2.5 it is known that the breaking parameter increases with increasing Iribarren parameter (Eq. 5.20), hence with increasing relative steepness of the slope. A larger relative bottom slope (larger bottom slope or longer wave) would therefore slightly decrease the sediment transport, at least according to the CERC formula. This is, however, only a

weak dependence in the CERC equation, and for all practical purposes one may consider the formula to be independent of wave period or bottom slope.

In some applications it is more practical to use deep-water wave parameters in the equations. The conversion to deep-water parameters is quite straightforward, when using an important finding of Sect. 5.5.5. There, it was explained that if the water depth contours in the area are all parallel, S_{yx} does not vary outside the breaker zone. Hence: $P = S_{yx,b}c_b = S_{yx,0}c_b$. We can thus evaluate S_{yx} using deep-water wave characteristics, which means that all wave parameters can be taken as deep-water parameters, except c_b. Remember that in deep water we need to take $n_0 = \frac{1}{2}$. This yields for straight, parallel depth contours:

$$S = \frac{K}{32(s-1)(1-p)} c_b \sin 2\varphi_0 H_0^2 \tag{8.10}$$

There are many equivalent forms of the CERC equation and all have at least one wave parameter at the breaker line. Due to the different representations, any application of the CERC formula must be made carefully (like, of course, all sediment transport formulas). This holds in particular for the value of the coefficient, the choice of H_{rms} or H_s and the choice between deep-water wave parameters and parameters at the breaker line.

Limitations of the CERC formula

Due to its simplicity the CERC formula can be helpful in understanding and solving many practical problems. However, the simplicity of the CERC formula has the following limitations (some of which have already been mentioned):

1. *Only the wave-induced longshore current is taken into account;* all other alongshore current driving forces, such as tidal currents, are ignored. In order to take the latter into account, more general transport formulas need to be applied. In a formula of the form Eq. 8.6, in principle, also tidal and wind-driven alongshore currents could be used;
2. *The sand transport is independent of sand properties such as grain size.* Also, the beach slope and hence the type of breakers is ignored (although the breaker index may be assumed to be dependent on the breaker type). Eq. 8.8 already suggested a dependency on beach slope and grain properties. To include these variables, the formula of Kamphuis (below) can be used;
3. *Only the total sediment transport in the breaker zone is given.* It is often of practical importance to know how this transport is distributed over the width of the breaker zone, for instance if bars are present in the coastal profile, or if coastal structures are considered that do not entirely cover the breaker zone (such as groynes: see Ch. 10). However, this distribution could be estimated from a distribution for the longshore current velocity and wave-stirring capacity. [§1.1]For example, Unibest-CL+ determines the cross-shore distribution of

the CERC transport by assuming that the transport is proportional to the third power of the longshore current velocity $V(x)^3$. This procedure is followed for the CERC transport in Figs. 8.1b and 8.5b. [p372]

Grain size and beach slope

Dean et al. (1982) suggested that the coefficient K in Eq. 8.5 should be dependent on the grain size, see Fig. 8.3.

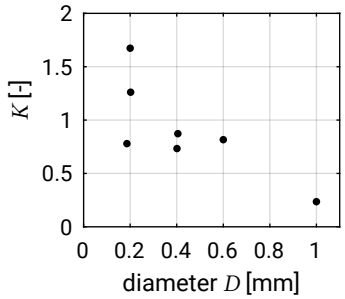

Figure 8.3: Variation in K with grain size (denoted by D) according to Dean et al. (1982). Note that the dependency of K on D is convincing only for larger grain sizes.

Such a relation is not unexpected since the CERC formula only has the wave characteristics and one can expect the sediment transport to depend on the sediment properties too, with larger transport for smaller grain sizes. It is often believed that the transport should be inversely proportional to the grain size to a power of about three, hence $S = f(D^{-3})$. The CERC formula was originally derived for beaches with uniform sand ranging between 175 §1.1 ~~m~~ §1.1 µm to 1000 §1.1 ~~m~~ §1.1 µm [p372] and thus represents an average over this range of conditions.

Kamphuis (1991) made an analysis of field and lab data and suggested an alternative bulk longshore transport formula that includes the effects of not only grain size but beach slope and wave steepness as well.

His formula for the immersed mass of transported sediment $I_m = \rho(s-1)(1-p)S$ (see Eq. 6.17) reads:

$$I_m = 2.27 H_{s,b}^2 T_p^{1.5} \left(\tan\alpha_b\right)^{0.75} D^{-0.25} \left(\sin 2\varphi_b\right)^{0.6} \tag{8.11}$$

with $\tan\alpha_b$ the beach slope at the breaker point.

The wave period, grain size and beach slope (absent in the CERC equations) now influence the longshore transport rate. Note that the dependency on the wave angle

seems relatively weak, compared to the CERC formula. The grain size proportionality with $D^{-0.25}$ also seems rather weak. However, it should be noted that the variables in the empirically derived Eq. 8.11 are interdependent. For example: given constant hydraulic conditions, coarser beach materials tend to form steeper slopes[1]; gravel beaches are far steeper than sand beaches. On the other hand, if the beach material is of a given diameter, then higher waves tend to result in flatter beach slopes. Similarly, the wave parameters T_p, φ_b and $H_{s,b}$ are interrelated.

Recent bulk longshore transport formula

Bayram et al. (2007) presented a new bulk formula based on the energetics concept, similar to Inman and Bagnold's model in Intermezzo 8.1. By assuming that the dissipated fluid power maintaining the sediment load is dissipated by bottom friction, Inman and Bagnold considered bed load sediment transport. By contrast, Bayram et al. assume that *suspended* sediment transport is the dominant mode of transport in the surf zone, as a result of turbulence induced by breaking waves. They assume that the dissipated fluid power per unit shore length used in suspending sediment is $\varepsilon \left(Ec_g\right)_b \cos\varphi_b$ (similar to Intermezzo 8.1). In contrast with Intermezzo 8.1, the work done (per unit time), in maintaining the suspended load at a certain level, is the product of W times the fall velocity w_s. Hence: $W = \varepsilon \left(Ec_g\right)_b \cos\varphi_b / w_s$.

Instead of Eq. 8.6 we now get:

$$I = WV = \frac{\varepsilon \left(Ec_g\right)_b \cos\varphi_b}{w_s} V \tag{8.12}$$

For V an analytical solution is used for the mean longshore current velocity that is derived using a Bruun-Dean's equilibrium profile (Eq. 7.1) instead of a constant bed slope. Based on comparison with field and laboratory data, Bayram et al. (2007) conclude that the predictive capability of their formula is higher than of the CERC, Inman-Bagnold and Kamphuis formulas. A recent attempt to improve the accuracies of these bulk longshore transport formulas is Mil-Homens et al. (2013).

8.2.4. The (S,φ)-curve

According to Eq. 8.5, bulk longshore sediment transport S is proportional to $H_{s,b}^{2.5} \sin 2\varphi_b$. The power 2.5 was explained in Intermezzo 8.1 as a sediment load proportional to $H_{s,b}^2$ transported by a wave-induced longshore current velocity proportional to $\sqrt{H_{s,b}}$. Both $H_{s,b}$ and φ_b depend on the offshore wave height, wave period and angle of incidence φ_0.

[1] Kamphuis (2000) mentions this as the probable reason for the absence of the grain size and beach slope dependency in the CERC formula. In addition, for grain sizes in the order of 200 µm, the grain size dependency is not so clear according to Fig. 8.3.

The angle of incidence is relative to the local depth contours, which, in the nearshore zone, are often approximately parallel to the shoreline. Given a relatively constant wave climate along a stretch of coast, alongshore variations in coastline orientation cause gradients in longshore sediment transport and hence cause the coastline orientation to change over time. The relationship between sediment transport S and angle of wave incidence φ is therefore a central concept in shoreline modelling (see also Sect. 8.3). In order to examine the effect of the angle of incidence on longshore sediment transport, we consider the situation of straight depth contour lines parallel to the shoreline and compute the sediment transport rate S from Eq. 8.10 for a constant offshore wave height and period and for a range of angles of attack $^{\S 1.1}\varphi_0$ [p374] (Example 8.1).

Example 8.1
Bulk longshore sediment transport rate S for different values of φ_0

Input parameters

Offshore wave height:	$H_{rms,0} = 2\,\mathrm{m}$
Wave period:	$T = 7\,\mathrm{s}$

Required Longshore sediment transport rate S for different values of φ_0

Method We consider the simple situation of straight depth contour lines parallel to the shoreline. In that case we can use the relation between S and the deep-water wave angle φ_0 (Eq. 8.10). For H_0 we use the deep-water root-mean-square wave height $H_{rms,0}$ and a corresponding value for K of $K_{rms} \approx 0.7$. With a value for the porosity $p = 0.4$ and the relative density $s = 2.65$, this equation can be written as:

$$S \approx 0.02 c_b H_{rms,0}^2 \sin 2\varphi_0 \tag{8.13}$$

We compute h_b as $H_{rms,b}/\gamma$ with $\gamma = 0.8$. This is a rather large value for the breaker index based on H_{rms}, but consistent with the determination of the coefficient value for K.

First choose φ_0. Then calculate c_b using for instance Table A.3 (alternatively, the dispersion relation can be solved using a small computer routine or an explicit approximation). The computation of h_b requires an iteration (choose h_b, calculate $H_{rms,b}$ according to Table A.3, check whether $H_{rms,b}/h_b = \gamma$; if not, choose new h_b, repeat process). The sediment transport rate can now be computed using Eq. 8.13. The results can be found in Table 8.1 and Fig. 8.4.

Table 8.1: Bulk longshore transport rates as a function of the deep-water wave angle §1.1 φ_0. §1.1 ~~In bold: the angle for which the maximum transport is found~~ §1.1 The maximum transport is found for $\varphi_0 = 43°$ [p375]. Note that $H_b = \gamma h_b$.

φ_0 [°]	h_b [m]	φ_b [°]	c_b [m/s]	S [m^3/s]
5	2.72	2.27	4.97	0.069
10	2.71	4.52	4.96	0.136
15	2.69	6.73	4.95	0.198
20	2.66	8.87	4.93	0.253
25	2.63	10.91	4.90	0.300
30	2.59	12.85	4.86	0.337
35	2.54	14.64	4.82	0.362
40	2.48	16.26	4.76	0.375
43	2.42	17.14	4.72	0.377
45	2.40	17.68	4.69	0.376
50	2.31	18.87	4.61	0.364
55	2.21	19.79	4.52	0.340
60	2.09	20.42	4.40	0.305
65	1.95	20.69	4.26	0.261
70	1.79	20.58	4.09	0.210
75	1.59	19.99	3.87	0.155
80	1.35	18.77	3.57	0.098
85	1.01	16.46	3.11	0.043

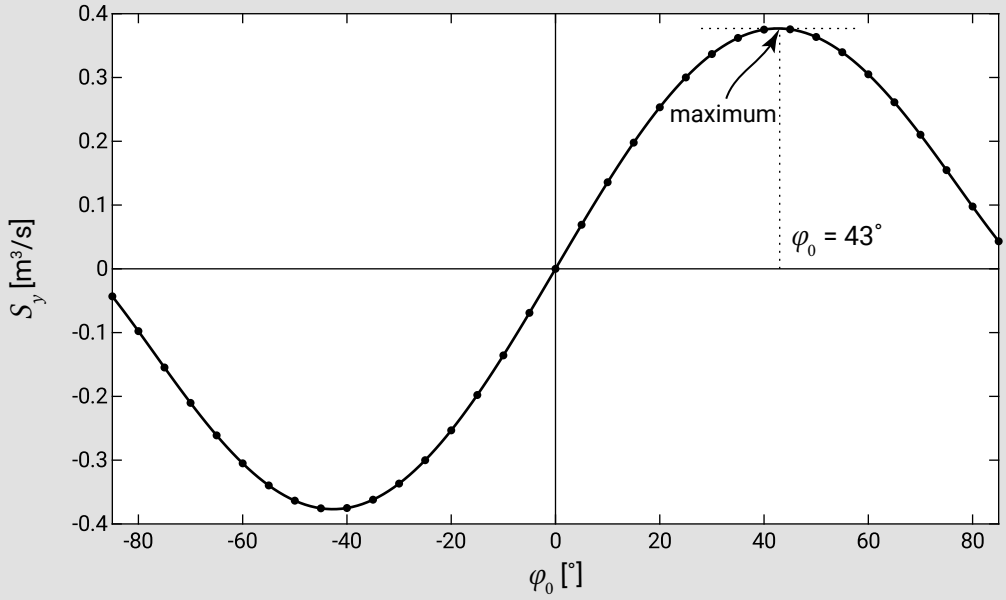

Figure 8.4: Bulk longshore transport rates S as a function of the deep-water wave angle φ_0. The dotted line indicates $\varphi_0 = 43°$. The maximum transport occurs for deep-water wave angles somewhat smaller than 45° (43° in this case). The angle φ is positive for a transport S in the direction of a positive alongshore coordinate axis and vice versa.

Figure 8.4 shows the longshore sediment transport against the wave angle in deep water. This is a so-called (S, φ)-curve; it gives the transport as a function of the wave angle for a given set of wave conditions. The (S, φ)-curve indicates that the maximum longshore transport occurs for an angle somewhat smaller than $\varphi_0 = 45°$. The term $\sin(2\varphi_0)$ in Eq. 8.10 suggests a maximum of S at exactly $\varphi_0 = 45°$. However, the wave propagation speed at the breaker line (as a function of the local depth) also depends on the deep-water wave angle, as it depends on the wave refraction from deep water to the breaker line: for larger values of φ_0, wave-breaking takes place at smaller water depths, reducing c_b (Sect. 5.2.3). This slightly affects the angle at which the maximum occurs. The longshore transport reduces to zero if φ_0 goes to 0° or 90°. An angle $\varphi_0 = 0°$ implies normally incident waves at the breaker line and hence only wave stirring and no longshore current. Note that for small angles, φ_0 up to approximately 20° to 30°, the longshore transport varies almost linearly with the wave angle. Table 8.1 furthermore shows that, due to refraction, the angle of incidence at the breaker line is smaller than about 20° for all values of φ_0.

8.2.5. Yearly-averaged sediment transport

In Sect. 8.2.4, we discussed the longshore transport rate for a single wave state (represented by its root-mean-square wave height and wave period) and examined the effect of the angle of incidence on the transport rates. The maximum computed transport rate (for a deep-water wave angle of 43°) amounts to 0.38 m^3/s. In the (unrealistic) situation that this wave condition is present all year round, we would find a net longshore transport of the order 10×10^6 m^3 per year.

In order to obtain a realistic estimate of the long-term average annual longshore sediment transport rate, we need to take the variability of the wave climate into account. Wave heights, periods and angles are weather-dependent. Different wave heights and periods result in different transport magnitudes. Changes in the wave angle may lead to transports that not only have different magnitudes, but opposite directions as well.

The wave climate variability can be taken into account by schematization of the wave climate in several classes (see Sect. 3.6). This requires that the wave climate is divided into sectors of for instance 30°, 0.5 s $T_p$and 0.5 m H_s with a certain percentage of occurrence. For morphological computations, such a full wave climate is then often reduced to a limited number of wave conditions. For the §1.1reduced wave §1.1climate [p376] to be representative of the full climate, it must reflect the dominant wave directions and also represent a morphological criterion of interest. Such a criterion could for instance be that the net longshore sediment transport at some coastal sections for the reduced climate must be identical to the net transport rate for the full climate. A reduced wave climate typically has 10 conditions, but sometimes a single representative wave condition is chosen that reproduces the net longshore transport rate of the full

climate. The net longshore transport rate is defined as the residual transport rate as a result of all conditions and is generally much smaller than the gross longshore transport rates up and down the coast. Of course, for a single wave condition, the gross and net longshore transport rates are identical.

As an example we consider the wave climate for the Dutch coast, which is characterised by relatively short-period waves (of about 5 s). Waves offshore exceed 2 m approximately 10 % of the time and 3 m approximately 2 % of the time. Most waves arrive arrive from directions between southwest and northwest, so that the average wave incidence is almost normal to the coast. The highest waves come from the northwest direction, because of the longer fetches in this sector. Swell is also predominantly from the northwest direction. The orientation of the central Dutch coast is approximately N-S (e.g. 7°N at Egmond, or 277°N for the shore-normal direction, and 15°N at IJmuiden). Along this coast, storms arriving from the northwest generate longshore currents and a southwards longshore transport. Conversely, waves from the southwest result in a northward-directed transport.

Figure 8.5 shows the cross-shore distribution of the longshore transport around Noordwijk according to model computations with Unibest-CL+. A distinction is made between northward and southward transport. For engineering purposes, we are interested in the gross transport rates as well as in the *net* transport rate (which is directed northward for most of the central Dutch coast).

Gradients in net transport rates determine the long-term evolution of a stretch of coast. Gross transport rates are important to determine the coastal response near breakwaters and groynes. This is because these structures provide shadow zones on either side for part of the wave conditions (see Sect. 8.4.2). Especially when the *gross* longshore transport rates along a coast are quite similar in magnitude, the magnitude (and direction!) of the *net* longshore transport is very difficult to determine with sufficient accuracy. This is because two large and inaccurate numbers are subtracted. Note further that net longshore transport rates (per metre width) are generally much higher than net cross-shore transport rates (per metre width).

A strongly reduced wave climate for the Dutch coast, taking into account the two dominant directions, may for instance consist of the following two wave conditions:

1. From southwesterly directions (say 225°N), occurring 20 % of the time and with $H_s = 1.7$ m and $T_p = 5$ s;
2. From northwesterly directions (say 315°N), occurring 8 % of the time and with $H_s = 1.8$ m, $T_p = 6$ s.

For a coastline orientation of about 15°N and hence a shore-normal of 285°N (IJmuiden), this means angles of wave incidence in deep water of 60° and −30° for condition 1 and 2 respectively. This would yield (using Eq. 8.13 as in Example 8.1) a net northward directed sediment transport of 250 000 m^3/yr as a result of:

1. Northward transport of ±530 000 m^3/yr;

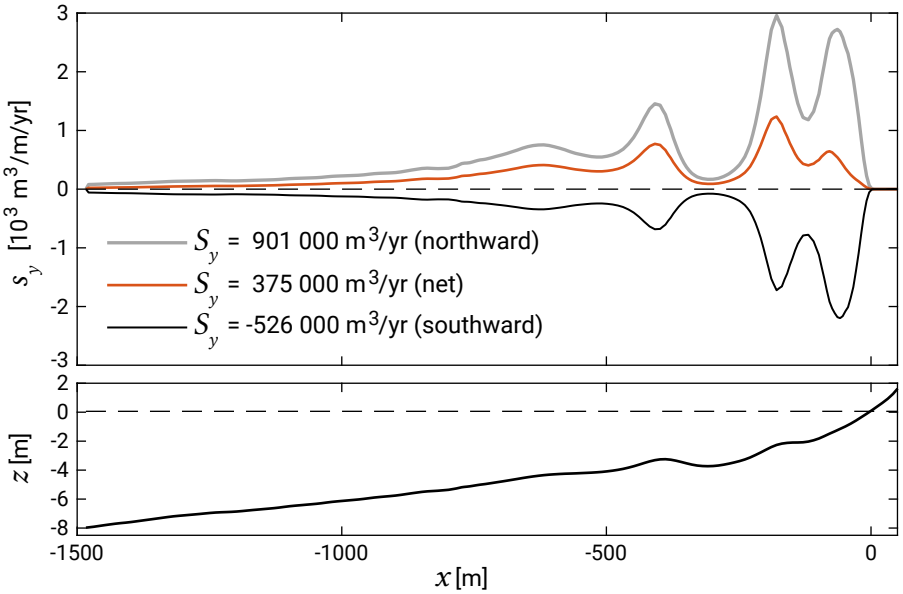

(a) net transport rates $s_y(x)$ and S_y (integrated over the cross-shore) using the Bijker transport formula and separated into gross (northward and southward) components

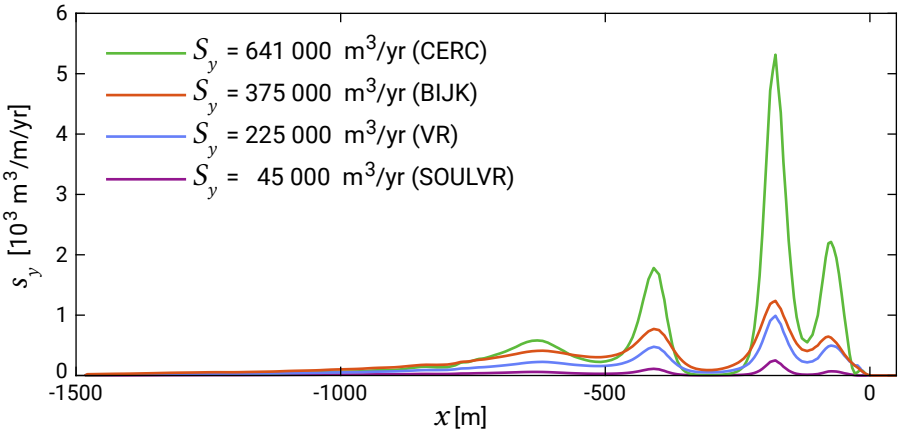

(b) net transport rates $s_y(x)$ and S_y (integrated over the cross-shore) using the transport formulas according to CERC, Bijker (BIJK), Van Rijn (VR) and Soulsby Van Rijn (SOULVR) without calibration (i.e. default settings are used)

Figure 8.5: Cross-shore distribution of longshore transport at Noordwijk according to model computations with Unibest-CL+ (https://www.deltares.nl/en/software/unibest-cl) using a yearly wave climate from a wave look-up table developed by Deltares for the Building with Nature project HK 3.2. §1.1 The cross-shore distribution of the CERC transport is determined by assuming that the transport is proportional to the third power of the longshore current velocity $V(x)^3$. [p378]

2. Southward transport of $\pm 280\,000\ \mathrm{m}^3/\mathrm{yr}$.

Note that we have chosen the two conditions such that: 1) they reflect the prevailing wave conditions; and 2) the net transport magnitude and direction correspond with estimates based on sediment balance considerations. As a reference: the net yearly transport in the central part of the Dutch coast (from Wassenaar to Zandvoort) is thought

to be around 200 000 m^3/yr northwards. We could further finetune our wave conditions to arrive at the figure of 200 000 m^3/yr rather than 250 000 m^3/yr. This is the process of defining a morphologically representative reduced wave climate. Note that in practice we would generally take more conditions into account.

8.3. Calculation of coastline position

8.3.1. Introduction

On high-energy coasts, long-term (years to decades) shoreline changes are predominantly due to human-induced longshore effects. Cross-shore movement of sediment typically occurs on short timescales (days) and has little direct influence on the longer-term changes in beach position, unless material is permanently lost from or introduced to the system. Possible sediment sinks are offshore canyons from where any deposited sediment cannot return, the hinterland (through aeolian transport) or sand mining from the beaches (for instance for construction purposes). Examples of sediment sources are dredge disposal or sediment input from rivers. Often however, longshore effects are the most important cause of shoreline changes on the longer timescales. Coastal change due to longshore processes will be the focus in the following.

> Please note that the coastline is aligned with the x-axis in the remainder of this chapter. This is different from the other parts of this book.

The long-term coastline changes are governed by net, yearly-averaged longshore sediment transport rates, averaged over several wave conditions with varying magnitudes and directions. In computations these are taken into account by a schematised wave climate with a limited number of conditions (as discussed in Sect. 8.2.5). The very presence of sediment transport does not lead to either erosion or deposition. Indeed, if one considers a portion of beach as sketched in plan in Fig. 8.6, the coastline will remain stable as long as S_{in} is equal to S_{out}. On the other hand, if S_{out} is greater than S_{in} (S increases as we move along the beach, $\frac{dS}{dx} > 0$, or sediment transport divergence), material must be eroded in the area under consideration in order to maintain a sediment mass balance. The coastal profile, including the shoreline, will recede. The shoreline will move seawards (accretion) if the longshore sediment transport decreases in the transport direction ($\frac{dS}{dx} < 0$ or sediment transport convergence). [§1.1]A sediment mass balance relates morphological changes to sediment transport gradients, and to sediment sinks and sources, see e.g. Eq. 1.1 [p379].

There are different ways to solve coastal changes from a sediment balance (Eq. 1.1):

- In complex morphological computer models (such as Delft3D), the sediment balance is computed for each cell in a fine grid that covers the area of interest. At every time step, a field of sediment transport rates is computed, based on the relevant hydrodynamic parameters. Subsequently, the bed levels are updated for

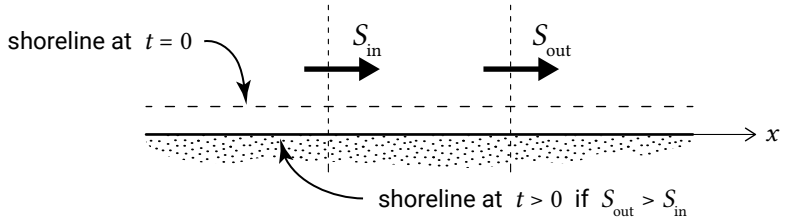

Figure 8.6: Longshore transport continuity.[§1.1] [Annotation for dotted line changed to 'shoreline at t = 0'] [p379]

every grid[§1.1] cell, [p380] based on sediment continuity. Such detailed morphological models are generally used in complex areas or in complex applications in which cross-shore and longshore transports are important. They are relatively expensive to run and it is complex to interpret the computational results. At Delft University of Technology, students will be taught to use these models in Coastal Dynamics II (CIE4309);

- If wave-induced longshore transport is the dominant mechanism, we can simplify the problem. The coarsest schematization is made by the *single-line* or *one-line* theory, in which the behaviour of the coast is mapped onto a single line, the coastline. In this approach it is assumed that the shape of the coastal profile itself does not change over the considered period of time or along the coast. The coast can thus be schematised as one single line, which moves seaward (accretion) or landward (erosion), depending on the sediment balance. This is what we (implicitly) assumed in Fig. 8.6. The single-line theory is discussed in Sect. 8.3.2 and analytical solutions in Sect. 8.3.3. It gives a valuable insight into the principles of coastline dynamics;
- Multiple (two and more) line theories (Sect. 8.3.4) are based on the same principle, but now the coastal (cross-shore) profile is schematized into a number of sections (depth zones), which can each be represented by one line in the alongshore direction. This is a method to account for the fact that different depth zones respond differently to changing sediment budgets.

8.3.2. Single-line theory

Beach profile schematization

The basic assumption is that the shape of the cross-shore profile does not change in time, which implies an equilibrium profile of arbitrary shape. As the coast erodes or accretes, the entire profile moves seaward or landward with a horizontal distance a. Figure 8.7 shows that this assumption also requires the assumption that there is a more or less horizontal part in the underwater profile; otherwise, unrealisticly large quantities of sand would be required for a small seaward movement of the shoreline.

In practical applications, the closure depth (see Sects. 1.5.1 and 7.2.3) is taken as the lower limit of the coastal profile. Depth changes seaward of this closure depth are

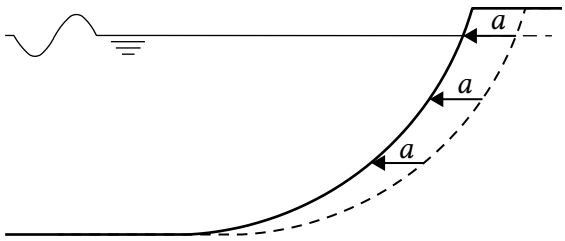

Figure 8.7: Beach profile schematization in single line or one-line theory.

assumed to not directly contribute to shoreline dynamics. The closure depth is governed by the highest waves that may occur in a certain period of time (normally several years). For the Holland coast (the central Dutch coast) the order of magnitude of the closure depth is MSL−6 m to MSL−12 m.

The upper limit of the coastal profile that needs to be taken into account depends – on shorter timescales – on whether the coast is eroding or not. For an eroding coast, the upper limit should be the dune height, allowing volume changes of the dunes. In the case of accretion, the upper limit is determined by the representative wave run-up added to the high-water level. (It is thus assumed that the build-up of dunes by aeolian transport is a very slow process). This is usually about 1 m to 3 m above MSL. In the discussion below, we simply assume that the active profile has a height d.

The wave characteristics in the assumed horizontal part are needed to compute changes in the schematised beach. Note that these characteristics are not necessarily equal to the deep-water characteristics.

Governing equations

Consider a stretch of a beach that is changing – either eroding or accreting. The x-axis is roughly parallel to the coastline, the y-axis is normal to the coast, see Fig. 8.8. The position of the coastline is at $y = Y$.

If during a short time interval Δt the shoreline moves forward with ΔY, the amount of accumulated volume over a distance Δx is:

$$\Delta x \Delta Y d \tag{8.14}$$

The net volume of sediment entering the segment with length Δx during time Δt is:

$$-\frac{\partial S}{\partial x}\Delta x \Delta t \tag{8.15}$$

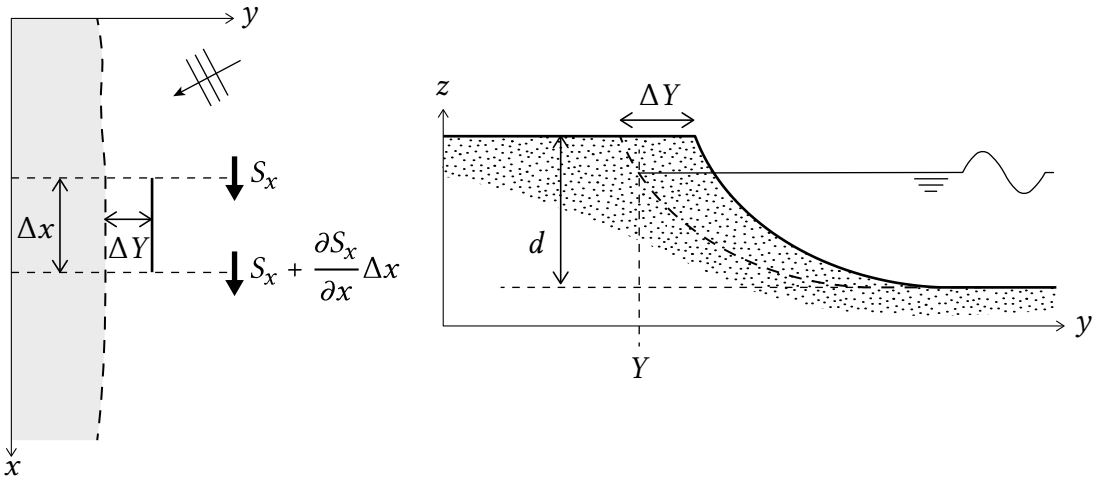

Figure 8.8: Longshore transport S_x and coastal change ΔY in a coastline model.

Equating the accumulation of sediment and the net inflow of sediment yields the following continuity equation:

$$\frac{\partial Y}{\partial t} + \frac{1}{d}\frac{\partial S_x}{\partial x} = 0 \tag{8.16}$$

In Sect. 8.2.3 we have seen that the angle of wave attack relative to the coastline φ [p382] is an important variable in determining the sediment transport S_x. Via the chain rule we can therefore write Eq. 8.16 as:

$$\frac{\partial Y}{\partial t} + \frac{1}{d}\frac{\partial S_x}{\partial x}\frac{\partial \varphi}{\partial x} = 0 \text{[p382]} \tag{8.17}$$

The term $\partial S_x/\partial\varphi$ follows from any longshore transport formula that we choose to use. In Sect. 8.3.3 we will do this analytically, by assuming that the sediment transport is a linear function of the angle of incidence. With a more complicated sediment transport formula, we can empirically determine $\partial S_x/\partial\varphi$ by varying the angle slightly in the formula and calculating the transport rates. The term $\partial\varphi/\partial x$ is directly related to the shoreline position that we are trying to solve for. This can be understood from Fig. 8.9, where an originally straight coastline is shown together with the coastline after some time.

The shoreline has rotated with an angle $\partial Y/\partial x$. This directly implies a reduction of the angle of wave attack φ with $\partial Y/\partial x$, since the wave angle is relative to the coastline. Hence, $\varphi = \varphi' - \partial Y/\partial x$ and $\partial\varphi = -\partial Y/\partial x$. Substituting this in Eq. 8.17 gives:

$$\frac{\partial Y}{\partial t} - \frac{1}{d}\frac{\partial S_x}{\partial \varphi}\frac{\partial^2 Y}{\partial x^2} = 0 \tag{8.18}$$

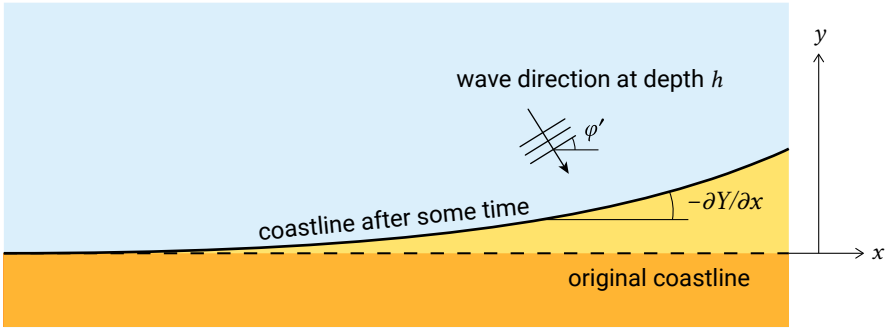

Figure 8.9: Shoreline position Y in original position and after some time. In this figure §1.1φ' [p382] is the original angle of wave incidence. After the change in shoreline orientation, this angle has been reduced with $\partial Y/\partial x$.

Equation 8.18 is a parabolic partial differential equation for the coastline position Y and must generally be solved numerically. This equation is solved in coastline development models (such as Unibest-CL+ or Genesis, see Szmytkiewicz et al. (2000)). In this equation the angle φ is the *angle of incidence at the closure depth.*

In Sect. 8.2.4, the (S, φ)-curve was introduced. We determined this curve by changing the angle of wave attack relative to a fixed coast. Since φ is the angle of wave attack relative to the coastline, we could just as well determine the curve by changing the coastline orientation relative to the waves, which is what is done in coastline modelling. The longshore sediment transport rate as a function of the changes in coastline orientation must be determined for the stretch of coast and the wave climate under consideration. This is done by calculating the longshore transport rates for the initial coastline orientation. Subsequently, the coastline orientation is changed a little bit and the longshore transport calculation is carried out again for the entire wave climate. This is equivalent to constructing a (S, φ)-curve. An example of such a procedure is given in Intermezzo 8.2.

Intermezzo 8.2 Transport curve as computed in a coastline model

A transport curve in a coastline model describes the relation between the yearly averaged longshore transport S_x and the coastline orientation. To determine this curve, the full local wave climate needs to be taken into account, generally schematised as a limited set of individual conditions (see Sect. 8.2.5) that are each described by a number of parameters, namely:

- The significant wave height H_s (e.g. at the deep-water boundary);
- The peak wave period T_p;
- The angle of wave approach φ (e.g. at the deep-water boundary);
- The storm-related set-up h_s;
- The percentage of occurrence.

Each of the conditions contributes to the yearly-averaged transport, weighted with their percentage of occurrence. The sum of the percentages of occurrence equals 100 % (or 365 days per year, although one of the conditions may be a zero to small wave height).

Figure 8.10 shows such a transport curve as computed with the coastline model Unibest-CL+ (https://www.deltares.nl/en/software/unibest-cl). For this computation a bottom slope of 1 : 100 was assumed from MSL to MSL−20 m. The sediment grain size $D_{50} = 200\,\mu m$. The transport zone was assumed to extend to MSL−10 m. The wave input at MSL−20 m is given in Table 8.2 (wave angles are defined such that positive wave angles give positive sediment transports). A total of 16 wave conditions were defined in four wave height classes and four directional sectors. From the table it can be seen that the number of days per year with hardly any waves is $365 - 181 = 184$.

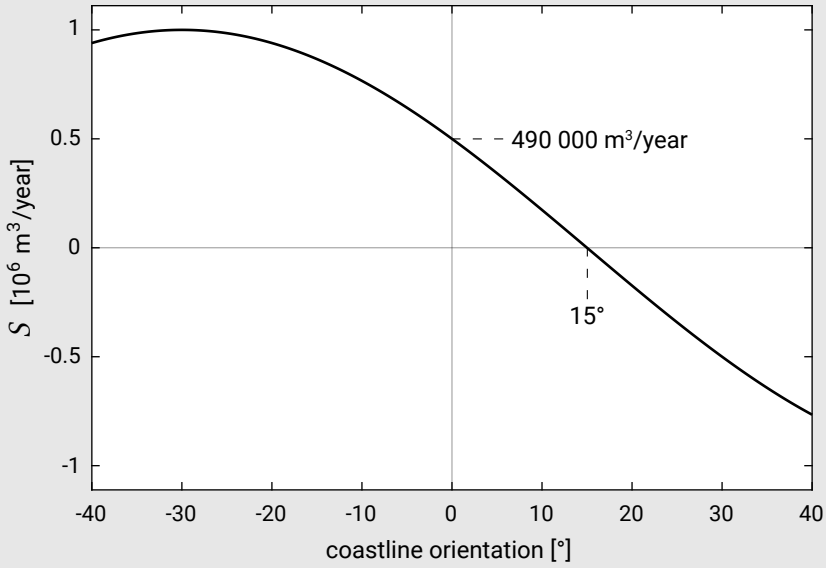

Figure 8.10: Yearly-averaged transport as a function of changes in coastline orientation. The reference (initial) coastline orientation is 0°.

Table 8.2: Wave input: number of days with certain wave conditions (combination of wave height and direction).

	direction with respect to shore normal				
H_s	−45°	−15°	15°	45°	
0.5	10	10	25	8	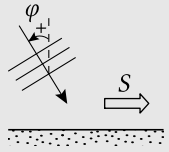
1.0	8	15	35	16	
2.0	4	10	21	11	
4.0	1	1	4	2	

For the reference coastline orientation the yearly-averaged longshore transport is 490 000 m^3/yr. If the coastline would rotate with 15°, the total longshore transport becomes zero. The angle for which $S = 0$ is sometimes called the equilibrium orientation, which is somewhat confusing since equilibrium requires zero gradients and not necessarily zero transports.

More insight in how to apply Unibest-CL+ can be obtained through e.g. Luijendijk et al. (2011) and Van der Salm (2013).

Note that the transport curve computed in this way as a function of changing coastline orientation is not necessarily constant along the coast, for instance where local wave conditions are affected by wave sheltering. As an example, at either side of a shore-normal breakwater, waves from certain directions are affected by diffraction, so that wave heights are reduced and the directions of the wave rays are more shore-normal. The alongshore variation of the yearly wave climate can be taken into account by relating a specific wave climate to a specific alongshore position and computing transport curves for various alongshore positions. In areas where the wave conditions are affected by non-uniform bottom topographies, by natural coastal features like headlands, or by man-made structures like breakwaters, the shape of the transport curve should be allowed to change alongshore.

8.3.3. Analytical solution for accretion near breakwater or jetty

The first person to describe the single line theory was Pelnard-Considère (1956). He came up with an analytical solution that can be used for a quick assessment of the effects of a structure, for instance a breakwater, on a coastline.

In order to find analytical solutions, we need to simplify Eq. 8.18. If we restrict ourselves to small changes in the angle of wave attack, we can assume $\partial S_x/\partial\varphi$ to be constant. Such an assumption implies that a segment of the (S,φ)-curve has been replaced by a straight line, which is reasonable for relatively small changes in φ. We can now write:

$$\frac{\partial S_x}{\partial \varphi} = s \tag{8.19}$$

in which s is a coastal constant. For $-20° < \varphi < 20°$, S is a linear function of the wave angle, such that $s = S/\varphi'$ (see Sect. 8.2.5). Note that S is the transport for the original angle of incidence φ'.

Substituting Eq. 8.19 in Eq. 8.18 changes the parabolic differential equation to:

$$\frac{\partial Y}{\partial t} - \frac{s}{d}\frac{\partial^2 Y}{\partial x^2} = 0 \tag{8.20}$$

This equation shows that the curvature in the coastline, scaled by the coastal constant, determines the coastal change. To solve Eq. 8.20, we need one initial condition and two boundary conditions. Very often these conditions are the position of the coastline at $t = 0$ (the initial situation) and the sediment transport on both borders of the coastal area as a function of time.

Consider the §1.1 ~~(sudden)~~ construction of a breakwater or a jetty running perpendicular to an initially straight shoreline (Fig. 8.11)§1.1 and assume, for simplicity, that the construction time of the structure is negligible [p385]. If the longshore transport is from left to right, then the coast to the left of the structure is called the updrift coast, whereas the coast to the right of the breakwater is called the downdrift coast. The breakwater is assumed to extend into the sea until at least the depth of closure.

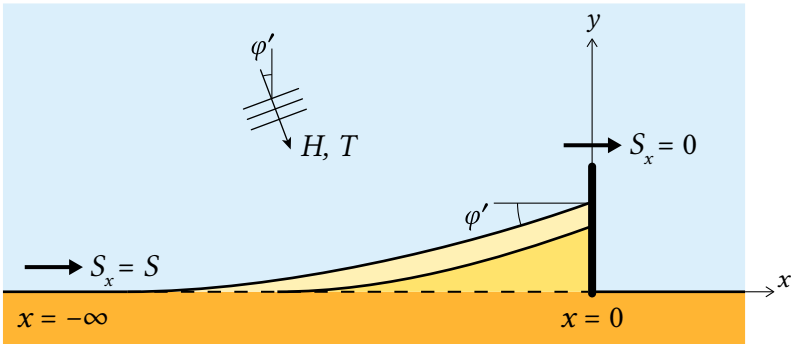

Figure 8.11: Accretion of the shore near a breakwater at different times. The wave conditions given in the sketch refer to the conditions at the assumed horizontal part in the coastal area.

The *initial condition* is the shape of the coastline at time $t = 0$:

$$Y = 0, \quad \text{for} \quad t = 0 \quad \text{and for} \quad -\infty < x < 0 \tag{8.21}$$

One boundary condition is that at a great distance from the breakwater, $x = -\infty$, the sand transport remains constant and equal to its value before breakwater construction:

$$S_x = S, \quad \text{for} \quad x = -\infty \quad \text{and for all} \quad t \tag{8.22}$$

The *second boundary condition* is imposed at the breakwater; it is impermeable to sand (no sand particles slipping through the pores of the breakwater). This means that the local longshore transport at the breakwater must be zero (100 % blocking):

$$S_x = 0, \quad \text{for} \quad x = 0 \quad \text{and for all} \quad t \tag{8.23}$$

This boundary condition is only valid as long as the breakwater blocks the entire transport, viz. as long as the active zone has not moved past the tip of the breakwater. Note that a zero transport means that the wave angle with respect to the orientation of the coastline must be zero as well. Since the offshore wave direction does not change, this

can only be accomplished by a shoreline rotation, such that the wave angle relative to this rotated coastline becomes zero (Fig. 8.11). The boundary condition at $x = 0$ can therefore also be written as:

$$\partial Y/\partial x = \varphi', \quad \text{for} \quad x = 0 \quad \text{and for all} \quad t \tag{8.24}$$

In other words, the beach accretion progresses seaward, always making an angle φ' with respect to the x-axis at the breakwater. Hence, at the breakwater, the coastline and the depth contours tend to become parallel to the approaching waves.

With the help of Eq. 8.20, applying the reference system of Fig. 8.11 and using the initial and boundary conditions mentioned above, the shape of the coastline $Y(x,t)$ on the updrift side of the breakwater can be solved as a function of time. Here, we only give some characteristics of the resulting solution (see also Fig. 8.12). First, the outward growth of the coastline at the breakwater $L(t)$ at $x = 0$ is found to be:

$$L(t) = 2\sqrt{\frac{\varphi' St}{\pi d}} = \varphi' \sqrt{\frac{4at}{\pi}} \tag{8.25}$$

where:

t	time	yr
d	profile height	m
a	$= \frac{s}{d} = \frac{S}{\varphi' d}$	$(m^3/yr)/rad/m$

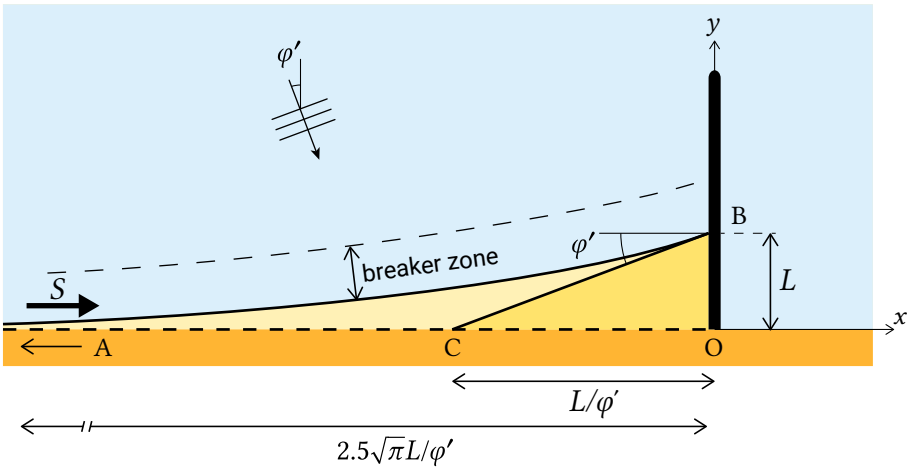

Figure 8.12: Accretion geometry. Note that line CB is tangential to the coastline at the breakwater.

Secondly, it can be shown that the influence of the breakwater (in terms of accretion of the shoreline relative to the accretion at the breakwater) is negligible at a distance $5\sqrt{at} = 2.5\sqrt{\pi}L/\varphi'$ from the breakwater. So, the influenced shoreline is dependent on the steepness s of the considered segment of the (S,φ)-curve and the height of the

active zone d (both of which are strongly dependent on the wave height). Both the horizontal extent of the influenced zone and the seaward growth at the breakwater vary with $\sqrt{t}$. This means that the progress of the shoreline gradually slows down; suppose that after a time t_1 the accretion length at the breakwater is L_1. At $t_2 = 2t_1$ the accretion length has not doubled, but only increased to $L_2 = \sqrt{2}L_1$. Equation 8.25 furthermore shows that, of course, the accretion speed increases with increasing sediment transport S. The surface area OCB in Fig. 8.12 is equal to:

$$\text{surface OCB} = \frac{1}{2}\frac{L^2}{\varphi'} = \frac{2}{\pi}\frac{St}{d} \tag{8.26}$$

Also, from continuity, the total surface area AOB is:

$$\text{surface OAB} = \frac{St}{d} \tag{8.27}$$

Therefore, 64 % §1.1(viz. $2/\pi$) [p388] of the total accretion is stored in the shaded area OCB.

For the coastal changes on the lee side of the breakwater (downdrift), an analogous analytical solution can be derived. In principle, the coastline changes on the updrift side are mirrored on the downdrift side and the total volume of updrift-accreted sediment equals the total volume of downdrift-eroded material. This is illustrated in Fig. 8.13.

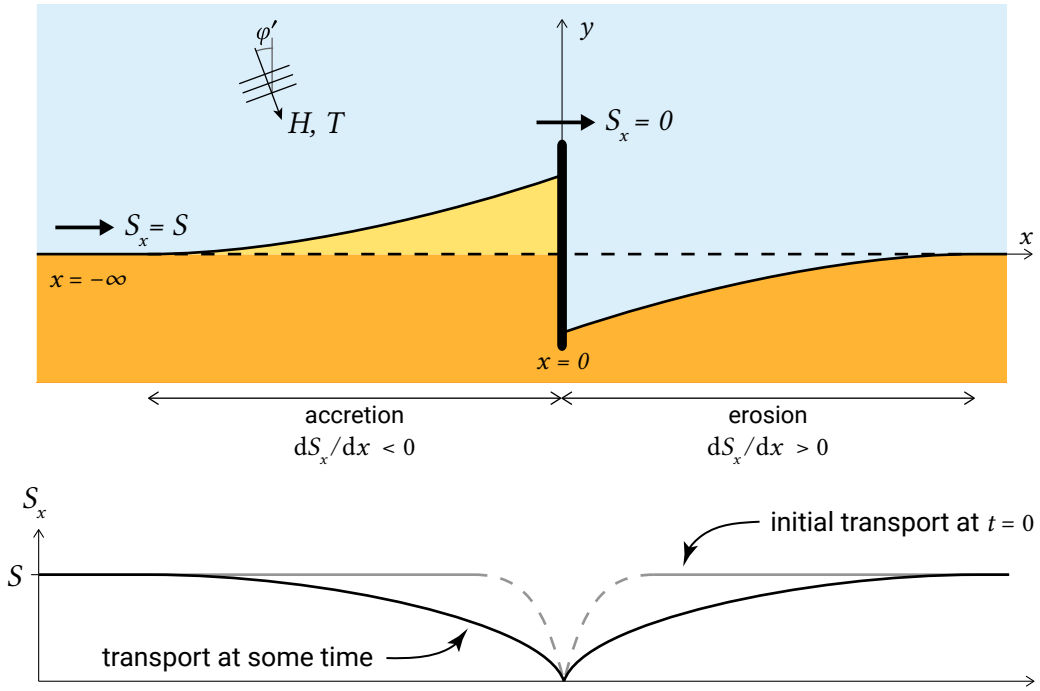

Figure 8.13: Shoreline development on the lee side of a breakwater. As a first approximation we may say that at the breakwater ($x = 0$) the lee-side shoreline orientation reflects the angle of wave attack (since $S_x = 0$), just as was the case for the updrift side. Thus, the shoreline at the lee side (or the downdrift shoreline) is the mirror image of the updrift shoreline.

In reality, however, there is a difference in the wave attack between the updrift and downdrift side. At the downstream side, a part of the shore is sheltered from wave attack by the breakwater. Waves propagating past the end of the breakwater diffract into the shadow zone (see Sect. 5.2.4). As a result, the wave heights are significantly lower than in the undisturbed region (see Fig. 8.14). Furthermore, the wave angles are significantly altered, since the wave rays turn somewhat towards the breakwater. At the breakwater, the rays run parallel to the breakwater. In principle, at the breakwater (zero transport), the coastline reorients itself normal to the local waves (hence parallel to the original coastline). There is, however, an additional shadow zone effect due to alongshore set-up differences. Due to the alongshore differences in wave height, the wave set-up in the surf zone changes along the shore (Sect. 5.5.4). The lower wave heights just behind the breakwater result in a lower set-up at the shoreline close to the breakwater, than elsewhere along the coast. The alongshore water level gradients result in a secondary current pattern that – close to the coast – is directed towards the breakwater (Fig. 5.45) and induce sediment transport towards the breakwater.

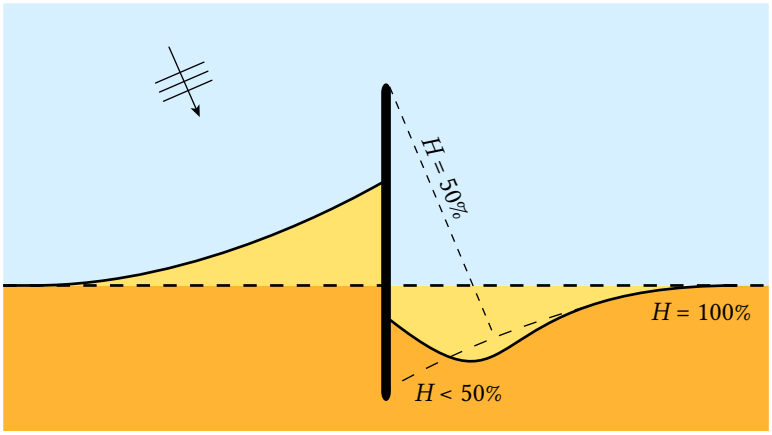

Figure 8.14: Wave height reduction and shoreline development on the lee side of the breakwater with, at the wave ray that separates the shadow zone from the wave zone, a wave height of 50 % of the original wave height according to linear theory. The dashed line shows the mirrored image of the accretion. The solid line is the equilibrium orientation, including shadow zone effects.

The resulting downdrift coastline development depends on the combination of all effects. The transport must increase from 0 at the breakwater to S in the undisturbed region. However, shadow zone effects will reduce the transport magnitude directed away from the breakwater or may even cause a net transport towards the breakwater. This leads to a coastline development as shown schematically in Fig. 8.14 (solid line).

Analytical solutions also exist for different boundary conditions at the breakwater and for different breakwater layouts. For example, after some time a beach can build up on the updrift side to such an extent that sand will be transported around the breakwater tip. This bypassing of sediment can be taken into account. Analytical solutions make hand computations of coastline changes possible and hence facilitate a quick assessment of the impact of certain coastal structures on the shoreline development.

Neither tidal influences (see Fig. 5.60 for tidal currents passing a breakwater) nor variations along the coast of wave height, wave direction or sediment characteristics can be taken into account. Besides, shoreline evolution is calculated under the assumption of steady wave conditions. This means that, as in the above example, only a single wave condition is taken into account. This limits the applicability of these analytical solutions, especially in the vicinity of structures where sheltering effects are important and vary strongly with the wave direction. In Sect. 8.4.2 this is further explained.

Numerical methods based on Eq. 8.18 often include the above-mentioned processes. These methods still suffer from limitations as a result of the basic assumption that coastline models are based on, namely the assumed equilibrium coastal profile. This assumption does not allow for profile changes over time or along the coast and assumes an instantaneous cross-shore redistribution of sediment when erosion of accretion occurs. This may be appropriate in the case of for instance a perturbation by a nourishment (Sect. 8.4.4). However, many situations are truly 2D, which implies that cross-shore and alongshore processes are not physically independent and the assumption of an instantaneous equilibrium cross-shore profile is invalid. Two examples of two-dimensional effects are the lee-side circulation patterns, as mentioned before, and 'outbreaking' longshore currents as they approach the breakwater. The latter refers to the fact that the water flowing towards the breakwater on the updrift side has no other option than to go offshore, since the longshore current decreases to zero at the breakwater (Fig. 8.15). This contributes to the redistribution of material in the cross-shore direction.

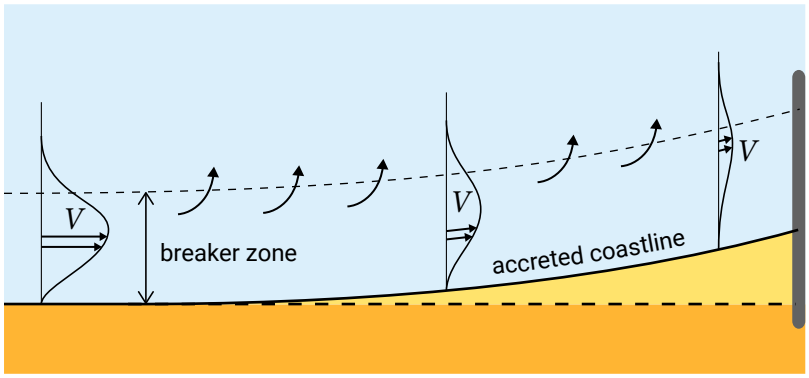

Figure 8.15: Longshore current approaching a breakwater. The current is diverted offshore while decreasing in strength.

8.3.4. Multiple-line theory

If the single-line shoreline approach is considered to be over-schematised, it is possible to use multiple-line theory. The principles of multiple- and single-line theory are the same. The most significant difference is that cross-shore exchange of sediment is taken into account in multiple-line theory, which allows a non-equilibrium cross-section to

be considered. Furthermore, the shore (cross-section) can be schematised in two or more zones of the profile.

Bakker (1968) proposed a two-line approach in order to study the dynamics of a coast with a groyne system that only partially blocked the longshore transport (since the groynes were shorter than the width of the breaker zone). He recognised the two distinct transport zones shoreward and seaward of the tip of structure and made a schematization into two zones, as shown in Fig. 8.16. In some special cases he found analytical solutions to the two-line approach.

For each zone in a two- (or more-) line model, a computation of the development of one depth contour can be made, similar to the computation of the single line in the single-line coastline models, but with the addition of an extra term in the continuity equation, viz. the cross-shore sediment transport component. In a schematization as in Fig. 8.16 each longshore transport component S_{xi} is directed parallel to the coast and describes the littoral sand movement in its zone. The horizontal planes, the boundaries between the zones, should in principle be selected at elevations which correspond more or less to flat portions of the total profile. If structures, such as groynes, are present, the boundaries between the zones can be chosen such that they correspond to the limits of a transport zone. The longshore transport components can be determined with any longshore transport formula, except for bulk longshore transport formulas. The cross-shore sediment transport exchange can be evaluated based on deviations from an equilibrium profile (see Sect. 1.5.4 and Sect. 7.2).

In addition to the analytical models, numerical models have been developed based on an arbitrary number of lines connected by cross-shore sediment transport. As with the single-line theory, a multi-line model assumes that the cross-shore and alongshore physics are decoupled. It has proven to be difficult to specify realistic formulas for both the cross-shore sediment transport and the cross-shore distribution of the longshore sediment transport. Hence, for strongly 2D coastlines, a more physics-based area model should be applied instead.

8.4. Coastal features and coastal change due to longshore transport

8.4.1. Introduction

The knowledge acquired in the previous sections will be used in this section to explain a variety of coastal features and coastline changes as observed in nature. The basis of the explanations lies in the *gradients* in littoral transport rates. The littoral transport rates are dependent on the nearshore wave exposure and wave incidence angle, as explained in Sect. 8.2. Hence, for a given offshore wave climate, coastal changes are determined by changes in the depth contours and shoreline orientation and the degree to which waves refract, shoal and diffract along the shoreline.

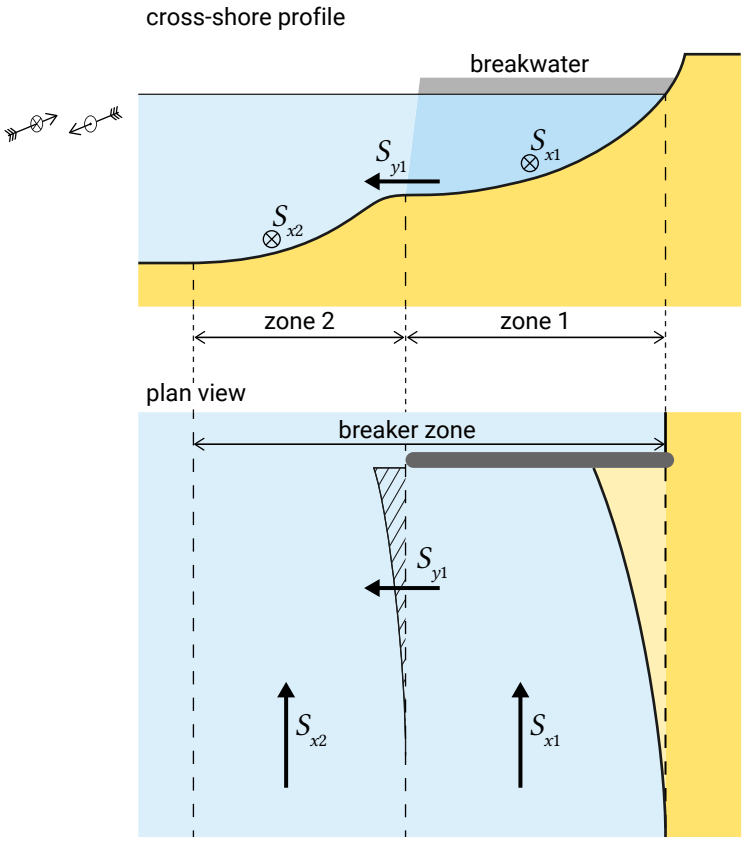

Figure 8.16: Shore plan and profile (two-line schematization).

Assuming the offshore wave conditions do not vary along the shore (which is a reasonable assumption on a scale of the order of 10 km), a curved coastline will always be subject to a longshore sediment transport gradient. This is because:

1. The changes in coastline orientation are reflected in changes in the angle of wave incidence. Changes in shallow-water depth contours and coastline orientation are generally more important than directional changes in offshore wave climate along the coast;
2. Due to refraction, convergence and divergence of wave energy occurs (Fig. 5.6).

As long as the wave angles are relatively small, viz. a deep-water wave angle with respect to the shoreline smaller than about 45°, the transport rates increase with increasing wave angle (Fig. 8.4). This implies that convex depth contours result in sediment transport divergence along the coast and thus in erosion, whereas concave depth contours lead to sedimentation (see Fig. 8.17). Note that convex and concave are here defined as seen from the sea.

As a consequence, a shoreline has a tendency to flatten out bumps and dents until the straight, equilibrium coastline is restored (hence a negative feedback process, see Sect. 1.5.2). The specific case of high-angle waves is discussed in Sect. 8.4.4.

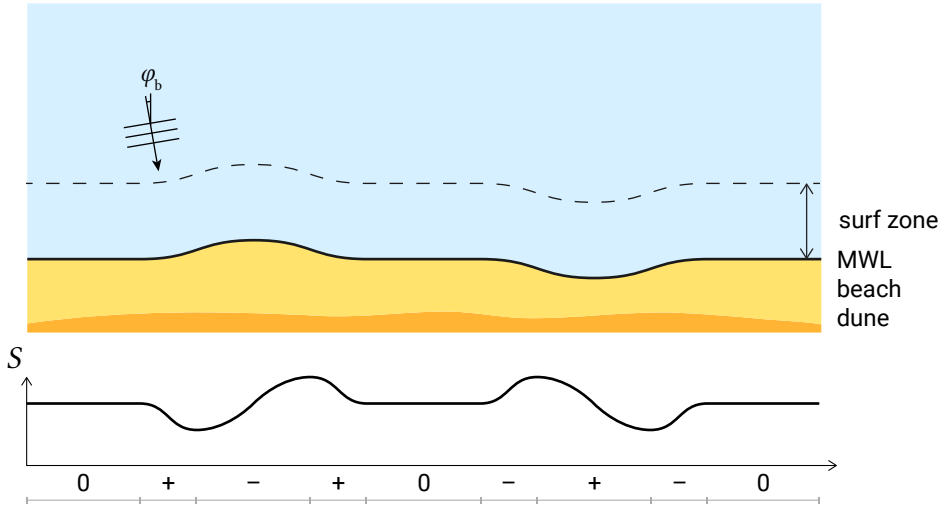

Figure 8.17: Longshore sediment transport along a coast for small, deep-water wave angles. Zones with positive transport gradients (transport divergence, erosion) are indicated by '−' and zones with negative transport gradients (transport convergence, accretion) by '+'. The 'bump' in the shoreline erodes and the 'dent' accretes.

In this section, we consider the structural coastal response to large disturbances or interruptions (natural and human-induced) that can be explained based solely on longshore transport gradients. The onshore and offshore movements of sediment that take place on short timescales, such as storm-induced erosion and seasonal variations, are assumed to cancel out on the longer timescales of shoreline change. Any net gains or losses of sediment in the cross-shore direction (e.g. due to offshore canyons or inland aeolian transport) can be considered as sinks or sources. Natural disturbances are for instance coastline interruptions by tidal basins or rivers, the presence of an offshore island and river sediment supply. Human-induced disturbances are for instance harbour moles, shore protection structures, river regulation works, nourishment schemes and maintenance dredging.

8.4.2. Blockage of longshore transport by shore-normal structures

In this section, we discuss the effect of (partial) blockage of longshore transport by groynes and breakwaters. As in Sect. 8.3.3, we expect updrift accretion and downdrift erosion. Figure 8.18 (in Example 8.2) serves as a further illustration. Whereas in Sect. 8.3.3 we considered steady wave conditions, here we consider a full wave climate as well a schematization into primary and secondary waves. Primary or prevailing waves are waves that give a gross transport in the net transport direction, averaged over all wave conditions. By contrast, secondary waves give a gross transport smaller in magnitude and in the opposite direction.

Example 8.2 Coastline development in lee of jettied entrance

The development in the lee side of a jettied entrance is illustrated in Fig. 8.18. Let us consider irregular wave conditions from one primary direction. The transport away from the downdrift jetty by the alongshore current is $S_{x,1}$. It is reduced in the lee side of the jetty due to the reduced wave heights (changes in wave angle are neglected). The shoreline development in response to $S_{x,1}$ only is shown at the top left of the figure. The secondary transport component due to set-up-driven currents is $S_{x,2}$ and is directed towards the downdrift jetty. The total transport is $S_{x,3} = S_{x,1} + S_{x,2}$. In the zone directly downdrift of the jetty the transport gradient $dS_{x,3}/dx$ is negative, resulting in sedimentation (see top right of the figure). Erosion occurs where $dS_{x,3}/dx$ is positive. Further away from the jetty, a constant $dS_{x,3}/dx$ implies no coastline change.

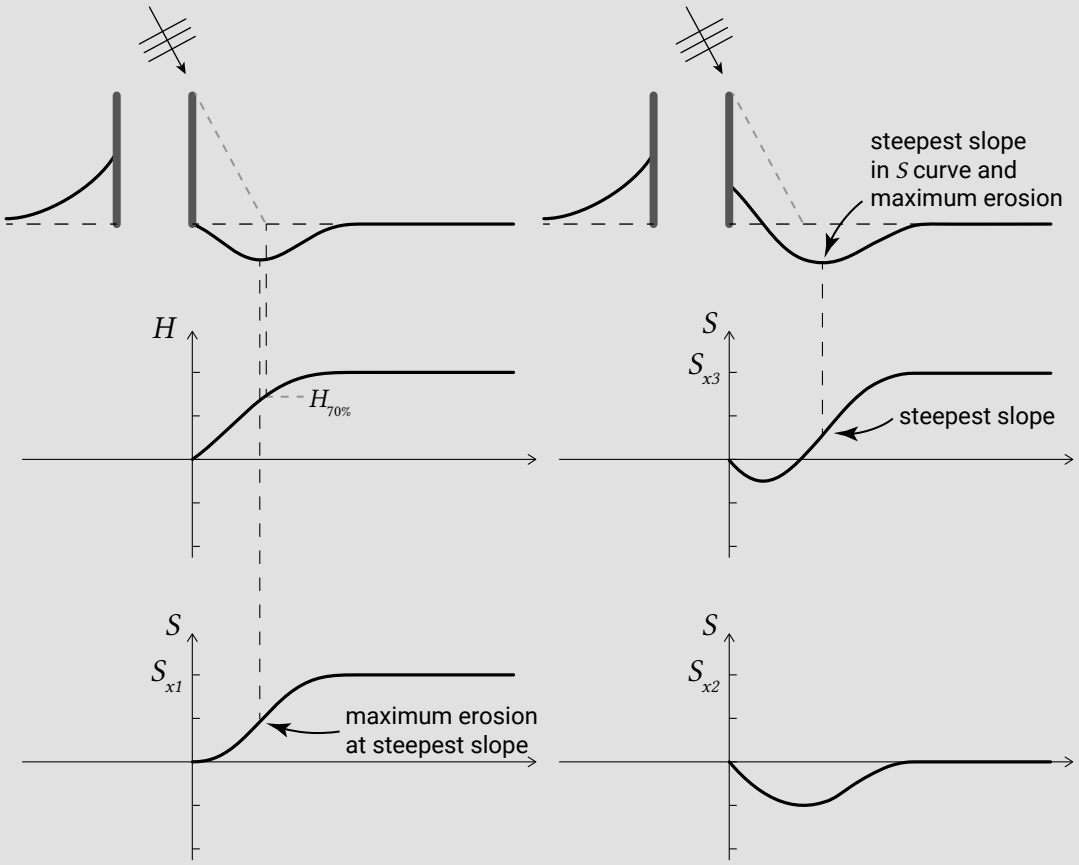

Figure 8.18: Shoreline development on the lee side of a jettied entrance. Left: Assuming irregular waves, the wave height H, at the wave ray that separates the shadow zone from the wave zone, is order 70 % of the original wave height. Since the transport depends nonlinearly on the wave height, the transport $S_{x,1}$ away from the jetty is reduced even more, for example by 50 %. The shoreline development in response to $S_{x,1}$ is shown at the top. Right: due to set-up differences, a transport $S_{x,2}$ towards the breakwater occurs, yielding a total transport $S_{x,3} = S_{x,1} + S_{x,2}$. The shoreline development in response to $S_{x,3}$ is shown at the top.

Let us – as in Sect. 8.3.3 – consider a long breakwater that extends far beyond the surf zone, such that at least initially no appreciable transport will take place around the tip of the breakwater. The wave conditions are as given in Intermezzo 8.2 and hence Fig. 8.10 shows the transport curve. This curve is valid for the undisturbed coastline far from the breakwater, that is reached by waves from all directions. On the updrift side of the breakwater, the secondary waves with negative angles of attack are initially blocked by the long breakwater. This locally increases the yearly-averaged transport rate (i.e. only the gross positive transport should be considered) and hence not only the transport for the unchanged coastline orientation, but the coastline orientation for zero transport as well. This means that the equilibrium coastline orientation, to be expected on the updrift side of the breakwater at $x = 0$, is initially larger than 15°. Similarly, on the downdrift side, the waves with positive angles of attack are blocked by the breakwater. Waves with negative wave angles will reach the breakwater and result in a transport towards the breakwater, such that local accretion can be expected at the breakwater. Note that the term *downdrift* refers to the net transport direction along the undisturbed coast averaged over all conditions. The angle of the accretion at the breakwater is determined by the condition of zero transport for the waves that can reach the ray just on the lee side of the breakwater. This angle follows from a transport curve (for the conditions giving a negative transport only), that intersects the y-axis at a negative transport rate and the x-axis at a negative angle. Note that the effects of diffraction of the waves with positive wave angles into the sheltered area (see Fig. 8.14) and corresponding set-up-induced currents are not yet taken into account in the discussion above about the downdrift equilibrium angle at the breakwater.

The expected development of the coastline for a comparable case (from Mangor, 2004) is shown in Fig. 8.19. The wave climate is schematised into prevailing waves from the NW and secondary waves from the NE. The 'representative wave condition' shown in Fig. 8.19 is a single condition that would reproduce the net transport of the full climate as well as the corresponding shoreline equilibrium angle. The wave angles are smaller than 45°. The figure shows the longshore transport rates along the coast, both initially after construction of the harbour and after bypass has started. The transport rates are expressed in units LDR (Longshore Drift Rate). The prevailing and secondary waves give transports of 10 LDR eastward (E) and 5 LDR westward (W) respectively. Hence, the net transport far from the breakwater is 5 LDR eastward.

Initially, the transport on the updrift side increases from 5 LDR E (outside the area of influence of the breakwater) to 10 LDR E closer to the breakwater, where the secondary waves do not penetrate. At the breakwater, of course, the transport is zero. In the beginning therefore, the zone on the updrift side that is sheltered from secondary waves, shows accretion close to the breakwater (where the transport gradients are negative) and a smaller (only initial) erosion a bit further away from the breakwater (in the zone with positive transport gradients). The updrift side as a whole has a sediment surplus of 5 LDR and hence experiences accretion.

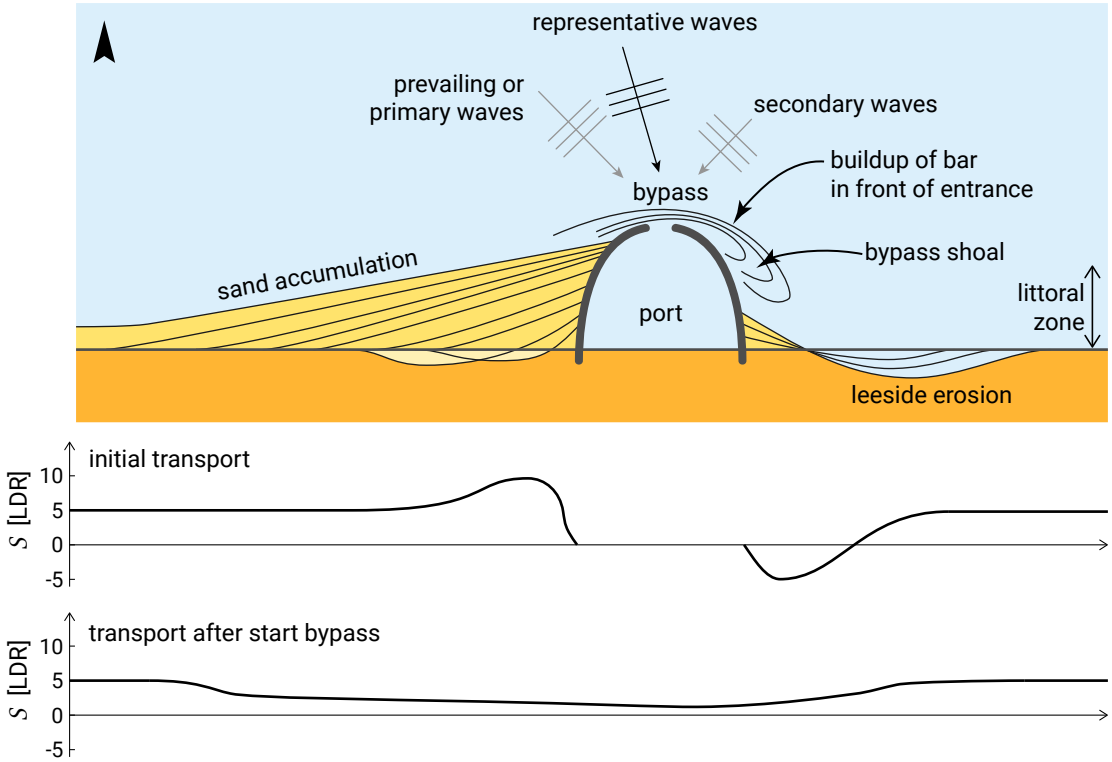

Figure 8.19: Schematic shoreline development, morphological development and net littoral drift budgets (in unspecified units of Longshore Drift Rate (LDR)) for a port at a coast with a slightly oblique resulting wave attack (after Mangor, 2004). Given the fact that continuity requires equal accreted and eroded volumes, we expect that the lee-side erosion must stretch over a much longer length.

Downdrift of the breakwater the expected initial transport rates are 5 LDR E further from the breakwater. Very close to the breakwater – in the shadow zone for the prevailing waves – the transport is 5 LDR W (resulting in a small accumulation at the breakwater). The lee side as a whole has a sediment deficit of 5 LDR and therefore experiences erosion. From sediment continuity considerations, it follows that the deposited sediment volumes in the entire affected area must match the eroded volumes.

At any given time the coastline orientation at the breakwater (updrift) is normal to the direction of the waves that can reach the advanced coastline. The angle can therefore be seen to gradually change from normal to the direction of the prevailing waves to normal to the direction of the 'resulting' (representative for the net transport) waves.

After the bypass starts, a bar will build up in the harbour entrance and the updrift coastline will try to re-orientate itself towards the original direction (but will never succeed). Although the downdrift coastline will continue to experience erosion, the erosion will diminish after the coastline receives sediment via the migrating bypass shoal.

8.4.3. Shadow effects due to obstacles away from the shoreline

An obstacle in front of a coast, such as a rocky outcrop, an offshore breakwater or even a shipwreck, will reduce the wave activity in the zone of wave shadow between the object and the shore. Since the reduced wave activity in the shadow zone will result in a reduced sediment transport capacity, material being carried along the shore will be deposited in the shadow zone, forming a tombolo. Initially only a shoal will form, which we call a *salient*. This can, however, develop into a point of land connecting the original shoreline to the obstacle (see Figs. 8.20 and 8.21). We now speak of *tombolo*. A tombolo completely blocks longshore transport in the zone landward of the obstacle.

Figure 8.20: The holocenic tombolo of Mariscal formed behind an island in Bombinhas, Brazil. The photo was taken from a hill in the original island (see black arrow in map) which is now connected to the Porto Belo peninsula by the tombolo. Photo by Carolina Piccoli, map OpenStreetMap ('Credits' on page 579).

These shadow zone effects can be used to stimulate and preserve a recreational beach (Sect. 10.5.4). Have a look at Fig. 10.41, which shows salient and tombolo formation behind a series of emerged (i.e. having their crests above MSL) offshore breakwaters.

The development of a tombolo, as explained above, depends upon a transport of material parallel to the coast; the reasoning is that in the shadow zones behind obstacles, the breaking wave heights and thus longshore transport capacity are reduced and sediment is deposited. Note that due to diffraction of waves around the ends of the breakwater, still some wave action will be present behind the breakwater (the wave heights

Figure 8.21: Tombolo formed behind a detached breakwater in Alicante, Spain. Photo by Leonid Andronov (‘Credits’ on page 579).

at the end of the breakwater are in the order of magnitude of 50 % of the original incoming wave height, see Sect. 5.2.4). Example 8.3 discusses the shoreline development resulting from an emerged breakwater (partly) blocking the longshore sediment transport by obliquely incident waves.

Besides the shoreline development, as a result of breaking wave height reduction in the shadow zone and subsequent gradients in longshore sediment transport (illustrated in Example 8.3), two subtler effects play a role, namely: 1) changes in wave angles in the shadow zone; and 2) secondary current patterns as a result of set-up differences. These *additional* or secondary effects enhance the pattern of deposition behind the obstacle for obliquely incident waves and are the reason that even with normally incident waves a salient or tombolo can be formed (Fig. 8.23). This can be explained as follows. Due to diffraction into the shadow zone, not only the wave heights, but also the wave angles are affected. Hence, even in the case of normally incident waves, the diffracted waves behind the breakwater approach the original coastline at some angle. This results in an initial sediment transport pattern with transports from both breakwater ends towards the shadow zone. Furthermore, as shown in Fig. 5.46, nearshore currents run towards the shadow zone from both sides of an emerged obstacle. This secondary current pattern also enhances transport towards the shadow zone.

Example 8.3 Coastline development near an emerged detached breakwater as a result of longshore transport gradients

Consider an emerged detached breakwater along a coast with initially straight and parallel depth contours (Fig. 8.22). Waves are incident at an angle of 15°. The natural surf zone width is smaller than the distance between the breakwater and the shore. The length of the breakwater is equal to its distance from the

shore. As in Fig. 8.17, Fig. 8.22 qualitatively shows the sediment transport as a function of the distance alongshore, for the initially straight shoreline, estimated based on a hypothesised variation of the wave height behind the breakwater. Next, the areas where the expected shoreline response is accretive (negative transport gradients, sediment transport convergence, indicated with '+') and erosive (positive transport gradients, sediment transport divergence, indicated with '−') can be identified. Based on the initial sediment transport variations alongshore, the expected shoreline development can be sketched. The result is a wave-like initial pattern of updrift accretion (the shoreline bulges seaward) and downdrift erosion (the shoreline curves landward) as in Fig. 8.22.

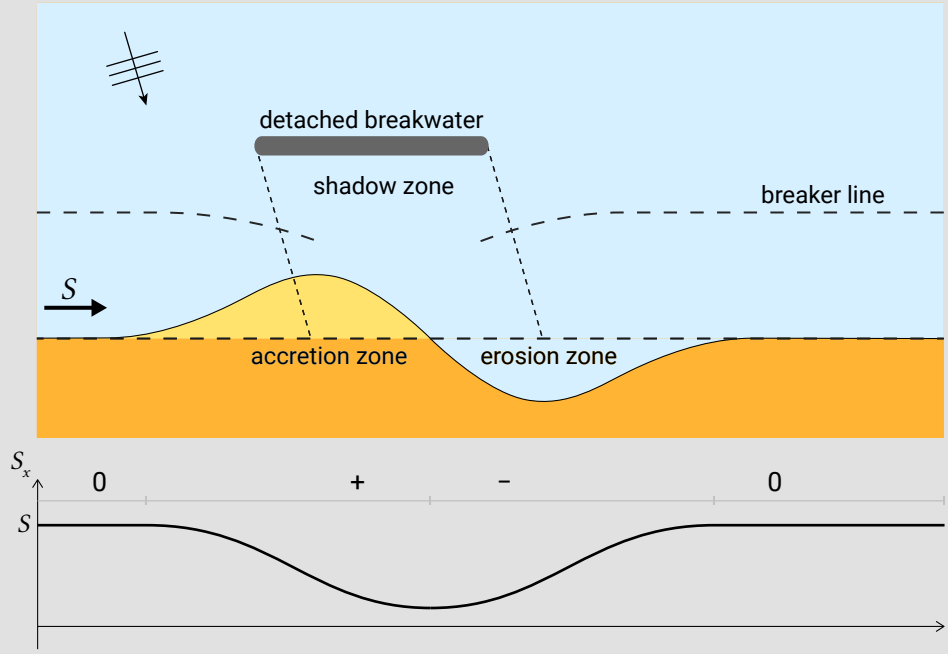

Figure 8.22: Shoreline development behind an emerged breakwater for obliquely incident waves from one direction. Only the development due to the longshore transport gradients is considered; other mechanisms are ignored. Note that continuity requires that accreted volumes are equal to eroded volumes.

Figure 8.23 shows the resulting symmetrical shoreline development, for normally incident waves, with erosion on either side of the breakwater and accretion behind the structure. The initial shoreline development takes the form of a salient (lower panel), which may or may not develop over time into a tombolo (upper panel). A tombolo is more likely to develop if the breakwater is located in or just outside the surf zone (since the responsible currents are generated in the surf zone) and if its length is relatively large. If the length is larger than, say, twice the distance from the coast, the diffracted wave heights reduce to zero in the centreline of the structure (Fig. 8.24, left figure). In that case the sediment stirring and transporting capacity behind the breakwater is

not enough to keep a passage open. For a relatively short breakwater, the equilibrium shoreline will take the form of a salient (Fig. 8.24, right figure).

In the case of *submerged* obstacles, tombolos or salients may also develop. However, in those cases, any accretional tendency may be counteracted by a (possibly stronger) erosional effect. This is related to the wave-induced current pattern as shown in Fig. 5.49. The onshore-directed wave forces, as a result of waves breaking on a shoal or submerged breakwater, result in a large on-shore flow of water. This is compensated for by rip currents returning seaward at either side of the shoal or breakwater. These

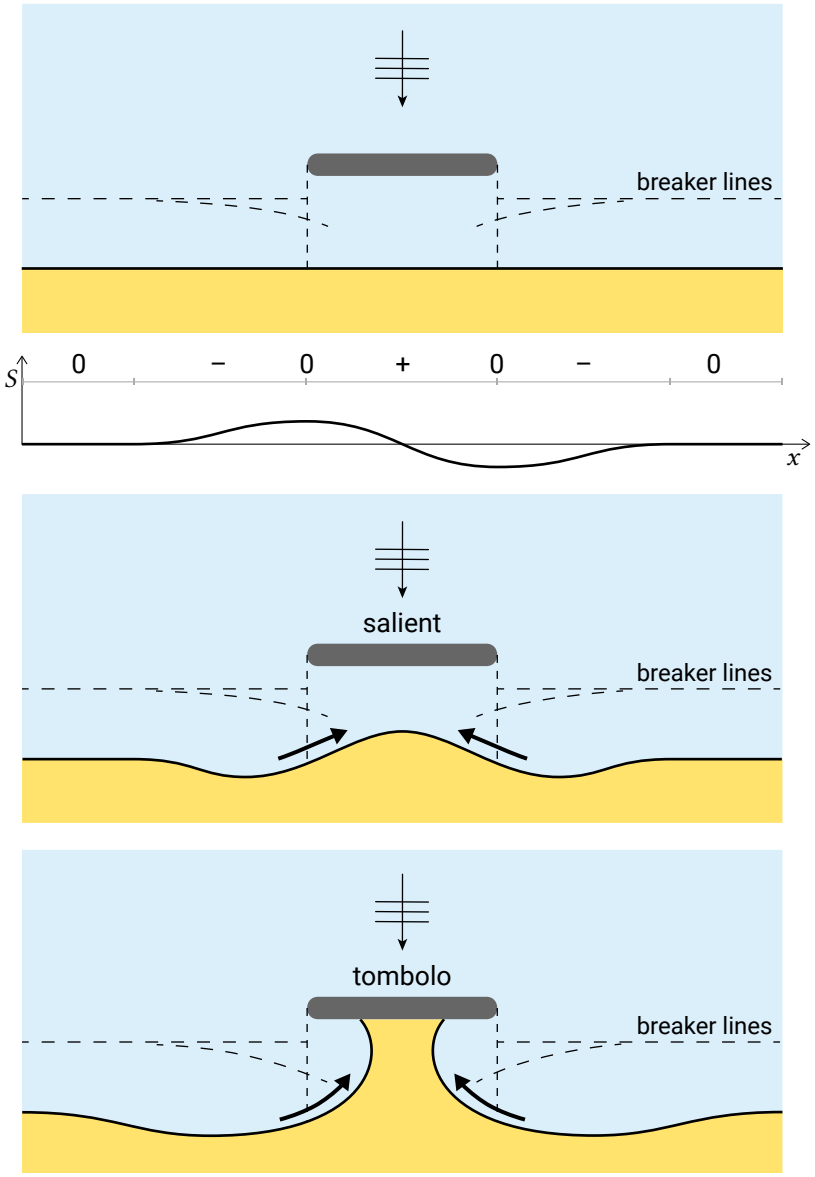

Figure 8.23: Shoreline development behind an emerged breakwater for normally incident waves. In this situation, the approach angles of the diffracted waves and the current patterns induced by the set-up gradients determine the coastline development. The figure also shows the *initial* sediment transport variations. Note that the coastline development is symmetrical (as opposed to the development for oblique incidence as sketched in Fig. 8.22) and that the accretion behind the obstacle necessarily means erosion on both sides of the obstacle.

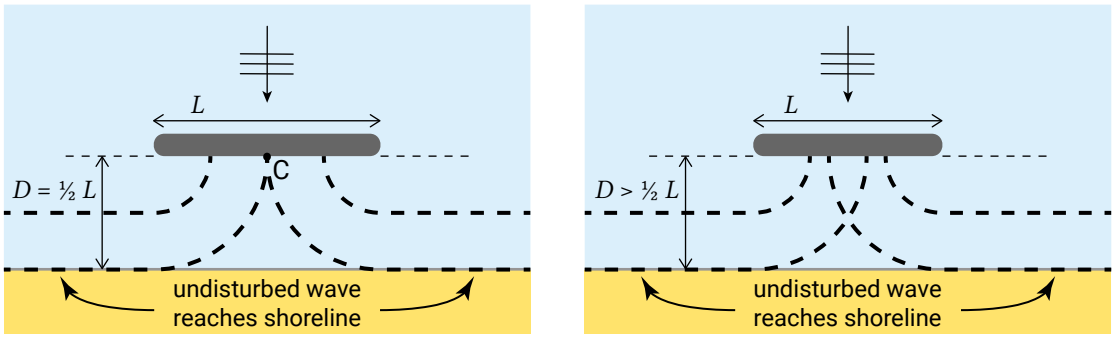

Figure 8.24: Wave diffraction behind a detached emerged breakwater with length L and distance to the shore D. Left: wave heights reduce to zero in the centreline of the structure. Right: wave energy penetrates in the entire zone between the emerged breakwater and the shoreline.

currents can carry large amounts of sediments from the shadow zone seaward and hence create large levels of erosion. Some consequences for submerged breakwater design are discussed in Sect. 10.5.4.

8.4.4. Shoreline perturbation

This section discusses the evolution of a single perturbation (a 'bump') in the shoreline. Such a bump in the shoreline can have various origins, for instance a nourishment scheme or a significant supply of sediment by rivers, leading to delta formation (see Sect. 8.4.6). In Example 8.4, we consider an initial disturbance of the system by a nourishment; the same development occurs for any other perturbation of the coastline.

Example 8.4 Coastline change caused by a perturbation of the shoreline

Assume a beach nourishment has recently been executed on an initially straight stretch of coast. Some time after the nourishment, the sediment has become redistributed over the cross-shore and the shoreline is given by the dotted line in Fig. 8.25. As a result of the nourishment, the shoreline has advanced, after cross-shore redistribution, over an alongshore distance of 1000 m. The maximum shoreline advance is 50 m. The angle between the original and nourished coastline is everywhere smaller than 10°.

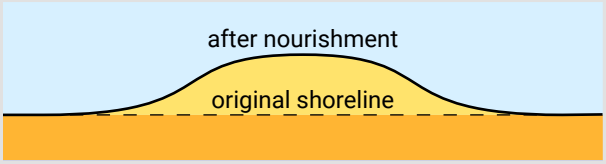

Figure 8.25: Shoreline some time after a beach nourishment, over a limited alongshore distance.

Questions

1. The waves are normally incident to the original shoreline. Sketch how the coastline will qualitatively develop over time. In order to substantiate your answer, draw the initial longshore transport rates as a function of the distance along the coast (as in the middle panel of Fig. 8.19) and indicate, based on the longshore transport gradients, where erosion and accretion take place. What are the locations with the largest shoreline change?
2. As 1. but now the waves have an angle of incidence in deep water of 20° with respect to the original shoreline;
3. As 1. but now the waves have a deep-water angle of incidence of 70° with respect to the original shoreline.

Figure 8.26, based upon concepts by Ashton and Murray (2006), contains some of the answers to the questions in Example 8.4. Figure 8.26b shows the transport as a function of the deep-water wave angle relative to the shore (denoted φ_0 in this book). It can be seen that for low-angle waves the transport increases with larger relative angles (from 1 to 2 to 3 in Fig. 8.26b). By contrast, for high-angle waves the transport decreases with increasing angle (from 4 to 5 to 6 in Fig. 8.26b).

Figure 8.26c shows the shoreline response to low-angle waves. At the 'horizontal' parts of the shoreline the transport magnitude is equal and given by point 2 in Fig. 8.26. However, at the 'left' and the 'right' flank of the 'bump', the relative wave angles and thus the transport magnitudes are smaller (point 1) and larger (point 3) respectively. The crest of the bump erodes, since there the transport increases (diverges) in the transport direction (positive transport gradient). A decreasing (converging) transport in the transport direction (negative transport gradient) causes deposition. The end result is a flattening of the shape towards a straight coastline, for which no further changes occur. For high-angle waves (greater than 45°) the pattern of erosion and deposition is reversed, leading to growth of the bump (Fig. 8.26d).

The shoreline response to low-angle waves is a clear example of negative feedbacks stabilising the shoreline by eroding the perturbations (see Sect. 1.5.2). For high-angle waves, positive feedbacks promote the growth of perturbations, leading to self-organised patterns (see also Intermezzo 7.2).

8.4.5. Interrupted coasts: spits

A spit is a pointed tongue extending into the sea. Spits develop where the longshore transport capacity is diminished due to coastline interruptions (river, estuary, end of island). The direction of a spit usually is a continuation of the shoreline from which sediment is supplied. An example of a spit is shown in Fig. 8.27. Waves coming predominantly from the southwest cause a sand transport toward the north along the western slope of the island. As the water becomes deeper at the north end of the island, the waves no longer break, the sediment transport decreases (hence a negative

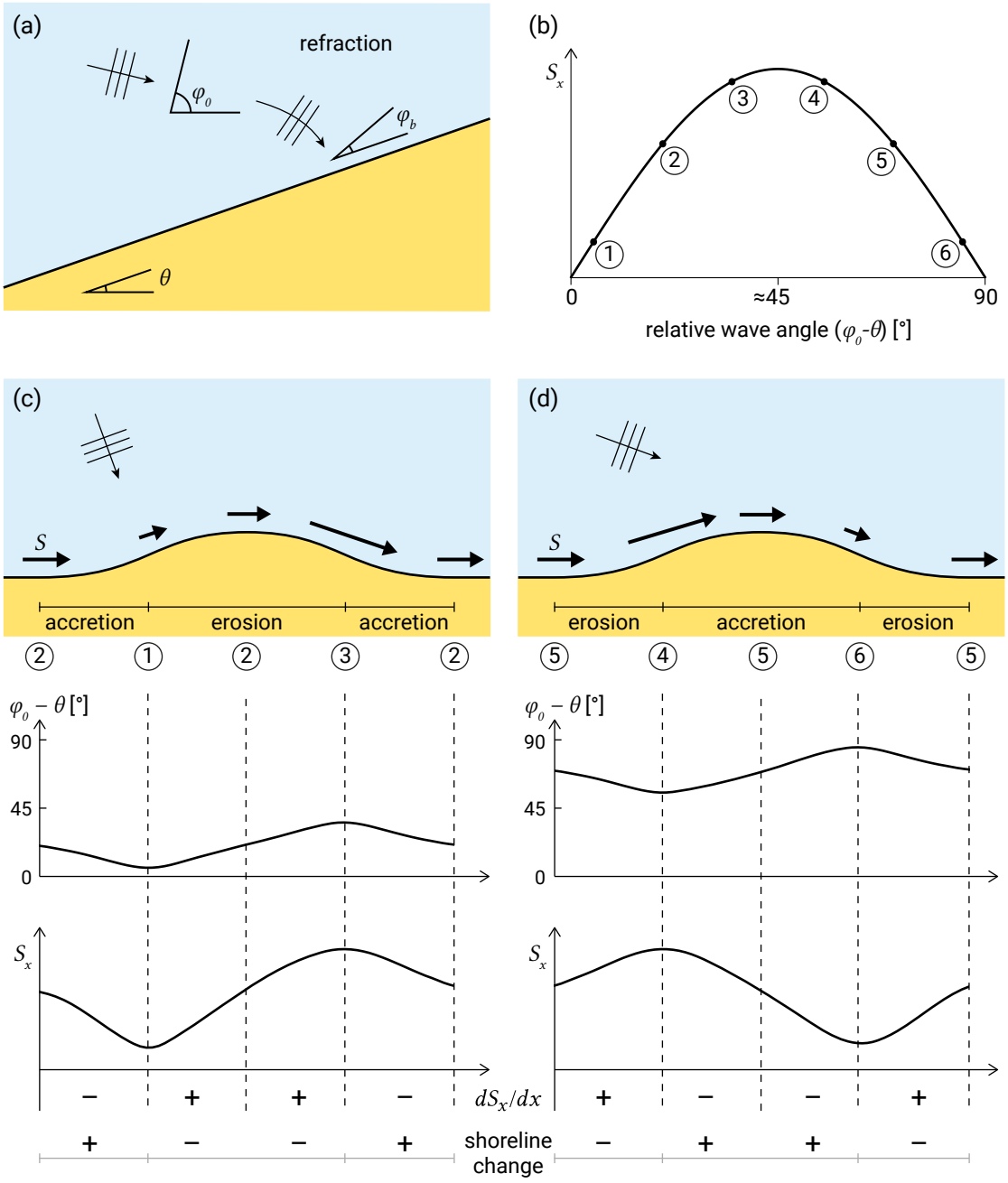

Figure 8.26: Response of a perturbation (a 'bump') in the shoreline, based on concepts by Ashton and Murray (2006) with (a) depiction of the terms and axes; (b) the transport curve as a function of the relative deep-water wave angle ($\varphi_0 - \theta$) showing a maximum for an angle of around 45°; (c) response to low-angle waves (smaller than 45°) for which the transport increases with larger relative angles resulting in flattening of the shape and (d) response to high-angle waves (greater than 45°) for which the transport decreases for increasing angle, resulting in growth of the bump. The bottom figures represent the initial variation of the wave angle and sediment transport along the shore and indicate the zones where sedimentation and erosion can be expected. The numbered transport magnitudes in (b) correspond to the numbers in (c) and (d).

transport gradient is created), the sand settles and the spit gradually builds out as an extension of the coastline.

Figure 8.27: Spit at north end of Block Island, USA. High Resolution Orthophotos obtained in April 2014. From U.S. Geological Survey ('Credits' on page 579).

The spit of Block Island is a good example of a spit formed at the end of a beach, where the longshore current loses its transport capacity. For the same reasons, spits can also form near the entrances of harbours or estuaries or where a river mouth interrupts an otherwise straight coast. Let us consider the situation of a modest river flowing into the open sea (see Fig. 8.28). The undisturbed longshore transport rate is S m^3/yr. If the river mouth is sufficiently wide and deep to strongly reduce the longshore transport rate (hence a negative transport gradient), coastal material is deposited on the updrift side of the entrance, narrowing the mouth. At the downdrift side the waves regain their capacity to transport sediment (capacity is S m^3/yr), whereas only a fraction of this bypasses the river mouth. The positive transport gradient results in erosion on the downdrift side. The result is a slow displacement of the river mouth in the direction of the longshore transport; a spit develops and grows over time.

Landward of the spit, the river flows more or less parallel to the coast for some distance. Because of the growing of the spit, the length of the river increases, and as a result the water levels in the river behind the spit rise, eventually forcing a breakthrough somewhere on the updrift side of the spit. This is a periodic process for a fully natural river mouth with breakthroughs of the slender spits occurring during periods of large river discharges (e.g. during a wet season).

Spits may also develop where coastlines with sufficient longshore sediment transport are interrupted by lagoons or bays instead of by a river. If the longshore transport rate is large enough, a spit can also develop in combination with a delta (see for instance Fig. 8.32). Spits may eventually close off a lagoon or bay, acting as a 'bay barrier' (Fig. 8.29a). Figure 8.29b shows a barrier spit that separates a tidal basin from the marine environment; tidal action keeps the entrance open. Breaches in long barriers can lead to barrier island formation.

The coastline interruptions may not only locally diminish wave-induced longshore transport capacity, but act as a source (e.g. a river, see Sect. 8.4.6) or sink (e.g. a tidal basin) of sediment as well. Tidal basins (bays, lagoons, estuaries) are known to

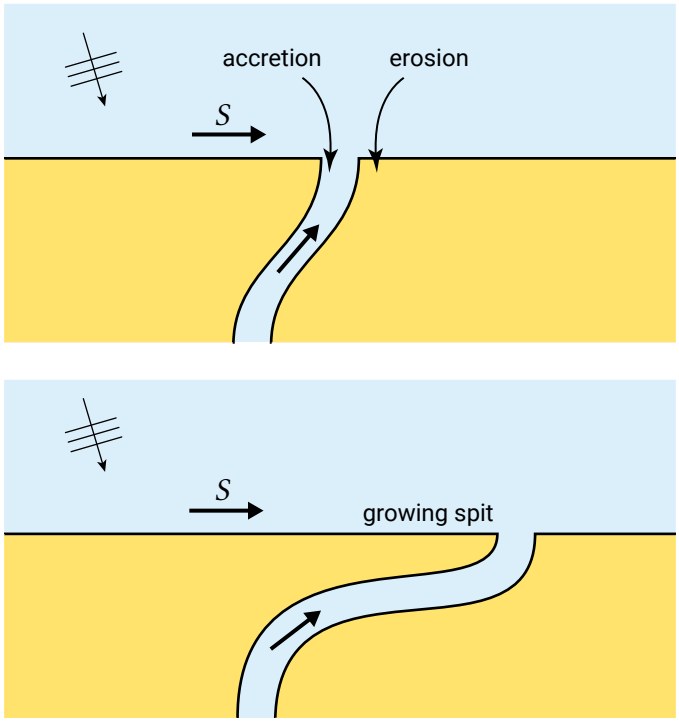

Figure 8.28: Spit and river mouth.

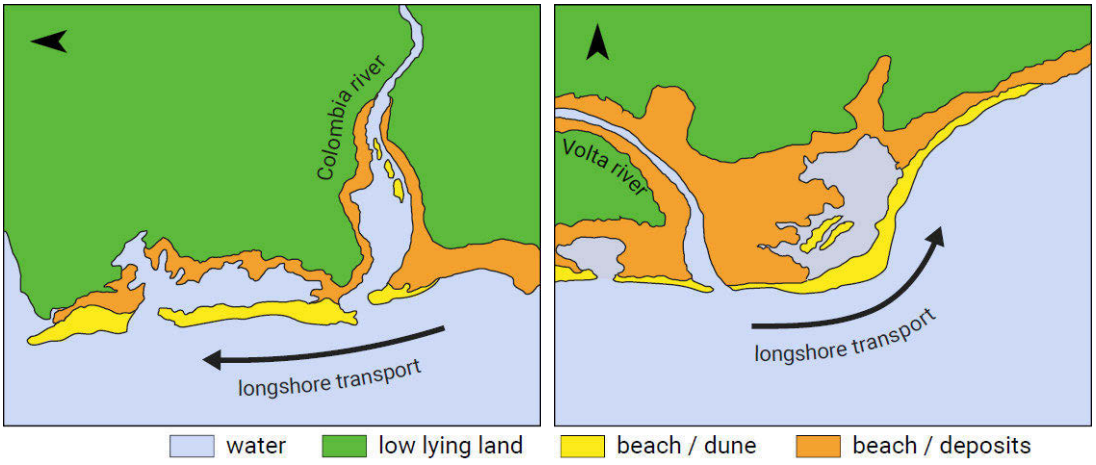

(a) Willapa Bay, Washington, USA (b) Keta Lagoon, Ghana

Figure 8.29: Barrier spit development as a result of longshore transport.

act as a sink for longshore sediment transport, thereby depriving adjacent coastlines of sediment. Tidal basins and their interaction with adjacent coasts are discussed in Ch. 9.

8.4.6. Deltaic coastlines

Built primarily from river-borne sediments, deltas form when the amount of sediment delivered at the mouth of a river exceeds the amount removed by waves and tidal currents (see Ch. 2). The main effect of waves and tides is to redistribute the sediment

along the coast. Section 2.7.3 has discussed the classification of deltas based on the relative river, wave and tidal influence.

Figure 8.30 shows the schematised development of a wave-dominated deltaic coastline (cf. Fig. 1.7). An equilibrium coastline position requires that all of the sediment supplied by the river is transported to the coastlines on either side of the river mouth by the wave-driven longshore currents. From the wave characteristics and the river sediment supply, the equilibrium coastline orientation (see Fig. 8.30) can be calculated; at the delta mouth the angle φ with the waves, which are normally incident to the initial coastline, will be such that the longshore transport rate is equal to $\frac{1}{2}S_r$.

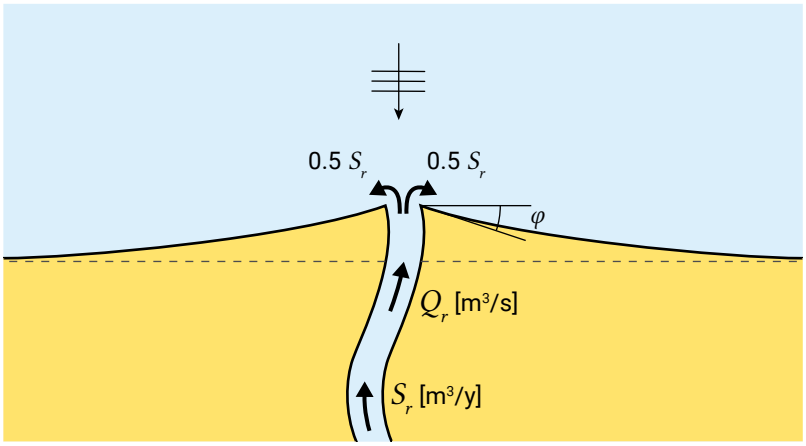

Figure 8.30: Development of deltaic coastline with waves that are normally incident to the original coastline and without tidal influence. The river discharge is Q_r and the sediment discharge S_r. The angle ϕ is determined by the sediment discharge and wave conditions.

Man-induced changes in the characteristics of the river (e.g. sand mining in the river bed or damming of the river for irrigation or hydro-power purposes) might change the natural accreting tendency of the coast to an eroding tendency in the vicinity of the river outlet (see Fig. 8.31).

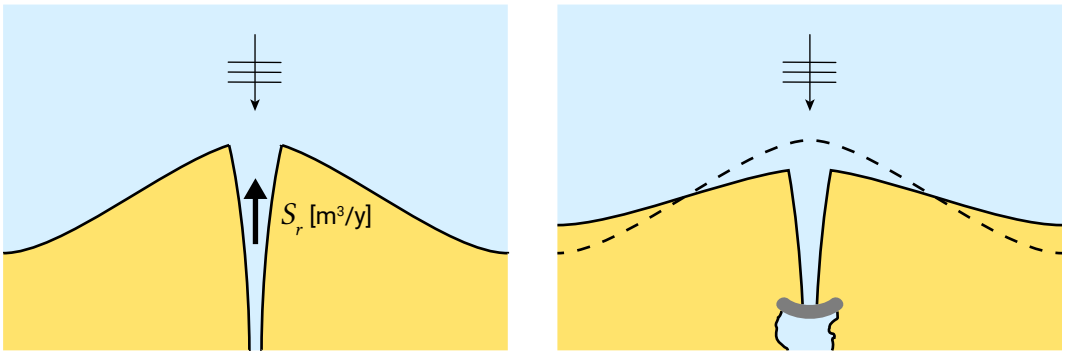

Figure 8.31: Delta erosion after the sediment supply is cut off. Due to wave-induced longshore transport gradients, sediments are redistributed along the coast, resulting in erosion of the delta (cf. the development of a shoreline perturbation in Sect. 8.4.4).

For obliquely incident waves, the redistribution of the river sediment along the shore is asymmetric. Also, a sand spit can develop in these cases due to a strong longshore

sediment transport, as already described in Sect. 8.4.5. Section 2.7.3 gives examples of various wave-dominated deltas. The Ebro delta (Fig. 2.49) and the Senegal delta (Fig. 8.32) are examples of spit formation in a deltaic environment.

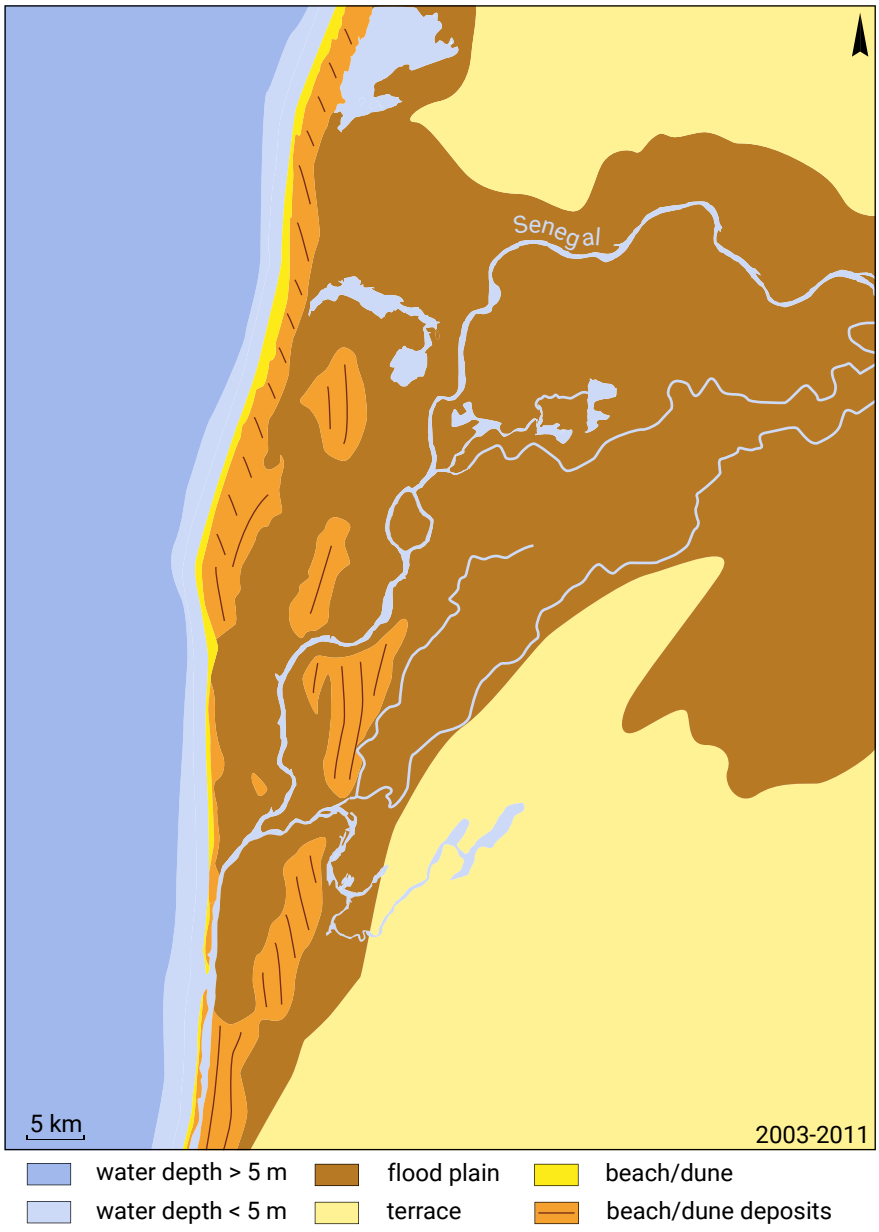

Figure 8.32: Senegal river delta.

9

Coastal inlets and tidal basins

9.1. Introduction

In the previous two chapters, we mainly focused on wave-dominated coastal systems. These coastal systems, with well-developed beaches, are typically shaped by waves and wave-generated currents. The moderate to high wave energy (see Sect. 4.3.1) overwhelms any tidal energy present, for which reason these coasts are called wave-dominated. The shoreline in wave-dominated environments is characterised by elongated sediment (mainly sand) bodies. These include spits (Ch. 8), alongshore bars (Ch. 7) and beaches. Besides straight coastlines – whether or not they are interrupted by breakwaters, groynes, rivers and lagoon entrances – pocket beaches may also fall into the wave-dominated category.

So far we have only encountered tidal influence in deeper water outside the surf zone, around long structures and at low wave-energy coastlines. In general, tidal conditions dominate where wave energy is relatively low. The word 'relative' is crucial here, since it is the *relative* influence of waves and tides that determines the morphology (Fig. 4.13). Tide-dominated environments may occur due to restricted fetch or where incident wave energy is trapped or reflected. Such environments include tidal basins.

As discussed in Ch. 2, tidal basins are the result of breakthroughs and flooding of low-lying areas due to the global rise of the post-glacial sea level. Processes contributing to basin formation include tectonic subsidence, fluvial erosion and glacial action. Bottom subsidence of the coastal plains due to human interference (peat harvesting, impoldering and water, oil and gas extraction) can be an additional cause for the creation of tidal basins. Finally, basins can also evolve due to the formation of barriers enclosing a body of water.

A few examples of tidal basins are Chesapeake Bay, San Francisco Bay, Waddenzee and Baie d'Arcachon. All of these were created by flooding of low-lying coastal plains on

coasts with a strong tidal energy and with little sediment discharge from rivers. The emphasis in this chapter is on understanding the relevant physics in order to make predictions about changes, which are expected to occur on the scale of the tidal basin itself. This does not only concern changes in water motion, but also changes in the physical structure of the basin, i.e. the morphology. Relevant practical questions are amongst others:

- What is the response of a tidal basin to sea level rise (does the basin floor follow the sea level rise by sedimentation)?
- What are the consequences of dredging for navigation or sand extraction (does sedimentation increase)?
- What is the effect of a dike or breaching of a beach barrier (does a new tidal basin form)?
- What are the impacts of land reclamation (does the inlet close, does sedimentation or erosion occur)?
- How do basin changes influence the adjacent coast (will the adjacent coast erode or accrete)?

The answers to a few of these practical questions are discussed in the final section of this chapter, Sect. 9.8, where the knowledge acquired in the preceding sections is applied. We start this chapter with a discussion of general basin and inlet types (Sect. 9.2) and a description of the main morphological units of tidal inlet systems (Sect. 9.3). The subsequent three sections focus on the three important morphological units, viz. the ebb-tidal delta (Sect. 9.4), the entrance or inlet channel (Sect. 9.5) and the inner basin (Sect. 9.6). Besides relevant processes, these sections discuss how the stability of these morphological units can be described with empirical relations, relating the geometric properties to hydraulic boundary conditions. In Sect. 9.7 the mechanisms responsible for net sediment import into and export from basins are discussed.

9.2. Basin and inlet types

9.2.1. Bays, lagoons and estuaries

Three distinct types of tidal basins can be discerned (Carter (1988), see Table 9.1 for a summary):

- *Tidal lagoons* are basins that are enclosed by wave-shaped coastal barrier islands or barrier spits. Almost 12 % of the world's coastline is made up of barriers, many of them enclosing lagoons. The Dutch Wadden Sea is a good example. Due to the presence of the barriers, the penetration of waves into the lagoons is limited. Water flows into the lagoon with the flood and out during the ebb through passes or inlets between the barrier islands. These narrow waterways are also called throats or gorges. In most cases the tidal fluxes in and out of the lagoon are balanced over a tidal period. Sometimes it is a sub-surface rather than a surface

connection with the open sea that allows the water levels in the basin to be modulated by the tide. Where the basins proper are tide-dominated, the inlets to the basins experience both wave and tidal influence. Sediment tends to be finer in the more protected regions away from the entrances. The freshwater run-off is typically limited;

- In the absence of barrier islands, *tidal bays* are basins that are more open to the deep water of the sea or ocean. Bays have a limited freshwater run-off. The Baie de St. Michel is a good example. Waves can enter unhindered, but generally lose their energy not far from the entrance (mouth) before the shorelines in the bay are reached, due to depth-limited breaking (Sect. 5.2.5) and bottom friction;
- *Estuaries* are different from bays in that they experience a (strong) fresh-water run-off. Therefore, the seawater in these basins is measurably diluted by fresh-water. But unlike river mouths, estuaries are typically tide-dominated; the water motion in estuaries is controlled more by the tides than by the river discharge. Also, sedimentation is primarily controlled by import from the adjacent coastal region. The coarser sediment (sand) settles predominantly in the seaward regions, while the finer sediment (silt) settles in the more protected landward regions. The entrances of some estuaries may be constricted by the development of spits, shoals or barriers across their mouths, as a result of wave effects.

Table 9.1: Distinctive attributes of tidal environments (according to Carter, 1988)

Environment	Distinctive attributes
Tidal bays • Baie de St. Michel, France (Normandy/Brittany) • West coast of South Korea • Hangzhou Bay, China	• High levels of wave dissipation • Little freshwater runoff
Tidal lagoons • Wadden Sea, Netherlands/Germany/Denmark • Laguna Madre, Texas	• Waves excluded by barriers • Tidal flows via passes • Infilling wetlands • Little freshwater runoff
Estuaries • Bay of Fundy, Nova Scotia • Bristol Channel	• Waves possibly excluded by barriers or sand shoals • High freshwater runoff

The three types of basins mainly differ in terms of the characteristics of the entrance and the importance of freshwater run-off. The basins are either interlinked with the

adjacent coast or barrier islands through tidal inlets, openings in the shoreline, such as between two barrier islands, or wider entrances such as estuary mouths. Freshwater run-off and hence the interaction between salt- and freshwater is a fundamental characteristic of estuaries (see Intermezzo 9.1). Based on the degree of mixing of the two water masses, estuaries can be classified as stratified, partially mixed/stratified and mixed or homogeneous. One of the phenomena related to fresh-salt water mixing is the turbidity maximum. In this book we mostly neglect the mixing between freshwater and saltwater, a topic which would require a rather extensive treatment. We therefore mostly assume a negligible influence of freshwater run-off in this chapter.

Intermezzo 9.1 Estuarine circulation

In estuaries, there exists a transitional region between salt- and freshwater. In the case of small and medium freshwater discharges the salt-freshwater transition region is located near the estuary head (the location of the river mouth). Seaward of the transition region the tidal water motion dominates and the water is mainly saline. More landward, the river flow dominates and the water is mainly fresh. The pressure gradient associated with the density difference between the saline (of sea origin mainly) water and the upstream fresh river water drives a vertical flow circulation, the so-called estuarine circulation (see Fig. 9.1). When the freshwater meets the saline water, the less dense freshwater overrides the denser saline water. Hence, along the bottom the net (i.e. tidally-averaged) flow is in the landward direction, while it is seaward along the surface. Note that wide estuaries may show little salinity variation with depth, but considerable variation with width; as a result of Coriolis, the denser flood and less dense ebb currents are concentrated along different banks.

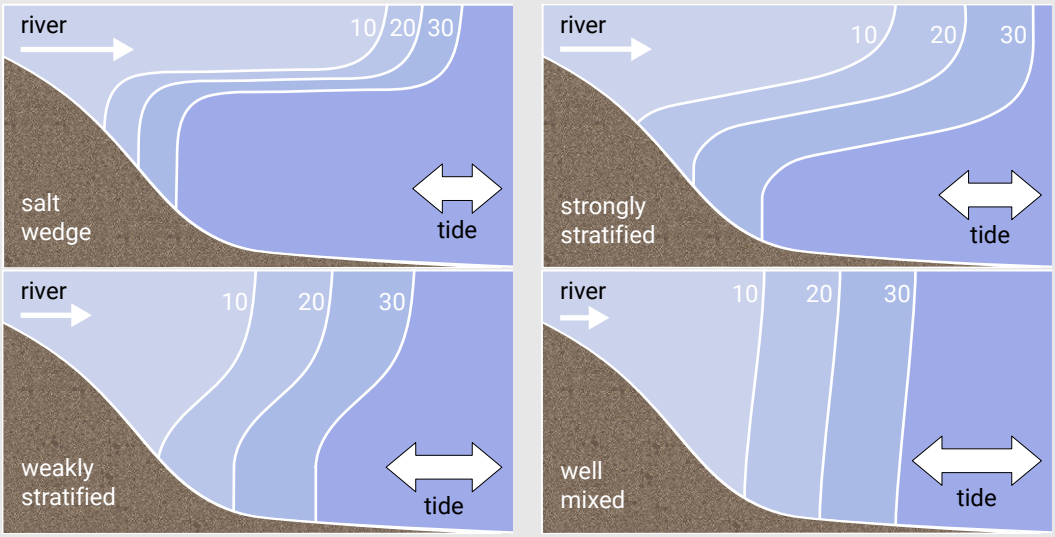

Figure 9.1: Isohalines (lines of equal salinity) and estuarine circulation for four different salinity distributions. The basic flow pattern is a surface flow of less dense freshwater towards the ocean and an opposite flow of salty seawater into the estuary along the bottom.

As suspended sediment concentrations are higher near the bed, estuarine circulation promotes sediment import. A related phenomenon is the formation of a turbidity maximum, which is the concentration of fine sediments not far from the end of a saltwater wedge. It occurs since saltwater stimulates the flocculation of clay particles being transported by the river.

When discussing lagoons, we assume an approximately equal influx and outflux of water (as is the case for the Wadden Sea basins). This means that we exclude lagoons for which the seawater inflow exceeds the outflow due to evaporation. These lagoons are called sabkhas and are common on low-latitude arid coasts.

In this book we often use the two distinct types of Dutch coastal basins, the estuaries of the Southwest Delta[1] and the Wadden Sea barrier inlet systems, to illustrate the above described differences. They are indicated in Fig. 9.2. Three of the estuaries in the Southwest Delta were partly or entirely closed as part of the Delta Works (numbers 3, 4 and 5 in Fig. 9.2). The Delta Works are a series of dams, sluices, locks, dikes and storm surge barriers built between 1950 and 1997 (Maeslant storm surge barrier) to protect a large area of land around the Southwest Delta from the sea. In the Dutch Wadden Sea system, two closure barriers have also been constructed in the 20th century (numbers 1 and 2 in Fig. 9.2). The morphological response to (semi-)closures of tidal basins is further discussed in Sect. 9.8.

9.2.2. Hydrodynamical classification

Following our preferred process-based classification, we could make a slightly different distinction between the different basin types than in Sect. 9.2.1.

Tidal basins (estuaries, bays, lagoons) are of course *tide-dominated*, see Sect. 2.7.1. The influence of the tide is evident from tidal current ridges, extensive salt marshes and tidal flats. In tidal basins with an extremely strong tide (amplitudes of the order of 10 m) the tidal wave is deformed so strongly that a tidal bore may develop (see Intermezzo 5.7). Examples of such basins are the Amazon, the Qiantang and the Severn.

We can distinguish between tidal basins with and without a strong river influence:

- Examples of tide-dominated coastal systems with strong river influence are the estuaries of the Western Scheldt, the Thames, the Elbe (all three in the winter season), the Seine, the Yangtze, the Mekong, the Ganges-Brahmaputra, the Fly River, Chesapeake Bay and the Rio de la Plata;

[1] The southwest coast of the Netherlands is often called our Delta Coast. It is here that Rhine, Meuse and Scheldt rivers exit into the North Sea. However, there is no real delta present and these rivers have mainly indirectly contributed to the Holocene formation of this coastal area; marine feeding (with reworked Pleistocene riverine sediments) was the major source of sediment.

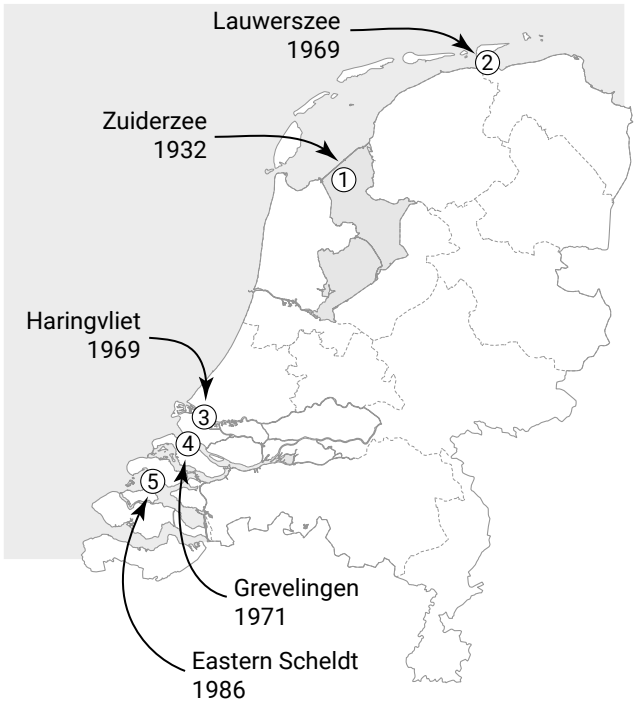

Figure 9.2: Closure of tidal basins in the Dutch coastal system, with the estuaries of the southwestern delta area and the northern Wadden Sea. The Western Scheldt (not numbered) is located to the south of the Eastern Scheldt.

- Examples of tidal basins without strong river influence are the (eastern) Wadden Sea, the (present) Eastern Scheldt, the Gulf of St. Lawrence, the Colorado River and San Francisco Bay (the latter two in summer).

In the entrance area of the basins (the inlet, see Intermezzo 9.2), which is maintained by the tide, wave and tidal influences are combined. The tidal range outside an inlet depends primarily on the ocean tides and their interaction with the continental shelf. Micro-tidal, meso-tidal and macro-tidal ranges can be distinguished (see Sect. 4.4.1). The wave conditions are generated further seaward and thus independent of the inlet. Wave energy can be classified as low, medium and high according to Sect. 4.3.1. Since both wave energy and tidal energy in the entrance area of basins are independent of the inlet system configuration, they are very suitable to be used for inlet classification.

Hayes (1979) and Davis Jr. and Hayes (1984) distinguish five hydrodynamical classes, from wave-dominant to tide-dominant, based on the above-mentioned tidal range and wave energy classification (see Sect. 4.4.2). Each class develops its own specific morphologic features. For instance, in Sects. 9.3 and 9.4 we will see that the relative sizes of the flood- and ebb-tidal deltas and the mechanism for sand-bypassing of entrances are dependent on the relative wave/tide dominance. Barrier islands are typically wave-built features and the entrance areas to barrier tidal inlet systems (see nr 7 in Fig. 2.42) are typically mixed-energy or wave-dominant systems. As an example, Fig. 9.4 classifies the Frisian Inlet (Friesche Zeegat in Dutch), one of the inlets of the Dutch Wadden

Sea as a mixed-energy environment. The Dutch Delta Coast can be classified as a mixed-energy environment as well.

Intermezzo 9.2 Terminology

Note that the term 'tidal inlet' generally refers to an opening in the shore that provides a connection between the ocean or sea and a basin, that is maintained by tidal currents. Alternatively, the term 'inlet' is used in a broader sense to describe the entire morphological system consisting of the entrance itself, the ebb-tidal delta (outside) and the flood basin, with possibly a distinct flood-tidal delta. In this book, we want to make a clear distinction between the two definitions and will use the term *inlet* only to refer to the short, narrow waterway that lets the tide in (the inlet, gorge or throat). The gorge is usually dominated by a main channel, but some are split by a shoal or a small island (cf. the Frisian Inlet, between the isles of Ameland and Schiermonnikoog in the western (Dutch) Wadden Sea). We use the term *tidal inlet system* to refer to the combined system of inlet, ebb-tidal delta and basin.

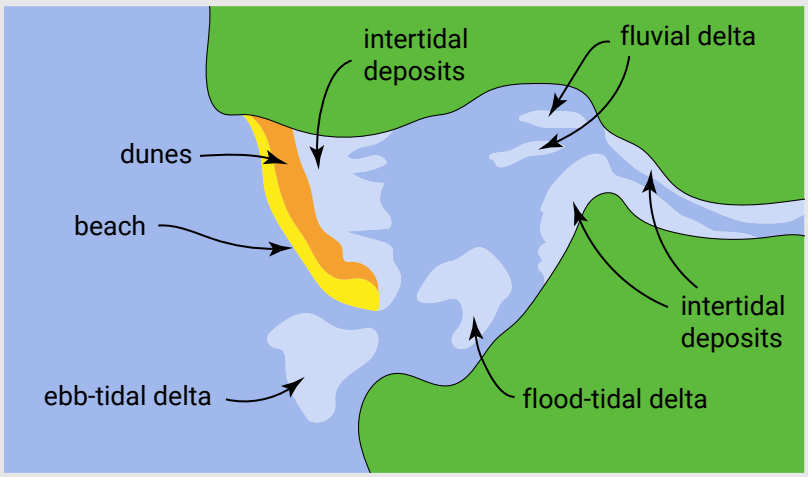

Figure 9.3: An estuary along a wave-dominated coast with a barrier constricting the mouth. On either side of the narrow inlet deltas are present, built by the flood and ebb tide respectively (see Sect. 9.3.2). Loosely based on Dingle Bay and Danube delta.

Tidal inlets mostly exist at places where there are breaks in a barrier coast. The term tidal inlet is generally not used for entrances to estuaries or bays with large unconstricted mouths, such as the Western Scheldt, although the tide may enter through inlet channels cutting through sand shoals. We will just speak of an *estuary entrance* or *mouth*. Entrances to estuaries along wave-dominated coasts or lagoons may also be constricted by wave-built barrier spits (Fig. 9.3 and Ch. 8). In that case it makes sense to speak of an *inlet*.

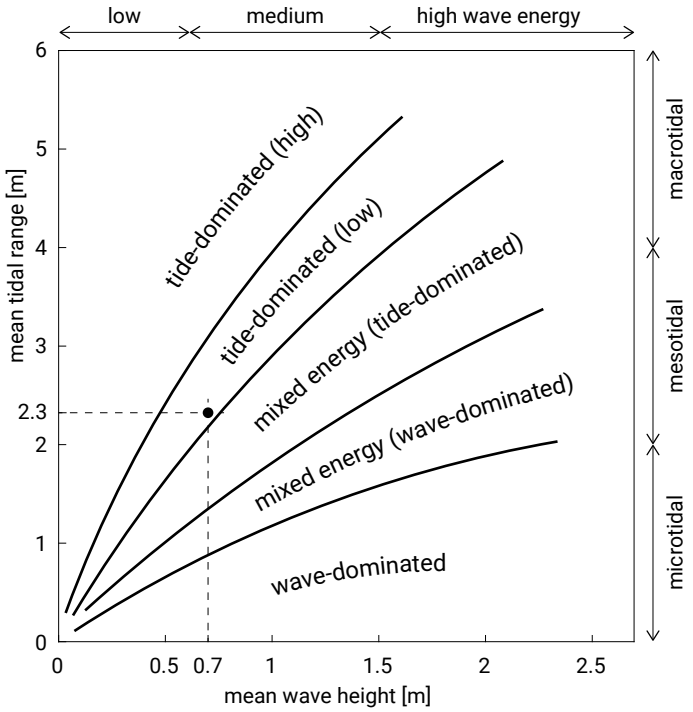

Figure 9.4: Hydrodynamical classification according to Hayes (1979) and Davis Jr. and Hayes (1984) with, as an example, the classification of the Frisian Inlet (Fig. 9.5), one of the inlets of the Dutch Wadden Sea. Every class covers a spectrum of tidal ranges and wave heights; the relative effects of waves and tides rather than the absolute tidal ranges and wave height are important.

9.2.3. Hydraulic boundary conditions and geometric controls

The hydraulic boundary conditions are crucial for determining the morphology of tidal basins and inlets. Not only is the relative dominance of waves or tides important, but other hydraulic conditions also control the morphodynamic behaviour. At the same time, the basin morphology has an influence on the hydraulic conditions. Due to this feedback mechanism, the basin in essence determines its own evolution, although external conditions such as sediment availability and storm surges also play a role.

The following geometric and hydraulic controls will be further explained in this chapter:

1. The *surface area of the basin*, in combination with the *tidal range*, determine in principle the *tidal prism* (Intermezzo 9.3), the volume of water that has to flow in and out through the inlet during one tidal cycle (excluding any freshwater). For a short basin[2], this is usually estimated by multiplying the mean surface area of the estuary by the mean tidal range in the estuary. This is only valid in the case of a negligible river discharge, since a river flow will also contribute to the filling of the basin. The tidal prism has empirically been found to determine the equilibrium, or minimal stable cross-sectional channel area of an inlet (Sect. 9.5.2). The channel cross-sectional area and volume (Sect. 9.6.2) as well as

[2]Try to answer the following question: why is this method to estimate the tidal prism only appropriate for a short basin? See also Intermezzo 9.3 and App. E.

the sand volume stored in the ebb delta (Sect. 9.4.3) have also been empirically related to the tidal prism;

2. The morphologically active part of basins consists of deeper areas, where the flow is concentrated during lower tidal water levels and of tidal flats, that are covered during higher water and exposed during lower water. Because of the different geometry (surface area, water depths) during low tide and high tide, the high tide propagates at a different phase speed (see Sect. 5.7.4) than the low tide. This can either strengthen or weaken the magnitude of the maximum flood flow, compared to the maximum ebb flow (and thus shorten or lengthen the flood duration compared to the ebb duration). This leads to a net import or a net export of sediment respectively and hence steers the morphological development of the basin in time. The important controls for the tidal distortion are the *surface areas at low and high water* and the *mean water depth at high and low water*, both of which are determined by a combination of *tidal range, channel depth and intertidal storage areas or flats* (see Sect. 9.7.2);
3. Tidal waves propagating into basins may be either progressive or standing, or a mixture of the two, depending on, amongst other factors, the *length of the basin* (see Sect. 5.7.3). The length of tidal basins is generally much shorter than the tidal wavelength. In short tidal basins, the tidal wave is reflected and has a standing character. The tidal range in the basin is of similar magnitude as in the open sea. In longer basins, resonance can occur when the basin length is approximately a quarter of the tidal wavelength (or a multiple of that). The tidal amplitude will then increase. The longer the basin, the more the tidal wave is dampened by friction. The resulting weakening of the reflected wave, assures that the tidal wave has a stronger propagating character;
4. In very short basins (length much smaller than the tidal resonance length), the combination of *tidal range, channel depth and intertidal storage areas or flats* results in a different type of asymmetry than asymmetry between ebb and flood duration (see under 2.). In the case of a short basin, the duration of the flow change is different at §1.1 ~~HW and at LW slack~~ §1.1 HWS and LWS [p417] (see Sect. 5.7.4). As we will discuss later, this asymmetry is of great importance for the net transport of fine sediment in the basin (Sect. 9.7.3).

Intermezzo 9.3 Tidal prism

The tidal prism is defined as the volume of water entering a tidal basin during flood tide and leaving the basin again during ebb tide. Neglecting freshwater outflow, the tidal prism P is equal to half the time integral of the inflow and outflow during a tidal cycle:

$$P = \frac{1}{2}\int_0^T |Q(t,0)|dt \tag{9.1}$$

with $Q(t, 0)$ the tidal discharge in the inlet of the basin.

For a short basin the size of the basin is small compared to the tidal wavelength, such that the spatial variation of the water level in the basin can be neglected (Sect. 5.7.3). From Eq. 5.108, we have $Q(t, 0) = \partial\eta_0/\partial t A_b$ with A_b the surface area of the basin. With this, Eq. 9.1 can be approximated as $P = A_b H$. Therefore, the tidal prism is often estimated by multiplying the mean surface area of the basin by the mean tidal range H in the basin.

For longer basins, the spatial variation of the water level in the basin cannot be neglected and the full Eq. 9.1 must be computed. Also, for quite long basins the tidal wave may exhibit a (partly) standing wave pattern with nodes and antinodes in the surface elevation and discharge (Fig. 5.63). A node in the discharge at a particular location implies that no water is exchanged through that cross-section during the tidal cycle. As a consequence, only the part of the basin from the inlet to the antinode contributes to the tidal prism. An example is given in App. E.

Under calm conditions, a basin like the Wadden Sea can be thought to consist of multiple basins – each with their 'own' tidal prism – separated by tidal divides or watersheds (Fig. 9.5).

9.3. The main morphological elements

9.3.1. Introduction

The morphodynamic behaviour of tidal inlet systems is highly dynamic and strongly determined by the tide. As an illustration of the complex tidal dynamics, Fig. 9.5 and Table 9.2 give an overview of the Wadden Sea. Many of the Wadden Sea inlet systems have distinct catchment areas, which in calm conditions are separated by a watershed (or tidal divide or *wantide* – from the Dutch *wantij*). The locations of the tidal divides in the Wadden Sea are not fixed, but can move due to human interference.

Table 9.2: Wadden Sea basin data (Data from Lodder et al., 2019).

Inlet	A_b [km^2]	H [m]
Texel	655	1.65
Eierland	157.7	1.65
Vlie	715	1.9
Ameland	276.3	2.15
Pinke	49.6	2.15
Zoutkamperlaag	105	2.25

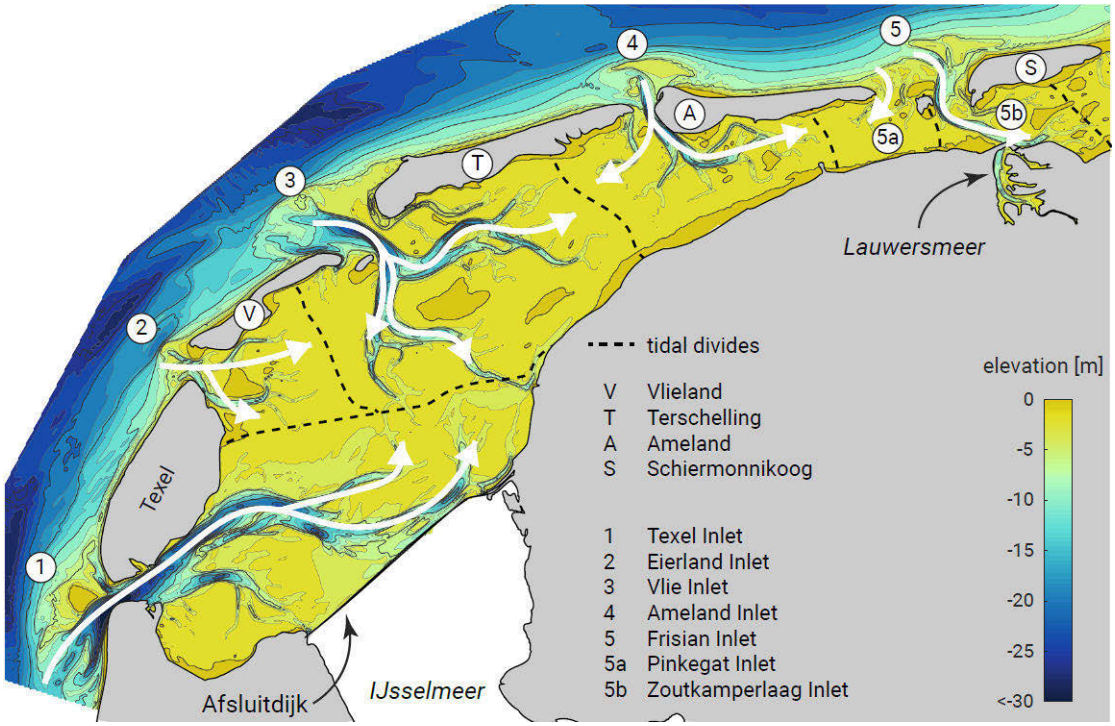

Figure 9.5: Wadden Sea tidal dynamics model, displaying the types of tidal passes and the wantide zones. The movement of the tide on the North Sea is from left to right.

At watersheds the inflowing flood currents through different inlets meet and tidal currents are practically zero. The watersheds are conducive to fine-grain deposition. This is because the low current velocities permit the fines to settle. Large tidal eddies are common along the back barrier flanks, sometimes superimposed on a unidirectional stream creating a spiralling current. Each catchment area exchanges large volumes of water with the outside area (the tidal prism – dependent on the tidal range and the surface area of the catchment area). This results in large inflowing flood and outflowing ebb currents that keep the inlets from closing naturally. The basin area consists of deeper areas where the flow is concentrated during lower tidal water levels and of tidal flats that are covered during higher water and exposed during lower water. In the Wadden Sea, the tidal flats are covered by salt marshes, but they may be covered with mangroves in other climatic regions (Sect. 2.6.6).

Although the Wadden Sea can be conceptually divided into separate basins during calm conditions, wind-driven currents and storm surges may lead to inter-basin flow and transport over the tidal watersheds (Duran-Matute et al., 2016).

9.3.2. Tidal deltas

Because of the large tidal discharges and hence velocities in the inlet or estuary mouth, there is a strong sediment exchange between the basin and the outside area. Especially in constricted inlets, this leads to the formation of extensive sand deposits at either side of the entrance, which are called tidal deltas. In the divergent ebb-tidal discharging

flow, the flow velocities decrease and sediment is deposited, thus creating the ebb-tidal delta. Just as the ebb-tidal delta consists of material deposited by the diverging ebb flow leaving the inlet, the flood-tidal delta is created by sediment deposited by the inflowing flood current. Consequently, basins with large tidal ranges (and limited wave influence) tend to have well-developed ebb- and flood-tidal deltas and very deep inlet gorges.

The ebb- and flood-tidal deltas are bisected by channels followed by the tidal currents. The flats and channels exhibit a highly dynamic behaviour; their locations are continuously changing with time.

Figure 9.6 shows a sketch of a barrier inlet system with typical flood- and ebb-tidal deltas. The boundaries of the ebb-tidal delta can be found via the no-inlet bathymetry, where the differences in bottom height are nil between the actual and no-inlet bathymetry of the adjacent coast (Fig. 9.20).

A typical ebb-tidal delta includes:

Marginal flood channels The term *marginal* in the context of marginal flood channels is used to indicate the positioning of the flood channels to the sides of the inlet. It is *not* used to indicate that they are of marginal importance or marginal in size; for instance, in the estuaries at the SW of the Netherlands the marginal flood channels are quite distinct.

Main ebb channel The occurrence of separate ebb- and flood-dominated tidal channels can be explained as follows. In the beginning of the flood cycle, the water in the main ebb channel continues to flow seaward as a result of inertia. As a consequence, water initially enters the basin via the path of least resistance, around the margin of the delta.

Channel margin linear bars These flank the ebb-tidal channel and are built up from deposits as a result of the interaction of flood- and ebb-tidal currents with wave-generated currents. In the Dutch inlet systems, these distinct bars are not present; instead, there are wide flats.

Terminal lobe A rather steep seaward-sloping body of sand, which forms the outer end of the ebb-tidal delta.

Swash platforms and bars The main ebb channel is flanked by swash platforms, which are broad sheets of sand. On these swash platforms, isolated swash bars can be recognised, built up by swash action of waves (the water that washes up on the platforms after waves have broken). Marginal flood channels are usually found between the the coast of the barrier islands and the swash platforms.

The flood-tidal delta may be fan- or horseshoe-shaped, with a flood ramp that slopes upward ending in the ebb shield, that is, the most elevated outer edge of the flood-tidal delta (Fig. 9.6). The ebb shield is the flood-tidal delta's equivalent of the terminal lobe and helps to divert ebb-currents along the margins of the flood-tidal delta. The flood currents follow the shallowing flood ramp and the flood channels that continue from

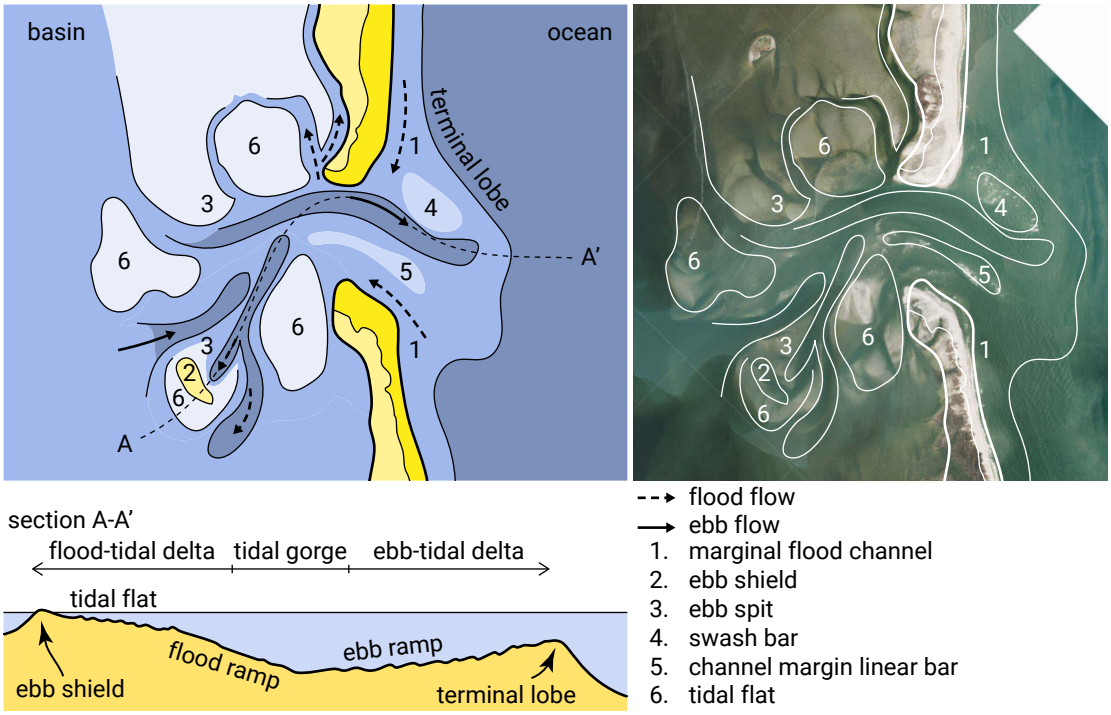

Figure 9.6: Sketch of the morphological elements of a tidal inlet system based on a photo from an inlet near Sheep Island, North Carolina (2016 imagery from NC OneMap Geospatial Portal (2020), 'Credits' on page 579). The lower part of the figure shows a cross-section of the depth variation along the inlet system.

the flood ramp. The ebb currents (and their interaction with the flood currents) are responsible for the ebb spits and the bar-like spillover lobes.

For relatively small basins with abundant sediment supply, such as the Wadden Sea, the flood-tidal delta spans the entire basin area, viz. flood-tidal deposits are found everywhere in the basin. For the Wadden Sea we therefore generally only speak of the outer delta () and the basin; the term flood-tidal delta is not used as a separate morphological unit. This is quite contrary to, for instance, the USA East Coast basins, which have relatively small, distinct flood-tidal deltas (as in Fig. 9.6). In these cases, the flood-tidal deltas can be regarded as the morphologically active parts of otherwise morphologically inactive basins. Following our Dutch experience, where the entire basin acts as a flood-tidal delta, we will focus on the ebb-tidal delta in Sect. 9.4. The flood-tidal delta is not treated separately, but in Sect. 9.6 on basins.

The overall morphology of the tidal deltas, especially the ebb-tidal delta, depends on the combined action of waves and tides. Wave action is generally considered to act as a bulldozer on the ebb-tidal delta morphology (Hageman, 1969); it moves sediment onshore and limits the area over which the ebb-tidal delta can spread out. Hence the ebb-tidal delta morphology is generally determined by the (dynamic) balance between a net offshore-directed sediment flux induced by the inlet currents (building up the ebb-tidal delta) and a net onshore-directed sediment flux induced by offshore waves (removing sediment from the ebb-tidal delta). It is the flood-tidal delta that benefits

from this onshore sediment flux. Therefore, for tide-dominated entrances, viz. with limited wave action, ebb-tidal deltas tend to be large relative to the flood-tidal delta. For wave-dominated entrances, the ebb-tidal deltas tend to be relatively small, whereas the flood-tidal deltas are well developed, with flood shoals that can be emergent at low tide.

9.3.3. Basin characteristics

The tides fill and empty the basin via channels that cut through (large) lower and higher tidal sand and mud flats. The intertidal flats serve to accommodate the tidal prism: at low water these flats fall dry, while at high water they are submerged. Intertidal flats are called *platen*, *slikken* or *wadden* in Dutch[3]. Only the most landward, higher parts remain dry at high water; these vegetated parts are named *supra*tidal flats or salt marshes (in Dutch: *schorren* or *kwelders*[3]).

The combined action of amongst others centrifugal forces, earth rotation (Coriolis) and inertia, causes the existence of separate ebb and flood channels, channel sills and channel bifurcations (Sect. 9.6). In general, ebb-dominant channels follow a meandering course, whereas flood-dominant channels shoal landwards.

A very good description of the ebb and flood channel systems is found in Van Veen et al. (2005). It was originally published in Dutch by Van Veen (1950), translated and annotated by Van Veen et al. (2002) and republished by Van Veen et al. (2005). Along barrier island coasts, the basins are often rectangular or nearly square, and the channel structure is often more branched than braided (Fig. 9.7). The branching structure is found to show fractal characteristics, viz. if you zoom in on a part, you find subsets that look like the whole figure.

In the case of larger rivers discharging into tidal basins, the tidal basin is often funnel-shaped, and the channel structure is not as branched, but is potentially braided (Figs. 9.8 and 9.9). In areas without width restriction (very large estuaries, e.g. Thames estuary), the channels followed by the flood current are generally different from the channels followed by the ebb current. They may connect due to meander action. If the width is more restricted (e.g. Scheldt estuary), the flood and ebb currents partly follow the same pathways.

Section 9.6.1 describes the complex geometry of ebb and flood channels in a bit more detail.

[3]The terms *slikken* and *schorren* are mostly used for the southwestern delta area, whereas the terms *wadden* and *kwelders* are exclusively used for the Wadden Sea.

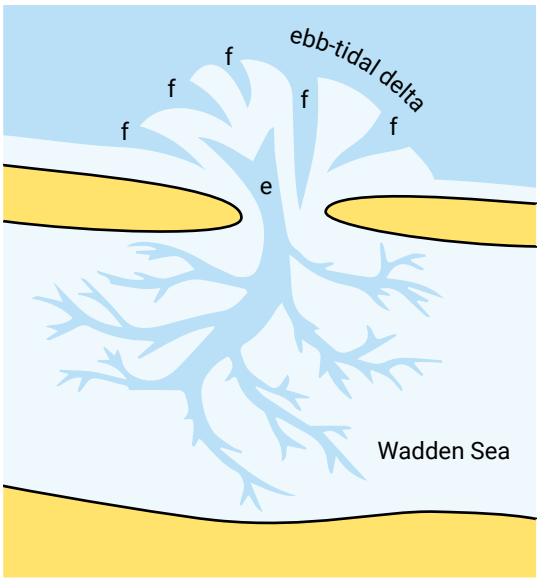

Figure 9.7: Sketch of ebb and flood channels in a typical Wadden Sea basin with an inlet between dune-islands, several flood channels coming in (indicated with §1.1V§1.1f) and an ebb channel (§1.1E§1.1e [p423]) and delta with a tendency to turn to the left, due to the ebb tide leaving to the left, consistent with the propagation direction of the tidal wave along the Dutch coast (see Fig. 3.31). After Van Veen et al. (2005).

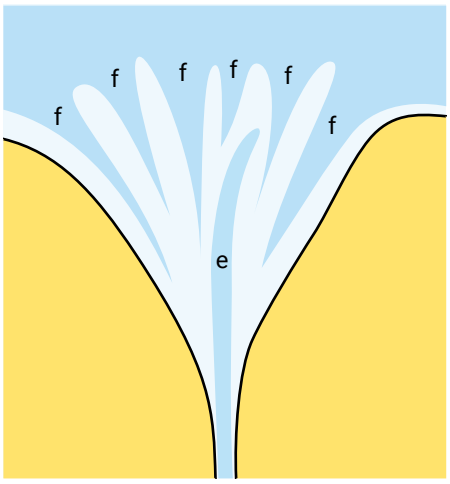

Figure 9.8: Sketch of ebb (§1.1E§1.1e) and flood channels (§1.1V§1.1f [p423]) in a wide estuary (for example, the Thames or Wash). Meander action may bring the ebb channel in connection with any of the flood channels (after Van Veen et al., 2005).

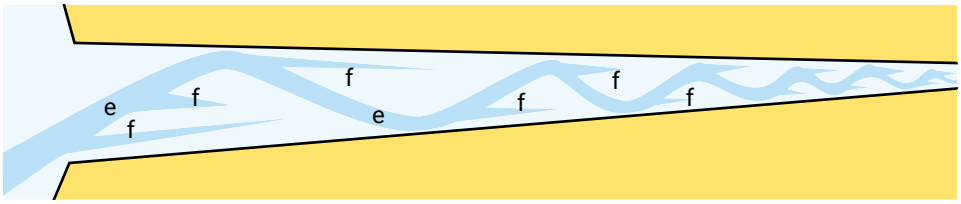

Figure 9.9: Sketch of an ideal system of ebb (§1.1E§1.1e) and flood (§1.1V§1.1f [p423]) channels (Scheldt estuary). It has a meandering main (ebb) channel and flood channels starting in every bend. The latter have a double function; viz. 1. filling the tidal sand flat in the inner bend of the main channel; 2. serving the cut-off current of the bend. After Van Veen et al. (2005).

9.4. The ebb-tidal delta or outer delta

9.4.1. Waves and currents at the outer delta

Clearly, the morphology of the outer delta is highly complicated and variable. This means that waves and currents encounter a very complex bed topography, with length scales which are not much larger than the wavelength of wind waves or swell, for instance. Via refraction, diffraction and reflection, this can lead to complex wave patterns with a strong spatial variability.

The currents in the vicinity of a tidal inlet are partly tidal, partly wave-driven and partly wind-driven. The tidal currents are primarily concentrated in the main channels, the wave-driven currents in areas where waves are breaking. Wind-driven currents occur mainly during storm events and are therefore rather episodic, but nonetheless important (though often forgotten in modelling studies!).

Wave patterns

As to the overall pattern of the waves, there are a few points to consider, such as the penetration of wave energy into the gorge and the sheltering from wave exposure in various parts of the system. Let us consider a typical inlet between two barrier islands, representative of one of the Wadden Sea inlets. In the case of normally incident waves, the entire delta edge and the gorge are exposed to wave energy. Due to refraction, the wave crests turn to run more and more parallel to the depth contours. Therefore, wave energy is concentrated in the central front edge of the ebb-tidal delta, whereas the side lobes of the delta will be less exposed than the central front part. Due to breaking on the shoals of the outer delta, the gorge will also be less exposed (Fig. 9.10).

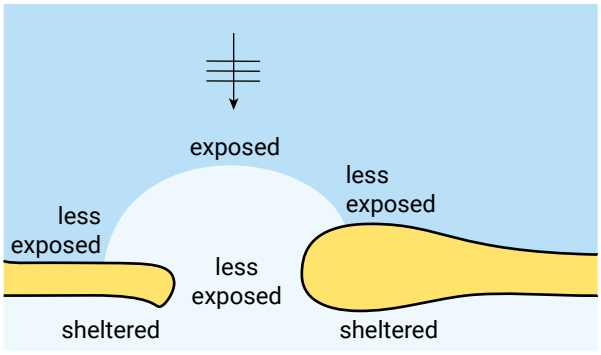

Figure 9.10: Exposure of outer delta to normally incident waves.

In the case of obliquely incident waves, one side lobe will be exposed, while the other will be sheltered. By implication, the wave climate at the sheltered side lobe will be different from that offshore or at the front edge of the delta. The western lobe in Fig. 9.11, for instance, will be fully exposed to westerly waves, less exposed (due to refraction) to northerly waves and sheltered from easterly waves. As a consequence,

wave-driven longshore currents in the vicinity of this western lobe are predominantly eastbound. Similarly, the currents near the eastern lobe are predominantly westbound.

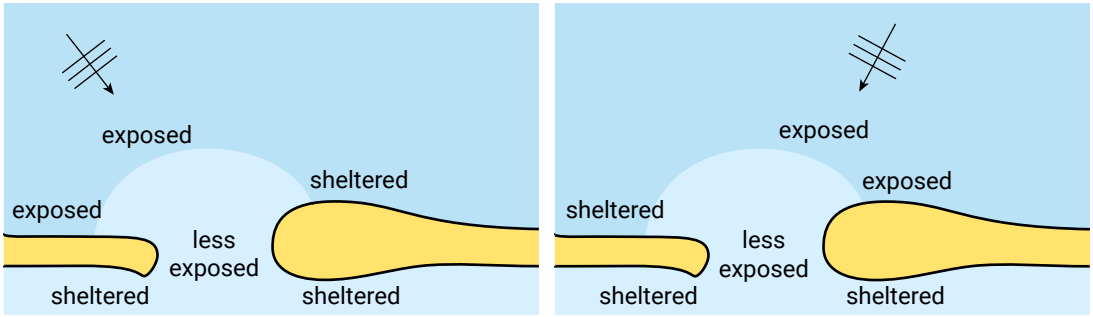

Figure 9.11: Sheltering and exposure to obliquely incident waves.

Another aspect which deserves attention is wave penetration into the inlet system. Clearly, the barrier islands provide considerable shelter to the basin, but wave energy can penetrate through the gorge. The latter, however, is sheltered to a certain extent from the open sea by the outer delta. Hence, the wave energy which reaches the back of the gorge is much less than offshore. Subsequently, this energy usually radiates into the basin, where the energy density and the wave height rapidly decay. As a consequence, the wave energy which penetrates from the open sea into the basin is usually rather small and is restricted to the area right behind the gorge. Wave energy further into the basin is generally due to waves generated inside the basin, if the prevailing wind meets a sufficiently long fetch.

A drastically different situation may arise if *channelling* of the wave energy occurs (Fig. 9.12). This phenomenon is associated with trapping of the waves in the channel if the wave ray direction is almost parallel to the banks. In such a case, areas which are at first sight sheltered from sea waves can be exposed to relatively high wave energy and thus to much more erosion than expected.

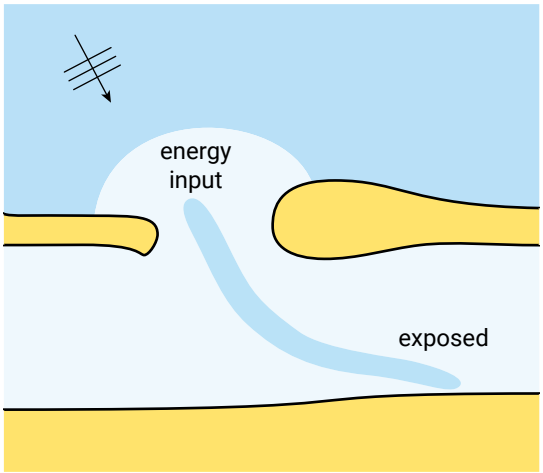

Figure 9.12: Exposure of a sheltered area due to wave channelling.

The complexity of the bed topography and the mixture of sea/swell waves coming from offshore, and locally generated waves of a much shorter period inside the basin,

make wave modelling for tidal inlets particularly difficult. A model for long-crested monochromatic waves (i.e. wave fields with one direction, one period and one height in each point of the model domain) will not work here. Instead, one would need a wave model which allows for irregular, short-crested waves of various periods and includes wave generation. Such (often fully spectral) wave models have been available for some time for deep-water wave prediction, but this concept has been translated only relatively recently to shallower water.

Tidal residual currents

In Sect. 5.7.6 we already discussed the tidal residual flow pattern as a result of the accelerating flow through the inlet gorge. The tidal residual current pattern in the highly schematised situation discussed there boils down to a quadruplet of gyres, two at either side of the inlet (Fig. 5.74). In reality, the residual current picture is much more complicated than this. There is usually a distinct ebb-dominated current (i.e. averaged over the tide the flow is in the ebb direction) over the outer delta, and often there are flood channels near the tips of the islands. In the Wadden Sea, well-developed flood deltas are hardly found: the entire basin acts as a flood delta, and the corresponding flood-residual current is difficult to distinguish. Many inlets on the East Coast of the USA, however, do exhibit such a feature and have a well-developed residual circulation inside the inlet.

Another type of residual current is Stokes drift (Sect. 5.7.6) which is dependent on the phase-coupling between the horizontal and the vertical tide. It was shown that if the horizontal tide and the vertical tide are more or less in phase ($\varphi \approx 0$), there can be a considerable residual current. This becomes even more apparent for shoals bordering a tidal channel which are flooding and drying during the tide. There, the largest part of the flooded stage coincides with the flood tide, so there must be a flood-dominated residual current (averaged over the tide the flow is in the flood direction). By implication, the residual current in the channel must be ebb-dominated.

Secondary flow components can arise from, amongst others, the curvature of the tidal current (Sect. 5.7.6). The curvature-induced secondary flow does not change sign as the tide turns and is therefore, in the upper part of the water column, always directed away from the centre of curvature of the flow; in the lower part always towards it. Thus the curvature-induced secondary flow contributes, for instance, to the maintenance of shoals (see Fig. 9.13).

Curvature-induced secondary flow on an outer delta has been hypothesised to play an important role in the case of the groyne which was built in 1995 to protect the north part of the coast of Texel, one of the barrier islands of the Dutch Wadden Sea (Fig. 9.14). The idea was to let this groyne interrupt the longshore drift into the inlet called Eierland Inlet (Eierlandse Gat in Dutch). Studies with 2D depth-averaged models (thus not resolving secondary flow patterns) revealed that this would lead to the 'textbook' pattern of updrift accretion and downdrift erosion, that is to say, to strong erosion

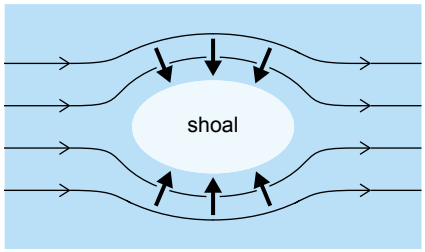

Figure 9.13: Curvature-induced secondary flow: near the bed the flow is always directed towards the shoal.

north of the groyne. It was foreseen that the groyne would have to be connected by a hard structure to the existing revetment which protects the tip of the island. Once the groyne had been built, however, accretion occurred at either side of it (Fig. 9.14), to the effect that it is now largely buried in sand (so the project turned out to be extremely successful, although at the cost of other coastal elements). Based on model computations by Steijn et al. (1998), amongst others, this has been attributed to a large extent to the curvature-induced secondary flow in the gully around the tip of the groyne, which consistently brings sediment towards the groyne (see Fig. 9.14). However, new computations suggest that the ebb-tidal currents during spring tides, rather than the secondary flow, are responsible for the large amounts of sedimentation at the north side of the dam (see Visser, 2014).

(a) 1990 (b) 1999

(c) 2005 (d) 2011

Figure 9.14: Observed morphological evolution around the Eierlandsedam, a long groyne at the north point of Texel built in 1995. Photos from Rijkswaterstaat (see 'Credits' on page 579).

In summary, there is a variety of mechanisms which lead to tidal residual currents, and hence to residual sediment transports and morphological changes. In shallow areas such as a tidal inlet system, we should not think of the tide as a small-amplitude wave.

Wave-induced currents

As stated before, an outer delta is nowhere near a straight prismatic coast. This means that the way of thinking about wave-driven currents as used in Ch. 5 is hardly applicable here. In that chapter, the alongshore and cross-shore momentum equations were separated, the former describing the momentum balance for a uniform longshore current and the latter the set-up balance. In the case of a complex topography with interrupted breaking, however, the situation is much more complicated; the momentum equations cannot be separated and need to be resolved in two horizontal dimensions; in principle, the wave-driven current in this type of situation is 3D. A relatively simple example, a shoal on which waves are breaking, was already given in Sect. 5.5.7 (Fig. 5.49). The general pattern was a net flow in the wave direction over the shoal, turning seaward again via the channels between the shoals. In tidal inlets, the wave-driven currents around shoals on the outer delta can be so strong that they dominate the tidal residual currents. This has strong implications for the sediment bypassing mechanism, see Sect. 9.4.2.

Wind-induced currents

An often forgotten type of currents in tidal inlet systems are wind-driven currents, either directly, via the wind-induced shear stress on the water surface, or indirectly, via the set-up of the water level against the coast. This means that the wind shear stress components need to be added to the depth-averaged momentum equations. These wind stress terms have the water depth in the denominator, which means that the wind tends to be more effective in driving a current when it acts on shallower water. Due to the large variations in water depth which are inherent to a tidal inlet system, the wind-driven current field will therefore strongly vary in space. In general, the flow will tend to follow the wind in the shallower parts, and to oppose it in the deeper parts, but this picture can be complicated greatly by spatial interactions via water level gradients.

As the wind forcing acts at the water surface, there will also be an effect on the vertical structure of the flow: the primary flow profile (e.g. logarithmic) will be disturbed by a ‘secondary’ flow component which follows the wind in the upper part of the water column and goes against it in the lower part. Note that this secondary flow has to be superimposed on the primary flow (the depth-averaged circulation with a primary flow profile). The result can be a complex 3D flow pattern.

Probably even more important than the direct wind-induced forcing is the effect of the water level set-up during a severe storm (Sect. 5.6). Although the peak of the

wind speed usually does not last much more than a few hours, the water level set-up can last much longer. However, it takes time for the backbarrier basin to follow the water level in the open sea, as raising the water level of such a basin by a few metres takes huge amounts of water, all of which has to be squeezed in through the inlets. Hence it sometimes occurs that the ebb current is entirely suppressed and that there is a flood current in the inlet for a day or more. Clearly, such events may influence the inlet morphology considerably. It is also clear that new inlets and channels will preferentially be created under such conditions, when there is a large head difference between the sea and the basin.

3D combined current field

In summary, we have seen that the current field around an inlet is essentially more complex than on a uniform straight coast, and that all constituents of this field are essentially 3D. So when modelling currents around inlets, we have to think 3D, even if we decide to use a 2D depth-averaged model. The interpretation and post-processing of the results (e.g. bed shear stress to be put into the sediment transport model) is much less straightforward here.

Wave-current interaction

The tidal and wave-driven current pattern on the outer delta is largely concentrated in the deeper channels. Consequently, there can be strong currents which affect the wave propagation via *current refraction* (see Sect. 5.2.3). This may even go as far as wave blocking (for a wave with opposing current). When standing on the coast overlooking a tidal inlet, one often observes a sharp distinction between areas with waves and areas with a flat water surface. This is simply because the current is strong enough to prevent the waves from entering this area. Moreover, where waves do occur, their pattern is often quite irregular, again as a consequence of refraction on a strongly varying current field. This form of wave-current interaction makes it particularly difficult to predict the wave field on the outer delta. Such a prediction should be based on a combined wave and current model, and both should be carefully calibrated in order to find the right pattern.

A more straightforward form of wave-current interaction is the effect of waves on bottom shear stress experienced by the current (see Sect. 5.5.5 and Sect. 6.5). The mechanisms underlying this effect are not essentially different from those in the case of a prismatic coast, though waves and near-bed currents can have arbitrary directions now. The result is a complex 3D boundary layer with a strongly veering velocity vector and a non-trivial direction of the bed shear stress. In large-scale models like the ones we use for tidal inlet systems, however, the effect on the *direction* is usually ignored and the shear stress is assumed to be opposite to the mean current. What we do have to take into account, however, is the bed shear stress *enhancement* induced by the waves. This may have major effects on the current pattern: especially the tidal flow

will tend to avoid shallow areas, where wave action and shear stress enhancement are strongest.

9.4.2. Sediment transport patterns

Figure 9.15 shows the effect of wave-driven alongshore sediment transport gradients on the shape of barrier islands. The combination of wave, current and sediment transport mechanisms on the outer delta gives rise to a typical residual sediment circulation pattern. Figure 9.16 shows a highly schematised picture. Reality is usually more irregular and diffuse (Fig. 9.17).

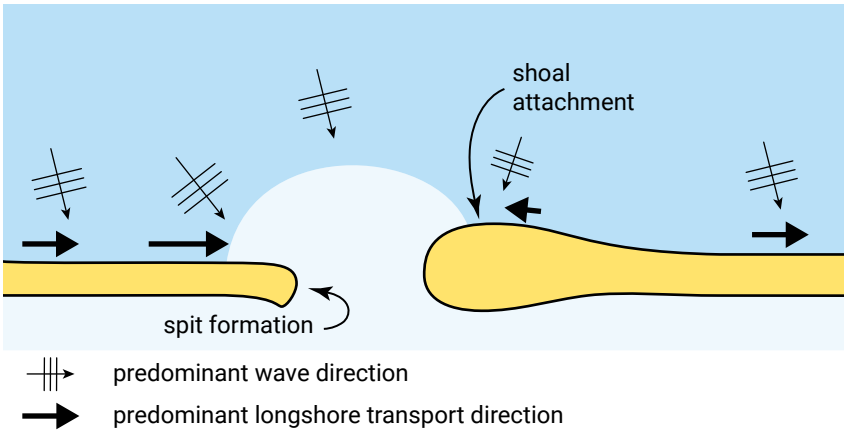

Figure 9.15: Wave-driven longshore sediment transport along the barrier islands on either side of a tidal inlet. The transport gradients lead to spit formation (left) and a drumstick-shaped barrier island (right).

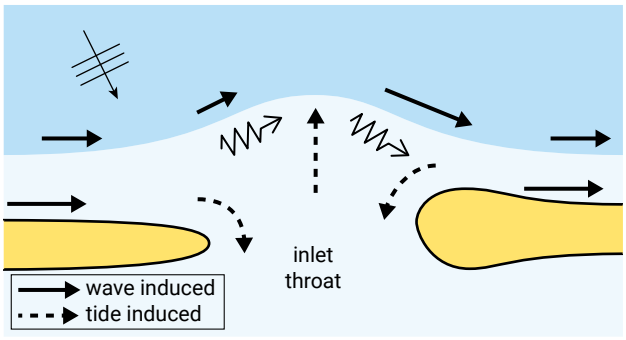

Figure 9.16: Schematic diagram of the outer delta residual sediment transport (hypothesised by De Vriend et al., 1994): 1) the wave-induced longshore sediment transport that bypasses the inlet; 2) the ebb-dominated main channel that exports sediment and 3) the flood channels that import sediment. In this case the tidal wave is assumed to propagate along the coast from west (left) to east (right).

In general, the flood channels on the outer delta carry sediment from the adjacent coasts to the inlet, mostly during episodic events. Depending on the demand[4] of the

[4]For the sand demand (as opposed to sand surplus) of a basin, the term 'sand hunger' is commonly used in the Netherlands. Internationally more established is the geological term 'accommodation space',

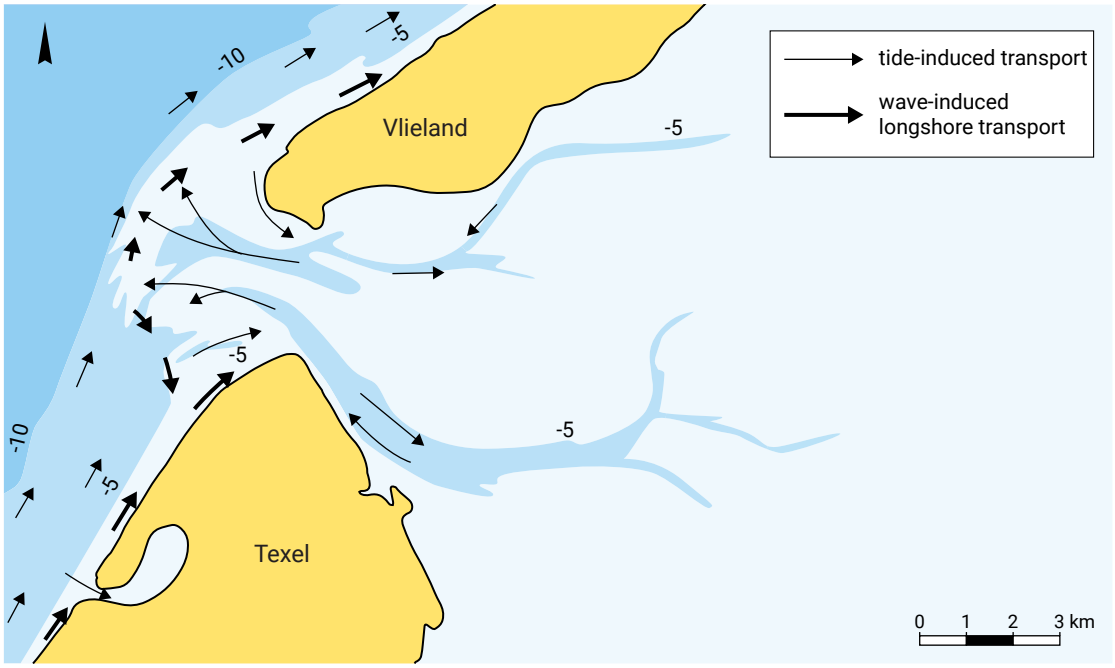

Figure 9.17: Residual sediment transport in the Eierland Inlet before the Eierlandsedam was built, composed from observations and various numerical modelling studies according to Ribberink et al. (1992).

basin, this sediment is transported either into the basin or sometimes into the main ebb channel and then towards the edge of the outer delta. There, part of it is picked up by wave-driven and/or tidal longshore currents and transported along the delta edge, ultimately towards the downdrift island, or towards the updrift one, depending on the local tidal state and wave direction.

Another part of the sediment from the ebb channel, as well as part of what is brought into the area by the longshore drift along the updrift island, ends up in the shoal system on the outer delta. Due to the various hydrodynamic and sediment transport processes around these shoals, there is a long-term residual transport and a slow migration of the shoals in the direction of the longshore drift (Fig. 9.18). The time needed for a shoal to cross the inlet may be tens of years (for instance, for the Borndiep, also called Ameland Inlet, between Terschelling and Ameland, it is typically 40 years).

It can be concluded that part of the littoral drift continues its way over the ebb-tidal delta to the downdrift coast, while another part is diverted into the tidal inlet by the flood. During ebb, part or all of the sediment carried into the tidal inlet is returned to the ebb-tidal delta, from where it can be transported to the downdrift coast again. The ratio between the volumes of littoral drift that are bypassed directly and that are bypassed via the ebb-tidal delta depends on the tidal prism and the magnitude of the littoral drift.

which can be both positive and negative and could apply to a backbarrier area as well as to a shoreface (see Sect. 7.4).

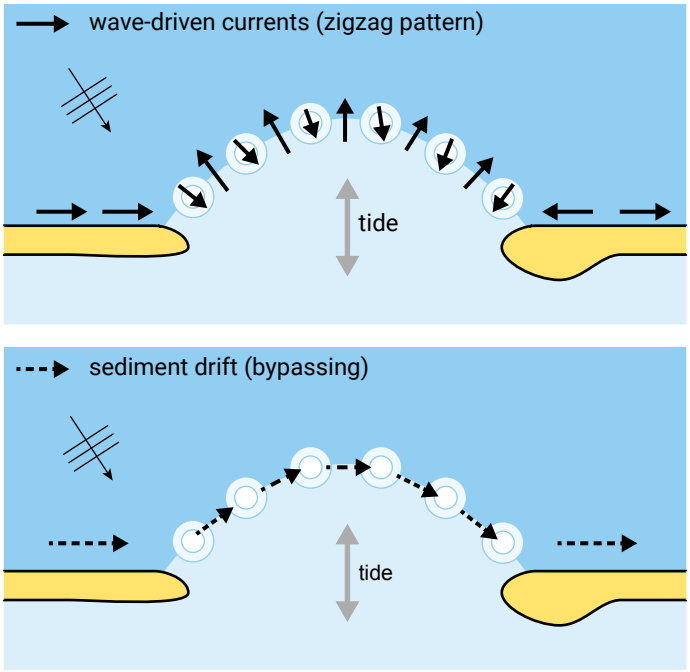

Figure 9.18: Sediment bypassing via shoal migration on the outer delta. The zigzag pattern of wave-driven currents results in a net sediment drift from the updrift to the downdrift island. (concept by De Vriend et al., 1994; Ehlers, 1988).

Bruun and Gerritsen (1959) propose a parameter r to indicate the type of bypassing. Later Bruun and Gerritsen (1960) and Bruun (1978) converted the original formula for r to:

$$r = \frac{P}{M_{\text{tot}}} \tag{9.2}$$

in which:

P	the tidal prism	m^3
M_{tot}	the total littoral drift	m^3/yr

The tidal prism is the volume of water entering or leaving the basin per half tidal cycle. Note that the parameter r is a measure for the relative wave/tide influence at the inlet. For large values of r (tidal prism much larger than the wave-induced littoral drift), the inlet is tide-dominated. For values of $r > 300$, the bypassing of sand is predominantly via the inlet. On the other hand, for small values of r (wave-dominance) the bypassing is predominantly via shoals on the ebb-tidal delta.

In Table 9.3 some values for r are given. The tidal inlets along the West Frisian Barrier islands all show a large value fFor r, which indicates that tidal flow bypassing is dominant. In general, increased values of r produce greater seaward displacement of inlet bars (Oertel, 1988). The first eight inlets in Table 9.3 are Wadden Sea inlets. The given values for r show that r decreases in an eastward direction. This seems to correspond with the occurrence of tidal sand ridges at the more easterly located inlets.

Figure 9.19 shows one of those inlets, viz. the Wichter Ee (r[§1.1] ~ 60 [p433]), one of the meso-tidal inlets of the eastern (German) Wadden Sea. The wave-induced longshore sediment transport along most of the North Sea coast is from west to east (left to right in the photo), as can be seen from the sand abundance at the eastern tip of Norderney and the lack of sand at the western tip of Baltrum. Apparently, the sand bypasses the inlet via a number of shoals, which migrate in the outer delta from the updrift to the downdrift island. This probably forms the principal sediment bypass mechanism across the inlet. The shoals get welded with the coast of Baltrum somewhere east of the tip, where sand abundance is found again.

Table 9.3: Values for r (Eq. 9.2) of some tidal inlets (from: Bruun, 1978).[§1.1] [Tidal prism of Texel Inlet corrected to 1000×10^6 m^3] [p433]

	Inlet	Tidal Prism P [10^6 m^3]	Total Littoral Drift M_{tot} [10^6 m^3/yr]	r
Wadden Sea Inlets from west to east	Inlet of Texel, Holland	1000	~1	~1000
	Eierlandse Gat, Holland	200	~1	~ 200
	Inlet of the Vlie, Holland	1000	~1	~1000
	Borndiep, Holland	500	~1	~ 500
	Friesche Zeegat, Holland	300	<1 [e]	~ 400
	Nordeneyer Seegat, Germany	160	<1 [e]	~ 250
	Wichter Ee, Germany	42	<1 [e]	~ 60
	Otzumer Balje, Germany	110	<1 [e]	~ 150
	John's Pass, Florida	14	0.1	140
	Longboat Pass, Florida	20	0.1	200
	Aveiro, Portugal	60	1	60
	Big Pass, Florida	10	0.01	100
	Masonboro Inlet, Florida	20	0.3	70
	Saratosa Pass, Florida	3	0.1	30
	Penang Harbour, Malaysia	700	0.6	~1000
	Krishnapatam, India	10	0.6	17
	Thyborøn, Denmark[a]	100	0.8	120
	East Pass, Florida[b]	40	0.1	400
	Oregon Inlet, N. Carolina	60	1	60
	Tan My, Vietnam	47	1.6	30

[a] jettied inlet
[b] weir jetty
[e] estimate

The shoals are separated by distinct channels, which all branch off from the main channel. In this particular case, the latter is strongly deflected eastward, but other inlets show that the main channel can just as well have a different direction. Furthermore, the main channel tends to migrate and change direction through time. The

(a) date: 2.8.1982

(b) date: 10.9.1982

Figure 9.19: Aerial photographs of the morphology of the tidal inlet Wichter Ee, between the islands Norderney (left) and Baltrum (right). Copyright Ehlers (1988), see 'Credits' on page 579. The date convention as used by Ehlers (1988) is unknown to us, but we expect that the photos are from 2 August and 10 September 1982 – hence a good month apart – and can be considered as pre-storm and post-storm, respectively.

main channel and its branches are probably all ebb-dominated (in this case meaning that, averaged over the tide, there is a residual flow in the ebb direction). If this is true, the principle of conservation of water mass requires that other parts of the area are flood-dominated. Often there are more or less distinct flood channels, e.g. around the tip of the updrift island. In the case of the Wichter Ee, at least at the time that the photos of Fig. 9.19 were taken, these flood channels were not very well developed.

From a project at Nerang River, Australia, it becomes clear what can go wrong when ignoring the nature of this sediment circulation. Here, an inlet to a tidal lagoon was

converted into a shipping channel by building groynes at either side of the inlet and bypassing the longshore drift via a pumping system. This scheme works well from the point of view of downdrift erosion, but it does a much worse job for the outer delta and where the hydrodynamic conditions in the inlet are concerned. By artificially bypassing all the sediment which arrived on the updrift side of the inlet, the shoal bypassing system was cut off from its sand supply, the shoals rapidly degraded, and the outer delta disappeared. As a consequence, the tidal motion into and out of the lagoon was no longer hampered by the delta and increased considerably. This led to a dramatic increase of the flow velocities in the inlet, due to which its navigational function (the prime reason for carrying out the scheme) has become heavily threatened.

9.4.3. Empirical relationships: volume of the ebb-tidal delta

The great importance of the ebb-tidal delta is evident from the large volume of sand that is accumulated in this delta. This ebb-tidal delta volume (Fig. 9.20) will be larger for low onshore-directed wave energy and large tidal forces. Under these circumstances the ebb-tidal delta can extend far seawards, without a distinct terminal lobe. Quite often the volume of sand deposited in an ebb-tidal delta is much larger than the total volume of the adjacent beaches. Although the governing physical processes (Sects. 9.4.1 and 9.4.2) are complex and not yet fully understood, it is beyond dispute that sediment exchange takes place between the adjacent barrier beaches and the ebb-tidal delta.

The volume of sand stored in the ebb-tidal delta has empirically been related to the tidal prism of the backbarrier system (Fig. 9.21). The relationship in Fig. 9.21 was first derived for outer deltas in the USA and reads:

$$V_{od} = C_{od} P^{1.23} \tag{9.3}$$

in which:

V_{od}	sand volume stored in the outer delta	m^3
C_{od}	empirical coefficient	$m^{-0.69}$
P	tidal prism	m^3

Figure 9.21 shows that the coefficient is dependent on the wave climate, in such a way that for the same tidal prism the volume in the ebb-tidal delta is smaller for more energetic waves. In Fig. 9.21 the tidal prism is determined based upon the spring or diurnal tidal range. Using the mean tidal prism P rather than the spring tidal prism, Eysink and Biegel (1992) found $c_{od} = 63.3 \times 10^{-4}$ for the Wadden Sea ($P_s/P \approx 1.15$).

Even small changes in the tidal prism or the wave conditions (by nature or human interferences) may result in changes in the sand volume of the ebb-tidal delta. For example, suppose the tidal prism of an inlet is enlarged after flooding of part of the

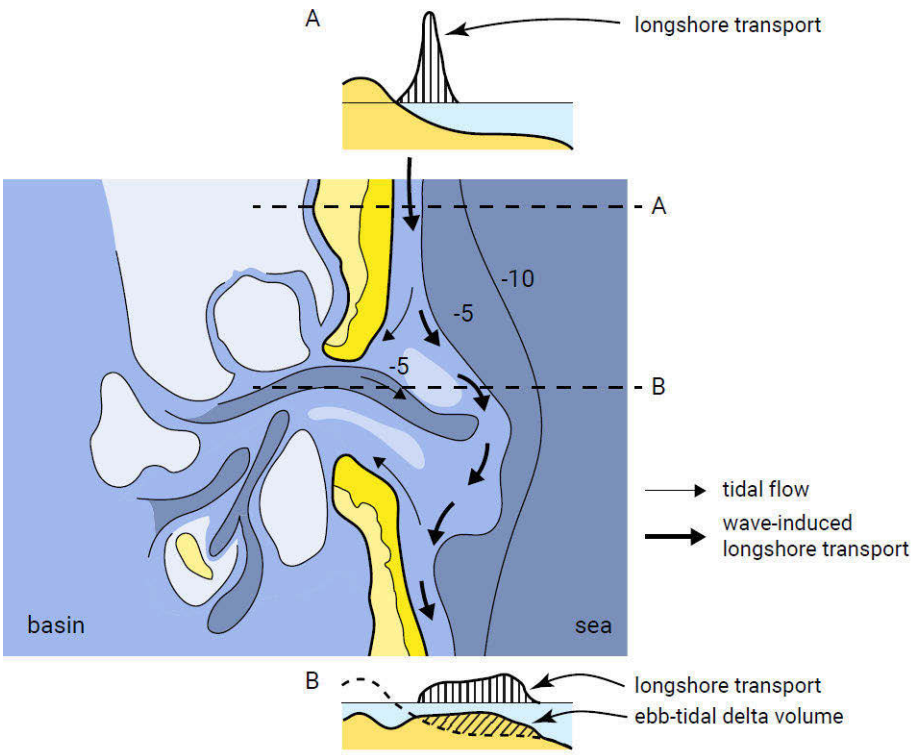

Figure 9.20: Definition of the ebb-tidal delta volume. A: the no-inlet bathymetry. B: the ebb-tidal delta bathymetry. The ebb-tidal delta volume is defined as the difference in bottom height between the actual and the no-inlet bathymetry of the adjacent coast for the entire extent of the ebb-tidal delta along the shore (see middle panel).

hinterland. According to the empirical relationships (Fig. 9.21), this will result in an enlargement of the volume of sand in the ebb-tidal delta. The sediment required for this enlargement may originate from the adjacent barrier coast, the backbarrier system (i.e. the basin) or from offshore. Most probably it will be a combination of these three sources, the distribution of which is very hard to determine without thorough knowledge of the underlying physics. Probably, erosion of tidal gullies will contribute most to the 'sand demand' of the (ebb)-tidal delta. Because of the relatively small morphological timescales of such adjustments, they are able to respond fast. Due to increased flow velocities, the tidal channels will (immediately) start to erode. The eroded material will mainly be deposited on the ebb-tidal delta where the flow decelerates. On the other hand, the contributions of the adjacent barrier coasts may be smaller, but these coasts are more vulnerable, as small changes in the sediment balance may cause severe coastline retreats.

Removal of sand from the outer delta

The sand in the outer delta may be used as a sand source for e.g. beach nourishment, or it may be necessary to dredge navigation channels through the outer delta. In both of these cases the sand is removed from the inlet system and the system will be disturbed from its 'equilibrium state'. Since the tidal prism and the protrusion rate of the delta

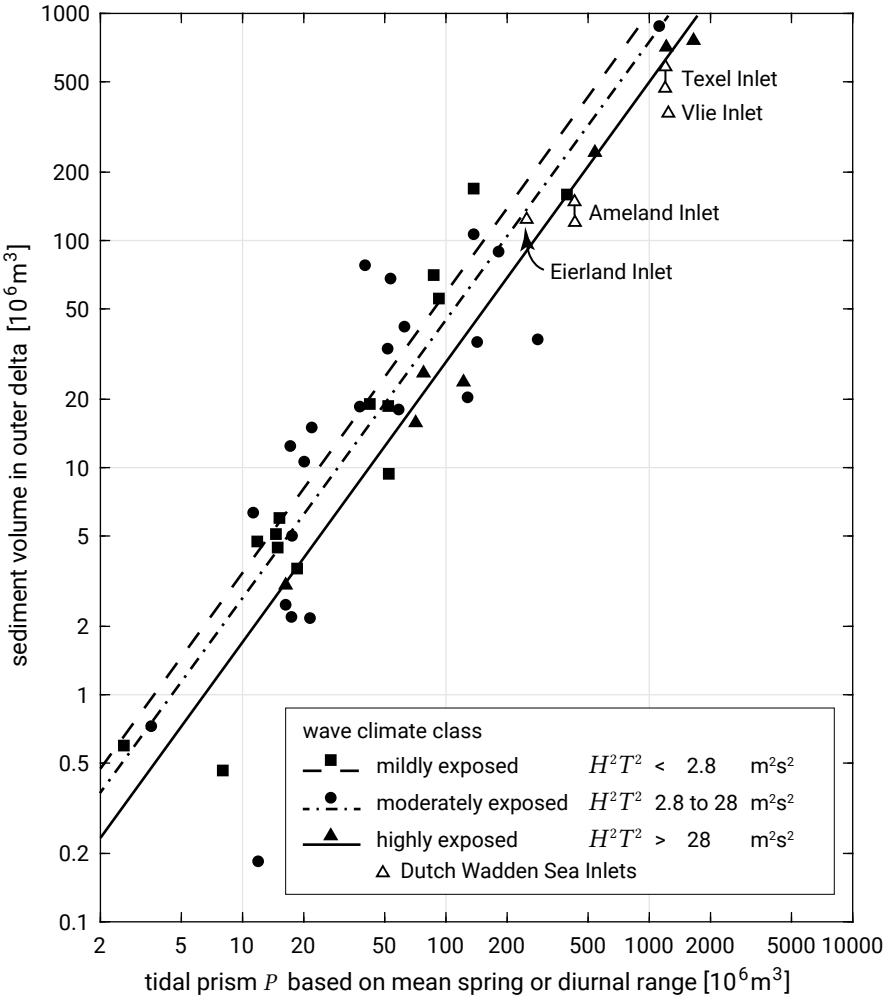

Figure 9.21: Empirical relationship between volume of sand in the outer delta and the tidal prism. The effect of the wave climate on this relationship is also shown; the general trend is that the ebb-tidal delta sand volume reduces with increasing wave activity. USA data from Walton and Adams (1976), Dutch data from Eysink and Biegel (1992).

remain constant, the supply of sand into the basin via the flood channels does not change.

In the first years after the start of dredging operations, the delta will retreat as a result of sand loss, while the barrier islands are not affected. This trend reverses, however, as the outer delta will demand sand in order to return to its equilibrium state. Assuming that the inlet system is a 'closed system', the demanded sand will be supplied by the adjacent coastlines, mainly by the downdrift coastline that will be cut off from its supply. The erosion of the barrier islands will begin on the foreshore, the beach profile steepens and gradually the erosion of the beach will become evident. Since the erosion of the barrier islands occurs tens of years after the dredging, the cause of the erosion may not be linked to the dredging operation.

In order to minimise the additional erosion it may be wise to consider the option of dredging sand from the inner (flood-tide) delta instead of from the outer delta. If the

amount of sand removed from the inlet system per year is less than or equal to the total volume of sand transported into the basin per year via the flood channels, then the effects of dredging the inner and outer delta on the long term (decades to centuries) will be the same. However, the outer delta retreat and thus the additional erosion on the downdrift island will be slower in the case of dredging of the inner delta.

Effects of the construction of a groyne on the updrift island

The construction of a groyne on the updrift island will trap sediment that previously entered the inlet via the updrift flood channels. Not only can lee-side erosion be expected, but erosion of the outer delta and the downdrift island as well. The outer delta acts as a buffer for the other elements of the inlet system. When sand is removed from one portion of the inlet system, the outer delta will respond by sharing sand with the other elements. This supply, however, is only a 'short-term loan' which will be repaid by the adjacent coastlines in the longer term. So erosion of the outer delta can be expected to occur rapidly, while on the downdrift island this will take place after tens of years. In the case of a longer groyne, more sand will be trapped behind the groyne and it will also take more time before bypassing begins. Consequently the erosion of the outer delta and the downdrift island will be more severe.

9.5. Stability of the inlet cross-sectional area

9.5.1. Escoffier's model

A tidal inlet is not fixed, but a dynamic entity governed by important factors such as tidal currents, storms, the tidal prism (the storage volume of the estuary between low tide and high tide level) and littoral sediment transport. Escoffier (1940) was the first to study the stability of the cross-sectional area of the inlet proper. Because of the littoral drift leaving and entering the inlet with the tide, there can be considerable variation in the cross-sectional area.

Escoffier's predominantly qualitative study led to a relationship for the maximum cross-sectionally-averaged entrance channel velocity (u_e, with the subscript indicating the entrance) for a given estuary or inlet (see Intermezzo 9.4 for an approximation). He related u_e to the hydraulic radius of the channel (R), its cross-sectional area (A_e) and the tidal range in the estuary (Δh). Since this calculation is made for a given inlet, other variables such as the channel bed roughness, its length, the surface area of the inlet, and the tidal range at sea have then all become more or less constant. Escoffier combined the variables for a given inlet into a single parameter x, such that a larger entrance cross-section results in a larger value of x. Qualitatively, he found that u_e varied as a function of x more or less as shown in Fig. 9.22.

A curve like in Fig. 9.22 is called a closure curve. In the range from A to C on this curve, the entrance channel is so small that it chokes off the tidal flow, so that the tidal

difference within the estuary will be less than at sea. For that reason the channel velocity will increase for an increasing cross-section. In terms of Eq. 9.5: with increasing A_e, P increases so much that $\hat{u}_e$ increases. On section C–E of the curve, the tidal flow is not choked off any longer (now P remains constant for increasing A), so that the maximum current velocity decreases as the channel becomes larger. For any estuary or inlet, a closure curve can be computed using a hydrodynamic model. This can be either a numerical model or a simpler analytical model. Simplified analytical solutions can for instance be obtained by assuming a short basin that responds in pumping mode (a uniformly fluctuating water level, see Sect. 5.7.3).

Intermezzo 9.4 Cross-sectional velocity for a sinusoidal tide

The maximum cross-sectional velocity is the maximum velocity during the tidal cycle. To understand its behaviour as a function of the cross-sectional area, it can be approximated as the amplitude $\hat{u}_e$ of a sinusoidal tidal motion u. In that case we can relate the maximum cross-sectionally-averaged entrance velocity $u_e = \hat{u}_e$ to the tidal prism P. The tidal prism P is equal to the time integral of the inflow during flood or to the outflow during ebb (cf. Eq. 9.1):

$$P = \int_0^{\S1.1\ 1/2T\ \S1.1\ 1/2T} A_e u dt = \int_0^{\S1.1\ 1/2T\ \S1.1\ 1/2T} A_e \hat{u}_e \sin\left(\frac{2\pi}{T}t\right) dt = \frac{TA_e}{\pi}\hat{u}_e \text{[p439]} \tag{9.4}$$

and thus:

$$\boxed{\hat{u}_e = \frac{\pi P}{A_e T}} \tag{9.5}$$

with T being the tidal period.

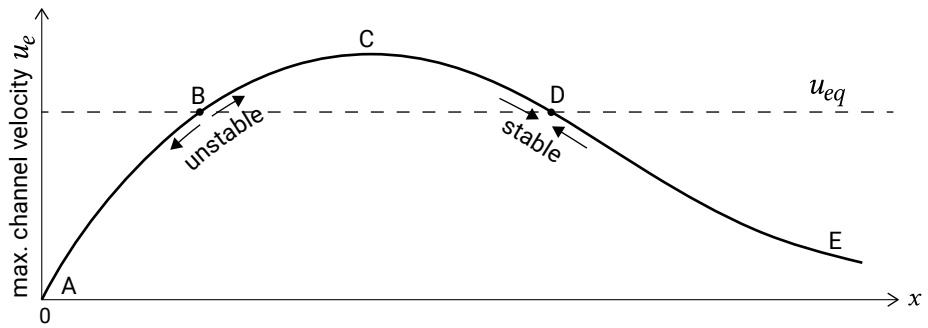

Figure 9.22: Channel velocity geometry relationship.

Escoffier's next step was to introduce the concept of an *equilibrium* maximum velocity u_{eq}, below which the velocity in the channel is too low to erode sediment and keep the

entrance channel open. This critical velocity is more or less independent of the channel geometry, according to Escoffier, and he plotted it as a horizontal line on Fig. 9.22, viz. independent of the cross-section. In reality u_{eq} is generally a weak function of the cross-sectional area, but at first order this effect can be neglected.

The fate of an estuary or tidal inlet can now be predicted by examining the curve ACE in relation to u_{eq}. Obviously, if u_e is always less than u_{eq} (for all values of x the closure curve lies below u_{eq}), then any sediment deposited in the entrance will remain there and the estuary will be closed off eventually. However, if a curve of u_e versus x intersects the u_{eq} line as shown at B and D in Fig. 9.22, then a variety of situations can exist. If, for example, the channel dimensions place it on section A–B of the curve in Fig. 9.22, then the channel is too small and the friction too high to maintain itself; so it will be closed by natural processes. If the channel geometry places it on section D–E of the curve, it will also become smaller, but as it does so, the velocity §1.1 ~~, ue,~~ §1.1 u_e [p440] will increase; sedimentation continues until point D is reached. Lastly, if the channel configuration places it on section B–D of the curve, then erosion takes place until point D is again reached; point D represents a stable situation. Since $u_e = u_{eq}$ represents the stable (D) and unstable (B) equilibrium conditions, the relationship for u_{eq} is called the equilibrium flow curve or the stability curve. The equilibrium velocity curve that Escoffier introduced assumes that the equilibrium velocity u_{eq} is a constant that depends only on the sediment diameter, and suggests that a good approximation of the velocity is 3 ft/s (0.9 m/s).

With this insight, it is now possible to evaluate the influence of changes in an estuary mouth. Since point D represents a naturally stable situation, most natural estuaries will tend to lie more or less in that region. Of course, a severe storm can cause severe sedimentation, largely filling the entrance, which is then suddenly in the state represented by section A–B of the curve. In such a situation, immediate dredging is called for to prevent complete closure. It is not necessary to restore the original situation, however, since, once the entrance geometry places it on section B–C–D of the curve in the figure, nature will do the rest of the work given enough time. Apparently, Escoffier's model incorporates a feedback between hydrodynamics and morphology and can therefore be seen as a morphodynamic model for the entrance of tidal basin.

Shipping interests may make it desirable to enlarge the entrance of a given estuary to accommodate larger ships. If such an expansion scheme places the channel on section D–E of the curve, continual dredging operations will be necessary. It may be possible to carry out the expansion and prevent the need for continual dredging by changing the channel alignment and artificially constricting its width – techniques often used in rivers – so that the larger channel cross-section remains stable. Translating such changes into a figure such as Fig. 9.22 means that a new curve of u_e versus x has been generated, which generally yields a slightly higher value of u_e for a given x value. This results in point D, the equilibrium situation, being moved to the right in the figure.

9.5.2. Empirical equilibrium cross-sectional area

One of the most important questions to be answered in order to use the approach by Escoffier outlined above is "what is the stable equilibrium condition of a basin?" or in other words, "when has point D in Fig. 9.22 been reached?"

Probably, the first relevant reference in this context is LeConte (1905), who, based on observations of a small number of inlet entrances and harbours on the Pacific coast of the USA, found an empirical relationship between the inlet cross-sectional area and the tidal prism. The pioneering work of LeConte (1905) was then followed up by O'Brien (1931), O'Brien (1969) and Jarrett (1976).

The general form of the empirical relationship for the equilibrium cross-section based on the tidal prism is as follows:

$$A_{eq} = CP^q \tag{9.6}$$

in which:

A_{eq}	the minimum equilibrium cross-section of the entrance channel (throat), measured below MSL	m^2
P	the tidal prism, often the spring tidal prism	m^3
q	coefficient	–
C	coefficient	m^{2-3q}

This equation seems to be equally valid for large estuary mouths, bays and tidal lagoons. The coefficients C and q are empirical parameters obtained from observational data. The coefficient C is not dimensionless and has dimensions of $L^{(2-3q)}$. Several researchers have reported values for C and q that vary with the type of inlets considered (Dutch Wadden Sea inlets give different values than the USA Atlantic coast inlets, for instance). The coefficient q is order of magnitude 1. In metric units, C is in the range 10^{-4} to 10^{-5}. For instance, O'Brien (1969) showed that for 28 USA entrances $C = 4.69 \times 10^{-4}$ and $q = 0.85$ are best-fit values applicable to all entrances, when P is measured in cubic metres (m^3) and A in square metres (m^2). But, when limited to 8 non-jettied entrances, he derived $C = 1.08 \times 10^{-4}$ and $q = 1$ as best-fit values. The assumption of Escoffier that the equilibrium velocity u_{eq} is approximately 0.9 m/s implies assuming $q = 1$ and $C = 7.8 \times 10^{-5}\ m^{-1}$. This is demonstrated in Intermezzo 9.5.

A certain combination of values for C and q is valid only for a set of inlets that have the same sediment characteristics (which determine how easily sediment is transported) and that are subject to the same wave conditions (important for the littoral sediment transport that reaches the inlet) and tidal conditions (since tidal prism and tidal period determine the current velocity – see Intermezzo 9.4 – and therefore the tidal transport capacity). Obviously, the 28 inlets in O'Brien's dataset do not all have the same littoral

drift and tide conditions, and it is doubtful whether this is the case for the 8 non-jettied entrances.

The dependencies of C and q on littoral drift and tidal conditions can be understood when looking at the equilibrium condition from the perspective of sediment balance. The sediment that is transported to the inlet entrance by wave-induced longshore currents is carried into the basin by the flood-tidal currents. When the inlet is in equilibrium, this sediment is transported back in the seaward direction by the ebb-tidal currents. The annual mean flux of sand entering the inlet on the flood is M (m^3/s). M is assumed a constant fraction of the annual mean longshore sediment transport and is assumed to remain constant over time. The remaining fraction is assumed to bypass the inlet via the ebb-tidal delta (see Sect. 9.4.2). When in equilibrium, the annual mean flux M equals the annual mean ebb-tidal sediment flux.

Intermezzo 9.5 The C and q values according to Escoffier's equilibrium velocity

In the approximation of a sinusoidal tidal motion, we have according to Eq. 9.5:

$$\hat{u}_{eq} = \frac{\pi P}{A_{eq} T} \tag{9.7}$$

Combining Eq. 9.7 with the equilibrium condition Eq. 9.6 and eliminating P leads to the following formula for the equilibrium velocity:

$$\hat{u}_{eq} = \pi A_{eq}^{1/q-1} C^{-1/q} T^{-1} \tag{9.8}$$

For $q \neq 1$ the equilibrium velocity must be dependent on the cross-sectional area, (see also Stive et al., 2009). Escoffier assumed a constant equilibrium velocity u_{eq} that depends only on the sediment diameter, and suggested an approximate value of 0.9 m/s (Sect. 9.5.1). His assumption implies that $q = 1$ and $C = \pi \hat{u}_{eq}^{-1} T^{-1} = 3.49\,\mathrm{m/s} \cdot T^{-1}$. Assuming a semi-diurnal tide with $T = 44\,700$ s, we find $C = 7.8 \times 10^{-5}\,\mathrm{m}^{-1}$. This is the order of magnitude of C values found empirically for $q = 1$.

Assuming a power law for the sediment transport and a sinusoidal velocity, the ebb-tidal sediment transport rate in the entrance TR is taken proportional to the power n of the velocity amplitude and the power m of a length dimension l of the cross-section:

$$TR = k \hat{u}_e^n l^m \tag{9.9}$$

The coefficient k is a constant and its value is dependent on the sediment characteristics. The values of n and m depend on the adopted sediment transport formula, where

n is in the range 3 to 6 and m of order 1, and the length scale l is either the annually averaged width or depth, the final choice depending on the way sediment enters and leaves the inlet entrance (Van de Kreeke, 1992, 2004). In the following we will adopt the assumption that for a given offshore tide, u_e is a unique function of the entrance cross-sectional area A_e.

After a change in the entrance cross-sectional area, the shape of the cross-section is assumed to remain geometrically similar. This allows the length scale to be expressed as a constant α times the square root of the annual mean cross-sectional area A_e:

$$l = \alpha\sqrt{A_e} \tag{9.10}$$

The value of α depends on the shape of the cross-section and the definition of l.

Substituting Eq. 9.10 for l in Eq. 9.9 results in a formula for the annual mean ebb-tidal sediment transport as function of the cross-sectional area:

$$TR = k\alpha^m \hat{u}_e^n A_e^{m/2} \tag{9.11}$$

In this equation $\hat{u}_e$ is a function of Ae (see Eq. 9.5). When the cross-section is in equilibrium:

$$TR = M \tag{9.12}$$

The shapes of the functions, which are independent for realistic values of the parameters k, α and m, represented by Eqs. 9.11 and 9.12, are plotted in Fig. 9.23. In general, there will be two values of the cross-sectional area for which the annual mean ebb-tidal transport equals the mean annual influx of sediment M (A_{eq1} and A_{eq2}).

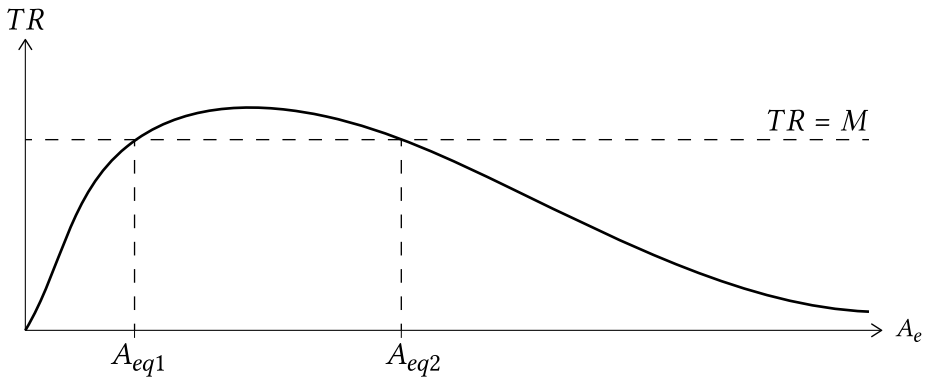

Figure 9.23: Equilibrium cross-sectional areas (Eqs. 9.11 and 9.12).

For a given inlet situation with a mean annual influx of sediment M, a difficulty in determining the value of A_{eq1} and A_{eq2} from Eqs. 9.11 and 9.12 is ascertaining the values k, n, m and α. An elegant way to circumvent ascertaining the parameters was

put forward by Van de Kreeke (2004). For inlets at equilibrium §1.1 $A_e = A_{eq}$ and $u_e = u_{eq}$ [p444] and we find from Eqs. 9.11 and 9.12:

$$M = k\alpha^m \hat{u}_e^n A_e^{m/2} \tag{9.13}$$

Subsequently, Van de Kreeke substitutes the relationship between the velocity amplitude of a sinusoidal tide $\hat{u}_{eq}$ and the cross-sectional area A_{eq} (Eq. 9.7). This yields after some algebra:

$$C = \left(\frac{MT^n}{k\alpha^m \pi^n} \right)^{\left(\frac{2}{m-2n}\right)} \tag{9.14}$$

and

$$q = \frac{n}{n - m/2} \tag{9.15}$$

Equations 9.14 and 9.15 imply that for a set of inlets in equilibrium that have the same values of M, T, k, α, m and n, values of C and q theoretically should be the same. It also follows that $q > 1$, at least under the present assumptions. This means that datasets used to determine the constants C and q in Eq. 9.6 should ideally consist of inlets that show phenomenological similarity (i.e., have similar values for k, n, m and α for a given inlet situation with mean annual influx of sediment M), implying that the datasets should be clustered while ensuring:

- similar wave-driven littoral drift;
- similar tide characteristics (form factor, Eq. 4.1, and amplitude);
- similar grain size and grain density;
- similar shape of the cross-section.

Most of the data sets published do not fulfil these recommendations and should therefore be considered with care (see Stive et al. (2009) for a review of the datasets). The resolution of this issue is important, because slightly different values of q result in significantly variable values for the equilibrium cross-sectional value of the tidal entrance. This may have significant implications in determining the true stable equilibrium entrance cross-sectional area.

9.6. The inner basin geometry

9.6.1. Complex geometry of tidal basins

The interaction between bottom morphology and tidal motion is the cause of a complex three-dimensional structure of residual circulations, which are both the cause and the result of the morphology of a basin. The residual circulations in meandering channels

play an active role in the morphological evolution of channel meanders and of ebb and flood chutes, as will be described below. Sedimentation, erosion, channels and flats are connected by these flow structures.

Section 5.7.6 described the transversal secondary flow induced by the curvature of the tidal current in channel bends and by the Coriolis effect. This secondary flow, though rather weak compared to the maximum tidal current, can have a significant residual effect on the current, and also on the sediment transport and the bed topography. The curvature-induced secondary flow does not change sign as the tide turns: in the upper part of the water column, it is always directed away from the centre of curvature of the flow; in the lower part always towards. This means that near the bottom the secondary flow is towards the inner bend, generating a transport of sediment from the outer bend, which erodes, towards the inner bend, which accretes. Hence, this phenomenon has a positive feedback mechanism (see Sect. 1.5.2). Straight channels are inherently unstable; a small eccentricity in the channel alignment will be inclined to grow. Similarly, curvature-induced secondary flow components contribute to the maintenance of shoals, see Fig. 9.13. Note that Coriolis (as well as density gradients) may substantially alter this simple picture.

As a result of Coriolis, amongst others factors, channels will be inclined to split up in an ebb-dominated and a flood-dominated channel. In areas where the width of the basin is not restricted, two mainly independent channel systems can develop; the ebb current concentrates in one set of channels, while the flood current is often strongest in a different set of channels. Flood channels can usually be recognised because they tend to be shallower than ebb channels and they tend to die out; they lead to progressively shallower water and finally spread out on a shoal. Conversely, ebb channels are continuous and tend to be deeper. Often the maximum ebb current occurs when the tide level is lower than that corresponding to the maximum flood current (for a velocity leading the surface elevation by less than 90°, see Sect. 5.7.3). Furthermore, in the case of a river discharge, the total discharge during ebb is larger than during flood. The combined effect of higher total ebb flow and the lower tidal level during this flow tends to increase the velocity and intensify erosion in ebb channels.

Due to inertia, the tidal current is inclined to overshoot the bend pathway (or take a wider bend; in Dutch: *uit de bocht schieten*), both during ebb and flood. Since the currents try to take a wider bend, ebb and flood chutes occur at the ending of the bends and are directed into the flat areas. Due to the fact that the mean water level during flood (especially near the ending of the flood) is higher than during ebb, the flood chutes are generally better developed than the ebb chutes. During the flood tide, the water spreads over the flats, while the ebb current primarily follows the main channel. Figure 9.24 sketches the characteristic structure of ebb and flood channels in a meandering channel system, with an indication of the depth-mean residual flow pattern.

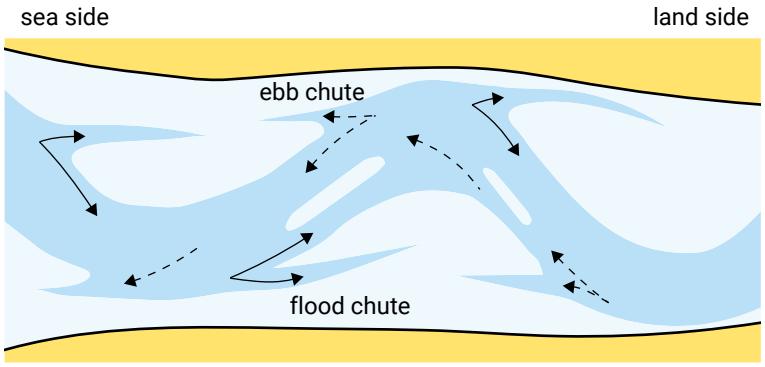

Figure 9.24: Meandering tidal channel with ebb and flood chutes (in Dutch: *ebscharen* and *vloedscharen*).

The flats are mostly fed with sand through the ebb and flood chutes. This feeding process causes the existence of sills between the ebb and flood chutes. When a sill breaches, the channel bend is cut off. A new, straighter channel is formed, while the old main channel accretes. However, in the course of time, the new channel will start to increase its curvature. Hence, the morphology of tidal basins is not static but dynamic; cycles of increasing channel curvature and channel cut-off are an important part of these internal dynamics.

9.6.2. Equilibrium relations for tidal channels and flats

The stability of the various morphological units of the inlet system can be described with empirical relations. These relationships relate geometric properties to hydraulic boundary conditions. In Sect. 9.5.2 we discussed the stability of the entrance of the inlet and described the cross-sectional area of the entrance as a function of the tidal prism. The sand volume stored in the ebb-tidal delta, which was discussed in Sect. 9.4.3, is also related to the tidal prism. In this section two other morphological units of an inlet and basin system are described: the tidal channels and tidal flats in the basin.

Equation 9.6 relates the equilibrium cross-sectional area in the throat, A_e, to the tidal prism P (with $q = 1$). From data of a tidal channel in the Wadden Sea it appeared that also *along a channel* the flow area was related to the tidal volume passing the local cross-section. Later on it was found that this relation is valid for various tidal channels in the Wadden Sea and in the estuaries of the Delta in the southern Netherlands. This relation is given by:

$$A_{\mathrm{MSL}} = C_A P_{AB} \tag{9.16}$$

in which:

A_{MSL}	the equilibrium flow area in a certain cross-section AB of the basin, measured below mean sea level	m^2
P_{AB}	the tidal prism landward of the cross-section AB under consideration	m^3
C_A	empirical coefficient	m^{-1}

The tidal prism now is the tidal prism behind the cross-section under consideration (and not the total tidal prism for the entire basin). The flow area below MSL could be considered as the channel cross-sectional area A_c. The flats are then defined as lying above MSL (but note that in other cases, they may be defined as lying above MLW, see also Fig. 9.25).

In the case that the flood-tidal delta spans the entire basin area (as is the case for e.g. the Wadden Sea), an empirical relationship for the total basin channel volume is:

$$V_c = C_V P^{3/2} \tag{9.17}$$

in which:

V_c	the equilibrium total channel volume below mean sea level	m^3
P	the tidal prism	m^3
C_V	empirical coefficient	$\text{m}^{-3/2}$

For example, the empirical coefficient C_V is $65 \times 10^{-6}\ \text{m}^{-3/2}$ for the Wadden Sea and $73 \times 10^{-6}\ \text{m}^{-3/2}$ to $80 \times 10^{-6}\ \text{m}^{-3/2}$ for the Eastern Scheldt and the Grevelingen (Eysink, 1991).

The power ½ in Eq. 9.17 can be understood as follows. We have found that the cross-sectional area of the channels is proportional to the tidal prism (Eq. 9.16). Furthermore, the length of the channels is proportional to the square root of the basin surface area (channels and flats), which in turn is proportional to the square root of the tidal prism. We then have:

$$\begin{aligned} A_c &\propto P \\ L_c &\propto \sqrt{A_b} \propto \sqrt{P} \end{aligned} \quad \Rightarrow \quad V_c = A_c L_c \propto P\sqrt{A_b} \propto P^{3/2} \tag{9.18}$$

in which:

A_c	the channel cross-section	m^2
P	the tidal prism	m^3
L_c	length of channels	m
V_c	volume of channels	m^3
A_b	the gross basin area (flats and channels)	m^2

From the proportionalities of Eq. 9.17, we can also deduce a relation between the tidal flat area and the total basin area. The flats area is equal to the total basin area minus the channels area (Fig. 9.25):

$$A_f = A_b - A_{ch} = A_b - \frac{V_c}{D_c} \approx A_b - \alpha \frac{P\sqrt{A_b}}{D_c} \approx A_b - \beta \frac{H_m}{D_c} A_b^{3/2} \tag{9.19}$$

in which

A_f	flats area, i.e. the area above MSL	m^2
A_{ch}	the horizontal area below MSL covered by all channels	m^2
α, β	constants of proportionality	m^{-1}
D_c	typical channel depth	m
H_m	mean tidal range	m

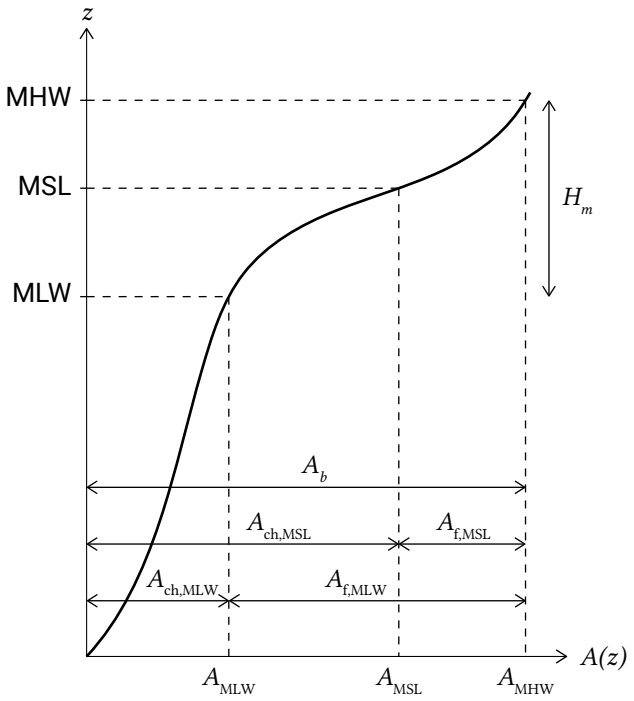

Figure 9.25: Definition of the basin area, channel area and flats area relative to the tidal levels.

§1.1~~Renger and Partenscky~~§1.1Renger and Partenscky (1974) found for the German Bight§1.1, with the flats defined as lying above LW: [p448]

$$A_f = A_b - 0.025 A_b^{3/2} \tag{9.20}$$

Figure 9.26 shows similar relationships for the estuaries in the south of the Netherlands and for the Wadden Sea basins. An explanation for the trend of the relation could be the increasing activity of local wind waves in larger basins (since waves act as an eroding agent on the flats).

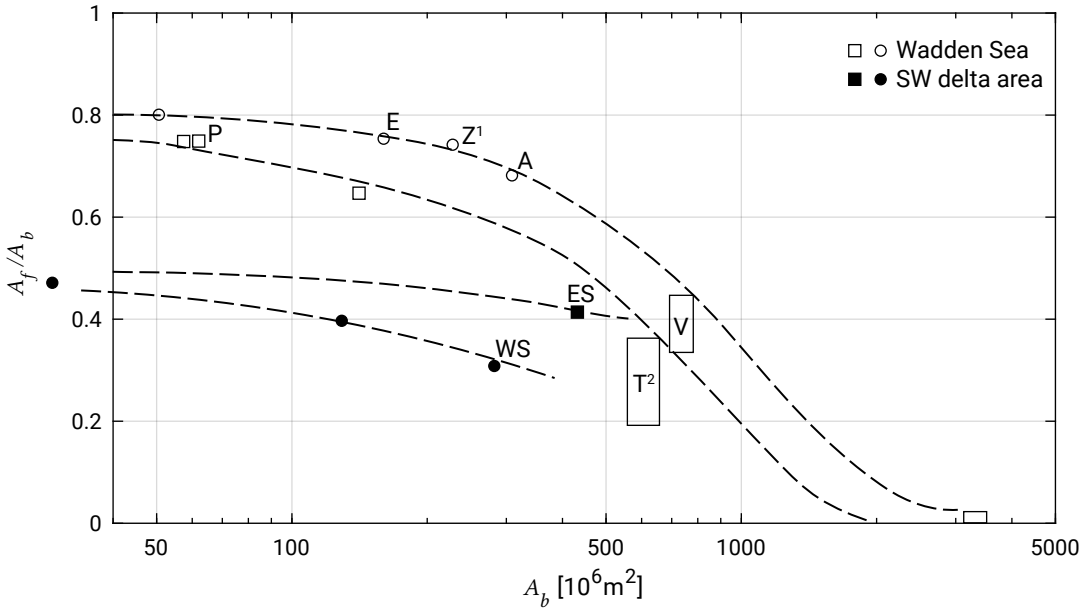

Wadden Sea
T Texel Inlet
E Eierland Inlet
V Vlie Inlet
A Ameland Inlet
Z Zoutkamperlaag Inlet
P Pinke Inlet

southwestern (SW) delta area
WS Western Scheldt
ES Eastern Scheldt

[1] before closure of the Lauwerszee
[2] after closure of the Zuiderzee (IJsselmeer); no equilibrium yet

Figure 9.26: Relative area of the intertidal zones in the Dutch Wadden Sea (upper two lines) and the delta area in the southern Netherlands (lower two lines). Some of the inlet systems are indicated by letters.

9.7. Net sediment import or export

9.7.1. Introduction

Within the basin, the tide is strongly deformed by bottom friction and other non-linear effects associated with the basin geometry (see Sects. 5.7.3 and 5.7.4). This tidal distortion can either strengthen or weaken the magnitude of the maximum flood flow compared to the maximum ebb flow (flood versus ebb dominance) and causes an asymmetry between durations of the slack water periods as well. These asymmetries greatly impact the net movement of sediment, both sand and silt, and thus the morphological development of the basin over time. As mentioned before, due to this feedback mechanism the basin in essence determines its own evolution (if we ignore external conditions such as sediment availability, storm surges and the tidal conditions at sea).

So-called hypsometric[5] curves give information about the depth of the channels and the extent of the flats (see Fig. 9.27). In Sect. 5.7.4, these parameters were found to control ebb and flood dominance in the following way:

- A large tidal amplitude and shallow channels enhance flood dominance;

[5]The term hypsometry refers to the topographical characteristics of tidal basins.

- A large intertidal storage volume (as compared to channel volume) enhances ebb dominance.

The import or export of sand is strongly determined by the velocity signal being flood-dominant or ebb-dominant, as we will see in Sect. 9.7.2.

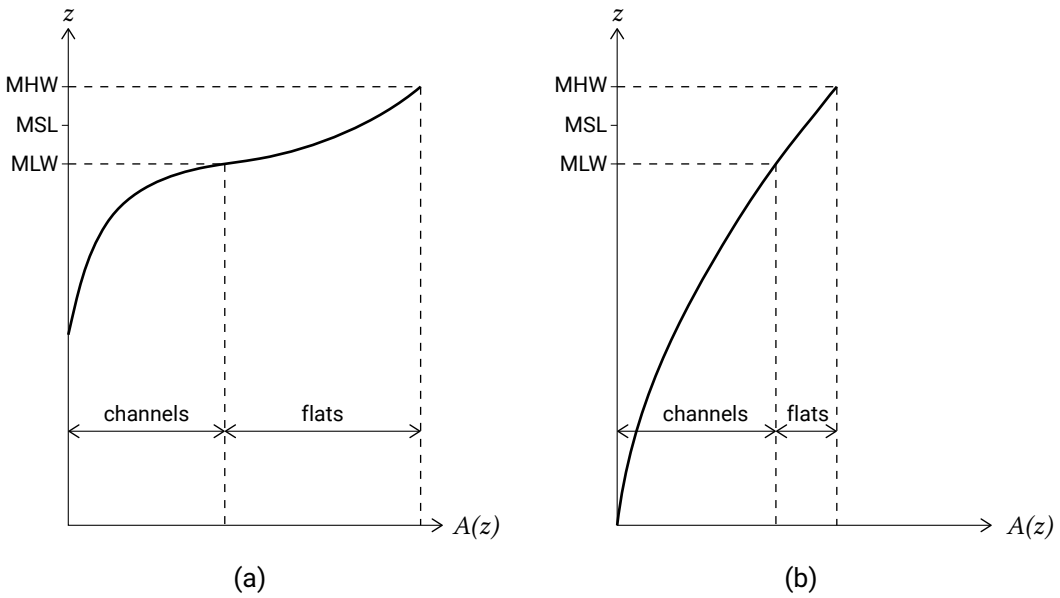

Figure 9.27: Hypsometric curves for two different basin types; the wetted basin surface area $O(z)$ as a function of the water level. The left figure is representative of a situation with shallow channels and large intertidal storage areas. The right situation is the opposite: deep channels and small intertidal areas. Here the flats are defined as lying above MLW.

9.7.2. Tide-induced residual transport of (medium to) coarse sediment

In this paragraph, we explore the sediment flux averaged over the tide and analyse the conditions under which a net import or export of *(medium to) coarse* sediment in the basin will occur (for fine sediment an *additional* effect occurs which is discussed in Sect. 9.7.3). A larger influx than outflux of sediment leads to a net landward directed sediment flux; as a result, the basin will import sediment. The opposite applies for basins exporting sediment.

In Ch. 5 we discussed in detail the mechanisms that contribute to a residual sediment transport, either landwards or seawards:

- The asymmetry of the horizontal tide (Sects. 5.7.4 and 5.7.5);
- Tide-averaged residual currents (Sect. 5.7.6) *along the channels*.

The residual flow along the channels may be composed of for instance contributions due to river flow and as compensation for Stokes drift. The secondary flow patterns as discussed in Sect. 5.7.6 have no direct impact on the import or export of sediment from the basin.

In the analysis below, we approximate the tide-averaged residual flow by a constant and depth-averaged residual tidal velocity u_0 in the channel direction. We further assume that M2 (semi-diurnal, 12.42 h period) is the dominant tidal-current constituent and that all other constituents are of a lesser order of magnitude. Furthermore, the residual flow velocity u_0 is assumed to be small compared to the amplitude of the M2 tidal current. These conditions roughly apply in most tidal basins in the Netherlands.

Coarse sediment was defined in Ch. 6 as having a diameter such that $w_s/u_* > 1$, where w_s is the fall velocity and u_* is the shear velocity. Coarse sediment is thought to respond instantaneously to the flow velocity (or alternatively the bed shear stress). In terms of the flow velocity we can write for the bed load transport (defined as volumetric transport excluding pores in $m^3/s/m$) in the case of small bottom slopes:

$$S \approx c \left|u^{n-1}\right| u \tag{9.21}$$

The coefficient n is thought to lie in the range 3 to 5. Here, we propose $n = 3$, consistent with the Bagnold-type formulation (see Eq. 6.50) for bed load in the case of small bed slopes. Furthermore $c = 10^{-7}\,\mathrm{m^{2-n}s^{n-1}}$ to $10^{-4}\,\mathrm{m^{2-n}s^{n-1}}$. In this transport formula, initiation of motion is not taken into account. This would further enhance the effect of asymmetry.

For suspended load transport of medium to coarse, non-cohesive bottom material (sand), a similar relationship is often used, but with a higher velocity power ($n = 4$, in agreement with Bagnold's suspended load formulation).

For suspended load transport of fine (cohesive) sediment, other formulations need to be adopted, which take account of the time lags related to settling and resuspension. This is treated in Sect. 9.7.3.

The velocity signal u(t) considered by Van de Kreeke and Robaczewska (1993) can be written as:

$$u(t) = u_0 + \hat{u}_{\mathrm{M2}} \cos\left(\omega_{\mathrm{M2}} t\right) + \sum_i \hat{u}_i \cos\left(\omega_i t - \varphi_i\right) \tag{9.22}$$

in which:

u_0	the Eulerian residual flow	1
$\hat{u}_{\mathrm{M2}}$	the amplitude of the M2 tidal current	m/s
$\hat{u}_i$	the amplitude of the other tidal-current constituents	m/s
ω_{M2}	the angular frequency of the M2 constituent	rad/s
ω_i	the angular frequency of the other tidal-current constituents	rad/s
φ_i	the phase lag between M2 and the other tidal constituents	rad

By substituting this velocity signal (Eq. 9.22) in Eq. 9.21, Van de Kreeke and Robaczewska (1993) demonstrated, under the assumption of M2 dominance and $n = 3$ (and thus $S \propto u^3$), what the most important contributions to net tide-induced bed load transport of coarse sediment are. Note that their approach is quite similar to the decomposition of the wave-induced cross-shore transport, as discussed in Sect. 7.5.

The resulting formula for bed load transport averaged over the long term, valid under the above-mentioned restrictions, is:

$$\frac{S}{c\hat{u}_{M2}^3} = \underbrace{\frac{3}{2}\frac{u_0}{\hat{u}_{M2}}}_{1} + \underbrace{\frac{3}{4}\frac{\hat{u}_{M4}}{\hat{u}_{M2}}\cos\varphi_{M4\text{-}2}}_{2} + \underbrace{\frac{3}{2}\frac{\hat{u}_{M4}}{\hat{u}_{M2}}\frac{\hat{u}_{M6}}{\hat{u}_{M2}}\cos\left(\varphi_{M4\text{-}2} - \varphi_{M6\text{-}2}\right)}_{3} \tag{9.23}$$

in which:

u_0	the Eulerian residual flow	1
$\hat{u}_{M2}$	the amplitude of the M2 tidal current	m/s
$\hat{u}_{M4}$	the amplitude of the M4 tidal current	m/s
$\hat{u}_{M6}$	the amplitude of the M6 tidal current	m/s
$\varphi_{M4\text{-}2}$	the phase lag $^{\S 1.1}\varphi_{M4} - 2\varphi_{M2}$ [p452] between M2 and M4 (cf. Eq. 5.111)	rad
$\varphi_{M6\text{-}2}$	the phase lag $^{\S 1.1}\varphi_{M6} - 3\varphi_{M2}$ [p452] between M2 and M6	rad
c	coefficient defined through Eq. 9.21	

Apparently, the long-term-averaged bed load transport is predominantly determined by:

- the residual flow velocity u_0;
- the amplitude of the M2 tidal current;
- the amplitudes and phases (relative to the M2 tidal current) of the M4 (quarter-diurnal, 6.21 h period) and M6 tidal-current constituents.

Although higher odd and even overtides also contribute, the first even overtide M4 and first odd overtide M6 are the most important contributing overtides. The components K1, S2, N2 and MS4 were also included in the analysis, but were found to only cause fluctuations of the transport rates that would average out in the longer term. For example, the effect of inclusion of S2 is only to give a beating of the transport flux with a period of 14.77 days (cf. Fig. 3.25). The inclusion of the diurnal component merely gives a daily fluctuation, but does not influence the longer-term net transport (cf. Fig. 3.26).

The three numbered terms on the right-hand side of Eq. 9.23 represent the net transport as a result of:

1. The asymmetry introduced by the addition of a small residual flow to the sinusoidal M2 tidal current component (cf. Fig. 5.72 for a mean river discharge, although in that case u_0 is not small);
2. The asymmetric velocity signal of the M2+M4 tidal current combined. The tide-averaged *velocity* of the M2 + M4 tidal current is zero. However, due to the non-linear response of the sediment transport to the velocity, larger (positive and negative) velocities get relatively more weight in contributing to the *transport*. The result is a net transport in the ebb or flood direction respectively, depending on the phase angle $\varphi_{\text{M4-2}}$ (cf. Fig. 5.71); For $\varphi_{\text{M4-2}} = \pi/2$ or $3\pi/2$ the ebb and flood velocity are of the same size and the signal has a sawtooth shape. The net transport (averaged over the tidal cycle) is zero. For other values of $\varphi_{\text{M4-2}}$ the maximum ebb velocities differ from the maximum flood velocities (either larger or smaller in the case of ebb or flood dominance respectively), causing a net sediment transport. The net transport is largest for the maximum skewness of the velocity signal ($\varphi_{\text{M4-2}} = 0$ or π);
3. An interaction term among M2, M4 and M6 (smaller than the first two contributions). Its importance is governed by the phase angles $\varphi_{\text{M4-2}}$ and $\varphi_{\text{M6-2}}$.

The first two terms in Eq. 9.23 are the most important. Their origin can be further clarified by considering the effect of the addition to the M2 sinusoidal current signal of u_0 and the M4 tidal current separately. We will also explore the effect of inclusion of M6.

Let us first consider $u(t) = u_0 + \hat{u}_{\text{M2}} \cos\left(\omega_{\text{M2}} t\right)$. If we substitute this in Eq. 9.21 and use $n = 3$, we find for the time-dependent transport:

$$
\begin{aligned}
S(t) &\approx c u(t)^3 = c\left(u_0 + \hat{u}_{\text{M2}} \cos\left(\omega_{\text{M2}} t\right)\right)^3 \Rightarrow \\
\frac{S}{c\hat{u}_{\text{M2}}^3} &= \underbrace{\left(\frac{u_0}{\hat{u}_{\text{M2}}}\right)^3}_{1} + \\
&\quad \underbrace{3\left(\frac{u_0}{\hat{u}_{\text{M2}}}\right)^2 \cos\left(\omega_{\text{M2}} t\right) + \cos^3\left(\omega_{\text{M2}} t\right)}_{2} + \\
&\quad \underbrace{3\left(\frac{u_0}{\hat{u}_{\text{M2}}}\right) \cos^2\left(\omega_{\text{M2}} t\right)}_{3}
\end{aligned}
\tag{9.24}
$$

The term denoted '1' can be neglected relative to the other terms, since we had assumed that $u_0/\hat{u}_{\text{M2}}$ is a small quantity (M2 being dominant). The remaining formula could also be obtained by using a Taylor expansion, as in Intermezzo 7.3, now with the residual flow velocity being the perturbation. The terms denoted '2' are symmetrical about the horizontal axis and will not give a contribution when averaged over the M2 tidal

period. The only term of interest for the tide-averaged sediment transport is term '3'. Integration over the tidal period results in:

$$\frac{\langle S \rangle}{c\hat{u}_{\mathrm{M2}}^3} = \frac{3}{2}\left(\frac{u_0}{\hat{u}_{\mathrm{M2}}}\right) \tag{9.25}$$

which is identical to the first term in Eq. 9.23 and represents the effect of the interaction of a (small) residual flow and the M2 tidal current.

The next step is to look at the interaction of M2 and M4. The velocity can now be written as $u(t) = \hat{u}_{\mathrm{M2}} \cos\left(\omega_{\mathrm{M2}} t\right) + \hat{u}_{\mathrm{M4}} \cos\left(\omega_{\mathrm{M4}} t - \varphi_{\mathrm{M4\text{-}2}}\right)$ with $\omega_{\mathrm{M4}} = 2\omega_{\mathrm{M2}}$. The phase lag $\varphi_{\mathrm{M4\text{-}2}}$ between M2 and M4 is $\varphi_{\mathrm{M4}} - 2\varphi_{\mathrm{M2}}$. The effects of the phase angle on the velocity signal and u^3 are illustrated in Figs. 9.28 and 9.29.

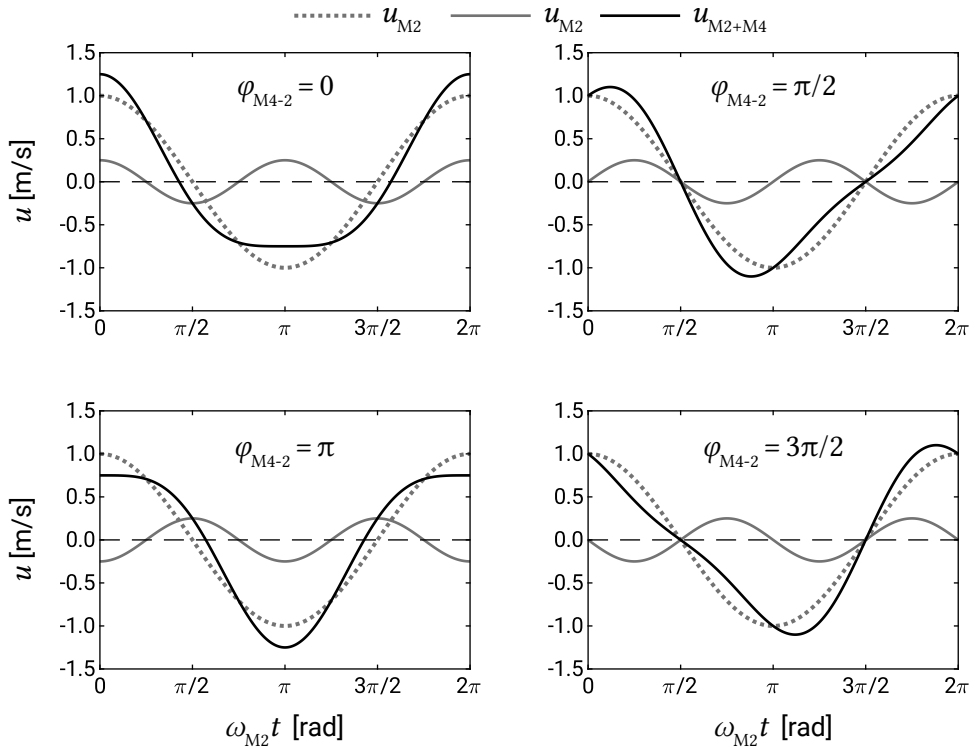

Figure 9.28: M2 and M4 tidal-current constituents. Flood dominance is found for $-\pi/2 < \varphi_{\mathrm{M4\text{-}2}} < \pi/2$ and ebb dominance for $\pi/2 < \varphi_{\mathrm{M4\text{-}2}} < 3\pi/2$. Flow reversal from flood to ebb (HWS) is of shorter duration than flow reversal from ebb to flood (LWS) for $0 < \varphi_{\mathrm{M4\text{-}2}} < \pi$ and of longer duration for $\pi < \varphi_{\mathrm{M4\text{-}2}} < 2\pi$.

We now get:

$$S(t) \approx c\left(\hat{u}_{\mathrm{M2}} \cos\left(\omega_{\mathrm{M2}} t\right) + \hat{u}_{\mathrm{M4}} \cos\left(\omega_{\mathrm{M4}} t - \varphi_{\mathrm{M4\text{-}2}}\right)\right)^3 \tag{9.26}$$

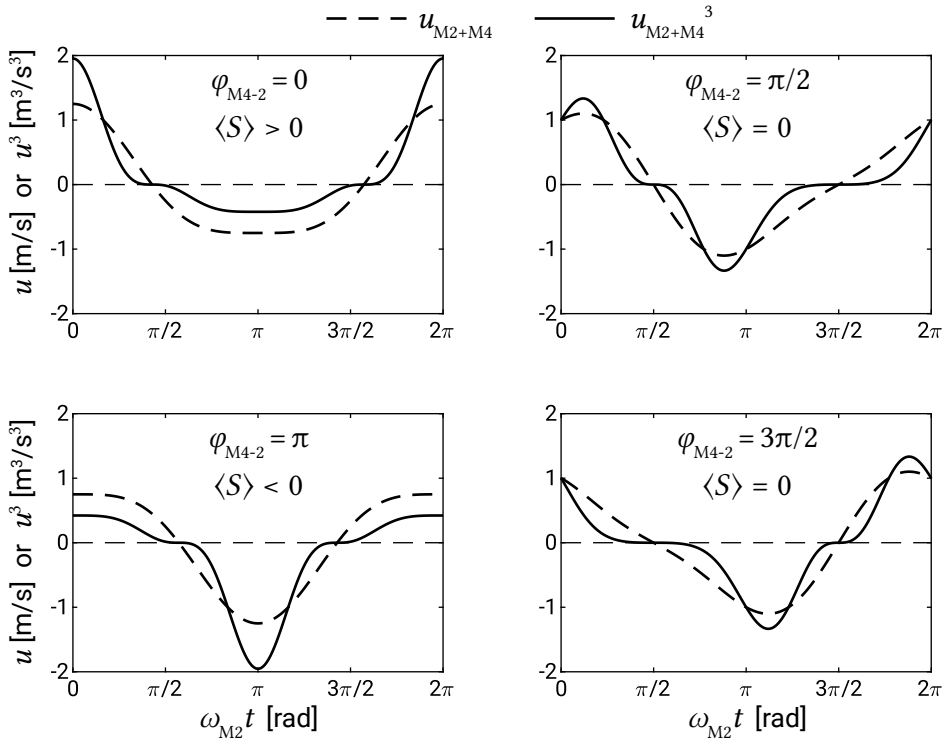

Figure 9.29: u and $\langle u^3 \rangle$ for u consisting of M2 and M4 tidal-current constituents with four different phase angles between M2 and M4. Since $\langle S \rangle \propto \langle u^3 \rangle$ we find $\langle S \rangle > 0$ for $-\pi/2 < \varphi_{M4\text{-}2} < \pi/2$ and $\langle S \rangle < 0$ for $\pi/2 < \varphi_{M4\text{-}2} < 3\pi/2$. $\langle S \rangle = 0$ for $\varphi_{M4\text{-}2} = \pi/2$ and for $\varphi_{M4\text{-}2} = 3/2\pi$.

The tide-averaged transport can be obtained by integration of Eq. 9.26. Analogous to the derivation of the M2-residual flow interaction, we neglect the third power of $\hat{u}_{M4}/\hat{u}_{M2}$. This leads to:

$$\frac{\langle S \rangle}{c\hat{u}_{M2}^3} = \frac{3}{4}\left(\frac{\hat{u}_{M4}}{\hat{u}_{M2}}\right)\cos\varphi_{M4\text{-}2} \tag{9.27}$$

In this formula we can recognise term '2' from Eq. 9.23. It represents the effect of the interaction of the M2 tidal current and its M4 overtide. As mentioned already, for $\cos\varphi_{M4\text{-}2} = \pm 1$, this interaction term is at its maximum. This corresponds to the situation that the ebb and flood velocities differ the most in magnitude. In the case of $\cos\varphi_{M4\text{-}2} = 1$ ($\varphi_{M4\text{-}2} = 0$) the velocity signal is flood-dominant (see Fig. 9.28, top left) without any sawtooth asymmetry, leading to a maximum net import of (coarse) sediment (Fig. 9.29, top left). For $\cos\varphi_{M4\text{-}2} = -1$ ($\varphi_{M4\text{-}2} = \pi$), the velocity is ebb-dominant and the system exports sediment (see Figs. 9.28 and 9.29, bottom left). There is no contribution to the net sediment transport for $\cos\varphi_{M4\text{-}2} = 0$ ($\varphi_{M4\text{-}2} = \pi/2$ or $3\pi/2$), see the right panels of Figs. 9.28 and 9.29. This corresponds to a velocity signal that demonstrates sawtooth asymmetry, but has equal flood and ebb current magnitudes and durations.

Why is a comparable term containing the odd overtide M6 not visible in Eq. 9.23? Apparently the interaction between the M2 and M6 does not lead to a net sediment transport, regardless of the phase angle. The combination of M2 and M6 leads to saw-tooth asymmetry only (see Fig. 9.30), and therefore does not give a residual sediment transport (Fig. 9.31).

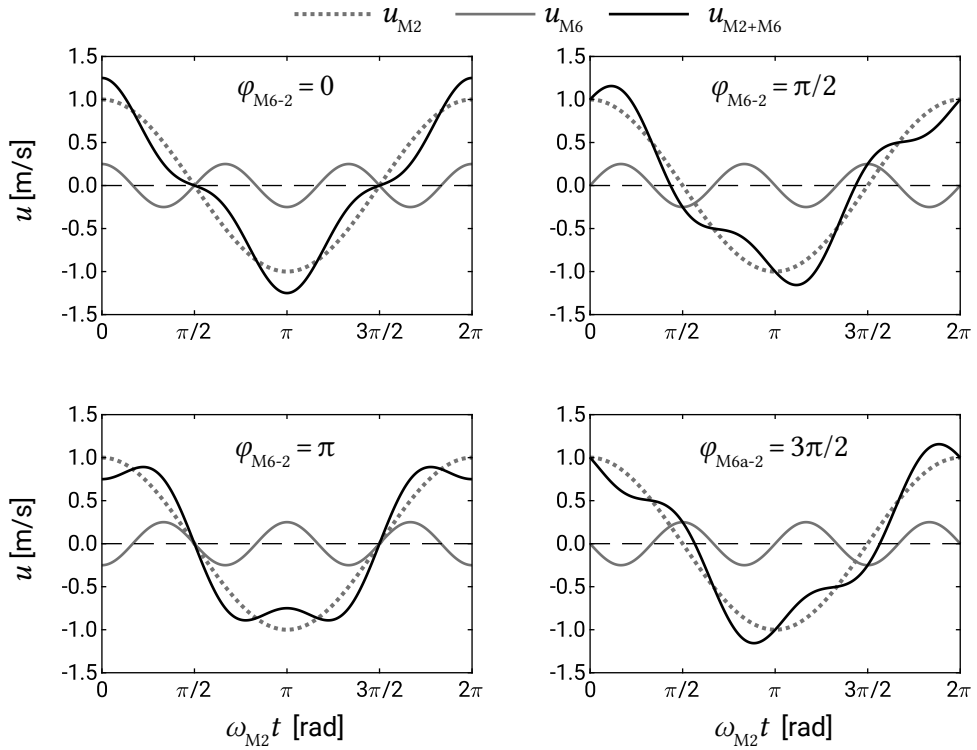

Figure 9.30: M2 and M6 tidal-current constituents for four different phase angles between M2 and M6.

Combining the above with our knowledge about how the basin influences the tidal asymmetry, we may conclude:

> Flood-dominant systems (with shallow channels and limited intertidal storage) enhance landward near-bed transport and tend to fill in their channels with coarse material, whereas ebb-dominant systems (with deep channels and large intertidal storage) enhance seaward near-bed transport and flush coarse sediment seaward.

9.7.3. Fine sediment transport and siltation

For coarse sediment, the bed load as well as the suspended load transport are determined largely by the hydrodynamic conditions and the sediment properties at the point of consideration. This can be modelled with a sediment transport formula (e.g. the Bijker or the Bailard formula, much like in the previous section), or with an intra-wave model which describes the suspension process during a wave cycle (Ch. 6). In the case of fine sediment, the suspended sediment transport not only depends on the

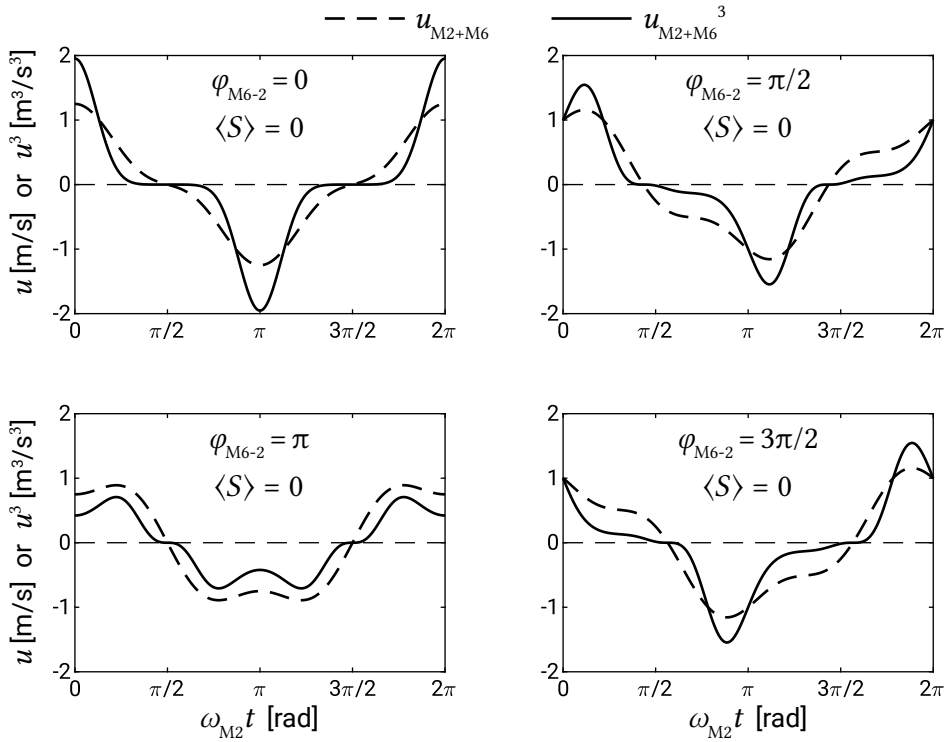

Figure 9.31: u and $\langle u^3 \rangle$ for u consisting of M2 and M6 tidal-current constituents with four different phase angles between M2 and M6. $\langle S \rangle \propto \langle u^3 \rangle = 0$ for all phase angles.

local instantaneous flow velocity, but also on the flow conditions upstream and in the past. We therefore need to include a 'memory effect' that makes the sediment concentration at a certain point respond to the conditions in all points the suspended sediment has come through in the past (Sect. 6.8.1). The timescales of erosion and sedimentation become important, a characteristic that causes an essential difference in the tidal dynamics of fine sediment (silt) compared to coarser sediment (sand). For sand this timescale is an order of magnitude smaller than the tidal period (so that we can assume an instantaneous response), whereas for fine sediment the timescales are of similar order. For fine sediment we denote this timescale as T_{sed}. If we assume that, under the condition of a constant flow velocity, after some time an equilibrium concentration c_{eq} is reached, then T_{sed} is the timescale for which the suspended concentration c approaches the equilibrium concentration. In formula form:

$$\frac{Dc}{Dt} = \frac{1}{T_{sed}} \left(c_{eq} - c \right) \tag{9.28}$$

Note that this is identical to Eq. 6.53. In principle a distinction must be made between the relaxation timescales T_{sed} for erosion and for sedimentation, respectively T_{Er} and T_{Se}. The equilibrium concentration §1.1 ~~eeq~~ §1.1 c_{eq} [p457] can be determined experimentally; it turns out that often

$$c_{eq} \approx \beta \, |u|^{n-1} \tag{9.29}$$

in which n = 3 to 5 (depending on the type of sediment) and β a constant. Please note the resemblance between Eq. 9.21 and Eq. 9.29. A (theoretical) example of the solution to this equation is shown in Fig. 9.32. The velocity signal $u(t) = \cos(\omega t) + {}^1/_4 \cos(2\omega t - {}^{\S 1.1}\varphi_{\text{M4-2}} = 3\pi/2)$ [p458] has been chosen such that the flood velocities are equal in magnitude to the ebb velocities. Hence, no residual bed load transport of coarse material will occur. For the equilibrium concentration, Eq. 9.29 has been used with $n = 5$, resulting in $c_{eq} \propto u^4$. In the case of an instantaneous sediment response (coarser material), the concentration would be equal to the equilibrium concentration and the net suspended sediment transport would be zero. In the case of finer sediment, the sediment needs time to respond and will follow the §1.1 red dotted §1.1 dash-dotted [p458] line. This is computed from Eq. 9.28 using $T_{sed}/T_{\text{M2}} = 0.2$. It can be seen that now the concentration is generally higher during the flood period than during the ebb period. As a result, the sediment flux uc during flood is 31 % larger than during ebb, leading to a net landward-directed flux of fine sediment.

The asymmetry in the concentration stems from the asymmetry in the slack water periods. In the schematised situation of Fig. 9.32, the duration of flow reversal from flood to ebb (HWS) is longer than the duration of flow reversal from ebb to flood (LWS). Hence, a strong sedimentation occurs around HWS; in the initial ebb phase only a small amount of material is in suspension. Later in the ebb period, more fine sediment is suspended. Around LWS part of this sediment settles, but not so much because of the short slack water duration. When the flood current increases in strength, a relatively large amount of suspended material is immediately transported. Subsequently, the suspended concentration increases even further. It is clear that, averaged over the flood, the concentration of suspended sediment is therefore larger than that during ebb. Over the whole tidal period, we therefore observe a net landward-directed transport.

In practice, both types of tidal asymmetry can be present at the same time (Fig. 9.33). A §1.2 short §1.2 long HWS duration and a net §1.2 seaward-directed §1.2 landward-directed [p458] transport of fines can be observed in Fig. 9.33. The slack durations before ebb ($T_{1,\text{slack}}$) and flood ($T_{2,\text{slack}}$) are defined by the flow velocity ($u_{\text{crit,flood}}$, $u_{\text{crit,ebb}}$); for smaller velocity magnitudes, sedimentation takes place. Since $T_{1,\text{slack}} > T_{2,\text{slack}}$, an import of fines is likely to happen. For coarser sediment (sand) slack water duration does not play a role of importance because of the short sedimentation timescale. Generally speaking, we may state that we have net flood transport for $u_{\text{max,flood}} > u_{\text{max,ebb}}$, and net ebb transport in the reverse case. In the present example, the maximum ebb velocity is larger than the maximum flood velocity. Hence, an export of coarse sediment can be expected.

In Sect. 5.7.4 we discussed 'sawtooth asymmetry of the horizontal tide'. We concluded that for a short basin, with shallow channels and little storage-offering flats, the HWS duration is longer than the LWS duration. On the other hand, in a basin with vast storage-offering tidal flats and deep channels, the HWS duration is shorter than the LWS duration. This suggests that import of fines is a characteristic property of a tidal

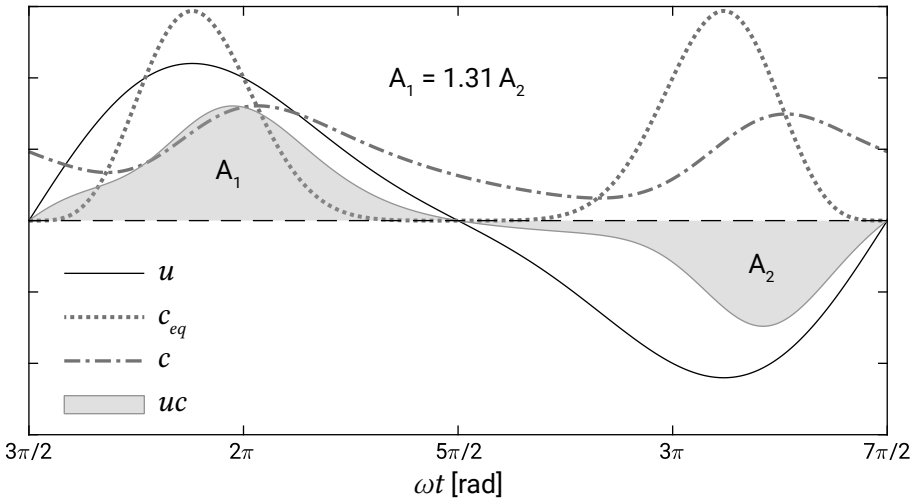

Figure 9.32: Lag effects on the residual sediment transport ($\hat{u}_{M4}/\hat{u}_{M2} = 0.25$ and $\varphi_{M4\text{-}2} = 3\pi/2$). Positive values for u §1.1(above the dashed line) indicate flood velocities. Since the duration of HWS (flow reversal from flood to ebb) is longer than the duration of LWS (flow reversal from §1.1~~flood to ebb~~§1.1ebb to flood [p459]), the sediment concentration is higher during the flood period than during the ebb period and a residual transport occurs in the flood direction.

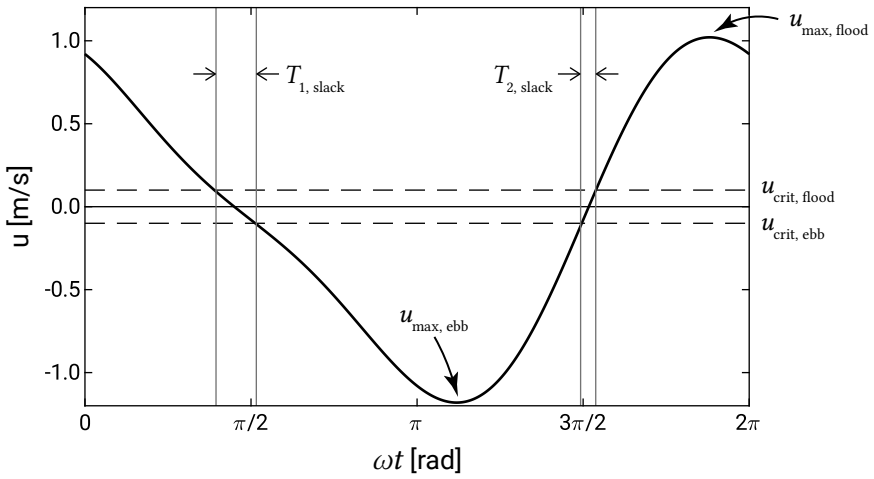

Figure 9.33: Asymmetry of the horizontal tide. The signal combines a small ebb current with M2 and M4 tidal-current components with $\varphi_{M4\text{-}2} = 3\pi/2$.

basin with shallow channels and limited tidal storage flats. Similarly, one may expect that basins with deep channels and large intertidal storage are likely to export fines. However, the latter is often not true, due to a counteracting effect that is especially important when large intertidal flats are present.

This counteracting effect is related to differences of sedimentation at HW and at LW. The relaxation timescale for sedimentation T_{Se} is, amongst other factors, dependent on the water depth, viz. $T_{Se} \approx h/$§1.1~~w_s~~§1.1w_s [p459]. Hence, the amount of sedimentation at HW can strongly differ from that at LW. This is particularly the case when the wet surface of the basin is much larger at HW than at LW (large intertidal storage),

implying an on average smaller water depth at HW than at LW. The result is a larger sedimentation at HW than at LW, reducing the concentration and sediment flux during the ebb period.

Apparently, a large storage-offering flat area has two opposing effects on the net transport of fine sediment: on the one hand a large storage prism causes a short slack duration in the flow channel at HWS; on the other hand, in this short period a strong settling can occur due to the small water depth. If the latter effect dominates this leads to a net import of fines, even in the case of large storage areas. This may be one of the reasons that many tidal basins are deposition areas for fine sediments (silt).

Furthermore, wave stirring and storm surges can cause a strong erosion and export of fine sediment. Waves can be expected to stir up sediment very effectively, and more so for smaller water depths. This increases fine sediment concentrations in the initial ebb phase, enhancing an ebb-transport.

9.7.4. Overview of the relation between morphology and sediment transport

From the above, we may derive qualitative relations between net sediment transport and the morphological characteristics of tidal basins. Table 9.4 and Table 9.5 give an overview of, respectively, the conditions for net flood and ebb transport for sediment in general and for fine sediment only. In the tables, the role of external conditions (tides, waves) is also indicated.

Table 9.4: Conditions for net import or export of sediment

Net flood transport	Net ebb transport	Tidal asymmetry
Small storage flat area	Large storage flat area	u_{max} flood/ebb
Long shallow channels	Long deep channels	u_{max} flood/ebb
Fast tidal rise at sea	Fast tidal fall at sea	u_{max} flood/ebb

Table 9.5: Conditions for net transport of fine sediment (silt)

Net flood transport	Net ebb transport	tidal asymmetry
Small storage flat area	Large storage flat area	u_{max} flood/ebb slack duration HW/LW
Large storage flat area	Small storage flat area	sedimentation HW/LW
Shallow channels	Deep channels	u_{max} flood/ebb slack duration HW/LW
Long HW period at sea	Short HW period at sea	slack duration HW/LW
Protected location, few waves	Open, many waves	sedimentation HW/LW

9.7.5. Large-scale morphodynamics

Basins are said to be flood-dominant or ebb-dominant, which refers to net sand import or sand export. In the case of neither flood nor ebb dominance, there is no net sediment gain or loss and the system is said to be in equilibrium (on the scale of the basin). Morphological equilibrium is dependent on external conditions, but if we assume these to be neutral, different basin geometries may fulfil the condition for equilibrium:

- Shallow channels and large intertidal (storage) flat area (e.g. Wadden Sea);
- Deep channels and small intertidal (storage) flat area (e.g. Eastern Scheldt);
- Intermediate geometries.

In the equilibrium condition, the geometrical characteristics of the basin are such that the durations of ebb and flood are approximately equal. (Dronkers, 1998) derived a formula for this equilibrium condition, based on the assumption that the tidal asymmetry at sea is not strong. This condition is shown in Fig. 9.34. It indicates that for Dutch tidal basins the ratio between the average channel depths and flat surface area is such that net ebb and flood transports are approximately equal, but have a slight flood-dominant tendency.

The tidal basins in the Wadden Sea (especially in the eastern Wadden Sea) are generally considered to be in morphological equilibrium. The flood dominance found in Fig. 9.34 could be the result of the neglect of residual currents in the derivation. As a result of Stokes drift, a compensating Eulerian current will enhance the ebb flow (see Sect. 5.7.6). It could also be that the flood dominance is the result of a sediment demand of the basin as a result of sea level rise (Sect. 9.8.3).

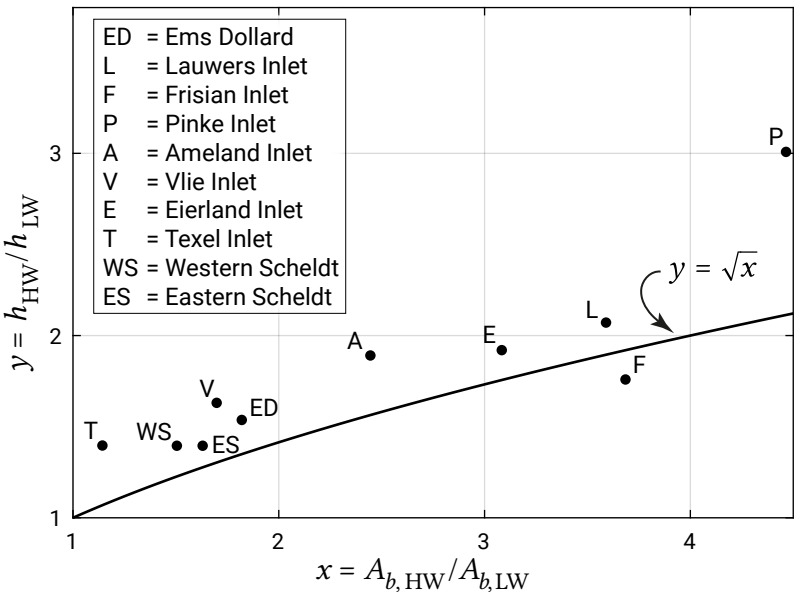

Figure 9.34: Relation between basin-averaged channel depth and flat area for Dutch tidal basins (after Dronkers, 2005). The ratio of water depths at HW and LW (y-axis) becomes larger for shallower channels. The wet surface area ratio on the x-axis increases for larger intertidal storage areas.

What happens if we disturb this equilibrium slightly? An increase of the channel depth will enhance the ebb dominance and cause a net sediment export. The result is a further deepening of the channels; this is a case of an unstable morphological equilibrium (Sect. 1.5.2). An increase of the channel width is equivalent to a relative decrease of the intertidal areas. In this case a net sediment import occurs, annihilating the initial disturbance (stable equilibrium, see Sect. 1.5.2).

Some tidal basins are unstable and silt up (with sand and/or finer fractions) in a relatively short period, such as the Zwin that[§1.1], in the Middle Ages, [p462] gave navigational access to the town of Bruges. In other basins there is a dynamic equilibrium between import and export of sediment. This is for instance the case for the eastern Wadden Sea, which has had the same topography for nearly a thousand years. The locations of flats and channels fluctuate over timescales of tens to hundreds of years.

The fact that tidal basins exist implies that they display a large degree of morphological stability. This stability requires that channel width, channel depth, flat width and flat depth are dynamically coupled. Especially the transversal transports (between flats and channels) in tidal basins are responsible for this dynamic coupling. This internal dynamic coupling can restore the morphological stability of the basin, for instance after the channel depth is disturbed by deepening or filling.

9.8. Changes in dynamic equilibrium

The various empirical relationships as described in this chapter can help understand the large-scale morphological response to changes in the dynamic equilibrium of tidal basins. A few examples will be given.

9.8.1. Closure of a part of a tidal basin

The closure of a part of a tidal basin will result in a reduction of the channel volume V_c and the tidal prism P. [§1.2]With the help of Fig. 9.35 and Table 9.6 we will demonstrate how the[§1.2]~~The~~ basin[§1.2]~~s~~ will adapt to [§1.2]~~the new situation, see Fig. 9.35~~[§1.2]two different closures [p462]. In this example we will neglect the role of the flats and assume that they are already more or less in equilibrium immediately after the closure.

The [§1.2]~~two lines~~[§1.2]dashed lines in Fig. 9.35 represent the power relationship between the channel volume [§1.2]V_c and the tidal prism ([§1.2]Eq. 9.17, with C_V is 65×10^{-6} m$^{-3/2}$)[§1.2]. The solid lines represent[§1.2]~~ and~~ the power relationship between the sand volume of the outer delta [§1.2]V_{od} and the tidal prism ([§1.2]Eq. 9.3, with C_{od} is [§1.2]~~65.7×10^{-4} m$^{-3/2}$~~[§1.2]65.7×10^{-4} m$^{-0.69}$)[§1.2]Since both the horizontal and vertical axes are logarithmic, the power relationships plot as straight lines. The slope of the lines is determined by the power in the power relationships, which means a larger slope for V_c than for V_{od}. The intercept with the vertical axis is given by the coefficient in the power relationships and is smaller for V_c than for V_{od}. [p462]

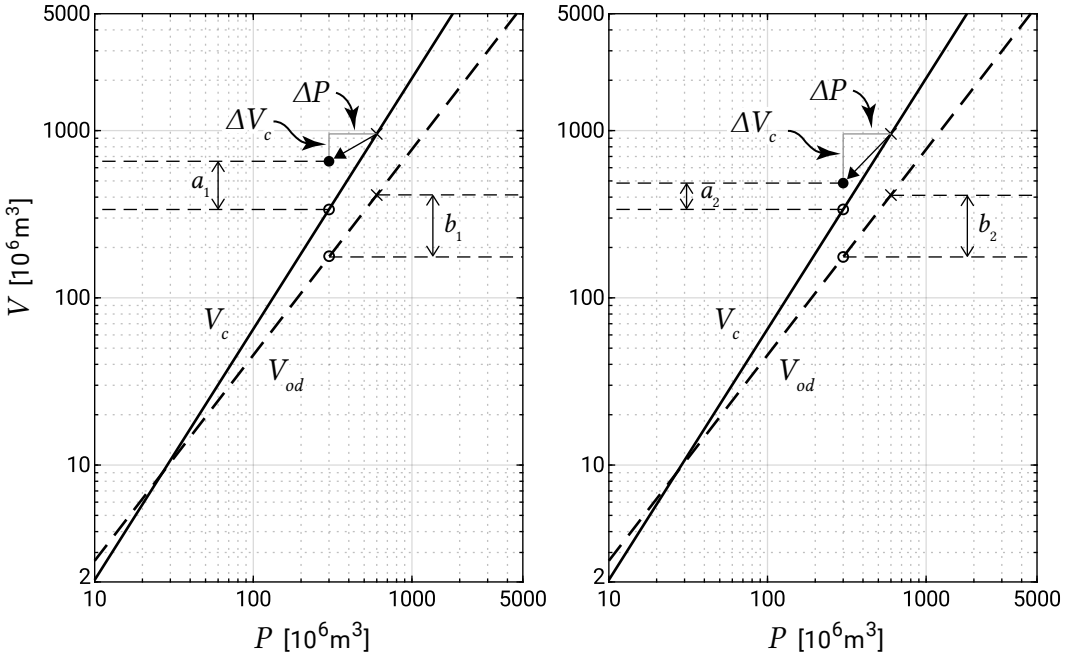

Figure 9.35: Effect of closure of part of the basin on the channel volume V_c and the volume of the outer delta V_{od} (crosses: initial situation, solid dots: immediately after closure, open dots: new equilibrium). §1.2 ~~From Eqs. 9.3 and 9.17 it can be seen that a change in the prism has a larger effect on the equilibrium channel volume than on the equilibrium volume of the outer delta.~~ Closure 1 (left) has a smaller ΔV_c than closure 2 (right). The reduction of the tidal prism ΔP is the same for both closures. Corresponding numbers are found in Table 9.6. [p463]

Now assume an §1.2 initial equilibrium situation with tidal prism P and corresponding channel volume V_c and sand volume of the outer delta V_{od} §1.2 (crosses in Fig. 9.35) [p462]. At a certain moment in time, a part of the tidal basin is closed off, which §1.2 immediately results in a reduction of the channel volume ΔV_c and a reduction of the tidal prism ΔP §1.2 (solid dots in Fig. 9.35). §1.2 Closure 1 (Fig. 9.35, left) and closure 2 (Fig. 9.35, right) differ in the magnitude of ΔV_c. The reduction of the tidal prism ΔP is the same for both closures. A new equilibrium §1.2 for V_c and V_{od} will arise at the equilibrium lines for tidal prism $P - \Delta P$ §1.2 (open dots in Fig. 9.35, the same for both closures). Note that the change in the prism has a larger absolute effect on the equilibrium channel volume than on the equilibrium volume of the outer delta ($V_{c,\,\text{before}} - V_{c,\,\text{after}} > V_{od,\,\text{before}} - V_{od,\,\text{after}}$). Due to the closures §1.2 ~~This means that~~ [p462] the channel volume is a m^3 too big and the sand volume of the outer delta is b m^3 too big. The sand of the outer delta is available for the adaptation of the channels (to an amount of b m^3). The rest, if a–$b > 0$, has to be supplied from outside (resulting in erosion of the downdrift coast). §1.2 The magnitude of b is given by $V_{od,\,\text{before}} - V_{od,\,\text{after}}$. The magnitude of a is determined as $V_{c,\,\text{before}} - V_{c,\,\text{after}} - \Delta V_c$ and is therefore different for closure 1 and closure 2. §1.2 ~~Closure 1 (Fig. 9.35, left) and closure 2 (Fig. 9.35, right)~~

~~differ in the magnitude of ΔV_c.~~ [p463] As a consequence $a–b > 0$ for closure 1 and $a–b < 0$ §1.2for closure 2 (see Table 9.6).

Table 9.6: Values corresponding to closure 1 (Fig. 9.35, left), closure 2 (Fig. 9.35, right) and accretion (Fig. 9.36). All variables in 10^6 m^3.

	closure 1	closure 2	accretion
Prism before	600	600	300
Prism after	300	300	225
ΔV_c	300	470	0
$V_{c,\text{ before}}$	955	955	338
$V_{c,\text{ after}}$	338	338	219
a	318	148	118
$V_{od,\text{ before}}$	412	412	176
$V_{od,\text{ after}}$	176	176	123
b	236	236	52
$a - b$	82	−88	66

An example of the above situation is the closure of the Lauwerszee in 1969 (see Fig. 9.2) as described in Wang et al. (2009), reprinted in App. E. Due to the decrease of the tidal basin area, the tidal prism and, as a result, the magnitude of the flow velocity decreased significantly. The tidal asymmetry changed such that it became more flood-dominant, favouring sediment input. The effect of the closure therefore was a sediment deficit that needed to be supplied from outside. Since the closure, the basin has been accumulating sediment and the ebb-tidal delta has been eroding. The sedimentation in the basin and the erosion of the ebb-tidal delta are more or less in balance. As a consequence the closure has not caused erosion of the adjacent coasts.

9.8.2. Accretion of new land

Natural accretion along the borders of the basin, due to the deposition of silt, is a very slow process. This process causes a gradual reduction of the tidal prism, see Fig. 9.36. Due to this reduction the channel volume is a m^3 too large and the sand volume of the ebb-tidal delta is b m^3 too big. This results in a sand demand from outside. Also in this case, not all the sand can be supplied from the outer delta; it will be supplied at the expense of the downdrift coast.

9.8.3. Relative sea level rise

The morphological response to sea level rise is more difficult to assess. From hypsometric curves of the different basins it follows that, without adaptation of the level of tidal flats, the tidal prism will increase and the area of intertidal zones will decrease. The latter effect will be most serious in the Wadden Sea, especially in the western part,

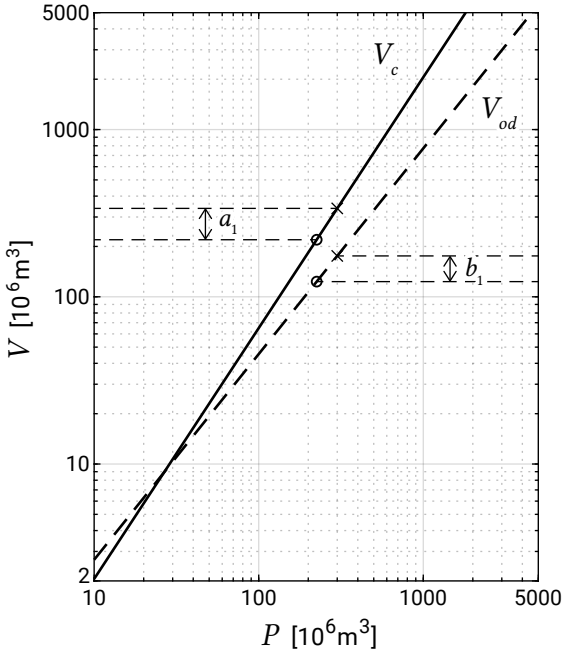

Figure 9.36: Accretion of new land (crosses: initial situation, open dots: new equilibrium). From Eqs. 9.3 and 9.17 it can be seen that a change in the prism has a larger effect on the equilibrium channel volume than on the equilibrium volume of the outer delta, such that $a - b > 0$.

where the tidal flats are low. If this scenario, without adaptation of the tidal flats, is realistic, the channels in the basin will widen and sand will be transported partly to the outer delta, which will extend, and partly will become available for accretion of the North Sea coast adjacent to the tidal inlet. However, an increase in sea level will also affect the level of the tidal flats. In a relative sense, the disturbance of the characteristic water depth on the flats will be much greater than in the channels. Hence, the sediment transport in the channels will be far less affected than that on the flats. Consequently, it seems realistic to assume that the response of nature will be strongest on the tidal flats. If it is assumed that the levels of the tidal flats can follow the sea level rise, this implies that the tidal prism of the basin remains unchanged, whereas the volume of the channels increases. Thus, this scenario results in a demand of sand from outside.

9.8.4. Adaptation time

The above-mentioned relationships only give an indication of the new equilibrium between morphology and hydrodynamic conditions in the case of changes. They do not give any information on how the adaptation will take place and what time this will take. In general, adaptation processes show a logarithmic character, see Fig. 9.37 and Eq. 1.2 in Sect. 1.5.4.

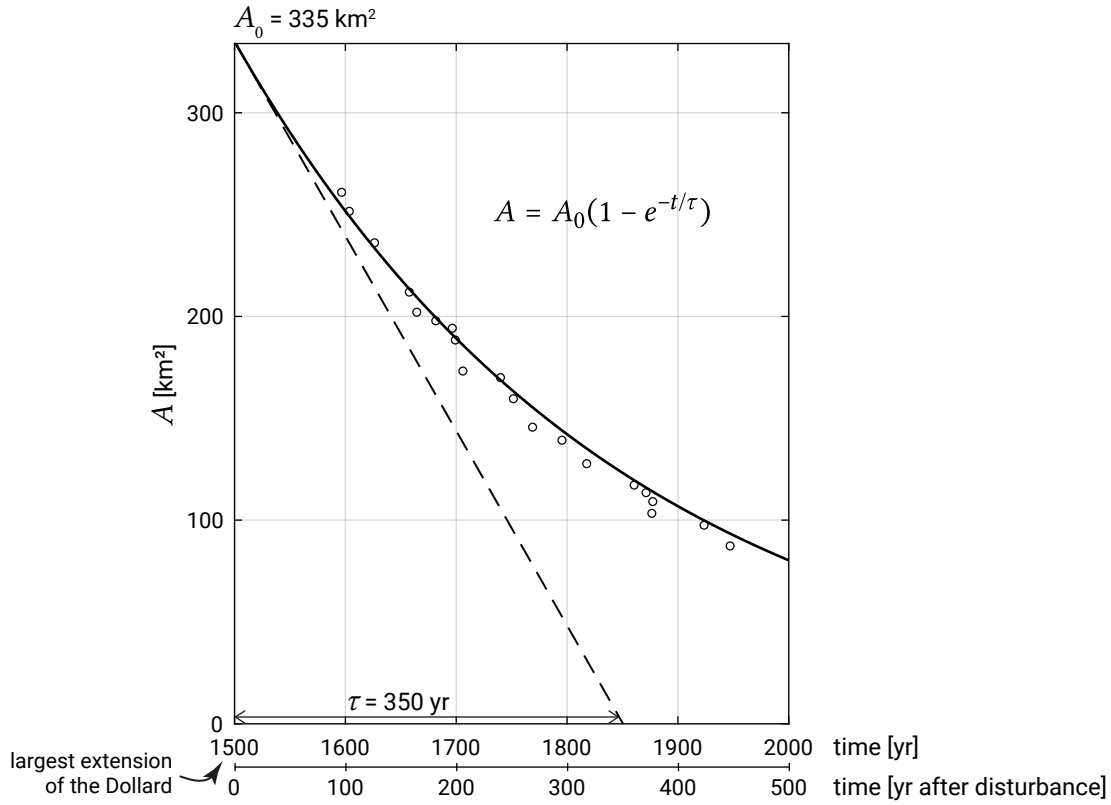

Figure 9.37: Accretion of the Dollard (according to Eysink, 1991). In the equation in the figure the t-origin is the time after the disturbance (extension), A is the area.

10

Coastal protection

10.1. Introduction

We have seen in the previous chapters how coasts can develop – can erode or accrete. Unfortunately, these processes may conflict with economic interests. A channel to a harbour may silt up, making the entrance too shallow for shipping, or a valuable structure (such as a hotel or jetty) may be washed away as a beach erodes. Beach accretion is rarely felt as a problem, except when the beach is too wide and the walking distance to the waterline is too far from a recreational point of view. We will therefore mainly focus on erosion problems.

Many sandy coasts all over the world suffer from structural erosion and/or dune and beach erosion during severe storm surges. In coastal engineering practice an important aim is the proper protection of these threatened coasts. Moreover, newly reclaimed areas or upgraded beaches have to be protected from the attacks by the sea. Furthermore, construction of harbours and other engineering works inevitably impacts the coastal system. The mitigation of adverse impacts should be an integral part of the design of these works (see Sect. 10.5.2).

Strategies and methods for coastal protection are introduced in Sect. 10.2. Next, the nature of coastal erosion (permanent or structural versus temporary) is extensively described in Sect. 10.3. Subsequently, Sect. 10.4 discusses the principle of interference in longshore transport rates to defend a structurally eroding stretch of coast. Section 10.5 deals with structures that are designed to interfere in longshore transport rates. Section 10.6 is devoted to structures that literally act as a barrier between the sea and the land. They prevent storm-induced, temporary loss of material from the dunes or land as well as flooding of the hinterland. Nourishment, a so-called 'soft' protection method, is treated in Sect. 10.7.

In the sections on structures, we focus on the functional design aspects of these structures. We will therefore discuss their effectiveness in coping with certain coastal problems and (briefly) the appropriate choices regarding position, crest height, length, etc. No attention will be paid to constructive and technical design aspects, like for example the required mass of stones of armour layers, thickness of various layers in the structures, etc. Other TU Delft courses like Bed, Bank and Shoreline Protection (CIE4310) and Breakwaters and closure dams (CIE5308) deal with this. We have, however, highlighted some interesting similarities between sediment transport and breakwater damage in App. D. Also, an overview of these topics can be found in Thorne et al. (1995) and in the CEM (see Sect. 1.7.3).

Although the term 'coastal protection' is usually not only used to mean protection against erosion, but against flooding as well, the determination of safety levels against flooding is not discussed in this book. The same holds for measures against sedimentation in approach channels to harbours. Dredging, the 'soft' solution to the latter problem, is discussed in detail in the course CIE5300 on Dredging Technology.

10.2. Coastal protection strategies and methods

10.2.1. Management strategies

In the last decade of the last century, especially in the context of raising awareness of the increased pressures on the coastal zone due to possibly accelerating climate change, management strategies to deal with coastal erosion were broadly divided into three categories (see Fig. 10.1):

Retreat do nothing and accept retreat and possibly flooding (as happened during the successive deglaciation periods since the earth came into existence).

Accommodate adapt coastal infrastructure to resist the increased risk of erosion and flooding.

Protect take protective measures to counteract erosion and flooding.

The management strategy 'retreat' may be applied in situations with strong coastline fluctuations without a clear long-term trend, or in situations where postponement of measures leads to more simple solutions in the future, because of the fact that erosion rates decrease as a function of time.

The chosen strategy as well as the chosen safety levels against flooding determine the methods to be used. Since we focus, in the present chapter, on protective measures to counteract erosion, we have implicitly assumed that the choice for protection as a management strategy has been made. However, protecting the coast is not necessarily the most appropriate strategy in all situations. The appropriate management strategy is closely linked to both the level of vulnerability and the land use (infrastructure, living, recreation, agriculture etc.) and thus to the social, economic and cultural value of the coast and the amount of available budget.

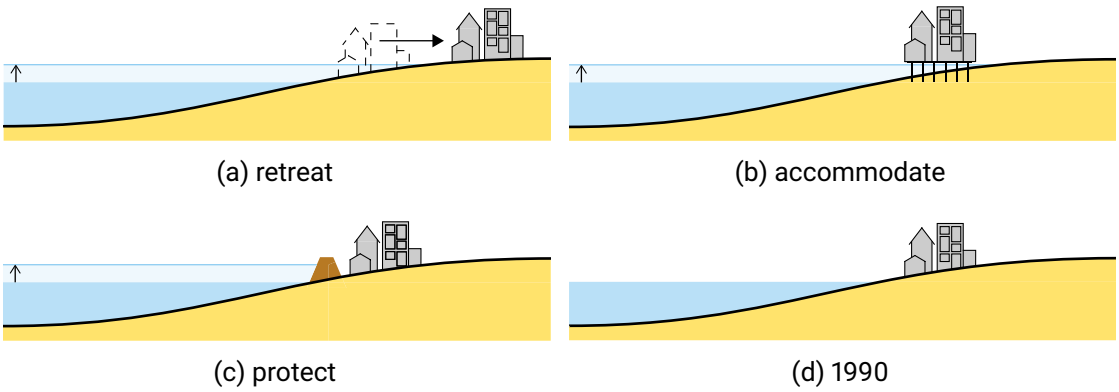

Figure 10.1: Management strategies for coastal erosion according to IPCC (1992) and World Coast Conference (1993): (a) retreat, (b) accomodate and (c) protect. Panel (d) refers to a specific situation in which a certain coastline (in this case the 1990 coastline in the Netherlands) is preserved using mainly sand nourishments.

10.2.2. Selection of protection method

In general, there are two possible solutions to coastal morphological problems, viz. 'hard' measures (coastal structures) and 'soft' (natural) measures.

'Soft' methods

The principle of 'soft' measures like beach or foreshore nourishment is to compensate for the eroded sand by nourishing sand, without great interference in the sediment transport patterns. This implies that the 'natural' erosion processes are allowed to continue. The eroded material is replaced on a regular basis with sand from somewhere else. This sand could be supplied, for instance, from deep-water borrow areas, or from the sediment deposited in an approach channel or upstream of a port. So the 'soft' solution to the erosion problem is in fact pumping sand towards the erosion area. Another example of a 'soft' solution is managed retreat in combination with protecting the retreated shoreline with a restored marsh.

Bypass systems form a special category of 'soft' solutions that artificially restore a (human-induced) blockage of the sediment transport. An example is a sand bypass system that brings sand from the accreting updrift shoreline to the eroding downdrift shoreline (see Fig. 10.2). In this way, the interruption of the sediment transport by the harbour is taken away.

Another example is a system in a river, which bypasses sediment from the upstream side of a hydropower dam to downstream in order not to interrupt the sediment supply to a river delta. The bypass system at the dam may take the form of a small cutter dredge that is continuously cleaning the basins upstream of the dam. The spoil is transported by a pipeline downstream of the dam into the river. Without such a system, river deltas may retreat after the construction of the dam.

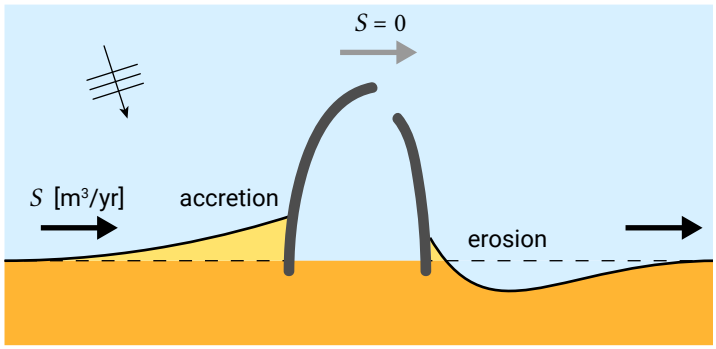

Figure 10.2: Typical structural downdrift erosion and updrift accretion.

'Hard' methods

Examples of 'hard' measures are series of groynes, series of offshore breakwaters, submerged breakwaters and revetments or seawalls (see Sect. 10.5.1 and Sect. 10.6). They ensure that sediment is not eroded, or to a lesser extent, by interfering in the sediment transports in alongshore and cross-shore directions of the coasts. This can be achieved in many ways, depending on the problem. For instance, undesired sedimentation can be prevented by structures that guide the currents in such a way that velocities and thus sediment transport rates increase. The 'hard' measures that counteract erosion can broadly be subdivided in:

1. Structures that primarily influence the rate of longshore transport under both normal and extreme conditions (groynes, a (long) dam to divert the wave- and tide-driven currents, detached breakwaters[1]);
2. Structures that prevent erosion during extreme storm events (seawall, revetment, sea dike).

The choice between a 'hard' or a 'soft' measure depends both on the characteristics of the problem concerned and on economic considerations. In Coastal Zone Management practice, the use of beach nourishment is becoming increasingly popular. Many of the frequently occurring adverse side effects of 'hard' measures can be avoided by using beach nourishments. It is noted, though, that beach nourishment in coastal zones that have a rich nearshore ecological value (e.g. sea grass meadows) is often problematic because of environmental reasons.

Nonetheless, the possible use of 'hard' measures for coastal protection still cannot be disregarded. A coastal engineer should at least have proper insight into the physical processes related to 'hard' measures. The desired effects (often: reduction or mitigation of the erosion potential in a given stretch of coast), and the often detrimental effects on adjacent coasts (lee-side erosion), have to be considered with care. Only then an appropriate choice can be made between the many coastal protection methods.

[1]Emerged detached breakwaters may also reduce storm-induced beach and dune erosion to a certain extent, see Sect. 10.5.4.

10.2.3. From problem definition to realisation

Coastal protection is an important task that requires skilled and experienced professionals. In some countries special institutes or Coastal Zone Authorities have been appointed to carry out the tasks involved. It is obvious that such authorities can only adequately operate if provided with governmental support and legal backing.

A few remarks can be made about the process from problem definition to implementation:

- The solution of a coastal erosion problem always starts with a clear understanding of the coastal processes that cause the coastal erosion problem (see for instance the erosion example of Fig. 10.7);
- Subsequently, the requirements for a possible solution have to be clearly defined. Should the erosion be prevented along the entire coast or only in a limited area? Is halting the erosion in a limited area enough or is recovery (accretion) in that area desirable? And are any changes in the future expected, which require adaptive intervention?
- In the next phase, different alternatives have to be analysed. Which alternatives meet the requirements? What are possible detrimental side effects? What are the costs involved?
- In the final selection phase, the best alternative has to be chosen, which is then designed in more detail, with respect to engineering, cost and implementation;
- After the implementation of the selected protection measure, it is strongly recommended to monitor the actual behaviour of the coast. Since 'art' and 'science' are still closely related in coastal engineering practice, the chosen solution may sometimes turn out to be far from ideal. The experience gained in this way can be very helpful in designing new projects.

10.3. Coastal erosion

10.3.1. Structural erosion of coasts

We speak about *structural erosion* in the case of a clear long-term erosional trend. Hence, structural erosion is a *permanent* erosion phenomenon. A typical example of a (human-induced) structural erosion problem is the erosion of a sandy coast on the lee side of port entrances sheltered by two breakwaters (see Fig. 10.2). As mentioned before, structural erosion also occurs at river deltas as a result of upstream damming of the river. This reduces the sediment supply from the river to the coastal zone and causes long-term retreat of the delta. Sometimes structural erosion problems have (partly) natural reasons, for instance if the wave climate varies along the coast due to sheltering effects or in the case of interruptions in the coastline (see Sect. 10.3.3) or if delta lobe switching occurs (see Intermezzo 2.2).

Structural coastal erosion means that the volume of sand in an arbitrary cross-section between well-chosen boundaries in that cross-section (control volume in m^3/m, see as shown in Fig. 10.4) gradually reduces as a function of time. The volume reduction is typically in the order of magnitude of 10 m^3/m to 50 m^3/m *per year* and the structural coastal retreat in the order of a few metres *per year* (Fig. 10.3). Intermezzo 10.1 provides some more information on the rate of recession versus the volume rate of erosion.

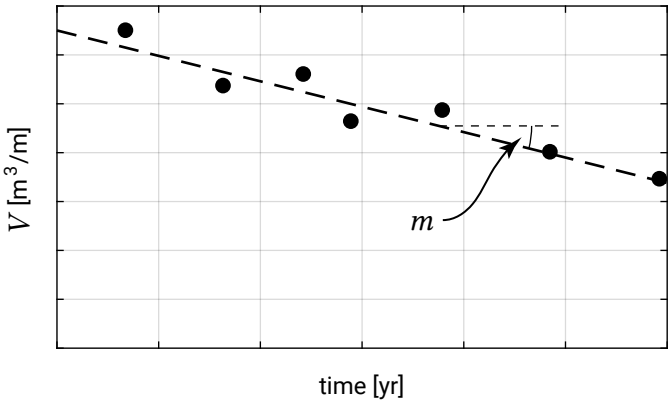

Figure 10.3: Volume loss out of control volume due to structural erosion.The slope $m = dV/dt$ [$m^3/m/yr$].

Intermezzo 10.1 Rate of recession versus volume rate of erosion

The two cross-shore profiles in Fig. 10.4 represent the position of the profiles at two different moments. As a first approximation it is assumed that the shape of the profiles remains identical (since the boundary conditions, e.g. wave climate and tides, are unchanged, see Sect. 7.2). The new profile can be found by shifting the old profile horizontally. It is assumed that not only the waterline shifts in the landward direction with a certain speed but that this holds in fact for all depth contours (cf. Sect. 7.4).

If the waterline shows a recession of R m/yr on average, the annual loss of volume out of the control volume area $^{\S 1.1}\Delta V$ [p472] ($m^3/m/yr$) is $R \times (h + d)$; see Fig. 10.4 for the definition of h and d. The dune height d with respect to MSL is easy to measure. The underwater part of the cross-shore profile h which has to be taken into account is more difficult to determine. Often an empirical relation for the depth of the so-called active part of the profile is taken as representative (depth of closure, see Sects. 1.5.1 and 7.2.3). This relates the depth at the end of the active part of the profile to the annual wave climate. A first approximation, the depth h can be found by multiplying the significant wave height which is exceeded for one day a year, with a factor of 2 to 3 (see the wave-breaking criterion in Sect. 5.2.5 and Hallermeier's closure depth in Sect. 7.2.3). With actual profile measurements often a more accurate estimate of h can be determined.

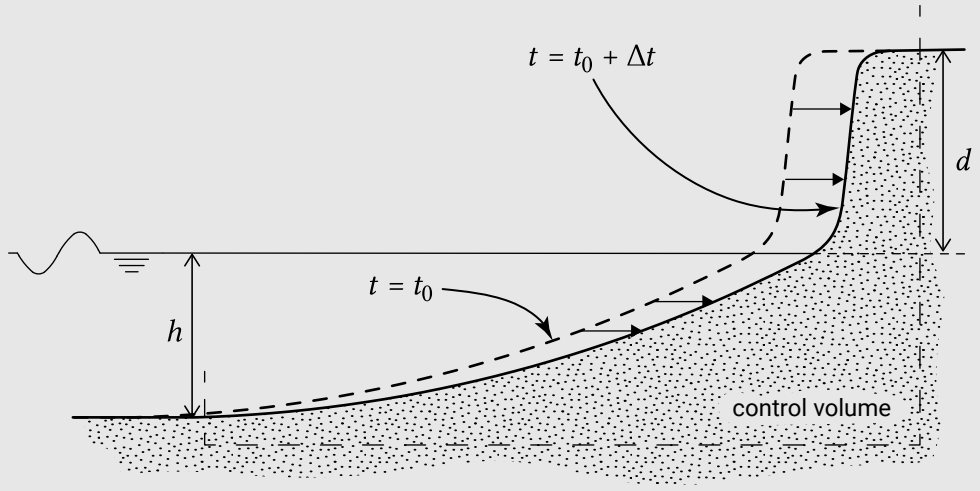

Figure 10.4: Retreat of the coastal profile due to structural erosion.

In Fig. 10.3, the development with time of the volume V in the cross-shore profile has been given. The slope $m = dV/dt$ (m^3/m/yr) is in this case a measure of the severity of the erosion problem. Of course a figure like Fig. 10.3 can also be made for an eroding profile in a structurally eroding part of the coast, by showing the recession of the position of the waterline (in metres with respect to a reference point) over time. The slope R (m/yr) is then a measure of the erosion rate. However, from a morphological point of view, it is preferable to represent erosion rates in terms of volumes instead of distances.

Although beach and dune erosion during a severe storm surge (see Sect. 10.3.2) is also considered as a typical erosion problem, it is not necessarily a *structural* erosion problem. Indeed, after the storm event the dunes and/or upper parts of the beaches may have lost sediment, which has disappeared from its pre-storm position. Often, however, the lost volume is found on the foreshore in the nearshore area (Fig. 10.5). Essentially, the total volume of sand in a cross-shore profile has not changed during the storm surge. In fact, only a redistribution of the sediment masses over the cross-sectional area has taken place. Depending of course on the severity of the storm surge, the volume of sand lost from the upper parts of the cross-section associated with this type of erosion is in the order of magnitude of 10 m^3/m to 100 m^3/m per event (per storm, that is to say, per day to a few days). In the period after the storm surge event, the normal natural conditions often force a recovery of the beaches and dunes. Thus, dune erosion during a severe storm surge is a *temporary* instead of a *permanent* erosion phenomenon.

In case of typical structural erosion problems, both normal conditions and storm conditions contribute to the eventual loss of sediment from a cross-section. Often a *gradient* in the longshore sediment transport is the main reason (gradient $dS/dx \neq 0$ with S the net yearly longshore sediment transport and x the coordinate directed along the coastline).

Structural erosion under normal conditions entails that the upper part of the profile (dry beach and slope of dune or mainland front) does not participate in the transport processes; the water and the waves do not reach this part of the cross-section. However, the erosion of the foreshore will continue under these normal conditions.

By contrast, under storm conditions, when the waves reach the dunes due to higher water levels and higher waves, the upper part of the cross-section forms an integral part of the entire active profile. In that case, the erosion of dunes and possibly hinterland will occur.

In an essentially stable situation, the storm-induced erosion of dunes and hinterland is only temporary. In a structurally eroding case, however, this erosion is partly permanent. This is because the eroded sediments from the upper part of the cross-section will not fully return under normal conditions, but will be removed in an alongshore direction. Hence, at the end of the day, by means of cross-shore transport processes, the structural erosion of the beach and the foreshore will also cause erosion of the dunes or the hinterland. This distinction is often not clear to the general public. Often permanent losses of dunes and firm land are incorrectly associated with storm surge events, while the basic problem is in fact structural erosion.

Structurally eroding coasts are often the source of serious problems for the various users of the coastal zone. Properties built close to the sea are lost; roads in the area disappear into the sea. Often society calls for action to be taken by the Coastal Zone Authorities in order to prevent the detrimental effects of structural erosion.

> In summary, the general public often thinks that storms are the reason for (permanent) beach and dune erosion problems, while the real reason is a gradient in longshore sediment transport rates. The storm just provides the necessary link in a chain of processes, by supplying sediments from the upper part of the profile to the active littoral zone.

10.3.2. Beach and dune erosion during severe storm surges

Coasts which over a number of years seem to be stable may suffer from the effects of severe storm surge events. During a severe storm, sediments from the dune and upper parts of the beach are eroded and deposited in deeper water within a short time period. This is a typical cross-shore sediment transport process. Severe storms are usually accompanied by higher water levels and higher waves. Under normal conditions, the shape of a cross-shore profile might be considered to be in equilibrium (cf. Sect. 7.2). During a storm, the initial profile shape (viz. the pre-storm profile) is far from the equilibrium shape that corresponds to the severe storm conditions. As a result, processes occur to reshape the profile, causing erosion of the upper part of the cross-shore profile, while the foreshore is accreting, resulting in flatter slopes in the post-storm profile (Fig. 10.5). Note that the control volume does not change during

the storm surge. This is because no sand is lost from the profile; sand is merely redistributed in the cross-shore direction. During the storm, while the profile flattens, the erosion process slows down. After the storm, generally a recovery towards the original situation occurs under the combined action of moderate waves and wind (the latter resulting in aeolian transport rebuilding the dunes).

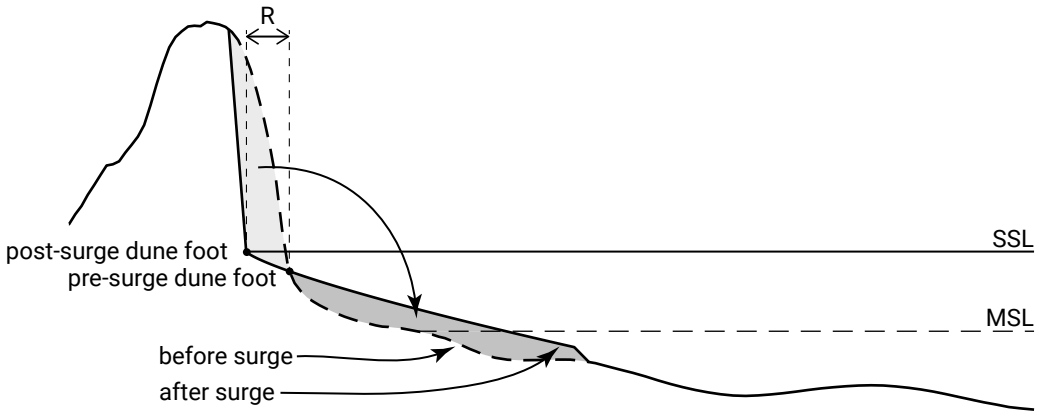

Figure 10.5: Dune erosion during a severe storm surge redistributes sediments in the cross-shore direction. There is no loss of sediment in the alongshore direction and hence the sediment will return under moderate conditions, through the combined action of small waves (under water) and onshore wind (on the beach).

These episodic events do occur along all types of coasts (along structurally eroding, stable and even along accreting coasts). As mentioned in the previous section, the rate of erosion can be very high (of course depending on the actual conditions, erosion rates of several metres per event, say per day to a few days). Associated with the loss of volumes of sediment from dune or firm land, a retreat R of the coast (see Fig. 10.5) of many metres may occur during a single event. Nowadays methods are available to reliably quantify the rate of dune erosion during arbitrary boundary conditions (see Sect. 7.3.5).

The effects of structural erosion or temporary storm-induced erosion on properties built too close to the shoreline are eventually the same. In both cases, the properties may be lost (see Fig. 10.6). However, it is beyond doubt that the countermeasures used to resolve or mitigate these different types of erosion must be quite different (see Sects. 10.5.1 and 10.6.1).

10.3.3. Dynamic behaviour of tidal inlets

Coasts near tidal inlets are often very dynamic. This is the result of a complicated sediment transport pattern, induced by tidal and wave-driven currents. Sediments from one side are imported into the tidal basin or are bypassed along the tidal bars, whereas the other side may receive sediments exported from the tidal basin or from direct bypass (see Sect. 9.4.2). The position of the main channel system may oscillate or gradually shift in one specific direction due to the accumulation of sediments at one

Figure 10.6: Historical photo of damage to a hotel at Schiermonnikoog due to dune erosion, circa 1923. From Rijkswaterstaat ('Credits' on page 579).

side of the inlet and erosion on the other side of the inlet. This may eventually lead to spit formation (cf. Fig. 8.28). This dynamic behaviour often hampers safe navigation and may cause damage to the properties adjacent of the inlet. The inlet may act as a sediment sink for longshore sediment transport, thus depriving the downdrift coastline of sediment.

10.4. Modification of longshore transport processes

In most cases, the use of structures for coastal protection relies on the ability of such structures to interfere with the existing sediment transport processes. The main reason for structural erosion is often a *gradient* in the net longshore sediment transport along a stretch of coast. Structures counteracting this erosion are designed to change the curve of the longshore transport S versus distance along the shore x, such that the transport gradients become zero and hence erosion is stopped. This situation is discussed in more detail below.

In Fig. 10.7, line a indicates the net yearly longshore sediment transport S along a coast (S: expressed in m^3/yr). The x-axis is the alongshore coordinate, with the positive transport direction coinciding with the positive x-direction. The increasing transport from A to B (difference V) causes an erosion problem in stretch A–B (along A–B $dS/dx \neq 0$). Such a situation may occur for a straight coastline that is subject to waves that increase in height in the positive x-direction along the coast.

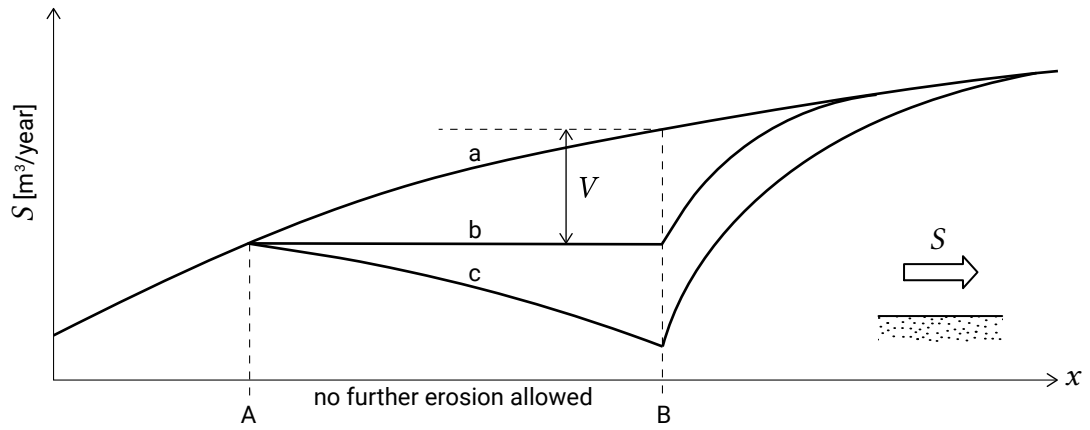

Figure 10.7: Longshore sediment transport distribution along eroding coast.

Assume that one wishes to protect only stretch A–B of the coast, for instance because important investments have been made in section A–B, which are at stake due to structural erosion. The erosion can be stopped by ensuring that the existing sediment transport distribution line *a* in Fig. 10.7 is changed to line *b* (along section A–B $dS/dx = 0$ in that case). At least in section A–B the erosion would stop if distribution *b* could be achieved. In the section to the left of A, the erosion will just continue, since the sediment transports have not changed. In the section to the right of B the existing erosion also continues, but at an even higher ratethan before, since the throughput of sediment through the cross-section in point B has been reduced, yielding steep gradients in the longshore sediment transport distribution. At the right-hand side of B, consequently, *lee-side erosion* occurs.

The formulation of the requirements of the sediment transport distribution in section A–B is rather simple; however, it is rather difficult to acquire curve *b*. Structures that, in principle, interfere with the process of longshore sediment transport rates can be used. Series of groynes or series of breakwaters with a crest either above (emerged) or below sea level (submerged) will undoubtedly affect the existing longshore sediment transport, but it is very difficult to ensure that these countermeasures are appropriate for specific cases. If the effectiveness of the countermeasure does not meet expectations, the erosion will be reduced but not entirely stopped. If the countermeasure is too effective in reducing the sediment transport, or in other words if the reduction of the sediment transport in stretch A–B is too great (see line *c* in Fig. 10.7), accretion in stretch A–B will be unavoidable. This might be beneficial for section A–B (accretion instead of the desired stabilization), but the lee-side erosion in the section at the right-hand side of B will grow worse. In fact, achieving line *c* in Fig. 10.7 represents an 'overkill' operation.

Even if the countermeasures in section A–B are well tuned, lee-side erosion is usually unavoidable. In fact, a solution for the erosion problem in section A–B, with the help of structures that decrease the sediment transport along A–B, always comes at the expense of the stretch of coast beyond B; the problem has simply been *shifted*. If the

extra lee-side erosion beyond B becomes unacceptable, countermeasures in this section are necessary as well. The lee-side erosion is then shifted further down the coast. Only if there is an accreting stretch of coast beyond B, or if position B represents the very end of a stretch of coast (e.g. if there is a tidal inlet beyond B), lee-side erosion is less obvious.

Alternatively, artificial nourishment could be selected as countermeasure in section A–B. The erosion problem is not permanently solved by artificial nourishment; the nourishment does not reduce the sediment transport involved, but eliminates the effects of the erosion instead. Since the erosion continues, the nourishment has to be repeated on a regular basis. In the example of Fig. 10.7, a volume V (in m^3/yr) must be nourished. It is not practical or economical to nourish every year, so usually a nourishment lifetime of 5 to 10 years is chosen.

At first sight, the limited lifetime of a nourishment may seem to be a drawback. In many cases, however, artificial nourishment is more cost-effective than solutions with permanent structures. This is certainly the case when the present-day value of the measures is calculated (the cost of future nourishment contributes little to the present-day cost). An additional advantage of artificial nourishment is that extra lee-side erosion does not take place.

10.5. Structures influencing longshore transport rates

10.5.1. Introduction

Structures of which the primary aim is to change the longshore transport rates under both normal and extreme conditions are:

- Jetties/shore-normal breakwaters;
- Series of groynes;
- Detached shore parallel offshore breakwaters (emerged and/or submerged).

The above-mentioned structures can all be observed along a Mediterranean coastal section of about 5 km in Sitges, Spain (Fig. 10.8). Open groyne cells with a spacing of about 500 m can be observed at the northern part of the beach and partly closed cells are present along the southern side of the beach. The harnessed solution with T-head groynes and detached breakwaters on the southern side is necessary to retain the beach sand within the cells (see further Sects. 10.5.3 and 10.5.4).

10.5.2. Jetties or shore-normal breakwaters

A jetty is a structure perpendicular to the coast that extends out into the sea and protects a harbour or stabilises a coastline. The crest heights of jetties are often well above MSL (see Figs. 10.8 and 10.9). They often function as breakwaters, in that they reduce

(a) south

(b) north

Figure 10.8: Coastal structures in Sitges, Spain. Orthophotos from ICGC obtained in May 2019 ('Credits' on page 579).

the wave action behind it. In the following, the morphological functions of these jetties or breakwaters are explored.

Figure 10.9: Port of Scheveningen in August 2010. From Rijkswaterstaat ('Credits' on page 579).

Function 1: Blocking the longshore transport of sand, which would otherwise settle into a dredged approach channel

When a longshore transport threatens to cause sedimentation in an entrance channel to a harbour or a river, this process can be interrupted by constructing a jetty slightly 'updrift' from the harbour or river (that is to say, where the sand is coming from). This jetty or breakwater should extend at least through the breaker zone, even during storms, and even after the coast has moved forward as a result of accretion. Material transported along the coast will accumulate against the jetty on the updrift side.

Generally, dredging is required to maintain an approach channel at the required depth for shipping. For example, the breakwaters of the Dutch port of IJmuiden extend about 2.5 km into the sea, thus (partly) preventing sedimentation in the approach channel. In many cases, the approach channel extends seaward of the end of the breakwaters. Here, the maintenance of an artificial channel is more expensive than in between the breakwaters. This is because large sedimentation may occur in the unprotected channel and dredging operations are less efficient here due to wave action. The optimum length of the breakwaters follows from a balance between the construction costs of the breakwater and the maintenance costs of the entrance channel.

The impact of long structures on the morphodynamics of the adjacent coasts can be very large. Since wave-induced longshore sediment transports are interrupted, sedimentation and coastline accretion on the updrift side is expected. On the downdrift side, erosion and coastline retreat will occur (see also Sect. 8.4.2). This sedimentation/erosion pattern is avoided with the implementation of an adequate sand bypass system.

Also, the further the breakwaters extend seaward, the more the (tidal) currents are affected (see Sect. 5.7.2). Contraction of the currents (high velocities) just near the entrance to the port hampers vessels to safely enter and depart the port. The contraction may further lead to local scour (possibly undermining the stability of the breakwaters). With a well-chosen layout of the breakwater, the currents can be guided such that the nuisance for shipping operations will be acceptable and scour is reduced as much as possible.

Figure 10.10 shows a nature-based port solution on the West African coast, which has been named the Sandbar Breakwater. Along the Gulf of Guinea coast, longshore sediment transport is unidirectional, and obstructions such as a breakwater result in strong sedimentation updrift and continuous coastal erosion on the downdrift side.

The Sandbar Breakwater concept makes the inevitably growing sandbar updrift the basis for the port protection, while restoring the natural sand balance by repetitive nourishments downdrift, at the Sand Engine (Van der Spek et al., 2020).

Long structures extending into open sea have an impact not only on the coastal morphology, but may also affect the transport patterns of silt and e.g. fish larvae. These impacts may be felt at rather large distances from the structures due to the low settling

Figure 10.10: Westward-looking aerial photo of the Sandbar Breakwater, including the sand engine, Lekki, Nigeria. Image courtesy of CDR International B.V.

rates. These aspects must be taken into account in the decision making process. Compare the discussion in The Netherlands of the impact of extensions of the Maasvlakte (Port of Rotterdam) on morphological processes in the Wadden Sea.

Function 2: Stabilizing a natural river mouth or coastal inlet

Natural river mouths and coastal inlets fronted by barrier spits typically have entrances that migrate over time (see Sect. 8.4.5). In order to protect existing infrastructure and property at the eroding side of the mouth and to accommodate shipping (yachts; fishery vessels), these entrances may be fixed at a certain position. This can be accomplished by constructing two jetties at either side of the mouth (see Fig. 10.11).

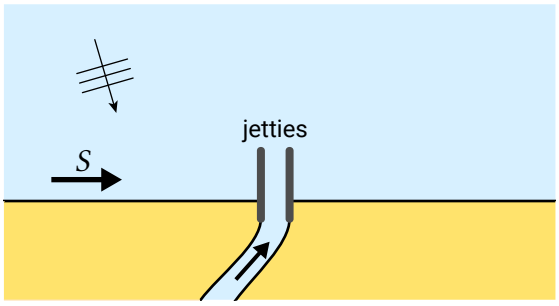

Figure 10.11: Stabilised river mouth.

Since in most cases these jetties will interrupt the natural longshore sediment transport, a proper design calls for additional measures in order to restore the sediment transport across the river mouth or tidal inlet. This can be done with a sand bypass system, which in fact should form an integral part of the design of the stabilizing structure.

Estimation of the required capacity of a sand bypass system is a difficult task. This is because the capacity should be based not only on the annual sediment transport

capacity but also on the fluctuation in time and the spatial distribution. Well-calibrated mathematical models may provide a good first estimate, based on the calculated actual sediment transport rates and their distribution over space and time.

It is tempting to consider the (yearly) growth of the spit (the migration speed of the mouth) as a measure for the annual net sediment transport. Be aware, however, that in natural systems often only a part of the annual net sediment transport contributes to the growth of the spit; the other part bypasses in a natural manner. If only the growth of the spit is taken into account, the rates of accretion and erosion after stabilization and the necessary capacity of a bypass system may be greatly underestimated. Therefore one may want to postpone the design of a bypass system until nature shows the real quantities involved, by accumulation on one side and by erosion on the other side. However, postponing the design of the bypass system ("let's wait and see") means in many cases that at the end of the day there is no money left to build a proper system. Without an adequate sand bypass system, the negative impact of the stabilization project, that is, erosion on the downdrift side of the jetties, is not mitigated.

As in the previous cases, stabilization of a river mouth or tidal inlet requires a comprehensive decision-making process, taking both the planned benefits as well as possible adverse consequences into account.

Function 3: Flushing the entrance channel to a harbour or river by constriction of the entrance

When a river with a sufficiently large sediment supply debouches into the sea, shoal formation may be expected slightly offshore from the river mouth. This shoal can be a major obstacle for shipping, especially during severe storms when waves are breaking on the shoal. In order to push the shoal formation to deeper water, two jetties can be built at the river mouth, in such a way that the entrance is kept narrow until deeper water is reached. In this way, the flow velocities in the entrance are increased, resulting in an increased sediment transport capacity, which tends to keep the entrance open.

Function 4: Preventing structural erosion of a sandy coast near a tidal inlet

The stretches of coasts near tidal inlets are generally very dynamic (see Sects. 9.4.2 and 10.3.3). Often one side of the inlet shows an accretive and the other side (the downdrift side) an erosional tendency. By building a long pier (dam) near the inlet at the end of the eroding coast (the crest level of the dam should be high enough to catch the sediments), one prevents that sediments disappear into the tidal basin. The construction of an 800 m long dam at the northern part of the Dutch island of Texel in 1995 is such an example (Fig. 10.12). Although this dam has stopped coastal erosion (see also Fig. 9.14), it is still unclear how the tidal inlet and tidal basin will respond on the long term to the reduction of the annual sediment supply. Due to the large surface area of the tidal basin, the short-term effects have been relatively small.

Figure 10.12: Long dam at the eastern tip of Wadden Island of Texel in August 2011. Photo from Rijkswaterstaat (see 'Credits' on page 579).

10.5.3. Groynes

A jetty only prevents accumulation of material in a small area or stimulates accumulation in another rather restricted area. Its influence is mostly local. A field of groynes, on the other hand, is a series of smaller jetties extending into the surf zone and spaced at relatively short intervals along a beach (see Fig. 10.13). They can be very effective in reducing the existing longshore sediment transport rate[2] along a coast. By keeping the coastal sand trapped between two adjacent groynes, they tend to stabilise the entire coast along which they are built. As such, they can be used to defend an eroding coast (for instance over a length of 5 km), to widen a beach or to extend the lifetime of beach fills.

Two main types of groynes can be distinguished:

Impermeable, high-crested structures with crest levels above MSL +1 m; these types of groynes are used to keep the sand within the compartment between adjacent groynes. The shoreline will be oriented perpendicular to the dominant wave direction within each compartment (sawtooth appearance of overall shoreline).

Permeable, low-crested structures with crest levels between the MLW and MHW lines, such that structure-induced eddy generation is reduced, at least at high tide (cf. Fig. 5.45). These types of groynes are generally used on beaches with a small sediment deficit; the function of the groynes is to slightly reduce the littoral drift in the inner surf zone and to create a more regular shoreline (without sawtooth effect). They are for instance made from sheet piles: a row of vertical

[2]Not only wave-induced longshore transport rates will be reduced, but tide-induced longshore transport rates as well, since groynes push the tidal current away from the coast.

(wooden or steel) piles purposely spaced so as to make a porous barrier, thus reducing but not totally blocking the longshore transport (Fig. 10.14).

Figure 10.13: Groynes on the Dutch southwestern delta coast, near Domburg, in November 2005. Photo from Rijkswaterstaat ('Credits' on page 579).

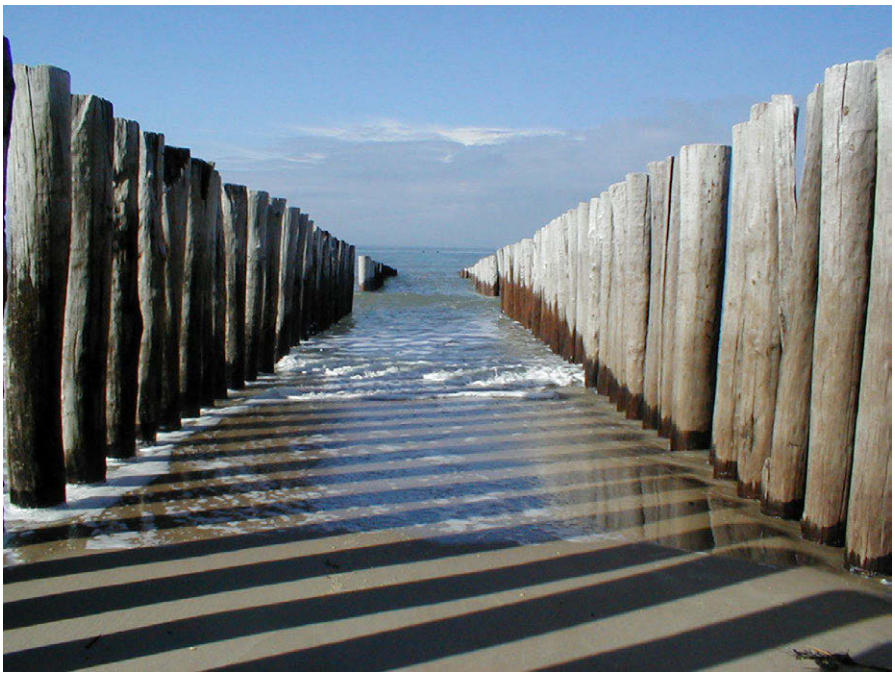

Figure 10.14: A row of piles serving as a groyne at the Zeeland coast in March 2004. This is only one of many types of groynes. Photo by Ad Reniers (see 'Credits' on page 579).

If properly designed, groynes can be used to achieve sediment transport curve b in Fig. 10.7, which is the ideal situation in that case. Proper design implies that the right choices for groyne length, height and permeability to sand are made. The finetuning problem (length and length/mutual spacing ratio) is, however, a difficult problem to

resolve. The physics of groyne systems are not completely understood, making the successful design of a groyne system more an art than a science. No generally applicable design rules are available, although there are some design guidelines (see below). A spacing equal to a few times the length of the groynes is common.

Since for solution *b* only a small portion of the sand transport must be stopped, the groynes should be short in this case, viz. shorter than the width of the breaker zone. Long groynes extending through the breaker zone tend to reduce the sediment transport curve to (nearly) zero in stretch A–B, which will unnecessarily maximise the lee-side erosion. A partial reduction can also be achieved with impermeable groynes.

In the example case of Fig. 10.7, in the cross-section through point B, the existing sediment transport had to be reduced by a factor of approximately 0.5 in order to fulfil the requirements (i.e. achieving line b in Fig. 10.7; $S_{B,new} \approx 0.5 S_{B,old}$). Note that for arbitrary cross-sections between A and B different, larger ratios are required. Let point C be half way between A and B. Then, according to Fig. 10.7, $S_{C,new} \approx 0.7 S_{C,old}$.

Another point of practical concern is the absolute magnitude of the net yearly longshore sediment transport involved. Although the transport *gradient* over section A–B (viz. the *difference* V between S_B and S_A over the considered length of coast) can be measured quite accurately (via measuring the volume loss in section A–B), the absolute values of the net yearly sediment transport of either S_B or S_A are in fact not automatically known. Since it is difficult to calculate these sediment transport rates, errors are easily made in the proper quantification of S_B and S_A. If in Fig. 10.7 both S_A and S_B are increased by ΔS, the difference V remains the same. But to achieve a constant sediment transport in section A–B, quite different reduction factors than mentioned previously are necessary.

Consider for example the following two situations:

1. Stretch of coast, 5 km: $S_{in} = 100\,000\ m^3/yr$; $S_{out} = 200\,000\ m^3/yr$;
2. Stretch of coast, 5 km: $S_{in} = 200\,000\ m^3/yr$; $S_{out} = 300\,000\ m^3/yr$.

In both cases, the annual loss is $100\,000\ m^3/yr$, which amounts to a rate of structural erosion of §1.1 ~~$20\ m^3/myr$~~ §1.1 $20\ m^3/m/yr$ [p485], a quite usual annual structural loss. However, an adequate groyne system for case 1 is quite different from an adequate groyne system for case 2. In case 1, the net sediment transport near the downdrift side of the stretch of coast must be reduced by 50 % in order to ensure that S_{out} equals S_{in}. In case 2 the reduction should be only 30 %.

The rate of reduction of the sediment transport depends among others of the length of the groynes. For an impermeable groyne, a rough estimate of the required length can be made by taking the cross-shore distribution of the undisturbed wave-induced longshore sediment transport as a starting point (see Fig. 10.15).

The transport reduction can now be estimated by simply assuming that the groyne completely blocks the transport and that seaward of the groyne the sediment transport

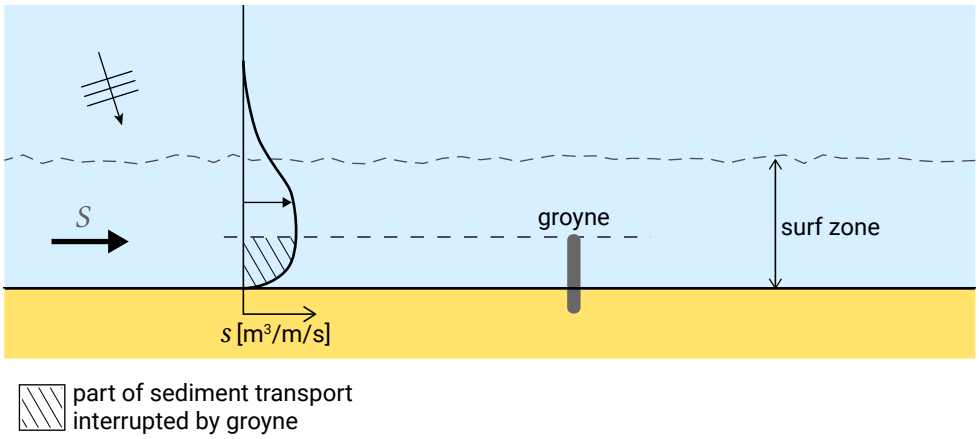

Figure 10.15: Rate of interruption of sediment transport by a groyne.

is unaffected by the groyne. Less crude estimates can be made by applying coastline models, such as Unibest-CL+ or Genesis (see Sect. 8.3.2). Such models take the impact of the shoreline development inside the groyne bays on the longshore sediment transport into account. Structure-induced eddies can also significantly impact the sediment transport patterns. These effects can only be taken into account in area models (2DH or 3D).

In the framework of Conscience, a European Union-funded research program, the efficiency of groyne systems was investigated and a number of design guidelines were presented (Van Rijn, 2010). It was concluded, amongst others, that:

- Nowadays, the design of groyne fields is generally combined with beach nourishment inside the groyne compartments in order to widen the beaches for recreation and to reduce the downdrift impacts;
- Long, curved groynes can be used to protect a major beachfill at both ends, creating a wide beach for recreational purposes (pocket beach) at locations where lee-side erosion is acceptable or manageable;
- The trapping efficiency can be enhanced by using, for instance, L-head or T-head groynes (see also Fig. 10.8) instead of straight groynes;
- Groynes preferably only extend over the inner surf zone (up to the landward flank of the inner bar trough), crest levels should be relatively low and spacings in the range of 1.5 to 3 times the length. This ensures sufficient sediment bypassing, so that lee-side erosion is prevented as much as possible.
- By reducing lengths at the downdrift end of the groyne field, downdrift erosion can be controlled and reduced (groyne tapering);
- By constructing groynes from downcoast to upcoast, initial erosion of the area to be protected is avoided.

10.5.4. Detached shore-parallel offshore breakwaters

Detached breakwaters are breakwaters parallel to the coast at a certain distance from the coastline (thus, 'detached'). They are often built from stone, just like ordinary harbour breakwaters or jetties, and may be segmented (Fig. 10.17). Disadvantages are the relatively high construction and maintenance costs and the inconvenience or even danger to swimmers and small boats. The breakwaters are either emerged (crest above MSL) or submerged (crest below MSL), see Fig. 10.16.

Emerged detached breakwaters with crest levels well above MSL are known to enhance accretion in their lee and have successfully been adopted for coastal protection for many decades. From an aesthetic point of view, submerged breakwaters are preferred to surface-piercing structures (see Fig. 10.18). However, submerged breakwaters have resulted in worse shoreline erosion in a number of cases (Ranasinghe & Turner, 2006; Van Rijn, 2010). Below, we separately discuss the morphological impact of emerged and submerged breakwaters.

Emerged detached breakwaters

Most emerged breakwaters have been built along micro-tidal beaches in Japan, in the USA and along the Mediterranean. Few have been built along open, exposed meso-tidal and macro-tidal beaches. In the shadow zone behind the structures, tombolo development is stimulated. The governing mechanisms for this shoreline accretion were treated in Sect. 8.4.3.

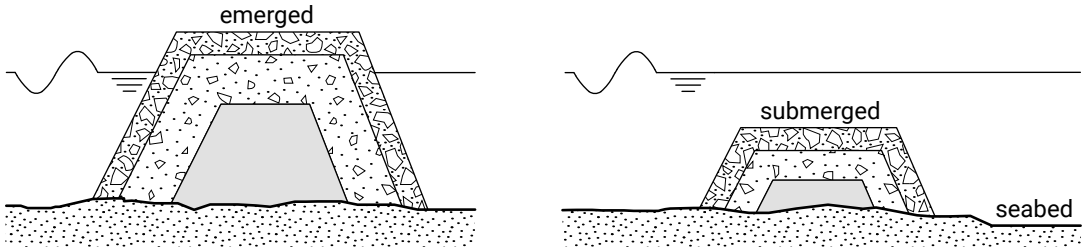

Figure 10.16: Detached shore parallel breakwaters (not to scale: slopes in figure are too steep).

Figure 10.17: Series of emerged detached breakwaters in Sea Palling, England. Note the salients and tombolos. Vertical aerial photography obtained in May 2019. From UK Environmental Agency ('Credits' on page 579).

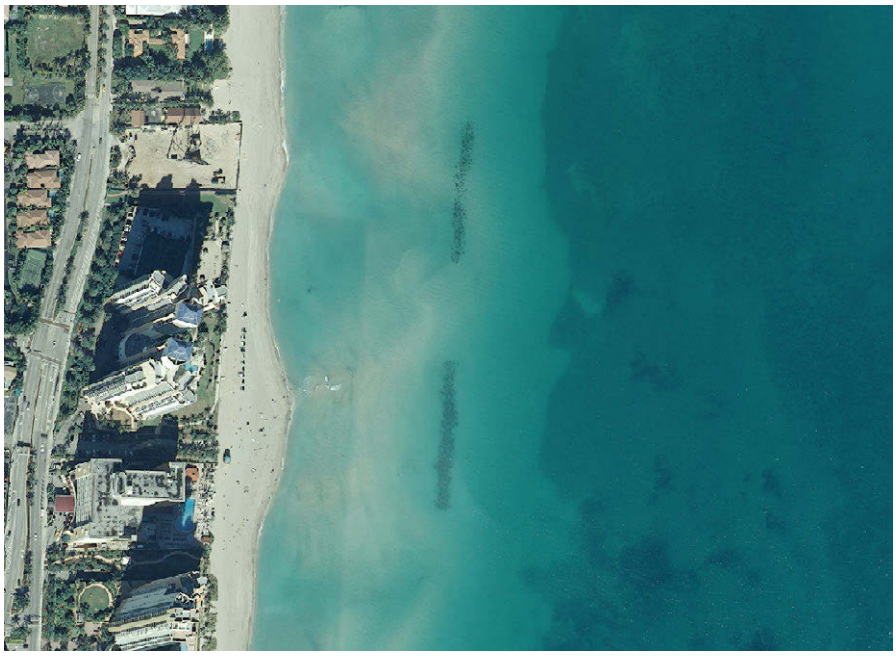

Figure 10.18: A coupled breakwater system containing two detached shore-normal submerged breakwaters, Sunny Isles, USA. Note the salients at the coast, behind the breakwaters. Orthophotos obtained in January 2009. From U.S. Geological Survey ('Credits' on page 579).

Since emerged breakwaters are effective in reducing the longshore sediment transport capacity in their shadow, structural coastal erosion can be solved with a series of *emerged* shore-parallel offshore breakwaters, as in Fig. 10.17. In the example of Fig. 10.7, the sediment transport in the cross-section through point B must be reduced from S_B to S_A (but not to zero, to avoid unnecessarily large lee-side erosion). Therefore, either in the area in the lee of an offshore breakwater near B or in the area seaward of that breakwater, a non-zero sediment transport is required. A salient occurs for a not too large negative longshore transport gradient behind the breakwater, but still allows sediment to be transported via the shadow zone behind of the breakwater to downdrift beaches. A tombolo prevents this.

What type of beach planform (the beach as viewed from above) evolves, strongly depends on dimensions and geometry (breakwater length L, offshore distance to original shoreline D and length of gap between segments L_{gap}, see Fig. 10.19). Bricio et al. (2008) analysed 27 detached breakwater projects along the northeast Catalonian coastline of Spain (which is almost tideless), based on pre- and post-project aerial photographs. The offshore distances D were in the range of 80 m to 230 m and the (emerged) breakwater lengths L in the range of 60 m to 240 m. Tombolos were found for $L/D > 1.3$ and salients for $0.5 < L/D < 1.3$. These findings are broadly in line with empirical relations found in other studies. In Sect. 8.4.3, we assumed tombolo formation for $L/D > 2$, based on non-interfering diffraction patterns.

Opposite the gaps, shoreline erosion may occur if the gaps are sufficiently large (say $L_{\text{gap}}/L > 1$ to 1.5).

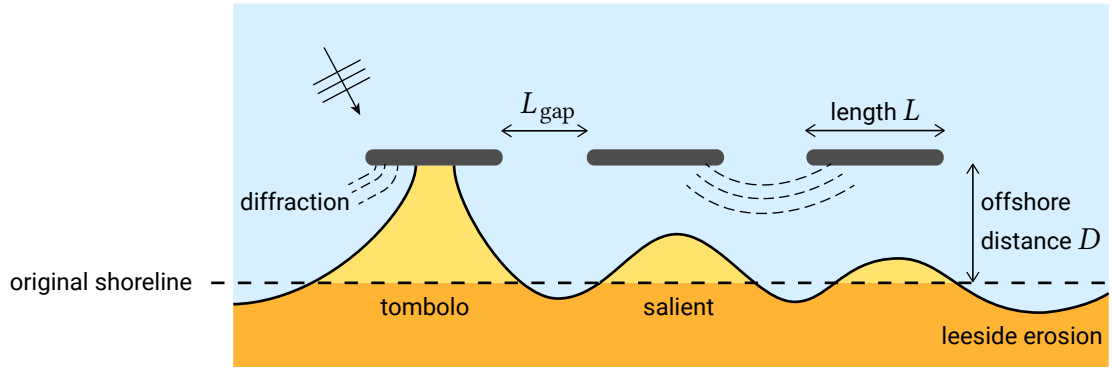

Figure 10.19: Detached shore-parallel breakwaters.

From the above, it follows that the optimal emerged breakwaters in terms of coastal protection are built close to the shore, with a high crest level and small gap lengths, but such a structure will block the horizon and is not attractive in terms of beach recreation.

Emerged breakwaters also reduce storm-induced beach and dune erosion to a certain extent. However, the still water level during a storm often increases (storm surge, see Sect. 5.6). Therefore, depending on the the height of the breakwaters above MSL, tidal range and storm surge levels, large storm waves may still pass over the structure, such that storm erosion cannot be completely stopped.

Submerged detached breakwaters

Examples are known from field and laboratory tests in which severe erosion is generated landward of submerged breakwaters. For example Dean et al. (1997) describe a striking example where the application of offshore breakwaters created more erosion than without this 'protection' measure: a single submerged breakwater built on the lower east coast of Florida (USA), approximately 7 km south of the entrance of the Port of Palm Beach, was later (in 1995) removed because of excessive erosion problems in the lee of the breakwater.

A *submerged* breakwater parallel to and at some distance from the shoreline will undoubtedly reduce the wave heights landward of the submerged breakwater (depending on the wave climate, the positioning and the crest height relative to the still water level). As in the case of emerged structures, this may result in accretion behind submerged structures. However, wave-breaking on the structure drives a current pattern, with diverging shore-parallel currents in the shadow zone of the submerged breakwater (see Sects. 5.5.7 and 8.4.3). Along the end sections of (segmented) breakwaters, the currents escape in the seaward direction (see Fig. 5.49). This current pattern can transport large amounts of sediment outside the area and counteract the accretional tendency. The erosional current pattern becomes stronger for decreasing distance between the breakwater and the shore. Hence, shoreline erosion may occur, for instance, if a submerged breakwater is built too close to the shore.

Unfortunately, very few guidelines are available for submerged breakwater design, as yet. Clearly, the successful application of submerged breakwaters requires a better understanding of the shoreline response. Any attempt to understand and model the morphodynamic impact of (submerged) structures requires the explicit consideration of the resulting complicated circulation currents.

Submerged structures have only a limited effect on storm-induced erosion, as most of the storm waves can be expected to pass over the structure and attack the dune or cliff front. Supplementary beach nourishments may be required to deal with local storm-induced shoreline erosion, especially opposite to gaps, where under storm conditions large amounts of sediment may irrevocably be carried seaward.

Sometimes, submerged breakwaters are constructed as sills between the tip of groynes to support the seaward toe of beach fills (perched beaches, see Fig. 10.39).

> In conclusion, in this paragraph the morphological consequences of detached shore parallel offshore breakwater were discussed. The finetuning of series of offshore breakwaters is a very difficult task, especially for submerged breakwaters. Waves from different directions and tidal effects (water level and currents) also seriously complicate the situation. A successful project may involve an initial design phase based on mathematical and physical modelling, the testing of the design by means of a field pilot project, including a detailed monitoring programme, and the finetuning of the design by modification of breakwater lengths based on practical experience.

If a submerged or low-crested emerged breakwater is not designed properly, additional negative morphological effects, such as local scour and shoreline erosion, may easily occur. Attention should further be paid to mitigation of downdrift (lee-side) erosion. This can be established by creating a transitional zone with gradually increasing gap lengths and/or decreasing crest levels. In addition, protection measures may be required against local toe scour in front of the breakwater, just as for seawalls (see Sect. 10.6.2).

10.5.5. Piers and trestles

Piers and trestles are rather long structures with a horizontal deck on a series of piles extending perpendicular to the coast into the sea (see Fig. 10.20). These structures serve as a landing place for vessels, as recreation facilities, as measuring facilities for coastal processes or as part of a sand bypass facility.

The supporting piles might impact the adjacent coast. Especially if a large number of large diameter piles have been applied, obliquely arriving waves will cause, in the lee of the rows of piles, an area with reduced wave heights. The sediment transports may be reduced as well; spots with some accretion might occur (in general at both sides, since

waves will approach from both sides). In this way a measuring pier creates atypical measuring conditions.

Figure 10.20: Recreation pier in Scheveningen in August 2010. Photo from Rijkswaterstaat (see 'Credits' on page 579).

10.5.6. Concluding remarks

Long breakwaters, series of groynes or detached offshore breakwaters can be used to solve structural erosion problems. The principle of these measures is that they locally reduceexisting longshore sediment transports and hence change the longshore transport gradients. Note that even for a well-designed protection scheme, lee-side erosion is unavoidable; downdrift of the protection scheme, longshore transport gradients will increase, leading to (additional) erosion. Coastal zone managers have to take these adverse consequences fully into account in the decision-making process.

The use of seawalls or revetments parallel to the shore, built along the front slope of the dunes or the firm land, does not provide an adequate solution to a structural erosion problem. This is because the cause of the erosion problem, namely longshore transport gradients, is not taken away. Although initially the loss of dunes or land is indeed prevented, the erosion of the beach and underwater profile will continue. The end result may be a complete loss of beaches and damage or failure of the seawall or revetments, exemplified in Fig. 10.21 and further discussed in Sects. 10.6.2 and 10.6.3.

Figure 10.21 shows the cross-shore and longshore damage of an incorrectly applied revetment. The picture is looking towards the north; to the south of this location, a non-periodic, episodic high river discharge event 25 years earlier had served as a source of sediment for two decades, counteracting sediment losses from Cua Dai beach in the northward direction. Around the beginning of the 21st century, the provincial authorities allowed resorts to be developed to the south of this location. However,

the absence of a new episodic source event eroded the beaches in front of the resorts and the resorts started to act as revetments and/or groynes. Hence, the coast north of the resorts started to erode, so that the beaches – important for tourism – were disappearing. Although this was a problem of alongshore transport gradients causing erosion, it was attempted to halt this erosion by geotextile bags, preventing the cross-shore supply of sediment to resolve the longshore transport erosive gradients. As a result two types of damage occurred: 1) although the erosion was diminished by the geotextile bags, wave attack on the bags caused toe erosion and damage to the bags' stability and the beaches in front disappeared; 2) the geotextile bags were initially successful in preventing further feeding of sediment to the alongshore transports, but shifted the alongshore transport gradients further to the north, causing erosion.

Figure 10.21: Cross-shore and longshore damage to an incorrectly applied revetment, Cua Dai beach, Hoi An, Vietnam, around 2016. Photo by Marcel J.F. Stive ('Credits' on page 579).

10.6. Structures protecting against storm-induced erosion

10.6.1. Introduction

If the rate of erosion due to a severe storm surge is unacceptably large during design conditions, the use of structures may be helpful in reducing the rate of erosion.

Series of groynes do not help to reduce the associated offshore-directed sediment transport. In principle, series of emerged breakwaters or submerged breakwaters reduce the wave heights landward of these structures and consequently may have the effect of reducing the rate of dune erosion. However, due to the increase of the still water level

associated with a storm (the surge), the effectiveness of these types of structures in reducing the wave heights under storm conditions is limited (see also Sect. 10.5.4). Also, wave overtopping of the breakwater segments may lead to concentrated rip currents in between the breakwater segments and therefore quite adverse effects (as is also the case for permanently submerged breakwaters). Furthermore, the use of detached breakwaters for the reduction of storm erosion may have undesirable consequences because of the inevitable impact on longshore transport gradients.

By contrast, the structures that can be effective in protection of the mainland against storm-induced erosion and flooding are:

- Seawalls;
- Revetments;
- Sea dikes.

10.6.2. Seawalls

A seawall is a shore-parallel and (nearly) vertical structure at the transition between the low-lying (sandy) beach and the (higher) mainland or dune (see Fig. 10.22). The seawall bridges the total height difference between beach and surface level of the mainland (often a boulevard, road or parking area). The seaward-sloping surface of a seawall is generally smooth and impermeable.

Seawalls are considered a relatively easy to build coastal protection measure. The philosophy behind the concept is that storm erosion will be prevented by simply cutting off the local supply of material. While in a situation without a seawall even a moderate storm (surge) will attack and erode the mainland, in the situation with a seawall this is prevented. Unfortunately, a rigid, massive seawall tends to reflect the incoming waves. The increased turbulence from this reflection may erode a deep trough along the toe of the seawall (as in Fig. 10.23a). The presence of this trough endangers the foundation, with the risk that the wall will fail by collapsing into the scour trough. This can be prevented by maintaining a beach in front of the seawall using some other means (e.g. regular artificial beach nourishments). If this is done, however, the logical question is: "why build a seawall, then?" The only purpose of the seawall is then to provide a clear and fixed distinction between the beach and the mainland (a boulevard or road), see Fig. 10.23b. Staircases are needed to facilitate access to the beach.

The design conditions for the seawall have to be properly chosen to provide the desired protection of infrastructure and buildings situated close to the edge of mainland or dunes. The larger the design wave conditions, the heavier the seawall must be; especially the foundation depth will increase accordingly. The crest height of a seawall determines (together with the boundary conditions at sea) to a great extent the rate of overtopping (water reaching the mainland by wave run-up, breaking waves and splashwater transported by landward-directed wind). With an additional wall and/or a slightly curved front, rates of overtopping might be reduced (see Fig. 10.24).

(a) normal conditions (photo taken in September 2015 by Wayland Smith 'Credits' on page 579)

(b) storm conditions (photo taken in 2014 by Carol Blaker ('Credits' on page 579)

Figure 10.22: A seawall in Dawlish, UK.

Let us consider a stretch of sandy coast. If unprotected, an extreme storm surge may cause a rate of mainland erosion of e.g. 40 m. With a seawall which is able to withstand these conditions, the erosion of the mainland will be zero. Instead, in front of the seawall a deep scour hole will be formed. The scour does not present any problems as long as the seawall does not fail; the scour hole will slowly be re-filled during moderate wave and wind conditions. If, however, the seawall partly collapses and locally a gap in the seawall is formed, a rather dangerous situation will occur. A large volume of sediment from the mainland may disappear through the gap and will flow in the

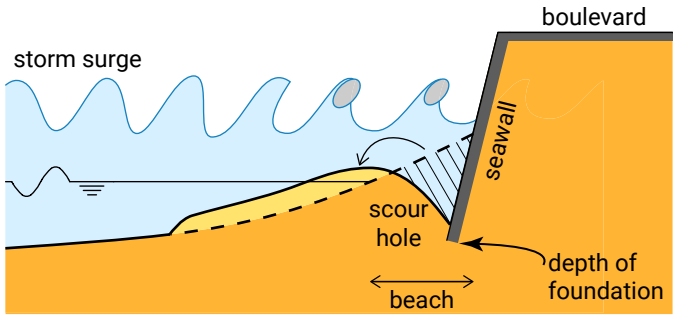

(a) scour in front of a seawall or revetment

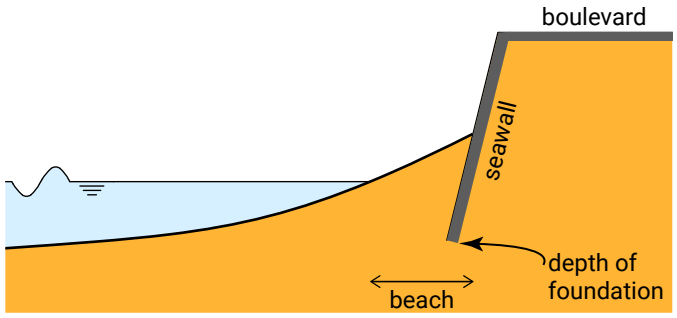

(b) maintaining a beach requires e.g. regular sand nourishments

Figure 10.23: Seawall or revetment separating the beach from the mainland (a boulevard in this case).

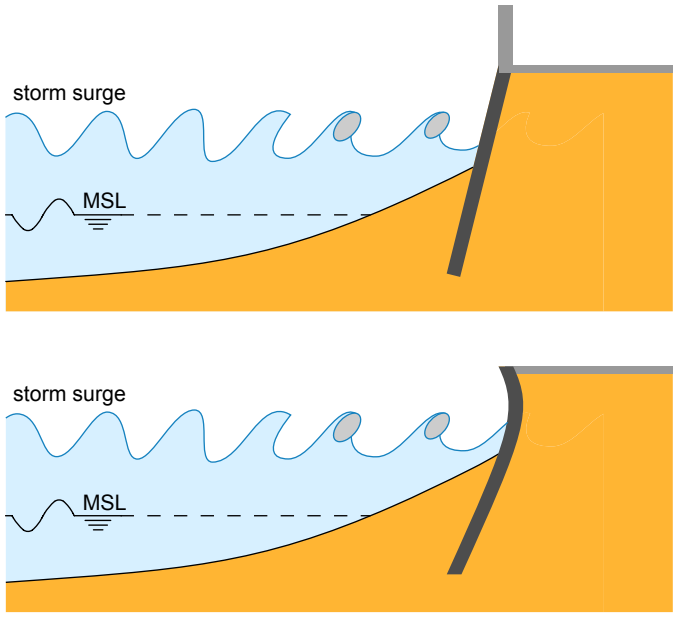

Figure 10.24: Seawall with measures to reduce overtopping.

alongshore direction along the sections of the seawall which are still in good condition, filling the scour trough. In this case, the final rate of erosion of the mainland behind the gap may be more than the 40 m mentioned for the unprotected case.

Similarly, the unprotected coastline adjacent to a seawall may suffer from extra storm erosion, since large amounts of sediment are lost to the scour trough.

Other than to prevent storm erosion, a seawall can be used to prevent flooding of low-lying hinterland, if the existing row of dunes does not meet safety requirements. The dunes may for instance be too slender to withstand the design wave and water level conditions.

Neither seawalls nor revetments can protect a coast from structural erosion due to longshore transport gradients. Nevertheless, a large number of cases are known world-wide where seawalls have been applied – unsuccessfully, however – to protect structurally-eroding coastlines.

Structural erosion as a result of a gradient in longshore sediment transport means that volumes of sediment are irrevocably lost from the area under consideration. Due to the low frequency of occurrence of extreme conditions, the majority of the longshore sediment transport is due to moderate wave conditions and occurs in the area below MSL. The presence of the seawall does not prevent this (see Fig. 10.25). Due to cross-shore redistribution of sediments during high tides and/or modest storms, the alongshore loss of sediment causes a recession of the entire cross-shore profile in front of the seawall. This causes loss of the beach and deepening in front of the seawall, which in turn results in an increased wave attack on the seawall and possibly in damage and failure of the seawall.

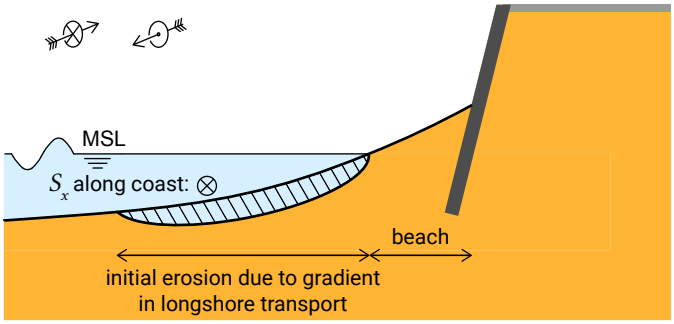

Figure 10.25: Seawalls and revetments cannot prevent structural erosion due to longshore transport gradients, since the longshore transports and transport gradients occur below the waterline in the surf zone.

In the short run, seawalls as a protective measure seem to solve erosion problems. Indeed, local citizens – whose property is endangered – have noticed in the past that every storm surge resulted in a loss of land. Just after the construction of a seawall, the 'protected' parts of the coast no longer show any signs of further erosion, whereas in the unprotected parts the erosion of the mainland continues. The seawall is therefore believed to function well. Unfortunately, after some time it will become clear that structural erosion has not been countered at all. If coastal zone managers decide to apply seawalls as a countermeasure against structural erosion, this must be due to either lack of knowledge or pressure by local citizens.

10.6.3. Revetments

A revetment (Fig. 10.26) is similar to a seawall in the sense that it is a shore-parallel structure that can prevent storm erosion, but is ineffective against structural erosion. Compared to a seawall, a revetment is more gently sloping (e.g. 1:2 or 1:4), can have either a rough or smooth surface and can also be applied over a limited vertical distance.

Two aspects call for some remarks, viz.:

1. Slope of revetment in relation to the depth of the scour hole;
2. Level of upper end of revetment.

(a) (b)

Figure 10.26: Wooden revetment and eroding cliffs in Sheringham, UK, in May 2008. This is a good example of a bad revetment; the revetment extends from the cliff to the waterline, whereas erosion can be expected below the waterline. Moreover, the revetment prevents supply of material from the cliff. Photos by Evelyn Simak ('Credits' on page 579).

For rather smooth revetments it has been demonstrated that the depth of the scour trench depends on the slope characteristics. During tests in the Delta Flume of Delft Hydraulics (now Deltares) it turned out that with a slope of 1:3.6, a deeper scour hole was created than with a slope of 1:1.8. The deepest point of a scour hole is not always found at the intersection point between revetment and cross-shore profile (see Fig. 10.27 for a sketch). For a rough slope, a smaller scour depth may be expected than for a smooth slope.

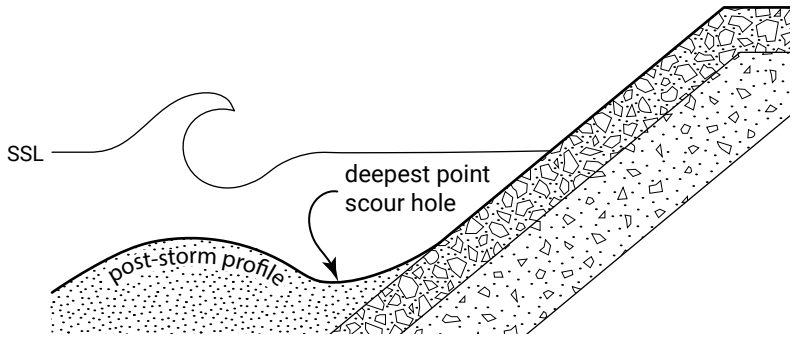

Figure 10.27: Scour in front of a revetment. Not to scale.

The level of the upper end of a revetment, above which the natural dune or cliff is unprotected, determines the amount of dune erosion above that level, but also to some extent the depth of the scour hole. The higher the level to which the revetment is applied, the smaller the dune erosion, but by implication also the deeper the scour trough (since no sediment is supplied from the dunes). If the level of the upper end of a revetment is equal to the storm surge level (or lower than that level), no reduction in dune erosion is found compared to a situation without any protection.

Summarizing, in a situation without longshore transport gradients, revetments as well as seawalls can be used to limit the rate of storm-induced erosion. These structures physically prevent the loss of material from dunes or land and thus reduce dune or mainland retreat. However, potential scouring in front of the structures has to be taken into account in the design.

10.6.4. Sea dikes

Sea dikes differ from revetments in the sense that a beach in front of the structure is absent (see Fig. 10.28). Just like dikes along e.g. a river, sea dikes are often meant to prevent flooding.

The design crest height of a sea dike has to be carefully chosen in order to prevent too much overtopping. In the Netherlands the former[3] Hondsbossche and Pettemer sea defence is an example of a sea dike (see Fig. 10.29). Because of the flat slope, the wave run-up under design conditions for the Dutch coast reaches rather high levels (about 8 m above design storm surge level). New (preliminary) insights in likely wave characteristics during design conditions showed that the crest level of the existing sea defence was too low. As a 'no-regret' measure, that is, a matter worth implementing in any case, the sea defence was partly supplemented with additional sheet piling (see Fig. 10.30). Note that the additional measures only prevent wave overtopping; the sheet piling cannot withstand hydraulic pressures in the case of high surge levels.

[3]Before the sandy reinforcement of the sea dike was completed, see also Fig. 7.14 and Sect. 10.7.1.

Figure 10.28: Sea dike, Westkapelle, the Netherlands, in June 1993. From Rijkswaterstaat ('Credits' on page 579).

Figure 10.29: Hondsbossche and Pettemer sea defence, The Netherlands, in June 1993. From Rijkswaterstaat ('Credits' on page 579).

An additional point of concern is the position of the (sandy) bottom just in front of the sea defence. The wave run-up depends on the local wave height at the toe of the sea defence, which is limited by the local depth. Therefore, when during design conditions erosion of the sandy bottom just in front of the sea defence is expected, the water depth and hence the typical wave height might be higher than expected.

Figure 10.30: Additional sheet piling at crest of dike, Hondsbossche and Pettemer sea defence. From Wikipedia, uploaded in 2005 ('Credits' on page 579).

10.7. Nourishments

10.7.1. Introduction

In this section, we discuss how coastal erosion problems can be solved by nourishments with sand instead of by building structures of quarry stone or concrete. These types of solutions are called 'soft' solutions. The basic idea is to supplement sand by artificial means (dredge, truck) in places where the loss or lack of sand is causing problems. Sand nourishment leaves the coast in a more natural state than permanent structures and preserves its recreational value. The method works if ample quantities of sand are available from a borrow area at a relatively short distance from the problem area.

An example is the sandy reinforcement of the Hondsbossche and Pettemer sea defence, completed in 2018 (Fig. 7.14). In order to meet current safety standards, the sea dike was reinforced in 2015 with a soft, natural barrier of 30×10^6 m^3 of sand on the sea side of the dike. It was renamed 'Hondsbossche Dunes' ('Hondsbossche Duinen' in Dutch). The design consists of a soft shallow foreshore (the beach) and a varied artificial dune landscape. In this way, the spatial quality of the primary flood defence was greatly improved.

Artificial nourishments can be applied for various reasons:

1. to compensate for losses as a result of structural erosion;

2. to enhance the safety of the hinterland against flooding and to protect the beach and dune area and properties built close to the edge of the dunes against storm erosion;
3. to broaden a beach, create new beaches (for recreation) or reclaim large areas of new land, such as artificial islands.

The second and third applications refer to situations in which the nourishment is, in principle, a once-only measure. However, in the case of structural erosion, which is an ongoing process, the nourishment will have to be repeated from time to time. The interval between successive supply operations depends on the rate of erosion and on the cost of mobilising the dredging equipment. Generally, an interval of 5 years between successive operations is considered acceptable.

With respect to structural erosion (application 1), a distinction between the 'hard' and the 'soft' methods is that the latter must be repeated from time to time, that it is flexible (in the sense that it is easy to modify the scheme if the results are not as expected) and that the cost of the operation is deferred, in the sense that it is spread out over a longer time. For conditions along the Dutch coast this makes 'soft' solutions more economical than 'hard' solutions. One could also argue that, since sediment is always added to the system, a nourishment can never go really wrong, although a badly designed nourishment may not be as effective as expected in counteracting the erosion problem under consideration, which may lead to damage to properties. Last but not least, lee-side erosion does not occur with 'soft' solutions, as would be the case with solid structures, like a series of groynes.

In Sect. 10.7.2 some design considerations are given. Next, the three different applications listed above are discussed in Sects. 10.7.3 to 10.7.5.

For further reference: many details related to the use of artificial nourishment are found in e.g. Dean (2002) and Van der Graaff et al. (1991) and in a reportVan Rijn (2010), prepared in the context of the European Union-funded project Conscience (Concepts and Science for Coastal Erosion Management). These publications also contain many references to papers specifically devoted to artificial nourishment.

10.7.2. Design aspects

Origin of the sand

The required volumes of sand are in the order of magnitude ranging from several hundreds of millions m^3 per project for large-scale reclamation projects to 10 million m^3 per project for smaller-scale nourishments.

The sand used for nourishments (borrow sand) can be obtained from land-based sources or from marine sources. Land-based sources may be river beds or dry sand deposits. Marine sources can be estuaries or the seabed. It is often attractive to try to combine excavation works with nourishment activities, to reduce the overall cost.

When marine material is used, it must be dredged at a sufficiently large distance from the shore to prevent extra erosion due to the presence of the borrow pits. Specifically, when material is dredged from the seabed, the question arises of whether it is better to dredge the material from small, deep borrow pits, or to dredge thin layers of material from an extended borrow area. Dredging thin layers means disturbing the biologically active surface layer over a large area, whereas creating deep borrow pits enhances the risk of stagnant water of poor quality remaining in the deeper parts. Although research into the effects of sand borrowing is being carried out, there is no clear conclusion yet. In the Netherlands, some sand is obtained by maintenance dredging in the access channels to the ports of Rotterdam and IJmuiden. The remaining amount of sand is extracted by dredging thin layers at a distance of at least 20 km from the shore.

Although sand nourishment may offer significant benefits, it may also be a costly method if life spans are fairly short or if the long-term availability of adequate volumes of compatible borrow sand at nearby (economic) locations is problematic. For example, suitable material cannot easily be found at most Italian and Spanish sites along the Mediterranean.

A special application of an artificial nourishment project is a sand-bypass system. A port built along a sandy coast or jetties to stabilise the mouth of a river flowing out into the sea often cause updrift sedimentation and downdrift erosion of the coast. To avoid erosion at the lee side, a sand-bypass system is a perfect tool. It artificially restores the blockage of the littoral drift by transporting sand from one side to the other. In Australia various examples are known of adequate and cost-effective systems (e.g. Nerang River project and Tweed River project).

Quality requirements for the sand

When sand is supplied to a(n) (eroding) stretch of coast, the newly supplied sand will tend to form a crust or blanket over the existing coastal formations. The supplied sand will follow the same laws of physics as the existing sand. For this reason, major changes in the slopes and other coastal features are to be expected when the grain size of the supplied sand differs from the original material. Usually, this is not acceptable, and one of the basic rules for beach nourishment is to use material that is relatively similar in grain size (and preferably grading) to the existing material (see also Sect. 10.7.3). However, in some cases the use of coarser material is preferable in order to diminish losses.

Another point of concern is the silt content of the borrow material. The borrow material sometimes contains some (immobile) silt (2 % silt is a quite normal percentage). During the dredging operation, silt is brought into the sea water via the overflow system of the dredge. This may have a negative impact on the marine environment. Moreover, any fines still present in the material when fed to the coast may disrupt the ecological equilibrium of the coastal zone. Since the bottom material of a sandy shore is extremely mobile, specifically in the breaker zone, fines will have been washed out

long ago, so that the water is relatively clear. It must therefore be ascertained that the beach nourishment material contains little or no fines. In the worst case, measures have to be taken to wash out the fines before placing the material on the beach.

Note that in Europe large areas have been declared Natura 2000 sites including dune and coastal areas. For these areas, environmental protection and prosperous development are policy aims. If a nourishment project is foreseen in the vicinity of Natura 2000 areas, an assessment has to be made whether negative effects are to be expected.

Location of the nourishment

Sand nourishments can be placed at different locations in the coastal profile, namely (see Fig. 10.31):

1. On the inner slope of the dunes;
2. On the outer slope of the dunes;
3. On the dry beach;
4. On the shoreface.

In theory, as long as the nourishment location is within the active zone, waves will redistribute material over time from the nourishment location over the entire coastal profile in order to achieve an equilibrium profile again. Hence, nourishments of the shoreface and beach can be regarded as local perturbations of the profile, which will be flattened out by cross-shore sediment transport processes.

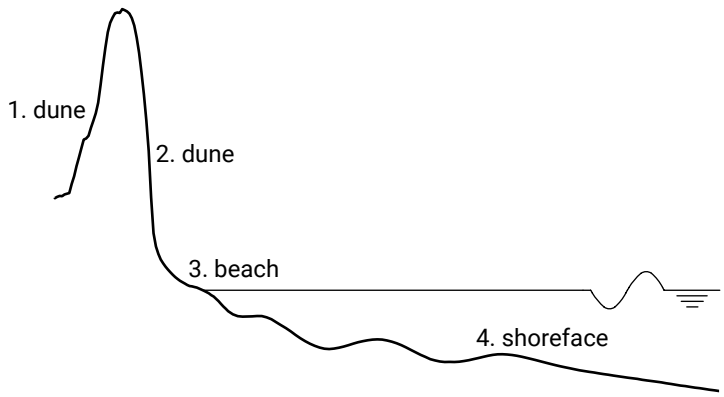

Figure 10.31: Locations of nourishments.

If a sand nourishment is carried out at locations 1 or 2, it is called a dune nourishment. The use of sand from land-based sources is a reasonably cost-effective option in these cases. This is even more important if the use of marine sand would cause a salt intrusion problem in a vulnerable region. A nourishment at location 3 is called a beach nourishment and at location 4 a shoreface nourishment. Placing sand on the dry beach is sometimes complicated, because it is necessary to cross the breaker zone with the dredging equipment (see Fig. 10.32). Since the breaker zone is a difficult place to work in, the costs of this option can be high. Furthermore, beach recreation is hampered as

a result of the pipelines that are needed to bring the sand to the beach and the noisy shovels needed to properly distribute the sand over the beach.

Figure 10.32: Beach suppletion during construction of the Sand Engine using pipelines (indicated by the black arrows) that cross the breaker zone in March 2011. From Rijkswaterstaat ('Credits' on page 579).

If compatible sand is available in nearby borrow areas, shoreface nourishments are more economical and recreation-friendly than beach nourishments, because the sediment can be placed at the seaward edge of the surf zone, where the navigational depth is sufficient for hopper dredgers. During calm wave conditions, material is dumped by shallow draft dredges (through doors in the bottom of the dredge or through rainbowing) at the shortest possible distance from the beach (see Fig. 10.33). Often shoreface nourishments are about half as expensive as beach nourishments.

The choice of the nourishment location further depends on the purpose of the nourishment. This is discussed in the next sections.

10.7.3. Counteracting structural erosion of coasts

When a beach suffers from structural erosion, artificial nourishments can be applied as a 'soft' remedy. Losses that occur are replenished from time to time. Regularly applying nourishments with borrow material that has the same size as the native material will, to a first approximation, not interfere in the longshore sediment transports and thus not influence the losses. Hence, the erosion does not stop and after a certain period the nourishment has to be repeated. The example of the Dutch coast shows that long-term and large-scale erosion can be stopped by massive beach and shoreface nourishment over long periods of time.

Figure 10.33: Shoreface nourishment at the Dutch coast through rainbowing in September 2005. From Rijkswaterstaat ('Credits' on page 579).

If a well-defined part of the coast has been assigned a minimum sand volume, then a re-nourishment project has to be carried out as soon as this minimum is reached (at $t/t_L = 1$ in Fig. 10.34).

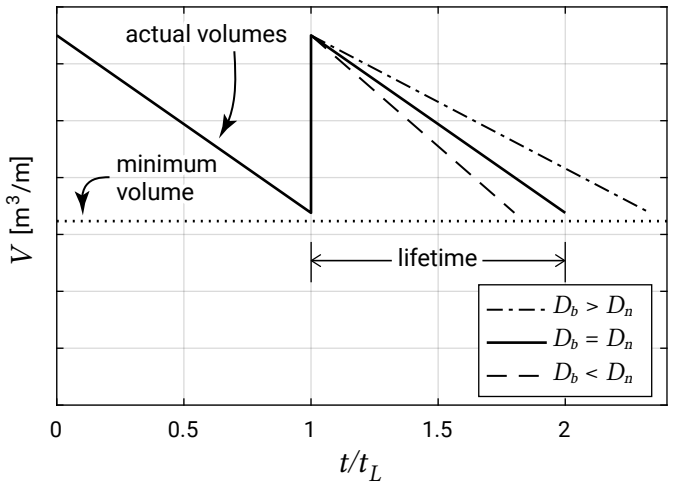

Figure 10.34: Schematised behaviour of an artificial nourishment with grain size of the borrow material D_b and grain size of the native material D_n. V is a sand volume per m along the shore.

If the borrow sand is the same as the native sand and if it is assumed that the morphological processes do not change, the erosional tendency after the nourishment is the same as before the nourishment (see the §1.1 ~~red~~ §1.1 solid [p505] line in Fig. 10.34, which has the same slope before and after the nourishment). The expected lifetime of the nourishment project then is $t_2 - t_1$. Generally lifetimes of 5 to 10 years are strived for, since the initial costs of a nourishment operation are often rather high due to mobilisation costs.

By contrast, if the grain size of the borrow sand is larger than that of the native sand, the longshore transport rate will be smaller than before. The time over which the beach volume will decrease to the minimum volume will be larger. The lifetime of the nourishment increases (see the §1.1~~black~~§1.1dash-dotted [p505] line in Fig. 10.34). However, when the grain size of the borrow sand is smaller than the native sand, the longshore transport in the nourished area increases. Therefore, the lifetime of a nourishment with finer sand is smaller than the lifetime of a nourishment with native sand (see the §1.1~~blue~~§1.1dashed [p505] line in Fig. 10.34).

With an average sand loss ΔV of 20 m^3/m per year (annual retreat of coastline of about 1 m per year; see Intermezzo 10.1) a time period between nourishments of 5 years means that about §1.1~~1000 m^3/m~~§1.1100 m^3/m [p506] has to be replenished every 5 years. This is a quite normal volume. If the relevant stretch of coast is 5 km long, a total volume of 500 000 m^3 has to be nourished every 5 years. This volume must be increased with 10 % to 20 % to account for additional losses of the fine-grained fraction§1.1, which may have been washed out [p506] during the execution of the nourishment works.

Artificial nourishments to combat structural erosion of a stretch of coast can be placed at various positions in a cross-shore profile (Fig. 10.35), viz. at the dry beach (Fig. 10.35b) or at the shoreface (Fig. 10.35a). In both cases cross-shore redistribution of sand will disperse the sediments. The dune reinforcement (Fig. 10.35d) and mega-nourishment (Fig. 10.35c) are described in the following sections.

In the case of a beach nourishment, sand is placed between the LW line and the dune foot. Eventually, the quantity supplied will be evenly distributed over the full height (and length) of the shoreface slope, following the equilibrium rules dictated by wave climate and grain size. This means that after a beach nourishment operation, large quantities of newly supplied material will soon disappear under water. The general public tends to call this phenomenon “erosion”, though we must understand that it is initially no more than a re-distribution of material within the natural cross-section of the coast.

For shoreface nourishments, the nourishment volume often is of the order of the volume of the outer breaker bar (ca. 300 m^3/m to 500 m^3/m). The length scale (alongshore 2 km to 5 km) of a shoreface nourishment is of the order of several times the width of the surf zone. Relatively large nourishment volumes are required, as only part of the nourishment volume (approximately 20 % to 30 %) will reach the beach zone after 5 years. Besides, because the costs per m^3 of a shoreface nourishment project are far less than the costs of a beach nourishment project, much larger volumes are often added to the system in the case of shoreface nourishments than in the case of beach nourishments (also called stockpile nourishments). Such large shoreface nourishments can be expected to significantly impact sediment transport processes. A large shoreface nourishment may behave in the same way as a submerged breakwater, although the effect diminishes over time. Examples are also known where the bar motion in

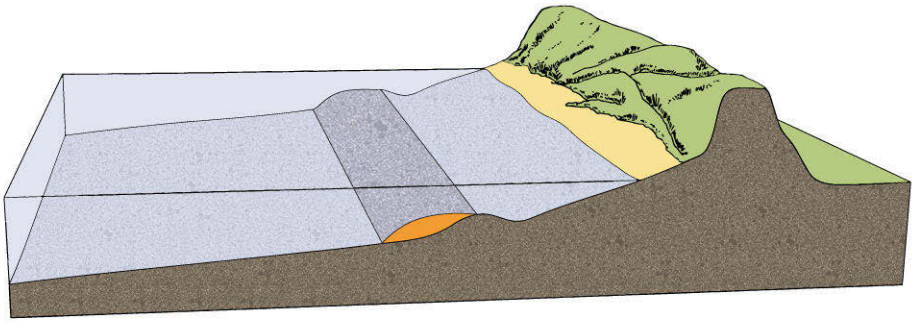

(a) shoreface nourishment

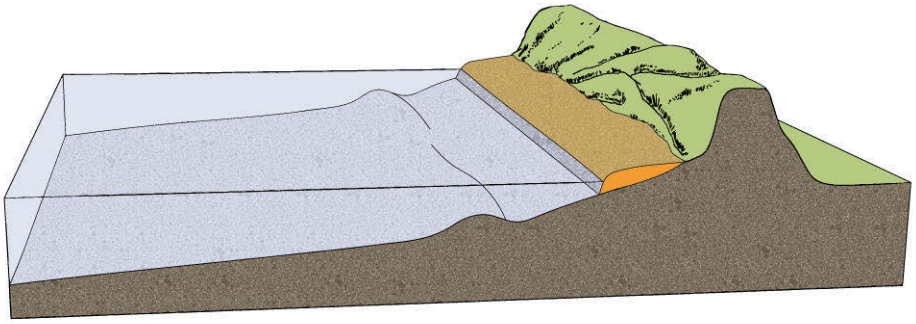

(b) beach nourishment

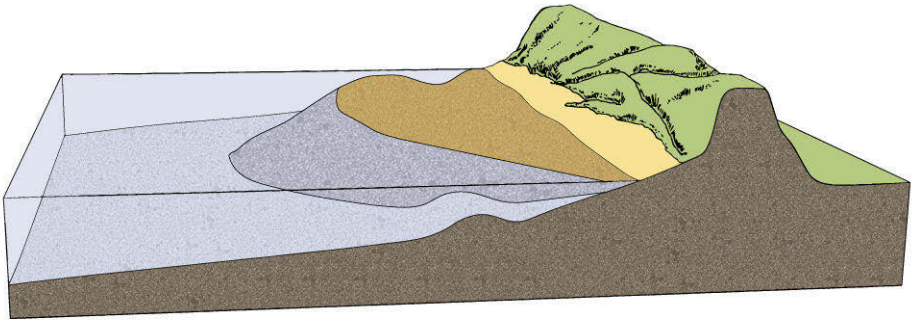

(c) mega-nourishment

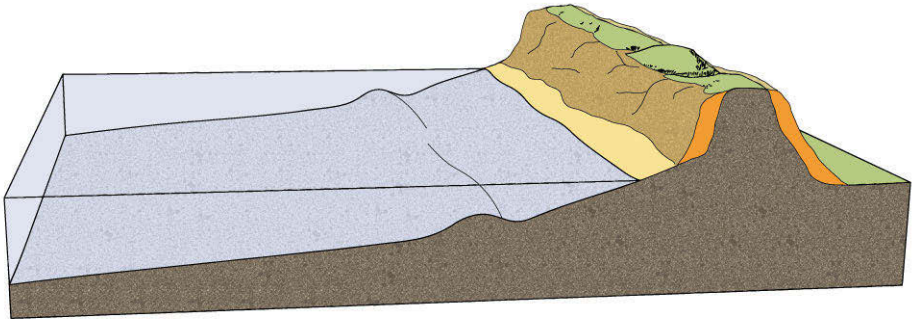

(d) dune reinforcement

Figure 10.35: Different types of nourishments.

the seaward direction is disturbed by a large shoreface nourishment project; see e.g. Spanhoff and Van de Graaff (2007).

Artificial nourishments can also be applied to counteract structural coastal retreat due to sea level rise, see also Sect. 7.4. If one chooses to maintain the current coastline (in the Netherlands the 1990 coastline is maintained, Fig. 10.1), nourishments should fill in the space created by sea level rise (between profile 1 and 2 in Fig. 10.36). A volume equal to the magnitude of sea level rise (SLR) times the fill distance L is necessary. With e.g. SLR = 1.0 m per century and L = 1000 m, a volume of 1000 m^3/m is required in 100 years. This volume of 10 m^3/m per year is a rather normal nourishment volume.

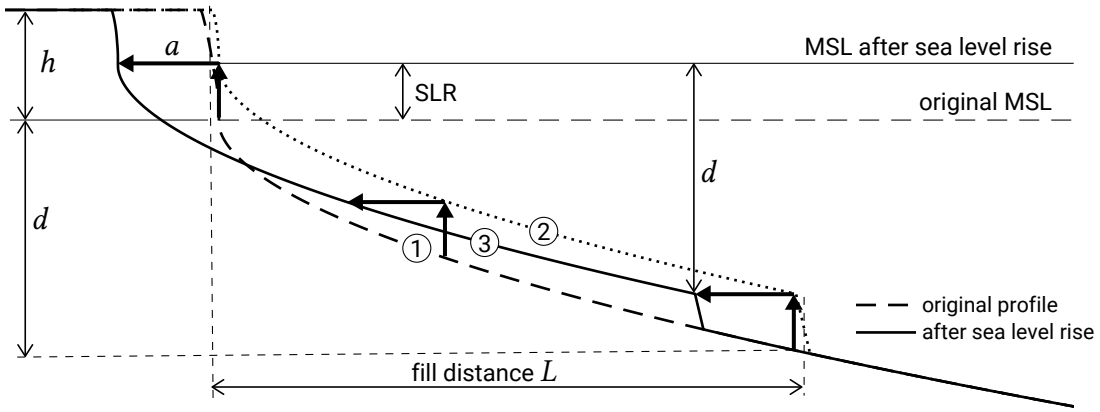

Figure 10.36: Profile adaptations and sea level rise (SLR).

Profile 3 in Fig. 10.36 represents the resulting equilibrium coastal profile without human interference; the new equilibrium is achieved by a horizontal shift a of profile 2 towards profile 3 in Fig. 10.36. The horizontal shift a can be determined from Eq. 7.13: $a = (\text{SLR} \times L)/(d + h)$. With SLR = 1.0 m (e.g. per century), L = 1000 m, d = 10 m and h = 10 m, a becomes 50 m. Whether such a gradual retreat of the coast (in the example 0.5 m per year) is acceptable depends on the situation. Note that in the situation of a very flat coastal profile (see Fig. 2.25, Bangladesh), the retreat will be significantly larger.

10.7.4. Dune reinforcement

Nourishment of the dune area is usually done if the volume of material in the dune ridge is insufficient to cope with dune erosion during the design storm[§1.1], the hypothetical extreme storm (consisting of a design wave condition, a design water level and a duration) a coastal protection structure is designed to withstand [p508]. In such cases, the hinterland may be exposed to flooding, not because of ongoing erosion, but simply because the existing dunes are not strong enough to withstand extreme conditions. The protection level of the land behind the dunes is increased more effectively by making a row of dunes wider than by making them higher.

Figure 10.35d repeats the two options to reinforce a row of dunes with sand. Reinforcement at the back of the dunes increases the safety level, but has no morphological impact. Often it may not be feasible to place sand at the landward side of the dune due to existing infrastructure and properties.

In the case of seaside reinforcement, it seems that only a relatively small volume of sand is required. However, the widening of the dunes in the seaward direction disturbs the dynamic equilibrium of the cross-shore profile (the dune foot being suddenly too close to the MSL). The same holds if the dry beach is nourished to compensate for storm losses. As a result, sand from the new dune or beach area is transported in the seaward direction and the new sand will be redistributed over a large part of the cross-shore profile (e.g. up to the active part of the cross-shore profile). Therefore, relatively large volumes of sand are required, since not only the face of the dune has to be shifted in the seaward direction, but also the active part of the cross-shore profile.

A similar redistribution of sand needs to be taken into account in the alongshore direction, as shown in Fig. 10.37. A purely local dune reinforcement will therefore have a short lifetime.

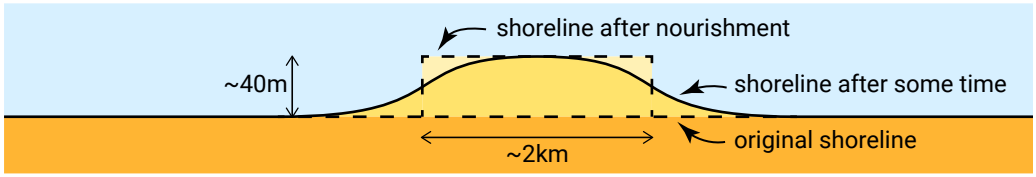

Figure 10.37: Dune reinforcement over a limited alongshore distance of 2 km, with a 40 m cross-shore extent, showing the expected alongshore redistribution. Cross-shore redistribution is not shown.

Widening and heightening of the dunes may not always be the preferred option of property owners close to the dune, because houses may end up further from the sea and sea views may be lost.

10.7.5. Beach widening and creation

Increasing urbanization of coastal areas often conflicts with natural shoreline fluctuations. An example is the Mediterranean, where overdevelopment often leads to a need to widen the beaches by nourishments, which in principle is a once-only measure. Shoreface nourishments mainly contribute to the sediment balance of the active surf zone, but are not very efficient for immediate beach widening for recreational purposes. Beach nourishments are about twice as expensive as shoreface nourishments, but directly benefit the beach. The lifetime of a beach fill can be extended by using coarser sediments.

More far-reaching is the situation in which a coast has to be extended over a considerable distance (for example in the order of magnitude of 2 km in the cross-shore direction and over 20 km in the alongshore direction). It is assumed that no serious

structural erosion occurs in the existing situation. The area is intensively used as a beach recreation area. One of the requirements is that, after the extension of the coast, recreation beaches are again available. This means that protection of the newly reclaimed area by a dike or revetment is not an acceptable option.

The most straightforward option for land reclamation would be an entire shift of the cross-shore profile of 2 km in the seaward direction. This applies not only to the waterline, but in principle also for all other depth contours to a water depth where natural adaptations of the profile are hardly to be expected (say 15 m below MSL). In order to achieve a 2 km shift of the coastline, a volume, per metre along the shore, of $2000\,\mathrm{m} \times 20\,\mathrm{m} = 40\,000\,\mathrm{m}^3/\mathrm{m}$ is required. The factor 20 m in the calculation is found by assuming a lower limit of MSL −15 m and an upper limit above MSL of 5 m. With an alongshore extension over 20 km, the total required volume of sediment is 800 million m^3, which means a very large project.

The large volume of sediment needed is the result of the new coast having a foundation that is identical to the old coast; a large part of the calculated volume is needed to make the new foundation. In order to restrict the volume of sediment needed for reclamation, one could consider an alternative. For example, the upper part of the cross-shore profile after reclamation is 'supported' with the help of a submerged breakwater (Fig. 10.38). The lower end of the profile can then be left as it was; a large reduction of the volume of sand is achieved in this way. This solution is called a 'perched beach'.

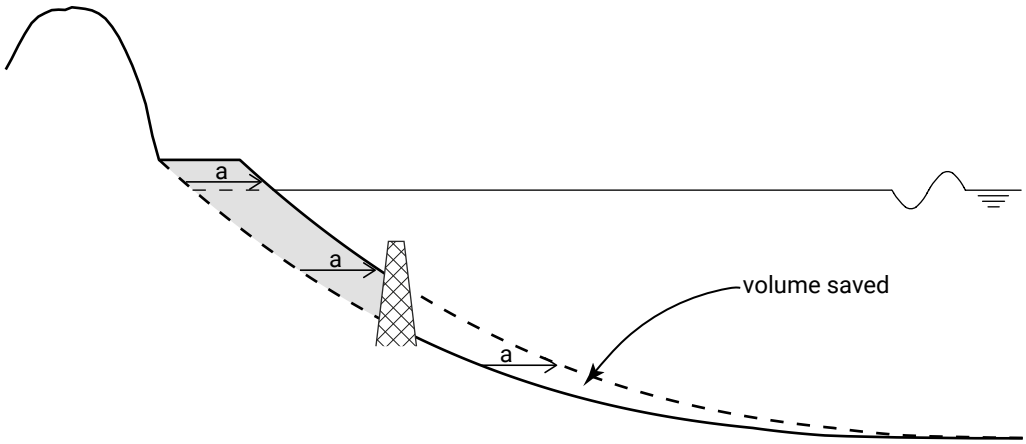

Figure 10.38: Cross-shore profiles in the case of large-scale land reclamation. The shaded volume is saved if a 'perched' beach supported by a submerged breakwater is chosen.

To prevent large alongshore losses, groynes can be applied. The seaward limit of the reclaimed area can also be moulded with series of detached breakwaters to confine sediment (Figs. 10.39 to 10.41). The design of this type of reclamation should include a thorough analysis of all relevant coastal processes and impacts.

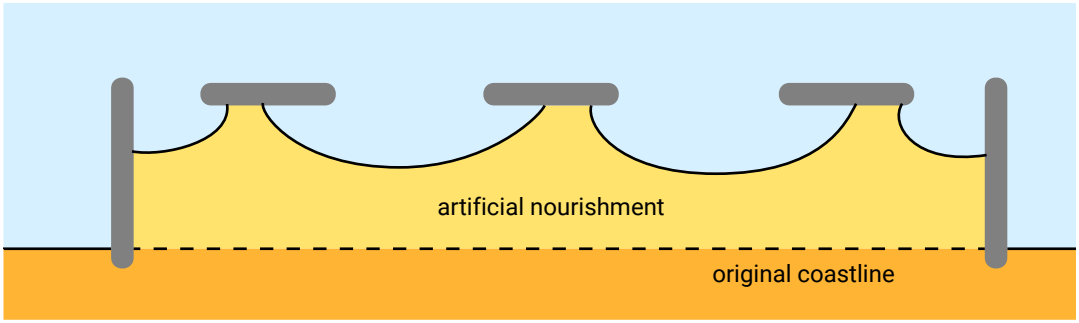

Figure 10.39: Application of structures to confine sand.

Figure 10.40: Submerged breakwater serving to perch the beach nourishment at the Pellestrina barrier island, in Venice, Italy. On the left side the Venetian Lagoon and on the right side the Adriatic Sea. Photo by Ni_Giri ('Credits' on page 579).

Figure 10.41: Real-life example: tombolos behind emerged (i.e. having their crests above MSL) offshore breakwaters in Malaga, Spain. Photo from SCNE ('Credits' on page 579).

10.7.6. A new nourishment strategy: the Sand Engine

Nourishment strategies applied in the Netherlands have historically developed as follows. From the 1970s onward, beach and dune nourishments, in which sand was placed directly on the beach and dunes, were used all over the world (Figs. 10.35b and 10.35d). Shoreface nourishments, initiated in the 1990s, make use of natural marine processes to redistribute the sand that is placed under water in the cross-shore direction and gradually create a wider coastal defense over time (Fig. 10.35a). This strategy is not very common globally. In the Netherlands nourishments over the last few decades are regularly executed to maintain the coastline position of 1990. Of these nourisments, roughly 50 % are traditional beach and dune nourishments and roughly 50 % shoreface nourishments. The average volume was 30 m^3/m/yr for the whole coast, while volumes per nourishment intervention varied roughly from 200 000 m^3 to 2 000 000 m^3 or 200 m^3/m to 500 m^3/m with typical time intervals of 3 to 5 years.

A new nourishment intervention, comprising an unprecedented 21.5×10^6 m^3 concentrated mega-nourishment known as the Sand Engine, was implemented in the Netherlands in the summer of 2011 (Stive et al., 2013). The nourishment advanced the coast locally in a bell shape with a maximum advancement of more than a km into the sea over a longshore distance of 1.5 km (Fig. 10.42).

This concentrated mega-nourishment exploits both marine and aeolian processes to redistribute the sand both in cross-shore and alongshore directions. The Sand Engine nourishment is a pilot project to test the efficacy of a local mega-nourishment as a countermeasure against the anticipated enhanced coastal recession in the 21st century. The proposed concept, a single mega-nourishment, is expected to be more efficient, economical, and environmentally-friendly in the long term than the traditional beach and shoreface nourishments presently in use to negate coastal recession. This local mega-nourishment is designed to widen the beach along a 10- to 20-km stretch of coastline and a beach area gain of 200 ha over a 20-year period. Observations since its construction show indeed a redistribution of the sand feeding the adjacent coasts, roughly 40 % toward the south and 60 % toward the north. While the jury is still out on this globally unique intervention, if proven successful it may well become an alternative worldwide solution for combatting coastal recession on open coasts driven by sea level rise.

(a) just after completion in 2011

(b) at low water on 27 March 2013

(c) at high water on 27 March 2013

Figure 10.42: Sand Engine mega-nourishment, the Netherlands, realised in 2011. Photos from Rijkswaterstaat (see 'Credits' on page 579).

A

Linear wave theory

In the theory for linear waves, equations are given for properties like:

the particle velocity (u, w) at any height in the water column	m/s
the particle acceleration (a_x, a_z) at any height in the water column §1.2 ~~m²/s~~ [p515]	m/s^2
the particle displacement (ξ, ζ) at any height in the water column	m
the pressure (p) at any height in the water column	N/m^2
the wave speed (c)	m/s
the wave group speed (c_g)	m/s
the wavelength (L)	m
the wave profile (η)	m
the wave energy per wavelength per unit crest length (E_t)	J/m
the energy per unit water surface area (E)	J/m^2
the wave power (U)	J/m×s

The general equations for these properties can be found in Table A.2 in the 'Transitional Water Depth' column. The equations for transitional water depth contain hyperbolic functions. It may be helpful to use standard tables containing the values of these hyperbolic functions, which can be found in the CEM. An extract of these tables is given in Table A.3.

For the specific cases of deep and shallow water (see Table A.1), simplifications can be made in the hyperbolic functions (see also Fig. A.1).

Table A.1: Criteria for deep- and shallow-water waves with an error of the order of 1 %

Shallow water			Deep water		
h/L_0	h/L	kh	h/L_0	h/L	kh
< 0.015	$< 1/20$	$< \pi/10$	> 0.5	> 0.5	$> \pi$

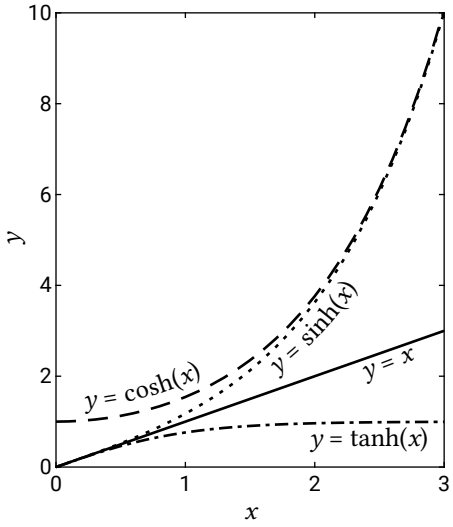

Figure A.1: Simplified hyperbolic functions.

For relatively deep water ($h > L/2$ so $kh > \pi$ where $k = 2\pi/L$ is the wavenumber):

$$\sinh kh = \frac{1}{2}\left(e^{kh} - e^{-kh}\right) = \frac{1}{2}e^{kh} \qquad \text{for } kh \to \infty \tag{A.1a}$$

$$\cosh kh = \frac{1}{2}\left(e^{kh} + e^{-kh}\right) = \frac{1}{2}e^{kh} \qquad \text{for } kh \to \infty \tag{A.1b}$$

$$\tanh kh = 1 \qquad \text{for } kh \to \infty \tag{A.1c}$$

For relatively shallow water ($h < L/20$ so $kh < \pi/10$):

$$\sinh kh = kh \qquad \text{for } kh \to 0 \tag{A.2a}$$

$$\cosh kh = 1 \qquad \text{for } kh \to 0 \tag{A.2b}$$

$$\tanh kh = kh \qquad \text{for } kh \to 0 \tag{A.2c}$$

Of the equations in Table A.2, the following are frequently used in this book:

$$\omega^2 = \left(\frac{2\pi}{T}\right)^2 = gk \tanh kh \qquad \text{dispersion relation } [1/\mathrm{s}^2] \tag{A.3a}$$

$$k = \frac{2\pi}{L} \qquad \text{wavenumber } [1/\mathrm{m}] \tag{A.3b}$$

$$n = \frac{c_g}{c} = 0.5\left(1 + \frac{2kh}{\sinh 2kh}\right) \qquad [-] \tag{A.3c}$$

The dispersion relation is implicit in terms of the wavenumber. This means that in order to solve the equation for transitional water depth, an iterative process is required (to calculate L from given h and T). There are also explicit formulas available that directly calculate L without iteration and approximate the solution closely. Alternatively, a look-up table may be used, like Table A.3 that gives h/L for given h/L_0 (with the deep-water wavelength $L_0 = gT^2/2\pi$).

The water particle displacement is shown in Fig. A.2 for a wave in shallow water and for a wave in deep water. In deep water the wave motion does not extend down to the bed; in shallow water the water makes an oscillating movement over the entire depth. Near the surface the water particles describe an elliptical path; near the bottom the water particles make a horizontal oscillating movement.

Figure A.3 shows the relation between the direction of the velocity and the acceleration of water particles at certain phases in the wave period.

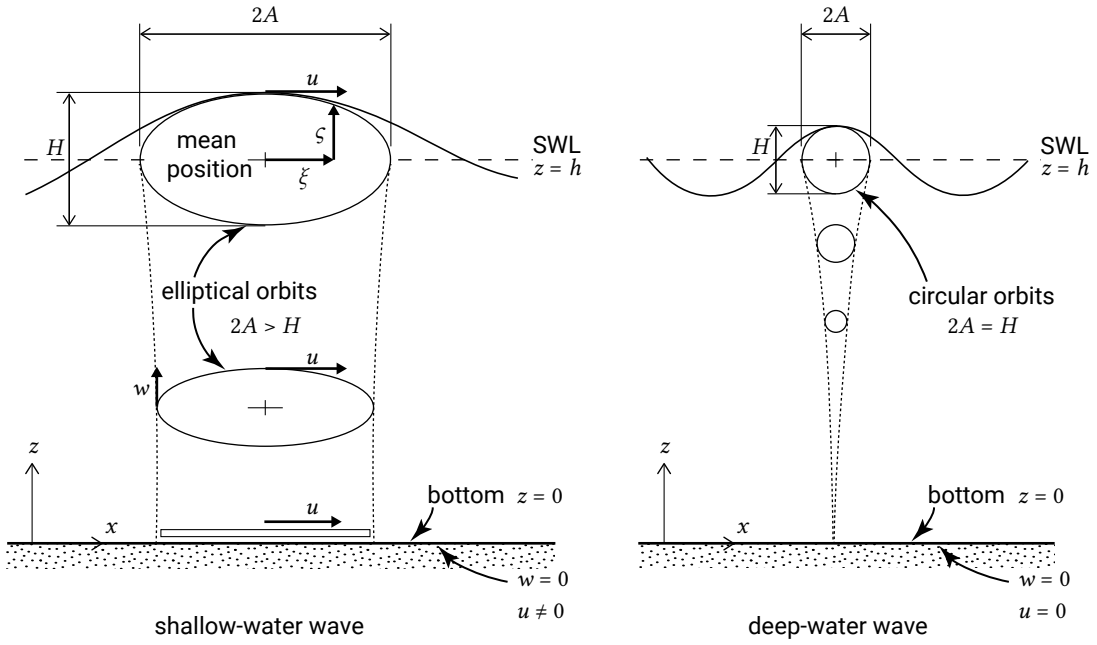

Figure A.2: Orbital motion under a shallow-water wave and a deep-water wave. Note that, as opposed to the definitions in Chapters 3 and 5, $z = 0$ at the bottom (instead of $z = -h$) and $z = h$ at the mean water level (instead of $z = 0$).

Table A.2: Formulas for shallow-, transitional- and deep-water wave computations according to linear wave theory. Note that as opposed to the definitions in Chapters 3 and 5, $z = 0$ at the bottom (instead of $z = -h$) and $z = h$ at the mean water level (instead of $z = 0$).

Parameter	Units	Shallow water	Transitional water depth	Deep water
wave profile	m	$\rightarrow$	$\eta = \frac{H}{2}\cos(kx - \omega t)$	$\leftarrow$
wave celerity	m/s	$c = \frac{L}{T} = \frac{\omega}{k} = \sqrt{gh}$	$c = \frac{L}{T} = \frac{\omega}{k} = \sqrt{\frac{g}{k}\tanh kh} = \frac{gT}{2\pi}\tanh kh$	$c = c_0 = \frac{L}{T} = \frac{gT}{2\pi} = \frac{g}{\omega} (\approx 1.56T)$
wave group celerity	m/s	$c_g = c = \sqrt{gh}$	$c_g = nc = \frac{1}{2}\left[1 + \frac{2kh}{\sinh 2kh}\right] c$	$c_{g0} = \frac{1}{2}c_0 = \frac{gT}{4\pi}$
wavelength	m	$L = cT = \sqrt{gh}T$	$L = cT = \frac{gT^2}{2\pi}\tanh kh$	$L = L_0 = c_0 T = \frac{\S JB\ \cancel{gT^w}}{2\pi} \frac{\S JB\ gT^2}{2\pi} (\approx 1.56T^2)$ [p518]
wave particle velocity horizontal	m/s	$u = \frac{\omega H}{2kh}\cos(kx - \omega t)$	$u = \frac{\omega H \cosh kz}{2\sinh kh}\cos(kx - \omega t)$	$u = \frac{\omega H_0}{2} e^{k_0(z_0 - h)}\cos(k_0 x - \omega t)$
... vertical	m/s	$w = \frac{\omega H z}{2h}\sin(kx - \omega t)$	$w = \frac{\omega H \sinh kz}{2\sinh kh}\sin(kx - \omega t)$	$w = \frac{\omega H_0}{2} e^{k_0(z-h)}\sin(k_0 x - \omega t)$
wave particle acceleration horizontal	m/s^2	$a_x = \frac{\omega^2 H}{2kh}\sin(kx - \omega t)$	$a_x = \frac{\omega^2 H \cosh kz}{2\sinh kh}\sin(kx - \omega t)$	$a_x = \frac{\omega^2 H_0}{2} e^{k_0(z-h)}\sin(k_0 x - \omega t)$
... vertical	m/s^2	$a_z = \frac{-\omega^2 H z}{2h}\cos(kx - \omega t)$	$a_z = \frac{-\omega^2 H \sinh kz}{2\sinh kh}\cos(kx - \omega t)$	$a_z = \frac{-\omega^2 H_0}{2} e^{k_0(z-h)}\cos(k_0 x - \omega t)$
wave particle displacement horizontal	m	$\xi = \frac{-H}{2kh}\sin(kx - \omega t)$	$\xi = \frac{-H \cosh kz}{2\sinh kh}\sin(kx - \omega t)$	$\xi = \frac{-H_0}{2} e^{k_0(z-h)}\sin(k_0 x - \omega t)$
... vertical	m	$\xi = \frac{Hz}{2h}\cos(kx - \omega t)$	$\xi = \frac{H \sinh kz}{2\sinh kh}\cos(kx - \omega t)$	$\xi = \frac{H_0}{2} e^{k_0(z-h)}\cos(k_0 x - \omega t)$
subsurface pressure	N/m^2	$p = \rho g(h - z) + \frac{\rho g H}{2}\cos(kx - \omega t)$	$p = \rho g(h - z) + \frac{\rho g H}{2}\frac{\cosh kz}{\cosh kh}\cos(kx - \omega t)$	$p = \rho g(h - z) + \frac{\rho g H_0}{2} e^{k_0(z-h)}\cos(kx - \omega t)$
wave energy per wavelength per unit crest length	J/m	$E_t = {}^1\!/\!_8 \rho g H^2 L$	$E_t = {}^1\!/\!_8 \rho g H^2 L$	$E_{t0} = {}^1\!/\!_8 \rho g H_0^2 L_0$
specific wave energy	J/m^2	$E_t = {}^1\!/\!_8 \rho g H^2$	$E_t = {}^1\!/\!_8 \rho g H^2$	$E_0 = {}^1\!/\!_8 \rho g H_0^2$
wave power	J/ms	$U = Ec_g = Enc = Ec$	$U = Ec_g = Enc$	$U_0 = E_0 n_0 c_0 = {}^1\!/\!_2 E_0 c_0$

Table A.3: Linear wave functions

h/L_0	$\tanh(kh)$	h/L	kh	$\sinh(kh)$	$\cosh(kh)$	K_{sh}	n	h/L_0	$\tanh(kh)$	h/L	kh	$\sinh(kh)$	$\cosh(kh)$	K_{sh}	n
0.000	0.000	0.0000	0.000	0.000	1.000	∞	1	0.200	0.888	0.225	1.41	1.926	2.170	0.918	0.6687
0.002	0.112	0.0179	0.112	0.112	1.006	2.12	0.9958	0.210	0.899	0.234	1.47	2.060	2.290	0.920	0.6559
0.004	0.158	0.0253	0.159	0.160	1.013	1.79	0.9917	0.220	0.909	0.242	1.52	2.177	2.395	0.923	0.6458
0.006	0.193	0.0311	0.195	0.196	1.019	1.62	0.9875	0.230	0.918	0.251	1.57	2.299	2.507	0.926	0.6362
0.008	0.222	0.0360	0.226	0.228	1.026	1.51	0.9834	0.240	0.926	0.259	1.63	2.454	2.650	0.929	0.6253
0.010	0.248	0.0403	0.253	0.256	1.032	1.43	0.9793	0.250	0.933	0.268	1.68	2.590	2.776	0.932	0.6169
0.015	0.302	0.0496	0.312	0.317	1.049	1.31	0.9690	0.260	0.940	0.277	1.74	2.761	2.936	0.936	0.6073
0.020	0.347	0.0576	0.362	0.370	1.066	1.23	0.9588	0.270	0.946	0.285	1.79	2.911	3.078	0.939	0.5999
0.025	0.386	0.0648	0.407	0.418	1.084	1.17	0.9488	0.280	0.952	0.294	1.85	3.101	3.259	0.942	0.5915
0.030	0.420	0.0713	0.448	0.463	1.102	1.13	0.9389	0.290	0.957	0.303	1.90	3.268	3.418	0.946	0.5851
0.035	0.452	0.0775	0.487	0.506	1.121	1.09	0.9289	0.300	0.961	0.312	1.96	3.479	3.620	0.949	0.5778
0.040	0.480	0.0833	0.523	0.547	1.140	1.06	0.9193	0.310	0.965	0.321	2.02	3.703	3.835	0.952	0.5711
0.045	0.507	0.0888	0.558	0.587	1.160	1.04	0.9095	0.320	0.969	0.330	2.08	3.940	4.065	0.955	0.5649
0.050	0.531	0.0942	0.592	0.627	1.180	1.02	0.8998	0.330	0.972	0.339	2.13	4.148	4.267	0.958	0.5602
0.055	0.554	0.0993	0.624	0.665	1.201	1.01	0.8905	0.340	0.975	0.349	2.19	4.412	4.524	0.961	0.5549
0.060	0.575	0.104	0.655	0.703	1.222	0.993	0.8812	0.350	0.978	0.358	2.25	4.691	4.797	0.964	0.5500
0.065	0.595	0.109	0.686	0.741	1.245	0.981	0.8719	0.360	0.980	0.367	2.31	4.988	5.087	0.967	0.5455
0.070	0.614	0.114	0.716	0.779	1.267	0.971	0.8627	0.370	0.983	0.377	2.37	5.302	5.395	0.969	0.5414
0.075	0.632	0.119	0.745	0.816	1.291	0.962	0.8538	0.380	0.984	0.386	2.43	5.635	5.723	0.972	0.5377
0.080	0.649	0.123	0.774	0.854	1.315	0.955	0.8448	0.390	0.986	0.395	2.48	5.929	6.013	0.974	0.5348
0.085	0.665	0.128	0.803	0.892	1.340	0.948	0.8358	0.400	0.988	0.405	2.54	6.300	6.379	0.976	0.5316
0.090	0.681	0.132	0.831	0.930	1.366	0.942	0.8272	0.410	0.989	0.415	2.60	6.695	6.769	0.978	0.5287
0.095	0.695	0.137	0.858	0.967	1.391	0.937	0.8188	0.420	0.990	0.424	2.66	7.113	7.183	0.980	0.5260
0.100	0.709	0.141	0.886	1.007	1.419	0.933	0.8102	0.430	0.991	0.434	2.73	7.634	7.699	0.982	0.5232
0.110	0.735	0.150	0.940	1.085	1.475	0.926	0.7937	0.440	0.992	0.443	2.79	8.110	8.171	0.983	0.5211
0.120	0.759	0.158	0.994	1.166	1.536	0.920	0.7775	0.450	0.993	0.453	2.85	8.615	8.673	0.985	0.5191
0.130	0.780	0.167	1.05	1.254	1.604	0.917	0.7611	0.460	0.994	0.463	2.91	9.151	9.206	0.968	0.5173
0.140	0.800	0.175	1.10	1.336	1.669	0.915	0.7468	0.470	0.995	0.472	2.97	9.720	9.772	0.987	0.5156
0.150	0.818	0.183	1.15	1.421	1.737	0.913	0.7329	0.480	0.995	0.482	3.03	10.324	10.373	0.988	0.5141
0.160	0.835	0.192	1.20	1.509	1.811	0.913	0.7195	0.490	0.996	0.492	3.09	10.966	11.011	0.990	0.5128
0.170	0.850	0.200	1.26	1.621	1.905	0.913	0.7041	0.500	0.996	0.502	3.15	11.647	11.689	0.990	0.5116
0.180	0.864	0.208	1.31	1.718	1.988	0.914	0.6918	1.000	1.000	1.000	6.28	266.893	266.895	1.000	0.5000
0.190	0.877	0.217	1.36	1.820	2.076	0.916	0.6800	∞	1.000	∞	∞	∞	∞	1.000	0.5000
0.200	0.888	0.225	1.41	1.926	2.170	0.918	0.6687								

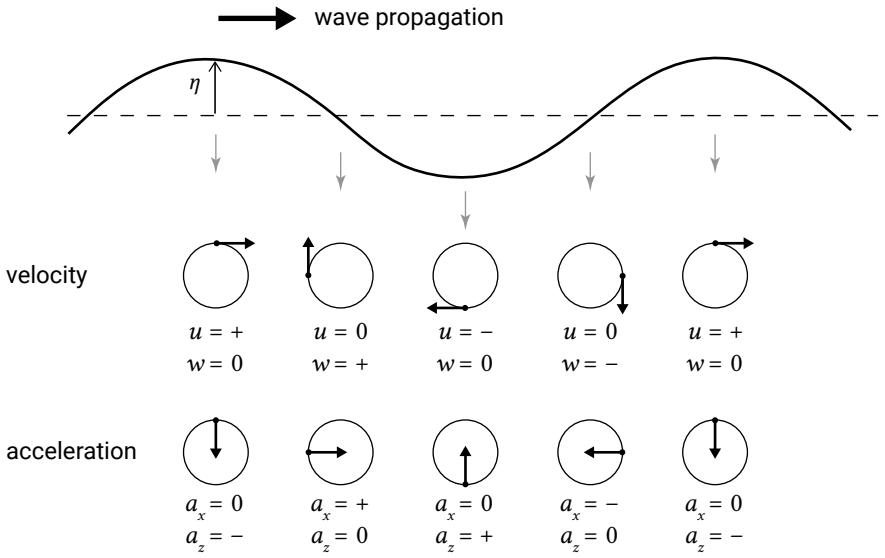

Figure A.3: Local fluid velocities and accelerations at certain phases in the wave period.

B

Waves breaking on a beach

B.1. Scale comparison

Stive (1985) performed flume experiments for periodic and random waves breaking on a gently sloping beach. Measurements were conducted in both a small-scale wave flume and a large-scale wave flume, such that a scale comparison could be performed. To that end, the small-scale measurements were scaled up geometrically by the length scale relation n_{length} and dynamically by the velocity scale relation according to Froude $n_{\text{velocity}} = n_{\text{length}}^{0.5}$.

B.2. Periodic wave results

The small-scale and large-scale results for periodic waves are compared in Fig. B.1 and Fig. B.2. Figure B.1 shows the wave height variation and the set-up and Fig. B.2 shows the characteristics of the velocity field. The small flume has a rigid bed and the large flume a sandbed, on which a breaker bar was formed. The variability in the large-scale results, amongst others the shift of the breakpoint during the first and second day, is related to the morphological development in these large-scale tests.

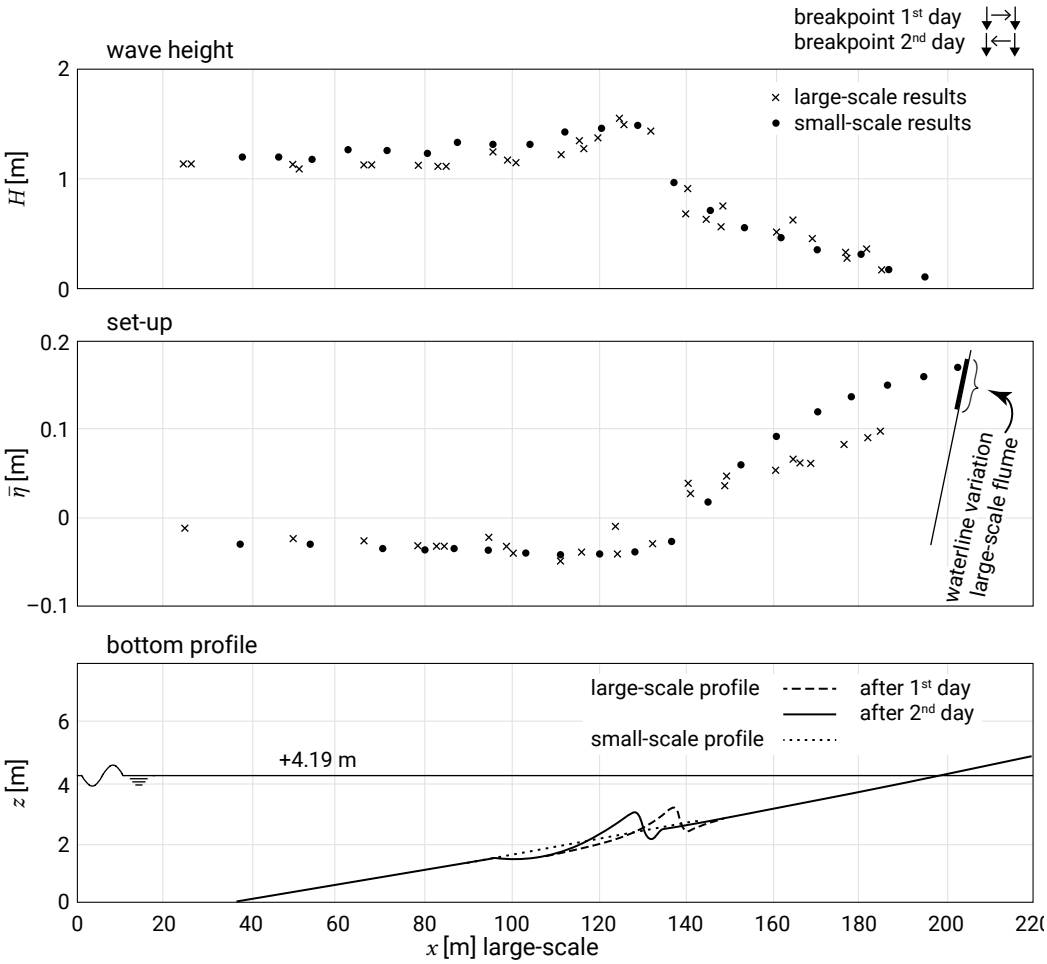

Figure B.1: Comparison between small-scale and large-scale flume measurements of wave height and set-up in periodic waves.

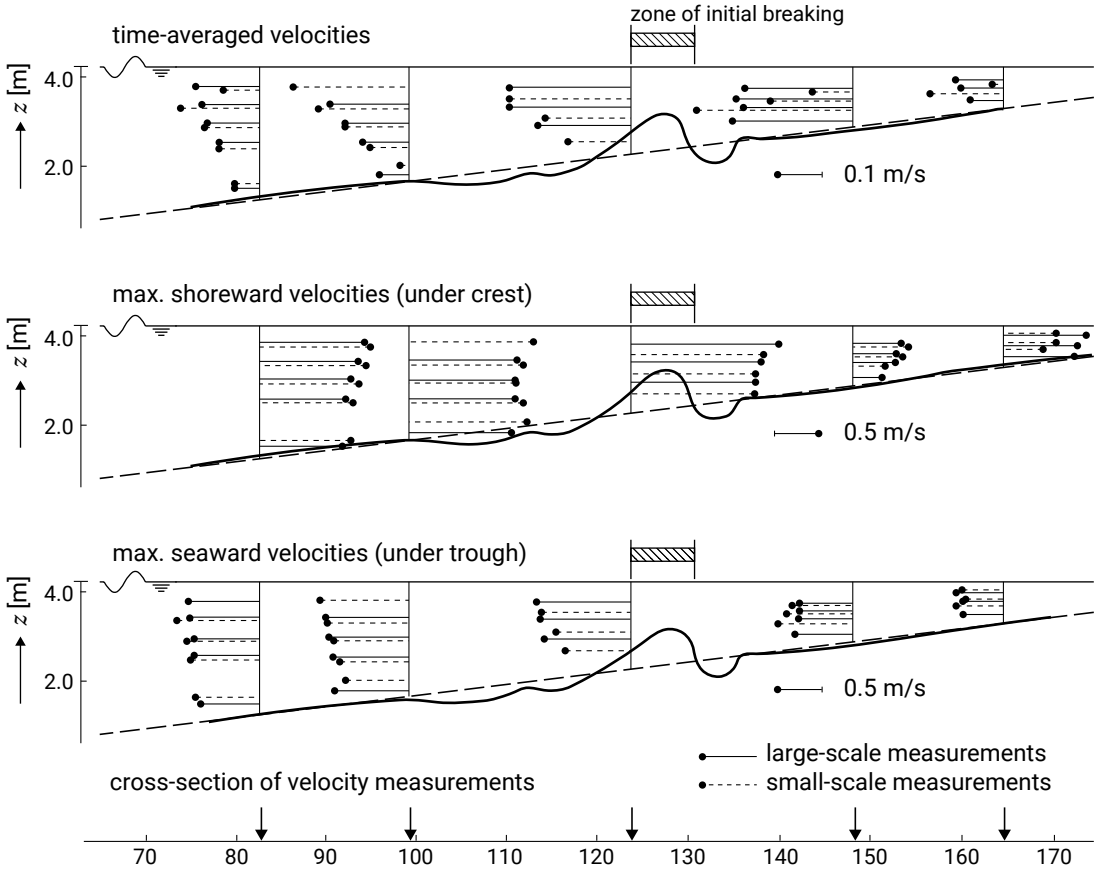

Figure B.2: Comparison between small-scale and large-scale flume measurements of time-averaged velocities, maximum shoreward velocities (under the wave crest) and maximum seaward velocities (under the wave trough).

B.3. Random wave results

For random waves, Fig. B.3 shows the wave height and set-up.

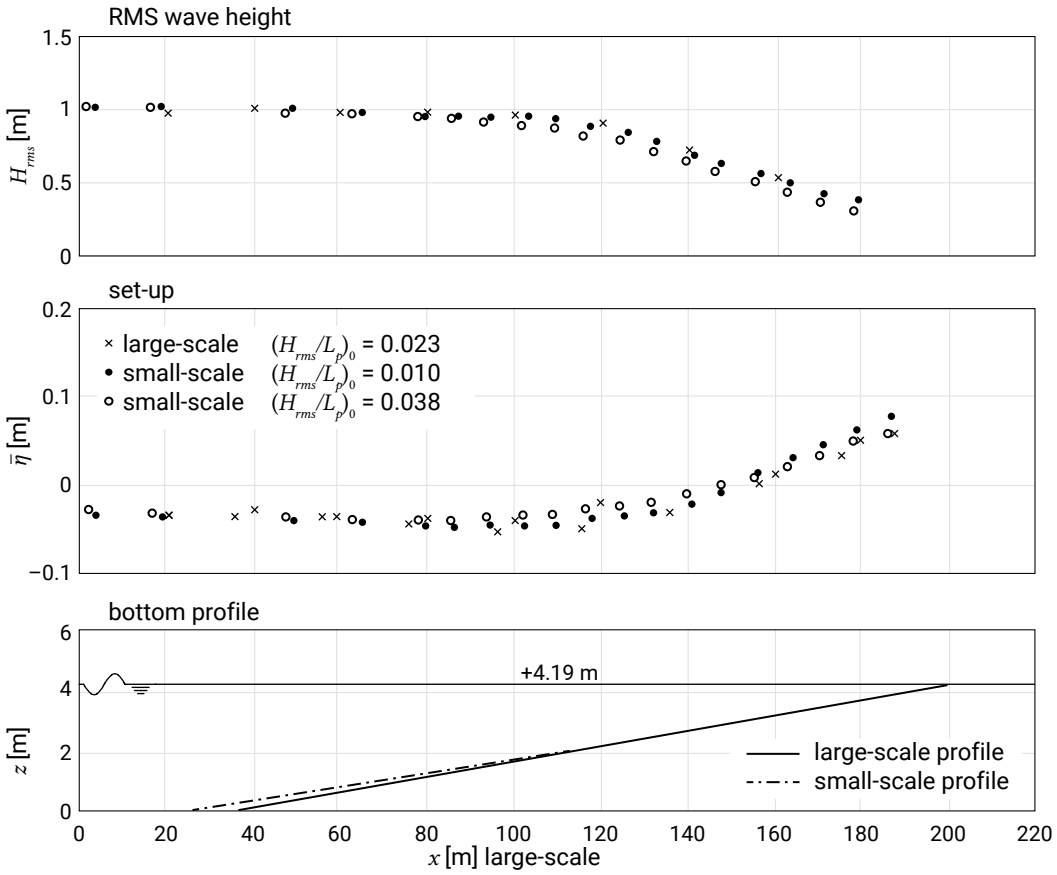

Figure B.3: Comparison between small-scale and large-scale flume measurements of root-mean-square wave height and set-up in random waves.

C

Hydrographic charts

C.1. Introduction

Maps are a very important source of information for coastal engineers. This is true for both maps of the land adjacent to the coast and charts of the seas and oceans. We expect that these maps will give accurate information about the topography of the area, but often additional information relating to land use, infrastructure, elevation, etc. is provided. For the coastal engineer, charts of the seas and oceans are of particular interest. Such charts have been produced for many centuries to provide information to seafarers. The production of these charts was originally in the hands of private enterprises that had an interest in the trade between Europe and the East and West Indies. In the early days of this trade, maps and charts represented a great commercial value and they were kept secret by institutes like VOC and the British East India Company. Later, from the early 19^{th} century, with the formal establishment of the colonies, the role of governments in various countries became more important. The task of making proper maps of sailing routes and ports was then transferred to the various navies. Up to today, in most countries the national navy has a hydrographic department that is responsible for providing up to date information for ocean navigation. An important part of that information is contained in hydrographic charts that give an impression of the local situation, including topography, bottom material, depths, sea levels, currents etc.

Such hydrographic charts are indispensable to sailors, and the presence of up-to-date charts is mandatory on board of seagoing vessels. When people cannot easily see what is below the surface of the water, maps and charts provide the only way for navigators to find out where it is safe for the ship to go and where it would be unwise to venture. Hydrographic charts are also an important tool for the coastal engineer, because these charts give reliable information on the conditions of the coastal zone. For engineers, however, not only the latest charts are of interest, but certainly also older maps that can

still be obtained from the archives of the various hydrographic institutes. A sequence of maps gives a good impression of long-term morphological developments.

This section shows the general principles governing the handling of maps and, more specifically, hydrographic charts, and indicates roughly what information can be obtained from them.

C.2. Units and their background

Hydrographic charts were meant to provide assistance to the navigators on board sailing vessels, who had little more in the way of instruments than a clock and a sextant. Positions were determined with respect to the position of the sun and the stars. The grid of the hydrographic chart is therefore the grid of the degrees latitude and longitude as drawn on the globe. Transformation of this spherical grid to a plane map causes distortions, either in the centre or in the corners of the map. This means that the coordinates of the grid as indicated along the borders of the map are not linear.

Since the mutual distance between the longitudinal coordinates (meridians) varies (they are long at the equator and zero at the poles), only the degrees of latitude (parallels) give a proper indication of the scale of the map. The circumference of the earth is 40 000 km, which is divided into 360° (degrees), each consisting of 60′ (minutes). This means that the 40 000 km are equal to $360 \times 6^{\S 1.1}0 = 21\,600'$ [p526]. The sailors used the minute as the basis for their unit of distance, the nautical mile, which thus equals slightly more than 1850 m. Early hydrographic charts were not based on the metric system. Their scales therefore appear unusual to people who are familiar only with the metric system of measurement.

The speeds of vessels and the velocities of currents are often expressed in nautical miles per hour (also called knots), which is slightly more than 0.5 m/s.

Water depths (soundings) are expressed either in the traditional nautical system, or in the metric system. This is always indicated on the map. The nautical system uses feet, fathoms (Dutch: vadem), or fathoms plus feet. A foot is equal to 0.3048 m; a fathom is equal to 6 feet or 1.83 m.

C.3. Explanatory notes

The first thing to do when looking at a map is to study the key. The following information may be found:

Horizontal scale The scale indicating the dimensions of details at the map. Most sailors look at the latitude border scales at the side of the map. 1 Minute equals 1 nautical mile. Most coastal engineers look at the linear scale. As a result of the projection of the globe on a plane, the scale changes over the map. The larger the area covered by the chart, the larger the deviations.

Vertical scale Depth on a hydrographic chart may be shown in metres, feet or fathoms. The reference level (Chart Datum) of the depths is also important. Chart Datum (CD) is often related to specific tidal data. This may be LAT, MSL or any other reference level. Different countries use different definitions of CD! A Belgian map of the Western Scheldt may thus give different depth values than a Dutch map of the same area. Even on one map, the CD may differ for different locations, because the tidal data differ from place to place. This poses a risk for coastal engineers, since we usually assume that the datum level of a map is horizontal. Specifically when we make hydraulic calculations, we must make sure that we use levels that find a reference to a horizontal plane, in order to eliminate errors in the gravitational forces. A striking example is given in Fig. C.1. The result of misinterpretation is given in Fig. C.2.

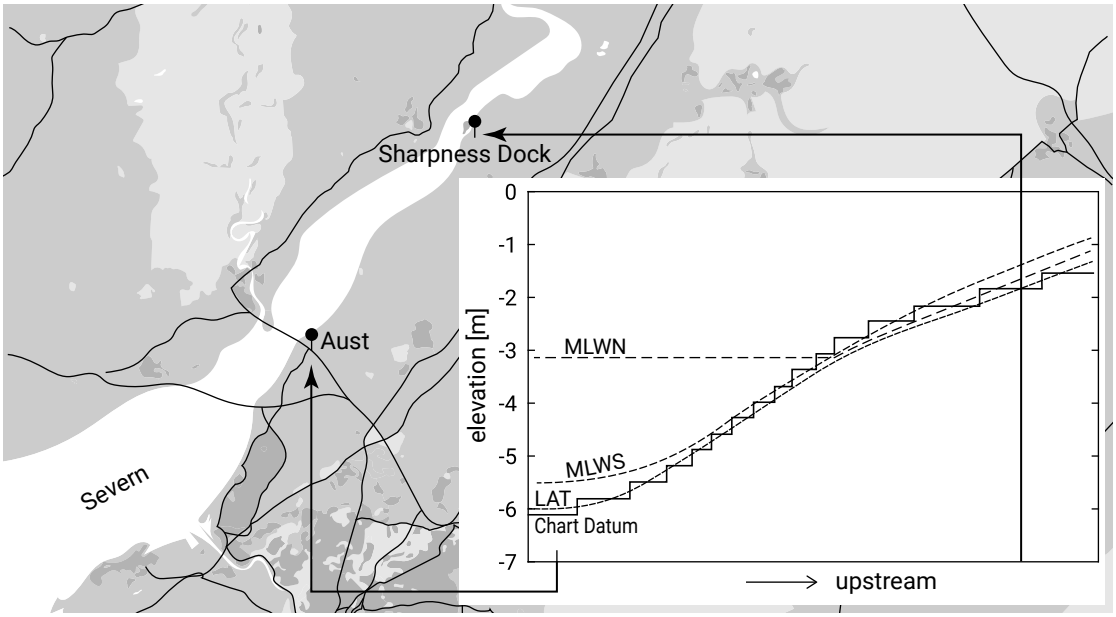

Figure C.1: River Severn (England).[§1.1] When CD is related to LAT, or another tidal level, it increases in upstream direction.[§1.1] [p527]
[Corrections in figure: vertical label and indication of Chart Datum]

- What happens to levels above the reference level, like mud flats or sandbanks? These levels are underlined and refer to CD. Levels at the shore may also be shown. For these levels, different reference levels are usually used, rather than CD;
- Tidal streams/currents are sometimes shown;
- Dates of publication and dates of smaller or larger corrections;
- Tidal levels are usually shown at some specific locations, as shown in Table C.1.

Terms related to tidal levels are summarised in Table C.2.

Figure C.2: §1.1 ~~Chart Datum is not horizontal!~~ §1.1 If a horizontal free-surface level is determined relative to a chart datum which is not horizontal, the free-surface level may be misinterpreted as non-horizontal. [p528]

Table C.1: Tabular statement of semi-diurnal or diurnal tides.

place	Lat. (N/S)	Lon. (E/W)	heights in metres/feet above datum			
(position for which tidal levels are tabulated)			MHWS	MHWN	MLWN	MLWS
			MHHW	MLHW	MHLW	MLLW

Table C.2: Terms related to tidal levels.

CD	Chart Datum
LAT	Lowest Astronomical Tide
HAT	Highest Astronomical Tide
MLW	Mean Low Water
MHW	Mean High Water
MSL	Mean Sea Level
MLWS	Mean Low Water Spring
MHWS	Mean High Water Spring
MLWN	Mean Low Water Neap
MHWN	Mean High Water Neap
MLLW	Mean Lower Low Water
MHHW	Mean Higher High Water
MHLW	Mean Higher Low Water
MLHW	Mean Lower High Water

MSL – Mean Sea Level the average height of the sea measured over a long period of time. This is the average level which would exist in the absence of tides.

LAT – Lowest Astronomical Tide the lowest tide level which can be predicted to occur under average meteorological conditions and under any combination of astronomical conditions.

HAT – Highest Astronomical Tide the highest tide level which can be predicted to occur under average meteorological conditions and under any combination of astronomical conditions.

MHW – Mean High Water the average height of all high tides.

MHHW – Mean Higher High water the average height of the higher of the two daily high tides over a long period of time. When only one high water occurs per day, this is taken as the higher high water.

MLW – Mean Low Water the average height of all low tides.

MLLW – Mean Lower Low Water the average height of the lower of the two daily low waters over a long period of time. When only one low water occurs per day, this is taken as the lower low water.

MHWS – Mean High Water Spring the long-term average of all high-water observations of the heights of two successive high waters during those periods of 24 hours (approximately once a fortnight) when the range of tide is greatest, at full and new moon.

MLWS – Mean Low Water Spring the long-term average of all low-water observations of the heights of two successive low waters during those periods of 24 hours (approximately once a fortnight) when the range of tide is greatest, at full and new moon.

MHWN – Mean High Water Neap the long-term average of all high-water observations of the heights of two successive high waters when the range of tide is the least, at the time of first and last quarter of the moon.

MLWN – Mean Low Water Neap the long-term average of all low-water observations of the heights of two successive low waters when the range of tide is the smallest, at the time of first and last quarter of the moon.

MLHW – Mean Lower High Water the mean of the lower of the two daily high waters over a long period of time. When only one high water occurs on most days, no value is printed in the MLHW column, indicating that the tide is usually diurnal.

MHLW – Mean Higher Low Water the mean of the higher of the two daily low waters over a long period of time. When only one low water occurs on most days, no value is printed in the MHLW column, indicating that the tide is usually diurnal.

C.4. The map itself

Once familiar with this information, the map itself may be studied. A complete list of symbols used on Admiralty Charts[1] may be found in *Symbols and Abbreviations Used on Admiralty Charts (NP5011)* (2020). A summary of frequently used symbols is shown in Table C.3.

Table C.3: A summary of frequently used symbols and abbreviations on Admiralty charts

Natural features	
	steep coast, cliffs
	flat coast
	sandy shore
	stony shore, shingle shore
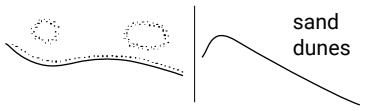	dunes
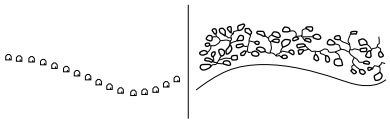	mangrove
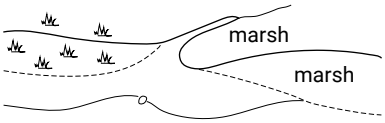	swamp, salt marsh
Cultural features	
	buildings
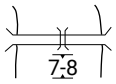	bridges
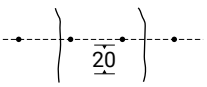	cables
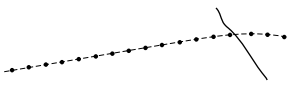	pipelines

[1] Admiralty charts are hydrographic charts issued by the United Kingdom Hydrographic Office.

Landmarks	
	examples of landmarks

Artificial features	
	dykes
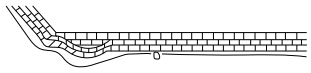	seawall
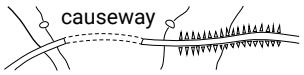	causeway
	breakwater
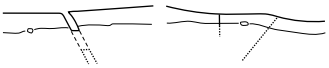	groyne
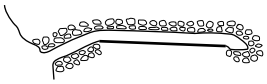	mole
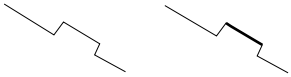	wharf
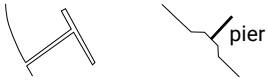	pier, jetty
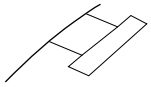	pontoon
	dolphins
	ramp

Nature of the seabed	
S	Sand
M	Mud
Cy	Clay
Si	Silt
St	Stones
G	Gravel
P	Pebbles
Cb	Cobbles
R	Rock
Co	Coral
Sh	Shells

C.5. Interpretation

Maps may also provide information about coastal processes like wind and wave directions and heavy breaking of waves. Many other phenomena can be derived by interpreting the coastal forms on the map: a spit indicates the direction of the longshore transport, and thus the dominant wave direction, and river sediment transport is shown by the presence of shoals and bars. If the map shows only a long, straight, sandy shore, little can be concluded about wave and wind direction and intensity. Only when there is an interruption to this shore, it is possible to determine the prevailing wave and wind direction and resulting sediment transport. For example, at a river mouth one may find out whether the river or the sea is dominant and the magnitude and direction of longshore and river sediment transport may be deduced. Another example is formed by protruding rocks or artificial features like groynes or breakwaters on a sandy coast. Here one may also find indications of the presence of longshore sediment transport (magnitude and direction) and, hence, the wind and wave direction. Detached obstacles (rocks or breakwaters) may give even more exact information about wave direction. In the lee of these obstacles sediment tends to settle, so the position of shoals indicates the lee side and thus the wave direction.

If dredged channels are present, it is clear that sediments have to be removed on a more or less regular basis. The location of the dumping grounds of dredged material sometimes gives an indication of the dredging method that is commonly used.

In large sandy areas, the bottom contours also indicate possible current patterns. Places with great depths probably indicate areas where the current will be concentrated. Shallow areas indicate low current velocities.

C.6. Limitations

Although hydrographic charts provide a very valuable contribution to our knowledge, the purpose of these charts is to assist navigators, rather than engineers. Soil data mentioned on the chart are generally only an indication of the surface of the seabed; they cannot be used in designing a foundation. The charts, and certainly the portions close to the shore, are meant to warn sailors against running aground. Relatively more attention is therefore paid to shoals and low water conditions, rather than to gullies and extremely high water levels. Moreover, the scale of the charts is generally unsuitable for construction work. For the specification needed in tenders and project drawings, more detailed maps are required.

When comparing old and recent charts, one must be aware that the locations of buoys and lighthouses may have changed since the survey or the drawing of the original chart. Therefore, one should remain vigilant when using older maps for comparison. The most recent maps will probably be based on positioning with DGPS, an electronic positioning system using satellites as beacons. This eliminates most errors.

D

Stability of structures

D.1. Introduction

In this book only the *functional* design of coastal engineering structures is treated, such as jetties/breakwaters, groynes, detached shore-parallel offshore breakwaters, seawalls and revetments (Ch. 10). We do not discuss the *technical* and *constructive* design of these structures, but refer to other TU Delft courses like Bed, Bank and Shoreline Protection (CIE4310) and Breakwaters and Closure Dams (CIE5308). Yet, we would like to point out some similarities between bottom sediment transport on the one hand and stone stability and structural damage approaches for slopes made of loose rock and of breakwater elements on the other hand in a more general way.

D.2. Initiation of transport and damage

In Sect. 6.3 the 'initiation of transport' concept of Shields (1936) was introduced for sediment particles under the impact of uniform flow. The parameter (θ) that he introduced is the ratio of the drag force due to the flow over the resisting force due to the underwater weight of the sediment. Initiation of motion occurs for a value of this parameter (θ_{cr}, Eq. 6.12) between 0.03 and 0.05 in practice. When, at a later stage, sediment transport formulas for uniform flow started to be developed, it turned out that Shields' parameter was not only a good parameter to describe threshold of motion, but also a fundamental parameter in empirical transport formulas, which nearly all can be expressed as a power function of θ or $\left(\theta - \theta_{cr}\right)$, with the power ranging from 1.5 to 3 (see Sect. 6.5). That is why θ or $\left(\theta - \theta_{cr}\right)$ is often referred to as the mobility number.

Sleath (1978) evaluated initiation of sediment motion under oscillatory flow from literature and his own experiments, and showed that by using the velocity amplitude

(specifically the orbital velocity amplitude) a Shields parameter for waves could be derived, where the empirical values for the initiation of motion only differ marginally from θ_{cr}, viz. in the range 0.02 to 0.05.

Interestingly, Iribarren (1938), two years after Shields' publication and most likely independently from him, proposed a stability criterion for a sloping rubble mound breakwater. The breakwater is stable if:

$$\underbrace{\rho_s g D^3}_{\text{stone weight}} \geq \frac{N \rho_s g H^3}{\Delta^3 (\mu \cos\alpha \pm \sin\alpha)^3} \tag{D.1}$$

in which the friction coefficient $\mu = \tan\varphi_r$ with φ_r is the natural angle of repose, $\Delta = (\rho_s - \rho)/\rho$, α is the angle of the bed slope, H is the wave height and N is a coefficient. The density ρ_s should now be interpreted as the density of the blocks or stones and D as a typical size.

We can rewrite this equation as:

$$\frac{H}{\Delta D(\mu \cos\alpha \pm \sin\alpha)} = \frac{\rho g D^2 H}{\left(\rho_s - \rho\right) g D^3 \left(\tan\varphi_r \cos\alpha \pm \sin\alpha\right)} \leq \frac{1}{\sqrt[3]{N}} \tag{D.2}$$

In the second term of this equation, we can recognize the ratio of drag force over the resisting force, just as Shields used (see Sect. 6.3.1). The numerator represents the drag force $\rho u^2 D^2$ taking $\sqrt{gH}$ as a typical value for u, assuming that the wave height of the order of magnitude of the water depth. The denominator reflects the resisting force proportional to $(\rho_s - \rho) g D^3$. We furthermore find in the denominator the effect of the bed slope, where the plus sign is for uprush and the minus sign for downrush. Once α approaches the natural angle of repose φ_r, the resisting force approaches zero for downrush. Furthermore, note the correspondence between the slope correction $\tan\varphi_r \cos\alpha \pm \sin\alpha$ and the denominator of Eq. 6.48a.

We can write Eq. D.2 as a slope-dependent criterion for the initiation of movement of a block of a certain size:

$$\frac{H_{cr}}{\Delta D} = \frac{(\mu \cos\alpha \pm \sin\alpha)}{\sqrt[3]{N}} \tag{D.3}$$

Later, many experiments were performed, mostly by Hudson (1952), to find the constants of proportionality in Eq. D.3. For practical reasons, Hudson finally proposed a criterion in which he indicated the proportionality constant as K_D and in which he changed the slope correction term, not based on physics, to $\cot\alpha$.

$$\frac{H_{cr}}{\Delta D} = \left(K_D \cot\alpha\right)^{1/3} \tag{D.4}$$

Note that what θ_{cr} is for the initiation of motion of sediment, $(K_D \cot\alpha)^{1/3}$ is for initiation of damage on a rocky slope. Both parameters are based on the same stability principle. Hudson's slope correction term limits the validity of this generally-applied formula to the range of $1.5 < \cot\alpha < 4$.

Just like the values of the Shields parameter, the values of K_D are based on experiments. Because structures represent a physically much more complex system than a flat sandy bed, the range of K_D values is larger. For instance, for natural rock K_D is 3–4 and for artificial elements, like Tetrapods or Xblocs®, it is 8–10. The higher values for artificial elements are due to the interlocking effect.

This would lead to values for $(K_D \cot\alpha)^{1/3}$ within the range of 1.5 to 3.5 and thus two orders of magnitude larger than the critical Shields parameter. What is the reason behind this difference? To answer this question, we rewrite the Shields parameter using $u = \sqrt{gH}$ as follows:

$$\theta = \frac{\tau_b}{(\rho_s - \rho)\, gD} = \frac{\rho c_f u^2}{(\rho_s - \rho)\, gD} = c_f \frac{H}{\Delta D} \tag{D.5}$$

Hence, the Shields parameter is related to $H/\Delta D$ through a friction factor c_f (order of magnitude 10^{-2}). This would lead to values for the critical Shields parameter that are two orders of magnitude smaller than critical values of $(K_D \cot\alpha)^{1/3}$, which agrees with the above-mentioned typical ranges.

The simplicity of Hudson's formula is very attractive, but the complex physics of rubble mound structures makes that these physics can only be included empirically in the K_D coefficient. These physics are in the loading, the structure's geometry and its permeability. Van der Meer (1988) conducted a lot of empirical research under various conditions and arrived at expressions for $(K_D \cot\alpha)^{1/3}$, where this parameter is a function of the structure's slope, the type of wave-breaking (Iribarren number), the number of waves, the permeability and the progressive damage.

As an example we present the equation of Van der Meer (1988) for plunging breakers on a loose rock slope, in which the right-hand term is a fit to $(K_D \cot\alpha)^{1/3}$ that includes the permeability (P), the damage (S), the number of waves (N) and the type of wave-breaking (ξ, the Iribarren parameter Eq. 5.20, which includes the slope as a property of the structure's geometry):

$$H_{s,cr}/(\Delta D) = 6.2 P^{0.18} (S/\sqrt{N})^{0.2} \xi^{-0.5} \tag{D.6}$$

Typically this leads to a progressive damage curve as shown in Fig. D.1. Note $S = 2$ means very little damage and $S = 20$ means serious damage.

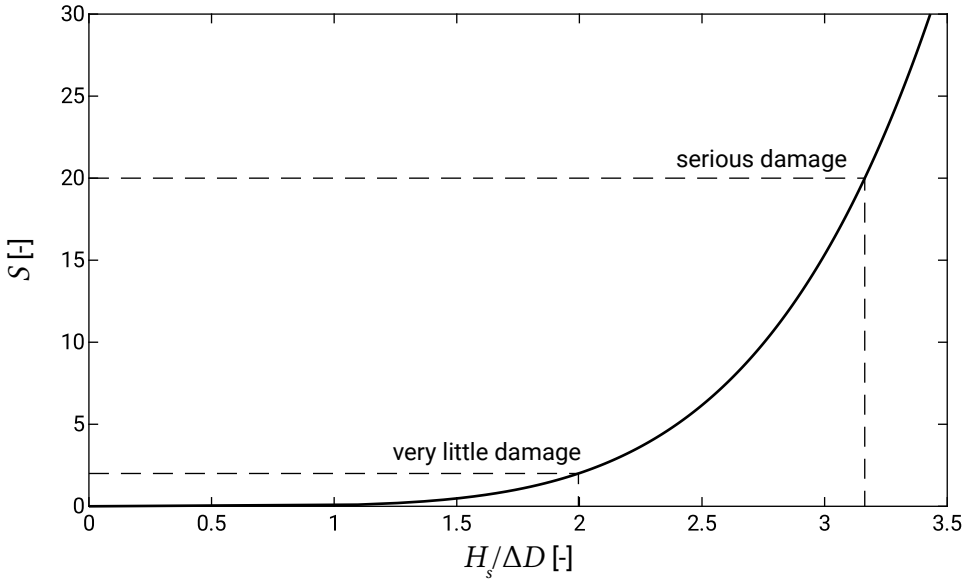

Figure D.1: Damage curve according to Eq. D.6 with $P = 0.5$ for a permeable core, $N = 3000$ (which for an average period of 6 s represents a storm of 5 hours duration) and ξ = 2.

In sediment transport terms, i.e. we solve for the damage that may be interpreted as transport, we may rewrite Eq. D.6 to:

$$S = \left(6.2P^{0.18}\right)^{-5} \sqrt{N}\xi^{2.5} \left(H_s/\Delta D\right)^5 \tag{D.7}$$

Note that damage now takes on a wider meaning: damage can now vary from initiation of motion to larger amounts of motion i.e. 'transport'. It appears that the damage is proportional to the power 5 of the Hudson parameter. Again we see a similarity with sediment, in that $H_s/\Delta D$ is used as a mobility number, so that we are talking about transport.

D.3. Other protections

In the above discussion, we assumed that the main loading of the structures was external, because of the large permeability of these rocky slope structures. When we consider coherent, semi-permeable, placed block revetments or impervious asphalt or concrete structures, the external loading also leads to internal loadings. The failure mechanisms thus become much more complex. We will not consider this here, but it is interesting to note that the empirical formulas for semi-impermeable structures also fall back on Iribarren's mobility parameter.

E

Responses to the closures of Dutch tidal basins

Reprinted with permission from: Wang, Z. B., De Ronde, J. G., Van der Spek, A. J. F. & Elias, E. P. L. Responses of the Dutch coastal system to the (semi-) closures of tidal basins. In: *International Conference on Estuaries and Coasts, Sendai, Japan.* 2009.

E.1. Introduction

The Dutch coastal system consists of the North Sea coast, a series of Wadden Sea tidal inlets in the north and various estuaries in the southwestern delta area. During the last century, various engineering works in the Dutch coastal system were carried out for flood defence and/or land reclamation purposes. Among these engineering works, two of the tidal inlets in the Dutch Wadden Sea and three of the estuaries in the southwestern delta were entirely or partly closed or semi-closed (Fig. E.1). The first closure is the Afsluitdijk, a dam of 30 km finished in 1932 and separating the former Zuiderzee from the Wadden Sea. The last of these closures is the Eastern Scheldt Storm Surge Barrier, finished in 1986, which semi-closed the Eastern Scheldt estuary.

These closures differ in type and location within the corresponding basins. Three of the five are fully closed dams: the Afsluitdijk, the closure of Lauwerszee and the closure of the Grevelingen. Haringvliet is closed by a dam in combination with sluices which only allow discharge of freshwater from the river upstream. The Eastern Scheldt Storm Surge Barrier only closes the basin under extreme conditions and allows tidal flow, although with reduced cross-section. The two closures in the Wadden Sea only close the landwards part of the tidal basin. The closures in the southwestern delta area almost completely close the entire corresponding basins, but their locations relative to the mouths of the basins differ from each other.

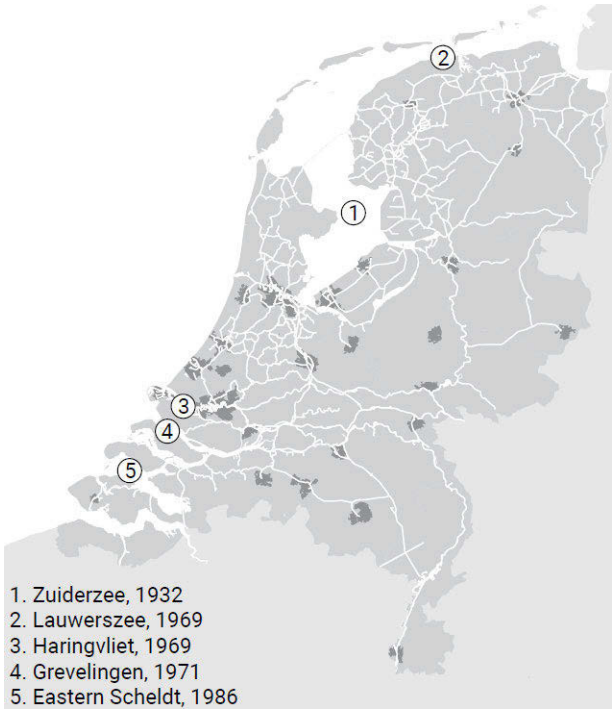

Figure E.1: Closures of tidal basins in the Dutch coastal system.

These closures of the tidal basins have impacted the development of not only the (semi-)enclosed basins themselves, but also the adjacent coast and tidal basins. They influence large-scale morphological developments and the sediment budget, and thereby impact the maintenance of the coast by sand nourishment. On a smaller scale they influence the developments of channels, intertidal flats and other morphological elements. Specifically the morphological developments of the intertidal flats make an impact on the ecological system.

In this paper we evaluate the effects of all these closures on the morphological development of the various parts of the Dutch coastal system. The evaluation is mainly based on analysis of field data. Bathymetric data have been collected since 1926. Furthermore, the results of earlier modelling studies are used. Special attention will be paid to the influence of the location of the closure and the type of the closure. It will e.g. be shown that the total sediment deficit for establishing the new morphological equilibrium caused by a closure is very much dependent on the location of the closure relative to the mouth of the tidal basin. We will also show the different environmental problems caused by the different types of closures. We believe that the lessons learned from the evaluation can also be relevant elsewhere in the world.

E.2. Closures in the Wadden Sea

E.2.1. Closure of Zuiderzee

The Afsluitdijk, a 30-km dam separating the former Zuiderzee from the Wadden Sea, was finished in 1932. After the closure, part of the Zuiderzee was reclaimed and the remaining part became a freshwater lake, the IJsselmeer.

Figure E.2 shows schematically how the closure dam influenced the vertical and horizontal tide. Before the closure, the basin was relatively long compared to the tidal wavelength. There was a place in the system where the tidal flow before the closure was minimal. The closure dam is located just seawards of this place. As the tidal range in the remaining basin became higher, the tidal prisms at the inlets (Texel and Vlie) even became slightly larger than before the closure.

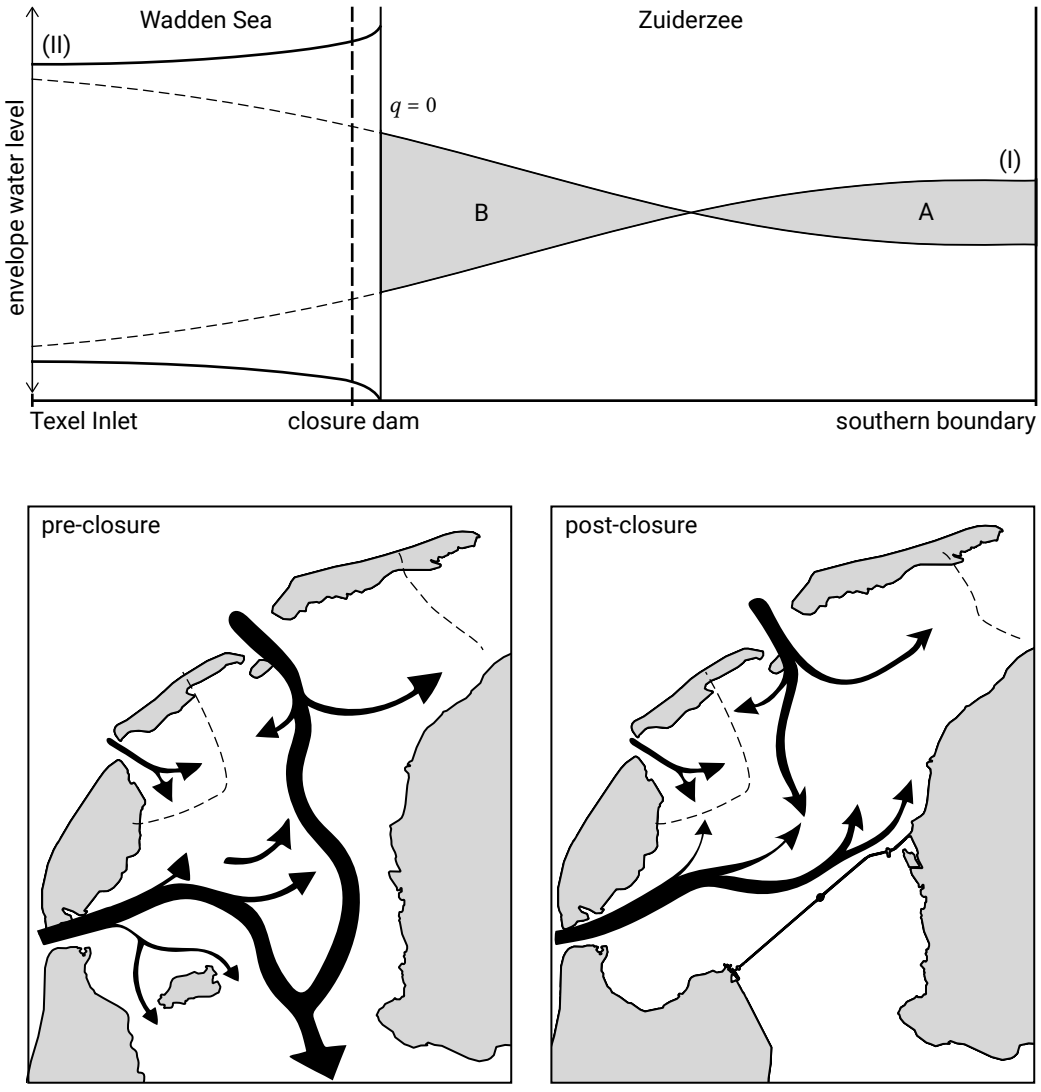

Figure E.2: Influence of the closure of the Zuiderzee on the tide (from Elias et al., 2003).

Although the closure has not caused significant changes in the total tidal prisms of the basins, it has induced morphological changes inside and outside the basins, especially the two large basins: Texel and Vlie. Figure E.3 shows the sediment budget of the three inlet systems. Note that the ebb-tidal delta is also included in the area indicated by 'coast'. Inside the two large (remaining) basins Texel and Vlie sedimentation has taken place since the closure. The sedimentation rates are much higher than necessary for keeping pace with the relative sea level rise. See also the total changes in the period 1927-2000 given in Table E.1. Outside the basins, i.e. in the coastal areas, erosion occurs and the total amount is more or less the same as the sedimentation inside the basins (Elias, 2006). Apparently, the closure has caused sediment deficits in the basins, which has driven sediment import from the coastal area into the basins.

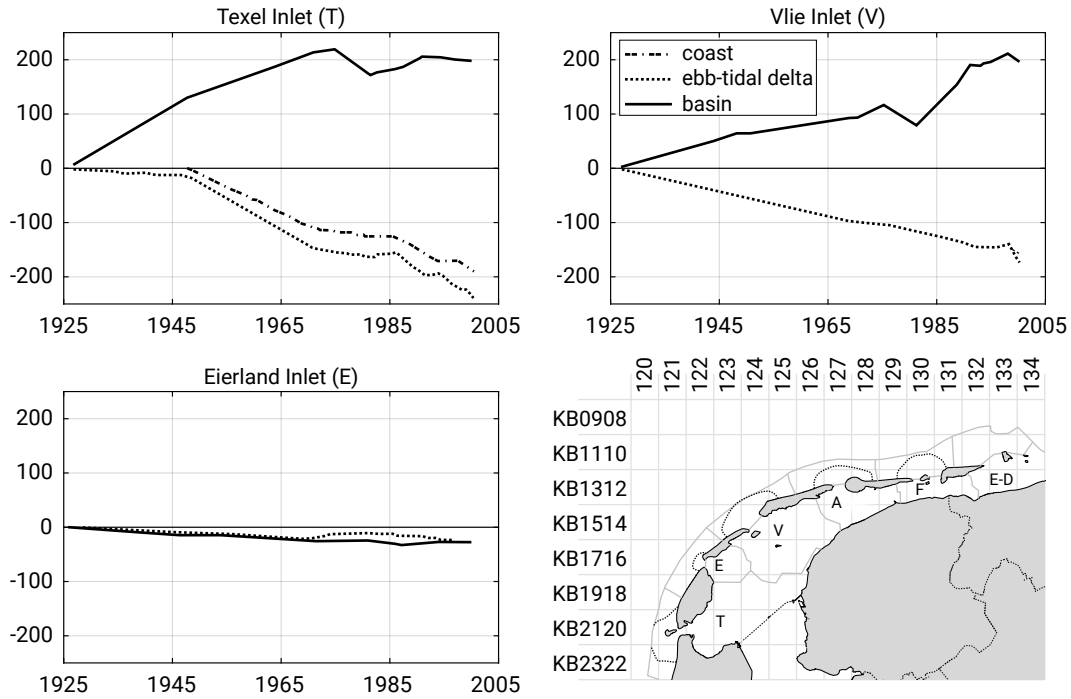

Figure E.3: Sediment budget of the three inlet systems influenced by the closure of Zuiderzee (Elias et al., 2012). On the vertical axes, cumulative sedimentation since 1927 in million m^3 is given.

Table E.1: Total changes in sediment budget of the Texel, Eierland and Vlie inlet systems in the period 1927-2000 (ebb-tidal delta forms part of coast).

	Coast [10^6 m^3]	Ebb-delta [10^6 m^3]	Basin [10^6 m^3]
Texel Inlet (T)	−240	−189	198
Eierland Inlet (E)	−26	5	−28
Vlie Inlet (V)	−175	−161	198

The erosion of the coastal area has caused retreat of the coastline, especially around the Texel Inlet. Since 1990 the Dutch coastline is maintained by sand nourishment. The coast around the Texel Inlet requires the largest volume of sand nourishment.

The morphological development within the basins has also caused movement of the tidal divide, i.e. the boundary between basins, between the Texel and Vlie basins. The movement is eastwards, enlarging the Texel basin at the cost of the Vlie basin. In the closed part of the basin, i.e. IJsselmeer, mud supplied by the IJssel River flowing into the basin accumulates. Locally this has resulted in a polluted lake bottom.

E.2.2. Closure of Lauwerszee

The Lauwerszee was closed in 1969 by a dam and it is nowadays a freshwater lake, Lauwersmeer. Before the closure it was a part of the Frisian Inlet basin, which is divided by the Engelsmanplaat into Zoutkamperlaag and Pinkegat (Fig. E.4). The closure caused a decrease of the basin area of the Frisian Inlet by about one third.

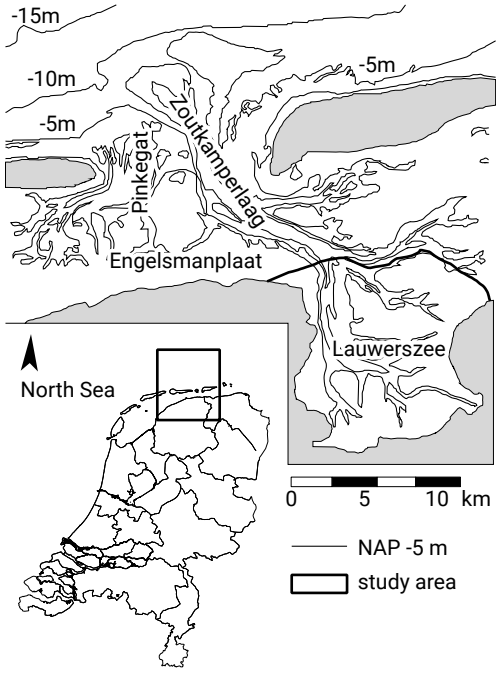

Figure E.4: Frisian Inlet and closure of Lauwerszee.

Figure E.5 shows the effects of the closure on the water level, flow velocity and sediment concentration at the centre of the Zoutkamperlaag Inlet, as calculated by Wang et al. (1995) using a 2DH model. The closure caused a small increase of the tidal range. However, due to the decrease of the tidal basin area, the tidal prism and, as a result, the magnitude of flow velocity decreased significantly. The tidal asymmetry changed such that it became more flood-dominant favouring sediment import.

Since the closure the tidal basin of Zoutkamperlaag has been accumulating sediment and the ebb-tidal delta has been eroding (Fig. E.6). The sedimentation in the basin and the erosion of the ebb-tidal delta are more or less in balance. As a consequence the closure has not caused erosion problems on the adjacent coasts, in contradiction to the closure of the Zuiderzee. However, to a lesser extent the closure has also caused movements of tidal divides, enlarging the tidal basin of Zoutkamperlaag.

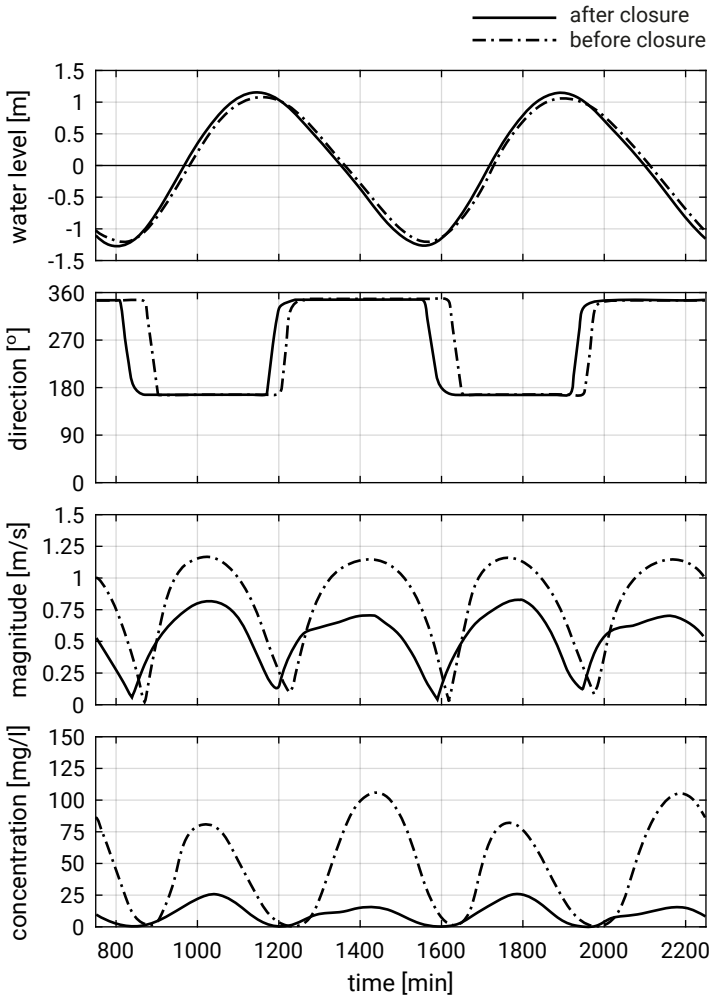

Figure E.5: Influence on tide and sediment transport at the centre of Zoutkamperlaag Inlet.

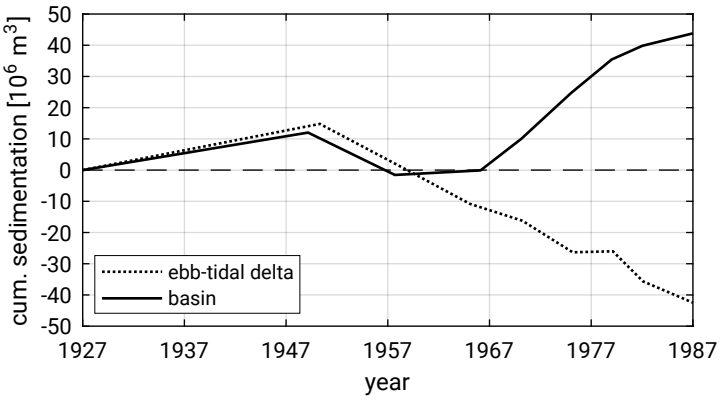

Figure E.6: Sediment budget of Zoutkamperlaag.

An environmental problem caused by the closure is the erosion of the Engelsmanplaat, the large intertidal flat between the Pinkegat and the Zoutkamperlaag. This is due to the fact that the tidal flow in the Zoutkamperlaag channel, which is a building force for the flat, became weaker due to the closure. The eroding force for the flat, the wave action, did not change due to the closure.

E.2.3. Discussion

It is interesting to compare the two closures in the Wadden Sea. The closure of the Zuiderzee took away a major part of the original tidal basin, whereas the closure of the Lauwerszee removed a relatively smaller part of the basin. However, the closure of the Lauwerszee caused a significant decrease of the tidal prism, while the closure of the Zuiderzee did not. The reason is that the Frisian Inlet is a short basin, while the Zuiderzee was originally a long basin, as well as the special location of the Afsluitdijk.

As for the morphological developments, both closures have in common that they caused sedimentation in the remaining tidal basins and erosion outside the inlet. The difference is that the closure of the Zuiderzee caused serious erosion of the coasts adjacent to the inlet, while the closure of the Lauwerszee did not. This can be explained by the fact that the equilibrium size of the ebb-tidal delta is related to the tidal prism. As the tidal prism did not decrease after the closure of the Zuiderzee, the equilibrium size of the ebb-tidal delta remained the same. This means that there is no sediment surplus in the ebb-tidal delta. The sediment deficit in the tidal basin can be the most easily satisfied by eroding the coast, as the size of the ebb-tidal delta would effectively increase when the coastline retreats. In other words, by eroding the coast and the ebb-tidal delta at the same time, the effective size of the ebb-tidal delta can remain the same. In the case of the closure of the Lauwerszee, the tidal prism decreased. This caused a sediment deficit in the basin, and at the same time a sediment surplus in the ebb-tidal delta area. The sediment deficit in the basin can then simply be satisfied by eroding the ebb-tidal delta. It is thus important to note that the tidal basin and the ebb-tidal delta form a sediment-sharing system. The closure of the Lauwerszee did not cause a sediment deficit in this sediment-sharing system as a whole, whereas the closure of the Zuiderzee did cause a sediment deficit of this sediment-sharing system.

E.3. Closures in the delta area

E.3.1. Overview of the closures

The Delta Works consist of a series of engineering works as shown in Fig. E.7. We consider the three closures at the mouths of the three estuaries: Haringvliet, Grevelingen and Eastern Scheldt Oosterschelde in Dutch. An overview of the characteristics of these three closures is listed in Table E.2. In the following two sections, the effects of

these closures on the development of the area seawards of the closures and the effects in the enclosed basins are discussed.

Figure E.7: Delta Works. The Eastern Scheldt, Grevelingen and Haringvliet are (semi-)closed off by the *Oosterscheldedam*, *Brouwersdam* and *Haringvlietdam*, respectively.

Table E.2: Characteristics of the three closures under consideration.

Closure	Type	Closed basin	Position	Year
Haringvliet	sluices, freshwater discharge	freshwater reservoir	more landwards	1969
Grevelingen	dam, fully closed	salt water lake	near mouth	1971
Eastern Scheldt	storm surge barrier, tidal flow	estuary/bay	near mouth	1986

E.3.2. Developments outside area

The influence of the Delta Works is reflected by changes in delta topography. The most important factors influencing the morphological geometry in ebb-tidal deltas are: 1) the relative influence of waves versus tidal flow, 2) the average wave direction and 3) the interaction between tidal flow offshore and in the nearshore channels (Sha & Van den Berg, 1993). The sedimentation-erosion pattern is shown in Fig. E.8.

The Haringvliet and the Grevelingen have in common that they are closed for tidal flow by the Delta Works. The Haringvliet Sluices only allow discharge of freshwater from the former estuary during periods with high river discharges. The Brouwersdam even forms a complete closure for the estuary. In both ebb-tidal delta areas, the influence of the tidal flow has significantly decreased after the closures, whereas the wave influence has not changed much. The morphological developments in the two areas also

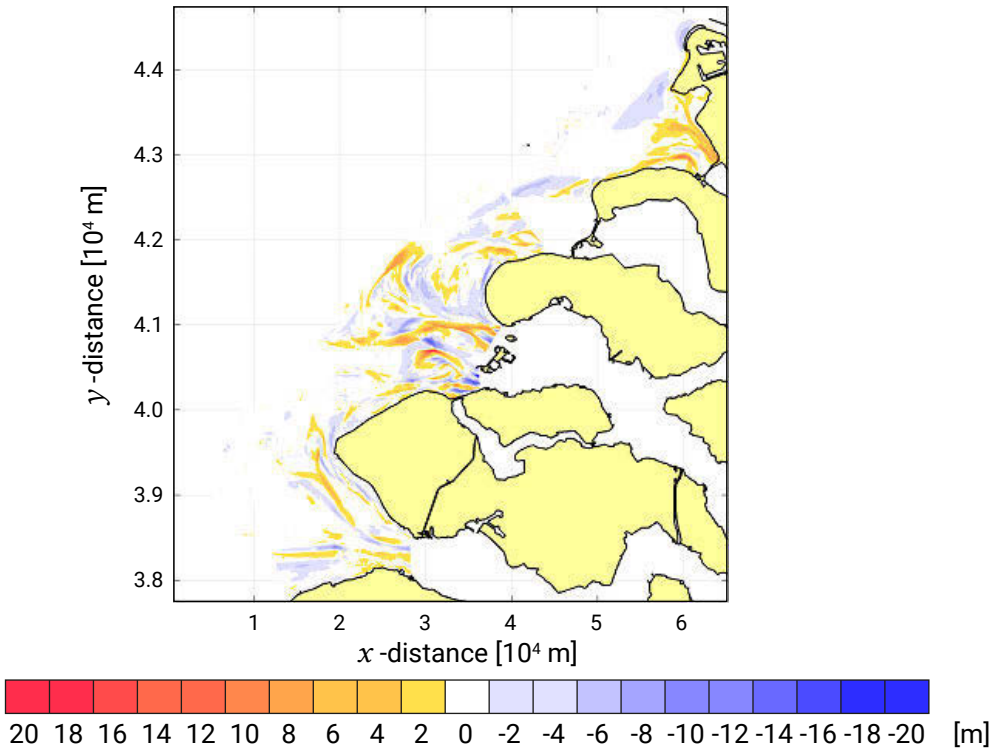

Figure E.8: Sedimentation and erosion in the period 1965-2006.

show similar patterns: erosion at the outer edge of the deltas (shoreface), formation of sand bars that retreat landwards at the north side of the deltas, and sedimentation in the former tidal channels. These developments can mainly be explained by the disappearance of the tidal flow in the cross-shore direction, and thus a significant decrease of the tidal volume. A smaller tidal volume means a smaller ebb-tidal delta and smaller tidal channels for the new equilibrium. This explains the erosion at the shoreface and the sedimentation in the tidal channels.

A difference in overall sediment balance exists due to the difference in relative position of the closures. The Haringvliet Sluices are located further landwards, partly due to the construction of the Maasvlakte (extension of the Port of Rotterdam). This means that the area outside the sluices with sediment-deficiting channels is relatively large. As a result, the sedimentation in the channels is dominating with respect to shoreface erosion, resulting in a positive overall sediment balance. The Brouwersdam is located relatively close to the sea, making the shoreface erosion dominant with respect to the sedimentation in the channels, resulting in a negative overall sediment balance. The morphological development in these two areas in fact tends to establish a continuous smooth coastline, because of the disconnection with the estuaries.

The influence of the tidal volume on the morphological development can also be observed at the Eastern Scheldt delta. The delta front propagated seaward from 1969 to 1980 due to an 8 % increase in tidal volume by the closure of Volkerak in 1969. After

the construction of the storm surge barrier in 1986, the tidal volume decreased, causing erosion of the shoreface (Aarninkhof & Van Kessel, 1999). The three remaining channels (Hammen, de Schaar van Roggenplaat and the Roompot), which form inlets in the barrier, deepened, and the lee side of the dam accreted. The other channels decreased in size and found a new orientation due to reduction and rotation (more in the alongshore direction instead of cross-shore) of the tidal flow.

E.3.3. Impact on the (semi-)closed basins

Regarding the effect within the (semi-)closed basins, only the most important environmental problems are discussed here. The problems appear to be mainly dependent on the type of closure.

The Haringvliet estuary is closed by sluices which only allow fresh river water to flow out, but no flow from the sea to the former estuary can occur through the sluices. The basin thus became a freshwater reservoir. As the cross-sectional area of the former estuary is too large to only discharge river water, accumulation of fluvial sediment occurred in the basin after the closure. In the first years after the closure, the quality of the fluvial sediment was poor. Therefore, polluted sediments are now present in the bottom of the basin, which creates an environmental problem.

In case of Grevelingen, the former estuary was fully closed by a dam, and became a saltwater lake. The only exchange of water between the lake and the sea takes place via a siphon structure. Due to the lack of sufficient refreshment of the water in the basin, water quality problems have started to occur in the basin in recent years.

The Eastern Scheldt has kept its estuarine characteristics because it is semi-closed by a storm surge barrier. Under normal conditions the barrier is open, allowing tidal flow through it. Only during severe storms the barrier is closed protecting the area behind it from the high sea. However, the construction of the barrier has reduced the cross-sectional area. In order to limit the decrease of the tidal range in the estuary, the basin area has been reduced by additional engineering works. The end result is that only limited change of the tidal range have ocurred after the closure. However, the tidal prism and the strength of the tidal flow have significantly decreased. As a consequence, the intertidal flats in the estuary suffer from serious erosion (Fig. E.9). This is an environmental problem, as the intertidal flats are used by birds for feeding and resting, when they are dry.

E.4. Conclusions

Five closures or semi-closures of tidal basins in the Dutch coastal system were considered in this paper. The two closures in the Wadden Sea separate part of the corresponding basin from the Wadden Sea. The three closures in the delta area close or semi-close practically the entire corresponding tidal basin, but they differ in the exact

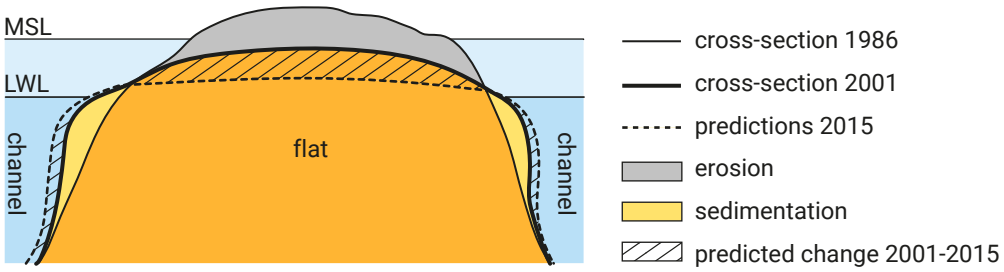

Figure E.9: Erosion of the intertidal flat in the Eastern Scheldt basin.

location with respect to the coastline and in the type of closures, varying from fully closed to allowing tidal flow under normal conditions. The effects of these closures have been analyzed from two management points of view, viz. the maintenance of the coast and environmental problems in the remaining and/or the closed basin.

From the coastal maintenance point of view, the ebb-tidal delta and the remaining tidal basin together form a sediment-sharing system. The sediment deficits and/or surpluses in the two elements together determine if the tidal inlet or estuary will be a source or sink for the coastal system after the closure. It is concluded that the position of the closure structure with respect to the coastline is important in this regard. When only part of the tidal basin is closed, as in the case of the two closures in the Wadden Sea, the tidal wavelength is also a relevant length scale to consider. The Texel Inlet became a sink of sediment after the closure of the Zuiderzee, causing serious erosion in the adjacent coasts. The sediment deficit in the basin of the Zoutkamperlaag and the sediment surplus in its ebb-tidal delta are almost in balance. When almost the entire basin is closed, as is the case for the closures in the delta area, the area outside the closure becomes a sink of sediment when the closure is located further landwards and vice versa.

The type of environmental problems in the remaining and/or closed basin caused by the closure mainly depends on the type of closure. When the closed basin becomes a freshwater lake/reservoir, accumulation of fluvial sediment can cause pollution of the bottom, as in the case of the closures of Zuiderzee and Haringvliet. If the refreshment of the water in the closed basin is too limited, as in the case of Grevelingen, water quality problems can occur in the long term. When the tidal flow is weakened, as in the case of Zoutkamperlaag and the Eastern Scheldt estuary, serious erosion of the intertidal flats can take place.

Acronyms and abbreviations

2DV 2D-vertical

AGU American Geophysical Union
ASBPA American Shore and Beach Preservation Association
ASCE American Society of Civil Engineers

CD Chart Datum
CEM Coastal Engineering Manual
CERC Coastal Engineering Research Council
COPEDEC Conference on Coastal and Port Engineering in Developing Countries

DGPS Differential Global Positioning System

GPS Global Positioning System

HW High Water
HWL High Water Level
HWS High Water Slack

ICCE International Conference on Coastal Engineering
IPCC International Panel on Climate Change
ITCZ Intertropical Convergence Zone

JONSWAP Joint North Sea Wave Observation Project

LAT Lowest Astronomical Tide
LOWT Large Oscillating Water Tunnel
LW Low Water
LWL Low Water Level
LWS Low Water Slack

MDPI Multidisciplinary Digital Publishing Institute
MHW Mean High Water
MHWN Mean High Water Neap
MHWS Mean High Water Spring
MLLW Mean Lower Low Water
MLW Mean Low Water
MLWN Mean Low Water Neap
MLWS Mean Low Water Spring
MSL Mean Sea Level

NAP *Normaal Amsterdams Peil*
NH Northern Hemisphere

RSL Relative Sea Level
RSLR Relative Sea Level Rise
RWS Rijkswaterstaat

SH Southern Hemisphere
SSL Storm Surge Level
SWL Still Water Level

TU Delft Delft University of Technology

USACE US Army Corps of Engineers

WMO World Meteorological Organisation

Bibliography

Aarninkhof, S. G. J. & Van Kessel, T. (1999). *Data analyse Voordelta. Grootschalige morfologische veranderingen 1960–1996.* (tech. rep. Z2694). Delft Hydraulics.

Ahrens, J. (2000). A fall velocity equation. *Journal of Waterway, Port, Coastal and Ocean Engineering*, *126*(2), 99–102. https://doi.org/https://doi.org/10.1061/(ASCE)0733-950X(2000)126:2(99)

Apel, J. R. (1987). *Principles of Ocean Physics.* Academic Press, London.

Apotsos, A., Raubenheimer, B., Elgar, S., Guza, R. & Smith, J. (2007). Effects of wave rollers and bottom stress on wave setup. *Journal of Geophysical Research*, *112*(C02003).

Ashton, A. D. & Murray, A. B. (2006). High-angle-wave instability and emergent shoreline shapes: 1. Modeling of sandwaves, flying spits, and capes. *Journal of Geophysical Research*, *111*(F04011). https://doi.org/10.1029/2005JF000422

Bagnold, R. A. (1956). The flow of cohesionless grains in Fluids. *Proceedings of the Royal Society of London, Series A*, *249*(964), 235–297.

Bagnold, R. A. (1962). Auto-suspension of transported sediment; turbidity currents. *Proceedings of the Royal Society of London, Series A*, *265*(1322), 315–319.

Bagnold, R. A. (1963). Mechanics of marine sedimentation. In M. N. Hill (Ed.), *The Sea* (pp. 507–528). Interscience.

Bagnold, R. A. (1966). *An approach to the sediment transport problem from general physics.* (tech. rep. No. 422-1). US Geological Survey Professional Paper. Washington, DC, US Government printing office.

Bailard, J. A. (1981). An energetics total load sediment transport model for a plane sloping beach. *Journal of Geophysical Research: Oceans*, *96*(C11), 10938–10954.

Bailard, J. A. (1982). Modelling on-offshore sediment transport in the surf zone. *Proceedings of the International Conference on Coastal Engineering*, *11*.

Bailard, J. A. & Inman, D. L. (1981). An energetics bedload model for a plane sloping beach: local transport. *Journal of Geophysical Research: Oceans*, *86*(C11), 2035–2043.

Bakker, W. T. (1968). A mathematical theory about sandwaves and its application on the Dutch Wadden Isle of Vlieland. *Shore and Beach*, *36*(2), 4–14.

Battjes, J. A. (1974). Surf similarity. *Proceedings of the 14th International Conference on Coastal Engineering*, *1*, 467–479. https://doi.org/10.1061/9780872621138.029

Battjes, J. A. (2006). *Short Waves.* Lecture Notes for CT4320, Technische Universiteit Delft.

Battjes, J. A. & Janssen, J. P. F. M. (1978). Energy loss and set-up due to breaking of random waves. *Proceedings of the 16th International Conference on Coastal Engineering.*, 569–587.

Bayram, A., Larson, M. & Hanson, H. (2007). A new formula for the total longshore sediment transport rate. *Coastal Engineering*, *54*(9), 700–710.

Bayram, A., Larson, M., Miller, H. C. & Kraus, N. C. (2001). Cross-shore distribution of longshore sediment transport: comparison between predictive formulas and filed measurements. *Coastal Engineering*, *44*(2), 79–99.

Bijker, E. W. (1967). *Some considerations about scales for coastal models with movable bed* (Doctoral dissertation) [Also: Publication No.50, Delft Hydraulics]. Delft University of Technology. Delft, The Netherlands.

Bijlsma, A. C., Bruinsma, R. & Vatvani, D. K. (1989). *Investigation of surge-tide interaction in the storm surge model CSM-16* (tech. rep. Z0311). Deltares.

Bird, E. C. F. (1985). *Coastline Changes: A Global Review.* Wiley Interscience.

Bosman, J. J. (1982). *Concentration measurements under oscillatory water motion* (Rep. M-1695 Part II). Delft Hydraulics Laboratory.

Bowen, A. J. (1980). Simple models of nearshore sedimentation; beach profiles and longshore bars. In S. B. McCann (Ed.), *The coastline of Canada.* (pp. 1–11).

Bowen, A. J. & Inman, D. L. (1971). Edge waves and crescentic bars. *Journal of Geophysical Research*, *76*(36), 8663–8671.

Boyd, R., Dalrymple, R. W. & Zaitlin, B. A. (1992). Classification of clastic coastal depositional environments. *Sedimentary Geology*, *80*(3–4), 139–150.

Breusers, H. N. C. (1983). *Lecture notes on sediment transport.* International course in hydraulic engineering.

Bricio, L., Negro, V. & Diez, J. J. (2008). Geometric detached breakwater indicators on the Spanish northeast coastline. *Journal of Coastal Research*, *24*(5), 1289–1303. https://doi.org/10.2112/07-0838.1

Bruun, P. (1954). *Coast erosion and the development of beach profiles* (Technical Memorandum No. 44). Beach Erosion Board, US Army Corps of Engineers. Vicksburg, MS.

Bruun, P. (1962). Sea level rise as a cause of shore erosion. *Journal of the Waterways and Harbors Division*, *88*(1), 117–130.

Bruun, P. (1978). Stability of Tidal Inlets: Theory and Engineering. *Developments in Geotechnical Engineering*, *23*, 13–38.

Bruun, P. & Gerritsen, F. (1959). Natural By-Passing of Sand at Coastal Inlets. *Journal of the Waterways and Harbors Division*, *85*(4), 75–108.

Bruun, P. & Gerritsen, F. (1960). Stability of coastal inlets. *Coastal Engineering Proceedings*, (7), 23–23.

Caballeria, M., Coco, G., Falqués, A. & Huntley, D. A. (2002). Self-organization mechanisms for the formation on nearshore crescentic and transverse sand bars. *Journal of Fluid Mechanics*, *465*, 379–410. https://doi.org/10.1017/S002211200200112X

Carter, R. W. G. (1988). *Coastal environments: An introduction to the physical, ecological, and cultural systems of coastlines.* Academic Press.

Clark, J. A., Farrell, W. E. & Peltier, W. R. (1978). Global changes in postglacial sea level: A numerical calculation. *Quaternary Research*, *9*(3), 265–287.

Coco, G. & Murray, A. B. (2007). Patterns in the sand: From forcing templates to self-organization. *Geomorphology*, *91*(3-4), 271–290.

Curray, J. R. (1964). Transgressions and regressions. In R. L. Miller (Ed.), *Papers in marine geology: Shepard commemorative volume* (pp. 175–203). Macmillan.

Dalrymple, R. W., Zaitlin, B. A. & Boyd, R. (1992). Estuarine facies models; conceptual basis and stratigraphic implications. *Journal of Sedimentary Research*, *62*(6), 1130–1146.

Davies, A. G., Van Rijn, L. C., Damgaard, J. S., Van de Graaff, J. & Ribberink, J. S. (2002). Intercomparison of research and practical sand transport models. *Coastal Engineering*, *46*(1), 1–23.

Davies, J. L. & Clayton, K. M. (1980). *Geographical variation in coastal development* (2nd ed.). Longman.

Davis Jr., R. A. (1994). *The Evolving Coast* (Vol. 48). Scientific American Library.

Davis Jr., R. A. & Hayes, M. O. (1984). What is a wave dominated coast? *Marine Geology*, *60*(1), 313–329.

De Blij, H. J. & Muller, P. O. (1993). *Physical geography: The global environment*. John Wiley; Sons, New York, USA.

De Vriend, H. J., Bakker, W. T. & Bilse, D. P. (1994). A morphological behaviour model for the outer delta of mixed-energy tidal inlets. *Coastal Engineering*, *23*, 305–327.

Dean, R. G. (1973). Heuristic models of sand transport in the surf zone. *Proceedings of the First Australian Conference of Coastal Engineering, 1973: Engineering Dynamics of the Coastal Zone*, 215–221.

Dean, R. G. (1977). *Equilibrium beach profiles: US Atlantic and Gulf coasts* (Ocean Engineering Report No. 12). Department of Civil Engineering and College of Marine Studies, University of Delaware.

Dean, R. G. (1987). Coastal Sediment Processes, Toward Engineering Solutions. *Proceedings of the Specialty Conference on Advances in Understanding of Coastal Sediment Processes*, *1*, 1–24.

Dean, R. G. (2002). *Beach Nourishment: Theory and Practice.* (Vol. 18: Advanced Series on Ocean Engineering). World Scientific Publishing.

Dean, R. G., Berek, E. P., Gable, C. G. & Seymour, R. J. (1982). Longshore transport determined by an efficient trap. *Proceedings of the 18th International Conference on Coastal Engineering*, 954–968.

Dean, R. G., Chen, R. & Browder, A. E. (1997). Full scale monitoring study of a submerged breakwater, Palm Beach, Florida, USA. *Coastal Engineering*, *29*(3-4), 291–315.

Dean, R. G. & Dalrymple, R. A. (2004). *Coastal processes with engineering applications*. Cambridge University Press.

Dibajnia, M. & Watanabe, A. (1993). Sheet flow under nonlinear waves and currents. *Proceedings of the 23rd International Conference on Coastal Engineering*, 2015–2028.

Doering, J. C. & Bowen, A. J. (1995). Parametrization of orbital velocity asymmetries of shoaling and breaking waves using bispectral analysis. *Coastal Engineering*, *26*(1–2), 15–33.

Dohmen-Janssen, C. M., Hassan, W. N. & Ribberink, J. S. (2001). Mobile-bed effects in oscillatory sheet flow. *Journal of Geophysical Research: Oceans*, *106*(C11), 27103–27115.

Dronkers, J. (1986). Tidal asymmetry and estuarine morphology. *Netherlands Journal of Sea Research*, *20*(2-3), 117–131.

Dronkers, J. (1998). Morphodynamics of the Dutch delta. *8th International Biennial Conference on Physics of Estuaries and Coastal Seas*, 297–304.

Dronkers, J. (2005). *Dynamics of Coastal Systems* (Vol. 25). World Scientific.

Duran-Matute, M., Gerkema, T. & Sassi, M. G. (2016). Quantifying the residual volume transport through a multiple-inlet system in response to wind forcing: The case of the western Dutch Wadden Sea. *Journal of Geophysical Research: Oceans*, *121*(12), 8888–8903. https://doi.org/https://doi.org/10.1002/2016JC011807

ECMWF. (n.d.). https://www.ecmwf.int/en/forecasts/datasets/reanalysis-datasets/era5

Egbert, G. D. & Erofeeva, S. Y. (2002). Efficient inverse modeling of barotropic ocean tides. *Journal of Atmospheric and Oceanic Technology*, *19*(2), 183–204. https://doi.org/10.1175/1520-0426(2002)019<0183:EIMOBO>2.0.CO;2

Ehlers, J. (1988). *The morphodynamics of the Wadden Sea*. Balkema.

Einstein, H. A. (1942). Formulas of the transportation of bed load. *Transactions of the American Society of Civil Engineers*, *107*(1), 561–577.

Einstein, H. A. (1950). *The bed-load function for sediment transportation in open channel flows.* (Vol. 1026). US Department of Agriculture Soil Conservation Service, Washington, DC.

Elias, E. P. L. (2006). *Morphodynamics of Texel Inlet.* (Doctoral dissertation). Delft University of Technology. IOS Press, The Netherlands.

Elias, E. P. L., Stive, M. J. F., Bonekamp, J. G. & Cleveringa, J. (2003). Tidal inlet dynamics in response to human interventions. *Journal of Coastal Engineering*, *45*(4), 629–658.

Elias, E. P. L., Van der Spek, A. J. F., Wang, Z. B. & De Ronde, J. (2012). Morphodynamic development and sediment budget of the Dutch Wadden Sea over the last century. *Netherlands Journal of Geosciences*, *91*(3), 293–310.

ENW. (2007). *Technisch rapport duinafslag* (tech. rep.). Expertisenetwerk waterveiligheid.

Erofeeva, S., Padman, L. & Howard, S. L. (2020). Tide Model Driver (TMD) version 2.5, Toolbox for Matlab.

Escoffier, F. F. (1940). The stability of tidal inlets. *Shore and Beach*, *8*, 111–114.

Eysink, W. D. (1991). Morphologic Response of Tidal Basins to Changes: The Dutch Coast. Paper No. 8. *22nd International Conference on Coastal Engineering*, 1948–1961.

Eysink, W. D. & Biegel, E. J. (1992). *Impact of sea level rise on the morphology of the Wadden Sea in the scope of its ecological function. ISOS*2 Project, phase 2* (tech. rep. Report H1300). Delft Hydraulics, Delft.

Farr, T. G. & Kobrick, M. (2000). Shuttle radar topography mission produces a wealth of data. *Eos Transactions AGU*, *81*(48), 583–585. https://doi.org/https://doi.org/10.1029/EO081i048p00583

FitzGerald, D. M. & Penland, S. (1987). Backbarrier dynamics of the east Friesian Islands. *Journal of Sedimentary Research*, *57*(4), 746–754.

Fredsøe, J. & Deigaard, R. (1992). *Mechanics of Coastal Sediment Transport.* (Vol. 3). World Scientific, Singapore.

Friedrichs, C. T. & Aubrey, D. G. (1988). Non-linear tidal distortion in shallow well-mixed estuaries: A synthesis. *Estuarine, Coastal and Shelf Science*, *27*(5), 521–545.

Galloway, W. E. (1975). Process framework for describing the morphologic and stratigraphic evolution of deltaic depositional systems. In M. L. Broussard (Ed.), *Deltas: Models for exploration* (pp. 87–98). Houston Geological Society.

Gornitz, V. & Lebedeff, S. (1987). Global sea-level changes during the past century. *Sea Level Fluctuation and coastal evolution*, *SEPM Special Publication No. 41*, 2–16.

Grant, W. D. & Madsen, O. S. (1979). Combined wave and current interaction with a rough bottom. *Journal of Geophysical Research: Oceans*, *84*(C4), 1797–1808.

Gyr, A. & Hoyer, K. (2006). Sediment Transport: A Geophysical Phenomenon. In R. Moreau (Ed.). Springer.

Hageman, B. P. (1969). Development of the western part of the Netherlands during the Holocene. *Geologie en Mijnbouw*, *48*, 373–388.

Hallermeier, R. J. (1978). Uses for a calculated limit depth to beach erosion. *Proceedings of the 16th Coastal Engineering Conference*, 1493–1512.

Hallermeier, R. J. (1981). A profile zonation for seasonal sand beaches from wave climate. *Coastal Engineering*, *4*, 253–277.

Hayes, M. O. (1967). Relationship between coastal climate and bottom sediment type on the inner continental shelf. *Marine Geology*, *5*(2), 111–132.

Hayes, M. O. (1979). Barrier island morphology as a function of tidal and wave regime. In S. P. Leatherman (Ed.), *Barrier Islands* (pp. 1–27).

Holman, R. A. & Bowen, A. J. (1982). Bars, bumps, and holes: Models for the generation of complex beach topography. *Journal of Geophysical Research: Oceans*, *87*(C1), 457–468.

Holman, R. A., Symonds, G., Thornton, E. & Ranasinghe, R. (2006). Rip spacing and persistence on an embayed beach. *Journal of Geophysical Research*, *111*(C01006).

Holthuijsen, L. H. (2007). *Waves in Oceanic and Coastal Waters*. Cambridge University Press.

Hudson, R. Y. (1952). Wave forces on breakwaters. *Proceedings of the American Society of Civil Engineers*, *78*(1), 1–22.

Hughes, S. A. & Chiu, T. Y. (1978). *The variations in beach profiles when approximated by a theoretical curve.* (tech. rep. TR/039). Coastal and Oceanographic Engineering Department, Univ. Florida, Gaines- ville, Florida.

Inman, D. L. & Bagnold, R. A. (1963). The Sea. In M. N. Hill (Ed.). Interscience, New York, N.Y.

Inman, D. L. & Nordstrom, C. E. (1971). On the Tectonic and Morphologic Classification of Coasts. *Journal of Geology*, *79*(1), 1–21.

IPCC. (1992). *Global climate change and the rising challengeof the sea.* Response Strategies WorkingGroup, CZM Subgroup, Ministry of Transport, Public Works andWater Management, DG Rijkswaterstaat.

IPCC. (2001). *Climate Change 2001: Synthesis Report. A Contribution of Working Groups I, II, and III to the Third Assessment Report of the Integovernmental Panel on Climate Change.* (R. T. Watson & the Core Writing Team, Eds.). Cambridge University Press, Cambridge, United Kingdom, and New York, NY, USA.

IPCC. (2007). *Climate Change 2007: Synthesis Report. Contribution of Working Groups I, II and III to the Fourth Assessment Report of the Intergovernmental Panel on Climate Change* (R. K. Pachauri & A. Reisinger, Eds.). IPCC, Geneva, Switzerland.

IPCC. (2014). *Climate Change 2014: Synthesis Report. Contribution of Working Groups I, II and III to the Fifth Assessment Report of the Intergovernmental Panel on Climate Change* (R. K. Pachauri & l. A. Meyer, Eds.). IPCC, Geneva, Switzerland.

IPCC. (2021). *Climate Change 2021: The Physical Science Basis. Contribution of Working Group I to the Sixth Assessment Report of the Intergovernmental Panel on Climate Change* (V. Masson-Delmotte, P. Zhai, A. Pirani, S. L. Connors, C. Péan, S. Berger, N. Caud, Y. Chen, L. Goldfarb, M. I. Gomis, M. Huang, M. Leitzell, E. Lonnoy, J. B. R. Matthews, T. K. Maycock, T. Waterfield, O. Yelekçi, R. Yu & B. Zhou, Eds.). Cambridge University Press. In press.

Iribarren, C. R. (1938). Una fórmula para el cálculo de los diques de escollera. *M. Bermejillo-Pasajes, Madrid, Spain.*

JARKUS. (n.d.). https://publicwiki.deltares.nl/display/OET/Dataset+documentation+JarKus

Jarrett, J. T. (1976). *Tidal prism-inlet area relationships* (General Investigation of Tidal Inlets Report No. 3). Vicksburg, MS, US Army Engineer Waterways Experiment Station.

Jonsson, I. G. (1967). Wave boundary layers and friction factors. *Proceedings of the 10^{th} Internation Conference on Coastal Engineering*, *2*, 127–148.

Kamphuis, J. W. (1991). Alongshore sediment transport rate. *Journal of Waterway, Port, Coastal and Ocean Engineering*, *117*(6), 624–641.

Kamphuis, J. W. (2000). *Introduction to Coastal Engineering and Management* (P. L.-F. Liu, Ed.; Vol. 16). World Scientific.

Katopodi, I. & Ribberink, J. S. (1992). Quasi-3D modelling of suspended sediment transport by currents and waves. *Coastal Engineering*, *18*(1-2), 83–110.

Kinsman, B. (1965). *Wind waves: their generation and propagation on the ocean surface.* Courier Corporation.

Klein, A. H. F. (2003). *Morphodynamics of Headland-bay Beaches: Examples from the coast of Santa Catarina State, Brazil.* (Doctoral dissertation). University of Algarve. Algarve, Portugal.

Klein, A. H. F., Da Silva, G. M., Ferreira, Ó. & Dias, J. A. (2005). Beach sediment distribution for a headland bay coast. *Journal of Coastal Research*, 285–293.

Komar, P. D. (1998). *Beach Processes and Sedimentation* (Second). Prentice-Hall, Upper Saddle River, New Jersey.

Komar, P. D. & Inman, D. L. (1970). Longshore sand transport on Beaches. *Journal of Geophysical Research*, *75*(30), 5914–5927.

Le Méhauté, B. (1976). *An Introduction to Hydrodynamics and Water Waves*. Springer, Berlin, Heidelberg. https://doi.org/10.1007/978-3-642-85567-2

LeConte, L. J. (1905). Discussion on the paper, "Notes on the improvement of river and harbor outlets in the United States" by D. A. Watt, paper no. 1009. *Trans. ASCE*, *55*, 306–308.

Lippmann, T. & Holman, R. A. (1990). The spatial and temporal variability of sand bar morphology. *Journal of Geophysical Research*, *95*(C7), 11575–11590.

List, J. H., Farris, A. & Sullivan, C. (2005). Reversing storm hotspots on sandy beaches: Spatial and temporal characteristics. *Marine Geology*, *226*, 261–279.

List, J. H. & Farris, A. S. (1999). Large-scale shoreline response to storms and fair weather. *Coastal Sediments '99: Proceedings of the 4th International Symposium on Coastal Engineering and Science of Coastal Sediment Processes.*, 1324–1338.

Lodder, Q. J., Wang, Z. B., Elias, E. P. L., Van der Spek, A. J. F., De Looff, H. & Townend, I. H. (2019). Future Response of the Wadden Sea Tidal Basins to Relative Sea-Level rise–An Aggregated Modelling Approach. *Water*, *11*(10), 2198.

Longuet-Higgins, M. S. (1953). Mass transport in water waves. *Philosophical Transactions of the Royal Society of London. Series A, Mathematical and Physical Sciences*, *245*, 535–581.

Longuet-Higgins, M. S. & Stewart, R. W. (1962). Radiation stress and mass transport in gravity waves, with application to 'surf beats'. *Journal of Fluid Mechanics*, *13*(4), 481–504.

Longuet-Higgins, M. S. & Stewart, R. W. (1964). Radiation stresses in water waves: a physical discussion with applications. *Deep-Sea Research*, *11*, 529–562.

Luijendijk, A., De Vroeg, H., Swinkels, C. & Walstra, D.-J. (2011). Coastal response on multiple scales: a pilot study on the IJmuiden Port. *The Proceedings of the Coastal Sediments 2011*. https://doi.org/DOI:10.1142/9789814355537_0046

Luijendijk, A., Hagenaars, G., Ranasinghe, R., Baart, F., Donchyts, G. & Aarninkhof, S. G. J. (2018). The State of the World's Beaches. *Scientific Reports*, *8*(5).

Mangor, K. (2004). *Shoreline Management Guidelines* (Ed. 3). DHI, Denmark.

Masselink, G. & Hughes, M. G. (2003). *Introduction to Coastal Processes and Geomorphology*. Hodder Arnold, London.

Masselink, G. & Short, A. D. (1993). The Effect of Tide Range on Beach Morphodynamics and Morphology: A Conceptual Beach Model. *Journal of Coastal Research*, *9*, 785–800.

Miche, R. (1944). *Mouvements ondulatoires des mers en profundeur constante on decroisante.* Annales des Ponts et Chaussees.

Mil-Homens, J., Ranasinghe, R., van Thiel de Vries, J. S. M. & Stive, M. J. F. (2013). Re-evaluation and improvement of three commonly used bulk longshore sediment transport formulas. *Coastal Engineering*, *75*, 29–39. https://doi.org/https://doi.org/10.1016/j.coastaleng.2013.01.004

Mitrovica, J. X. & Milne, G. (2002). On the origin of late Holocene sea-level highstands within equatorial ocean basins. *Quaternary Science Reviews*, *21*, 2179–2190. https://doi.org/10.1016/S0277-3791(02)00080-X

Mol, A. C. S. (2007). *Schematisation of boundary conditions for morphological simulations.* Deltares.

Moore, B. D. (1982). *Beach profile evolution in response to changes in water level and wave height* (Master's thesis). University of Delaware, Newark, DE.

Morton, R. A. (1977). Historical Shoreline Changes and Their Causes, Texas Gulf Coast. *Gulf Coast Association of Geological Societies Transactions*, *27*, 352–364.

Munk, W. H. (1950). Origin and generation of waves. *Coastal Engineering Proceedings*, *1*(1), 1–4. https://doi.org/10.9753/icce.v1.1

Nairn, R. B., Roelvink, J. A. & Southgate, H. N. (1990). Transition Zone Width and Implications for Modelling Surfzone Hydrodynamics. *22nd International Conference on Coastal Engineering* (pp. 68–81). https://doi.org/10.1061/9780872627765.007

NC OneMap Geospatial Portal. (2020). North Carolina Department of Information Technology, Government Data Analytics Center, Center for Geographic Information and Analysis. https://www.nconemap.gov

Nielsen, P. (1992). *Coastal Bottom Boundary Layers and Sediment Transport.* World Scientific. https://doi.org/10.1142/1269

Nielsen, P. (2009). *Coastal and Estuarine Processes.* World Scientific. https://doi.org/10.1142/7114

O'Brien, M. P. (1931). Estuary and Tidal Prisms Related to Entrance Areas. *Civil Engineering*, *1*(8), 738–739.

O'Brien, M. P. (1969). Equilibrium flow areas of inlets on sandy coasts. *Journal of the Waterways and Harbors Division, ASCE*, *95*(1), 43–53.

Oertel, G. F. (1988). Hydrodynamics and Sediment Dynamics of Tidal Inlets. Lecture Notes on Coastal and Estuarine Studies, vol 29. In D. G. Aubrey & L. Weishar (Eds.). Springer, New York, NY. https://doi.org/10.1007/978-1-4757-4057-8_17

Pelnard-Considère, R. (1956). *Essai de theorie de l'èvolution des formes de ravage en plages de sable et de galets.* (tech. rep. No. 3).

Ranasinghe, R. & Stive, M. J. F. (2009). Rising Seas and Retreating Coastlines. *Climate Change*, *97*, 465–468.

Ranasinghe, R., Symonds, G., Black, K. & Holman, R. A. (2004). Morphodynamics of intermediate beaches: a video imaging and numerical modelling study. *Coastal Engineering*, *51*, 629–655.

Ranasinghe, R., Symonds, G. & Holman, R. A. (1999). Quantitative characterisation of rip currents via video imaging. *Coastal Sediments '99*, 987–1002.

Ranasinghe, R. & Turner, I. L. (2006). Shoreline response to submerged structures: a review. *Coastal Engineering*, *53*(1), 65–79.

Renger, E. & Partenscky, H. W. (1974). Stability criteria for tidal basins. *Coastal Engineering Proceedings*, 1605–1618.

Reniers, A. J. H. M., Roelvink, J. A. & Thornton, E. B. (2004). Morphodynamic modeling of an embayed beach under wave group forcing. *Journal of Geophysical Research*, *109*(C01030).

Ribberink, J. S. (1998). Bed load transport for steady and unsteady oscillatory flow. *Coastal Engineering*, *34*, 59–82.

Ribberink, J. S., De Vroeg, J. H. & Van Overeem, J. (1992). *Kustverdediging Eierland (Texel) - hydraulische morfologische effektstudie (fase ii, deel iii) : morfologische berekeningen.* (tech. rep.). Delft Hydraulics.

Rijkswaterstaat. (1949). Getijtafels voor Nederland.

Roelvink, J. A., Reniers, A. J. H. M., Van Dongeren, A. R., Van Thiel de Vries, J., McCall, R. T. & Lescinski, J. (2009). Modelling storm impacts on beaches, dunes and barrier islands. *Coastal Engineering*, *56*(11-12), 1133–1152.

Roelvink, J. A. & Stive, M. J. F. (1989). Bar-generating cross-shore flow mechanisms on a beach. *Journal of Geophysical Research*, *94*, 4785–4800.

Rouse, H. (1937). Modern conceptions of the mechanics of turbulence. *Transactions of the American Society of Civil Engineers*, *102*, 463–505.

Schoonees, J. S. & Theron, A. K. (1993). Review of the field-data base for the longshore sediment transport. *Coastal Engineering*, *19*, 1–25.

Schoonees, J. S. & Theron, A. K. (1996). Improvement of the most accurate longshore transport formula. *Proceedings of the 25th International Conference on Coastal Engineering*, *3*, 3652–3665.

Sha, L. P. & Van den Berg, J. H. (1993). Variation in ebb-tidal delta geometry along the coast of the Netherlands and the German Bight. *Journal of Coastal Research*, *9*(3), 730–746.

Shields, A. (1936). *Anwendung der Ahnlichkeitsmechanik und der Turbulenzforschung auf die Geschiebebewegung.* (Doctoral dissertation). Mitt. Der Preuss. Versuchsanst. Fur Wasserbau und Schiffbau, Berlin, Germany.

Shore Protection Manual. (1984). U.S. Army Corps of Engineers.

Short, A. D. (2005). Sandy Coasts. In M. L. Schwartz (Ed.), *Encyclopedia of coastal science* (pp. 821–825). Springer Netherlands. https://doi.org/10.1007/1-4020-3880-1_267

Sleath, J. F. A. (1978). Measurements of bed load in oscillatory flow. *Journal of Waterway, Port, Coastal and Ocean Engineering, ASCE*, *104*(3), 291–307.

Smit, M. (2010). *Formation and evolution of nearshore sandbar patterns.* (Doctoral dissertation). TU Delft.

Smith, S. D. & Banke, E. G. (1975). Variation of the sea surface drag coefficient with wind speed. *Quarterly Journal of the Royal Meteorological Society*, *101*(429), 665–673. https://doi.org/https://doi.org/10.1002/qj.49710142920

Soulsby, R. L. (1994). *Manual of Marine Sands*. Thomas Telford, London.

Soulsby, R. L. (1997). *Dynamics of marine sands: a manual for practical applications*. Thomas Telford, London.

Soulsby, R. L., Hamm, L., Klopman, G., Myrhaug, D., Simons, R. R. & Thomas, G. P. (1993). Wave-current interaction within and outside the boundary layer. *Coastal Engineering*, *21*(1–3), 41–69.

Spanhoff, R. & Van de Graaff, J. (2007). Towards a better understanding and design of shoreface nourishments. *Proceedings of the 30th International Conference on Coastal Engineering*, 4141–4153.

Steetzel, H. J. (1993). *Cross-shore transport during storm-surges*. (Doctoral dissertation). Delft University of Technology.

Steijn, R. C., Van Banning, G. K. F. M. & Roelvink, J. A. (1998). *Gevoeligheidsberekeningen Eijerland en ZW-Texel – fase 2: ZW Texel. Rapport van het Samenwerkingsverband Alkyon / WL|Delft Hydraulics. (A266 / Z2430). June 1998. (Sensitivity computations Eijerland and Southwest Texel - phase 2: Southwest Texel)*. (tech. rep.).

Stewart, R. H. (2008). *Introduction to Physical Oceanography*. http://hdl.handle.net/1969.1/160216

Stive, M. J. F. (1985). A scale comparison of waves breaking on a beach. *Coastal Engineering*, *9*(2), 151–158.

Stive, M. J. F., De Schipper, M. A., Luijendijk, A. P., Aarninkhof, S. G. J., Van Gelder-Maas, C., Van Thiel de Vries, J. S. M., De Vries, S., Henriquez, M., Marx, S. & Ranasinghe, R. (2013). A new alternative to saving our beaches from local sea-level rise: the sand engine. *Journal of Coastal Research*, *29*(5).

Stive, M. J. F. & De Vriend, H. J. (1995). Modeling shoreface profile evolution. *Marine Geology*, *126*, 235–248.

Stive, M. J. F. & Reniers, A. J. H. M. (2003). Sandbars in motion. *Science*, *299*(5614), 1855–1856.

Stive, M. J. F., Van de Kreeke, J., Lam, N. T., Tung, T. T. & Ranasinghe, R. (2009). Empirical relationships between inlet cross-section and tidal prism: A review. *Proceedings of Coastal Dynamics, Tokyo, Japan, 2009*.

Svendsen, I. A. (1984). Wave heights and set-up in a surf zone. *Coastal Engineering*, *8*, 303–329. https://doi.org/10.1016/0378-3839(84)90028-0

Swart, D. H. (1974). *Offshore sediment transport and equilibrium beach profiles* (Doctoral dissertation). Delft University of Technology.

Symbols and abbreviations used on admiralty charts (np5011). (2020). United Kingdom Hydrographic Office.

Szmytkiewicz, M., Biegowski, J., Kaczmarek, L. M., Okrój, T., Ostrowski, R., Pruszak, Z., Ożyńsky, G. & Skaja, M. (2000). Coastline changes nearby harbour structures:

comparative analysis of one-line models versus field data. *Coastal Engineering*, *40*(2), 119–139. https://doi.org/https://doi.org/10.1016/S0378-3839(00)00008-9

Tamisiea, M. E., Mitrovica, J. X., Davis, J. L. & Milne, G. A. (2003). II: Solid Earth Physics: Long Wavelength Sea Level and Solid Surface Perturbations Driven by Polar Ice Mass Variations: Fingerprinting Greenland and Antarctic Ice Sheet Flux. *Space Science Reviews*, *108*, 81–93.

Thorne, C. R., Abt, S. R., Barends, F., Maynord, S. T. & Pilarczyk, K. W. (1995). *River, coastal, and shoreline protection : Erosion control using riprap and armourstone*.

Torfs, H. (1995). *Erosion of mud/sand mixtures* (Doctoral dissertation). Katholieke Universiteit Leuven.

Turner, I. L., Whyte, D., Ruessink, B. & Ranasinghe, R. (2007). Observations of rip spacing, persistence and mobility at a long, straight coastline. *Marine Geology*, *236*, 209–221.

Valentin, H. (1952). *Die Küsten der Erde: Beiträge zur allgemeinen und regionalen Küstenmorphologie* (Vol. 246). J. P. Gotha.

Van de Graaff, J. (1977). Dune erosion during a storm surge. *Coastal Engineering*, *1*, 99–134.

Van de Kreeke, J. (1992). Stability of tidal inlets; Escoffier's analysis. *Shore and Beach*, *60*(1).

Van de Kreeke, J. (2004). Equilibrium and cross-sectional stability of tidal inlets: application to the Frisian Inlet before and after basin reduction. *Coastal Engineering*, *51*, 337–350.

Van de Kreeke, J. & Robaczewska, K. (1993). Tide-induced residual transport of coarse sediment: Application to the Ems estuary. *Netherlands Journal of Sea Research*, *31*(3), 209–220.

Van de Meene, J. W. H. & Van Rijn, L. C. (2000). The shoreface-connected ridges along the central Dutch coast - Part 2: Morphological modelling. *Continental Shelf Research*, *20*, 2325–2345. https://doi.org/10.1016/S0278-4343(00)00049-2

Van der Graaff, J., Niemeyer, H. D. & Van Overeem, J. (Eds.). (1991). Coastal Engineering [Artificial Beach Nourishments], *16*(1).

Van der Meer, J. W. (1988). Stability of Cubes, Tetrapods and Accropode. *Proceedings of the Breakwaters Conference '88, Thomas Telford, London, United Kingdom*.

Van der Salm, G. L. S. (2013). *Coastline modelling with UNIBEST:Areas close to structures* (Master's thesis). Delft University of Technology.

Van der Spek, B.-J., Bijl, E., Van de Sande, B., Poortman, S., Heijboer, D. & Bliek, B. W. (2020). Sandbar Breakwater: An Innovative Nature-Based Port Solution. *Water*, *12*(5). https://doi.org/10.3390/w12051446

Van Ledden, M. & Wang, Z. B. (2001). Sand-mud morphodynamics in a former estuary. *IAHR Proceedings of the River, Coastal and Estuarine Morphodynamics Conference, Obihiro, Japan*, 505–514.

Van Rijn, L. C. (1984a). Sediment Transport, Part I: Bed Load Transport. *Journal of Hydraulic Engineering*, *110*(10).

Van Rijn, L. C. (1984b). Sediment Transport, Part II: Suspended Load Transport. *Journal of Hydraulic Engineering*, *110*(11).

Van Rijn, L. C. (1989). *Handbook of sediment transport by currents and waves.* Delft Hydraulics, Delft, The Netherlands.

Van Rijn, L. C. (1993). *Principles of sediment transport in rivers, estuaries and coastal seas.* Aqua Publications, Amsterdam, The Netherlands.

Van Rijn, L. C. (1999). *Principles of coastal morphology.* Aqua Publications, Amsterdam, the Netherlands.

Van Rijn, L. C. (2000). *General view on sand transport by currents and waves.* (tech. rep.) [Report Z2899.30]. Delft Hydraulics, Delft, The Netherlands.

Van Rijn, L. C. (2010). *Coastal erosion control based on the concept of sediment cells.* (tech. rep.). EU Conscience project: Concepts and Science for Coastal Erosion Management.

Van Thiel de Vries, J. S. M. (2009). *Dune Erosion During Storm Surges* (Doctoral dissertation). Delft University of Technology.

Van Veen, J. (1950). Eb-en vloedschaarsystemen in de Nederlandse getijwateren. *Tijdschrift koninklijk Nederlands Aardrijkskundig Genootschap*, *67*(2), 303–352.

Van Veen, J., Van der Spek, A. J. F., Stive, M. J. F. & Zitman, T. (2002). *Ebb and flood channel systems in the Netherlands tidal waters.* VSSD, Delft, The Netherlands.

Van Veen, J., Van der Spek, A. J. F., Stive, M. J. F. & Zitman, T. (2005). Ebb and flood channel systems in the Netherlands tidal waters. *Journal of Coastal Research*, *21*(6).

Vanoni, V. A. (1975). Sedimentation Engineering. ASCE, New York.

Vellinga, P. (1986). *Beach and dune erosion during storm surges.* (Doctoral dissertation). Delft University of Technology.

Vellinga, P. & Leatherman, S. P. (1989). Sea level rise, consequences and policies. *Climate Change*, *15*, 175–189.

Visser, P. (2014). *Short Term Morphological Impact of the Eierlandsedam.* (Master's thesis). Delft University of Technology.

Vollmers, H. J. (1989). The state of art of physical modelling of sediment transport. *Proceedings of the International Symposium on Sediment Transport Modeling, ASCE, New York*, 7–12.

Walton, T. L. & Adams, W. D. (1976). Capacity of inlet outer bars to store sand. *Proceedings of the 15th International Conference on Coastal Engineering, ASCE*, 1919–1937. https://doi.org/10.1061/9780872620834.112

Wang, Z. B., De Ronde, J. G., Van der Spek, A. J. F. & Elias, E. P. L. Responses of the Dutch coastal system to the (semi-) closures of tidal basins. In: *International Conference on Estuaries and Coasts, Sendai, Japan.* 2009.

Wang, Z. B., Louters, T. & de Vriend, H. J. (1995). Morphodynamic modelling of a tidal inlet in the Wadden Sea. *Journal of Marine Geology*, *126*, 289–300.

Wang, Z. B. & Ribberink, J. S. (1986). The validity of a depth-integrated model for suspended sediment transport. *Journal of Hydraulic Research*, *24*(1), 53–67. https://doi.org/10.1080/00221688609499332

Wegener, A. (1912). Die Entstehung der Kontinente. *Geologische Rundschau*, *3*, 276–292.

Wegener, A. (1929). *Die Entstehung der Kontinente und Ozeane. 4^{th} edition (1^{st} edition 1915).* [(rev. eds. 1920,1922,1929; in German, from 1922 also in English)]. Vieweg & Sohn, Braunschweig.

Whitehouse, R. J. S. (1998). *Scour at marine structures: a manual for practical applications.* Thomas Telford, London.

World Coast Conference. Preparing to meet the coastal challenges of the 21st century. In: (Noordwijk, The Netherlands). 1993.

Wright, L. D. & Short, A. D. (1984). Morphodynamic variability of surf zones and beaches: A synthesis. *Marine Geology*, *56*, 93–118. https://doi.org/10.1016/0025-3227(84)90008-2

Zhang, K., Douglas, B. C. & Leatherman, S. P. (2004). Global Warming and Coastal Erosion. *Climate Change*, *64*(41).

Subject index

Credits

Lecture notes

In the 1960s, the topic of coastal engineering at the faculty of Civil Engineering of TU Delft was not really taught as a separate graduate course. It was rather an integral part of the hydraulic engineering chairs and courses of Professors Van Bendegom and Jansen with more focus on rivers than coasts. In 1972 Professor Bijker was appointed the first chair focusing on coastal engineering alone. He asked Associate Professor Massie to compose the first coastal engineering lecture notes, which still serve as inspiration for our current notes. In 1988 Professor D'Angremond succeeded Professor Bijker, who invited both MSc graduate Van de Velden and Associate Professor Van de Graaff to develop two new courses and lecture notes, viz. Introduction to Coastal Engineering (CT4300) and Coastal Morphology and Protection (CT5309) respectively. In 1994, the topic of Coastal Inlets and Tidal Basins was added as a separate third course (CT5303) developed by Professor Stive, newly appointed in a part-time position. With the dedicated assistance of MScs Elias and Hibma, he composed lecture notes by integrating existing material of Professors De Vriend, Dronkersand Wang and Drs Eijsink, Van der Spek and Van Dongeren. Per the academic year 2009-2010, the courses CT4300, CT5309 and CT5303 were replaced with two larger courses Coastal Dynamics I (CIE4305) and Coastal Dynamics II (CIE4309), for which the lecture notes were developed that formed the basis of this book. The development of these two new courses was driven by our wish to update and streamline our coastal engineering curriculum and make room for new developments in coastal and morphodynamic process knowledge and modelling. We wish to acknowledge the efforts of all our colleagues who developed these earlier courses.

Photos

Figure	Source
Fig. 2.5	Matthijs Buijs
Fig. 2.8	Marcel Stive
Fig. 2.11	Marcel Stive
Fig. 2.12	Marcel Stive
Fig. 2.13	Alejandra Gijón Mancheño
Fig. 2.15	Blenda Gomes Rocha
Fig. 2.16	Ascha Simons

Last change date: 2023-01-11

Fig. 2.31 Erik Mosselman
Fig. 2.37 Marcel Stive
Fig. 2.39 Marcel Stive
Fig. 2.40 Marcel Stive
Fig. 3.9 beeldbank.rws.nl, Rijkswaterstaat
Fig. 3.12 Stefanie Ross
Fig. 5.8 Roberto Lo Savio / Shutterstock.com
Fig. 5.68 Marcel Stive
Fig. 5.69 Richard P Long / Shutterstock.com
Fig. 6.18 beeldbank.rws.nl, Rijkswaterstaat
Fig. 7.9 Jurriaan Brobbel / Rijkswaterstaat
Fig. 8.20 Photo by Carolina Piccoli / map by OpenStreetMap contributors
Fig. 8.21 Leonid Andronov / Shutterstock.com
Fig. 8.27 U.S. Geological Survey, Department of the Interior / USGS
Fig. 9.6 NC OneMap Geospatial Portal (2020)
Fig. 9.14a beeldbank.rws.nl, Rijkswaterstaat
Fig. 9.14b Rens Jacobs / beeldbank.rws.nl, Rijkswaterstaat
Fig. 9.14c Rens Jacobs / beeldbank.rws.nl, Rijkswaterstaat
Fig. 9.14d Joop van Houdt / beeldbank.rws.nl, Rijkswaterstaat
Fig. 9.19 Ehlers (1988)
Fig. 10.6 beeldbank.rws.nl, Rijkswaterstaat
Fig. 10.8 Institut Cartogràfic i Geològic de Catalunya (ICGC)
Fig. 10.9 Joop van Houdt / beeldbank.rws.nl, Rijkswaterstaat
Fig. 10.10 Courtesy of CDR International B.V., from Van der Spek et al. (2020)
Fig. 10.12 Joop van Houdt / beeldbank.rws.nl, Rijkswaterstaat
Fig. 10.13 Rens Jacobs / beeldbank.rws.nl, Rijkswaterstaat
Fig. 10.14 Ad Reniers
Fig. 10.17 UK Environmental Agency under an Open Government Licence
Fig. 10.18 U.S. Geological Survey, Department of the Interior / USGS
Fig. 10.20 Joop van Houdt / beeldbank.rws.nl, Rijkswaterstaat
Fig. 10.21 Marcel Stive
Fig. 10.22a Wayland Smith / Shutterstock.com
Fig. 10.22b Carol Blaker / Shutterstock.com
Fig. 10.26a Evelyn Simak / Wikipedia Commons
Fig. 10.26b Evelyn Simak / Wikipedia Commons
Fig. 10.28 beeldbank.rws.nl, Rijkswaterstaat
Fig. 10.29 beeldbank.rws.nl, Rijkswaterstaat
Fig. 10.30 Ceinturion Wikipedia Commons
Fig. 10.32 Joop van Houdt / beeldbank.rws.nl, Rijkswaterstaat
Fig. 10.33 beeldbank.rws.nl, Rijkswaterstaat
Fig. 10.40 Ni_Giri / Shutterstock.com
Fig. 10.41 OrtoPNOA 2019 scne.es
Fig. 10.42a Joop van Houdt / beeldbank.rws.nl, Rijkswaterstaat

Fig. 10.42b Joop van Houdt / Rijkswaterstaat
Fig. 10.42c Joop van Houdt / Rijkswaterstaat

Errata and improvements

Version history

This section provides a record of changes made to this textbook since its initial publication as an open textbook (January 2021). If the edits are minor, the version number increases by 0.1. If the changes involve substantial updates, the edition number increases to the next whole number. The e-book always reflects the most recent version and is available for online use and free download from the TU Delft Open Textbook repository at textbooks.open.tudelft.nl.

Version	Date	Change
1.0	January, 2021	Original
1.1	January, 2022	Corrected misspellings, typographical errors and punctuation errors in text Added missing symbols in text Corrected misspellings and other minor errors in figures Corrected typographical errors in equations Added some brief clarifications Updated or corrected a few references Added 'Errata and improvements' on page 583
1.2	January, 2023	Corrected misspellings, typographical errors and punctuation errors in text Updated Figs. 1.14, 2.18, 2.19 and 3.8 Corrected typographical errors in equations Added some brief clarifications

List of changes

When the version number increases by 0.1, students (and other readers) can continue to use their softback of the previous version, as long as they copy the most important changes in their hardcopy. To this end, an e-book with markup, serving as an overview of errata and improvements, is available via the TU Delft Open Textbook repository by selecting *Errata and improvements*. These corrections are considered important for understanding the material. Other, less crucial changes are not tracked.

Errata and improvements that are suggested, but not yet part of a new version, are recorded on online errata and improvements lists, respectively, to which we invite our readers to contribute. In order to suggest a correction or improvement, please fill out the suggestion form. These lists as well as the suggestion form are also accessible by selecting *Errata and improvements* on the TU Delft Open Textbook repository.